molecules

Special Issue Reprint

Nanostructured Materials

Synthesis, Functionalization and Applications in Biomedicine—2nd Edition

Edited by
Ying-Jie Zhu and Heng Li

mdpi.com/journal/molecules

MDPI

Nanostructured Materials: Synthesis, Functionalization and Applications in Biomedicine—2nd Edition

Nanostructured Materials: Synthesis, Functionalization and Applications in Biomedicine—2nd Edition

Guest Editors

Ying-Jie Zhu
Heng Li

Assisted by

Hanping Yu

MDPI

Basel • Beijing • Wuhan • Barcelona • Belgrade • Novi Sad • Cluj • Manchester

Guest Editors

Ying-Jie Zhu
Biomaterials and Tissue Engineering Research Center
Shanghai Institute of Ceramics, Chinese Academy of Sciences
Shanghai
China

Heng Li
Biomaterials and Tissue Engineering Research Center
Shanghai Institute of Ceramics, Chinese Academy of Sciences
Shanghai
China

Editorial Office
MDPI AG
Grosspeteranlage 5
4052 Basel, Switzerland

This is a reprint of the Special Issue, published open access by the journal *Molecules* (ISSN 1420-3049), freely accessible at: https://www.mdpi.com/journal/molecules/special_issues/4LDY02692Q.

For citation purposes, cite each article independently as indicated on the article page online and as indicated below:

Lastname, A.A.; Lastname, B.B. Article Title. *Journal Name* **Year**, *Volume Number*, Page Range.

ISBN 978-3-7258-9249-5 (Hbk)
ISBN 978-3-7258-9250-1 (PDF)
https://doi.org/10.3390/books978-3-7258-9250-1

© 2026 by the authors. Articles in this reprint are Open Access and distributed under the Creative Commons Attribution (CC BY) license. The reprint as a whole is distributed by MDPI under the terms and conditions of the Creative Commons Attribution-NonCommercial-NoDerivs (CC BY-NC-ND) license (https://creativecommons.org/licenses/by-nc-nd/4.0/).

Contents

About the Editors . . . . . **vii**

Anish Prasad Lohani, Mohamed Elosta, Mahmoud Maksoud and Nimer Murshid
Functionalized Carbon Nanotubes: Emerging Nanomaterials for Enhanced Cancer Diagnosis and Imaging
Reprinted from: *Molecules* **2025**, *30*, 2364, https://doi.org/10.3390/molecules30112364 . . . . . **1**

Subin Antony Jose, Benjamin Crutchfield, Mario Caballero, Eadrian Carreon, Ian Davis and Pradeep L. Menezes
Nanoparticles for Drug Delivery: Design, Mechanisms, and Clinical Translation
Reprinted from: *Molecules* **2026**, *31*, 3121, https://doi.org/10.3390/molecules31173121 . . . . . **35**

Adriana-Gabriela Schiopu, Elena Andreea Vijan, Ecaterina Magdalena Modan, Sorin Georgian Moga, Denis Aurelian Negrea, Daniela Istrate, et al.
Ovalbumin-Mediated Biogenic Synthesis of ZnO and MgO Nanostructures: A Path Toward Green Nanotechnology
Reprinted from: *Molecules* **2025**, *30*, 1164, https://doi.org/10.3390/molecules30051164 . . . . . **64**

Thúlio Wliandon Lemos Barbosa, Laurent Lemaire, Isabelle Verdu, Larissa Santos, Natália Galvão de Freitas, Mariana Picchi Salto and Leila Aparecida Chiavacci
Bimodal Poly(lactic-co-glycolic acid) Nanocarrier with Zinc Oxide and Iron Oxide for Fluorescence and Magnetic Resonance Imaging
Reprinted from: *Molecules* **2025**, *30*, 1818, https://doi.org/10.3390/molecules30081818 . . . . . **83**

Liang Chen, Qiao Wu, Chen Yang, Xiulan Xin, Zhaochu Xu, Shuai Luo and Hao Liang
Construction and Anti-Cancer Activity of a Self-Assembly Composite Nano-Delivery System Loaded with Curcumin
Reprinted from: *Molecules* **2025**, *30*, 2940, https://doi.org/10.3390/molecules30142940 . . . . . **101**

Huan Yue, Tirusew Tegafaw, Shuwen Liu, Ying Liu, Dejun Zhao, Endale Mulugeta, et al.
Physicochemical and Multimodal Imaging Properties of Core–Shell Ln_2O_3@Carbon Nanoparticles (Ln = Tb and Ho)
Reprinted from: *Molecules* **2025**, *30*, 4064, https://doi.org/10.3390/molecules30204064 . . . . . **116**

Dan Adrian Vasile, Ludmila Motelica, Luiza-Andreea Mîrț, Gabriel Vasilievici, Oana-Maria Memecică, Ovidiu Cristian Oprea, et al.
Antimicrobial Functionalized Mesoporous Silica FDU-12 Loaded with Bacitracin
Reprinted from: *Molecules* **2026**, *31*, 340, https://doi.org/10.3390/molecules31020340 . . . . . **131**

Hayrettin Eroglu, Arif Kürsad Ayan and Ayse Yenilmez
Biodistribution of Tc-99m-Labeled Solid Lipid Nanoparticles and Evaluation of Their Possibility as a Radiopharmaceutical
Reprinted from: *Molecules* **2026**, *31*, 654, https://doi.org/10.3390/molecules31040654 . . . . . **162**

Javiera Carrasco-Rojas, Javiera Solas-Soto, Rubén Veas-Albornoz, Carlos F. Lagos, Mario J. Simirgiotis, Francisco Arriagada and Andrea C. Ortiz
Nanostructured Lipid Carriers as Physicochemical Modulators of Complex Natural Extracts: Release Behavior and Bile-Induced Remodeling in Biorelevant Media
Reprinted from: *Molecules* **2026**, *31*, 1028, https://doi.org/10.3390/molecules31061028 . . . . . **175**

Egemen Uzel, Meltem Ezgi Durgun, Neriman Aydilek, Mayram Hacıoğlu, Sevgi Güngör and Yıldız Özsoy
A Dual-Drug Nanocarrier Strategy for Ocular Fungal Infections: Micelles Embedded in Electrospun Nanofibers
Reprinted from: *Molecules* **2026**, *31*, 1235, https://doi.org/10.3390/molecules31081235 . . . . . **195**

About the Editors

Ying-Jie Zhu

Ying-Jie Zhu received his Master's degree and Ph.D. from the University of Science and Technology of China in 1992 and 1994, respectively. He served as an assistant professor and associate professor at the University of Science and Technology of China from 1994 to 1997. From 1997 to 1998, he was a visiting scholar in the University of Western Ontario, Canada. From 1998 to 1999, he was an Alexander von Humboldt Research Fellow at the Fritz-Haber Institute of the Max Planck Society, Germany. He subsequently worked as a postdoctoral fellow at the University of Utah and the University of Delaware, USA, from 1999 to 2002. In 2002, he was recruited by the Chinese Academy of Sciences (CAS) through the Program for Recruiting Overseas Outstanding Talents and began his tenure as a full professor and research group leader at the Shanghai Institute of Ceramics, CAS. He has received many honors, including being selected as "Scientific Chinese Person of the Year 2006", recognition as an Outstanding Leader of the Shanghai Subject Chief Scientist Program in 2007, being awarded the ZhuLiYueHua Excellent Teacher Prize of the CAS in 2008, and receiving the First-Class Prize of Natural Sciences from the Shanghai Municipality in 2009 (shared with colleagues). He has published more than 400 peer-reviewed journal papers, 1 monograph, and 7 book chapters, with his research being cited approximately 25,000 times, including many ESI highly cited papers. From 2014 to 2025, he was listed 12 times among Elsevier's Annual List of Most Cited Chinese Researchers. He also holds 72 authorized patents. His research interests include nanostructured materials and biomaterials.

Heng Li

Heng Li received his Ph.D. from the Shanghai Institute of Ceramics, Chinese Academy of Sciences, in 2019, and he subsequently worked at the Center of Super-Diamond and Advanced Films, the City University of Hong Kong. He is currently an associate professor and group leader at the Shanghai Institute of Ceramics, CAS. His research interest focuses on high-safety and biocompatible battery materials.

molecules

MDPI

Review

Functionalized Carbon Nanotubes: Emerging Nanomaterials for Enhanced Cancer Diagnosis and Imaging

Anish Prasad Lohani †, Mohamed Elosta †, Mahmoud Maksoud and Nimer Murshid *

Biological Sciences, Carnegie Mellon University in Qatar, Educational City, Doha P.O. Box 24866, Qatar
* Correspondence: nmurshid@andrew.cmu.edu
† These authors contributed equally to this work.

Abstract: Cancer remains a leading global cause of mortality, highlighting the critical need for effective early diagnosis. Despite advancements in treatment, early detection and imaging continue to pose significant challenges. Functionalized carbon nanotubes (CNTs) have emerged as promising nanomaterials due to their unique structural properties and versatile functionalization strategies. This review explores the role of both covalent (e.g., fluorination, hydrogenation, cycloadditions, aryldiazonium salt reduction, organometallic ion attachment, carboxylation, amidation, esterification, and metallic nanoparticle attachments) and non-covalent functionalization methods (e.g., surfactant coating, polymer wrapping, biomolecule attachment, and polymer encapsulation) in enhancing CNT biocompatibility and diagnostic efficiency. Functionalized CNTs are extensively applied in cancer detection through highly sensitive biosensors, including electrochemical, optical, and field-effect transistor-based systems, capable of detecting various cancer biomarkers with exceptional sensitivity. Additionally, they offer significant advantages in cancer imaging modalities such as fluorescence imaging, magnetic resonance imaging (MRI), computed tomography (CT), and ultrasound imaging, improving contrast, resolution, and specificity. This review also discusses the challenges and future directions in the development of CNT-based diagnostic platforms, emphasizing the need for continued research to advance their clinical translation and integration into routine cancer diagnostics.

Keywords: carbon nanotubes (CNTs); cancer; diagnosis; biosensors; functionalization

1. Introduction

Cancer is a leading cause of mortality and disability worldwide, characterized by unregulated cell proliferation that can spread and destroy normal tissues [1]. The World Health Organization (WHO) recognizes cancer as a major public health concern. The disease is a significant focus of healthcare efforts [2–4].

Research in the field of cancer is crucial, with efforts focused on improved diagnosis [5–7], early detection [8], and development of effective therapies [5,9]. Early detection is essential to improving patient outcomes [8,10–13]. The development of targeted therapies is another critical area of research that seeks to minimize the side effects of cancer treatment and increase recovery rates [14–17].

Various approaches to cancer treatment are being explored, and nanotechnology has emerged as a promising field for developing novel diagnostic and therapeutic strategies [8,18,19]. Nanomaterials, including carbon nanotubes (CNTs), are being investigated for their potential in cancer therapy. CNTs have arisen as a significant area of study, especially for their roles in both diagnosis and therapy [20–22].

CNTs offer several advantages in biomedical applications [23,24]. They have a high surface area, which allows them to carry a large number of therapeutic molecules [21,22,25–27]. Additionally, CNTs can be functionalized to enhance their biocompatibility, target cancer cells, and deliver drugs directly to tumor sites [28–30]. Furthermore, CNTs' unique properties make them useful as biosensors and in bioimaging for early cancer detection [31–34].

CNTs have a unique structure, with diameters in the nanometer range and lengths that can reach micrometers. They can be single-walled (SWCNTs) or multi-walled (MWCNTs), which affects their properties. The carbon atoms in CNTs are arranged in a hexagonal lattice, giving CNTs their unique electronic, thermal, and mechanical characteristics. These properties are influenced by the type of CNT, whether single-walled or multi-walled [20].

The structural functionality of CNTs allows for diverse applications in biomedicine, including drug delivery, tissue engineering, and biosensing. Their ability to be functionalized provides further opportunities for modifying their characteristics to suit various applications [35,36].

This review explores recent progress and advancements in the application of functionalized carbon nanotubes (fCNTs) for cancer diagnosis. It begins by discussing the functionalization strategies of CNTs, focusing on both covalent and noncovalent modifications. The review then examines various approaches for utilizing CNTs in cancer diagnosis, particularly in biosensing and bioimaging, before concluding with insights on future directions.

2. Cancer and Carbon Nanotubes: Overview

2.1. Cancer

Cancer is one of the most dangerous and concerning health problems globally because of its complexity and high mortality rates. Cancer is characterized by uncontrolled cell growth, the potential to spread to other parts of the body, and resistance to treatment. It can often bypass the immune system, remain undetected until it reaches advanced stages, and return after therapy, making treatment more difficult [2].

Another concerning aspect of cancer is its ongoing global burden, which continues to grow at an alarming rate, with both the number of incidents and deaths increasing year by year [2]. In 2022, there were approximately 20 million new cases and nearly 9.74 million cancer-related deaths. Trachea, bronchus, and lung cancer had the highest incidence, accounting for about 12% of global cancer cases, followed by breast cancer at 11%, prostate cancer at 7%, colon cancer at 6%, and stomach cancer at 5% (Figure 1a) [3]. The numbers of incidents and deaths are expected to increase over time, with new cancer cases predicted to hit 35.3 million and about 18.5 million cancer-related deaths by 2050 (Figure 1b) [4]. This escalating burden is expected to strain healthcare systems, deplete critical resources, and impose significant pressure on global economies. As the demand for medical services, research, and treatment rises, it could lead to potential shortages in care and increased inequality in access to treatment [2–4].

A study conducted by a group of researchers [37] estimated that the economic cost of cancer from 2020 to 2050 is projected to reach an alarming $25.2 trillion. This estimate includes not only the direct expenses related to cancer treatments but also the broader economic impacts, such as productivity losses and changes in savings and investment patterns resulting from the costs of cancer care.

As cancer rates rise globally, the long-term economic impact will be significant, highlighting the urgent need for early diagnosis and treatment to improve survival, reduce morbidity, lower treatment costs, and decrease the overall economic burden.

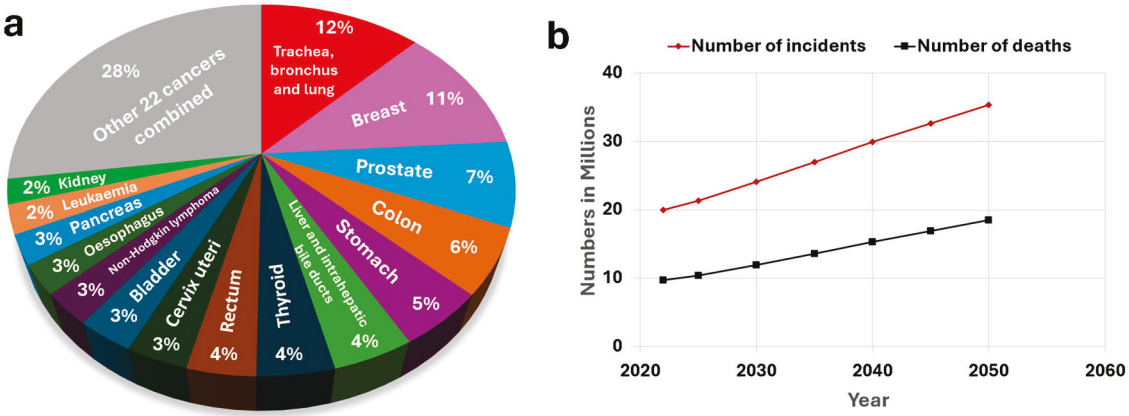

Figure 1. (**a**): Pie chart representation of total global cancer incidences in 2022. (**b**) Number of cancer incidents and cancer-related deaths expected between 2022 and 2050. Data gathered from Refs [2,3].

2.2. Carbon Nanotubes

Due to their exceptional structure (cylindrical hollow nanostructures made from rolled-up sheets of graphene), CNTs exhibit outstanding mechanical properties, including high tensile strength [38], optical properties [39], electronic properties [40], thermal properties [41], electric conductivity [42], and high surface area [43]. These unique characteristics make CNTs ideal for a wide range of applications, including aerospace, composite materials, advanced nanoelectronics, optical sensors, energy storage in batteries and supercapacitors, quantum computing, catalysis, adsorption, and biomedical fields such as drug delivery, medical imaging, and sensing [35].

As shown in Figure 2, CNTs can be classified into three categories: single-walled nanotubes (SWNTs), double-walled nanotubes (DWNTs), and multi-walled nanotubes (MWNTs). SWNTs consist of a single sheet of graphene rolled into a cylindrical structure. In contrast, DWNTs and MWNTs are composed of two and multiple concentric layers of graphene, respectively, wrapped around one another like a "Russian doll" [44].

The way the graphene sheet is rolled (the chiral vector or orientation) determines the arrangement of the hexagonal graphene network and leads to three types of CNTs: armchair, zigzag, and chiral, each with a distinct geometric structure. The unique structure of each type of nanotube contributes to their distinct mechanical, electrical, and thermal properties. For example, the armchair structure is metallic, whereas zigzag and chiral structures can be metallic or semiconducting [45].

What makes CNTs particularly remarkable is their ability to have their properties tailored, modified, or enhanced through functionalization. As illustrated in Figure 2, functionalization can be categorized into two types: covalent and non-covalent [35]. Covalent functionalization includes methods such as fluorination, carboxylation, 1,3-dipolar cycloadditions, and the attachment of metallic nanoparticles. Non-covalent functionalization, on the other hand, involves techniques like polymer wrapping, polymer encapsulation, protein attachment, and antibody attachment. These modifications can significantly improve the electronic properties of CNTs, enhance their solubility, improve imaging contrast, facilitate targeted therapy and controlled drug release, as well as increase biocompatibility and biosensor performance. Types of CNTs, their functionality, and biomedical applications are discussed and summarized in the following sections.

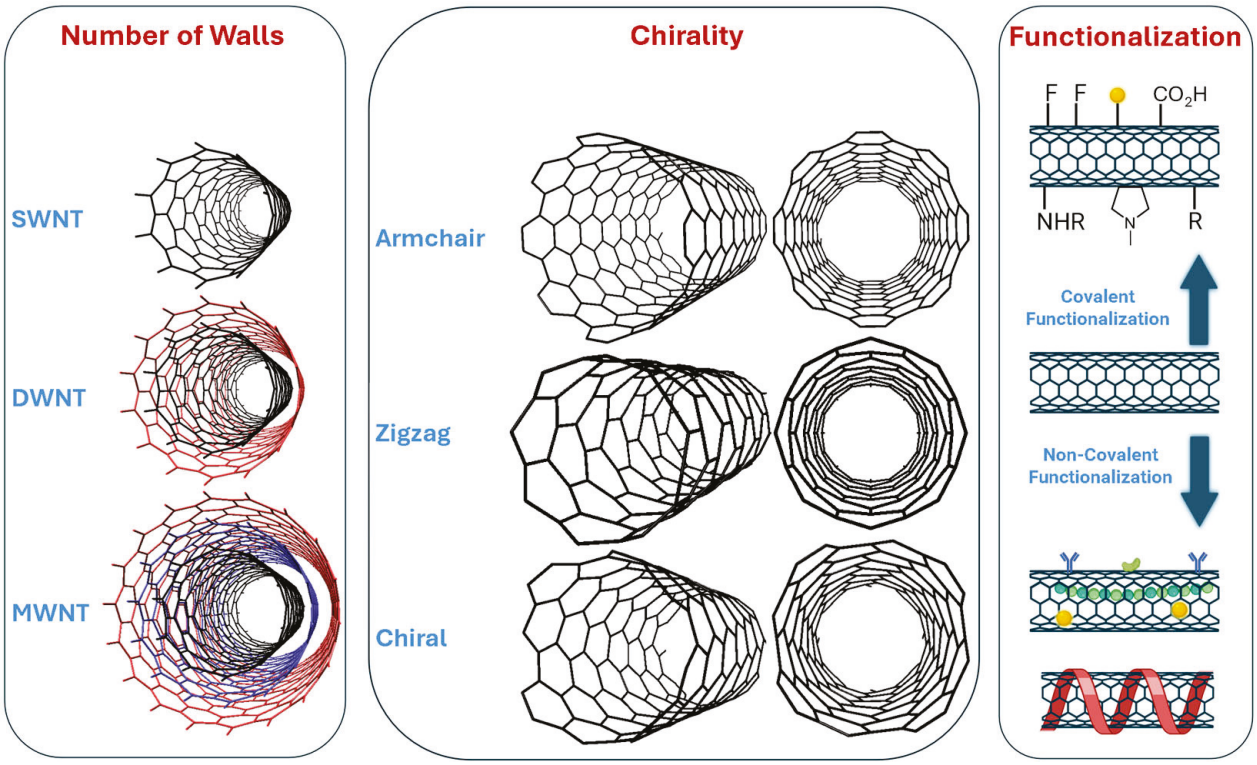

Figure 2. Classification of carbon nanotubes based on number of walls, chirality, and type of functionalization.

3. Functionalization Strategies for CNTs

Section 3 focuses on the diverse functionalization strategies for CNTs, differentiating between covalent and noncovalent modification methods. These critical processes are used to tailor CNT properties, enhancing their performance for specific applications, including improvements in electronic properties, solubility, imaging, and drug delivery. These strategies will be discussed in the following subsections, with their details and comparison summarized in Figure 3.

Functionalized CNTs have emerged as a pivotal tool in the realm of cancer diagnostics and treatment, showcasing their versatility across various cancer types. Recent studies have highlighted their application in targeted drug delivery systems, significantly enhancing the efficacy of chemotherapeutic agents. For instance, dual-targeting multi-walled carbon nanotubes have been utilized to improve the delivery of neratinib in breast cancer, demonstrating superior cytotoxic effects compared to conventional methods [46]. Gelatin-functionalized CNTs loaded with cisplatin have shown promising results in anti-cancer therapy, indicating that functionalization is crucial for maximizing therapeutic outcomes [47]. In the context of photothermal therapy, hyaluronic acid-modified CNTs have been effective in promoting apoptosis in nasopharyngeal carcinoma cells, showcasing their potential in localized cancer treatment [48]. The integration of CNTs in combination therapies, such as those involving radiation sensitizers, has been explored to enhance the effectiveness of radiotherapy in breast cancer [49]. Overall, the application of faunctionalized carbon nanotubes spans various cancer types, including breast cancer and nasopharyngeal carcinoma, underscoring their role as a transformative approach in cancer diagnostics and treatment [48,49].

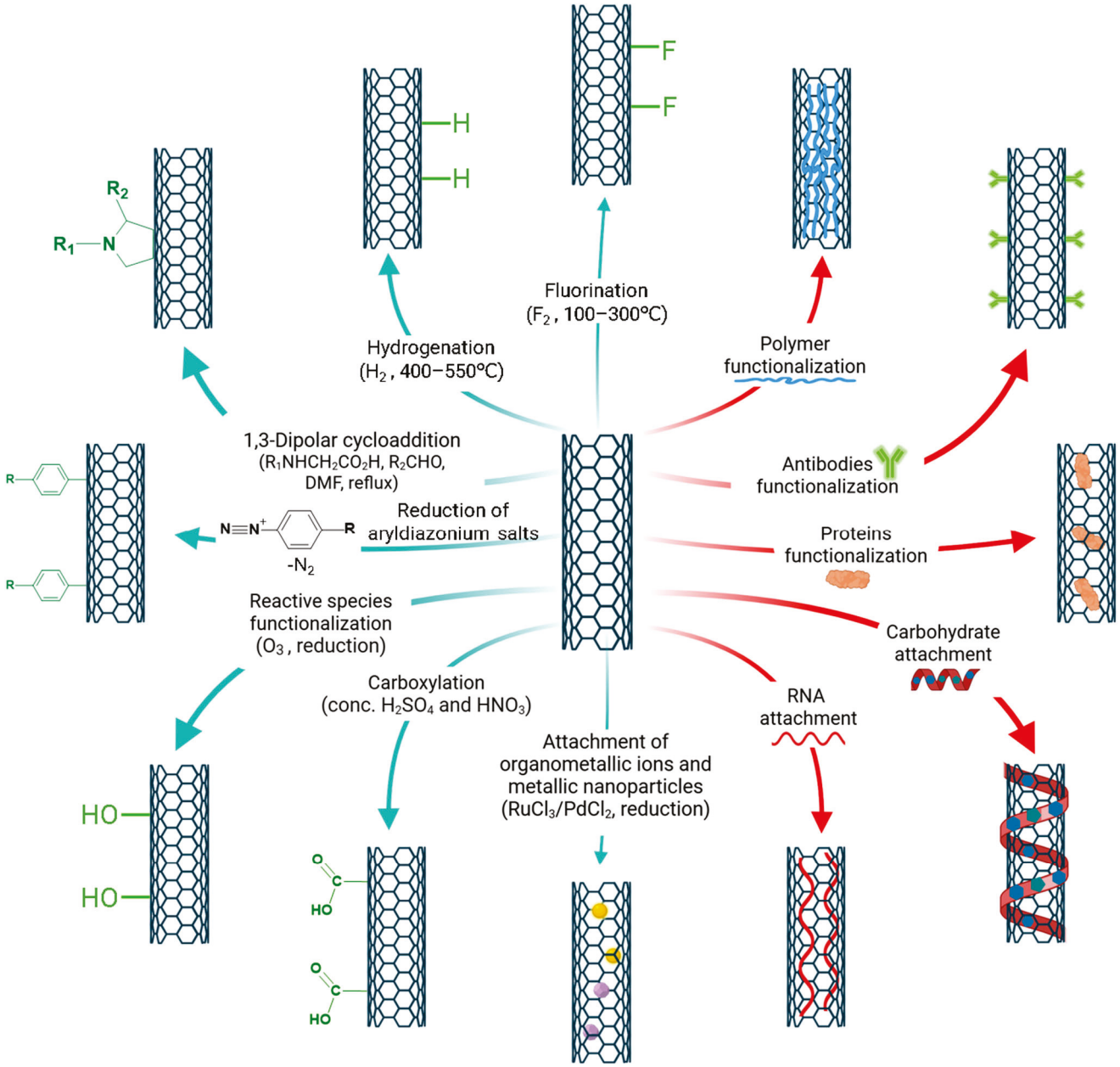

Figure 3. Schematic representation of CNT functionalization strategies: covalent (blue arrows) and noncovalent (red arrows) approaches. Created with BioRender.com.

3.1. Covalent Functionalization

The covalent functionalization strategies of CNTs discussed in this subsection are summarized in Figure 3 and indicated by the green arrows.

3.1.1. Fluorination

The fluorination of CNTs has gathered significant attention due to its potential to modify the electronic and chemical properties of these nanomaterials. Fluorination typically introduces C–F bonds, which can alter the electronic structure and enhance the reactivity of CNTs. For instance, it has been observed that fluorinated SWCNTs (fSWCNTs) maintain their structural integrity while exhibiting dispersed fluorine patterns, characterized by a low fluorination degree and a reduced concentration of edge C–F groups [50]. This unique behavior is attributed to the high crystallinity of the carbon network, which allows for selective fluorination without compromising the overall tube structure. Furthermore, the

introduction of fluorine can significantly increase the solubility of CNTs in polar organic solvents, enhancing their compatibility with various chemical environments due to dipole interactions [51].

Moreover, the fluorination process can lead to the formation of both covalent and semi-ionic C–F bonds, which are crucial for applications in energy storage and catalysis. For example, studies have shown that fluorination can enhance the electrochemical properties of CNTs, making them suitable for use in lithium batteries and as electrocatalysts [52,53]. The presence of fluorine modifies the electronic properties and influences the hydrophobicity of the CNT surface, which can be beneficial in applications requiring water stability and proton conductivity [54]. Additionally, the interaction between fluorinated CNTs and other materials, such as fluorosumanenes, has been explored to further enhance carrier doping and improve the performance of electronic devices [55]. Overall, the fluorination of carbon nanotubes represents a promising avenue for advancing the functionality of these versatile nanomaterials across various applications. Wang et al. [56] added silver nanoparticles (AgNps) to construct hydro-soluble fluorinated carbon fiber oxide (FCO)/Ag composite, which proved to be a highly effective targeted nanocarrier for photothermal therapy and also demonstrated antibacterial activity. FCO/Ag acts as a fluorescence quencher for doxorubicin, enabling visual monitoring of drug adsorption processes through a "turn-off" fluorescence mechanism. Fluorinated graphene and CNTs have been utilized in a surface plasmon resonance (SPR) sensor proposed by Uniyal et al. for the detection of SARS-CoV-2 viral particles [57].

3.1.2. Hydrogenation

The hydrogenation of CNTs is a significant area of research due to its potential to enhance the chemical reactivity and electronic properties of these nanomaterials. Hydrogenation can introduce hydrogen atoms into the CNT structure, leading to the formation of C–H bonds, which can modify the electronic band structure and improve the material's catalytic properties. For instance, studies have shown that hydrogenation can enhance the adsorption capacity of CNTs for various gases, including hydrogen itself, thereby making them suitable candidates for applications in hydrogen storage and fuel cells [58]. Additionally, the hydrogenation process can facilitate the growth of nitrogen-doped carbon nanotubes (NCNTs) on substrates like foamed nickel, which can further improve their performance in catalytic reactions. Research indicates that the curvature and electronic properties of CNTs can be optimized through controlled hydrogenation, leading to improved catalytic performance [59]. The interaction between hydrogenated CNTs and metal nanoparticles, such as platinum, has also been explored, revealing that hydrogenation can enhance the bonding strength between the metal and the CNT, thus improving the overall efficiency of catalytic processes [60]. The synthesis of CNTs through hydrogen-rich environments, such as during pyrolysis processes, has been shown to yield high-quality CNTs with desirable properties for various applications, including energy conversion and storage [61].

3.1.3. 1,3-Dipolar Cycloadditions

The 1,3-dipolar cycloaddition (1,3-DC) of carbon nanotubes (CNTs) has emerged as a promising strategy for functionalizing these nanomaterials, enhancing their chemical reactivity, and expanding their application potential. This reaction typically involves the interaction of a dipolar species, such as azomethine ylides, with a suitable dipolarophile, leading to the formation of five-membered heterocycles. Recent studies have demonstrated that encapsulating 1,3-dipolar cycloaddition reactions within CNTs can significantly influence the regioselectivity and stereochemistry of the products, offering a unique environment

that can stabilize transition states and intermediates [62]. Theoretical investigations have provided insights into the mechanisms underlying these reactions, revealing that the confinement within CNTs can enhance the reactivity of the dipoles and facilitate the formation of desired cyclic adducts [62]. Furthermore, the use of metal-catalyzed approaches, such as copper-catalyzed azide–alkyne cycloaddition (CuAAC), has been shown to be particularly effective in promoting 1,3-DC reactions [63]. The involvement of CNTs has led to the synthesis of functionalized derivatives that exhibit improved properties for applications in drug delivery and materials science.

Recent research indicates that the functionalization of MWCNTs using the 1,3-dipolar cycloaddition approach with azomethine ylides leads to the development of hybrid materials with improved photodynamic and photothermal properties, making them suitable for treating various cancers, including melanoma and breast cancer [64]. The regioselectivity of these cycloadditions, modulated by the confinement effects within the nanotubes, allows for the precise synthesis of triazole derivatives, which can be utilized as drug delivery vehicles or imaging agents in cancer diagnostics [62,65]. The incorporation of therapeutic agents into these functionalized CNTs has shown promise in enhancing the efficacy of chemotherapy, particularly in colorectal cancer, where targeted delivery can significantly reduce systemic toxicity [19,66]. The versatility of 1,3-dipolar cycloaddition in modifying CNTs underscores its potential in advancing cancer treatment modalities, including targeted therapies and diagnostics across a spectrum of cancer types, such as skin cancer and nasopharyngeal carcinoma [67,68].

3.1.4. Reduction of Aryldiazonium Salts

The reduction of aryldiazonium salts enables the generation of aryl radicals that can participate in various coupling reactions. Aryldiazonium salts, typically formed from aniline derivatives, can be reduced using a variety of methods, including electrochemical reduction and chemical reduction with reducing agents such as zinc or sodium sulfite. Recent advancements have highlighted the utility of transition metal catalysts in facilitating these reductions, which can enhance the selectivity and efficiency of the process [69]. For example, studies have shown that the use of palladium or copper catalysts can significantly improve the yields of aryl radicals from aryldiazonium salts, allowing for more efficient coupling with nucleophiles or other electrophiles [70]. The reduction of aryldiazonium salts can also be performed under mild conditions, making it a versatile method for synthesizing functionalized aromatic compounds]. The generated aryl radicals can then be utilized in various reactions, including the formation of C–C and C–N bonds, thereby expanding the synthetic utility of aryldiazonium salts in the development of complex organic molecules [71].

Recent studies demonstrate that the electrochemical reduction of aryldiazonium salts can effectively modify the surface of CNTs, enabling the attachment of various biomolecules (nucleic acids, proteins, carbohydrates, etc.), thereby enhancing their targeting capabilities for cancer cells. For instance, functionalized CNTs have been utilized for the targeted delivery of chemotherapeutic agents in breast cancer, improving drug efficacy while minimizing side effects [72]. Additionally, the incorporation of these modified CNTs in biosensors has facilitated the detection of cancer biomarkers, allowing for early diagnosis of cancers such as colorectal and gastric cancer [24,73]. The ability to create controlled monolayer films through the reduction of diazonium salts further enhances the specificity and sensitivity of these biosensors, making them invaluable in the clinical setting [74]. The functionalization of CNTs via aryldiazonium salt reduction not only aids in the targeted treatment of cancers, including breast and colorectal cancer, but also plays an essential role in the development of advanced diagnostic tools that can detect cancer at earlier stages [24].

3.1.5. Reactive Species Functionalization

This process often includes adding functional groups onto the CNT surface through various chemical reactions, including the use of aryldiazonium salts, which can covalently bond to the CNTs, thereby modifying their electronic and chemical properties [75]. The functionalization can also be achieved through hydrogenation, where molecular hydrogen reacts with the CNTs, leading to the formation of stable C–H bonds that can further facilitate additional chemical modifications [76,77]. The incorporation of transition metals or metal oxides into CNTs has been shown to improve their catalytic properties, particularly in hydrogen storage applications, where the presence of these metals enhances the adsorption capacity of hydrogen [78].

The use of reactive oxygen species generated from CNTs has been investigated for their ability to induce oxidative stress in biological systems, which can be harnessed for therapeutic applications [79]. The functionalization of CNTs with various reactive species not only improves their compatibility with different solvents and matrices but also enhances their performance in potential applications such as sensors, drug delivery systems, and catalysis [80].

3.1.6. Organometallic Ions

Organometallic ions play a crucial role in various chemical processes, particularly in catalysis and functionalization reactions involving carbon nanostructures such as CNTs and graphene. These ions can facilitate the formation of covalent bonds between organometallic species and carbon nanostructures, enhancing their reactivity and enabling the development of novel materials with tailored properties. For instance, the functionalization of CNTs through 1,3-dipolar cycloaddition reactions has been shown to effectively incorporate organometallic ions, leading to improved electronic and catalytic properties [81].

Moreover, the use of organometallic ions in conjunction with transition metals has been explored to enhance the selectivity and efficiency of cycloaddition reactions involving CNTs. Studies have demonstrated that the presence of these ions can stabilize transition states and intermediates, thereby promoting desired reaction pathways and improving product yields [82]. The confinement of reactive species within the unique geometry of CNTs can lead to distinct regioselectivity in functionalization reactions, further highlighting the importance of organometallic ions in these processes [65].

Recent studies have demonstrated that the functionalization of CNTs with organometallic ions, such as ruthenium and palladium, enhances their efficacy in drug delivery systems, particularly for breast and prostate cancers [83,84]. These organometallic-functionalized CNTs can effectively carry chemotherapeutic agents, allowing for controlled release and improved targeting of cancer cells, thus minimizing side effects associated with traditional chemotherapy [19]. Furthermore, the integration of organometallic ions into CNTs has been explored for their role in enhancing imaging techniques, such as magnetic resonance imaging (MRI) and computed tomography (CT), facilitating the early detection of cancers like colorectal and lung cancer [19,85]. The ability of these modified CNTs to act as biosensors for detecting cancer biomarkers also highlights their dual role in both diagnostics and treatment, making them invaluable in the fight against various cancer types [19,86].

3.1.7. Carboxylation and Further Derivation

Recent findings indicate that carboxylation can be effectively achieved using aryldiazonium salts as reactive intermediates, facilitating the introduction of carboxylic acid functional groups onto the CNT surface [87]. The functionalization of CNTs through carboxylation can lead to the formation of various derivatives that are useful in drug delivery systems, sensors, and catalysis. The introduction of carboxyl groups can also facilitate

subsequent reactions, such as amidation or esterification, thereby enabling the synthesis of more complex organic structures [88]. The ability to control the degree of carboxylation and the nature of the substituents on the CNTs allows for the fine-tuning of their properties, making them suitable for specific applications in materials science and nanotechnology [89].

Recent studies have demonstrated that carboxylated MWCNTs (c-MWCNTs) can effectively serve as carriers for targeted drug delivery systems, significantly improving the therapeutic efficacy of chemotherapeutic agents in various cancers, including breast and colorectal cancer [46]. For instance, c-MWCNTs have proven to boost the cytotoxic effects of cisplatin against breast cancer cells, facilitating preferential drug delivery to cancerous tissues [46]. The functionalization of CNTs with carboxyl groups has been utilized in the development of electrochemical immunosensors for detecting cancer biomarkers, such as nuclear matrix protein 22, which is relevant for bladder cancer diagnostics [90]. The ability of SWCNTs to form stable dispersions in aqueous solutions also enhances their application in biosensing technologies, allowing for the early detection of cancers like gastric and lung cancer [75]. Studies have been done on utilizing carboxylated MWCNTs (MWCNTs-COOH) as a drug delivery system for enhanced ovarian cancer treatment [91]. A system was designed where MWCNTs-COOH was coupled with folic acid to target ovarian tumors and loaded with curcumin (CUR). The carboxyl functional group (-COOH) of MWCNTs-COOH facilitates conjugation with targeting ligands like folic acid, improves drug loading, and enhances cellular absorption. This approach aims to overcome the drawbacks of conventional chemotherapy by enabling more specific and effective drug delivery [91]. The carboxylation of CNTs not only improves their utility in drug delivery systems but also plays a crucial role in advancing diagnostic tools for various cancer types, thereby contributing to more effective cancer management strategies.

Further functionalization of carbonylated CNTs has also been explored, including amidation and esterification of carboxylic groups, which are essential transformations in organic synthesis. Recent advancements in these reactions have focused on improving efficiency and selectivity through innovative catalytic and electrochemical systems [92,93]. Recent research indicates that the functionalization of CNTs through amidation can improve their biocompatibility and facilitate the targeted delivery of chemotherapeutic agents, particularly in breast and colorectal cancers [47,66]. For example, gelatin-functionalized CNTs, achieved through esterification, have been utilized to create pH-responsive drug delivery systems that enhance the release of cisplatin—a common chemotherapeutic agent—specifically in tumor environments [47]. The incorporation of organometallic compounds has been explored to enhance the efficacy of photothermal therapy, where modified CNTs can selectively target and ablate cancer cells without harming healthy tissues [94]. Additionally, the functionalization of CNTs with carboxylic groups allows for the development of advanced biosensors capable of detecting cancer biomarkers, facilitating early diagnosis of cancers such as gastric and lung cancer [73,90].

In addition to amidation, etherification of CNTs has emerged as a significant strategy in enhancing cancer diagnostics and treatment, primarily through the functionalization of CNTs to improve their biocompatibility and drug delivery capabilities. Recent studies have demonstrated that etherified CNTs can effectively serve as carriers for anticancer drugs, allowing for targeted delivery systems that enhance the therapeutic efficacy of agents such as cisplatin in breast and colorectal cancers [24,47]. For instance, the incorporation of ether linkages facilitates the attachment of various biomolecules, which can improve the selectivity of drug delivery to cancer cells while minimizing off-target effects [95]. Additionally, etherified CNTs have been utilized in the development of biosensors for detecting cancer biomarkers, thereby aiding in the early diagnosis of cancers such as prostate and gastric cancer. The ability of these modified CNTs to form stable dispersions

in biological fluids further enhances their application in both therapeutic and diagnostic contexts, making them versatile tools in the fight against various cancer types.

Ionic functionalization of carboxylic groups has emerged as a significant area of research, particularly in enhancing the properties of various materials for applications in energy storage and separation technologies [96–98]. The ionic functionalization of carboxylic groups not only improves the performance of materials in various applications but also opens new avenues for the design of advanced functional materials such as CNTs.

3.1.8. Attachment of Metallic Nanoparticles

The attachment of metallic nanoparticles to various substrates, particularly to CNTs, has garnered significant attention due to their potential applications in fields such as catalysis, sensing, and biomedical technologies. Recent studies have highlighted innovative methods for the synthesis and functionalization of metallic nanoparticles, particularly through green synthesis approaches that utilize plant extracts and biological systems. For instance, the use of plant-derived extract as reducing and stabilizing agents has been shown to facilitate the eco-friendly synthesis of nanoparticles that, when combined with CNTs, exhibit enhanced properties for various applications such as photothermal cancer therapy [94]. Additionally, research has demonstrated that the coordination-assisted surface functionalization method can effectively graft organic ligands onto substrates like MXene, promoting the uniform growth of ultrafine metal nanoparticles [97]. This method not only enhances the stability of the nanoparticles but also allows for precise control over their size and distribution, which is crucial for optimizing their performance in applications such as drug delivery and catalysis [97]. Overall, the attachment and functionalization of metallic nanoparticles through these innovative approaches represent a significant advancement in nanotechnology, paving the way for the development of next-generation materials with tailored functionalities. For instance, gold nanoparticles have been shown to act as radiosensitizers, enhancing the effectiveness of radiotherapy by increasing the localized radiation dose delivered to tumor cells while minimizing damage to surrounding healthy tissues [49]. The integration of metallic nanoparticles with CNTs not only enhances drug delivery systems but also plays a crucial role in the advancement of diagnostic tools, making it a promising strategy in the fight against various cancer types.

3.2. Non-Covalent Functionalization

The non-covalent functionalization strategies of CNTs discussed in this subsection are summarized in Figure 3 and indicated by the red arrows.

3.2.1. Polymer Functionalized CNTs

CNTs can be non-covalently functionalized by polymers through wrapping, encapsulation, or absorption approaches. Polymer wrapping of CNTs has emerged as a promising approach to enhance the stability, functionality, and application potential of these nanomaterials. Recent studies have demonstrated that encapsulating CNTs within polymer matrices can significantly improve their mechanical and thermal properties, making them suitable for various applications, including electronics and energy storage. For instance, a study on PVC/CNT electrospun composites revealed that while some CNTs were not fully encapsulated due to their non-uniformity, the overall morphology and thermal behavior of the composites were positively influenced by the presence of CNTs, suggesting that proper alignment and dispersion are crucial for maximizing performance [99]. The encapsulation of CNTs in N,P-doped graphene has been explored as a method to create high-efficiency trifunctional electrocatalysts, where the polymer wrapping not only stabilizes the CNTs but also enhances their electrochemical activities for applications in flexible batteries and water splitting [100]. Furthermore, the development of dye-encapsulated CNTs has shown

potential in photocatalytic applications, indicating that polymer wrapping can facilitate the integration of functional materials for advanced technological uses [101].

Recent studies have shown that wrapping CNTs with conjugated polymers can significantly enhance their drug delivery capabilities, allowing for the effective transport of chemotherapeutic agents such as doxorubicin and cisplatin to cancer cells, particularly in breast and lung cancers [102]. For instance, the polymer wrapping not only stabilizes the CNTs in biological environments but also facilitates the controlled release of drugs in response to specific stimuli, such as pH changes in tumor microenvironments [103]. Additionally, polymer-wrapped CNTs have been utilized in the development of biosensors for detecting cancer biomarkers, enabling early diagnosis of cancers such as colorectal and prostate cancer [104]. The ability of these modified CNTs to form stable dispersions enhances their application in both therapeutic and diagnostic contexts, making them versatile tools in the fight against various cancer types [105].

Moreover, the incorporation of surfactants into polymer matrices has been explored to improve the mechanical and thermal properties of the resulting materials. For example, the addition of dodecyl surfactants to polyamide-6 nanofibers has been found to induce crystalline modifications, transforming the crystalline phase from γ to α-form, which enhances the material's overall performance including wettability of surfaces, facilitating better fluid movement in microfluidic devices, which is critical for biomedical applications [106,107].

Polymer encapsulation of CNTs has appeared as a vital strategy for enhancing the properties and functionalities of these nanomaterials in various applications. Recent studies have demonstrated that the encapsulation of CNTs within polymers can significantly improve their mechanical, thermal, and electrical properties. For instance, the use of conjugated polymers has been shown to spontaneously wrap around semiconducting SWCNTs, effectively preventing charge dissipation and enhancing the performance of optoelectronic devices [108]. This encapsulation not only stabilizes the CNTs but also facilitates their integration into polymer matrices, leading to composites with improved conductivity and mechanical strength. Additionally, research has indicated that the encapsulation of CNTs in polymers can enhance their compatibility with various solvents and matrices, which is crucial for applications in drug delivery and biosensing [109]. Furthermore, the incorporation of CNTs into polymer systems has been explored for developing advanced materials with multifunctional properties, such as shape memory and electromagnetic shielding [109,110].

Polymer absorption into CNTs enhances the mechanical, thermal, and electrical properties of composite materials. The absorption of sulfur-containing polymers onto CNTs has been demonstrated to create composite cathode materials for lithium–sulfur batteries, resulting in enhanced electrochemical performance due to the effective interaction between the polymer and the CNTs [111]. Additionally, the optimization of polyamide-based nanocomposites with CNTs has highlighted the role of polymer absorption in increasing the impact strength and elastic modulus of the resulting materials, showcasing the importance of uniform dispersion and interfacial bonding for maximizing mechanical properties [112]. Furthermore, the development of biodegradable polymer-CNT composites has been explored for their potential in electromagnetic shielding applications, where the absorption of polymers contributes to the overall performance of the composite [113].

3.2.2. Antibodies Functionalized CNTs

The attachment of antibodies to CNTs has emerged as a promising strategy in cancer diagnostics and treatment, leveraging the unique properties of CNTs to enhance the specificity and efficacy of therapeutic agents. CNTs functionalized with antibodies can selectively target cancer cell markers, thereby facilitating the precise delivery of chemotherapeutic agents. For instance, a study highlighted the use of antibody-conjugated CNTs

to detect E-cadherin and keratin-19, which are highly expressed in breast cancer cells, showcasing the potential of these nanoprobes for targeted diagnostics [105]. This approach improves the accuracy of cancer detection and allows for real-time monitoring of treatment responses, making it a valuable tool in personalized medicine.

In addition to diagnostics, antibody attachment to CNTs plays a crucial role in enhancing therapeutic outcomes. By conjugating antibodies that specifically bind to cancer cell surface antigens, CNTs can facilitate the targeted delivery of cytotoxic drugs directly to tumor cells, minimizing systemic toxicity. For example, dual-targeting strategies using CNTs have been developed to improve the delivery of neratinib in breast cancer, demonstrating enhanced therapeutic efficacy compared to conventional delivery methods [46]. This targeted approach is particularly beneficial in treating aggressive cancer types, such as triple-negative breast cancer, where conventional therapies often fall short [114]. The ability to deliver drugs directly to cancer cells while sparing healthy tissues represents a significant advancement in cancer treatment. By enhancing the specificity of drug delivery and enabling sensitive biomarker detection, this strategy holds great promise for advancing personalized cancer therapies and improving diagnostic accuracy.

3.2.3. Proteins Functionalized CNTs

Recent studies have shown that functionalizing CNTs with proteins can facilitate targeted drug delivery and improve the detection of cancer biomarkers. For instance, the conjugation of CNTs with tumor suppressor proteins, such as PTEN, has been demonstrated to enhance antitumor activity in breast cancer cells, promoting apoptosis and inhibiting cell proliferation [27]. This targeted approach allows for a more effective treatment strategy, particularly in aggressive cancer types where conventional therapies may be less effective. By leveraging the unique properties of CNTs, researchers are able to create more efficient drug delivery systems that can directly interact with cancer cells, thereby improving therapeutic outcomes.

The protein attachment to CNTs plays a crucial role in enhancing the biocompatibility and stability of these nanomaterials in biological environments. The formation of a protein corona around CNTs can significantly influence their biological interactions and cellular uptake, which is essential for effective drug delivery [115]. For example, studies have indicated that the interaction between CNTs and specific proteins can enhance the targeting of cancer cells, allowing for the selective delivery of chemotherapeutic agents to tumors while minimizing systemic toxicity [116], which is particularly relevant in the treatment of cancers such as colorectal and prostate cancer.

Overall, the attachment of proteins to CNTs offers a promising strategy for advancing cancer therapies and diagnostics. By enhancing drug delivery systems and enabling sensitive biomarker detection, this approach holds great potential for improving personalized cancer treatments and diagnostic accuracy. As research continues to evolve, the applications of protein-functionalized CNTs in oncology are likely to expand, paving the way for innovative solutions in cancer care [68,117].

3.2.4. Carbohydrate Attachment

Recent studies have demonstrated that functionalizing CNTs with carbohydrates, such as hyaluronic acid and mannose, can improve the specificity of drug delivery systems. Hyaluronic acid-modified CNTs have been shown to effectively target specific cancer cell receptors, which are promoting apoptosis in various cancer cells, as a targeted approach, including breast and lung cancers [48]. The incorporation of carbohydrates on CNT surfaces can facilitate the specific binding of cancer biomarkers, allowing for sensitive detection of cancerous cells. For example, studies have shown that glucose-functionalized CNTs

can be employed to detect specific glycoproteins linked to colorectal cancer, allowing for early diagnosis and monitoring of treatment responses [66,118]. The high surface area and conductivity of CNTs, combined with the specificity provided by carbohydrate attachments, make these biosensors highly effective for cancer biomarker detection, which is crucial for timely intervention.

In combination with chemotherapeutic agents, carbohydrate-functionalized CNTs have shown promise in enhancing therapeutic outcomes. Research indicates that attaching carbohydrates to CNTs can improve the solubility and stability of anticancer drugs, such as doxorubicin, leading to enhanced drug loading and controlled release profiles [118]. This is particularly beneficial in treating aggressive cancer types, such as triple-negative breast cancer, where conventional therapies often face challenges due to drug resistance [119]. As research continues to evolve, the applications of carbohydrate-functionalized CNTs in oncology are likely to expand, paving the way for innovative solutions in cancer care [19,115].

3.2.5. RNA Attachment

RNA-functionalized CNTs can serve as effective carriers for targeted drug delivery, particularly in the treatment of various cancers such as breast and lung cancer. The conjugation of small interfering RNA (siRNA) to CNTs has been shown to facilitate the targeted silencing of oncogenes, leading to reduced tumor growth and improved therapeutic outcomes [120]. This targeted approach not only enhances the specificity of drug delivery but also minimizes off-target effects, making it a valuable tool in personalized cancer therapy. Moreover, RNA attachment to CNTs has been utilized in the development of advanced biosensors for cancer diagnostics. The incorporation of RNA molecules on CNT surfaces can facilitate the specific binding of cancer-related biomarkers, enabling sensitive detection of cancerous cells. For example, studies have demonstrated that RNA aptamers can effectively capture specific tumor markers, such as prostate-specific antigen (PSA) for prostate cancer detection [121]. Incorporating these aptamers in CNTs is expected to enhance early diagnosis and monitoring of treatment responses.

Research indicates that attaching RNA molecules to CNTs can improve the solubility and stability of therapeutic agents, leading to enhanced drug loading and controlled release profiles [122]. This is particularly beneficial in treating aggressive cancer types, such as triple-negative breast cancer, where conventional therapies often face challenges due to drug resistance [123]. Overall, the attachment of RNA to carbon nanotubes represents a multifaceted approach to advancing cancer diagnostics and treatment. By enhancing drug delivery systems, enabling sensitive biomarker detection, and improving the therapeutic efficacy of anticancer agents, this strategy holds great potential for improving patient outcomes in various cancer types, including breast, lung, and prostate cancers. As research continues to evolve, the applications of RNA-functionalized CNTs in oncology are likely to expand, paving the way for innovative solutions in cancer care [118,124]. Table 1 summarizes the different types of CNTs' functionality and their biomedical applications.

Table 1. Summary of the type of functionalization and example applications.

Type of Functionalization	Functionality Method	Example	Benefit	Application	Reference
Covalent Functionalization	Fluorination	Introduction of fluorine atoms to CNTs	Improves dispersion; enhances electronic properties; and increases reactivity	Drug delivery, photothermal therapy	[51,53,56]
	Hydrogenation	Attachment of hydrogen atoms	Modifies electrical conductivity and improves catalytic activity. Works with cisplatin for anticancer properties.	Drug delivery, fuel cells	[19,58,59]
	1,3-Dipolar cycloadditions	Reaction with azomethine ylides	Enhances bioconjugation and allows precise functionalization	Cancer treatment, photodynamic therapy	[62,66]
	Reduction of aryldiazonium salts	Arylation via diazonium salt chemistry	Enables attachment of functional groups for improved targeting	Drug delivery, biosensors	[24,72]
	Reactive species functionalization	Functionalization using reactive oxygen species	Enhances surface reactivity and interactions with biomolecules	Sensors, catalysis, medical applications	[30]
	Organometallic ions	Coordination with transition metals	Improves electronic and catalytic properties	Biosensors, imaging	[81,85,86]
	Carboxylation and further derivation	Carboxyl (-COOH) groups on CNTs	Enhances solubility; allows further modifications	Drug delivery, biosensors	[30,90]
	Amidation and esterification of carboxylic groups	Reaction of carboxylated CNTs with amines/esters	Improves biocompatibility and drug-loading efficiency	Drug delivery, biosensors	[90,91]
	Ionic functionalization of carboxylic groups	Functionalization with ionic groups	Enhances dispersibility in aqueous solutions; improves targeting	Drug delivery, diagnostics	[90]
	Attachment of metallic nanoparticles	Deposition of Au, Ag, and Pt nanoparticles	Improves imaging contrast; enhances targeted therapy	Imaging, cancer treatment	[47,94]
Non-Covalent Functionalization	Surfactant functionalization	Use of anionic (SDS, NaDDBS), cationic (CTAB, MATMAC), or non-ionic (Triton X-100) surfactants	Enhances dispersibility and stability in biological systems	Drug delivery, antimicrobial applications	[75]
	Polymer wrapping	Wrapping CNTs with conjugated polymers	Stabilizes CNTs in biological environments; improves targeting	Drug delivery, biosensors	[102]
	Polymer encapsulation	Encapsulation in biocompatible polymers	Improves biocompatibility; enables controlled drug release	Drug delivery, regenerative medicine	[109]
	Polymer absorption	Adsorption of functional polymers onto CNTs	Enhances stability; provides controlled release properties	Drug delivery, biosensors	[112]

Table 1. *Cont.*

Type of Functionalization	Functionality Method	Example	Benefit	Application	Reference
Non-Covalent Functionalization	RNA attachment	Conjugation of RNA to CNTs	Enables gene silencing; improves targeted drug delivery	Cancer therapy, genetic engineering	[120,122]
	Protein attachment	Functionalization of CNTs with proteins	Enhances biocompatibility; enables targeted therapy	Cancer treatment, biosensors	[27]
	Antibodies attachment	Conjugation of antibodies to CNTs	Enables specific targeting of cancer cells; enhances biosensor performance	Cancer detection, immunotherapy	[105]
	Carbohydrate attachment	Functionalization with sugars like hyaluronic acid	Improves cellular recognition; enables targeted drug delivery	Cancer therapy, biosensors	[48]

4. Carbon Nanotubes in Cancer Diagnosis

4.1. Overview

Carbon nanotubes (CNTs) have become a key component in cancer diagnosis due to their unique physical and chemical properties. Their high surface area, electrical conductivity, and mechanical strength make them well-suited for biomedical applications, particularly in detecting cancer biomarkers. Integrating CNTs into diagnostic tools has significantly improved early cancer detection, allowing for more sensitive and accurate identification of malignant cells compared to traditional methods [125–128].

Beyond detection, CNTs offer versatility through functionalization, which enhances their biocompatibility and targeting abilities. By attaching targeting ligands or drugs, CNTs can selectively bind to cancer cells, improving the accuracy of diagnostic assays [127,129–131]. This targeted approach not only aids in diagnosis but also enables therapeutic applications, as CNTs can deliver chemotherapeutic agents directly to tumors, reducing systemic toxicity [132,133]. Their dual role in diagnosis and treatment makes CNTs a crucial tool in advancing nanomedicine.

In addition to biosensing, CNTs are being explored for imaging applications. Their unique optical properties allow them to act as contrast agents in imaging techniques such as fluorescence imaging and magnetic resonance imaging (MRI). Incorporating CNTs into these methods enhances tumor visibility, making it easier to monitor cancer progression and treatment effects [134]. Furthermore, combining CNTs with MRI and computed tomography (CT) has shown potential for real-time tumor tracking and response assessment [135,136]. With their ability to improve both detection and imaging while also offering therapeutic potential, CNTs are shaping the future of cancer diagnostics and treatment, bringing precision and efficiency to modern medicine.

A biosensor is a device used for analysis that combines a biological recognition component with a transducer, allowing it to detect and measure specific biological substances in different types of samples. It transduces biological responses into a detectable and measurable electrical signal (Figure 4).

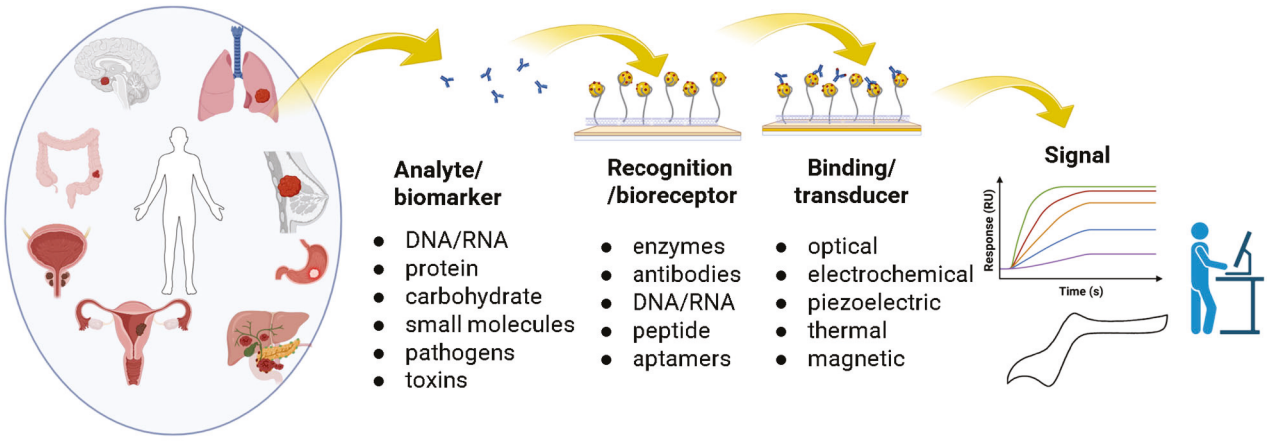

Figure 4. Biosensor components and biosensing processes. Created with BioRender.com.

CNT-based biosensors can be categorized into various types, such as electrochemical sensors, optical sensors, field-effect transistor (FET) sensors, and hybrid biosensors. Electrochemical biosensors incorporating CNTs have demonstrated exceptional sensitivity and specificity, largely due to CNTs' high surface area, which facilitates functionality and efficient immobilization of biomolecules [137,138]. These sensors detect target analytes by detecting variations in current or potential upon binding to immobilized biomolecules. The presence of CNTs in the sensor matrix enhances electron transfer kinetics, significantly improving detection limits [137–139].

Optical biosensors utilize CNTs' unique optical properties, such as their ability to quench fluorescence via Förster resonance energy transfer (FRET). This phenomenon has been exploited to create highly sensitive fluorescence-based biosensors capable of detecting low concentrations of biomolecules [140,141]. Additionally, non-covalent functionalization of CNTs with biopolymers and surfactants improves their dispersion in aqueous solutions, further enhancing their performance in optical sensing applications) [141,142].

Field-effect transistor (FET) biosensors based on CNTs offer another promising approach for biosensing. These devices rely on CNTs' electrical properties to detect changes in the charge state of the sensor surface upon target analyte binding. The high sensitivity of CNT-FETs is attributed to the pronounced change in CNT conductivity in response to biomolecule adsorption. Furthermore, integrating CNTs into flexible and miniaturized sensor platforms has opened new possibilities for point-of-care diagnostics and wearable biosensing devices [142,143].

Beyond individual sensor types, CNTs are also used in hybrid biosensing systems, where they are combined with other nanomaterials, such as graphene and metal nanoparticles, to develop multifunctional sensors. These hybrid systems leverage the complementary properties of different nanomaterials to enhance overall sensing performance [144–147]. For example, incorporating CNTs with gold and silver nanoparticles has been shown to improve the sensitivity and selectivity of electrochemical biosensors for detecting specific biomolecules [144–148].

4.2. CNT-Biosensors for Selective Cancer Detection

Recent advancements in carbon nanotube (CNT)-based biosensors have shown significant promise in the detection of cancer biomarkers. This review categorizes the applications of CNT-biosensors into four main types: electrochemical sensors, optical sensors, field-effect transistor (FET) sensors, and hybrid biosensors. Each category is supported by recent primary research papers that highlight specific CNT-based biosensors, the cancer biomarkers detected, and detailed experimental results.

4.2.1. Electrochemical Biosensors

Electrochemical biosensors have been widely used in the detection of various cancer biomarkers [149–151], especially CNT-based electrochemical biosensors [152]. Kumar and co-workers developed a highly sensitive electrochemical immunosensor using a nano-engineered material of magnesium oxide (MgO) on functionalized MWCNTs (f-MWCNT), further modified with APTES, for the early diagnosis of lung cancer biomarker CKAP4. This biosensor achieved a low limit of detection of 6.25 pg/mL. The incorporation of f-MWCNTs enhanced electrical conductivity and provided a large surface area, which improved the biosensor's sensitivity compared to other metal oxide-based sensors [152]. Figure 5 shows the fabrication methods for the working electrode in electrochemical biosensors.

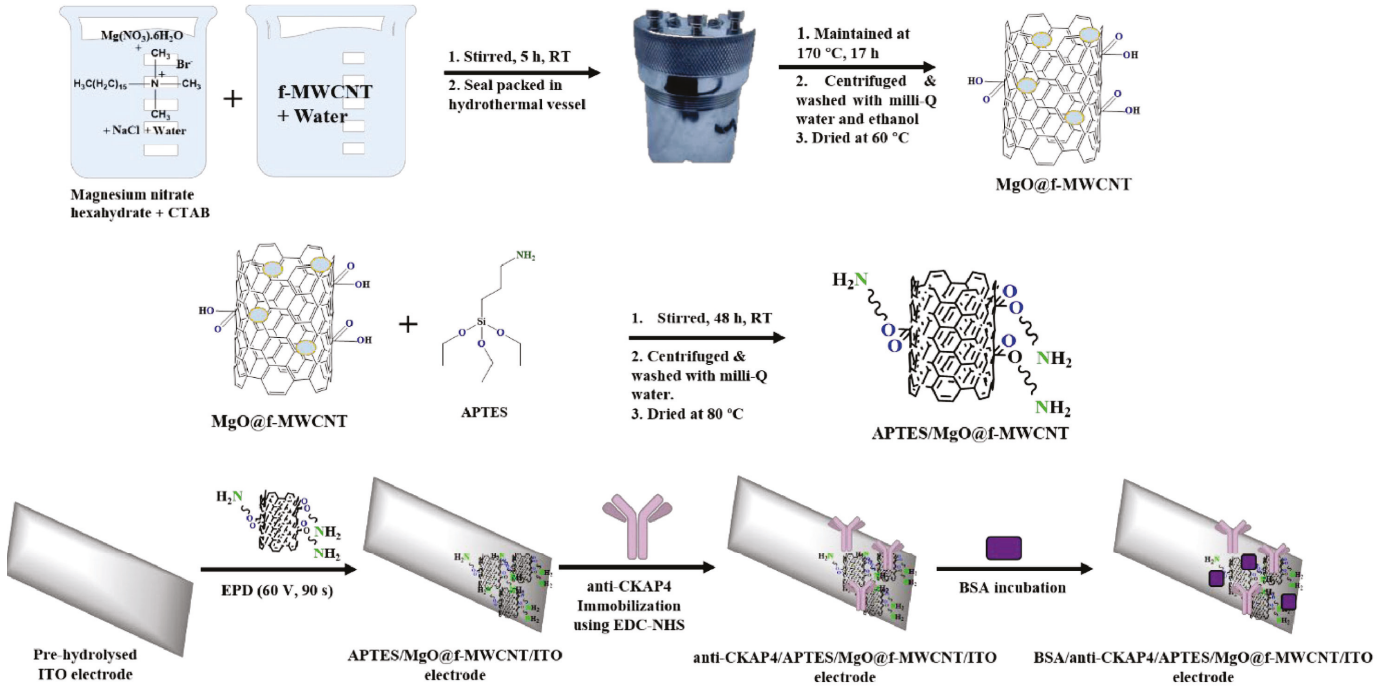

Figure 5. Fabrication process of the working electrode in an electrochemical biosensor for the detection of the lung cancer biomarker CKAP4 (Reused from Shanker et al. [152]).

Bhattacharjee et al. developed an electrochemical biosensor by employing a gold nanoparticle (AuNPs) functionalized MWCNT nanocomposite for the detection of the non-small cell lung cancer (NSCLC) biomarker miR-223. The MWCNTs enhance the surface area and facilitate electron transfer, while AuNPs further improve conductivity, contributing to the sensor's high sensitivity. This design, along with a sandwich hybridization assay and a ferrocene-labeled bioconjugate for signal amplification, enables a low detection limit of 0.73 pM and good selectivity for miR-223 over homologous sequences (Figure 6a) [153].

In another study conducted by Zhang et al., a label-free electrochemical sensor was developed by utilizing MWCNTs for the detection of CD44, a cell surface glycoprotein that is overexpressed in various cancers, including lung and breast cancers [154]. The fabricated sensor was constructed on an indium tin oxide (ITO) electrode modified with MWCNTs and polydiallyldimethylammonium (PDDA) to enhance the electrochemical performance. The sensor showed a linear response to CD44-positive cancer cells, indicating its reliability for clinical applications. The electrochemical response was significantly enhanced due to the high surface area and conductivity of the MWCNTs, which facilitated the binding of CD44. The detection was based on the electrochemical impedance spectroscopy (EIS)

technique, which allowed for real-time monitoring of the binding events between the sensor and the cancer cells (Figure 6b) [154].

Electrochemical biosensing approaches were also explored for the detection of biomarkers for cancer [155–157]. Yang and co-workers reported an electrochemical immunosensor utilizing MWCNTs-COOH functionalized with Fe_3O_4 and AuNPs for the detection of the liver cancer marker alpha-fetoprotein (AFP). The use of functionalized MWCNTs-COOH provides a large surface area for stable antibody immobilization through covalent bonding, enhancing the electrochemical signal and contributing to high sensitivity and selectivity for AFP. The developed sensor achieved a low detection limit of 1.09034 pg/mL [158]. The fabrication of the functionalized MWCNTs-COOH working electrode for the electrochemical sensors is illustrated in Figure 6c.

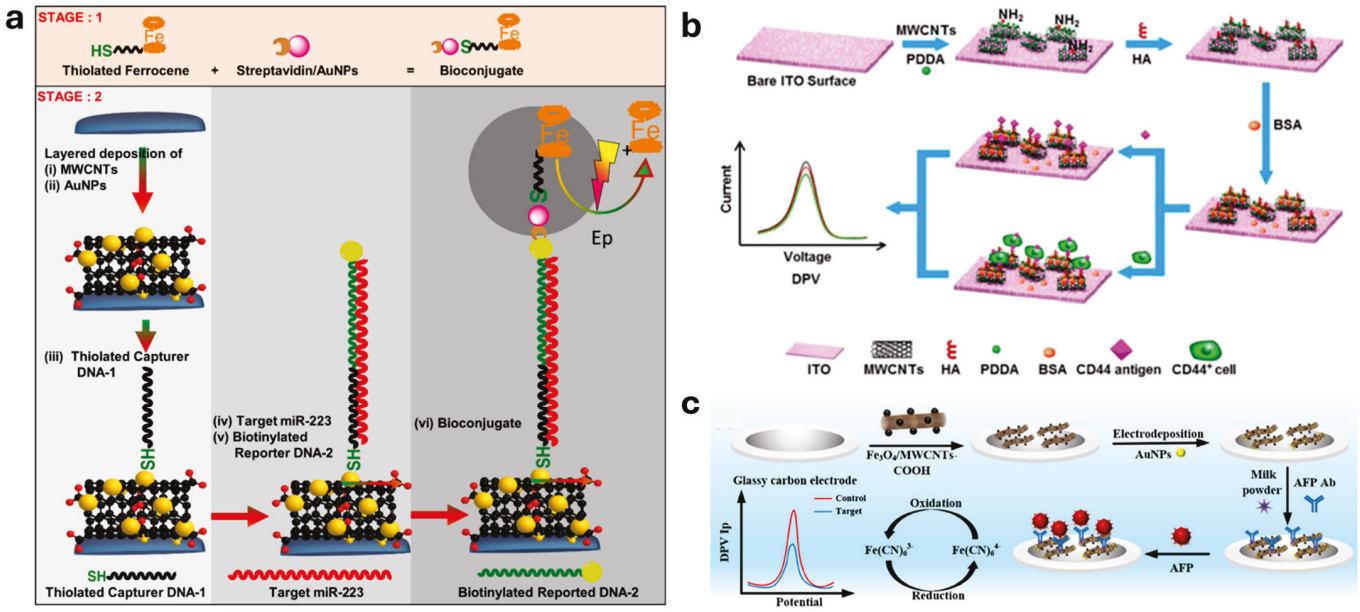

Figure 6. Schematic diagram illustrating the synthesis of: (**a**) a sandwich-type gold/MWCNT nanocomposite–based electrochemical biosensor for non-small cell lung cancer (NSCLC) miR-223 biomarkers (Ref. Bhattacharjee et al. [153]); (**b**) a label-free electrochemical sensor targeting CD44, based on ligand–protein interactions, designed to detect CD44 in human serum and cancer cells (Ref. Zhang et al. [154]; and (**c**) an electrochemical immunosensor for AFP utilizing a modified electrode surface composed of Fe_3O_4 nanoparticles, MWCNTs-COOH, and gold nanoparticles (AuNPs) for enhanced sensitivity and performance (Ref. Wu et al. [158]).

Xu et al. investigated a CNT-based electrochemical sensor for the detection of alpha-fetoprotein (AFP), a well-known biomarker for hepatocellular carcinoma (liver cancer) [159]. The sensor utilized a composite of conducting polymers and CNTs, which provided a highly effective electrochemical sensing material. The study reported a detection limit of 0.20 µM for AFP, which is significant for early diagnosis and monitoring of liver cancer. The electrochemical detection was performed using cyclic voltammetry (CV), which allowed for the assessment of the electrochemical behavior of the AFP biomarker upon binding to the sensor surface [159]. Makableh et al. developed an electrochemical Aptasensor for the early detection of HER2, a biomarker for breast cancer. The biosensor utilizes a screen-printed carbon electrode modified with gold nanoparticles (GNPs) and MWCNTs to enhance response and selectivity. Employing electrochemical techniques like differential pulse voltammetry (DPV), the Aptasensor achieved a very low detection limit of 4.4 Pg/mL with a response time of approximately 5 min [160].

4.2.2. Field-Effect Transistor (FET) Sensors

Field-Effect Transistor (FET) Sensors based on functionalized CNTs have been explored for the detection of biomarkers for diverse cancers, including liver, breast, prostate, and lung cancer [161–163]. Recently, You and co-workers developed a portable field-effect transistor (FET) biosensor utilizing a novel semiconductor material composed of metal carbide@carbon nanotubes (MC@CNTs) for the non-invasive detection of exosomal microRNA-122, a biomarker for liver cancer, in urine. The incorporation of CNTs enhances the electrical conductivity and transconductance of the metal carbide, contributing to significantly improved sensitivity. This MC@CNT-iFETs device achieved an ultralow detection limit of 0.12 fM for microRNA-122, and its high specificity is attributed to the use of a specific aptamer for microRNA-122 recognition (Figure 7a) [163].

Choi and co-workers reported a method for the real-time and highly sensitive monitoring of adenosine receptor activities in non-small cell lung cancer (NSCLC) cells. The method utilizes an electrochemical transduction mechanism via a carbon nanotube field-effect transistor (CNT-FET) hybridized with NSCLC cells. The CNT-FET is functionalized with a fibronectin coating for stable immobilization of the cancer cells expressing adenosine receptors. This platform enables the detection of adenosine, a key molecule in lung cancer biology, with an ultralow detection limit of 1 fM [162].

In another study, a CNT FET biosensor was developed for the detection of carcinoembryonic antigen (CEA), a well-known biomarker for lung cancer. The biosensor was functionalized with specific antibodies against CEA and operated using electrostatic coupling to detect biomolecular interactions. The results indicated a wide detection range from 1 fg/mL to 1 ng/mL and sensitivity of 72 ag/mL, demonstrating its effectiveness in clinical applications for lung cancer diagnostics [164].

Liu et al. developed a semiconductor carbon nanotube (CNT)-based field-effect transistor (FET) DNA sensor designed for the detection of the BRCA1 gene, a key biomarker associated with breast cancer. The CNT-FET, featuring a floating gate and high κ dielectric, was optimally functionalized with peptide nucleic acid (PNA) probes. It achieved excellent sensitivity with a low detection limit of 1.38 aM and successfully distinguished between patients and healthy individuals [165].

Li et al. presented a CNT field-effect transistor (FET) biosensor specifically designed for the ultrasensitive and label-free detection of exosomal miRNA21, a biomarker associated with breast cancer. The biosensor exhibited a detection limit of 0.87 aM, showcasing its potential for early diagnosis. The study highlighted the ability of the CNT FET to provide real-time monitoring of biomarker levels, which is crucial for timely intervention in breast cancer treatment [166].

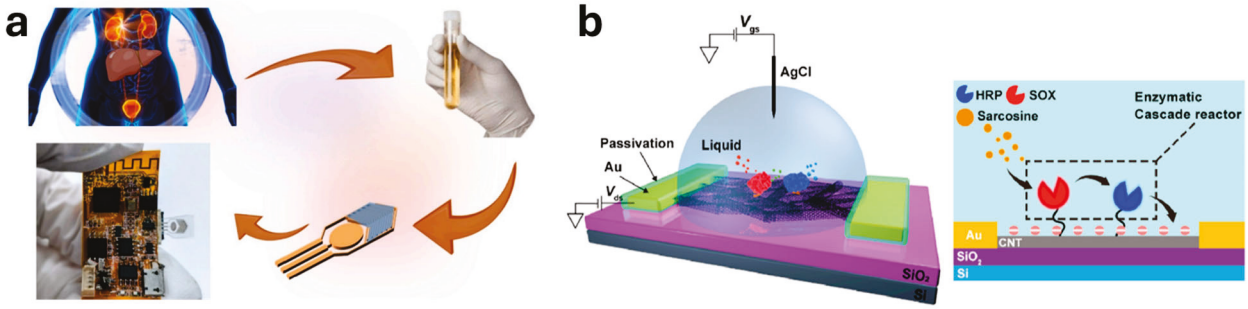

Figure 7. Schematic diagram illustrating FET immunosensors: (**a**) a non-invasive approach for detecting exosomal microRNA-122 in the urine of liver cancer patients using MC@CNT-iFETs (Ref. Zhang et al. [163]); and (**b**) a CNT-FET modified with enzymatic cascade reactors (Ref. Liu et al. [167]).

Wei and colleagues recently developed a high-purity semiconductor carbon nanotube-based field-effect transistor (CNT-FET) integrated with enzymatic cascade reactors, enabling highly sensitive detection of sarcosine, a biomarker associated with biopsy-positive prostate cancer. The CNT network improves reaction efficiency, enhancing signal transduction, leading to a limit of detection as low as 105 zM. This CNT-FET sensor demonstrated the ability to precisely distinguish prostate cancer samples from benign prostatic hyperplasia samples with higher accuracy than conventional PSA testing (Figure 7b) [167].

4.2.3. Optical Sensors

Several types of optical biosensors have been developed and used for the early detection of cancer biomarkers, including photonic crystals, surface plasmon resonance (SPR) spectroscopy [168,169], surface-enhanced Raman spectroscopy (SERS), and colorimetric sensors [170,171]. Due to the advantages of the localized surface plasmon resonance (LSPR) phenomenon, optical SPR biosensors for biomolecule and cancer detection have been extensively studied [155–157,172]. However, plasmonic nanoparticles (NPs) are commonly used to enhance electrochemical detection with CNT-SPR biosensors, and there are limited recent studies investigating SPR optical detection of CNT-SPR optical biosensors. Recently, Karki et al. proposed a surface plasmon resonance (SPR) sensor incorporating carbon nanotubes (CNTs) for the ultra-sensitive detection of colorectal cancer. The sensor, utilizing a CaF_2 prism/Cu/CNT/$HfSe_2$ multilayer structure, detects changes in the refractive index between healthy and cancerous colorectal tissue via shifts in the resonance angle, leveraging the optical property of SPR. The inclusion of a 1 nm thick CNT layer enhances the sensor's sensitivity, achieving a maximum sensitivity of 387.60 deg/RIU specifically for colorectal cancer detection. This design presents a promising approach for early and less invasive colorectal cancer detection [157]. The study by Uniyal et al. proposes a surface plasmon resonance (SPR) sensor utilizing fluorinated graphene and carbon nanotubes (CNTs) for the detection of SARS-CoV-2 viral particles. This work highlights the diagnostic potential of this sensor configuration, with the Introduction mentioning the vital role of diagnostic testing in outbreak containment. The use of fluorinated graphene and CNTs is explored to enhance the sensitivity of the SPR sensor for this diagnostic application [57]. The study also calculates the Limit of Detection (LOD) for the considered SARS-CoV-2 concentrations. For the suggested sensor configuration with one layer of fluorinated graphene and five layers of CNTs, the maximum LOD attained is 3.07×10^{-6} RIU for a 125 nM concentration of coronavirus [57].

An optical biosensor for Chronic Lymphocytic Leukemia (CLL) biomarker detection using MWCNTs has been developed by Kala and co-workers. The MWCNTs are functionalized with silane to enable antibody immobilization. The sensing mechanism relies on monitoring Fermi level fluctuations induced by the binding of CLL cells, detected through photocurrent and photoconductive response using a 635 nm laser. The developed biosensor achieved a limit of detection of 27 cells/mL [173].

CNT-based fluorescence sensors are widely used [174], with CNTs also serving as effective fluorescence quenchers. Bio-recognition elements, such as oligonucleotides, can be fluorescently labeled and non-covalently attached to CNTs, where their fluorescence is quenched via Förster resonance energy transfer (FRET). In the presence of analyte molecules, these oligonucleotides preferentially bind to the analyte, displacing the CNTs and leading to a significant fluorescence increase [175].

Williams et al. utilized fluorescent SWCNTs as optical transducers for in vivo nanobiosensors. These SWCNTs are often combined with materials like ssDNA, antibodies, peptides, or polymers for dispersion and specific biomarker recognition. While various biomarkers are detected, including the ovarian cancer biomarker HE4 and surface

proteins on prostate cancer cells (PSMA), and pH change detection is demonstrated in ovarian cancer xenografts, this review specifies different detection levels for various analytes rather than a singular limit for a specific cancer type. For instance, the HE4 sensor could discriminate between mice injected with 10 pmol of HE4 and controls [176].

Table 2 summarizes the types of functionalized CNTs that have been explored for the detection of diverse types of cancers and their biomarkers. Recent primary research on CNT-based biosensors for cancer detection has revealed significant advancements across various sensor types. Electrochemical and FET sensors have demonstrated high sensitivity and specificity for cancer biomarkers, making them promising candidates for clinical applications. Additionally, while optical biosensors have been extensively explored for cancer biomarker detection, research on CNT-based optical sensors, particularly fluorescence-based sensors, has primarily focused on their applications in cancer imaging rather than biomarker detection.

Table 2. Summary of the types of biosensors and example applications.

Type of Biosensor	Type of CNT Used	Type of Cancer/Biomarker/ Molecule Detected	Type of Recorded Signal	Detection Limit	Ref.
Electrochemical	Functionalized MWCNT (f-MWCNT)	Lung cancer/CKAP4	Change in current or potential (implied)	6.25 pg/mL	[152]
	Gold nanoparticle (AuNPs) functionalized MWCNT	Non-small cell lung cancer (NSCLC)/miR-223	Change in current or potential (implied)	0.73 pM	[153]
	MWCNTs	Lung and breast cancers/CD44 (cancer cells)	Electrochemical impedance spectroscopy (EIS)	5.94 pg/mL	[154]
	MWCNTs-COOH functionalized with Fe_3O_4 and AuNPs	Liver cancer/alpha-fetoprotein (AFP)	Electrochemical signal	1.09034 pg/mL	[158]
	CNTs combined with conducting polymer	Liver cancer/alpha-fetoprotein (AFP)	Cyclic voltammetry (CV)	0.20 μM	[159]
	MWCNTs modified with gold nanoparticles (GNPs)	Breast cancer/HER2	Differential pulse voltammetry (DPV)	4.4 Pg/mL	[160]
Field-Effect Transistor (FET)	Metal carbide@carbon nanotubes (MC@CNTs)	Liver cancer/exosomal microRNA-122	Change in electrical conductivity/transconductance	0.12 fM	[163]
	CNT	Non-small cell lung cancer (NSCLC) cells/adenosine receptor activity/adenosine	Electrochemical transduction (implied through hybridization with CNT-FET)	1 fM	[162]
	CNT functionalized with specific antibodies	Lung cancer/carcinoembryonic antigen (CEA)	Change in electrical conductivity (implied)	72 ag/mL	[164]
	Semiconductor CNT functionalized with peptide nucleic acid (PNA) probes	Breast cancer/BRCA1 gene	Change in electrical conductivity (implied)	1.38 aM	[165]
	CNT-FET coated with fibronectin	Breast cancer/exosomal miRNA21	Change in electrical conductivity (implied)	0.87 aM	[166]
	High-purity semiconductor CNT modified with enzymatic cascade reactors	Prostate cancer/sarcosine	Enhanced signal transduction (change in electrical conductivity implied)	105 zM	[167]

Table 2. *Cont.*

Type of Biosensor	Type of CNT Used	Type of Cancer/Biomarker/ Molecule Detected	Type of Recorded Signal	Detection Limit	Ref.
Optical	CNTs in a CaF_2 prism/Cu/CNT/HfSe2 multilayer structure	Colorectal cancer/refractive index difference between healthy and cancerous tissue	Shift in resonance angle	Maximum sensitivity of 387.60 deg/RIU (for colorectal cancer detection)	[157]
	MWCNTs functionalized with silane	Chronic Lymphocytic Leukemia (CLL)/CLL cells	Photocurrent and photoconductive response	Limit of detection of 27 cells/mL	[173]
	SWCNTs (as quenchers)	Ovarian cancer/HE4; prostate cancer/PSMA (among others not specific to one cancer in this description)	Fluorescence increases upon analyte binding	For HE4: could discriminate between mice injected with 10 pmol and controls	[176]

4.3. CNTs in Cancer Imaging Modalities

Recent advancements in CNT-based biosensors have demonstrated significant potential in enhancing cancer imaging modalities [177–179]. CNTs have gained significant attention in the field of fluorescence imaging due to their unique optical properties, including strong fluorescence, low photobleaching, and tunable emission wavelengths. Recent studies have explored various applications of CNTs in fluorescence imaging, particularly in biological systems for cancer detection and monitoring [174]. This section reviews recent primary research papers that highlight the advancements in CNT-based fluorescence imaging.

4.3.1. CNTs in Fluorescence Imaging

Hendler-Neumark et al. investigated the use of SWCNTs as fluorescent probes for in vivo imaging within the gastrointestinal tract of *Caenorhabditis elegans* (*C. elegans*) nematodes. The study demonstrated that DNA-functionalized SWCNTs exhibit remarkable photostability compared to traditional organic fluorescent dyes, allowing for prolonged imaging of dynamic biological processes without significant photobleaching. The researchers reported that SWCNTs enabled real-time imaging of cellular events over extended periods, showcasing their potential for long-term tracking of biological phenomena) [180]. This property is particularly advantageous in cancer research, where continuous monitoring of tumor dynamics is crucial.

In their study, Zhou et al. enhanced imaging capabilities by creating a nanocomposite, GdN@CQDs-MWCNTs, which combines the deep tissue penetration of magnetic resonance imaging (MRI) with the single-cell sensitivity of fluorescence imaging (FI). The research focused on imaging and treating A549 lung cancer cells in living mice. The main finding was the successful development of a magnetofluorescent nanocomposite capable of targeted drug delivery and synergistic chemo/photothermal therapy, with fluorescence imaging used to track cellular uptake and in vivo distribution [177].

Kojima et al. explored the effects of oxygen-doping on SWCNTs to enhance their fluorescence properties for use as near-infrared labels in immunoassays. The introduction of oxygen atoms into the CNT structure resulted in a red shift in the fluorescence wavelength, improving the contrast in biological imaging applications. The study demonstrated that Streptavidin oxygen-doped SWCNTs could effectively reduce autofluorescence in living cells, thereby increasing the detected signal and enhancing image quality [181]. This functionalization strategy opens new avenues for using CNTs in fluorescence imaging, particularly in complex biological environments where background noise can obscure signals.

In a recent study, Wu et al. developed an artificial cell-based sensing system where embedding carbon nanotubes (CNTs) in the artificial cell membranes significantly enhances

fluorescence imaging of intracellular biomarkers. These embedded CNTs function as artificial channels, facilitating the faster and more efficient transfer of signal probes, such as nucleic acids and fluorescent dyes, across cell membranes. This enhanced probe transfer, mediated by CNTs, leads to improved fusion between the artificial cells and target cells, allowing the probes to selectively hybridize with intracellular target miRNAs and trigger a fluorescence signal. Consequently, the study demonstrates enhanced fluorescence signal and improved visualization of let-7a miRNA within living colon cancer cells, showcasing the potential of CNTs to overcome limitations in probe delivery for intracellular imaging (Figure 8) [182].

Chen et al. investigated the photoluminescence properties of unzipped MWCNTs (uMWCNTs) and their potential applications in fluorescence imaging. The study reported that uMWCNTs exhibited strong fluorescence with a peak emission of around 550 nm, which is suitable for various imaging applications. The authors noted that the unique electronic properties of CNTs allow for efficient charge separation and migration, which enhances their fluorescence intensity (Figure 9) [183]. This property can be leveraged to improve the sensitivity of fluorescence imaging techniques in detecting cancer biomarkers.

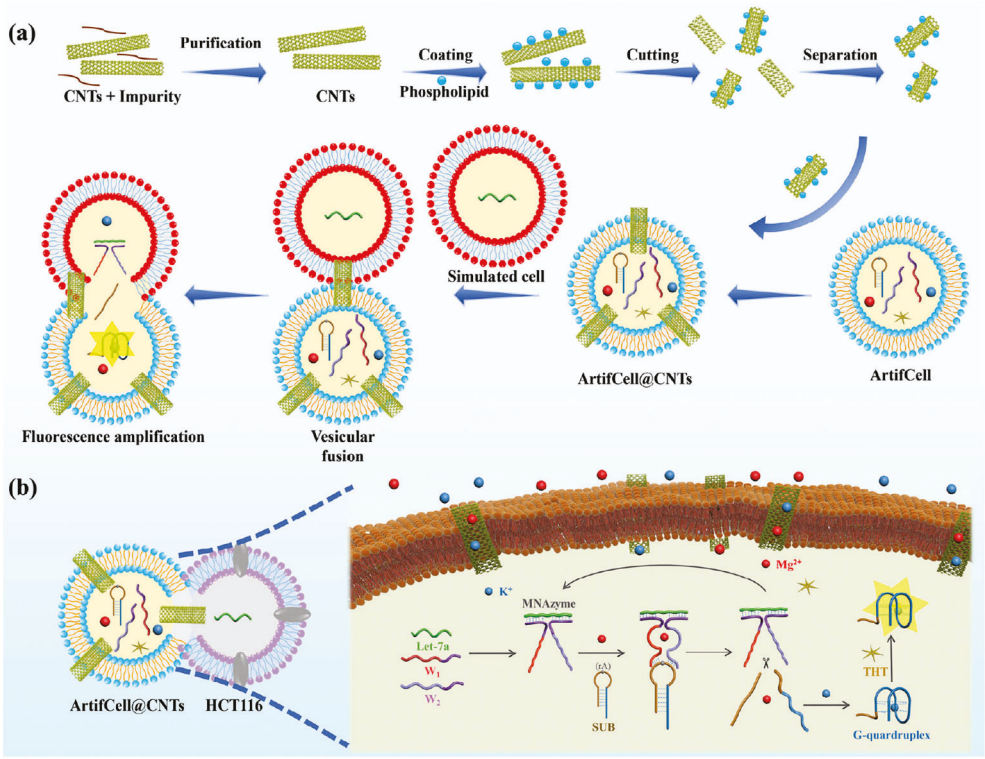

Figure 8. Schematic of the ArtifCell@CNTs-based probe transfer-enhanced sensing strategy. (**a**) Purification of CNTs and the preparation of Artif-Celll@CNTs for fluorescence sensing. (**b**) Illustration of the ArtifCell@CNTs-based sensing specifically targeting let-7a (Ref. Wu et al. [182]).

Mandal et al. demonstrated the use of sp^3 defect-tailored CNTs for near-infrared (NIR-II) single-particle imaging in live brain slices. The study achieved high signal-to-noise ratios using low excitation intensities, which is crucial for minimizing photodamage in sensitive biological tissues. This work highlights the potential of CNTs as single-molecule probes for advanced imaging techniques, paving the way for their application in real-time monitoring of tumor microenvironments [184]. The study also shows that para-nitroaryl functionalized SWCNTs (f-SWCNTs) exhibit brighter fluorescence in the NIR-II region with significantly lower excitation intensities compared to non-functionalized SWCNTs (unf-SWCNTs). This enhanced performance of f-SWCNTs allows for higher signal-to-noise

ratio imaging in live tissue using an order of magnitude less light excitation than required for unf-SWCNTs [184]. The ability to visualize individual CNTs in biological systems could lead to breakthroughs in understanding cancer biology and treatment responses.

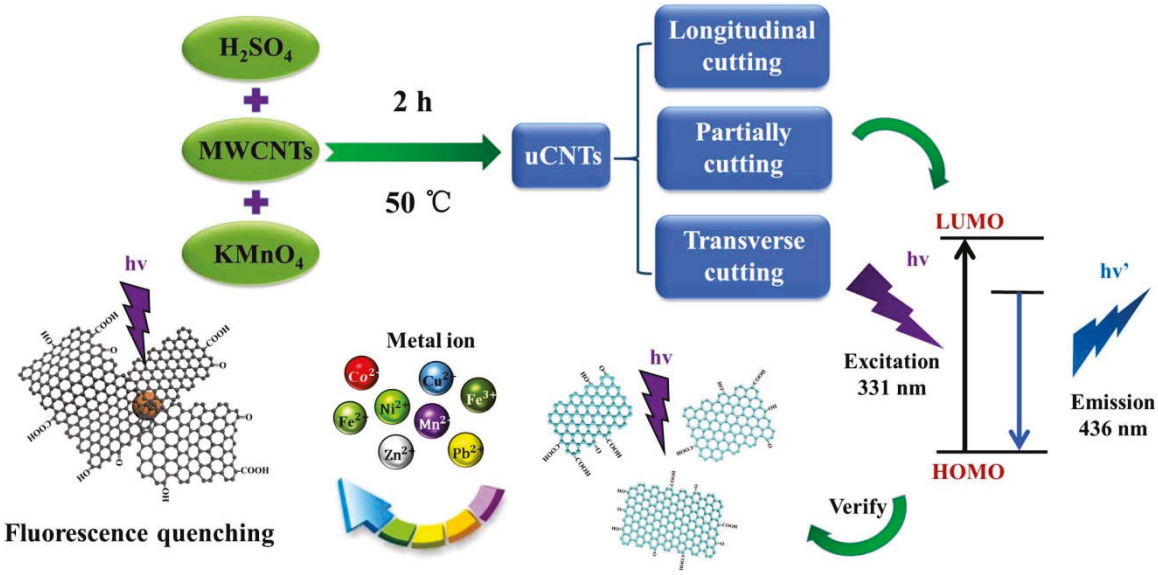

Figure 9. Illustration of the unzipping process of a carbon nanotube (CNT) into a graphene nanoribbon, along with the corresponding energy profile (Ref. Chen et al. [183]).

The application of carbon nanotubes in fluorescence imaging represents a significant advancement in biomedical imaging technology. Recent studies have demonstrated that CNTs, particularly SWCNTs and MWCNTs, possess unique optical properties that make them suitable for long-term imaging, enhanced contrast, and live tracking of biological functions. The functionalization of CNTs further enhances their imaging capabilities, allowing for targeted applications in cancer diagnostics and therapy. As research continues to evolve, CNTs are willing to play a critical role in advancing fluorescence imaging techniques in oncology and beyond.

4.3.2. CNT-Enhanced MRI

Carbon nanotubes (CNTs) have emerged as promising materials in the field of magnetic resonance imaging (MRI), primarily due to their unique properties that can enhance imaging contrast and provide multifunctional capabilities. Furthermore, Gao et al., in their recent review, highlighted the potential of functionalized CNTs in enhancing MRI capabilities. They discussed how surface modifications could be tailored to optimize the targeting of specific cancer biomarkers, thereby increasing the specificity of MRI imaging [19]. This targeted approach can lead to more accurate tumor detection and characterization, which is vital for effective treatment planning. This section reviews recent studies focusing on the application of CNTs in MRI, detailing the specific types of CNTs used, their functionalization, and the experimental results related to their effectiveness as contrast agents.

One significant study by Mehri-Kakavand et al. investigated the use of gadolinium (Gd)-loaded CNTs as MRI contrast agents. The researchers synthesized Gd_{3+}@CNTs-PEG and compared their performance with Gadovist®, a commercially available contrast agent. The results indicated that Gd_{3+}@CNTs-PEG exhibited superior relaxivity, enhancing the proton transverse relaxation times (T2) significantly. The study reported a relaxivity value of 12.5 $mM^{-1}s^{-1}$ for the CNT-based contrast agent, compared to 5.5 $mM^{-1}s^{-1}$ for Gadovist® [185]. This enhanced relaxivity suggests that CNTs can provide improved imaging quality and sensitivity in MRI applications.

In another study, Wolski et al. designed a multimodal, pH-sensitive drug carrier using CNTs that could be visualized via MRI due to the presence of superparamagnetic nanoparticles. The study demonstrated that these constructs could effectively unload their drug cargo at the tumor site, while also enhancing MRI contrast. The superparamagnetic nanoparticles increased the proton transverse relaxation times, acting as effective MRI contrast agents [186]. This dual functionality of drug delivery and imaging is particularly advantageous in cancer therapy, where monitoring treatment response is crucial.

The functionalization of CNTs plays a critical role in their effectiveness as MRI contrast agents. For instance, Glória et al. explored the solubilization and characterization of MWCNTs for biomedical applications. They found that the adsorption of polymers significantly improved the dispersion of CNTs in biological media, enhancing their compatibility for use in MRI [187]. This improved solubilization is essential for ensuring that CNTs can circulate effectively in the bloodstream and reach target tissues.

The application of carbon nanotubes in MRI represents a significant advancement in imaging technology. Their unique properties, including enhanced relaxivity and the ability to be functionalized for targeted delivery, position CNTs as valuable tools in the field of medical imaging. Ongoing research into the optimization of CNTs for MRI will likely yield further improvements in imaging quality and specificity, ultimately benefiting patient care in oncology.

4.3.3. CNTs in Computed Tomography (CT)

In the field of computed tomography (CT), carbon nanotubes (CNTs) have attracted a lot of interest because of their special chemical and physical characteristics that potentially improve imaging capabilities. Recent research has examined a number of CNT applications in CT, with an emphasis on their usage as contrast agents and X-ray sources. This section summarizes the most recent research on CNTs in CT imaging, including particular studies, CNT types, and experimental outcomes [188–191]. Jo reported a study on optimizing image quality in a carbon nanotube (CNT)-based rectilinear Digital Tomosynthesis System (DTS). This system is explored as an alternative to traditional CT in External Beam Radiation Therapy (EBRT) for cancer treatment, aiming to reduce radiation exposure and acquisition time. The research highlights the importance of balancing image quality and computational efficiency for real-time patient positioning in radiotherapy [192].

Dillon et al. presented a novel hardware configuration using carbon nanotube (CNT) field emission source arrays for fast 3D X-ray imaging in radiotherapy. This technology aims to improve upon current CT imaging limitations, particularly for cancers affected by respiratory motion. Their simulation study uses a 4D patient phantom with an implanted tumor moving due to respiration, suggesting a focus on lung cancer imaging. The goal is to enable volumetric imaging before and during treatment delivery [193].

One of the most promising applications of CNTs in CT is their use as X-ray sources. Kim et al. developed a carbon nanotube emitter X-ray source aimed at improving the resolution of micro-computed tomography. Their research demonstrated that CNT-based X-ray sources could significantly reduce radiation exposure while maintaining high resolution. The study reported that the CNT emitter achieved a spatial resolution of 2.5 μm, which is a substantial improvement over traditional X-ray sources [189]. This advancement is crucial for applications requiring detailed imaging, such as in oncology, where precise tumor localization is essential [194]. In another study, Kim et al. further explored the development of a high-speed micro-computed tomography system based on a CNT emitter X-ray source. This system was designed to enhance imaging speed while maintaining image quality. The results indicated that the CNT-based system could achieve imaging speeds of up to 30 frames per second, which is significantly faster than conventional systems [191]. The

ability to capture high-speed images is particularly beneficial in dynamic imaging scenarios, such as monitoring tumor response to treatment.

Moreover, Zulkifli et al. examined the effects of CNTs on the flexural properties of carbon fiber/epoxy composites, indirectly suggesting that CNTs could enhance the mechanical properties of materials used in CT imaging systems [195]. While this study did not focus directly on CT imaging, it underscores the potential of CNTs to improve the structural integrity of imaging devices, which could lead to better imaging outcomes.

The application of carbon nanotubes in acoustic imaging represents a significant advancement in the field of cancer diagnostics. Studies have revealed that CNT-based ultrasound contrast agents can enhance imaging sensitivity and specificity, providing valuable tools for early cancer detection. As research continues to evolve, the potential for CNTs to revolutionize ultrasound imaging in oncology remains substantial.

5. Conclusions

Functionalized CNTs hold significant promise as versatile tools for advancing cancer diagnosis and imaging. The urgent global need for effective early cancer detection, highlighted by high incidence and mortality rates and substantial economic costs, underscores the importance of innovative diagnostic approaches. While advances in cancer treatment exist, early detection and imaging remain critical challenges that CNTs are poised to address.

The unique structural properties of CNTs, coupled with the ability to tailor their characteristics through various functionalization strategies (both covalent and non-covalent), enable enhanced biocompatibility, selectivity, and performance in biomedical applications. This review has explored the application of functionalized CNTs in diverse diagnostic modalities, including highly sensitive biosensors such as electrochemical, optical, and field-effect transistor (FET) sensors capable of detecting a wide range of cancer biomarkers with impressive detection limits across various cancer types. Furthermore, the utility of CNTs extends to enhancing cancer imaging techniques such as fluorescence imaging, magnetic resonance imaging (MRI), computed tomography (CT), and ultrasound imaging, often improving contrast, resolution, and targeting capabilities.

Despite these advancements, there is a continued need for the development of improved CNT-based diagnostic platforms and strategies to overcome the challenges associated with their widespread adoption in medical practice. Further research should focus on optimizing functionalization techniques, enhancing biocompatibility and long-term safety, and translating these promising findings into clinically viable tools for earlier and more accurate cancer diagnosis. Future direction in this field includes utilizing CNTs as carriers for testing cancer biomarkers and this necessitates robust diagnostic clinical trials to explore their full potential as safe, effective, and accurate diagnostic tools in Cancer diagnostics. The continued exploration of novel functionalization methods and their integration into diverse diagnostic and imaging modalities will undoubtedly pave the way for significant progress in mitigating the consequences of this global health concern.

Funding: This research received no external funding.

Institutional Review Board Statement: Not applicable.

Informed Consent Statement: Not applicable.

Data Availability Statement: No new data were created or analyzed in this study. Data sharing is not applicable to this article.

Acknowledgments: The authors would like to acknowledge the Research Office, the Library, and the Biological Sciences Department at CMU-Q for their support in publishing this work.

Conflicts of Interest: The authors declare no conflicts of interest.

References

1. Wu, Z.; Xia, F.; Lin, R. Global Burden of Cancer and Associated Risk Factors in 204 Countries and Territories, 1980–2021: A Systematic Analysis for the GBD 2021. *J. Hematol. Oncol.* **2024**, *17*, 119. [CrossRef] [PubMed]
2. Cancer Key Facts. Available online: https://www.who.int/Health-Topics/Cancer#tab=tab_1 (accessed on 9 April 2025).
3. Cancer Today. Available online: https://gco.iarc.who.int/today/ (accessed on 2 March 2025).
4. Cancer Tomorrow. Available online: https://gco.iarc.who.int/tomorrow/ (accessed on 2 March 2025).
5. Zhang, Z.; Wang, J.; Hou, L.; Zhu, D.; Xiao, H.-J.; Wang, K. Graphene/Carbohydrate Polymer Composites as Emerging Hybrid Materials in Tumor Therapy and Diagnosis. *Int. J. Biol. Macromol.* **2025**, *287*, 138621. [CrossRef] [PubMed]
6. Alshammari, M.M.; Almuhanna, A.; Alhiyafi, J. Mammography Image-Based Diagnosis of Breast Cancer Using Machine Learning: A Pilot Study. *Sensors* **2022**, *22*, 203. [CrossRef] [PubMed]
7. Bui, C.N.; Hong, S.; Suh, M.; Jun, J.K.; Jung, K.W.; Lim, M.C.; Choi, K.S. Effect of Pap Smear Screening on Cervical Cancer Stage at Diagnosis: Results from the Korean National Cancer Screening Program. *J. Gynecol. Oncol.* **2021**, *32*, e81. [CrossRef]
8. *Biosensors Based on Graphene, Graphene Oxide and Graphynes for Early Detection of Cancer*; Jain, P., Verma, C., Raman, A.P.S., Kumari, K., Singh, P., Eds.; CRC Press: Boca Raton, FL, USA, 2024; ISBN 978-1-00-349136-1.
9. Alwabel, S.A.M.; Alwadai, M.S.M.; AlQahtani, H.A.M.; Almutairi, F.S.B.; Almutairi, M.A.M.; Otaibi, F.S.J.A. Novel Drug Delivery Systems: Advancements And Challenges. *J. Popul. Ther. Clin. Pharmacol.* **2022**, *29*, 2573–2576. [CrossRef]
10. Bargahi, N.; Ghasemali, S.; Jahandar-Lashaki, S.; Nazari, A. Recent Advances for Cancer Detection and Treatment by Microfluidic Technology, Review and Update. *Biol. Proced. Online* **2022**, *24*, 5. [CrossRef] [PubMed]
11. Das, S.; Devireddy, R.; Gartia, M.R. Surface Plasmon Resonance (SPR) Sensor for Cancer Biomarker Detection. *Biosensors* **2023**, *13*, 396. [CrossRef]
12. Li, J.; Xu, L.; Zou, Y.; Li, Z. Self-Powered Sensors for Biomarker Detection. *Sens. Diagn.* **2023**, *2*, 1097–1122. [CrossRef]
13. Yu, S.-Q.; Li, P.; Li, H.-J.; Shang, L.-J.; Guo, R.; Sun, X.-M.; Ren, Q.-Q. Highly Sensitive Detection of Hydrogen Peroxide in Cancer Tissue Based on 3D Reduced Graphene Oxide–MXene–Multi-Walled Carbon Nanotubes Electrode. *Biosensors* **2024**, *14*, 261. [CrossRef]
14. Chandradoss, S.D.; Schirle, N.T.; Szczepaniak, M.; MacRae, I.J.; Joo, C. A Dynamic Search Process Underlies MicroRNA Targeting. *Cell* **2015**, *162*, 96–107. [CrossRef]
15. Chen, C. Identification of a Fully Human Antibody VH Domain Targeting Anaplastic Lymphoma Kinase (ALK) With Applications in ALK-Positive Solid Tumor Immunotherapy. *Antibodies* **2024**, *13*, 39. [CrossRef]
16. Kamazani, F.M.; Nematalahi, F.S.; Siadat, S.D.; Pornour, M.; Sheikhpour, M. A Success Targeted Nano Delivery to Lung Cancer Cells With Multi-Walled Carbon Nanotubes Conjugated to Bromocriptine. *Sci. Rep.* **2021**, *11*, 24419. [CrossRef] [PubMed]
17. Wang, L.; Wu, M.; Pan, Y.; Xie, D.; Hong, C.; Li, J.; Ma, X.; Xu, H.; Li, H.; Chen, T.; et al. Sequential Targeting Biomimetic Nano Platform for Enhanced Mild Photothermal Therapy and Chemotherapy of Tumor. *Comput. Struct. Biotechnol. J.* **2023**, *21*, 2780–2791. [CrossRef]
18. Bohunicky, B.; Mousa, S.A. Biosensors: The New Wave in Cancer Diagnosis. *Nanotechnol. Sci. Appl.* **2010**, *4*, 1–10. [CrossRef]
19. Gao, S.; Xu, B.; Sun, J.; Zhang, Z. Nanotechnological Advances in Cancer: Therapy a Comprehensive Review of Carbon Nanotube Applications. *Front. Bioeng. Biotechnol.* **2024**, *12*, 1351787. [CrossRef] [PubMed]
20. *Carbon Nanotubes*; Topics in applied physics; Dresselhaus, M.S., Dresselhaus, G., Avouris, P., Eds.; Springer: Berlin/Heidelberg, Germany, 2001; Volume 80, ISBN 978-3-540-41086-7.
21. Chadar, R.; Afzal, O.; Alqahtani, S.M.; Kesharwani, P. Carbon Nanotubes as an Emerging Nanocarrier for the Delivery of Doxorubicin for Improved Chemotherapy. *Colloids Surf. B Biointerfaces* **2021**, *208*, 112044. [CrossRef] [PubMed]
22. Elhissi, A.M.A.; Ahmed, W.; Hassan, I.U.; Dhanak, V.R.; D'Emanuele, A. Carbon Nanotubes in Cancer Therapy and Drug Delivery. *J. Drug Deliv.* **2012**, *2012*, 837327. [CrossRef]
23. Shabnum, S.S.; Siranjeevi, R.; Raj, C.K.; Nivetha, P.; Benazir, K. A Comprehensive Review on Recent Progress in Carbon Nanotubes for Biomedical Application. *Environ. Qual. Manag.* **2025**, *34*, e70040. [CrossRef]
24. Kumar, S.; Ansari, A.; Basu, M.; Ghosh, S.; Begam, S.; Ghosh, M.K. Carbon Nanotubes in Cancer Diagnosis and Treatment: Current Trends and Future Perspectives. *Adv. Ther.* **2025**, *8*, 2400283. [CrossRef]
25. Rahmanifar, E.; Saheb, V.; Yoosefian, M. Carbon Nanotube Coated with Tryptophan as a pH-Sensitive Nanocarrier in the Delivery and Smart Release of the Anticancer Drug Topotecan. *J. Mol. Liq.* **2025**, *419*, 126767. [CrossRef]
26. Contreras, L.; Villarroel, I.; Torres, C.; Rozas, R. Doxorubicin Encapsulation in Carbon Nanotubes Having Haeckelite or Stone–Wales Defects as Drug Carriers: A Molecular Dynamics Approach. *Molecules* **2021**, *26*, 1586. [CrossRef] [PubMed]
27. Papi, R.M.; Tasioulis, K.S.; Kechagioglou, P.V.; Papaioannou, M.A.; Andriotis, E.G.; Kyriakidis, D.A. Carbon Nanotube-Mediated Delivery of PTEN Variants: In Vitro Antitumor Activity in Breast Cancer Cells. *Molecules* **2024**, *29*, 2785. [CrossRef] [PubMed]

28. Al-Jamal, K.T.; Nunes, A.; Methven, L.; Ali-Boucetta, H.; Li, S.; Toma, F.M.; Herrero, M.A.; Al-Jamal, W.T.; ten Eikelder, H.M.M.; Foster, J.; et al. Degree of Chemical Functionalization of Carbon Nanotubes Determines Tissue Distribution and Excretion Profile. *Angew. Chem.* **2012**, *124*, 6495–6499. [CrossRef]
29. Dubey, R.; Dutta, D.; Sarkar, A.; Chattopadhyay, P. Functionalized Carbon Nanotubes: Synthesis, Properties and Applications in Water Purification, Drug Delivery, and Material and Biomedical Sciences. *Nanoscale Adv.* **2021**, *3*, 5722–5744. [CrossRef]
30. AbouAitah, K.; Abdelaziz, A.M.; Higazy, I.M.; Swiderska-Sroda, A.; Hassan, A.M.E.; Shaker, O.G.; Szałaj, U.; Stobinski, L.; Malolepszy, A.; Lojkowski, W. Functionalized Carbon Nanotubes for Delivery of Ferulic Acid and Diosgenin Anticancer Natural Agents. *ACS Appl. Bio Mater.* **2024**, *7*, 791–811. [CrossRef]
31. John, B.K.; John, N.; Mathew, J.; Mathew, B. Carbon Nanotubes for Bioimaging. In *Carbon Nanotubes for Biomedical Applications and Healthcare*; Apple Academic Press: Point Pleasant, NJ, USA, 2024; ISBN 978-1-00-339639-0.
32. Acharya, R.; Patil, T.V.; Dutta, S.D.; Lee, J.; Ganguly, K.; Kim, H.; Randhawa, A.; Lim, K.-T. Single-Walled Carbon Nanotube-Based Optical Nano/Biosensors for Biomedical Applications: Role in Bioimaging, Disease Diagnosis, and Biomarkers Detection. *Adv. Mater. Technol.* **2024**, *9*, 2400279. [CrossRef]
33. Chou, H.-T.; Wang, T.-P.; Lee, C.-Y.; Tai, N.-H.; Chang, H.-Y. Photothermal Effects of Multi-Walled Carbon Nanotubes on the Viability of BT-474 Cancer Cells. *Mater. Sci. Eng. C* **2013**, *33*, 989–995. [CrossRef]
34. Farbod, M.; Sharif, L.; Rezatofighi, S.E. Photothermal Performance of Carbon Nanotubes in the Visible and Near-Infrared Regions: Applications in Water Evaporation and Destroying Cancer Cells. *Colloid Polym. Sci.* **2025**, *303*, 25–31. [CrossRef]
35. Murmu, M.; Dey, D.; Murmu, N.C.; Banerjee, P. Carbon Nanotubes. In *Functionalized Carbon Nanotubes for Biomedical Applications*; John Wiley & Sons, Ltd.: Beverly, MA, USA, 2023; pp. 49–73, ISBN 978-1-119-90508-0.
36. Kamoun, E.A.; Elsabahy, M.; Mohamed Elbadry, A.M.; Abdelazim, E.B.; Mohsen, A.A.; Aleem, M.A.; Gao, H.; Eissa, N.G.; Elghamry, I.; Salim, S.A. Recent Progress of Polymer-Based Biosensors for Cancer Diagnostic Applications: Natural versus Synthetic Polymers. *ACS Omega* **2025**, *10*, 8816–8831. [CrossRef]
37. Chen, S.; Cao, Z.; Prettner, K.; Kuhn, M.; Yang, J.; Jiao, L.; Wang, Z.; Li, W.; Geldsetzer, P.; Bärnighausen, T.; et al. Estimates and Projections of the Global Economic Cost of 29 Cancers in 204 Countries and Territories From 2020 to 2050. *JAMA Oncol.* **2023**, *9*, 465. [CrossRef]
38. Yu, M.-F.; Lourie, O.; Dyer, M.J.; Moloni, K.; Kelly, T.F.; Ruoff, R.S. Strength and Breaking Mechanism of Multiwalled Carbon Nanotubes Under Tensile Load. *Science* **2000**, *287*, 637–640. [CrossRef] [PubMed]
39. Kataura, H.; Kumazawa, Y.; Maniwa, Y.; Umezu, I.; Suzuki, S.; Ohtsuka, Y.; Achiba, Y. Optical Properties of Single-Wall Carbon Nanotubes. *Synth. Met.* **1999**, *103*, 2555–2558. [CrossRef]
40. Issi, J.-P.; Langer, L.; Heremans, J.; Olk, C.H. Electronic Properties of Carbon Nanotubes: Experimental Results. *Carbon* **1995**, *33*, 941–948. [CrossRef]
41. Hone, J.; Llaguno, M.C.; Biercuk, M.J.; Johnson, A.T.; Batlogg, B.; Benes, Z.; Fischer, J.E. Thermal Properties of Carbon Nanotubes and Nanotube-Based Materials. *Appl. Phys. A Mater. Sci. Process.* **2002**, *74*, 339–343. [CrossRef]
42. Ebbesen, T.W.; Lezec, H.J.; Hiura, H.; Bennett, J.W.; Ghaemi, H.F.; Thio, T. Electrical Conductivity of Individual Carbon Nanotubes. *Nature* **1996**, *382*, 54–56. [CrossRef]
43. Raymundo-Piñero, E.; Cazorla-Amorós, D.; Linares-Solano, A.; Delpeux, S.; Frackowiak, E.; Szostak, K.; Béguin, F. High Surface Area Carbon Nanotubes Prepared by Chemical Activation. *Carbon* **2002**, *40*, 1614–1617. [CrossRef]
44. Iijima, S. Helical Microtubules of Graphitic Carbon. *Nature* **1991**, *354*, 56–58. [CrossRef]
45. Dresselhaus, M.S.; Dresselhaus, G.; Charlier, J.C.; Hernández, E. Electronic, Thermal and Mechanical Properties of Carbon Nanotubes. *Philos. Trans. R. Soc. London. Ser. A Math. Phys. Eng. Sci.* **2004**, *362*, 2065–2098. [CrossRef]
46. Abu Lila, A.S.; Bhattacharya, R.; Moin, A.; Hagbani, T.A.; Abdallah, M.H.; Danish Rizvi, S.M.; Khafagy, E.-S.; Hussain, T.; Gangadharappa, H.V. Dual Targeting Multiwalled Carbon Nanotubes for Improved Neratinib Delivery in Breast Cancer. *RSC Adv.* **2023**, *13*, 24309–24318. [CrossRef]
47. Li, R.; Bao, Z.; Wang, P.; Deng, Y.; Fan, J.; Zhu, X.; Xia, X.; Song, Y.; Yao, H.; Li, D. Gelatin-Functionalized Carbon Nanotubes Loaded With Cisplatin for Anti-Cancer Therapy. *Polymers* **2023**, *15*, 3333. [CrossRef]
48. Guo, Z.; Liu, X.; Lin, Y.; Sang, Z.; Chen, D. Hyaluronic Acid Modified Carbon Nanotubes Using for Photothermal Therapy by Promoting Apoptosis of Nasopharyngeal Carcinoma Cells. *Front. Bioeng. Biotechnol.* **2023**, *11*, 1229852. [CrossRef] [PubMed]
49. Mohammadi, A.; Hashemi, N.; Asghariha, Z.; Hosseini, M.S.; Danafar, H. SWCNTs functionalized with gold nanoradiosensitizers as radiosensitizers for enhanced radiotherapy in breast cancer. *Results Chem.* **2024**, *14*, 102113. [CrossRef]
50. Li, Z.; Xu, Y.; Li, S.; Liu, J.; Tang, N. Mechanism of Elemental Superdoping of Low-Dimensional Carbon Materials. *Chem. Mater.* **2024**, *36*, 8369–8377. [CrossRef]
51. Liu, Y.; Zhang, Y.; Wang, Z.; Lai, W.; Zhang, X.; Wang, X.; Liu, X. Investigation of the Dispersion Behavior of Fluorinated MWCNTs in Various Solvents. *Phys. Chem. Chem. Phys.* **2017**, *19*, 21565–21574. [CrossRef]
52. Raudsepp, R. Boron and Fluorine Co-Doped Graphene/Few-Walled Carbon Nanotube Composite as Highly Active Electrocatalyst for Oxygen Reduction Reaction. *Chemnanomat* **2024**, *10*, e202300546. [CrossRef]

53. Ahmad, Y.; Dubois, M.; Guerin, K.; Hamwi, A.; Flahaut, E. High Energy Density of Primary Lithium Batteries Working with Sub-Fluorinated Few Walled Carbon Nanotubes Cathode. *J. Alloys Compd.* **2017**, *726*, 852–859. [CrossRef]
54. Ami, T. Highly Fluorinated Nanospace in Porous Organic Salts With High Water Stability/Capability and Proton Conductivity. *Angew. Chem.* **2024**, *136*, e202407484. [CrossRef]
55. Uchiyama, H. Carrier Doping in Semiconducting Carbon Nanotubes With Fluorosumanenes. *J. Phys. Chem. C* **2024**, *128*, 17668–17673. [CrossRef]
56. Wang, D.; Peng, J.; Huang, Y.; Sun, L.; Liu, M.; Li, H.; Chao, M.; Gong, P.; Liu, Z.; You, J. Rational Construction of Fluorescence Turn-Off Fluorinated Carbon Fiber/Ag Composites and Their Anticancer and Antibacterial Activities. *ACS Appl. Bio Mater.* **2021**, *4*, 1749–1759. [CrossRef]
57. Uniyal, A.; Srivastava, G.; Sarkar, P.; Kumar, M.; Singh, S.; Taya, S.A.; Muduli, A.; Pal, A. Fluorinated Graphene and CNT-Based Surface Plasmon Resonance Sensor for Detecting the Viral Particles of SARS-CoV-2. *Phys. B Condens. Matter* **2023**, *669*, 415282. [CrossRef]
58. Yan, J.-Y. Mechanism of NCNTs Growth on Foamed Nickel and Thus-Prepared PS Hydrogenation High-Performance Carrier NCNTs@FN. *Langmuir* **2024**, *40*, 6786–6805. [CrossRef] [PubMed]
59. Zhao, W. Curvature-Switched Activity of Carbon Nanotube-Supported Single Atom Catalysts for the Hydrogen Evolution Reaction. *J. Mater. Chem. A* **2024**, *12*, 16476–16481. [CrossRef]
60. Tang, H.; Kojima, T.; Kazumi, K.; Fukami, K.; Sakaguchi, H. Platinum nanoparticles bonded with carbon nanotubes for high-performance ampere-level all-water splitting. *ACS Omega* **2024**, *9*, 21378–21387. [CrossRef]
61. Duraia, E.M. Efficient Eco-Friendly Synthesis of Carbon Nanotubes Over Graphite Nanosheets From Yellow Corn: A One-Step Green Approach. *Sci. Rep.* **2024**, *14*, 16405. [CrossRef] [PubMed]
62. Tomasini, M. Computational Insights Into the Regioselectivity of 1,3-Dipolar Cycloadditions Inside Carbon Nanotubes. *J. Phys. Chem. C* **2024**, *128*, 14961–14971. [CrossRef]
63. Pacholak, P. Ethynyl-Substituted Benzosiloxaboroles: The Role of C(π)$\cdots$B Interactions in Their Crystal Packing and Use in Cu(i)-Catalyzed 1,3-Dipolar Cycloaddition. *RSC Adv.* **2024**, *14*, 16069–16082. [CrossRef]
64. Rebelo, S.L.H.; Laia, C.A.; Szefczyk, M.; Guedes, A.; Silva, A.M.; Freire, C. Hybrid Zn-B-Aminoporphyrin–Carbon Nanotubes: Pyrrolidine and Direct Covalent Linkage Recognition, and Multiple-Photo Response. *Molecules* **2023**, *28*, 7438. [CrossRef]
65. Fukuura, S. Roles of Carbon Nanotube Confinement in Modulating Regioselectivity of 1,3-Dipolar Cycloadditions. *J. Phys. Chem. A* **2023**, *127*, 6962–6973. [CrossRef]
66. Ma, J.; Wang, G.; Ding, X.; Wang, F.; Zhu, C.; Rong, Y. Carbon-Based Nanomaterials as Drug Delivery Agents for Colorectal Cancer: Clinical Preface to Colorectal Cancer Citing Their Markers and Existing Theranostic Approaches. *ACS Omega* **2023**, *8*, 10656–10668. [CrossRef]
67. Ding, K.; Zhu, Y.; Lang, Y.; Zhu, L.; Zhang, T.-T.; Zhang, R.; Li, Q.; Xie, B.; Ding, L.; Shang, L.; et al. Multiwalled Carbon Nanotubes-Reprogrammed Macrophages Facilitate Breast Cancer Metastasis via NBR2/TBX1 Axis. *ACS Nano* **2024**, *18*, 11103–11119. [CrossRef]
68. Adamus-Grabicka, A.A.; Hikisz, P.; Sikora, J. Nanotechnology as a Promising Method in the Treatment of Skin Cancer. *Int. J. Mol. Sci.* **2024**, *25*, 2165. [CrossRef]
69. Zhang, G.; Fu, Y.; Xiang, J.; Guan, C.; Sang, Z.; Ding, C. Nickel-Catalyzed Cross-Coupling of Aryl Diazonium Salts with Aryl Bromides. *Org. Lett.* **2024**, *26*, 6687–6691. [CrossRef]
70. Han, H. 1,3-Dipolar Cycloaddition of Polycyclic Aromatic Azomethine Ylides and Alkynylbenziodoxoles for Synthesis of Functional Dibenzoullazines. *Chin. J. Chem.* **2024**, *42*, 1079–1083. [CrossRef]
71. Kvasovs, N.; Gevorgyan, V. Contemporary Methods for Generation of Aryl Radicals. *Chem. Soc. Rev.* **2021**, *50*, 2244–2259. [CrossRef] [PubMed]
72. Zhang, W.; Zhang, Z.; Zhang, Y. The Application of Carbon Nanotubes in Target Drug Delivery Systems for Cancer Therapies. *Nanoscale Res. Lett.* **2011**, *6*, 555. [CrossRef] [PubMed]
73. Alrushaid, N.; Khan, F.A.; Al-Suhaimi, E.A.; Elaissari, A. Nanotechnology in Cancer Diagnosis and Treatment. *Pharmaceutics* **2023**, *15*, 1025. [CrossRef]
74. Billon, J.; Omelchuk, A.; Shkirskiy, V.; Dabos-Seignon, S.; Alévêque, O.; Levillain, E.; Breton, T.; Gautier, C. An Innovative Method for Controlled Synthesis of Bicomponent Monolayer Films Obtained by Reduction of Diazonium. *Nanoscale* **2023**, *15*, 19213–19218. [CrossRef]
75. Hilmer, A.J.; McNicholas, T.P.; Lin, S.; Zhang, J.; Wang, Q.H.; Mendenhall, J.D.; Song, C.; Heller, D.A.; Barone, P.W.; Blankschtein, D.; et al. Role of Adsorbed Surfactant in the Reaction of Aryl Diazonium Salts With Single-Walled Carbon Nanotubes. *Langmuir* **2012**, *28*, 1309–1321. [CrossRef]
76. Talyzin, A.V.; Luzan, S.M.; Anoshkin, I.V.; Nasibulin, A.G.; Jiang, H.; Kauppinen, E.I.; Mikoushkin, V.M.; Shnitov, V.V.; Marchenko, D.; Noréus, D. Hydrogenation, Purification, and Unzipping of Carbon Nanotubes by Reaction With Molecular Hydrogen: Road to Graphane Nanoribbons. *ACS Nano* **2011**, *5*, 5132–5140. [CrossRef]

77. Bhowmick, R.; Rajasekaran, S.; Friebel, D.; Beasley, C.; Jiao, L.; Ogasawara, H.; Dai, H.; Clemens, B.M.; Nilsson, A. Hydrogen Spillover in Pt-Single-Walled Carbon Nanotube Composites: Formation of Stable C–H Bonds. *J. Am. Chem. Soc.* **2011**, *133*, 5580–5586. [CrossRef]
78. Larijani, M.M.; Safa, S. Increase of Hydrogen Storage Capacity of CNTs by Using Transition Metal, Metal Oxide-CNT Nanocomposites. *Acta Phys. Pol. A* **2014**, *126*, 732–736. [CrossRef]
79. Zhornik, E.V.; Baranova, L.A.; Emel'yanova, V.P.; Volotovsky, I.D. The Generation of Reactive Oxygen Species and Induction of Lipid Peroxidation in Human Lymphocytes Under the Influence of Carbon Nanotubes. In Proceedings of the 2010 International Kharkov Symposium on Physics and Engineering of Microwaves, Millimeter, and Submillimeter Waves, Kharkiv, Ukraine, Kharkiv, Ukraine, 21–26 June 2010. [CrossRef]
80. Szymański, T.; Kempa, M.; Giersig, M.; Rybka, J.D. Carbon Nanotubes Interference With Luminescence-Based Assays. *Materials* **2020**, *13*, 4270. [CrossRef]
81. Gu, X.; Qi, W.; Xu, X.; Sun, Z.; Zhang, L.; Liu, W.; Pan, X.; Su, D. Covalently Functionalized Carbon Nanotube Supported Pd Nanoparticles for Catalytic Reduction of 4-Nitrophenol. *Nanoscale* **2014**, *6*, 6609–6616. [CrossRef]
82. Bayazit, M.K.; Coleman, K.S. Probing the Selectivity of Azomethine Imine Cycloaddition to Single-Walled Carbon Nanotubes by Resonance Raman Spectroscopy. *Chem. Asian J.* **2012**, *7*, 2925–2930. [CrossRef]
83. Veerakumar, P.; Vinothkumar, V.; Chen, S.-M.; Sangili, A.; Lin, K.-C. Ultrafine Rhenium–Ruthenium Nanoparticles Decorated on Functionalized Carbon Nanotubes for the Simultaneous Determination of Antibiotic (Nitrofurantoin) and Anti-Testosterone (Flutamide) Drugs. *J. Mater. Chem. C* **2021**, *9*, 15949–15966. [CrossRef]
84. Safarkhani, M.; Moghaddam, S.S.; Taghavimandi, F.; Bagherzadeh, M.; Fatahi, Y.; Park, U.; Radmanesh, F.; Huh, Y.S.; Rabiee, N. Bioengineered Smart Nanocarriers for Breast Cancer Treatment: Adorned Carbon-Based Nanocomposites with Silver and Palladium Complexes for Efficient Drug Delivery. *ACS Omega* **2024**, *9*, 1183–1195. [CrossRef]
85. Saghatchi, F.; Mohseni-Dargah, M.; Akbari-Birgani, S.; Saghatchi, S.; Kaboudin, B. Cancer Therapy and Imaging Through Functionalized Carbon Nanotubes Decorated with Magnetite and Gold Nanoparticles as a Multimodal Tool. *Appl. Biochem. Biotechnol.* **2020**, *191*, 1280–1293. [CrossRef] [PubMed]
86. Yan, Y.; Liu, Z.; Pang, W.; Huang, S.; Deng, M.; Yao, J.; Huang, Q.; Jin, M.; Shui, L. Integrated Biosensor Array for Multiplex Biomarkers Cancer Diagnosis via in-Situ Self-Assembly Carbon Nanotubes with an Ordered Inverse-Opal Structure. *Biosens. Bioelectron.* **2024**, *262*, 116528. [CrossRef]
87. Mo, F.; Qiu, D.; Zhang, L.; Wang, J. Recent Development of Aryl Diazonium Chemistry for the Derivatization of Aromatic Compounds. *Chem. Rev.* **2021**, *121*, 5741–5829. [CrossRef]
88. Sonam; Shinde, V.N.; Kumar, A. KPF6-Mediated Esterification and Amidation of Carboxylic Acids. *J. Org. Chem.* **2022**, *87*, 2651–2661. [CrossRef]
89. Wu, Z.; Wang, Z.; Yu, F.; Thakkar, M.; Mitra, S. Variation in Chemical, Colloidal and Electrochemical Properties of Carbon Nanotubes with the Degree of Carboxylation. *J. Nanopart Res.* **2017**, *19*, 16. [CrossRef]
90. DanDan, W.; Luo, L.; Deng, D.; Gong, G.; Qin, J.; Cai, K.; Gu, Y.; Mei, Y. Electrochemical Immunosensor for the Determination of Nuclear Matrix Protein 22 in Urine Using Carboxylated MWCNTs and Zeolitic Imidazolate Framework Modified with AgNPs. *ACS Appl. Nano Mater.* **2023**, *6*, 18328–18336. [CrossRef]
91. Chattaraj, A.; Mishra, Y.; Aljabali, A.A.A.; Mishra, V. Development and Evaluation of Folic Acid Conjugated Curcumin-Loaded Functionalized Multiwalled Carbon Nanotubes for Enhanced Efficacy in Ovarian Cancer Treatment. *Carbon Trends* **2025**, *19*, 100464. [CrossRef]
92. Zuo, D. Highly Efficient Esterification of Carboxylic Acids With O–H Nucleophiles Through Acid/Iodide Cooperative Catalysis. *Org. Biomol. Chem.* **2024**, *22*, 6181–6188. [CrossRef]
93. Yu, P. Electrochemical Decarboxylative Cross-Coupling With Nucleophiles. *Chem. A Eur. J.* **2024**, *30*, e202402124. [CrossRef]
94. Naief, M.F.; Khalaf, Y.H.; Mohammed, A.M. Novel Photothermal Therapy Using Multi-Walled Carbon Nanotubes and Platinum Nanocomposite for Human Prostate Cancer PC3 Cell Line. *J. Organomet. Chem.* **2022**, *975*, 122422. [CrossRef]
95. Shi, J.; Ma, R.; Wang, L.; Zhang, J.; Liu, R.; Li, L.; Liu, Y.; Hou, L.; Yu, X.; Gao, J.; et al. The Application of Hyaluronic Acid-Derivatized Carbon Nanotubes in Hematoporphyrin Monomethyl Ether-Based Photodynamic Therapy for in Vivo and in Vitro Cancer Treatment. *Int. J. Nanomed.* **2013**, *8*, 2361–2373. [CrossRef]
96. Song, T. Electrospun Polyimide Nanofiber-based Separators Containing Carboxyl Groups for Lithium-ion Batteries. *J. Appl. Polym. Sci.* **2024**, *141*, e55721. [CrossRef]
97. Yang, E. Harnessing Coordination-Assisted Surface Functionalization for Ligand-Induced Growth of Ultrafine Metal Nanoparticles on MXene. *Adv. Funct. Mater.* **2024**, *34*, 2408444. [CrossRef]
98. Scaglione, N. Tailored Carbon Dioxide Capacity in Carboxylate-Based Ionic Liquids. *Faraday Discuss.* **2024**, *253*, 233–250. [CrossRef]
99. Briesemeister, M. PVC/CNT Electrospun Composites: Morphology and Thermal and Impedance Behavior. *Polymers* **2024**, *16*, 2867. [CrossRef] [PubMed]

100. Ngo, Q.P. The Mott–Schottky Co_2P/Co Heterocatalyst Encapsulated by N,p-Doped Graphene/Carbon Nanotubes as High-Efficiency Trifunctional Electrocatalysts for Cable-Type Flexible Zn–air Batteries and Water Splitting. *J. Mater. Chem. A* **2024**, *12*, 1185–1199. [CrossRef]
101. Tajima, T. Photocatalytic Ammonia Decomposition Using Dye-Encapsulated Single-Walled Carbon Nanotubes. *Catalysts* **2024**, *14*, 715. [CrossRef]
102. Wu, S.; Zhu, H.; Hong, L.; Nakashima, N.; Yang, C. Modulation for Redox States of Single-Walled Carbon Nanotubes: Effect of Wrapping Conjugated Polymers. *Chem. Asian J.* **2024**, *20*, e202400879. [CrossRef]
103. Das, S.; Roy, S.; Dinda, S.C.; Bose, A.; Mahapatra, C.; Basu, B.; Prajapati, B. Carbon Nanotubes in Brain Targeted Drug Delivery: A Comprehensive Review. *Results Chem.* **2025**, *15*, 102206. [CrossRef]
104. Niidome, Y.; Matsumoto, H.; Hamano, R.; Kato, K.; Fujigaya, T.; Shiraki, T. Polymer Wrapping State Changes at Defect Sites of Locally Functionalized Single-Walled Carbon Nanotubes. *J. Phys. Chem. C* **2024**, *128*, 5146–5155. [CrossRef]
105. Mal, S.; e Souza, L.D.; Allard, C.; David, C.; Blais-Ouellette, S.; Gaboury, L.; Tang, N.; Martel, R. Duplex Phenotype Detection and Targeting of Breast Cancer Cells Using Nanotube Nanoprobes and Raman Imaging. *ACS Appl. Bio Mater.* **2023**, *6*, 1173–1184. [CrossRef]
106. Minu, S. Dodecyl Surfactants Induced Crystalline Modifications in Polyamide-6 Nanofibers. *ACS Appl. Polym. Mater.* **2024**, *6*, 10891–10905. [CrossRef]
107. Gonçalves, M. Polydimethylsiloxane Surface Modification of Microfluidic Devices for Blood Plasma Separation. *Polymers* **2024**, *16*, 1416. [CrossRef]
108. Sui, N. Photoprogrammed Multifunctional Optoelectronic Synaptic Transistor Arrays Based on Photosensitive Polymer-Sorted Semiconducting Single-Walled Carbon Nanotubes for Image Recognition. *Adv. Sci.* **2024**, *11*, e2401794. [CrossRef]
109. Mousavi, S.M. Recent Advances in Bioactive Carbon Nanotubes Based on Polymer Composites for Biosensor Applications. *Chem. Biodivers.* **2024**, *21*, e202301288. [CrossRef] [PubMed]
110. da Silva, M.M. Shape-Memory Polymers Based on Carbon Nanotube Composites. *Micromachines* **2024**, *15*, 748. [CrossRef] [PubMed]
111. Wang, S.; Wu, Y.; Yang, M.; Sun, L.; Tao, Y.; Yang, C.-A. Sulfur-Containing Polymer/Carbon Nanotube Composite Cathode Materials for High-Energy Lithium–Sulfur Batteries. *New J. Chem.* **2024**, *48*, 621–630. [CrossRef]
112. Panahizadeh, V. Optimization of Impact Strength and Elastic Modulus of Polyamide-Based Nanocomposites: Using Particle Swarm Optimization Method. *J. Elastomers Plast.* **2024**, *56*, 244–261. [CrossRef]
113. Pietrzak, Ł. The Electromagnetic Shielding Properties of Biodegradable Carbon Nanotube–Polymer Composites. *Electronics* **2024**, *13*, 2169. [CrossRef]
114. Choi, H.R.; Kim, K. Theranostics for Triple-Negative Breast Cancer. *Diagnostics* **2023**, *13*, 272. [CrossRef]
115. Suleman, M.; Murshed, A.; Imran, K.; Khan, A.; Ali, Z.; Albekairi, N.A.; Wei, D.; Yassine, H.M.; Crovella, S. Abrogation of ORF8–IRF3 Binding Interface With Carbon Nanotube Derivatives to Rescue the Host Immune System Against SARS-CoV-2 by Using Molecular Screening and Simulation Approaches. *BMC Chem.* **2024**, *18*, 99. [CrossRef]
116. Rida, J.F. The Employment of Carbon Nanotubes in Biomedical Applications. *Scalable Comput. Pract. Exp.* **2024**, *25*, 4283–4300. [CrossRef]
117. Saini, S.; Bhattacharjee, A.K.; Gouda, G.M. Switching Behavior of the Composite Low Dimensional Structural Hybrids of Carbon After UV Exposure. In Proceedings of the Iop Conference Series Materials Science and Engineering, Mangalore, India, 21–23 September 2024. [CrossRef]
118. Thakur, C.K.; Martins, F.G.; Karthikeyan, C.; Bhal, S.; Kundu, C.N.; Hari Moorthy, N.S.; Sousa, S.F. In Silico-Guided Discovery and in Vitro Validation of Novel Sugar-Tethered Lysinated Carbon Nanotubes for Targeted Drug Delivery of Doxorubicin. *J. Mol. Model.* **2024**, *30*, 261. [CrossRef]
119. Pandey, R.P.; Dhiman, R.; Bazad, N.; Mukerjee, R.; Vidić, J.; Leal, É.; Raj, V.S.; Chang, C.-M. Enhancing Breast Cancer Therapy: Nanocarrier-Based Targeted Drug Delivery. *Preprints* **2023**. [CrossRef]
120. Son, K.H.; Hong, J.H.; Lee, J.W. Carbon Nanotubes as Cancer Therapeutic Carriers and Mediators. *Int. J. Nanomed.* **2016**, *11*, 5163–5185. [CrossRef] [PubMed]
121. Svobodova, M.; Bunka, D.H.J.; Nadal, P.; Stockley, P.G.; O'Sullivan, C.K. Selection of 2′F-Modified RNA Aptamers against Prostate-Specific Antigen and Their Evaluation for Diagnostic and Therapeutic Applications. *Anal. Bioanal. Chem.* **2013**, *405*, 9149–9157. [CrossRef]
122. Alidori, S.; Asqiriba, K.; Londero, P.; Bergkvist, M.; Leona, M.; Scheinberg, D.A.; McDevitt, M.R. Deploying RNA and DNA with Functionalized Carbon Nanotubes. *J. Phys. Chem. C* **2013**, *117*, 5982–5992. [CrossRef]
123. Mahor, A.; Singh, P.P.; Bharadwaj, P.; Sharma, N.; Yadav, S.; Rosenholm, J.M.; Bansal, K.K. Carbon-Based Nanomaterials for Delivery of Biologicals and Therapeutics: A Cutting-Edge Technology. *C* **2021**, *7*, 19. [CrossRef]
124. Cygert, S.; Pastuszak, K.; Górski, F.; Sieczczyński, M.; Juszczyk, P.; Rutkowski, A.; Lewalski, S.; Różański, R.; Jopek, M.A.; Jassem, J.; et al. Platelet-Based Liquid Biopsies Through the Lens of Machine Learning. *Cancers* **2023**, *15*, 2336. [CrossRef] [PubMed]

125. Ji, S.; Liu, C.; Zhang, B.; Yang, F.; Xu, J.; Long, J.; Jin, C.; Fu, D.; Ni, Q.; Yu, X. Carbon Nanotubes in Cancer Diagnosis and Therapy. *Biochim. Biophys. Acta BBA Rev. Cancer* **2010**, *1806*, 29–35. [CrossRef] [PubMed]
126. Jaishree, V.; Gupta, P.D. Nanotechnology: A Revolution in Cancer Diagnosis. *Ind. J. Clin. Biochem.* **2012**, *27*, 214–220. [CrossRef]
127. Huang, S.; Li, H.; Yang, M.; Liu, X.; Fang, Y.; Xiao, Q.; Zhang, Y. MX/MWCNTs Composite Material Aids New Strategy for HBV-DNA Electrochemical Biosensor: Achieving Multi-Level Signal Amplification and Unlabeled Detection. *Adv. Compos. Hybrid. Mater.* **2025**, *8*, 127. [CrossRef]
128. Surana, K.; Ahire, E.; Aher, P.; Laddha, U.; Talele, S.; Mahajan, S.; Kshirsagar, S.; Gajbhiye, S. Role of Carbon Nanotube in Biosensor Developments. In *Carbon Nanotubes for Biomedical Applications and Healthcare*; Apple Academic Press: Point Pleasant, NJ, USA, 2024; ISBN 978-1-00-339639-0.
129. Nagaraju, K.; Reddy, R.; Reddy, N. A Review on Protein Functionalized Carbon Nanotubes. *J. Appl. Biomater. Funct. Mater.* **2015**, *13*, 301–312. [CrossRef]
130. Li, R.; Wu, R.; Zhao, L.; Qin, H.; Wu, J.; Zhang, J.; Bao, R.; Zou, H. In Vivo Detection of Magnetic Labeled Oxidized Multi-Walled Carbon Nanotubes by Magnetic Resonance Imaging. *Nanotechnology* **2014**, *25*, 495102. [CrossRef]
131. Li, X.; Fan, Y.; Watari, F. Current Investigations into Carbon Nanotubes for Biomedical Application. *Biomed. Mater.* **2010**, *5*, 022001. [CrossRef] [PubMed]
132. Meredith, J.R. Biomedical Applications of Carbon-Nanotube Composites. *Front. Biosci.* **2013**, *5*, 610–621. [CrossRef]
133. Singh, R.; Kumar, S. Cancer Targeting and Diagnosis: Recent Trends with Carbon Nanotubes. *Nanomaterials* **2022**, *12*, 2283. [CrossRef] [PubMed]
134. Simon, J.; Flahaut, E.; Golzio, M. Overview of Carbon Nanotubes for Biomedical Applications. *Materials* **2019**, *12*, 624. [CrossRef]
135. Jampilek, J.; Kralova, K. Advances in Drug Delivery Nanosystems Using Graphene-Based Materials and Carbon Nanotubes. *Materials* **2021**, *14*, 1059. [CrossRef] [PubMed]
136. Augustine, S.; Singh, J.; Srivastava, M.; Sharma, M.; Das, A.; Malhotra, B.D. Recent Advances in Carbon Based Nanosystems for Cancer Theranostics. *Biomater. Sci.* **2017**, *5*, 901–952. [CrossRef]
137. Sinha, A.; Dhanjai; Jain, R.; Zhao, H.; Karolia, P.; Jadon, N. Voltammetric Sensing Based on the Use of Advanced Carbonaceous Nanomaterials: A Review. *Microchim. Acta* **2018**, *185*, 89. [CrossRef]
138. Zhou, Y.; Fang, Y.; Ramasamy, R. Non-Covalent Functionalization of Carbon Nanotubes for Electrochemical Biosensor Development. *Sensors* **2019**, *19*, 392. [CrossRef]
139. Tîlmaciu, C.-M.; Morris, M.C. Carbon Nanotube Biosensors. *Front. Chem.* **2015**, *3*, 59. [CrossRef]
140. Ding, S.; Cargill, A.; Das, S.; Medintz, I.; Claussen, J. Biosensing with Förster Resonance Energy Transfer Coupling between Fluorophores and Nanocarbon Allotropes. *Sensors* **2015**, *15*, 14766–14787. [CrossRef]
141. Gillen, A.J.; Boghossian, A.A. Non-Covalent Methods of Engineering Optical Sensors Based on Single-Walled Carbon Nanotubes. *Front. Chem.* **2019**, *7*, 612. [CrossRef] [PubMed]
142. Chik, M.W.; Hussain, Z.; Zulkefeli, M.; Tripathy, M.; Kumar, S.; Majeed, A.B.A.; Byrappa, K. Polymer-Wrapped Single-Walled Carbon Nanotubes: A Transformation toward Better Applications in Healthcare. *Drug Deliv. Transl. Res.* **2019**, *9*, 578–594. [CrossRef] [PubMed]
143. Hwang, H.S.; Jeong, J.W.; Kim, Y.A.; Chang, M. Carbon Nanomaterials as Versatile Platforms for Biosensing Applications. *Micromachines* **2020**, *11*, 814. [CrossRef] [PubMed]
144. Gao, J.; He, S.; Nag, A.; Wong, J.W.C. A Review of the Use of Carbon Nanotubes and Graphene-Based Sensors for the Detection of Aflatoxin M1 Compounds in Milk. *Sensors* **2021**, *21*, 3602. [CrossRef]
145. Pan, M.; Yin, Z.; Liu, K.; Du, X.; Liu, H.; Wang, S. Carbon-Based Nanomaterials in Sensors for Food Safety. *Nanomaterials* **2019**, *9*, 1330. [CrossRef]
146. Ahmad, I.; Sead, F.F.; Kanjariya, P.; Kumar, A.; Rajivm, A.; Shankhyan, A.; Jaidka, S.; Kumar, H.; Aminov, Z. Nanomaterial Sensors for Enhanced Detection of Serotonin. *Clin. Chim. Acta* **2025**, *569*, 120160. [CrossRef]
147. Govindasamy, M.; Chen, S.-M.; Mani, V.; Devasenathipathy, R.; Umamaheswari, R.; Joseph Santhanaraj, K.; Sathiyan, A. Molybdenum Disulfide Nanosheets Coated Multiwalled Carbon Nanotubes Composite for Highly Sensitive Determination of Chloramphenicol in Food Samples Milk, Honey and Powdered Milk. *J. Colloid Interface Sci.* **2017**, *485*, 129–136. [CrossRef]
148. Yari, A.; Shams, A. Silver-Filled MWCNT Nanocomposite as a Sensing Element for Voltammetric Determination of Sulfamethoxazole. *Anal. Chim. Acta* **2018**, *1039*, 51–58. [CrossRef]
149. An, J.; Zhang, M.; Fu, Y.; Zhang, Q.; Si, Y.; Zhang, Y.; Fang, Y.; Zhang, D. Emerging Electrochemical Biosensors for Lung Cancer-Associated Protein Biomarker and miRNA Detection. *Int. J. Biol. Macromol.* **2024**, *280*, 135972. [CrossRef]
150. Zheng, R.; Wu, A.; Li, J.; Tang, Z.; Zhang, J.; Zhang, M.; Wei, Z. Progress and Outlook on Electrochemical Sensing of Lung Cancer Biomarkers. *Molecules* **2024**, *29*, 3156. [CrossRef]
151. Noreen, S.; Ishaq, I.; Saleem, M.H.; Ali, B.; Muhammad, A.; Syed, M.A.; Iqbal, J. Electrochemical Biosensing in Oncology: A Review Advancements and Prospects for Cancer Diagnosis. *Cancer Biol. Ther.* **2025**, *26*, 2475581. [CrossRef] [PubMed]

152. Shankar, S.; Kumar, Y.; Kumar, N.; Yadav, B.K.; Sharma, N.; Chandra, R.; Kumar, S. Nanoengineered Multiwalled Carbon Nanotube for Lung Cancer Diagnosis. *J. Mol. Struct.* **2025**, *1320*, 139629. [CrossRef]
153. Bhattacharjee, S.; George, M.; Neppolian, B.; Das, J. Electrochemical Detection of Non-Small Cell Lung Cancer (NSCLC) Mir-223 Biomarker Employing Gold/MWCNT Nanocomposite–Based Sandwich Platform. *J. Solid State Electrochem.* **2025**, *29*, 669–680. [CrossRef]
154. Zhang, R.; Rejeeth, C.; Xu, W.; Zhu, C.; Liu, X.; Wan, J.; Jiang, M.; Qian, K. Label-Free Electrochemical Sensor for CD44 by Ligand-Protein Interaction. *Anal. Chem.* **2019**, *91*, 7078–7085. [CrossRef] [PubMed]
155. Kim, N.; Bae, M.; Cho, E.; Kim, K.S.; Lee, J.-H. Plasmonic Biosensors in Cancer-Associated miRNA Detection. *Biosensors* **2025**, *15*, 165. [CrossRef]
156. Saadh, M.J.; Saeed, T.N.; Alfarttoosi, K.H.; Sanghvi, G.; Roopashree, R.; Thakur, V.; Lakshmi, L.; Aminov, Z.; Taher, W.M.; Alwan, M.; et al. Plasmonic Nanoparticles: Enhancing Early Breast Cancer Detection Through Biosensors. *Plasmonics* **2025**, *20*, 1–18. [CrossRef]
157. Karki, B.; Pal, A.; Dhiman, G.; Ahmed, M.Z. Ultra-Sensitive Early Detection of Colorectal Cancer Using Surface Plasmon Resonance Sensor: Theoretical Analysis. *Microchim. Acta* **2025**, *192*, 126. [CrossRef]
158. Wu, H.; Zhang, G.; Yang, X. Electrochemical Immunosensor Based on Fe3O4/MWCNTs-COOH/AuNPs Nanocomposites for Trace Liver Cancer Marker Alpha-Fetoprotein Detection. *Talanta* **2023**, *259*, 124492. [CrossRef]
159. Xu, S.; Zhao, W.; Lin, G.; Wu, Q.; Xu, M.; Huang, X.; Luo, J.; Zhu, Y.; Liu, X. Long Conducting and Water-Compatible Polymer/Carbon Nanotubes Nanocomposite with "Beads-on-a-String" Structure as a Highly Effective Electrochemical Sensing Material. *ACS Sustain. Chem. Eng.* **2019**, *7*, 3556–3566. [CrossRef]
160. Makableh, Y.; Athamneh, T.; Ajlouni, M.; Hijazi, S.; Alnaimi, A. Enhanced Response and Selective Gold Nanoparticles/Carbon Nanotubes Biosensor for the Early Detection of HER2 Biomarker. *Sens. Actuators Rep.* **2023**, *5*, 100158. [CrossRef]
161. Kim, J.P.; Lee, B.Y.; Lee, J.; Hong, S.; Sim, S.J. Enhancement of Sensitivity and Specificity by Surface Modification of Carbon Nanotubes in Diagnosis of Prostate Cancer Based on Carbon Nanotube Field Effect Transistors. *Biosens. Bioelectron.* **2009**, *24*, 3372–3378. [CrossRef] [PubMed]
162. Choi, Y.; Jeong, J.-Y.; Hong, S. Highly Sensitive Real-Time Monitoring of Adenosine Receptor Activities in Nonsmall Cell Lung Cancer Cells Using Carbon Nanotube Field-Effect Transistors. *ACS Appl. Mater. Interfaces* **2024**, *16*, 2101–2109. [CrossRef]
163. Zhang, W.; Luo, Y.; Tao, J.; Liu, G.; Li, B.; Teng, Y.; Xu, J.; Feng, L.; You, Z. Miniaturized and Portable Device for Noninvasive, Ultrasensitive and Point-of-Care Diagnosis by Engineered Metal-Carbide-Based Field Effect Transistor. *Chem. Eng. J.* **2025**, *506*, 160264. [CrossRef]
164. Li, L.; Liu, X.; Wei, T.; Wang, K.; Zhao, Z.; Cao, J.; Liu, Y.; Zhang, Z. Carbon Nanotube Field-Effect Transistor Biosensor with an Enlarged Gate Area for Ultra-Sensitive Detection of a Lung Cancer Biomarker. *ACS Appl. Mater. Interfaces* **2023**, *15*, 27299–27306. [CrossRef]
165. Liu, P.; Liu, Y.; Cai, B.; Li, J.; Zhang, G. Probe-Screened Carbon Nanotube Field-Effect Transistor Biosensor to Enhance Breast Cancer-Related Gene Assay. In Proceedings of the SPIE Third International Conference on Biomedical and Intelligent Systems (IC-BIS 2024), Nanchang, China, 26–28 April 2024; Volume 13208, pp. 26–35.
166. Li, T.; Liang, Y.; Li, J.; Yu, Y.; Xiao, M.-M.; Ni, W.; Zhang, Z.; Zhang, G.-J. Carbon Nanotube Field-Effect Transistor Biosensor for Ultrasensitive and Label-Free Detection of Breast Cancer Exosomal miRNA21. *Anal. Chem.* **2021**, *93*, 15501–15507. [CrossRef] [PubMed]
167. Liu, W.; Wang, X.; Dong, B.; Liu, Y.; Wei, D. Enzymatic Cascade Reactors on Carbon Nanotube Transistor Detecting Trace Prostate Cancer Biomarker. *Biosens. Bioelectron.* **2024**, *263*, 116603. [CrossRef]
168. Murshid, N.; Keogh, D.; Kitaev, V. Optimized Synthetic Protocols for Preparation of Versatile Plasmonic Platform Based on Silver Nanoparticles with Pentagonal Symmetries. *Part. Part. Syst. Charact.* **2014**, *31*, 178–189. [CrossRef]
169. Cathcart, N.; Murshid, N.; Campbell, P.; Kitaev, V. Selective Plasmonic Sensing and Highly Ordered Metallodielectrics via Encapsulation of Plasmonic Metal Nanoparticles with Metal Oxides. *ACS Appl. Nano Mater.* **2018**, *1*, 6514–6524. [CrossRef]
170. Ahmed Taha, B.; Kadhim, A.C.; Addie, A.J.; Haider, A.J.; Azzahrani, A.S.; Raizada, P.; Rustagi, S.; Chaudhary, V.; Arsad, N. Advancing Cancer Diagnostics through Multifaceted Optical Biosensors Supported by Nanomaterials and Artificial Intelligence: A Panoramic Outlook. *Microchem. J.* **2024**, *205*, 111307. [CrossRef]
171. Chen, C.; Wang, J. Optical Biosensors: An Exhaustive and Comprehensive Review. *Analyst* **2020**, *145*, 1605–1628. [CrossRef]
172. Špringer, T.; Bocková, M.; Slabý, J.; Sohrabi, F.; Čapková, M.; Homola, J. Surface Plasmon Resonance Biosensors and Their Medical Applications. *Biosens. Bioelectron.* **2025**, *278*, 117308. [CrossRef] [PubMed]
173. Kala, K.; Kumar, U.S.; Devi, K.Y.; Kapali, B.S.C.; Devi, N.B. Optical Biosensor Manufacturing for Chronic Lymphocytic Leukemia Biomarker Detection with-Walled Carbon Nano Tubes-Based Multi Electrodes. *Surf. Interfaces* **2023**, *42*, 103371. [CrossRef]
174. Ackermann, J.; Metternich, J.T.; Herbertz, S.; Kruss, S. Biosensing with Fluorescent Carbon Nanotubes. *Angew. Chem. Int. Ed.* **2022**, *61*, e202112372. [CrossRef]

175. Kruss, S.; Hilmer, A.J.; Zhang, J.; Reuel, N.F.; Mu, B.; Strano, M.S. Carbon Nanotubes as Optical Biomedical Sensors. *Adv. Drug Deliv. Rev.* **2013**, *65*, 1933–1950. [CrossRef]
176. Cohen, Z.; Williams, R.M. Single-Walled Carbon Nanotubes as Optical Transducers for Nanobiosensors In Vivo. *ACS Nano* **2024**, *18*, 35164–35181. [CrossRef] [PubMed]
177. Zhang, M.; Wang, W.; Wu, F.; Yuan, P.; Chi, C.; Zhou, N. Magnetic and Fluorescent Carbon Nanotubes for Dual Modal Imaging and Photothermal and Chemo-Therapy of Cancer Cells in Living Mice. *Carbon* **2017**, *123*, 70–83. [CrossRef]
178. Ghasemlou, M.; Pn, N.; Alexander, K.; Zavabeti, A.; Sherrell, P.C.; Ivanova, E.P.; Adhikari, B.; Naebe, M.; Bhargava, S.K. Fluorescent Nanocarbons: From Synthesis and Structure to Cancer Imaging and Therapy. *Adv. Mater.* **2024**, *36*, 2312474. [CrossRef]
179. Zhang, Z.; Yuan, Y.; Xue, Y.; Zhang, W.; Sun, X.; Xu, X.; Liu, C. Nanomaterials for Ultrasound Imaging- Guided Sonodynamic Therapy. *Technol. Cancer Res. Treat.* **2024**, *23*, 15330338241263197. [CrossRef]
180. Hendler-Neumark, A.; Wulf, V.; Bisker, G. In Vivo Imaging of Fluorescent Single-Walled Carbon Nanotubes within C. *elegans Nematodes Near-Infrared Window. Mater. Today Bio* **2021**, *12*, 100175. [CrossRef]
181. Kojima, K.; Iizumi, Y.; Zhang, M.; Okazaki, T. Streptavidin-Conjugated Oxygen-Doped Single-Walled Carbon Nanotubes as Near-Infrared Labels for Immunoassays. *Langmuir* **2022**, *38*, 1509–1513. [CrossRef]
182. Wu, J.; Zeng, X.; Wang, L.; Zhang, J.; Cui, S.; Ma, Z.; Pan, R.; Liu, C.; Kong, D.; Song, J.; et al. Embedding Carbon Nanotubes in Artificial Cells Enhances Probe Transfer. *Adv. Mater.* **2025**, *37*, 2418271. [CrossRef] [PubMed]
183. Chen, M.; Qi, X.; Zhang, W.; Yang, N.; Yang, D.; Wang, Y.; Zhang, L.; Yang, W.; Huang, L.; Zhang, M.; et al. Self-Photoluminescence of Unzipped Multi-Walled Carbon Nanotubes. *Nanomaterials* **2021**, *11*, 1632. [CrossRef] [PubMed]
184. Mandal, A.K.; Wu, X.; Ferreira, J.S.; Kim, M.; Powell, L.R.; Kwon, H.; Groc, L.; Wang, Y.; Cognet, L. Fluorescent Sp^3 Defect-Tailored Carbon Nanotubes Enable NIR-II Single Particle Imaging in Live Brain Slices at Ultra-Low Excitation Doses. *Sci. Rep.* **2019**, *10*, 5286. [CrossRef] [PubMed]
185. Mehri-Kakavand, G.; Hasanzadeh, H.; Jahanbakhsh, R.; Abdollahi, M.; Nasr, R.; Bitarafan-Rajabi, A.; Jadidi, M.; Darbandi-Azar, A.; Emadi, A. Gdn3+@CNTs-PEG versus Gadovist®: In Vitro Assay. *Oman Med. J.* **2019**, *34*, 147–155. [CrossRef]
186. Wolski, P.; Nieszporek, K.; Panczyk, T. Multimodal, pH Sensitive, and Magnetically Assisted Carrier of Doxorubicin Designed and Analyzed by Means of Computer Simulations. *Langmuir* **2018**, *34*, 2543–2550. [CrossRef]
187. Glória, J.; Brito, W.; Gandarilla, A.; Larrude, D.; Carlos, J.; Araújo, F.; Almeida, M.E.; Manzato, L.; Mariúba, L.A.M. Solubilization, Characterization, and Protein Coupling Analysis to Multiwalled Carbon Nanotubes. *High Perform. Polym.* **2021**, *33*, 338–344. [CrossRef]
188. Aher, P.; Surana, K.; Ahire, E.; Talele, S.; Talele, G.; Mahajan, S.; Kshirsagar, S. Carbon Nanotube: A Promising Role in Biomedical Imaging. In *Carbon Nanotubes for Biomedical Applications and Healthcare*; Apple Academic Press: Point Pleasant, NJ, USA, 2024; ISBN 978-1-00-339639-0.
189. Kim, W.; Ahn, J.S.; Ryu, J. Carbon Nanotube Emitter X-Ray Source for High-Resolution Micro-Computed Tomography. In *The Medical Imaging 2023: Physics of Medical Imaging*; Fahrig, R., Sabol, J.M., Yu, L., Eds.; SPIE: San Diego, CA, USA, 2023; p. 177.
190. Puett, C.; Inscoe, C.; Hartman, A.; Calliste, J.; Franceschi, D.K.; Lu, J.; Zhou, O.; Lee, Y.Z. An Update on Carbon Nanotube-Enabled X-Ray Sources for Biomedical Imaging. *WIREs Nanomed. Nanobiotechnol.* **2018**, *10*, e1475. [CrossRef]
191. Kim, W.; Jung, J.; Rajpoot, S.; Chung, W.-K.; Ahn, J.S.; Lee, B.-N.; Ryu, J. Development of High-Speed Micro Computed Tomography System Based on Carbon Nanotube Emitter x-Ray Source. In *The Medical Imaging 2022: Physics of Medical Imaging*; Zhao, W., Yu, L., Eds.; SPIE: San Diego, CA, US, 2022; p. 103.
192. Jo, B. Optimizing Image Quality in Carbon Nanotube-Based Rectilinear Digital Tomosynthesis System via Projection Number Variation. *J. Magn.* **2024**, *29*, 480–486. [CrossRef]
193. Dillon, O.; Reynolds, T.; O'Brien, R.T. X-Ray Source Arrays for Volumetric Imaging during Radiotherapy Treatment. *Sci. Rep.* **2023**, *13*, 9776. [CrossRef]
194. Choi, J.; Lee, H.; Jang, J.; Sharma, M.B.; Jung, J.; Yeo, S.J.; Kim, S.H.; Kong, M.; Lee, S.H.; Ryu, J. Innovative CNT X-Ray Source-Based 3D Hemispherical Multi-Beam Tomosynthesis for Medical Imaging. In *The Medical Imaging 2024: Physics of Medical Imaging*; Fahrig, R., Sabol, J.M., Li, K., Eds.; SPIE: San Diego, CA, USA, 2024; p. 143.
195. Zulkifli, N.A.; Ismail, N.H.; Jaafar, M.; Othman, A.R. Effect of Carbon Nanotubes on the Flexural Properties and Flammability of Carbon Fibre/Epoxy Multi-scale Composites. *Mater. Werkst* **2022**, *53*, 1544–1550. [CrossRef]

Disclaimer/Publisher's Note: The statements, opinions and data contained in all publications are solely those of the individual author(s) and contributor(s) and not of MDPI and/or the editor(s). MDPI and/or the editor(s) disclaim responsibility for any injury to people or property resulting from any ideas, methods, instructions or products referred to in the content.

molecules

MDPI

Review

Nanoparticles for Drug Delivery: Design, Mechanisms, and Clinical Translation

Subin Antony Jose, Benjamin Crutchfield, Mario Caballero, Eadrian Carreon, Ian Davis and Pradeep L. Menezes *

Department of Mechanical Engineering, University of Nevada, Reno, NV 89557, USA; subinj@unr.edu (S.A.J.); eadrianc@unr.edu (E.C.); iandavis@unr.edu (I.D.)
* Correspondence: pmenezes@unr.edu

Abstract

Nanoparticle-based drug delivery systems have become an important component of modern nanomedicine, enabling improved drug protection, controlled release, targeted delivery, and the modulation of pharmacokinetic behavior. Their therapeutic performance is governed by physicochemical properties such as size, shape, surface chemistry, and material composition, which influence biological interactions, biodistribution, cellular uptake, and clearance. This review examines major nanoparticle platforms, including polymeric, lipid-based, inorganic, carbon-based, and hybrid systems, together with passive and active targeting and endogenous and externally triggered release strategies. Current and emerging applications in oncology, infectious diseases, central nervous system disorders, gene therapy, and vaccines are discussed alongside theranostic and combination-delivery approaches. Particular emphasis is placed on computational modeling, artificial intelligence, and digital twins for formulation optimization and personalized nanomedicine. Key barriers to clinical translation, including manufacturing scalability, biological variability, limitations of EPR-mediated targeting, regulatory standardization, and long-term safety, are critically evaluated. Finally, emerging directions in sustainable nanomanufacturing and biomimetic delivery are discussed. By integrating biological mechanisms with computational, manufacturing, regulatory, and clinical considerations, this review provides a translational perspective on advancing nanoparticle drug-delivery systems from laboratory development toward clinical implementation.

Keywords: nanoparticles; drug delivery; nanomedicine; polymeric nanoparticles; clinical translation; artificial intelligence; green nanomanufacturing

1. Introduction

1.1. From Conventional Systems to Nanomedicine: Needs and Opportunities

The development of nanomedicine has been driven by the accumulating limitations of conventional drug delivery approaches, such as oral tablets, capsules, and parenteral injections, which were adequate for small-molecule pharmaceuticals but are proving increasingly insufficient for the complex, fragile, and highly potent therapeutic agents that dominate modern pipelines. Standard dosage forms suffer from poor aqueous solubility, rapid systemic clearance, nonspecific biodistribution, and resulting off-target toxicity, which reduces therapeutic index and treatment tolerability [1]. In oncology, cardiovascular diseases, and neurological disorders, these limitations are particularly consequential. Drugs must reach a localized disease site at therapeutic concentrations while sparing surrounding healthy tissue, a spatial discrimination that conventional formulations cannot achieve. The

progressive increase in the molecular complexity of biologics, nucleic acid therapeutics, and precision oncology agents has further widened the gap between drug potency and delivery capability, as many of these agents are inherently unstable in biological fluids, membrane-impermeable, or rapidly degraded before reaching the target cells [2,3].

Compared with conventional pharmaceutical formulations, nanoparticle-based delivery systems can provide additional control over drug solubility, protection from premature degradation, pharmacokinetics, biodistribution, and site-specific or stimulus-responsive release. These advantages are particularly relevant for poorly soluble drugs and biologics such as proteins and nucleic acids; however, they are accompanied by greater formulation complexity, manufacturing and characterization requirements, potential nanomaterial-specific safety concerns, and additional regulatory challenges [4,5].

Nanomedicine broadly refers to the application of nanoscale materials and technologies to the diagnosis, prevention, monitoring, and treatment of disease, including their use as engineered systems for therapeutic delivery. Within this field, nanoparticles are generally defined as materials or structures with dimensions in the nanoscale range, although pharmaceutical nanocarriers may extend beyond the conventional 1–100 nm definition depending on their composition and intended biomedical function [6]. In drug delivery, these systems are engineered to encapsulate, protect, transport, and release therapeutic agents while modifying their pharmacokinetic and biodistribution profiles [7]. Nanoparticles below approximately 200 nm exhibit preferential accumulation in tumor vasculature through the EPR effect, the passive extravasation of nanocarriers through fenestrated tumor blood vessels, and their retention due to impaired lymphatic drainage [3]. Beyond this passive mechanism, nanoparticles can be equipped with active targeting ligands, antibodies, peptides, and aptamers that selectively bind disease-associated receptors, enabling discrimination between diseased and healthy tissue at the molecular level [2]. The resulting combination of extended circulation, site-specific accumulation, and controlled release within the therapeutic target constitutes the central value proposition of nanomedicine over conventional dosage forms.

1.2. Core Advantages and Inherent Challenges

The advantages of nanoparticle-based drug delivery extend across multiple dimensions of therapeutic performance. Protection of labile cargo (nucleic acids, proteins, and unstable small molecules) from enzymatic degradation during systemic circulation is one of the most clinically significant benefits, enabling the delivery of therapeutic classes that were previously considered undruggable due to stability limitations [8]. Controlled and sustained drug release over hours to weeks reduces peak plasma concentration fluctuations, maintains drug levels within the therapeutic window for prolonged periods, and decreases dosing frequency, all of which improve both therapeutic consistency and patient adherence [9,10]. The multifunctionality of modern nanoparticle platforms, their ability to co-load multiple therapeutic agents at defined molar ratios, incorporate imaging reporters, and carry targeting moieties simultaneously, enables combination therapies, theranostics, and sequential drug release strategies that are structurally impossible with conventional single-molecule formulations [11,12].

Despite these advantages, several fundamental challenges continue to limit the broader clinical translation of nanomedicine. The complexity of nanoparticle systems introduces variability in synthesis, characterization, and batch reproducibility that is difficult to control at the manufacturing scale [13]. Protein corona formation (the rapid adsorption of serum proteins onto nanoparticle surfaces upon systemic injection) alters targeting ligand accessibility, accelerates immunological recognition, and modifies pharmacokinetic behavior in ways that are poorly predicted by in vitro testing [14,15]. Long-term biodis-

https://doi.org/10.3390/molecules31173121

tribution and organ accumulation of non-biodegradable materials, particularly inorganic nanoparticles, remain incompletely characterized, raising safety questions that regulatory agencies require extensive preclinical evidence to address [16,17]. Regulatory frameworks continue to evolve in response to the technological diversity of nanomedicines, and the absence of globally harmonized standards for nanoparticle characterization and safety assessment creates friction in the approval process [18]. Overcoming these barriers requires not only advances in materials science and formulation engineering, but also progress in manufacturing technology, computational design, and regulatory science.

Unlike conventional reviews that primarily classify nanoparticle platforms or summarize their biological applications, this review integrates therapeutic design with an engineering and translational perspective. Particular emphasis is placed on the convergence of AI-guided formulation design and digital twins, scalable and sustainable nanomanufacturing, and the regulatory and production challenges governing clinical translation. By connecting nanoparticle design, biological performance, computational optimization, manufacturing, and clinical implementation within a unified framework, this review aims to bridge the gap between laboratory-scale innovation and clinically deployable nanomedicines.

1.3. Scope and Organization of the Review

This review critically examines nanoparticle-based drug delivery from physicochemical design and biological interactions to therapeutic applications and clinical translation. Unlike reviews focused primarily on nanoparticle classification or biological applications, this review emphasizes the integration of AI-guided formulation design and digital twins, scalable and sustainable nanomanufacturing, and the engineering, safety, and regulatory considerations governing clinical translation. By connecting nanoparticle design, biological performance, computational optimization, manufacturing, and clinical implementation, the review aims to bridge the gap between laboratory-scale innovation and clinically deployable nanomedicines.

2. Fundamentals of Nanoparticle Design and Biological Interactions

2.1. Physicochemical Properties: Size, Shape, Surface Chemistry, and Drug Loading

The biological behavior of drug-delivery nanoparticles is governed by the interplay between their material composition, structural architecture, and physicochemical properties. The systems considered in this review include polymeric nanoparticles and micelles, lipid-based nanoparticles and liposomes, inorganic nanoparticles such as silica, gold, and iron oxide systems, carbon-based nanomaterials, and hybrid or biomimetic carriers. These platforms differ structurally, ranging from solid or porous matrices and inorganic cores to micellar assemblies and lipid bilayer vesicles, and these differences influence drug loading and release, protein adsorption, cellular interactions, biodistribution, and clearance [19]. Among their physicochemical characteristics, particle size is a particularly important determinant of circulation, tissue distribution, cellular uptake, and elimination. In general, larger nanoparticles (>200 nm) are more susceptible to recognition and clearance by the mononuclear phagocyte system (MPS), whereas nanoparticles with hydrodynamic diameters below approximately 5.5 nm, particularly small inorganic systems, may undergo efficient renal filtration and urinary excretion [7]. The optimal size window for passive tumor targeting via the EPR effect is generally cited as 10–200 nm, though the actual effective range varies with tumor type, vascularization density, and disease stage. Within this range, smaller particles penetrate deeper into tumor tissue, while larger particles may accumulate at the periphery [20]. Figure 1 summarizes the influence of nanoparticle size on biological fate and pharmacokinetic behavior in vivo.

https://doi.org/10.3390/molecules31173121

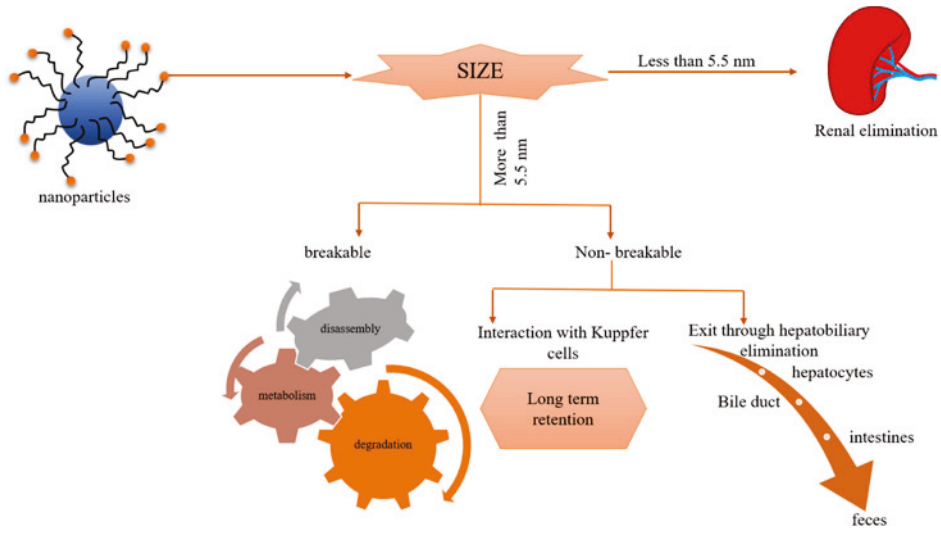

Figure 1. Effect of nanoparticle size on circulation behavior, biodistribution, tissue penetration, and clearance mechanisms in vivo, illustrating the size-dependent transition between renal elimination, prolonged systemic circulation, and uptake by the mononuclear phagocyte system. Reprinted from Ref. [21], under the terms of the Creative Commons CC BY license.

Shape is an equally important but often underappreciated design variable. Spherical nanoparticles are the most widely studied geometry and are favored for their predictable behavior and efficient endocytosis, but non-spherical morphologies confer distinct biological advantages. Rod-shaped particles exhibit prolonged circulation times relative to spheres of equivalent volume, attributed to their reduced phagocytic uptake due to asymmetric contact with macrophage membranes [20,22]. Worm-like filomicelles exhibit shape- and length-dependent biodistribution; early studies demonstrated markedly prolonged circulation compared with spherical micelles, whereas subsequent studies indicate that tumor accumulation and cellular uptake depend strongly on filament length and formulation characteristics [23]. Disk-shaped and platelet-mimicking particles have attracted interest for their ability to adhere to vascular walls and avoid margination from blood flow. The implications for drug delivery design are clear, where the shape must be selected in conjunction with the intended delivery route, target tissue, and cellular uptake pathway rather than defaulting to spherical geometry. Figure 2 illustrates representative examples of non-spherical nanoparticle geometries employed in drug delivery applications, including filomicelles, bottlebrush structures, worm-like vesicles, nanorods, prisms, cylinders, disks, and ellipsoids. These morphologies exhibit distinct hydrodynamic behavior, circulation profiles, and cellular interactions, further highlighting the importance of shape as a critical parameter in the rational design of nanocarriers [24].

Surface charge, quantified by zeta potential, governs colloidal stability, protein adsorption, and cellular interaction. Cationic surfaces facilitate electrostatic interaction with the negatively charged cell membrane, improving uptake efficiency for nucleic acid delivery, but also increase non-specific protein adsorption and MPS recognition in vivo. Anionic and neutral surfaces generally offer better systemic circulation but lower intrinsic cellular internalization [25]. Surface functionalization with hydrophilic polymers such as polyethylene glycol (PEG) is commonly used to generate a 'stealth' coating. PEG chains form a hydrated steric barrier around the nanoparticle surface that reduces nonspecific protein adsorption and recognition by the mononuclear phagocyte system, thereby prolonging systemic circulation [14]. Liposomes are vesicular nanocarriers composed of phospholipid bilayers surrounding an aqueous core, enabling the encapsulation of therapeutic compounds within the aqueous compartment or lipid bilayer [26]. A clinically established

example is PEGylated liposomal doxorubicin, in which doxorubicin is encapsulated within PEG-coated phospholipid liposomes. This formulation illustrates how surface PEGylation and liposomal encapsulation can alter drug pharmacokinetics and reduce systemic toxicity compared with free doxorubicin [27]. Drug loading efficiency depends on the physicochemical compatibility between the drug and the carrier matrix, and on whether passive (encapsulation during self-assembly) or active (post-formation loading driven by pH or ion gradients) loading strategies are employed. Active loading generally achieves higher efficiency and more controlled loading for ionizable drugs [28].

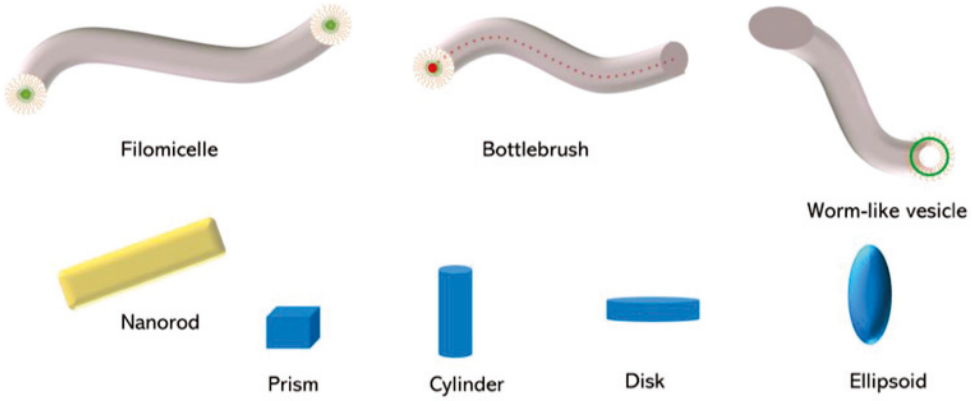

Figure 2. Representative non-spherical nanoparticle geometries used in drug delivery applications. Reprinted from Ref. [24], under the terms of the Creative Commons CC BY license.

2.2. Pharmacokinetics, Biodistribution, and Navigating Biological Barriers

The pharmacokinetics of nanoparticle-based therapeutics differ fundamentally from those of free drugs, and understanding these differences is essential for rational dosing and the prediction of therapeutic outcomes. Following systemic administration, nanoparticles encounter a sequential series of biological barriers, each of which can attenuate the fraction of the administered dose that ultimately reaches the therapeutic target [21]. The first barrier is the blood compartment, where protein corona formation occurs within seconds of injection, altering the particle's identity as perceived by the immune system and potentially redirecting biodistribution to MPS organs regardless of the engineered targeting strategy [15]. Stealth coatings mitigate but do not eliminate this effect, and anti-PEG antibodies generated after repeated dosing can accelerate clearance in a subset of patients, the accelerated blood clearance (ABC) phenomenon.

Vascular extravasation into solid tumors is typically achieved through the EPR effect for nanoparticles in the appropriate size range, but the magnitude of EPR-mediated accumulation is highly variable and has been called into question as a reliable basis for clinical performance [29]. Heterogeneous tumor vascularization, variable pericyte coverage, and inter-patient differences in lymphatic function mean that EPR-mediated targeting can differ by an order of magnitude across tumor types and patients, explaining in part why nanoparticle systems that show compelling efficacy in murine tumor models frequently underperform in human clinical trials [2]. Transcytosis, receptor-mediated endocytosis, and active targeting using ligands that bind disease-specific surface receptors provide more predictable targeting mechanisms that do not rely on the anatomical features of the tumor vasculature [2].

Cellular barriers constitute the final stage of delivery. Following uptake via endocytosis, nanoparticles enter the endo-lysosomal pathway, where progressively acidifying compartments (from pH 7.4 in early endosomes to pH 4.5–5.0 in lysosomes) can degrade acid-sensitive cargo and expose lysosomal nucleases that degrade unprotected nucleic acids [30]. Endosomal escape is therefore a critical design objective for the intracellular

delivery of biologics and gene therapies. Ionizable lipids that undergo protonation and membrane-disruptive conformational change at low pH, proton sponge polymers that buffer acidification and induce osmotic swelling, and photosensitizer-mediated membrane disruption are among the strategies employed to achieve cytoplasmic delivery after endosomal uptake [31,32]. Subcellular targeting (delivery to the nucleus for gene therapy, to the mitochondria for metabolic interventions, or to specific organelles for precision pharmacological action) represents the next frontier in intracellular targeting and requires additional targeting sequences beyond those sufficient for cell-level selectivity [22].

3. Material Systems, Synthesis, and Functionalization

3.1. Key Nanoparticle Platforms: Polymeric, Lipid-Based, Inorganic, Carbon-Based, and Hybrid

The choice of material platform is the most fundamental decision in nanoparticle design because it determines the physicochemical properties, drug loading capacity, degradation behavior, and biological interactions of the resulting system. Table 1 provides a systematic comparison of the principal nanoparticle platforms across these dimensions. Polymeric nanoparticles (PNPs) are among the most extensively studied platforms due to their compositional versatility, tunable degradation rates, and the wide range of drugs and biologics they can encapsulate. Polyesters such as poly(lactic-co-glycolic acid) (PLGA), polylactic acid (PLA), and polycaprolactone (PCL) degrade hydrolytically to non-toxic metabolites and are the basis of the majority of clinically progressed polymeric systems [10,33]. The polymer molecular weight, copolymer composition, and end-group chemistry collectively determine the degradation rate and drug release kinetics, providing extensive tunability for sustained-release applications ranging from days to months.

Table 1. Comparative overview of the principal nanoparticle drug delivery platforms: composition, size range, key advantages, primary limitations, and representative therapeutic applications.

Platform	Core Composition	Size Range	Key Advantages	Primary Limitations	Representative Applications	Ref.
Polymeric NPs	PLGA, PCL, PLA, chitosan, albumin	50–500 nm	Tunable degradation rate; high drug-loading capacity; surface versatility; stimuli-responsive variants available	Batch-to-batch variability; potential immunogenicity of degradation products; scale-up challenges	Oncology (paclitaxel, doxorubicin delivery); gene therapy; arthritis; CNS disorders	[7,10,33]
Lipid-based NPs (liposomes, LNPs)	Phospholipids, cholesterol, ionizable lipids	50–200 nm	Excellent biocompatibility; biodegradable; amphiphilic bilayer accommodates both hydrophilic and hydrophobic cargo; PEGylation extends circulation	Physical instability (aggregation, leakage); cold-chain storage requirements; hypersensitivity reactions in some patients	mRNA COVID-19 vaccines (Pfizer/Moderna); Doxil® (oncology); siRNA delivery (Onpattro®)	[7,31]
Mesoporous silica NPs (MSNs)	Amorphous SiO_2 with ordered pore channels	50–300 nm	High surface area and pore volume; tunable pore size; thermally and chemically stable; excellent drug-loading capacity; gatable pores for controlled release	Non-biodegradable in certain formulations; potential for long-term silica accumulation; synthesis complexity	Theranostics; pH/enzyme-responsive delivery; antifungal; anticancer drug loading	[34,35]
Inorganic NPs (gold, iron oxide)	Au, Fe_3O_4/Fe_2O_3, QDs, MnO_2	5–100 nm	Unique optical/magnetic properties; excellent imaging contrast; photothermal conversion efficiency; precise targeting under external field guidance	Potential long-term accumulation; regulatory uncertainty; cost; limited biodegradability of metallic cores	Photothermal cancer therapy; MRI contrast agents; magnetic hyperthermia; colorectal cancer biosensors	[36,37]

Table 1. *Cont.*

Platform	Core Composition	Size Range	Key Advantages	Primary Limitations	Representative Applications	Ref.
Hybrid (lipid-polymer) NPs	polymeric core + lipid shell	50–250 nm	Combines polymer stability with lipid biocompatibility; stealth coating; co-delivery of hydrophilic and hydrophobic drugs; reduced protein corona formation	More complex fabrication; additional quality control requirements; cost of manufacturing	Combination cancer chemotherapy; boron neutron capture therapy (BSH-LDH); targeted oncology	[7]
Carbon-based NPs (carbon dots, CNTs)	sp^2/sp^3 carbon; surface-functionalizable	1–10 nm (CDs)	Tunable photoluminescence; biocompatible surface chemistry; EPR-mediated tumor accumulation; dual drug and gene delivery	Heterogeneous size distribution; uncertain long-term toxicity; scale-up and clinical translation barriers	Cancer theranostics; gene silencing (siRNA); tumor microenvironment-responsive imaging	[38]
Exosomes/ biomimetic NPs	Cell-derived lipid vesicles; RBC membrane coatings	30–150 nm	Inherent immune evasion; natural targeting ability; low immunogenicity; capable of carrying proteins, nucleic acids, and small molecules	Complex and low-yield isolation; batch variability; challenges in large-scale production and standardization	siRNA delivery; immune modulation; CNS targeting; cancer immunotherapy	[15,39]

NPs = nanoparticles; LNPs = lipid nanoparticles; MSNs = mesoporous silica nanoparticles; CDs = carbon dots; RBC = red blood cell; EPR = enhanced permeability and retention.

Beyond their structural and compositional differences, modern nanoparticle platforms are increasingly designed as multifunctional systems capable of simultaneously integrating therapeutic, diagnostic, and targeting functionalities. Figure 3 illustrates representative nanocarrier architectures and the diverse range of payloads and functional moieties that can be incorporated into these systems [40].

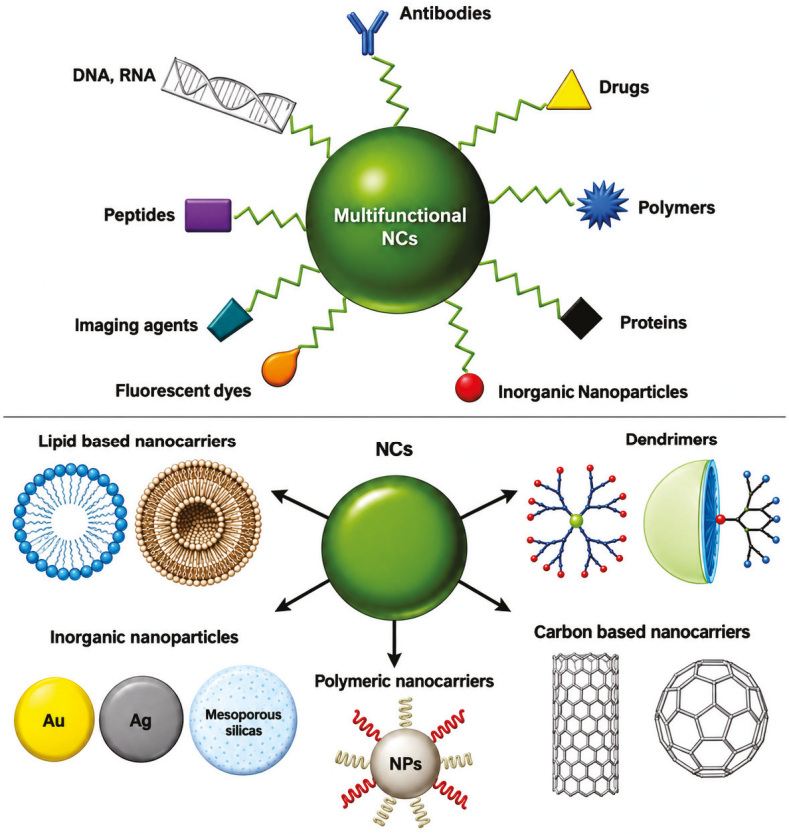

Figure 3. Representative nanoparticle platforms used in drug delivery and their multifunctional capabilities, including the incorporation of drugs, nucleic acids, proteins, imaging agents, and targeting ligands within a single nanocarrier system. Reprinted from Ref. [40], under the terms of the Creative Commons CC BY license.

Lipid-based nanoparticles, including liposomes and lipid nanoparticles (LNPs), represent the most clinically successful nanoparticle class to date, encompassing several FDA-approved products and the transformative COVID-19 mRNA vaccines [13,31]. Their biocompatibility, biodegradability, and the structural amphiphilicity that allows for the simultaneous encapsulation of hydrophilic cargo in the aqueous core and hydrophobic drugs in the lipid bilayer are key advantages. The development of ionizable lipids (lipids with pKa values in the range of 6–7 that are neutral at physiological pH but positively charged in acidic endosomal compartments) was a critical advance that enabled efficient siRNA and mRNA delivery by facilitating endosomal membrane disruption and cargo release [31]. Mesoporous silica nanoparticles (MSNs) offer a distinctive combination of high internal surface area (>1000 m^2 g^{-1}), tunable and uniform pore dimensions (2–50 nm), and chemical stability that makes them exceptionally capable drug reservoirs [35]. The pores can be functionalized with gating molecules (molecular machines such as nanovalves, pseudorotaxanes, and DNA duplexes) that open in response to specific stimuli, transforming the MSN into a precisely controlled drug release device [34].

Inorganic nanoparticles, including gold, iron oxide, and quantum dot systems, derive their clinical utility primarily from unique physical properties unavailable to organic carriers. Gold nanoparticles exhibit strong and size-tunable surface plasmon resonance, enabling both highly sensitive optical imaging and photothermal conversion, while superparamagnetic iron oxide nanoparticles (SPIONs) provide MRI contrast enhancement and are responsive to external magnetic fields for guided delivery and magnetic hyperthermia [36,37]. Hybrid nanoparticles that combine a polymeric core with a lipid shell (the lipid-polymer hybrid nanoparticle) represent an attempt to capture the stability and drug-loading advantages of polymers with the biocompatibility and surface versatility of lipids within a single architecture [7]. Carbon dots, a recently emerged class of photoluminescent carbon-based nanomaterials smaller than 10 nm, combine biocompatibility, tunable emission, and surface functionalizability with inherent EPR-mediated tumor accumulation, making them attractive candidates for simultaneous cancer imaging and drug/gene co-delivery [38]. Sustainable biopolymer-derived nanocarriers, including cellulose nanofibers and nanocellulose-based composites, are also emerging as promising platforms due to their biocompatibility, biodegradability, high surface area, and ease of surface functionalization for drug delivery and biomedical applications. Exosomes and red blood cell membrane-coated nanoparticles represent the biomimetic frontier, exploiting naturally derived lipid bilayers to achieve stealth circulation, and in the case of exosomes, inherent tissue targeting capabilities derived from their cell of origin [15,39].

3.2. Fabrication, Encapsulation Methods, and Manufacturing Scalability

The transition from materials design to a manufacturable product requires fabrication processes that reliably produce nanoparticles meeting defined critical quality attributes (CQAs), including specifications for size, polydispersity, surface charge, drug loading, and encapsulation efficiency, which are predictive of clinical performance [28]. Historically, liposomes and polymeric nanoparticles were formed by bulk mixing methods such as thin-film hydration, nanoprecipitation, and solvent emulsification, which produce acceptable laboratory-scale particles but suffer from poor process control, high batch-to-batch variability, and difficulty scaling to commercial volumes without reoptimization [28]. The introduction of microfluidic fabrication technologies represented a paradigm shift. By confining mixing to channels of defined geometry at controlled flow rates, microfluidic systems achieve rapid, reproducible nanoprecipitation with size control as fine as $\pm$5 nm, and the laminar-to-turbulent mixing transition can be precisely tuned to optimize nanoparticle formation kinetics [41]. More recently, impingement jet mixing (IJM) technology has

https://doi.org/10.3390/molecules31173121

enabled the scale-up of LNP manufacturing to commercial volumes while preserving the mixing precision achieved by microfluidics at smaller scales, with multi-jet configurations allowing proportional increases in throughput without altering the critical hydrodynamic mixing parameters [42]. Active loading strategies (post-formation drug loading driven by transmembrane pH or ammonium sulfate gradients) achieve significantly higher encapsulation efficiencies for ionizable drugs than passive co-encapsulation during particle formation, and are the basis of the remote loading strategy used in Doxil® and related pegylated liposomal products [28,43].

3.3. Surface Engineering: Targeting Ligands, Stealth Coatings, and Stimuli-Responsive Designs

Surface engineering is the process by which a nanoparticle with appropriate bulk properties is transformed into a precisely programmed biological agent, one that knows where to go, when to release its cargo, and how to avoid immune detection along the way. Stealth coatings are the most fundamental surface modification, and polyethylene glycol (PEG) has been the dominant strategy for more than three decades. PEGylation creates a hydrophilic, flexible polymer brush that sterically prevents protein adsorption, reduces MPS recognition, and extends circulation half-life from minutes to hours or days [14,44]. However, the clinical adoption of PEGylated systems has revealed a limitation. Repeated dosing in a subset of patients generates anti-PEG antibodies that accelerate clearance and can trigger hypersensitivity reactions. Polyzwitterionic coatings and naturally derived polymer coatings such as polysarcosine are being investigated as PEG alternatives that preserve stealth properties without immunogenic liability [45].

Active targeting is accomplished by conjugating targeting ligands (small molecules, peptides, aptamers, or antibodies) to the nanoparticle surface at densities that allow multivalent binding to disease-associated receptors while preserving the steric properties of the stealth layer. The folate receptor, transferrin receptor, ErbB2/HER2, EGFR, and PSMA are among the most intensively targeted receptors in cancer nanomedicine, while CXCR4 and VCAM-1 are studied in cardiovascular and inflammatory applications [2,46]. Folic acid-targeted carbon quantum dot systems have demonstrated dual siRNA delivery and selective cytotoxicity in folate receptor-overexpressing osteosarcoma cells, illustrating how ligand–receptor specificity can be combined with dual cargo delivery in a single platform [47]. Stimuli-responsive surface designs add a further level of programmability: pH-sensitive bonds that expose targeting ligands only in the acidic tumor microenvironment, enzyme-cleavable coatings that are stripped by tumor-associated proteases to reveal the active targeting surface, and thermo-responsive polymers that undergo conformational transitions at specified temperatures to release cargo or alter surface accessibility [10,48]. The convergence of stealth coatings, active targeting, and environmental responsiveness in hybrid surface architectures represents the current frontier of nanoparticle surface engineering.

4. Release Mechanisms and Advanced Delivery Strategies

4.1. Controlled Release via Diffusion, Degradation, and Endogenous Triggers

Controlled drug release from nanoparticles is rarely governed by a single mechanism. Rather, it typically reflects the simultaneous and coupled operation of diffusion, matrix degradation, and erosion, with their relative contributions determined by the specific polymer composition, drug physicochemical properties, and environmental conditions at the delivery site [10,49]. In biodegradable polymeric systems based on PLGA and PCL, drug molecules traverse the matrix through water-filled pores that develop as hydrolysis proceeds, and the rate of hydrolytic bond cleavage, which sets the degradation rate, is tunable through the adjustment of copolymer composition, molecular weight, and end-group chemistry [10]. As described by Kamaly et al. [10], drug release from biodegradable

https://doi.org/10.3390/molecules31173121

polymeric systems commonly results from the combined contributions of diffusion, degradation, and erosion rather than from a single mechanism. Understanding and controlling these interconnected processes through rational polymer design can enable the precise spatial and temporal regulation of drug release.

Endogenous chemical triggers exploit pathological features of disease sites to achieve selective drug release. pH-responsive systems exploit the acidic microenvironment of tumors (extracellular pH 6.5–7.0) and the even more acidic lysosomal compartment (pH 4.5–5.0) to activate acid-labile bonds or protonate ionizable lipids that then disrupt endosomal membranes, enabling cytoplasmic cargo escape [31,32]. Redox-responsive systems exploit the approximately 1000-fold difference in glutathione (GSH) concentration between the reducing cytoplasm of cancer cells (2–10 mM) and the oxidizing extracellular space (~2 μM), using disulfide crosslinks that are stable in circulation but cleaved intracellularly to trigger cargo release with high selectivity for cancerous over healthy tissue [12,50]. Enzyme-responsive designs use cleavable substrates for cathepsin B, matrix metalloproteinases (MMP-2/9), or other enzymes overexpressed in the tumor microenvironment as gatekeeping elements that remain intact in healthy tissue but are cleaved at the target site [34,51]. MSNs are particularly well-suited to enzyme-gated delivery because their pores can be sealed with supramolecular caps (pseudorotaxanes, DNA duplexes, protein gatekeepers) that are displaced or cleaved by specific biological signals, providing digital on/off control over drug release rather than the analog, diffusion-governed release of polymer systems [34]. Table 2 provides a systematic overview of the principal release mechanisms, their molecular bases, and their most relevant clinical application contexts.

Table 2. Systematic overview of nanoparticle drug release mechanisms: trigger type, representative carrier systems, molecular basis, and primary clinical application context.

Release Mechanism	Trigger	Nanoparticle System	Molecular Basis	Key Application Context	Ref.
Diffusion-controlled	Passive (concentration gradient)	Polymeric NPs, lipid vesicles	Drug diffuses through water-filled pores or polymer matrix without structural breakdown; rate governed by matrix permeability	Sustained systemic release; chronic disease management (hypertension, diabetes)	[9,10]
Hydrolytic degradation	Passive (aqueous environment)	PLGA, PLA, PCL nanoparticles	Ester bond hydrolysis in polyester backbone progressively fragments matrix; rate tunable via molecular weight and copolymer ratio	Long-term oncology; post-surgical local delivery; gene therapy depots	[10,49]
pH-responsive	Endosomal acidification (pH 5–6); tumor microenvironment (pH 6.5–7.0)	Ionizable LNPs; acid-labile polymers; MSN nanovalves	Ionizable lipids acquire positive charge at low pH, disrupting endosomal membrane; acid-labile linkers cleave to release cargo	Intracellular drug/siRNA delivery; cancer targeting; lysosomal escape for gene therapy	[31,32,34]
Redox-responsive	Elevated intracellular GSH (tumor cytoplasm ~10 mM vs. ~2 μM extracellular)	Disulfide-crosslinked polymeric NPs; thiolated MSNs	GSH cleaves disulfide bonds holding polymer crosslinks or gating agents, releasing encapsulated cargo selectively in reductive intracellular compartments	Cytoplasmic drug delivery; cancer-selective release; siRNA release in tumor cells	[12,50]
Enzyme-responsive	Cathepsin B, MMP-2/9 (overexpressed in tumors)	Peptide-capped MSNs; enzyme-cleavable polymer prodrugs; magnetic NPs	Enzyme cleaves substrate linker or gating peptide to open pore or activate drug; exploits tumor-associated overexpression	Tumor-selective delivery; personalized cancer therapy; precision oncology	[34,51]

Table 2. *Cont.*

Release Mechanism	Trigger	Nanoparticle System	Molecular Basis	Key Application Context	Ref.
Photothermal/ photo-triggered	NIR light (650–950 nm); UV	Au NPs, polymer-based NPs, azobenzene-gated MSNs	Light absorbed by plasmonic or photosensitizer moiety converted to heat; heat disrupts thermo-labile bonds or induces conformational change in gatekeepers	Photothermal tumor ablation; spatiotemporally precise drug release; theranostics	[37,52]
Magnetic hyperthermia	Alternating magnetic field (AMF)	Superparamagnetic iron oxide NPs (SPIONs)	AMF induces Néel/Brownian relaxation in magnetic cores, generating local heat that cleaves thermolabile bonds or disrupts lipid bilayers	Deep-tissue tumor therapy; MRI-guided drug release; combination with chemotherapy	[36]
Ultrasound-mediated	Focused ultrasound + microbubble cavitation	Drug-loaded microbubbles; echogenic liposomes	Acoustic cavitation transiently increases membrane permeability (sonoporation), enabling enhanced NP cellular uptake and focal drug delivery	Blood-brain barrier opening; cardiac and tumor delivery; non-invasive, focal drug activation	[53]

4.2. Externally Triggered Systems: Light, Magnetic Field, and Ultrasound

Externally triggered release systems give clinicians active spatiotemporal control over drug liberation by applying a physical stimulus that is absent during circulation and storage but applied precisely to the therapeutic target. Photothermal systems based on gold nanoparticles and polymer-embedded photothermal agents leverage the surface plasmon resonance of metal nanostructures (or the strong near-infrared (NIR) absorption of organic dye-loaded polymer matrices) to convert incident light energy into localized heat with high efficiency [37,52]. In photothermal cancer therapy, this heat selectively destroys tumor cells through protein denaturation and membrane disruption while simultaneously triggering the release of thermosensitive drug payloads. Gold nanoparticles offer shape-dependent tunability of the plasmon resonance. Nanorods can be tuned to absorb maximally in the tissue-transparent NIR window (650–950 nm), nanostars exhibit a "lightning rod" concentration of electromagnetic field intensity at their sharp tips, enabling deeper tissue penetration, and nanoshells provide a structurally robust option for clinical translation [37]. For photodynamic therapy, photosensitizer-loaded nanoparticles generate reactive oxygen species upon light irradiation, providing an alternative cytotoxic mechanism that is independent of thermal effects and suitable for oxygen-replete tumor microenvironments [54].

Magnetically triggered systems use superparamagnetic iron oxide nanoparticles (SPIONs) that can be simultaneously guided to the target site by an external magnetic field and activated by an alternating magnetic field (AMF) to generate local hyperthermia through Néel and Brownian relaxation [36]. The combination of spatial guidance and thermal activation provides two independent levels of targeting control that synergize to improve tumor-to-background drug accumulation while limiting systemic exposure. Functionalization with targeting ligands and enzyme-responsive drug linkers further extends the specificity of this platform [51]. Ultrasound-mediated drug delivery exploits acoustic cavitation (the oscillation and collapse of microbubbles in an ultrasonic field) to create transient pores in cell membranes (sonoporation) that dramatically increase the uptake of co-administered nanoparticles and drugs [53]. Focused ultrasound systems allow this effect to be spatially confined to a tissue volume of millimeter-scale precision, enabling

delivery through the blood–brain barrier by transient BBB opening. This approach has progressed to Phase I/II clinical evaluation, including studies in patients with recurrent glioblastoma (e.g., NCT03744026) [55].

4.3. Combination, Sequential, and Theranostic Delivery

The conceptual unification of diagnosis and therapy in theranostic nanoparticle systems, and the combination of multiple therapeutic modalities in a single carrier, represent logical extensions of the nanoparticle multifunctionality that distinguishes nanomedicine from conventional drug formulation. Co-delivery of cytotoxic drug combinations at defined molar ratios has demonstrated synergistic antiproliferative effects in cell culture and animal models, and the clinical success of Vyxeos® (CPX-351) (a liposomal formulation of daunorubicin and cytarabine at a fixed 5:1 molar ratio) provides proof-of-concept validation that nanoparticle-enforced drug ratio maintenance can translate into meaningful survival improvements in patients [13]. Sequential release strategies deliver multiple drugs in a defined temporal sequence from the same carrier, exploiting the different sensitivity of the target cells to different treatments at different stages. Amphiphilic Janus nanoparticles with distinct hydrophilic and hydrophobic domains enable the simultaneous loading of two drugs in separate compartments and their sequential release through independent triggers (for example, pH-responsive release of one agent in the endosome followed by NIR-triggered release of the second agent in the cytoplasm), generating synergistic effects not achievable through simultaneous co-delivery [11,12].

Photo-triggered theranostic nanoparticle systems combine NIR-light-activated drug release with photoacoustic or fluorescence imaging signals generated by the same chromophore, enabling the real-time monitoring of drug distribution and tumor response during treatment [54]. MSN-based theranostic systems incorporate imaging agents (MRI contrast agents, photoacoustic dyes, or radioactive tracers) directly into the silica framework or pore channels, allowing simultaneous CT, MR, and optical imaging to guide drug delivery in real-time [11,35]. The convergence of therapeutic action and diagnostic feedback in a single injectable agent eliminates the temporal and spatial uncertainty inherent in sequentially administering separate diagnostic and therapeutic agents and represents a fundamental advance in treatment monitoring capability. Polymeric nanoparticle platforms further extend this concept through the incorporation of "smart" stimuli-responsive elements that respond to the specific biochemical environment of the tumor, enabling both activation of the therapeutic payload and the generation of a detectable signal that confirms correct localization before drug release commences [33,47].

5. Therapeutic Applications and Preclinical to Clinical Translation

5.1. Major Disease Targets: Oncology, Infectious Diseases, and CNS/CVD Disorders

Oncology has been and remains the dominant application domain for nanoparticle-based drug delivery, driven by the unmet need for treatments that can improve the therapeutic index of highly toxic chemotherapeutic agents and the growing portfolio of molecularly targeted therapies that require intracellular delivery [2,56]. Nanoparticles accumulate preferentially in tumor tissue through EPR-mediated passive targeting, and the tumor microenvironment provides multiple endogenous stimuli (acidic pH, elevated GSH, hypoxia, overexpressed proteases) for triggered drug release [12,50]. Clinical translation is exemplified by PEGylated liposomal doxorubicin, which maintains antitumor activity while reducing cardiotoxicity compared with conventional doxorubicin, demonstrating how nanoparticle encapsulation can improve the therapeutic index of established chemotherapeutic agents [57]. Carbon dots have emerged as a functionally versatile nanoplatform for simultaneous cancer imaging and drug/gene delivery, exploiting their photolumines-

cent properties for tumor visualization while serving as carriers for therapeutic payloads including chemotherapeutic drugs, siRNAs, and targeted gene silencing agents [38]. Folic acid-functionalized carbon quantum dot systems incorporating macrophage cell membrane coatings demonstrated the simultaneous delivery of two siRNAs targeting osteosarcoma-relevant pathways (with in vivo results showing significant tumor regression and suppression of lung metastasis without systemic toxicity), representing the integration of biomimetic stealth, active targeting, and multi-cargo delivery in a single platform [47]. Gold nanoparticles functionalized for photothermal applications have shown significant preclinical efficacy in breast cancer models, with simulation studies confirming thermal confinement within tumor tissue without damage to surrounding normal tissue [37,58].

Polysaccharide-based nanoparticle platforms have demonstrated clinically relevant performance across multiple disease targets, including cancer, cardiovascular disease, and neurodegenerative disorders, by combining biocompatibility with the chemical versatility that polysaccharides offer for surface functionalization and stimuli-responsive design [12]. In glioblastoma treatment, silica nanoparticle systems and nanoparticle-stem cell combination approaches have shown preclinical promise by protecting therapeutic payloads, enabling sustained local drug delivery and improving gene/siRNA delivery within the immunosuppressive brain tumor microenvironment [32]. For cardiovascular applications, nanoparticle-based delivery of anti-inflammatory and antifibrotic agents to sites of vascular injury and myocardial infarction exploits the selectivity of targeted nanocarriers for activated endothelium and macrophage-rich plaques, with enzyme-responsive magnetic nanoparticles combining MRI-guided localization with spatially precise drug activation [51]. Clinical translation of CNS delivery is also being explored using focused ultrasound-mediated blood–brain barrier opening. Early-phase clinical evaluation, including a Phase I/II study in recurrent glioblastoma (NCT03744026), has demonstrated the feasibility of transient BBB opening to facilitate therapeutic delivery [55]. Infectious disease applications include both direct antimicrobial delivery, where nanoparticle-encapsulated antibiotics achieve sustained local concentrations at infection sites, and vaccine delivery, where nanoparticles serve as antigen carriers and adjuvant platforms that improve immunogenicity and reduce dosing frequency [59,60].

5.2. Gene Delivery and Vaccines

Gene therapy and RNA interference represent therapeutic modalities that fundamentally require nanoparticle delivery due to the inherent pharmacological limitations of nucleic acids as free agents. They are rapidly degraded by serum nucleases, do not cross cell membranes passively due to their large size and negative charge, and in the case of plasmid DNA, must reach the nucleus for transcription [30]. Lipid nanoparticles with ionizable lipid components are the leading platform for nucleic acid delivery, exemplified by the clinical success of patisiran, the first FDA-approved siRNA therapeutic, which uses LNPs to achieve efficient hepatocyte-targeted gene silencing in hereditary transthyretin amyloidosis, and by the COVID-19 mRNA vaccines, which established the largest clinical validation of LNP-mediated nucleic acid delivery in history [8,31]. In the pivotal Phase III APOLLO trial, patisiran significantly improved polyneuropathy and quality-of-life measures compared with the placebo, providing direct clinical validation of systemic LNP-mediated siRNA delivery [61]. Similarly, pivotal Phase III trials of LNP-formulated mRNA COVID-19 vaccines demonstrated 95.0% efficacy for BNT162b2 and 94.1% efficacy for mRNA-1273 against symptomatic COVID-19, providing large-scale clinical validation of LNP-mediated mRNA delivery [62–64]. The key mechanistic challenge addressed by ionizable LNPs is endosomal escape. At lysosomal pH, the ionizable lipid becomes protonated, assumes a positive charge, and disrupts the endosomal membrane through charge-driven lipid mixing,

releasing siRNA or mRNA into the cytoplasm, where it can access the RNA interference machinery or ribosomes [31].

Carbon dots and polymeric carriers have demonstrated capacity for multi-cargo nucleic acid delivery in preclinical cancer models, with folic acid-targeted platforms simultaneously delivering two siRNAs targeting complementary oncogenic pathways at the same tumor cell, demonstrating that nucleic acid cargo multiplicity is achievable without compromising targeting or cellular uptake efficiency [47]. Exosome-based delivery systems represent a biomimetic alternative to synthetic nucleic acid carriers that exploits the natural intracellular communication function of exosomes. Their inherent membrane stability, natural targeting capabilities encoded by surface proteins from their cell of origin, and reduced immunogenicity relative to synthetic liposomes are advantageous for gene therapy applications where repeated dosing may be required [39]. Vaccine delivery using nanoparticles extends beyond mRNA vaccines to encompass protein antigen delivery with polysaccharide-based systems that achieve sustained antigen release over three or more weeks, enabling single-dose immunization protocols that are particularly valuable for programs targeting vaccine-hesitant or geographically dispersed populations [20,59]. Hydrogel nanoparticle systems for intranasal vaccine delivery have demonstrated improved mucosal immune responses in animal models compared to conventional intranasal formulations, attributable to the improved mucoadhesion and prolonged antigen residence time at the nasal-associated lymphoid tissue [59].

5.3. Evaluation Pipeline: In Vitro Models, In Vivo Studies, and Clinical Trials

The evaluation pipeline for nanoparticle drug delivery systems follows a progression from in vitro cellular models through in vivo preclinical studies to clinical trials, each stage providing increasingly complex and predictive biological data at progressively higher cost and regulatory scrutiny. In vitro studies provide initial evidence of therapeutic activity, cellular uptake, and cytotoxicity selectivity at low cost and high throughput, with two-dimensional cell cultures being supplemented by more predictive three-dimensional tumor spheroids, organoids, and organ-on-chip systems that better replicate the spatial heterogeneity and mass transport barriers of solid tumors [47,65]. Assessment of in vitro drug release kinetics under physiologically relevant conditions (including buffer pH, enzyme concentration, and temperature matching the intended delivery environment) provides a mechanistic understanding of release behavior that informs in vivo dose prediction and study design. For folic acid-targeted carbon quantum dot systems, in vitro studies demonstrated the inhibition of osteosarcoma cell proliferation and invasion, dose-dependent cytotoxicity, and pH-responsive drug release profiles that provided the mechanistic rationale for in vivo testing [47].

In vivo studies in rodent xenograft and syngeneic tumor models provide evidence for systemic pharmacokinetics, biodistribution, tumor accumulation efficiency, and therapeutic efficacy in a living organism with intact vasculature and partially functional immune response [65]. Significant tumor regression and the suppression of distant metastasis without systemic toxicity in in vivo models represent the evidence threshold typically required before clinical investigation begins, and has been demonstrated for multiple carbon dot, polysaccharide, and MSN-based systems in preclinical oncology work [47,59]. However, the predictive value of murine preclinical data for human clinical outcomes has been consistently questioned, particularly for tumor targeting. This limitation has been demonstrated experimentally for lipid nanoparticle (LNP)-mediated mRNA delivery. In a comparative study evaluating 89 chemically distinct LNPs across murine, non-human-primate-derived, and human hepatocytes in vivo, delivery to non-human primate and human hepatocytes showed a strong correlation (R^2 = 0.83), whereas the correlation between murine and

human hepatocytes was substantially lower (R^2 = 0.53). These findings demonstrate that nanoparticle delivery performance can be species-dependent and highlight the importance of selecting physiologically relevant preclinical models before clinical translation [66]. The EPR effect is more pronounced and reproducible in subcutaneous xenograft models than in orthotopic, spontaneous, or patient-derived xenograft (PDX) models that better reflect the vascular and immunological complexity of human tumors [29]. This disconnect between preclinical promise and clinical performance is reflected in the substantial attrition of nanoparticle-based oncology therapeutics during clinical development, highlighting the limited predictive value of many conventional preclinical models for human outcomes [13]. Approved nanoparticle products such as Doxil®, Abraxane®, Onpattro®, and the mRNA vaccines confirm that clinical success is achievable, but that the pathway from compelling preclinical data to approved therapeutic is long, expensive, and uncertain [13]. Table 3 provides an overview of key approved and late-stage clinical nanoparticle products.

Table 3. Representative clinically approved and late-stage nanoparticle drug delivery products: platform type, active ingredient, indication, approval status, and key clinical benefit.

Product/Platform	NP Type	Active Ingredient	Indication	Approval Status	Current Market/Clinical Status	Key Clinical Benefit	Ref.
Doxil®/Caelyx®	PEGylated liposome	Doxorubicin	Ovarian cancer, Kaposi's sarcoma	FDA-approved (1995)	Currently marketed	Reduced cardiotoxicity vs. free doxorubicin; enhanced tumor accumulation via EPR effect	[13]
Abraxane®	Albumin-bound NP	Paclitaxel	Breast, lung, pancreatic cancer	FDA-approved (2005)	Currently marketed	Eliminates Cremophor® vehicle toxicity; improved tolerability; higher dose delivery	[13]
Onpattro® (patisiran)	Ionizable lipid NP	siRNA (transthyretin)	Hereditary transthyretin amyloidosis	FDA-approved (2018)	Currently marketed	First approved siRNA therapeutic; demonstrated liver-targeted gene silencing in humans	[8,31]
Comirnaty®/ Spikevax®	Ionizable lipid NP (LNP)	mRNA (SARS-CoV-2 spike)	COVID-19 prevention	FDA-approved (2021)	Currently approved; updated formulations remain in clinical use	First approved mRNA vaccines; validated LNP as clinical nucleic acid delivery platform	[63,64]
DepoCyt® (liposomal cytarabine)	Sustained-release liposome	Cytarabine	Lymphomatous meningitis	FDA-approved (1999)	Discontinued in the USA; marketing authorization withdrawn in the EU (2018)	Extended CSF drug residence time; reduced injection frequency from every 4 days to every 2 weeks	[43]
Vyxeos® (CPX-351)	Liposome (fixed molar ratio)	Daunorubicin + cytarabine	Acute myeloid leukemia (AML)	FDA-approved (2017)	Currently marketed	Synergistic dual drug delivery at fixed ratio; improved OS vs. conventional 7 + 3 regimen in high-risk AML	[13]
Gold NP photothermal (AuroLase®)	Silica-gold nanoshells	Photothermal agent	Prostate cancer (ablation)	Investigational; evaluated in clinical studies	Investigational; not FDA-approved for prostate cancer treatment	Focal tumor ablation using NIR laser; minimally invasive; targeted tissue destruction with thermal mapping	[37]

6. Computational Design, Artificial Intelligence, and Machine Learning

6.1. AI-Driven Design of Nanoparticle Formulations and Properties

The integration of artificial intelligence and machine learning into nanoparticle design represents a paradigm shift from the iterative empirical approach, namely synthesize, characterize, and modify, that has governed the field since its inception. The fundamental limitation of empirical optimization is that nanoparticle performance depends on the simultaneous interaction of dozens of formulation variables (lipid composition, molar ratios, polymer molecular weight, surface ligand density, drug loading method) and process variables (mixing conditions, temperature, flow rate), creating a parameter space too vast for exhaustive experimental exploration [3,67]. Machine learning models trained on existing experimental datasets can identify multivariate structure–property relationships across this space and predict optimal formulation orders of magnitude faster than laboratory synthesis, making them invaluable for initial formulation screening before physical experiments are undertaken.

Tunable Nanoparticles using Artificial Intelligence (TuNa-AI) is a hybrid machine-learning framework developed to guide nanoparticle formulation by learning relationships between formulation composition and experimentally measured performance. The approach integrates formulation data with predictive modeling to identify optimized nanoparticle compositions while reducing unnecessary formulation components and experimental iterations [67]. Notably, in a trametinib formulation, the AI-guided approach reduced excipient usage by 75% while preserving in vitro efficacy and in vivo pharmacokinetics relative to the standard formulation, demonstrating the potential of machine learning to simplify nanoparticle compositions while maintaining therapeutic performance [67]. The development of science-specific language models such as LightGBM for gradient-boosted decision tree learning, combined with microfluidic synthesis platforms that generate high-quality training data rapidly and reproducibly, is creating a closed-loop computational-experimental design cycle in which AI predictions are tested, results are fed back as new training data, and model accuracy improves iteratively [41,67]. For mRNA-LNP manufacturing, AI-coupled microfluidic systems have been demonstrated to achieve the precise control of particle size and morphology, parameters that critically influence mRNA delivery efficiency and immunogenicity, within a quality-by-design framework that is directly compatible with pharmaceutical manufacturing standards [41,42].

6.2. Modeling Drug Release, Pharmacokinetics, and Targeting Efficacy

Computational pharmacokinetic modeling occupies a critical role in the nanoparticle development pipeline by providing quantitative predictions of in vivo behavior that inform dose selection, schedule optimization, and the design of clinical studies before first-in-human testing. Multi-view learning neural networks trained on physicochemical nanoparticle descriptors and animal pharmacokinetic data have been demonstrated to predict key PK parameters (area under the curve (AUC), maximum plasma concentration, and clearance rate) across multiple nanoparticle classes with predictive accuracy sufficient for dose range selection in preclinical studies [68]. These predictive models accelerate the transition from formulation design to in vivo testing by reducing the number of pharmacokinetic studies required to characterize a new formulation, and their integration with population PK modeling approaches is enabling patient-specific dose personalization based on individual physiological parameters [68,69].

AI-based protein design tools, including RFdiffusion, enable de novo generation of proteins with specified structural and functional properties and may provide a foundation for the rational development of targeting ligands for nanoparticle delivery systems [70]. The ANIDS AI system has been proposed as a computational framework for optimizing

https://doi.org/10.3390/molecules31173121

nanoparticle formulations and illustrates the potential of AI-guided approaches for simultaneously considering targeting and drug-encapsulation parameters [22]. However, independent experimental validation across diverse nanoparticle systems is still required before the predictive performance and generalizability of such approaches can be established. Table 4 summarizes the principal AI and machine learning approaches being applied to nanoparticle research, their specific applications, and the key outcomes demonstrated.

Table 4. AI and machine learning approaches in nanoparticle drug delivery research: specific application, representative system, and key outcomes.

AI/ML Approach	Application in Nanomedicine	Representative System	Key Outcome	Ref.
Gradient boosting/LightGBM	Predict nanoparticle size, PDI, encapsulation efficiency from formulation inputs; screen polymer–lipid ratios	TuNa-AI	Reduced excipient usage by 75% in a trametinib formulation while maintaining in vitro efficacy and in vivo pharmacokinetics	[67]
Multi-view learning (neural networks)	Predict in vivo pharmacokinetics (AUC, Cmax, clearance) from physicochemical descriptors and animal model data	AI-PK model	Achieved high predictive accuracy for PK parameters from NP surface/size descriptors across multiple NP classes	[68]
Random forest/ensemble methods	High-throughput toxicity screening; predict cytotoxicity and genotoxicity from structural and surface descriptors	Nanotoxicology ML panel	Enables multi-variable safety assessment prior to synthesis, replacing one-at-a-time experimental testing	[71]
Convolutional neural networks (CNNs)	Image-based phenotypic analysis of NP-treated cells; pulmonary nodule malignancy classification from CT scans	AI-aided radiomics + adaptive NP surface design	Demonstrated automated lesion characterization enabling patient-specific NP surface modification strategy	[3,46]
In silico digital twins (ISTs)	Patient-specific simulation of NP pharmacokinetics, dose-response, and treatment optimization before clinical administration	IST platform	Personalizes NP dosing regimen based on patient age, genetics, organ function; reduces trial-and-error in clinical settings	[72]
Protein structure diffusion (RFdiffusion)	De novo design of targeting ligands and antibody fragments with optimized affinity for disease-associated receptors	RFdiffusion-guided ligand design	Enables rational design of targeting moieties with defined binding specificity; reduces reliance on empirical ligand screening	[70]
Microfluidics-coupled AI	Real-time process control of NP synthesis; adaptive feedback for size and PDI control during LNP manufacturing	AI-integrated microfluidic platform	Rapid formulation optimization; consistent particle quality; scalable integration with industrial LNP manufacturing	[41]

6.3. Predictive Toxicology and Personalized Nanomedicine

The application of AI to predictive nanotoxicology addresses one of the most time-consuming and resource-intensive aspects of nanoparticle development such as the characterization of safety profiles for materials with large compositional spaces. Traditional nanotoxicology testing evaluates one variable at a time (nanoparticle size, then surface charge, then composition, in sequence), generating incomplete safety pictures that cannot capture the interaction effects between multiple variables that commonly govern real biological responses [71]. Random forest ensemble models trained on multi-dimensional nanotoxicology datasets can simultaneously evaluate the size, surface chemistry, shape, and composition as predictors of cytotoxicity, genotoxicity, and inflammatory response,

identifying non-obvious safety signals that univariate testing would miss while dramatically reducing the animal experiment burden required to establish preliminary safety profiles [71]. These predictive toxicology tools are now being integrated into the early formulation design process, enabling the identification of potentially toxic compositions before laboratory synthesis, a true safety-by-design paradigm for nanomedicine.

Recent studies provide practical examples of this potential. TuNa-AI integrates automated high-throughput nanoparticle synthesis with machine learning to optimize both material selection and formulation composition. Using a dataset of 1275 formulations, the platform increased successful nanoparticle formation by 42.9% through composition optimization, and in a trametinib case study, reduced excipient use by 75% while maintaining in vitro efficacy and in vivo pharmacokinetics [67]. Such approaches illustrate how AI can move beyond retrospective data analysis toward closed-loop formulation design, in which computational predictions guide experimental synthesis and validation. Looking forward, integration with pharmacokinetic modeling and patient-specific digital twins could further support individualized formulation selection and dosing, although these applications still require substantial clinical validation.

The most transformative near-term prospect for AI in nanomedicine is the development of truly personalized nanoparticle therapeutics in which drug formulation, dose, and administration schedule are individually optimized for each patient based on their genomic, proteomic, and clinical data [13,73]. In silico digital twin (IST) frameworks implement this concept by creating a patient-specific computational replica (parameterized with the individual's age, genetic polymorphisms, organ function indices, and disease characteristics) that simulates the pharmacokinetics, tissue distribution, and pharmacodynamics of candidate nanoparticle formulations before any drug is administered [72]. By running thousands of simulated dosing scenarios on the patient's digital twin, the optimal formulation and schedule can be identified, and predicted adverse effects can be anticipated and mitigated before clinical exposure. This approach is particularly valuable for patient populations with variable metabolism (pediatric, elderly, renally impaired, and genetically polymorphic individuals) who are systematically underrepresented in the clinical trials that inform standard dosing recommendations [72].

7. Safety, Regulation, and Societal Impact

7.1. Biocompatibility, Long-Term Toxicity, and Immunogenicity

The assessment of nanoparticle biocompatibility demands a more comprehensive evaluation framework than is applied to conventional small-molecule drugs because nanoparticles interact with biological systems as physical objects through their geometry, surface area, and charge, in addition to their chemical properties, and because their behavior at the cellular and subcellular levels cannot be predicted from bulk material properties alone [17]. Cytotoxicity assessment in relevant cell lines provides an initial indication of cellular safety, but must be distinguished from systemic biocompatibility in multi-tissue organisms, where compensatory mechanisms, organ-level accumulation, and chronic exposure effects introduce complexities absent from cell culture models [17]. Robust safety evaluation therefore requires in vitro panels covering hepatic, renal, pulmonary, and immune cells, followed by in vivo studies assessing systemic toxicity, genotoxicity, carcinogenicity, and reproductive toxicity through standard toxicological protocols adapted for nanoparticle-specific considerations [17].

The immunogenicity of nanoparticle systems presents a particularly complex safety challenge because the immune system responds to nanoparticles through multiple overlapping mechanisms (complement activation, macrophage phagocytosis, T-cell activation, and antibody-mediated recognition), and these responses can be either beneficial (adjuvant

https://doi.org/10.3390/molecules31173121

effects in vaccines) or detrimental (inflammatory reactions, anti-drug antibody formation, accelerated blood clearance), depending on the specific nanoparticle composition and application [18]. The formation of anti-PEG antibodies following repeated dosing with PEGylated nanoparticles is a clinically established example of immunogenicity-driven pharmacokinetic variability that was not predicted by preclinical studies [15]. Long-term organ accumulation represents a critical safety concern for inorganic nanoparticles and carbon-based systems that are not fully biodegradable. The liver and spleen are primary sites of nanoparticle sequestration by resident macrophages, and the long-term consequences of progressive nanoparticle accumulation, including their degradation products' effects on hepatic and splenic function, require extensive longitudinal study before clinical approval [16]. As Kutner et al. [16] have emphasized, even biodegradable nanoparticle systems depend on the safety of their degradation products, since accumulated byproducts may themselves provoke inflammation or foreign body responses distinct from those caused by the intact carrier.

7.2. Regulatory Frameworks and Standardization Pathways

The regulatory classification of nanomedicine products is a fundamental determinant of the development pathway, approval timeline, and post-market surveillance requirements a product faces. The U.S. FDA, the European Medicines Agency (EMA), and the Japanese PMDA classify nanoproducts as drugs, biologics, or medical devices based on their primary mode of action, with each classification imposing different Chemistry, Manufacturing, and Controls (CMC) requirements, clinical trial designs, and safety evidence thresholds [17,18]. The complexity of nanoparticle systems (which can simultaneously exhibit drug-like pharmacological activity, device-like physical function, and biologic-like immune modulation) creates regulatory ambiguity that has been a persistent source of friction in the approval process. Nucleic acid nanoparticles represent the most acute example of regulatory boundary cases. The traditional pharmaceutical regulatory framework distinguishes between active pharmaceutical ingredients (APIs) and excipients, but a nucleic acid nanoparticle in which the lipid carrier is both the therapeutic enabler and the structural component challenges this binary classification in ways that require entirely new regulatory thinking [74].

The urgent need for standardized characterization and testing protocols for nanomedicines is recognized by regulatory agencies, standards organizations, and the academic community alike. Without agreed standards for measuring nanoparticle size distribution, surface charge, protein corona composition, and drug release profiles under physiologically relevant conditions, it is impossible to make meaningful cross-study comparisons, establish the material characterization requirements that a regulatory submission must meet, or define the performance specifications that a generic nanoparticle product must satisfy to demonstrate equivalence to an innovator product [15,17]. Organizations including ISO, ASTM, and the OECD are actively developing nanoparticle-specific standards and test guidelines to fill this gap, and the FDA and EMA have published nanotechnology-specific guidance documents that provide important initial frameworks, though global harmonization remains incomplete [17].

7.3. Ethical, Societal, and Cost-Accessibility Considerations

The integration of nanotechnology into clinical medicine raises ethical dimensions that extend beyond conventional pharmaceutical ethics to encompass questions specific to the novel capabilities and uncertainties of nanoscale systems. Informed consent for clinical nanoparticle trials, and eventually, approved nanoparticle therapies, require that patients receive meaningful information about nanoparticle compositions, potential long-term biodistribution, the possibility of multi-generational biological effects from persistent

https://doi.org/10.3390/molecules31173121

non-biodegradable materials, and the inherent uncertainty surrounding safety profiles that have not yet been characterized over full human lifetimes [17]. The asymmetry between the sophisticated technical understanding required to evaluate nanoparticle safety data and the lay understanding available to most patients creates a consent quality gap that is larger for nanomedicines than for conventional drugs.

Accessibility and cost equity arguably present the most consequential societal dimension of nanomedicine. The development and clinical translation of nanoparticle therapeutics can involve substantial costs associated with formulation optimization, scale-up, physicochemical characterization, preclinical evaluation, regulatory compliance, and clinical testing. These requirements may ultimately contribute to high product costs and create accessibility challenges, particularly for patients in low- and middle-income countries [75]. This economic structure risks creating a "two-tier medicine" in which the most powerful therapeutic tools available are preferentially accessible to the wealthy, widening rather than closing global health inequities. Extended-release and long-acting drug delivery formulations may improve treatment adherence by reducing dosing frequency and simplifying therapeutic regimens [75]. Sustainable manufacturing approaches using biopolymer-based and green chemistry synthesis routes directly address the cost and environmental burden dimensions of this equity challenge.

8. Challenges and Critical Barriers to Translation

Despite extensive preclinical research demonstrating nanoparticle efficacy across multiple disease areas, the vast majority of nanoparticle systems that show compelling laboratory performance do not reach clinical approval, reflecting a complex set of scientific, manufacturing, regulatory, and biological barriers that are distinct from those confronting conventional small-molecule drug development. Table 5 provides a structured overview of the principal barriers, their root causes, current mitigation strategies, and development status.

Table 5. Critical barriers to the clinical translation of nanoparticle drug delivery systems: root cause, current mitigation approaches, and development status.

Challenge	Root Cause	Current Mitigation Strategies	Development Status	Ref.
Batch-to-batch irreproducibility	Sensitivity of NP formation to mixing conditions, temperature, and reagent quality; lack of standardized protocols	Microfluidic manufacturing with real-time process control; AI-assisted parameter optimization; critical quality attribute (CQA) frameworks	Microfluidic scale-up demonstrated for LNPs; ISO and ICH Q8/Q10 frameworks being adopted; industrial IJM systems achieving consistent output	[28,41,42]
Protein corona formation	Serum proteins adsorb onto NP surface upon systemic injection, altering targeting ligand accessibility and accelerating clearance	PEG and zwitterionic stealth coatings; biomimetic cell-membrane cloaking; corona-resistant surface chemistries	PEGylation well-established but anti-PEG antibody formation reported; RBC membrane and CD47 'don't-eat-me' signals under active investigation	[7,14,15]
Inconsistent EPR-mediated targeting	EPR effect heterogeneous across tumor types, patient populations, and vascularization states; reduced in clinical vs. preclinical settings	Active targeting with receptor-specific ligands, antibodies, aptamers; multi-ligand systems targeting >1 receptor; tumor-penetrating peptides	Active targeting demonstrated in preclinical models; clinical benefit over passive targeting remains under investigation; EPR debate ongoing	[2,29]

Table 5. *Cont.*

Challenge	Root Cause	Current Mitigation Strategies	Development Status	Ref.
Limited CNS penetration	Blood–brain barrier (BBB) restricts most NPs; tight junctions exclude particles >8–10 nm by paracellular transport	Receptor-mediated transcytosis (transferrin, LDL); focused ultrasound + microbubbles for transient BBB opening; cell-membrane-coated NPs	Focused ultrasound-mediated BBB opening evaluated in Phase I/II clinical trials, including recurrent glioblastoma (NCT03744026); no clinically approved CNS nanoparticle product yet	[32,55,76]
Poor nucleic acid stability	Serum nucleases rapidly degrade unprotected RNA/DNA; endosomal trapping limits intracellular delivery efficiency	Ionizable lipid NPs with pH-responsive endosomal escape; chemical modification (2′-OMe, phosphorothioate); polymeric encapsulation	Demonstrated in approved Onpattro® and mRNA vaccines; liver targeting well-established; extrahepatic delivery still challenging	[8,30,31]
Manufacturing scale-up cost	High-resolution fabrication (plasma etching, CVD, lithography) incompatible with commercial volume production; high raw material costs	Roll-to-roll processing; impingement jet mixing (IJM); low-cost biopolymer substrates; green solvent synthesis	IJM demonstrated for LNP scale-up; biopolymer platforms in early development; full commercial scalability not yet universally demonstrated	[28,42]
Long-term safety and biodistribution	Unclear fate of non-degradable inorganic NPs (Au, Fe_3O_4) after repeated dosing; organ accumulation in liver/spleen; degradation product toxicity	Biodegradable coating strategies; comprehensive multi-organ toxicokinetic studies; AI-assisted toxicity prediction before synthesis	Extensive preclinical safety data required by FDA/EMA; standardized nanotoxicology protocols under development by ISO/OECD	[16,17]
Regulatory classification ambiguity	NPs classified differently (drug, biologic, device) depending on mode of action; nucleic acid NPs act as both API and excipient simultaneously	Harmonized nanotechnology-specific guidelines (FDA guidance 2022; EMA reflection paper); International harmonization via ICH	FDA and EMA guidance documents published; nucleic acid NP regulatory pathway being actively debated post-COVID vaccine approval	[18,74]

8.1. Reproducibility, Scalability, and Manufacturing Hurdles

Reproducibility at the batch level (the ability to produce nanoparticles with consistent size, loading, surface properties, and biological activity across independent manufacturing runs) is a fundamental requirement for clinical use that many laboratory-scale nanoparticle synthesis methods cannot reliably meet [28]. The sensitivity of nanoparticle formation to mixing conditions, reagent lot-to-lot variability, and minor process parameter deviations means that a synthesis protocol that produces excellent material in one laboratory may yield unacceptably variable material in another, or in the same laboratory at different times [77]. This reproducibility gap is not merely a regulatory inconvenience, it is a scientific problem that limits the ability to draw meaningful conclusions from clinical trial data when the nanoparticle formulation itself may vary between patients or even between treatment cycles within the same patient. The adoption of microfluidic and IJM manufacturing approaches with in-process analytical monitoring, combined with design of experiments (DoE) frameworks that systematically map the design space and identify process parameters critical to product quality, represents the current industrial approach to resolving this challenge [28,42].

Scalability from laboratory to commercial manufacturing is a distinct and equally challenging problem because the physical processes that govern nanoparticle formation (fluid mixing, interfacial energy minimization, nucleation and growth kinetics) do not

scale linearly with volume. Increasing batch size without changing mixing conditions alters the effective mixing time and shear rate that the formulation experiences, which can change particle size distribution, drug loading, and surface properties in ways that require complete reoptimization of the manufacturing process at each scale step [41]. Green-synthesized nanoparticles, which use biologically derived reducing agents and natural extract-mediated synthesis routes, offer a potentially more environmentally sustainable manufacturing pathway, but currently lack the process control and characterization data required for regulatory filing, representing an important research agenda for sustainable nanomedicine [78,79].

8.2. Biological Complexity, Patient Variability, and the EPR Debate

The enhanced permeability and retention (EPR) effect has served as the foundational rationale for passive nanoparticle targeting in oncology, and it underlies the design logic of virtually every passively targeted nanoparticle oncology product [3]. However, a growing body of clinical and meta-analytic evidence has called into question the reliability of EPR-mediated tumor accumulation as a predictable clinical phenomenon. A widely cited meta-analysis by Wilhelm et al. reported that the median delivery of systemically administered nanoparticles to solid tumors was approximately 0.7% of the injected dose, highlighting the substantial biological barriers that limit nanoparticle tumor accumulation. However, subsequent analyses have emphasized that estimates of nanoparticle delivery efficiency depend on the pharmacokinetic metrics and analytical approaches used [80]. The factors governing this variability include tumor vascular density and permeability, pericyte coverage and vessel maturation, interstitial fluid pressure, and lymphatic drainage function, all of which differ substantially between the transplanted subcutaneous xenografts used in most preclinical studies and the spontaneous, stromal-rich tumors encountered in clinical oncology. This EPR controversy does not negate the value of nanoparticle delivery (the improved tolerability and pharmacokinetics of Doxil® relative to free doxorubicin are real clinical benefits regardless of whether EPR is the mechanism). Still, it fundamentally undermines the assumption that passive targeting alone is sufficient for clinical efficacy and strengthens the case for active targeting strategies.

8.3. Standardization and Long-Term Safety Data

The absence of standardized characterization, testing, and reporting frameworks for nanoparticle drug delivery is a structural barrier that impedes progress at every stage from basic research to regulatory approval. Without agreed protocols for measuring nanoparticle size distribution by appropriate techniques (DLS, NTA, AF4-MALS), reporting protein corona composition under physiologically relevant conditions, and characterizing drug release under validated in vitro conditions that correlate with in vivo performance, the results of different research groups studying apparently similar systems cannot be meaningfully compared or synthesized into collective knowledge [15,17]. This fragmentation means that the global community of nanoparticle researchers is, to a significant degree, producing data that cannot be aggregated into the large, high-quality datasets needed to train the machine learning models and establish the mechanistic understanding required for reliable clinical translation prediction.

Long-term safety data gaps are particularly acute for nanoparticle systems containing non-biodegradable materials (gold, silica, iron oxide) that may persist in organs for months to years after administration. Preclinical toxicology studies conducted over weeks or months cannot capture the effects of years of organ accumulation that will occur in patients who receive repeated treatment cycles for chronic conditions. Similarly, the emergence of anti-PEG immune responses in clinical populations (not predicted by preclinical studies)

illustrates that nanoparticle-specific immunological effects may only become apparent after years of clinical use. The nanotoxicology community, in partnership with regulatory agencies and ISO/OECD standards bodies, is actively developing standardized in vitro and in vivo test batteries specifically designed for nanoparticle safety assessment, and the establishment of these standards is recognized as a prerequisite for the accelerated development of the next generation of nanomedicines [17,18].

9. Emerging Trends and Future Directions

9.1. Personalized and Biomimetic Nanomedicine

The convergence of personalized medicine and nanomedicine is producing a new generation of nanoparticle therapeutics whose composition, surface functionalization, and dosing are tailored to the molecular and physiological profile of individual patients. AI-powered in silico digital twin frameworks represent the most comprehensive implementation of this concept, enabling patient-specific simulation of nanoparticle pharmacokinetics and pharmacodynamics before clinical exposure and the optimization of formulation and dosing schedules for each individual [72]. The clinical utility of this approach is greatest for patient populations with high inter-individual variability in drug metabolism and tissue distribution, including pediatric, elderly, and genetically polymorphic populations, where standard population-average dosing is least reliable. Personalized surface functionalization, where targeting ligands are selected to match the specific receptor expression profile of a patient's tumor as determined by biopsy proteomics or liquid biopsy, represents a related frontier that is becoming technically feasible as next-generation protein design tools mature [46].

Biomimetic nanoparticle strategies exploit biological structures and materials (cell membranes, extracellular vesicles, protein cages, and naturally derived biopolymers) to construct delivery systems with inherent biological compatibility and targeting capabilities that synthetic materials cannot replicate. Red blood cell membrane-coated nanoparticles acquire the self-recognition "CD47" and "do not eat me" signals of erythrocytes, enabling immune evasion and prolonged circulation without PEGylation, while exosomes derived from tumor-homing immune cells, such as macrophages and NK cells, carry natural targeting ligands for tumor-associated antigens [15,39]. Wound healing and tissue regeneration applications have recently exploited nanocellulose-based scaffolds and nanomaterial-functionalized wound dressings that modulate inflammation, provide mechanical support for tissue reconstruction, and deliver therapeutic factors with spatial precision unavailable to conventional wound care formulations. These biomimetic platforms illustrate the broadening scope of nanomedicine beyond drug delivery into tissue engineering and regenerative medicine.

9.2. Sustainable Nanomanufacturing and Green Chemistry Approaches

The environmental footprint of nanoparticle synthesis is an increasingly important consideration as nanomedicine moves from small-scale laboratory production to industrial manufacturing. Conventional nanoparticle synthesis routes frequently employ non-biodegradable polymers, toxic organic solvents, and hazardous reducing agents whose waste streams require specialized treatment and generate significant environmental burden [78,79]. Green chemistry approaches for drug-delivery nanoparticles seek to replace hazardous solvents and reagents with safer alternatives and adopt resource-efficient manufacturing processes while preserving the physicochemical properties, biocompatibility, drug-loading capacity, and reproducibility required for therapeutic use. Table 6 summarizes representative sustainable manufacturing strategies directly relevant to nanoparticle drug-delivery systems.

Table 6. Green and sustainable manufacturing strategies for nanoparticle drug-delivery systems: approach, sustainability advantage, therapeutic relevance, and key findings.

Approach	Sustainable Strategy	Drug-Delivery Relevance	Key Findings	Ref.
Green-solvent PLGA nanoparticle synthesis	Replacement of conventional hazardous/petroleum-derived solvents with safer, more sustainable solvents	PLGA nanoparticles for therapeutic delivery	Green-solvent formulations produced stable PLGA nanoparticles with physicochemical properties and cellular uptake comparable to conventionally prepared nanoparticles	[81]
Sustainable PLGA formulation	Use of green/alternative solvents in nanoprecipitation and nanoemulsion processes	Biodegradable PLGA drug-delivery systems	Alternative solvents can reduce reliance on hazardous organic solvents while maintaining nanoparticle formation and relevant particle characteristics	[82]
Microfluidic PLGA nanoparticle production	Reduced material, energy, and reagent consumption through controlled microscale processing	Controlled production of PLGA drug carriers	Microfluidic processing provides improved control over particle properties while reducing material, energy, and processing requirements	[83]

For drug-delivery applications, green nanomanufacturing should focus not only on reducing environmental impact but also on preserving the physicochemical properties, biocompatibility, drug-loading capability, and reproducibility required for therapeutic use. Recent studies demonstrate that greener solvent systems can be employed for PLGA nanoparticle production while maintaining particle characteristics and cellular uptake comparable to conventional formulations [81]. Process-intensified approaches such as microfluidic synthesis may further reduce reagent and energy consumption while improving control over nanoparticle size and reproducibility [83]. Nevertheless, regulatory translation requires the rigorous characterization of residual solvents, batch consistency, stability, and biological performance before such sustainable manufacturing strategies can be adopted clinically.

9.3. Next-Generation Clinical Translation and Global Health Integration

The most impactful near-term opportunity for expanding nanomedicine's global health contribution lies in closing the substantial translational gap between the large number of nanoparticle systems reported in preclinical research and the comparatively limited number that have progressed to clinical approval [13]. The primary causes of this translational attrition, poor predictive validity of standard murine models, EPR effect variability in human tumors, unresolved long-term safety concerns, and manufacturing scalability barriers, are well-characterized, and targeted research investments addressing each barrier are likely to yield proportionate improvements in clinical trial success rates. Patient-derived tumor models, including organoids and humanized mouse models with reconstituted human immune systems, provide more predictive platforms for efficacy and safety assessment that may improve the pre-clinical-to-clinical translation rate [32]. Standardized regulatory pathways with pre-competitive collaborative development of characterization standards (modeled on the ICH guidelines that have harmonized small-molecule drug development across major regulatory jurisdictions) would reduce the per-product regulatory burden and accelerate approval timelines for nanoparticle therapeutics globally.

Nanotechnology education in medical training programs represents an underappreciated systemic barrier to clinical translation. Medical practitioners who will prescribe, administer, and monitor nanoparticle-based therapeutics must understand the fundamental properties of these systems well enough to select appropriate patients, recognize unique

adverse effects, and interpret performance deviations. Díaz-López et al. [84] documented significant gaps in nanotechnology awareness among postgraduate medical students and identified structural curricula limitations, including limited dedicated course time and the insufficient integration of nanotechnology into existing pharmacology and clinical oncology training, as root causes that require systemic educational reform rather than individual study. Addressing this knowledge gap is as important for clinical translation as the technical challenges, because therapeutic benefit can only be realized if clinicians possess the understanding needed to use nanomedicines correctly and safely.

10. Conclusions and Outlook

Nanoparticle-based drug delivery systems have moved from concept to clinical standard over the past three decades, with FDA-approved products spanning liposomal chemotherapeutics, albumin-bound nanoparticles, siRNA-LNP gene therapy, and mRNA vaccines that have collectively benefited hundreds of millions of patients. The fundamental scientific principles are well-established. The size, shape, surface charge, and composition jointly determine pharmacokinetic behavior and cellular fate; the EPR effect enables passive tumor accumulation, though with high patient-to-patient variability; stimuli-responsive mechanisms can achieve controlled, site-specific drug release with spatial and temporal precision; and multifunctional architectures integrating drug delivery with imaging and diagnostic functionality are now technically feasible across multiple material platforms.

The central challenge of the present moment is not discovery; enough nanoparticle platforms, surface engineering strategies, and targeting approaches have been characterized to fill an enormous clinical portfolio, but translation: reliably converting compelling laboratory demonstrations into manufacturable, safe, and clinically effective products that reach patients at an accessible cost. This translation challenge has multiple interacting dimensions. Manufacturing scalability requires engineering solutions that maintain nanoparticle quality attributes during commercial-scale production. Biological predictability requires improved preclinical models that faithfully replicate the immunological, vascular, and cellular complexity of human disease. Regulatory efficiency requires harmonized characterization standards and approval pathways designed for the unique properties of nanoparticle systems. Clinical utility requires patient-specific approaches that account for the inter-individual biological variability that causes population-average nanoparticle performance to diverge from the performance needed for each patient.

The emerging integration of artificial intelligence, machine learning, and digital twin frameworks into nanomedicine design is the most powerful accelerant currently available for addressing these challenges. By enabling multi-variable formulation optimization, predictive pharmacokinetics, high-throughput toxicity screening, and patient-specific treatment planning, AI tools compress the empirical iteration cycles that currently consume most of the time and cost of nanomedicine development. Sustainable green chemistry approaches address the cost and environmental barriers that limit the accessibility of nanomedicine in low-resource settings. Biomimetic platforms that exploit natural biological components for immune evasion and targeting address the immunogenicity and protein corona challenges that limit the in vivo performance of synthetic carriers. Together, these converging advances suggest that the third decade of clinical nanomedicine will be defined not by the technical achievement of ultralow friction or single-particle drug delivery precision, but by the achievement of manufacturing reliability, clinical predictability, regulatory clarity, and global accessibility that transforms nanoparticle platforms from specialized research tools into routine elements of personalized medical care.

https://doi.org/10.3390/molecules31173121

Author Contributions: Conceptualization, S.A.J. and P.L.M.; methodology, S.A.J., B.C., M.C., E.C. and I.D.; formal analysis, S.A.J., B.C., M.C., E.C. and I.D.; writing—original draft preparation, S.A.J., B.C., M.C., E.C. and I.D.; writing—review and editing, S.A.J., B.C., M.C., E.C., I.D. and P.L.M.; supervision, P.L.M. All authors have read and agreed to the published version of the manuscript.

Funding: This research received no external funding.

Data Availability Statement: No new data were created or analyzed in this study. Data sharing is not applicable to this article.

Conflicts of Interest: The authors declare no conflicts of interest.

References

1. Patra, J.K.; Das, G.; Fraceto, L.F.; Campos, E.V.R.; Rodriguez-Torres, M.D.P.; Acosta-Torres, L.S.; Diaz-Torres, L.A.; Grillo, R.; Swamy, M.K.; Sharma, S.; et al. Nano Based Drug Delivery Systems: Recent Developments and Future Prospects. *J. Nanobiotechnol.* **2018**, *16*, 71. [CrossRef] [PubMed]
2. Li, M.; Zhou, S.; Zhang, Y.; Li, J.; Zhang, K. Advancements in Tumor-Targeted Nanoparticles: Design Strategies and Multifunctional Therapeutic Approaches. *Nanomaterials* **2025**, *15*, 1262. [CrossRef] [PubMed]
3. Kantesaria, R.; Panda, H.S. A Review on AI-Based Data-Driven Models for Optimization of Nanocarriers as Drug Delivery Systems. *ACS Biomater. Sci. Eng.* **2026**, *12*, 1397–1418. [CrossRef] [PubMed]
4. Srivastava, A.; Ahmad, A.; Siddiqui, S.; Islam, A. Innovations in Targeted Drug Delivery: From Nanotechnology to Clinical Applications. *Next Nanotechnol.* **2026**, *9*, 100336. [CrossRef]
5. Liu, Y.; Liang, Y.; Yuhong, J.; Xin, P.; Han, J.L.; Du, Y.; Yu, X.; Zhu, R.; Zhang, M.; Chen, W.; et al. Advances in Nanotechnology for Enhancing the Solubility and Bioavailability of Poorly Soluble Drugs. *Drug Des. Dev. Ther.* **2024**, *18*, 1469–1495. [CrossRef] [PubMed]
6. Kurul, F.; Turkmen, H.; Cetin, A.E.; Topkaya, S.N. Nanomedicine: How Nanomaterials Are Transforming Drug Delivery, Bio-Imaging, and Diagnosis. *Next Nanotechnol.* **2025**, *7*, 100129. [CrossRef]
7. Jacob, S.; Varkey, N.R.; Boddu, S.H.S.; Gorain, B.; Rao, R.; Nair, A.B. Advances in Lipid-Polymer Hybrid Nanoparticles: Design Strategies, Functionalization, Oncological and Non-Oncological Clinical Prospects. *Pharmaceuticals* **2025**, *18*, 1772. [CrossRef] [PubMed]
8. Lu, M.; Xing, H.; Zheng, A.; Huang, Y.; Liang, X.-J. Overcoming Pharmaceutical Bottlenecks for Nucleic Acid Drug Development. *Acc. Chem. Res.* **2023**, *56*, 224–236. [CrossRef] [PubMed]
9. Perrigue, P.M.; Murray, R.A.; Mielcarek, A.; Henschke, A.; Moya, S.E. Degradation of Drug Delivery Nanocarriers and Payload Release: A Review of Physical Methods for Tracing Nanocarrier Biological Fate. *Pharmaceutics* **2021**, *13*, 770. [CrossRef] [PubMed]
10. Kamaly, N.; Yameen, B.; Wu, J.; Farokhzad, O.C. Degradable Controlled-Release Polymers and Polymeric Nanoparticles: Mechanisms of Controlling Drug Release. *Chem. Rev.* **2016**, *116*, 2602–2663. [CrossRef] [PubMed]
11. Zhang, L.; Zhang, M.; Zhou, L.; Han, Q.; Chen, X.; Li, S.; Li, L.; Su, Z.; Wang, C. Dual Drug Delivery and Sequential Release by Amphiphilic Janus Nanoparticles for Liver Cancer Theranostics. *Biomaterials* **2018**, *181*, 113–125. [CrossRef] [PubMed]
12. Sánchez-Orozco, J.L.; Aguirre-Loredo, R.; García-Uriostegui, L.; Meléndez-Ortiz, H.I. Drug Delivery Systems Based on Polysaccharides and Inorganic Nanoparticles: A Comprehensive Review on Their Therapeutic Applications and Recent Advances. *Next Mater.* **2026**, *11*, 101707. [CrossRef]
13. Desai, N.; Rana, D.; Patel, M.; Bajwa, N.; Prasad, R.; Vora, L.K. Nanoparticle Therapeutics in Clinical Perspective: Classification, Marketed Products, and Regulatory Landscape. *Small* **2025**, *21*, 2502315. [CrossRef] [PubMed]
14. Fam, S.Y.; Chee, C.F.; Yong, C.Y.; Ho, K.L.; Mariatulqabtiah, A.R.; Tan, W.S. Stealth Coating of Nanoparticles in Drug-Delivery Systems. *Nanomaterials* **2020**, *10*, 787. [CrossRef] [PubMed]
15. Hao, X.; Zhang, H.; Liu, R.; Che, J.; Zhang, D.; Liang, J.; Sun, L. Red Blood Cell Membrane Functionalized Biomimetic Nanoparticles for Systemic Lupus Erythematosus Treatment. *Mater. Today Adv.* **2022**, *16*, 100294. [CrossRef]
16. Kutner, N.; Kunduru, K.R.; Rizik, L.; Farah, S. Recent Advances for Improving Functionality, Biocompatibility, and Longevity of Implantable Medical Devices and Deliverable Drug Delivery Systems. *Adv. Funct. Mater.* **2021**, *31*, 2010929. [CrossRef]
17. Yusuf, A.; Almotairy, A.R.Z.; Henidi, H.; Alshehri, O.Y.; Aldughaim, M.S. Nanoparticles as Drug Delivery Systems: A Review of the Implication of Nanoparticles' Physicochemical Properties on Responses in Biological Systems. *Polymers* **2023**, *15*, 1596. [CrossRef] [PubMed]
18. Rodríguez-Gómez, F.D.; Monferrer, D.; Penon, O.; Rivera-Gil, P. Regulatory Pathways and Guidelines for Nanotechnology-Enabled Health Products: A Comparative Review of EU and US Frameworks. *Front. Med.* **2025**, *12*, 1544393. [CrossRef] [PubMed]

19. Akomolafe, O.A.; Akinsiku, A.A. Advances in Nanoparticles as Drug Delivery Systems: A Review. *Sci. Afr.* **2025**, *30*, e03101. [CrossRef]
20. Kaga, S.; Truong, N.P.; Esser, L.; Senyschyn, D.; Sanyal, A.; Sanyal, R.; Quinn, J.F.; Davis, T.P.; Kaminskas, L.M.; Whittaker, M.R. Influence of Size and Shape on the Biodistribution of Nanoparticles Prepared by Polymerization-Induced Self-Assembly. *Biomacromolecules* **2017**, *18*, 3963–3970. [CrossRef] [PubMed]
21. Haripriyaa, M.; Suthindhiran, K. Pharmacokinetics of Nanoparticles: Current Knowledge, Future Directions and Its Implications in Drug Delivery. *Future J. Pharm. Sci.* **2023**, *9*, 113. [CrossRef]
22. Mustahkimovna, J.; Khikmatuloyevna, M.; Harale, A. AI-Based Smart Drug Delivery Systems: Integrating Artificial Intelligence and Nanotechnology. *Int. J. Drug Deliv. Technol.* **2026**, *16*, 522–528. [CrossRef]
23. Geng, Y.; Dalhaimer, P.; Cai, S.; Tsai, R.; Tewari, M.; Minko, T.; Discher, D.E. Shape Effects of Filaments versus Spherical Particles in Flow and Drug Delivery. *Nat. Nanotechnol.* **2007**, *2*, 249–255. [CrossRef] [PubMed]
24. Lagarrigue, P.; Moncalvo, F.; Cellesi, F. Non-Spherical Polymeric Nanocarriers for Therapeutics: The Effect of Shape on Biological Systems and Drug Delivery Properties. *Pharmaceutics* **2023**, *15*, 32. [CrossRef] [PubMed]
25. Patil, S.; Sandberg, A.; Heckert, E.; Self, W.; Seal, S. Protein Adsorption and Cellular Uptake of Cerium Oxide Nanoparticles as a Function of Zeta Potential. *Biomaterials* **2007**, *28*, 4600–4607. [CrossRef] [PubMed]
26. Chelliah, R.; Rubab, M.; Vijayalakshmi, S.; Karuvelan, M.; Barathikannan, K.; Oh, D.-H. Liposomes for Drug Delivery: Classification, Therapeutic Applications, and Limitations. *Next Nanotechnol.* **2025**, *8*, 100209. [CrossRef]
27. Gabizon, A.A. Pegylated Liposomal Doxorubicin: Metamorphosis of an Old Drug into a New Form of Chemotherapy. *Cancer Investig.* **2001**, *19*, 424–436. [CrossRef] [PubMed]
28. Herdiana, Y. Bridging the Gap: The Role of Advanced Formulation Strategies in the Clinical Translation of Nanoparticle-Based Drug Delivery Systems. *Int. J. Nanomed.* **2025**, *20*, 13039–13053. [CrossRef] [PubMed]
29. Florence, A.T. Reductionism and Complexity in Nanoparticle-Vectored Drug Targeting. *J. Control. Release* **2012**, *161*, 399–402. [CrossRef] [PubMed]
30. Zhang, H.; Vandesompele, J.; Braeckmans, K.; De Smedt, S.C.; Remaut, K. Nucleic Acid Degradation as Barrier to Gene Delivery: A Guide to Understand and Overcome Nuclease Activity. *Chem. Soc. Rev.* **2024**, *53*, 317–360. [CrossRef] [PubMed]
31. Hu, M.; Li, X.; You, Z.; Cai, R.; Chen, C. Physiological Barriers and Strategies of Lipid-Based Nanoparticles for Nucleic Acid Drug Delivery. *Adv. Mater.* **2024**, *36*, 2303266. [CrossRef] [PubMed]
32. Munasir; Maulana, S.A.; Nurlaili, R.A.; Taufiq, A.; Faaizatunnisa, N.; Ariesta, M.N.; Suaebah, E.; Putri, N.P.; Sunaryono; Astuti, S.D.; et al. Engineering Silica Nanoparticle-Based Drug Delivery Systems for Glioblastoma Therapy. *J. Drug Deliv. Sci. Technol.* **2026**, *119*, 108178. [CrossRef]
33. Eltaib, L. Polymeric Nanoparticles in Targeted Drug Delivery: Unveiling the Impact of Polymer Characterization and Fabrication. *Polymers* **2025**, *17*, 833. [CrossRef] [PubMed]
34. Cheng, C.-A.; Deng, T.; Lin, F.-C.; Cai, Y.; Zink, J.I. Supramolecular Nanomachines as Stimuli-Responsive Gatekeepers on Mesoporous Silica Nanoparticles for Antibiotic and Cancer Drug Delivery. *Theranostics* **2019**, *9*, 3341–3364. [CrossRef] [PubMed]
35. Djayanti, K.; Maharjan, P.; Cho, K.H.; Jeong, S.; Kim, M.S.; Shin, M.C.; Min, K.A. Mesoporous Silica Nanoparticles as a Potential Nanoplatform: Therapeutic Applications and Considerations. *Int. J. Mol. Sci.* **2023**, *24*, 6349. [CrossRef] [PubMed]
36. Stueber, D.D.; Villanova, J.; Aponte, I.; Xiao, Z.; Colvin, V.L. Magnetic Nanoparticles in Biology and Medicine: Past, Present, and Future Trends. *Pharmaceutics* **2021**, *13*, 943. [CrossRef] [PubMed]
37. Almajidi, Y.Q.; Al-hakeem, M.A.; Abdulsahib, W.K.; Mustafa, W.W.; Jyothi, S.R.; Nayak, P.P.; Janney, J.B.; Singh, G.; Sinha, A.; Polatova, D. Engineering Plasmonic Gold Nanoparticles for Synergistic Photothermal Cancer Therapy. *Photonics Nanostruct.-Fundam. Appl.* **2026**, *70*, 101520. [CrossRef]
38. Kanagaraj, K.; Nangan, S.; Thirumalaivasan, N. Carbon Dots and Their Role in Cancer Immunotherapy: Targeted Drug Delivery and Tumor Microenvironment Modulation-a Narrative Review. *Next Mater.* **2026**, *11*, 101711. [CrossRef]
39. Saka, O.M.; Dora, D.D.; Kibar, G.; Tevlek, A. Expanding the Role of Exosomes in Drug, Biomolecule, and Nanoparticle Delivery. *Life Sci.* **2025**, *368*, 123499. [CrossRef] [PubMed]
40. Siafaka, P.I.; Üstündağ Okur, N.; Karavas, E.; Bikiaris, D.N. Surface Modified Multifunctional and Stimuli Responsive Nanoparticles for Drug Targeting: Current Status and Uses. *Int. J. Mol. Sci.* **2016**, *17*, 1440. [CrossRef] [PubMed]
41. Zhang, H.; Yang, J.; Sun, R.; Han, S.; Yang, Z.; Teng, L. Microfluidics for Nano-Drug Delivery Systems: From Fundamentals to Industrialization. *Acta Pharm. Sin. B* **2023**, *13*, 3277–3299. [CrossRef] [PubMed]
42. Devos, C.; Udepurkar, A.; Sagmeister, P.; Hodlewsky, A.S.; Chen, J.; Hatas, A.; Ostrovsky, N.; Al-Jazrawe, M.; Ren, J.I.; Liu, A.Y.; et al. Manufacturing mRNA-Loaded Lipid Nanoparticles with Precise Size and Morphology Control. *ACS Nano* **2025**, *19*, 33991–34002. [CrossRef] [PubMed]
43. Tan, Y.F.; Lao, L.L.; Xiong, G.M.; Venkatraman, S. Controlled-Release Nanotherapeutics: State of Translation. *J. Control. Release* **2018**, *284*, 39–48. [CrossRef] [PubMed]

44. Mukthavaram, R.; Tanis, S.P.; Sagi, A.; Parirokh, P.; Davis, M.; Hong, H.; Huynh, H.P.; Nguyen, M.; Lee, R.; Guo, Y.; et al. Peptide Substitutes of PEG: Biological Outcomes on Prospective Lipid Nanoparticle Shielding Materials. *Adv. Healthc. Mater.* **2026**, *15*, e05392. [CrossRef] [PubMed]
45. Kabil, M.F.; Azzazy, H.M.E.-S.; Nasr, M. Recent Progress on polySarcosine as an Alternative to PEGylation: Synthesis and Biomedical Applications. *Int. J. Pharm.* **2024**, *653*, 123871. [CrossRef] [PubMed]
46. Zhao, L.; Liu, X.; Deng, X. AI-Engineered Multifunctional Nanoplatforms: Synergistically Bridging Precision Diagnosis and Intelligent Therapy in next-Generation Oncology. *J. Nanobiotechnol.* **2025**, *24*, 73. [CrossRef] [PubMed]
47. Yao, E.; Li, Y.; Deng, K.; He, W.; Ashrafizadeh, M.; Conde, J.; Yang, L. Folic Acid-Targeted Macrophage Membrane-Coated Carbon Quantum Dot Nanoplatform for Dual Drug and Gene Delivery in Metastatic Osteosarcoma Therapy. *Chem. Eng. J.* **2025**, *515*, 163227. [CrossRef]
48. Huang, W.; Hsu, J.C.; Zhou, J.; Kwon, G.S.; Kang, L.; Hua, C.; Cai, W. Stimuli-Responsive Nanomaterials for Targeted Drug Delivery in Inflammatory Bowel Disease: Advances and Emerging Directions. *Matter* **2025**, *8*, 102249. [CrossRef] [PubMed]
49. Sivasubramanian, P.D.; Unnikrishnan, G.; Kolanthai, E.; Muthuswamy, S. Engineered Nanoparticle Systems: A Review on Emerging Strategies for Enhanced Cancer Therapeutics. *Next Mater.* **2025**, *6*, 100405. [CrossRef]
50. Liu, J.; Liu, J.; Mu, W.; Ma, Q.; Zhai, X.; Jin, B.; Liu, Y.; Zhang, N. Delivery Strategy to Enhance the Therapeutic Efficacy of Liver Fibrosis via Nanoparticle Drug Delivery Systems. *ACS Nano* **2024**, *18*, 20861–20885. [CrossRef] [PubMed]
51. Du, Z.; Saleh, E.A.M.; MMoharam, M.; Rab, S.O.; Ballal, S.; Singh, A.; Sabarivani, A.; Sahoo, S.; Hsu, C.-Y. Enzyme Responsive Magnetic Nanoparticles for Targeted Drug Delivery and Precision Medicine. *Drug Dev. Res.* **2025**, *86*, e70185. [CrossRef] [PubMed]
52. Pierini, F.; Nakielski, P.; Urbanek, O.; Pawłowska, S.; Lanzi, M.; De Sio, L.; Kowalewski, T.A. Polymer-Based Nanomaterials for Photothermal Therapy: From Light-Responsive to Multifunctional Nanoplatforms for Synergistically Combined Technologies. *Biomacromolecules* **2018**, *19*, 4147–4167. [CrossRef] [PubMed]
53. Seip, R.; Chin, C.T.; Hall, C.S.; Raju, B.I.; Ghanem, A.; Tiemann, K. Targeted Ultrasound-Mediated Delivery of Nanoparticles: On the Development of a New HIFU-Based Therapy and Imaging Device. *IEEE Trans. Biomed. Eng.* **2010**, *57*, 61–70. [CrossRef] [PubMed]
54. Abueva, C.D. Photo-Triggered Theranostic Nanoparticles in Cancer Therapy. *Med. Lasers* **2021**, *10*, 7–14. [CrossRef]
55. Carpentier, A.; Stupp, R.; Sonabend, A.M.; Dufour, H.; Chinot, O.; Mathon, B.; Ducray, F.; Guyotat, J.; Baize, N.; Menei, P.; et al. Repeated Blood–Brain Barrier Opening with a Nine-Emitter Implantable Ultrasound Device in Combination with Carboplatin in Recurrent Glioblastoma: A Phase I/II Clinical Trial. *Nat. Commun.* **2024**, *15*, 1650. [CrossRef] [PubMed]
56. Ghazal, H.; Waqar, A.; Yaseen, F.; Shahid, M.; Sultana, M.; Tariq, M.; Bashir, M.K.; Tahseen, H.; Raza, T.; Ahmad, F. Role of Nanoparticles in Enhancing Chemotherapy Efficacy for Cancer Treatment. *Next Mater.* **2024**, *2*, 100128. [CrossRef]
57. Ghahremanloo, A.; Erfani, B.; Asgharzadeh, F.; Mansoori, S.; Gheybi, F.; Hashemy, S.I. Reducing Toxicity and Enhancing Efficacy of Doxorubicin by Liposomal Doxorubicin and Aprepitant in Breast Cancer. *Sci. Rep.* **2025**, *15*, 9798. [CrossRef] [PubMed]
58. Dheyab, M.A.; Aziz, A.A.; Khaniabadi, P.M.; Jameel, M.S.; Oladzadabbasabadi, N.; Rahman, A.A.; Braim, F.S.; Mehrdel, B. Gold Nanoparticles-Based Photothermal Therapy for Breast Cancer. *Photodiagn. Photodyn. Ther.* **2023**, *42*, 103312. [CrossRef] [PubMed]
59. Salatin, S.; Barar, J.; Barzegar-Jalali, M.; Adibkia, K.; Milani, M.A.; Jelvehgari, M. Hydrogel Nanoparticles and Nanocomposites for Nasal Drug/Vaccine Delivery. *Arch. Pharm. Res.* **2016**, *39*, 1181–1192. [CrossRef] [PubMed]
60. Sharma, D.K. Current Advancements in Nanoparticles for Vaccines and Drug Delivery for the Treatment of Tuberculosis. *J. Microbiol. Methods* **2025**, *232–234*, 107138. [CrossRef] [PubMed]
61. Adams, D.; Gonzalez-Duarte, A.; O'Riordan, W.D.; Yang, C.-C.; Ueda, M.; Kristen, A.V.; Tournev, I.; Schmidt, H.H.; Coelho, T.; Berk, J.L.; et al. Patisiran, an RNAi Therapeutic, for Hereditary Transthyretin Amyloidosis. *N. Engl. J. Med.* **2018**, *379*, 11–21. [CrossRef] [PubMed]
62. Parvin, N.; Mandal, T.K.; Joo, S.-W. The Impact of COVID-19 on RNA Therapeutics: A Surge in Lipid Nanoparticles and Alternative Delivery Systems. *Pharmaceutics* **2024**, *16*, 1366. [CrossRef] [PubMed]
63. Baden, L.R.; El Sahly, H.M.; Essink, B.; Kotloff, K.; Frey, S.; Novak, R.; Diemert, D.; Spector, S.A.; Rouphael, N.; Creech, C.B.; et al. Efficacy and Safety of the mRNA-1273 SARS-CoV-2 Vaccine. *N. Engl. J. Med.* **2021**, *384*, 403–416. [CrossRef] [PubMed]
64. Polack, F.P.; Thomas, S.J.; Kitchin, N.; Absalon, J.; Gurtman, A.; Lockhart, S.; Perez, J.L.; Pérez Marc, G.; Moreira, E.D.; Zerbini, C.; et al. Safety and Efficacy of the BNT162b2 mRNA Covid-19 Vaccine. *N. Engl. J. Med.* **2020**, *383*, 2603–2615. [CrossRef] [PubMed]
65. Choi, G.; Rejinold, S.; Huiyan, P.; Choy, J.-H. Inorganic–Inorganic Nanohybrids for Drug Delivery, Imaging and Photo-Therapy: Recent Developments and Future Scope. *Chem. Sci.* **2021**, *12*, 5044–5063. [CrossRef] [PubMed]
66. Hatit, M.Z.C.; Lokugamage, M.P.; Dobrowolski, C.N.; Paunovska, K.; Ni, H.; Zhao, K.; Vanover, D.; Beyersdorf, J.; Peck, H.E.; Loughrey, D.; et al. Species-Dependent in Vivo mRNA Delivery and Cellular Responses to Nanoparticles. *Nat. Nanotechnol.* **2022**, *17*, 310–318. [CrossRef] [PubMed]

67. Zhang, Z.; Xiang, Y.; Laforet, J., Jr.; Spasojevic, I.; Fan, P.; Heffernan, A.; Eyler, C.E.; Wood, K.C.; Hartman, Z.C.; Reker, D. TuNa-AI: A Hybrid Kernel Machine to Design Tunable Nanoparticles for Drug Delivery. *ACS Nano* **2025**, *19*, 33288–33296. [CrossRef] [PubMed]
68. Khakpour, A.; Florescu, L.; Tilley, R.; Jiang, H.; Iyer, K.S.; Carneiro, G. AI-Powered Prediction of Nanoparticle Pharmacokinetics: A Multi-View Learning Approach. *Mater. Today Commun.* **2025**, *49*, 113742. [CrossRef]
69. Kardani, S.L. Nanocarrier-Based Formulations: Regulatory Challenges, Ethical and Safety Considerations in Pharmaceuticals. *Asian J. Pharm.* **2024**, *18*, 346–351. [CrossRef]
70. Watson, J.L.; Juergens, D.; Bennett, N.R.; Trippe, B.L.; Yim, J.; Eisenach, H.E.; Ahern, W.; Borst, A.J.; Ragotte, R.J.; Milles, L.F.; et al. De Novo Design of Protein Structure and Function with RFdiffusion. *Nature* **2023**, *620*, 1089–1100. [CrossRef] [PubMed]
71. Han, Y.; Kim, D.H.; Pack, S.P. Nanomaterials in Drug Delivery: Leveraging Artificial Intelligence and Big Data for Predictive Design. *Int. J. Mol. Sci.* **2025**, *26*, 11121. [CrossRef] [PubMed]
72. Alharthi, S. AI-Powered in Silico Twins: Redefining Precision Medicine through Simulation, Personalization, and Predictive Healthcare. *Saudi Pharm. J.* **2025**, *34*, 1. [CrossRef] [PubMed]
73. Alavi, S.E.; Alavi, S.F.; Koohi, M.; Raza, A.; Ebrahimi Shahmabadi, H. Nanoparticle-Integrated Metal–Organic Frameworks: A Revolution in next-Generation Drug Delivery Systems. *J. Pharm. Investig.* **2024**, *54*, 751–783. [CrossRef]
74. Kozlov, S.; Panigaj, M.; Rebolledo, L.; Bhaskaran, H.; Afonin, K.A. Nucleic Acid Nanoparticles Redefine Traditional Regulatory Terminology: The Blurred Line between Active Pharmaceutical Ingredients and Excipients. *ACS Nano Med.* **2026**, *1*, 5–17. [CrossRef] [PubMed]
75. Li, W.; Tang, J.; Lee, D.; Tice, T.R.; Schwendeman, S.P.; Prausnitz, M.R. Clinical Translation of Long-Acting Drug Delivery Formulations. *Nat. Rev. Mater.* **2022**, *7*, 406–420. [CrossRef]
76. Hammouda, S.; Husien, S.; Salakawy, N.E.; Mamdouh, W. Influence of Polymer Hydrophilicity/Hydrophobicity and Drug Loading Strategy (Free vs. Polycaprolactone/Chitosan Nanoparticle-Encapsulated) on Tamoxifen-Loaded Polyvinyl Alcohol and Polycaprolactone Nanofibers for Breast Cancer Therapy. *J. Drug Deliv. Sci. Technol.* **2026**, *117*, 108071. [CrossRef]
77. Zhang, J.; Liu, R.; Yang, Z.; Luo, C.; Chen, J.; Guo, B.; Weitz, D.A.; Chen, D. Physicochemical and Surface Properties of Nanoparticles: Effects on Cellular Pathway and Uptake. *ChemNanoMat* **2025**, *11*, e202500043. [CrossRef]
78. Abubakar, H.L.; Mustapha, S.; Mustapha, S.I.; Tijani, J.O.; Abdulkareem, A.S. Green Nanoparticles Engineering for Environmental and Biomedical Solutions: A Comprehensive Review of Parameter-Driven Synthesis. *Next Mater.* **2026**, *11*, 101750. [CrossRef]
79. Mobarak, M.H.; Al Mahmud, M.Z.; Hossain, A.; Abir, M.A.H.; Hossain, N.; Chowdhury, M.A. Advances of Green-Synthesized Nanoparticles for Biomedical Applications. *BioMed Res. Int.* **2026**, *2026*, 9207147. [CrossRef] [PubMed]
80. Wilhelm, S.; Tavares, A.J.; Dai, Q.; Ohta, S.; Audet, J.; Dvorak, H.F.; Chan, W.C.W. Analysis of Nanoparticle Delivery to Tumours. *Nat. Rev. Mater.* **2016**, *1*, 16014. [CrossRef]
81. Karmaker, S.; Joshi, R.; Viravalli, A.; Boehnke, N. Evaluating Green Solvents for Sustainable PLGA Nanoparticle Synthesis. *Biomater. Sci.* **2025**, *13*, 2883–2890. [CrossRef] [PubMed]
82. Fischer, D. Sustainability in Drug and Nanoparticle Processing. In *Drug Delivery and Targeting*; Schäfer-Korting, M., Schubert, U.S., Eds.; Handbook of Experimental Pharmacology; Springer International Publishing: Cham, Switzerland, 2023; Volume 284, pp. 45–68, ISBN 978-3-031-52863-7.
83. Rezvantalab, S.; Keshavarz Moraveji, M. Microfluidic Assisted Synthesis of PLGA Drug Delivery Systems. *RSC Adv.* **2019**, *9*, 2055–2072. [CrossRef] [PubMed]
84. Díaz-López, M.M.; Bustos, R.-H.; Guevara-Ramírez, J.F.; García, J.-C. Understanding Barriers to Nanotechnology Education in Medical Specialty Programs: A Qualitative Nominal Group Study Among Postgraduate Students. *Adv. Med. Educ. Pract.* **2025**, *16*, 1481–1499. [CrossRef] [PubMed]

Disclaimer/Publisher's Note: The statements, opinions and data contained in all publications are solely those of the individual author(s) and contributor(s) and not of MDPI and/or the editor(s). MDPI and/or the editor(s) disclaim responsibility for any injury to people or property resulting from any ideas, methods, instructions or products referred to in the content.

molecules

MDPI

Article

Ovalbumin-Mediated Biogenic Synthesis of ZnO and MgO Nanostructures: A Path Toward Green Nanotechnology

Adriana-Gabriela Schiopu [1,2], Elena Andreea Vijan [2], Ecaterina Magdalena Modan [3,*], Sorin Georgian Moga [3], Denis Aurelian Negrea [3], Daniela Istrate [2], Georgiana Cîrstea [3], Mihai Oproescu [4] and Şaban Hakan Atapek [5]

[1] Faculty of Mechanics and Technology, Pitesti University Centre, National University of Science and Technology POLITEHNICA Bucharest, 110040 Pitesti, Romania; gabriela.schiopu@upb.ro
[2] Doctoral School Materials Science and Engineering, National University of Science and Technology POLITEHNICA Bucharest, Splaiul Independentei no. 313, Sector 6, 060042 Bucharest, Romania; elena_andreea.vijan@stud.sim.upb.ro (E.A.V.); calin_istrate_daniela@yahoo.com (D.I.)
[3] Regional Center of Research & Development for Materials, Processes and Innovative Products Dedicated to the Automotive Industry (CRCD-AUTO), Pitesti University Centre, National University of Science and Technology POLITEHNICA Bucharest, 110040 Pitesti, Romania; sorin_georgian.moga@upb.ro (S.G.M.); aurelian.negrea@upb.ro (D.A.N.); georgiana.cirstea93@upb.ro (G.C.)
[4] Faculty of Electronics, Communication and Computers, Pitesti University Centre, National University of Science and Technology POLITEHNICA Bucharest, 110040 Pitesti, Romania; mihai.oproescu@upb.ro
[5] Department of Metallurgical and Materials Engineering, Kocaeli University, 41001 Kocaeli, Türkiye; hatapek@kocaeli.edu.tr
* Correspondence: ecaterina.modan@upb.ro

Abstract: Sustainable and eco-friendly synthesis methods for nanoparticles are crucial for advancing green nanotechnology. This study presents the biogenic synthesis of zinc oxide (ZnO) and magnesium oxide (MgO) nanoparticles using ovalbumin, an abundant and non-toxic protein from egg white. The synthesis process was optimized by varying metal ion concentrations to control particle size and morphology. Characterization using ATR-FTIR, XRD, SEM, and UV-VIS confirmed the successful formation of uniform, well-crystallized nanoparticles with sizes ranging from 7.9 to 13.5 nm. ZnO nanoparticles exhibited superior antimicrobial efficacy against *Escherichia coli* and *Enterococcus faecalis*, while MgO nanoparticles showed enhanced potential environmental remediation. These findings highlight ovalbumin as a versatile agent for the green synthesis of ZnO and MgO nanomaterials, with promising applications in the medical, environmental, and optoelectronic fields. The results indicate that this biogenic method can serve as a sustainable proposal to produce nanostructured materials with diverse applications in the medical and environmental fields, such as eliminating pathogenic bacteria and purifying contaminated environments. Overall, this study significantly contributes to the development of sustainable nanomaterials and opens up new perspectives on the use of ovalbumin protein in the synthesis of multifunctional nanostructured materials.

Keywords: ovalbumin; eco-friendly; biogenic synthesis; nanostructures; ZnO; MgO

1. Introduction

Nanostructures (NSs) have revolutionized scientific fields due to their unique properties, including small size, large specific surface area, high catalytic activity, and antibacterial and antimicrobial properties. The choice of elaboration method of NSs depends on various factors, including the desired properties of the nanoparticles, the scale of production, and the available resources. By carefully selecting the appropriate method, it is possible to synthesize metal oxide NSs with tailored properties for a wide range of applications.

Among the variety of nanostructured oxides, ZnO and MgO are versatile and accessible materials, making them excellent examples of the potential of nanotechnology across various industries [1–4]. Zinc oxide (ZnO) and magnesium oxide (MgO) are versatile semiconductors with a wide band gap (3.37 eV-ZnO, 7.8eV-MgO) and excellent optical and electrical properties. Due to their nanoscale size, both ZnO and MgO nanoparticles (NPs) possess a high surface-to-volume ratio, which enhances their reactivity and catalytic activity in various applications and photocatalytic properties [5–8]. They can act as catalysts in various chemical reactions, including oxidation, reduction, and decomposition reactions. Thermal stability makes them suitable for high-temperature applications. Due to their shared properties, both ZnO and MgO nanoparticles find applications in various fields: catalysis, sensors, electronics, and biomedical applications. These oxides are also now used as an antibacterial agent against a wide range of bacteria species [9,10]. ZnO exhibits antibacterial properties both in the dark and under the action of light. Their mechanisms of action include the generation of reactive oxygen species (ROS), the release of ions, and the damage of the bacterial cell membrane. Both can be used in water or air purification, due to their ability to degrade toxic organic compounds. Also, both oxides can be used in combination to modify and improve the optoelectronic properties of devices.

To highlight the differences and similarities between zinc oxide (ZnO) and magnesium oxide (MgO), the comparison in Table 1 is organized based on their main properties and applications.

Table 1. Main properties and applications of ZnO and MgO nanoparticles.

Characteristic	ZnO	MgO	Strengths	Reference
Structure and physical properties				
Crystal Structure	Hexagonal (wurtzite, zincite)	Cubic (halite)	ZnO: More suitable for optical devices due to the wurtzite structure. MgO: Excellent thermal stability due to its cubic structure.	[6–8]
Density	~5.61 g/cm^3	~3.58 g/cm^3	MgO: Lighter material, useful in porous material application.	
Resistance to High Temperatures	Moderate (~1975 °C melting point)	Excellent (~2852 °C melting point)	MgO: Ideal for refractory and thermal insulator applications.	
Optical and Electronic Properties				
Bandgap	3.37 eV	7.8 eV	ZnO: Ideal for photocatalysis and UV sensors. MgO: Excellent performance as an electrical insulator.	[9,11–14]
Conductivity	Semiconductor	Insulator	ZnO: Enables use in electronic and optoelectronic devices.	
UV Light Absorption	Excellent	Limited	ZnO: Superior performance in UV applications (e.g., sunscreens, photocatalysis).	
Catalytic properties				
Photocatalysis	Excellent due to UV absorption	Limited	ZnO: Used for degrading organic compounds and environmental purification.	[15–17]
Adsorption	Moderate	Excellent for gasses	MgO: Superior performance in CO_2 adsorption and removal of gaseous pollutants.	

Table 1. *Cont.*

Characteristic	ZnO	MgO	Strengths	Reference
Antimicrobial Activity				
Antibacterial	Active in a broad spectrum	Active in a broad spectrum	Both: Offer antimicrobial activity, but ZnO may be more effective against Gram-negative bacteria.	[9,10,13]
Toxicity	Non-toxic at low concentrations	Very safe for skin	MgO: Preferred in applications where skin safety is a priority.	

Top-down methods for metal oxide nanostructure synthesis involve breaking down bulk materials into smaller particles, often through physical or mechanical processes [11,12]. These methods are relatively simple and they can lead to variations in particle size and shape, as well as potential contamination from the processing equipment. Bottom-up methods involve building nanostructures from individual atoms or molecules. These methods offer greater control over particle size, shape, and crystallinity, making them highly desirable for many applications [5,13,14]. Previous studies have highlighted common synthesis methods for the two oxides, as well as the most used precursors, as shown in Table 2.

Table 2. Common synthesis methods for ZnO and MgO nanoparticles.

Method	Description	Precursors for ZnO	Precursors for MgO	Reference
Ablation	Solar concentrated energy on metal-oxide precursors.	Zinc oxide	Magnesium oxide	[15–17]
Chemical Vapor Deposition (CVD)	Chemical reaction between gaseous precursors, depositing solid material on a substrate.	Zinc acetate, diethylzinc, dimethylzinc	Magnesium chloride, magnesium nitrate	[4,18]
Sol–Gel Method	Formation of a sol, gelation, and heat treatment.	Zinc acetate, zinc nitrate	Magnesium nitrate, magnesium chloride	[19–21]
Hydrothermal	Reactions in a sealed autoclave under high temperature and pressure.	Zinc acetate, zinc nitrate	Magnesium nitrate, magnesium chloride	
Microwave-assisted synthesis	Microwave irradiation accelerates chemical reactions.	Zinc acetate, zinc nitrate	Magnesium nitrate, magnesium chloride	[22,23]
Electrospinning	Electrospinning polymer solution into fibers, followed by calcination.	Zinc acetate, zinc nitrate	Magnesium nitrate, magnesium chloride	[13,24–26]
Biosynthesis	Utilizes biological agents for eco-friendly synthesis.	Zinc nitrate, zinc acetate	Magnesium nitrate, magnesium chloride	[6,27–32]

The conventional synthesis of metal nanoparticles often involves the use of toxic chemicals and entails high costs. Against the backdrop of global sustainability concerns, nanoparticle synthesis methods based on natural agents are being paid more attention. Biosynthesis, which involves the use of natural resources such as plants, microorganisms, or organic substances, has become a promising alternative to traditional chemical methods due to its low impact on the environment. Plant extracts are an affordable and rich source of phytochemical compounds such as phenols, flavonoids, and tannins, which facilitate the reduction in metal ions. For example, the use of *Portulaca oleracea* for the synthesis of ZnO nanoparticles has shown that the pH of the solution influences particle size and photocatalytic efficiency for the degradation of toxic dyes such as methyl orange [33].

Microorganisms, including fungi and bacteria, provide a robust platform for the synthesis of nanoparticles through intracellular or extracellular processes. Fungi such as *Fusarium oxysporum* produce nanoparticles by secreting enzymes that reduce metal ions and stabilize the resulting products [34]. This process is considered cost-effective and easy to scale [10]. The use of *Abelmoschus esculentus* and *Salvia officinalis* extracts for the synthesis of ZnO nanoparticles showed degradation rates of up to 86% for blue methylene in the first 90 min [30].

Distinguishing themselves from the use of plants, some studies focus on the use of other proteins in the biogenic synthesis of nanoparticles. For example, one review article discusses various methods for the synthesis and control of nanoparticle growth, highlighting the importance of proteins and other biomolecules in the formation and stabilization of nanoparticles [35].

Ovalbumin, a protein from egg white, is one choice, due to its availability and unique chemical properties, proving a promising agent for the controlled synthesis of nanoparticles. Egg white proteins have been used for the synthesis of silver (Ag) nanoparticles and metal oxides. Egg white acts as a reducing and stabilizing agent, forming uniform nanoparticles of about 20–25 nm, ideal for biomedical and energy applications [36,37].

Unlike plant extracts or microorganisms, which exhibit batch-to-batch variability due to genetic and environmental factors, ovalbumin is a single, well-characterized protein with a consistent structure. Ovalbumin has a well-defined molecular structure with functional groups (e.g., hydroxyl, carboxyl, and amine) that can effectively coordinate metal ions (Zn^{2+} and Mg^{2+}), leading to the controlled nucleation and growth of ZnO and MgO nanostructures. This level of control is often challenging to achieve with plant extracts, which contain complex and variable compositions of biomolecules such as polyphenols, flavonoids, and alkaloids that can unpredictably influence particle morphology. Plant extracts contain a variety of organic compounds that may leave residual carbon and impurities after calcination, affecting the purity and functionality of the final nanomaterial. In contrast, ovalbumin undergoes a cleaner thermal degradation, leading to higher-purity ZnO and MgO nanoparticles with fewer organic contaminants. This allows for more reproducible synthesis conditions and uniform nanostructures, ensuring consistent size, shape, and characteristics, which are critical for applications in catalysis, sensing, and biomedicine. Egg white as source of ovalbumin is inexpensive, readily available, and easy to handle compared to plant extracts or microbial cultures, which require complex growth conditions, nutrient media, and precise environmental controls. This makes the ovalbumin-assisted synthesis method more scalable and economically viable for large-scale production.

Previous research focuses on ZnO nanoparticles' egg white-assisted synthesis using zinc nitrate and eggs of different origin (chickens and ducks) [32]. Nitrate generates nitrogen oxide bonding during the synthesis process, requiring additional removal measures.

This research explores a biogenic approach that overcomes this limitation using zinc and magnesium acetate as sources of metals. Acetates are a less oxidizing salt compared to nitrates, which can favorably influence the synthesis reactions. Acetate, on the other hand, produces carbon dioxide and water upon thermal decomposition, which are more environmentally friendly and easier to manage. Also, zinc or magnesium acetate is more economically accessible and easier to store compared to nitrate. In the presence of egg white (which contains proteins), acetate can interact more gently, avoiding a sudden change in pH, which contributes to better control of the morphology of the nanoparticles.

2. Results and Discussion

2.1. Compositional Characterization

In the frame of current study, the ATR-FTIR spectra from Figure 1a show absorption bands at 438 cm^{-1} and at 447 cm^{-1}, which had been attributed to ZnO the stretching frequency of ZnO bonds. The ATR-FTIR spectra from Figure 1b show absorption bands at 441 cm^{-1} and at 416 cm^{-1}, which can be attributed to the stretching frequency of Mg–O bonds, as reported by as reported by Seghir et al. [29]. Compared to ZnO nanoparticles synthesized using Portulaca oleracea extract [34], where ZnO bonds were identified at 450 cm^{-1}, the current study demonstrates slightly shifted peaks, which could be attributed to the ovalbumin-mediated synthesis process, leading to different bonding environments.

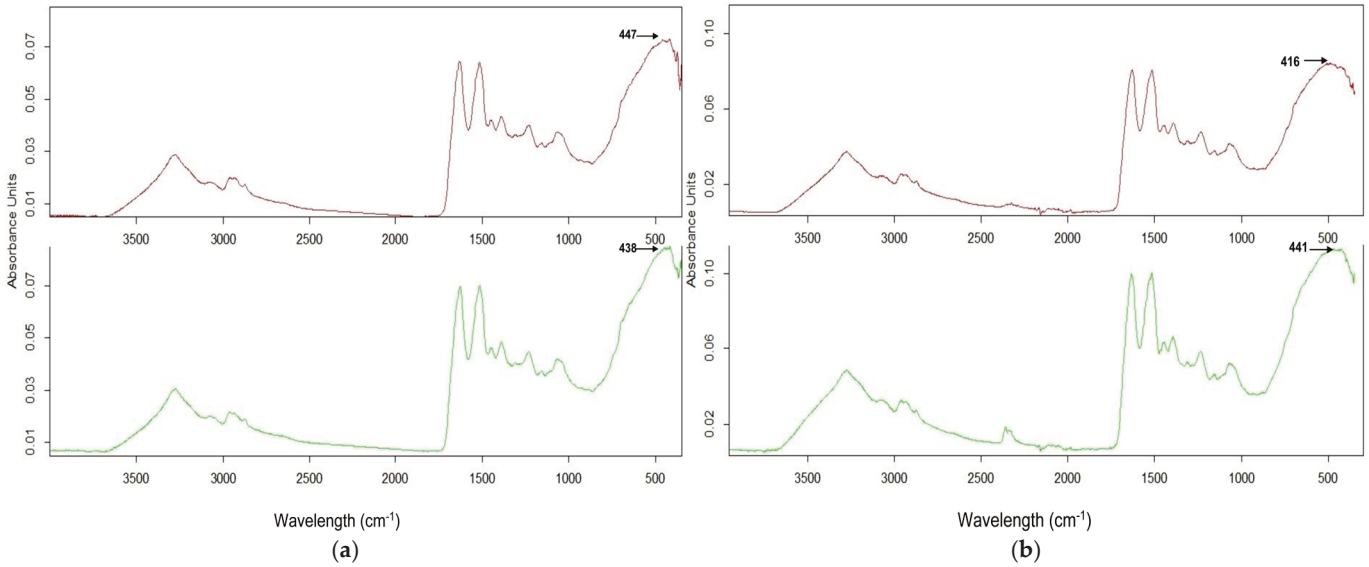

Figure 1. ATR-FTIR spectra of (**a**) ZnO NSs and (**b**) MgO NSs: 1M (magenta); 2M (green).

The band centered at 1630 cm^{-1} was ascribed to the presence of water molecules on the surface of oxides. Also, a peak at 1117 cm^{-1} was due to the re-absorption of water molecules from an ambient atmosphere. The presence of carboxyl chain residues in ovalbumin degraded during treatment at 120 °C is evidenced by the absorption bands at 1396 cm^{-1}, assigned to protein side-chain COO–. Carboxyl groups chelate metal ions and act as nucleation sites. Amino groups participate in metal ion binding and contribute to the reduction process. Thiol groups are strong reducing agents and can play a significant role in the reduction of metal ions. The amide I band from the C=O stretching vibrations of the peptide bond overlapped with the hydroxyl groups at 1630 cm^{-1}. The band around 1550 cm^{-1} corresponds to N–H vibration and indicates the presence of the amide II band. The peak near 1070 cm^{-1} was attributed to C–O vibration. For all spectra, the absorption band at 3343 cm^{-1} was due to the stretching frequency of hydroxyl groups of absorbed water. The peaks around 2300–2400 cm^{-1} correspond to CO_2 molecules from the air.

Table 3 exhibits the values of assignments of absorption bands of ZnO and MgO NSs synthesized with ovalbumin, starting from acetates after 4 h at 120 °C.

ATR-FTIR spectra of ZnO and MgO after 4 h reflect a predominance of inorganic components in the final composition.

For all samples calcinated at 550 °C for 2 h, the ATR-FTIR analysis consisted of a comparison with commercial ZnO and MgO powders of analytical purity, as shown in Figure 2. The pure ZnO presents an absorption band at 352 cm^{-1}, while the pure MgO presents an absorption band at 387 cm^{-1} (black line in Figure 2).

Table 3. ATR-FTIR peak assignments of ZnO and MgO NSs after 4 h at 120 °C.

Spectral Range (cm^{-1})	Vibrations for ZnO NSs	Vibrations for MgO NSs	Interpretation
350–500 cm^{-1}	Zn–O stretching and bending (438, 447 cm^{-1})	Mg–O stretching and bending (416, 441 cm^{-1})	Characteristic vibrations of the metal–oxide bond.
1000–1500 cm^{-1}	Organic contributions: C–O and C–N stretching (weak/moderate)		Contribution from carboxyl (COO–) or amide groups in proteins (ovalbumin).
1500–1700 cm^{-1}	Amide I (C=O, 1650 cm^{-1}) and Amide II (N–H, 1550 cm^{-1})		Amide bonds in denatured proteins (ovalbumin).
2500–3500 cm^{-1}	Broad O–H and N–H stretching (hydrogen bonds, hydration)		Hydroxyls on the surface of the materials or residual adsorbed water.
3000–3500 cm^{-1}	O–H stretching (wide)		Hydroxyl groups from water or proteins (hydrogen bonded to molecules adsorbed on ZnO and MgO NSs).

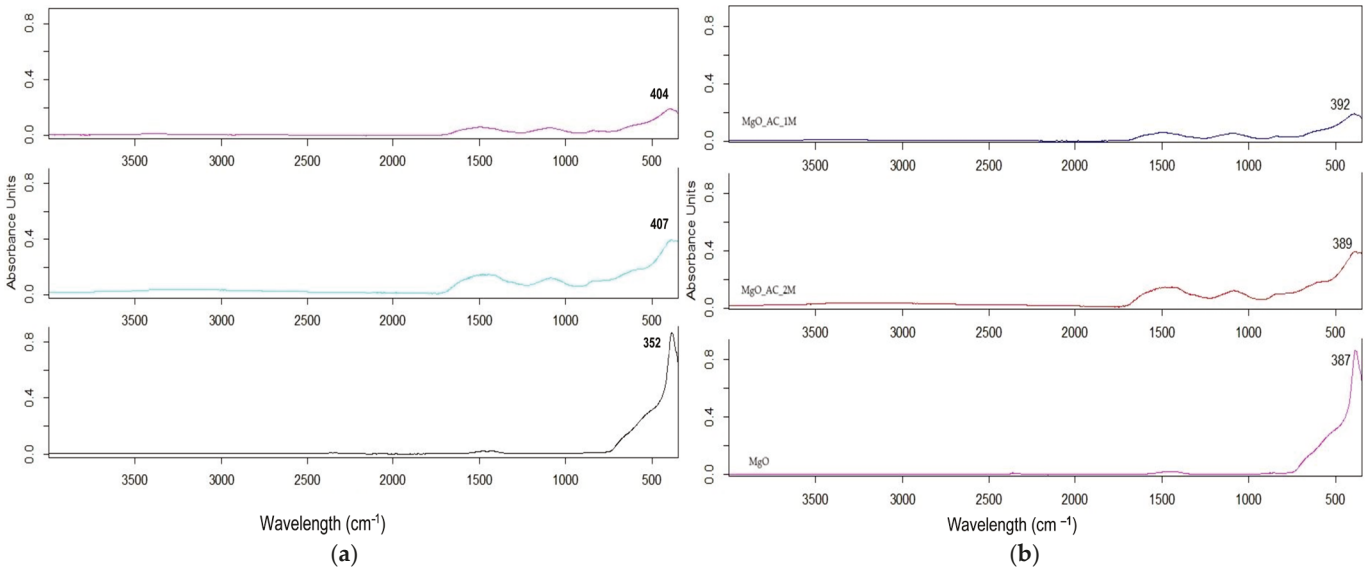

Figure 2. ATR-FTIR spectra of (**a**) ZnO NSs and (**b**) MgO NSs: 1M (magenta), 2M (green), and commercial (black) after calcination after 2 h at 550 °C.

Additionally, the disappearance of the broad O-H stretching band at 3343 cm^{-1} post-calcination at 550 °C indicates the successful removal of organic residues, which coincides with results obtained by Pachiyappan et al. [6], where the complete degradation of biogenic stabilizing agents was observed in ZnO and MgO hybrids. This confirms that the transformation of the hydroxide to the oxide phase occurred during the calcination process. The intensity of bands around 380–400 cm^{-1} suggests a well-crystallized ZnO NS and MgO NS, and the slight shift in the values in this region may be due to the interaction of ZnO with organic molecules (ovalbumin). Weak bands in the range of 1500–1000 cm^{-1} may be associated with functional groups of protein degradation, especially the C–O (carboxylic) and C–N (amide) stretching.

The mechanism of formation of metal oxides through biogenic synthesis is not fully known, even though there is previous research by Vijan et al. [33]. By analyzing the ATR-FTIR spectra after 4 h at 120 °C and after calcination at 550 °C for 2 h, we can propose the mechanism of ZnO and MgO formation via biogenic synthesis with ovalbumin. The

mechanism of metal oxide synthesis with ovalbumin is presented in Figure 3. Ovalbumin, with its rich amino acid composition, can chelate metal (Zn and Mg) ions through various functional groups like carboxyl, amino, and thiol groups. This initial binding step is crucial for the subsequent reduction and nucleation processes.

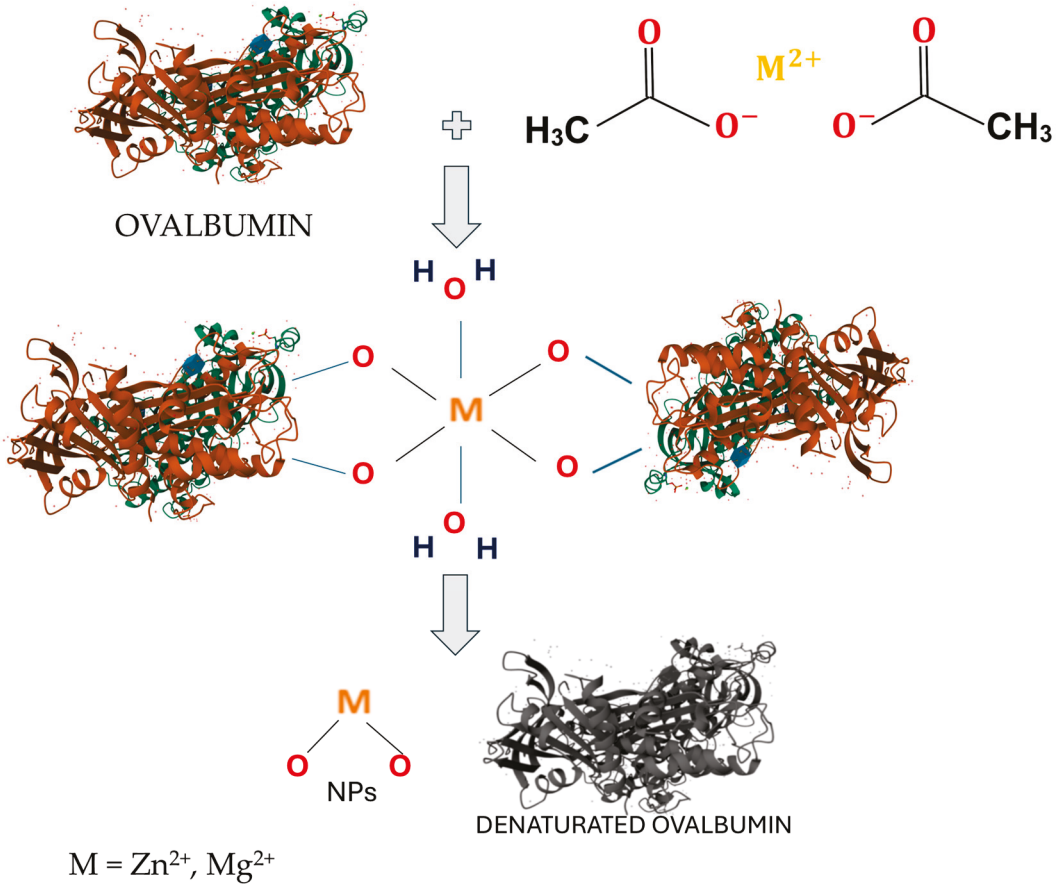

Figure 3. Mechanism of formation of metal oxides through biogenic synthesis using ovalbumin.

The chelated metal ions on the ovalbumin surface can serve as nucleation sites for the formation of metal oxide clusters. The protein can stabilize the formed NS by capping its surface. This capping action prevents agglomeration and ensures the formation of discrete NSs.

A higher concentration of ions (2M) accelerates chelation, but may lead to faster saturation and competition for binding sites. Heating induces the denaturation of proteins, exposing additional sites for nucleation.

2.2. Crystalline Characterization

To assess the crystalline structure, XRD analysis was performed. All the diffraction peaks of the calcinated ZnO samples can be indexed to a hexagonal structure, which is very well matched with card number 04-005-4711, as presented in Figure 4a. Also, all the diffraction peaks of the calcinated MgO samples can be indexed to a cubic structure, which is very well matched with card number 04-012-6481, as presented in Figure 4b.

No characteristic peaks of any impurities are detected, which demonstrates that the product has high phase purity. Ovalbumin decomposes during calcination at 550 °C, leaving behind metal oxides. The decomposition rate impacts the transition from organic–metal complexes to pure crystalline metal oxides. A controlled heating rate (20 °C/min) ensures uniform conversion.

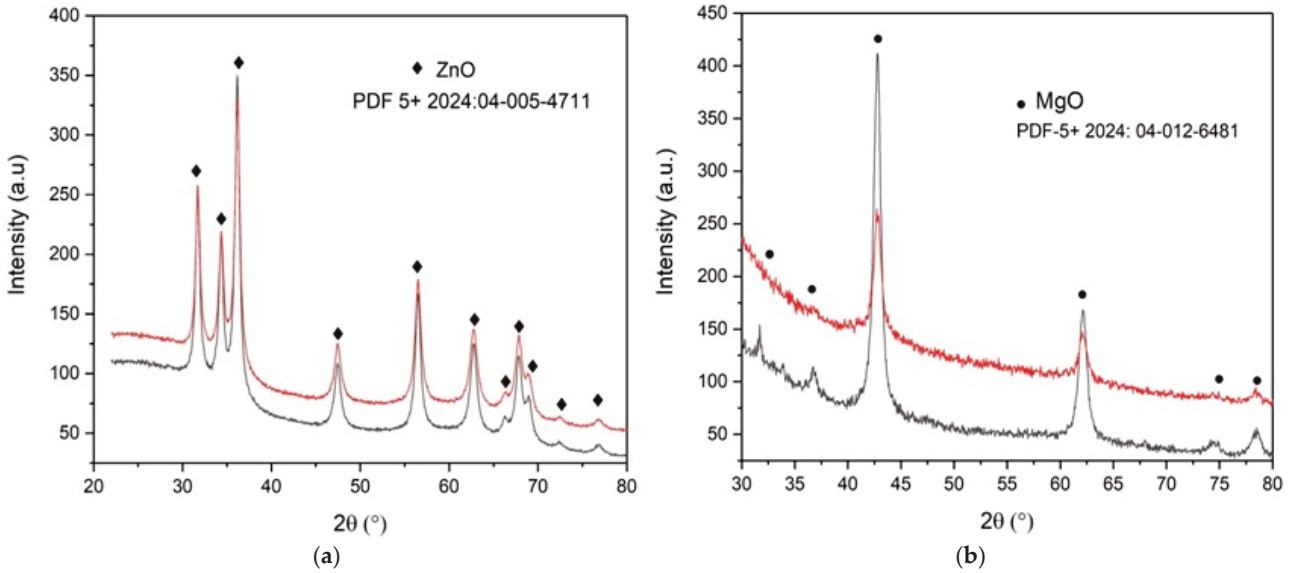

Figure 4. XRD patterns of (**a**) ZnO and (**b**) MgO NSs elaborated with ovalbumin, black 1M, and red 2M.

To understand the modification of the structural characteristics under biogenic synthesis using ovalbumin, the average crystallite size D (nm) of the nanoparticles was determined using the Williamson–Hall method:

$$\beta cos\theta = K\lambda / D + 4\varepsilon sin\theta \quad (1)$$

where β is the full-width-half-maximum (FWHM) of the prominent peaks in X-ray diffraction; K is the shape factor; λ is the X-ray wavelength (λ = 0.15418 nm); D is the particle size ($D_{W\text{-}H}$); and ε is the lattice strain of ZnO and MgO NSs. The lattice parameters a and c (Å), cell volume V (Å^3), and unit cell, volume u (Å) are also presented in Table 4. The values match well with the standard literature values [17,38,39].

Table 4. XRD data of ZnO and MgO NSs.

Sample	*D* (nm)	*a* (Å)	*c* (Å)	*c*/*a*	V (Å^3)	u (Å)
ZnO_1M	12.0 ± 1.7	3.2536	5.2126	1.6021	47.79 ± 0.2	3.6289
ZnO_2M	12.5 ± 0.4	3.2558	5.2167	1.6022	47.88 ± 1.8	3.6312
MgO_1M	7.9 ± 0.3	4.2190	4.2190	1	75.10 ± 0.4	4.2190
MgO_2M	13.5 ± 0.3	4.2230	4.2230	1	75.30 ± 0.7	4.2227

The perfect wurtzite structure of ZnO has four-fold coordination with a hexagonal unit cell, having the fraction c/a = 8/3 = 1.633. The perfect halite structure of MgO is body-centered cubic geometry, with each magnesium ion (Mg^{2+}) being surrounded by six oxygen ions (O^{2-}), and vice versa.

These values of a and c align well with the standard ZnO structure, confirming the expected hexagonal crystalline phase. The c/a ratio is approximately identical for both ZnO samples, which is very close to the ideal value for the wurtzite structure (1.633). This indicates well-ordered crystalline lattices with minimal distortion. The slight increase in crystallite size with increasing molarity suggests that ion concentration has an effect on nucleation kinetics, which is comparable to the conclusions of Hafef et al. [8], whereby ZnO-MgO composite structures showed increasing grain size with precursor concentration.

The c/a ratio aligns with standard wurtzite ZnO values, supporting the minimal lattice distortion observed in the biogenic synthesis approaches of Stepan et al. [5].

The difference in crystallite size between MgO NSs arises from higher concentrations of the metal solution. The unit cell volumes are consistent between the two samples ZnO_1M and ZnO_2M NSs, suggesting that the change in molarity has minimal effects on the ZnO crystal structure. The slight increase in crystallite size and consistent lattice parameters indicate that the ZnO NSs are well crystallized, and that the higher molarity leads to slightly better crystallinity. The corresponding ZnO NS results can be compared with the results of Ahmed et al. [40]. Other researchers, such as Gherbi et al., obtained ZnO crystals two times bigger via Portulaca oleracea extract [33].

The MgO_1M NS exhibits a significantly larger crystallite size compared to the MgO_2M NS. This large reduction in crystallite size, with increased molarity, suggests that higher molarity significantly impacts nucleation and growth dynamics, possibly due to enhanced supersaturation during synthesis. A higher concentration of Mg (II) leads to faster nucleation and smaller crystal sizes. The values of the lattice parameters of MgO NSs match the standard MgO cubic structure. The slight increase in the unit cells of the MgO_2M NS may be attributed to lattice strain, or small variations in the synthesis process. The substantial decrease in crystallite size for MgO at higher molarity suggests that nucleation is favored by overgrowth at a 2M concentration. Both samples exhibit perfect cubic symmetry, and the structural integrity of MgO is maintained.

These results demonstrate the critical role of molarity in tailoring nanomaterial properties, such as crystallite size and structural parameters, which are crucial for their potential applications.

2.3. Morphological Characterization

The nanoparticles of ZnO from Zn(II), 1M, exhibit a slightly elongated and rod-like shape, as observable in Figure 5a. There seems to be a relatively uniform size distribution with some agglomeration. The nanoparticles of ZnO from Zn(II), 2M, as shown in Figure 5b, display a more irregular and elongated morphology. There is a greater degree of agglomeration compared to Figure 5a. Compared to the research of Ahmed et al., the ZnO NSs obtained in this research are much more crowded, due to effect of a higher acetate concentration [40].

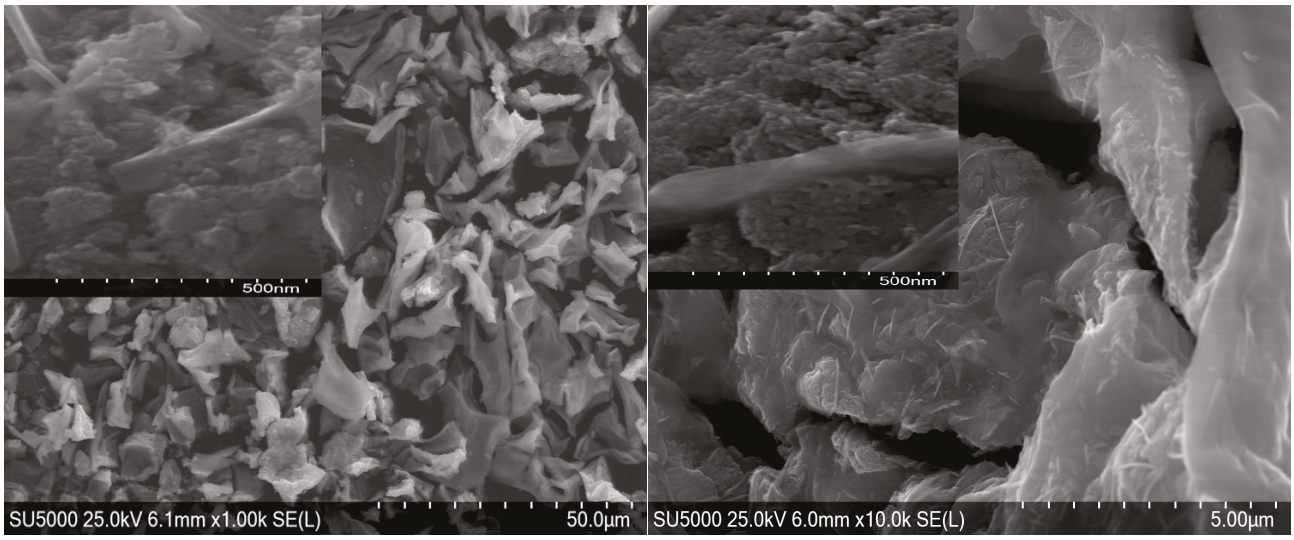

(**a**) (**b**)

Figure 5. SEM morphologies of ZnO NSs elaborated with ovalbumin from Zn(II) (**a**) 1M and (**b**) 2M.

MgO nanoparticles obtained with ovalbumin have a more regular shape, often semi-spheres, as shown in Figure 6. This may be due to a stronger interaction between magnesium ions and protein, which promotes a more isotropic growth of particles.

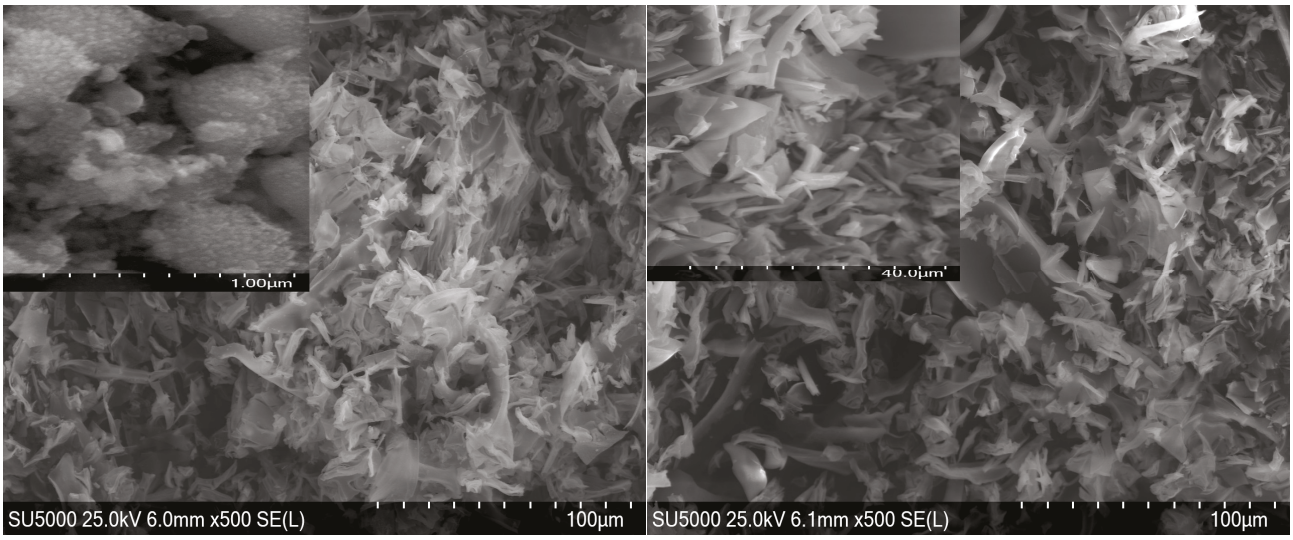

(**a**) (**b**)

Figure 6. SEM morphologies of MgO NSs elaborated with ovalbumin from Mg (II) (**a**) 1M and (**b**) 2M.

Similar morphologies were reported by Rode et al. [10], where biosynthesized ZnO nanoparticles showed anisotropic growth patterns due to variations in metal ion interaction with stabilizing biomolecules. The aggregation observed at higher ion concentrations aligns with previous reports from Selvi et al. [16], suggesting that increased nucleation sites in the presence of a higher precursor concentration led to densely packed nanostructures.

The higher concentration of Zn(II) and Mg(II) ions might have led to faster nucleation and growth, resulting in the observed changes in morphology and agglomeration. Faster nucleation and growth were due to the higher reactivity of Zn^{2+} ions, leading to elongated structures. Slow nucleation with isotropic growth causes semi-spherical particles of MgO.

For both ZnO and MgO, increasing the concentration of metal ions (from 1M to 2M) leads to a more irregular morphology and an increase in the degree of agglomeration.

The presence of ovalbumin in the synthesis process significantly influences the morphology of the particles, acting as a trapping agent and controlling crystal growth. In both cases, we observe a tendency towards the formation of agglomerates, especially at higher concentrations of metal ions. Slower nucleation with isotropic growth results in semi-spherical particles.

The role of ovalbumin as a morphological directing agent can be assumed from the well-defined shapes observed in the SEM images. This behavior aligns with the results of Lu et al. [36], who demonstrated that protein-mediated synthesis promotes isotropic growth, leading to defined structural features in metal oxide nanoparticles.

2.4. Optical Characterization

The UV-VIS spectra were measured in the range of 200–1000 nm. In Figure 7a show a clear increase in the Eg value for the ZnO_2M NS, consistent with a better-ordered crystal structure and a reduction in defects. The increase in Eg is attributed to an improvement in NS quality rather than quantum size effects, given the similar sizes of the crystallites.

The UV-VIS spectra in Figure 7b and Eg values show that the MgO_1M NS exhibits optical properties closer to those of the bulk material, with better crystalline quality and

fewer defects. MgO_2M, on the other hand, exhibits a reduced Eg and an absorption shifted towards longer wavelengths, due to the decrease in crystallite size and the increase in structural defects.

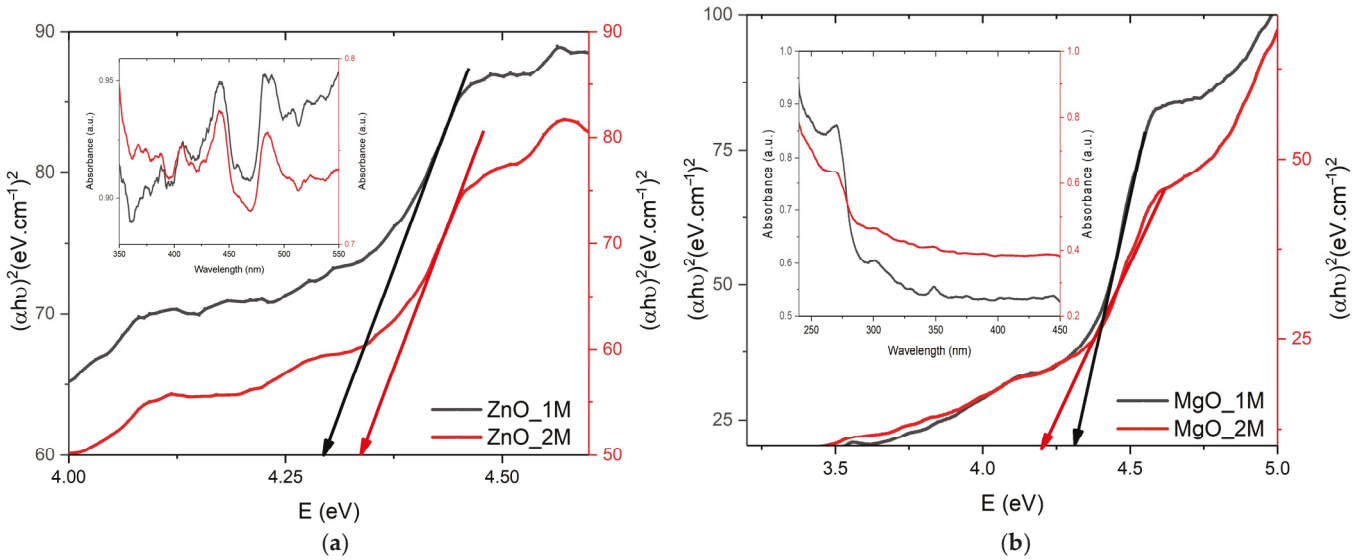

Figure 7. UV-VIS spectra and Eg plot of ZnO and MgO NSs elaborated with ovalbumin at (**a**) 1M and (**b**) 2M.

The calculated Eg value (4.29 eV) of the ZnO_1M NS is higher than the typical theoretical value for ZnO (~3.37 eV in bulk). This increase indicates quantum effects, which are consistent with the small crystallite size (~12 nm). Quantum size effects appear for particles below 20 nm, and shift the absorption edge to shorter wavelengths, a process called blue shift. A slight increase in the crystallite size of the ZnO_2M NS (12.5 nm compared to 12.02 nm) is observed, but the difference is small, as shown in Table 5. The increased Eg value to 4.34 eV suggests a slightly higher electronic separation, possibly due to increased purity. This shift corresponds to the quantum confinement effects reported by Haque et al. [39], where smaller ZnO nanoparticles exhibited an increased bandgap energy due to reduced electron–hole recombination.

Table 5. Average crystallite size correspondence with Eg of NS oxides.

Sample	Average Crystallite Size (nm)	Eg (eV)
ZnO_1M	12.02 ± 1.7	4.29
ZnO_2M	12.5 ± 0.4	4.34
MgO_1M	7.88 ± 0.3	4.31
MgO_2M	13.5 ± 0.3	4.20

MgO typically exhibits absorption in the UV region due to its broad band energy (~7.8 eV in bulk). The measured Eg value (4.31 eV) of the MgO_1M NS is lower than the theoretical one, suggesting structural changes due to the influence of ovalbumin. The reduced Eg value (4.20 eV compared to 4.31 eV) of the MgO_2M NS can be attributed to the additional effects induced by the particle sizes. The same effect was observed in studies by Eissa et al. [28]. The discrepancy between theoretical and measured Eg values suggests that the interaction of ovalbumin with MgO during synthesis alters electronic transitions, as was also reported by Maruthai et al. [15]. The absorption is shifted to lower energies (red shift).

The higher Eg values for ZnO (compared to the theoretical ~3.37 eV) indicate good crystalline quality and quantum effects. The Eg value for the MgO NS is lower than the

theoretical one (~7.8 eV), indicating the possible effects of functional groups of amino acid chains on the NS surface.

The UV-VIS spectra confirm the characteristic absorption of ZnO and MgO nanoparticles, influenced by concentration and size.

2.5. Characterization of Antibacterial Properties

ZnO_1M inhibited *E. coli* growth completely after 5 h of contact, as shown in Table 6. However, it had a limited effect on *E. faecalis*, with only a slight reduction in the colony-forming units (CFUs). ZnO_2M exhibited similar results to 1M ZnO, completely inhibiting *E. coli* growth after 5 h, but showing a less pronounced inhibition of *E. faecalis*. This performance aligns with studies by Ogunyemi et al. [27], whereby ZnO nanoparticles synthesized using green methods exhibited significant bacterial suppression through reactive oxygen species (ROS) generation. The mechanism involves the disruption of bacterial membranes via ROS, ion release, and electrostatic interactions, as reported by Seghir et al. [29].

Table 6. The antibacterial properties of the NS oxides.

Sample	Contact Time < 1 h	Contact Time 5 h	Contact Time < 1 h	Contact Time 5 h
	Escherichia coli **CFU/1 mL**	***Escherichia coli*** **CFU/1 mL**	***Enterococcus faecalis*** **CFU/1 mL**	***Enterococcus faecalis*** **CFU/1 mL**
Negative control sample	0	0	0	0
Positive control	~300	~300	44	29
ZnO_1M	~280	0	37	14
ZnO_2M	~270	0	36	8
MgO_1M	~300	89	43	7
MgO_2M	~300	87	34	20

MgO_1M demonstrated a moderate inhibitory effect on both bacteria, with a significant reduction in the CFUs after 5 h of contact. MgO_2M showed a slightly stronger inhibitory effect than 1M MgO, with a greater reduction in the CFUs for both bacteria after 5 h. The results that are in agreement with Bachhav et al. [19], whereby MgO showed selective inhibition against Gram-positive bacteria. The variation in efficacy between ZnO and MgO can be attributed to differences in ROS production and surface charge density, as discussed by Hafef et al. [8].

Following the contact of ZnO and MgO NSs with the bacterial suspension containing *Escherichia coli* and *Enterococcus faecalis* for ~5 h at 25 °C, good results on the inhibitory action of these NS oxides on bacterial growth were obtained. The longer the contact time between the oxides and the bacteria, the greater the inhibitory action on the bacterial growth was.

The antibacterial properties are in direct connection with the small band gaps of NS oxides, because the band gap of a semiconductor influences the photon energy required to excite electrons and generate ROS. Nanoparticles with a smaller band gap can be excited by a wider range of wavelengths of light, which gives them greater potential to generate ROS and have greater antibacterial activity.

3. Materials and Methods

3.1. Materials and Reagent for Synthesis

Free-range chicken egg whites were collected. These served as sources of ovalbumin for ZnO and MgO NP synthesis. The synthesis of ZnO and MgO nanostructures consisted

of the dropwise addition of 50 mL of Zn(II) and Mg(II) solution into 50 mL of ovalbumin foam from free-range chicken eggs.

Zinc acetate dehydrate a.p., CAS-5970-45-6, from Sigma Aldrich and magnesium acetate tetrahydrate a.p., CAS-16674-78-5, from Roth were used as sources of metallic ions. The Chromocult Coliform agar, Slanetz and Bartley agar, media for microbiology, and sterile distilled water were used for bacterial cultures during antibacterial testing. *Escherichia coli* ATCC25922 and *Enterococcus faecalis* ATCC19433 were used to evaluate the antibacterial efficacy of the biogenically synthesized NSs.

3.2. Synthesis of ZnO and MgO Nanoparticles with Ovalbumin

The ability of egg white proteins to form a gel upon heating and their water-binding and emulsifying capacity are important functional properties. Ovalbumin is the essential protein of egg white. It has a unique sequence located in the middle of the protein chain, rather than at the N-terminus, as in most proteins. In the literature, different terminologies are used for ovalbumin: native (N-), stable (S-), and intermediate (I-) ovalbumin. N-ovalbumin can be converted into S-ovalbumin through the formation of an intermediate (I-) [41]. All these species can aggregate. The ovalbumin can self-assemble into various nanostructures, such as fibers, spheres, and capsules. The specific arrangement of amino acids in the polypeptide chain determines the unique three-dimensional structure of ovalbumin and its functional properties. Ovalbumin aggregation is generally triggered by a heat-induced conformational change in the protein, or by the binding of metal ions that affect the folded structure [37,38,41]. Metal ions can be encapsulated within ovalbumin using various techniques, such as ionic cross-linking or electrostatic interactions.

Thus, ovalbumin can serve as a template for ZnO and MgO NS synthesis through various mechanisms:

1. Zn and Mg ions can coordinate with the functional groups present in ovalbumin, such as amino and carboxyl groups. Zn and Mg ions can be incorporated into these self-assembled structures, followed by calcination to remove the organic template and obtain metal oxide nanostructures with controlled morphology.
2. The protein can act as a reducing agent, converting metal ions into metal nanoparticles. The resulting metal nanoparticles can be further oxidized to form metal oxide nanoparticles.

The elaboration process flux presented in Figure 8 outlines each stage, from the initial solution preparation to the final powdered nanostructure product.

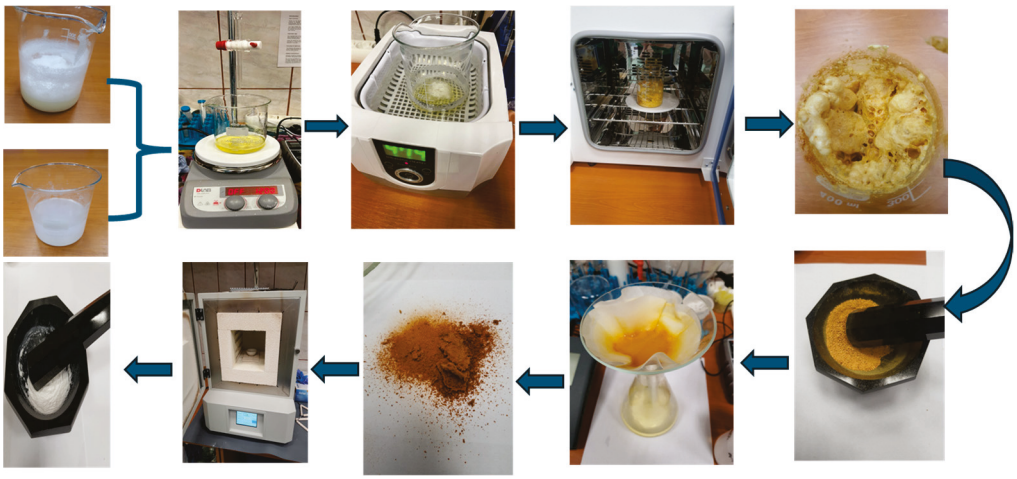

Figure 8. Elaboration process flux.

In total, 50 mL of egg white is separated from the yolk and collected in a beaker. The egg white serves as a natural source of ovalbumin, which acts as a stabilizing and templating agent. The 50 mL acetate solution of 1M and 2M concentration is added dropwise to the egg white foam. For each mL of acetate added, the pH is measured to identify the turning point corresponding to the formation of the ovalbumin–metal complex. This mixture is stirred without heating to ensure thorough mixing, forming a homogeneous solution. The mixture is subjected to sonication using an ultrasonic bath. This step helps to uniformly disperse the precursor within the egg white matrix and facilitates interaction between the ovalbumin and metal ions. After all the acetate solution has been added, the metal–foams are formed. The drying of foam was performed in a Biobase oven at 120 °C for 4 h. This removes the water content and converts the mixture into a solid foam structure. Yellow initial powders were obtained after grinding the dyed foam. The amount of obtained dried powders is presented in Table 7, in association with the amount of metallic acetate. These powders were again washed with deionized water and dried for 2 h at 120 °C.

Table 7. The amount of metallic acetate and of elaborated initial dried powders.

Sample	Metallic Acetate (g)	Dried Powders (g)
ZnO_1M	9.17	3.36
ZnO_2M	18.35	3.53
MgO_1M	10.72	3.42
MgO_2M	21.44	3.76

After dying, a Mikrotest MKF-05, Ankara, Türkiye, muffle oven was used for the calcination of powders at 550 °C, at a controlled rate of 20 °C/min, for 2 h to ensure the complete decomposition of the metal–ovalbumin complex. Cooling was performed at 20 °C/min to stabilize the properties. After calcination, a fine white powder was obtained.

The research was conducted at different concentrations of Zn(II) and Mg(II) to study whether a higher concentration led to a higher nucleation rate in ovalbumin foam, resulting in a larger number of smaller crystallites.

The addition of Zn(II) or Mg(II) might initially cause a change in pH, due to the interaction of the metal ions with the functional groups on the ovalbumin. The experiments were conducted at room temperature. The initial decrease in pH suggests that Zn(II) and Mg(II) displace protons from the protein. As more metal ions were added, the pH stabilized. This indicates a buffering region, as shown in Figure 9.

Amino acid residues from ovalbumin with ionizable groups (like carboxylic acids and amines) can act as buffers, resisting changes in the pH. This could indicate that the metal ions bind to specific sites on the ovalbumin, forming stable complexes, where the pH reaches a point at which the complex becomes insoluble.

The heat-induced denaturation of foams was studied using ATR-FTIR. Calcination is the critical step where the organic template decomposes, leaving behind metal oxide nanostructures.

3.3. Methods of Characterization of ZnO and MgO Nanostructures

ZnO and MgO's crystalline structures were assessed via XRD using the Rigaku Ultima IV diffractometer, Japan. The scan speed was set at 2°/min in Bragg–Brentano geometry using CuKα radiation (λ = 0.154 nm) at 45 kV and 40 mA, along with a one-dimensional D/teX Ultra detector equipped with a graphite monochromator. The X-ray diffractograms were recorded over a measuring range of 2θ: (28–105°), with a step size of 0.05°. The

XRD spectra were analyzed using the PDXL 2 program, and crystalline compounds were identified using the PDF 5+ database.

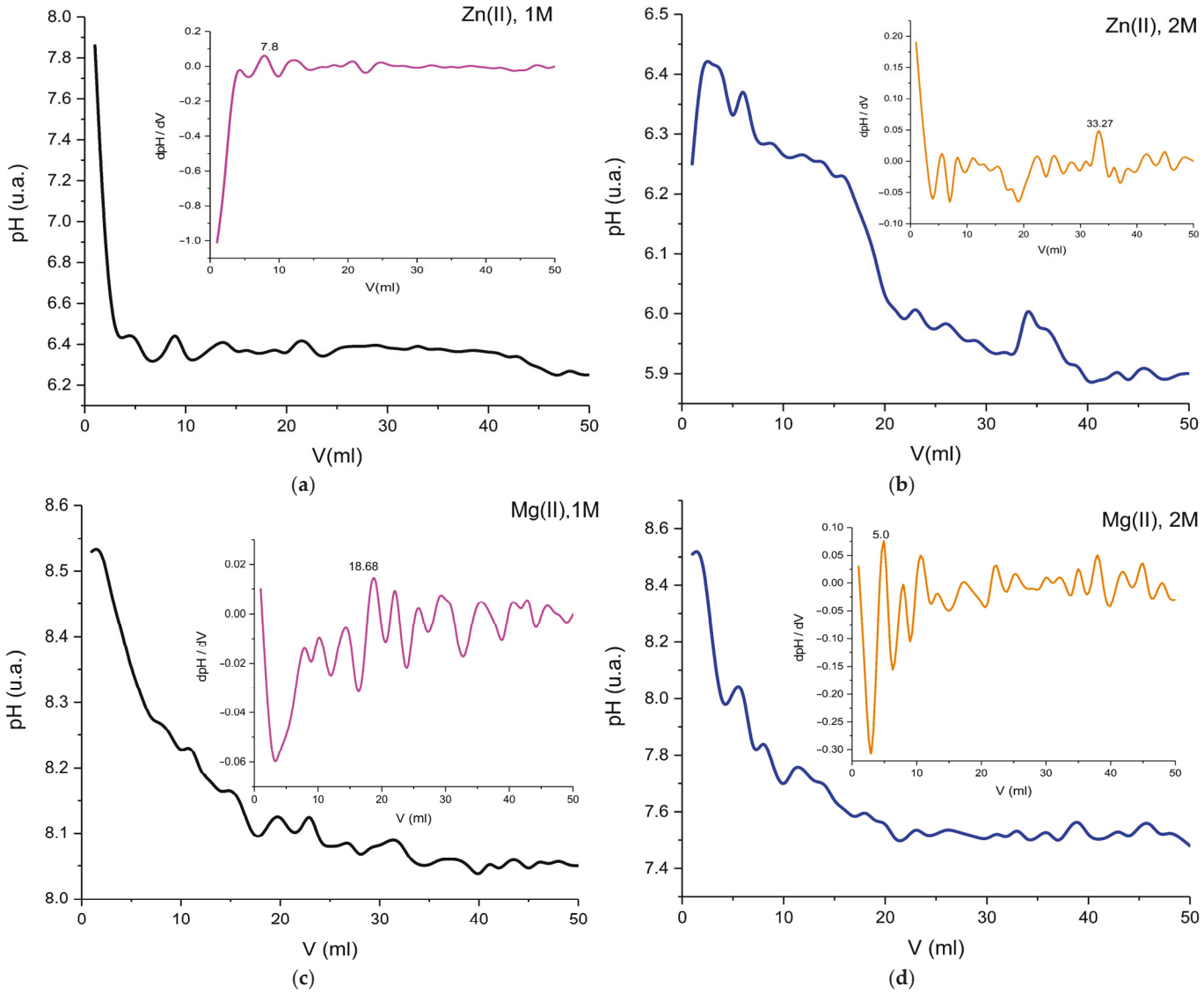

Figure 9. Graphical representation of the pH = f(V) variation for Zn(II) solutions ((**a**) 1M and (**b**) 2M) and Mg(II) ((**c**) 1M and (**d**) 2M).

To assess the role of ovalbumin, during the drying process, the samples were subjected to Attenuated Total Reflectance–Fourier Transform Infrared Spectroscopy analysis using a Tensor 27 spectrometer, Bruker, Germany, in the range of 350–4000 cm^{-1}, with a resolution of 4 cm^{-1}.

An Ocean Optics HR2000+ spectrometer was used to measure and record the UV–Vis absorption spectra of nanoparticle solutions. The optical energy band of a semiconductor was obtained using the following equation:

$$\alpha = \frac{k(h\vartheta - Eg)^{n/2}}{h\vartheta} \quad (2)$$

where k is a constant, α is the absorption coefficient, Eg is the energy band gap, and n is 1326 for a direct energy band gap. The Eg can be estimated from the Tauc plot of $(\alpha h\upsilon)^2$ versus the energy of a photon ($h\upsilon$) [30]. The intersection of the tangent on the Tauc plot gives a direct band gap for n = 1.

The shape and size of ZnO and MgO NS were analyzed using Scanning Electron Microscopy (SEM) (SU 5000 microscope, Hitachi, Tokyo, Japan). The samples were fixed on carbon tape. The morphology was analyzed at different magnifications at 25 kV acceleration voltage.

Nanoparticles can interact directly with the bacterial cell membrane, disrupting its integrity and leading to the loss of the cellular contents. Nanoparticles with a sharp or irregular shape can more easily penetrate the bacterial cell membrane. Also, the absorption of light by nanoparticles can lead to a local increase in temperature, which can denature bacterial proteins and damage the cell membrane.

The loops with bacterial load were hydrated, each in 1 mL of sterile distilled water, for 30 min at 37 °C, while sterile loop passages were made on the non-selective medium, Tryptic Soy agar, and incubated at 37 °C for 24 h. From these subcultures, work crops were carried out in the same way. From the working culture, a colony was unloaded into 10 mL of sterile distilled water, to determine the approximate number of bacteria. A McFarland densitometer was used. Knowing that a colony had a bacterial load of approximately 1.5×10^8 CFU/mL, decimal dilutions up to 10^{-6} were performed for *Escherichia coli* and 10^{-6} for Enterococus faecalis, followed by testing each dilution to establish the number of bacteria of interest and the number of developed colonies that could be read on the culture medium. The culture media used were the Chromocult Coliform agar and Merck's Slanetz and Bartley agar. They were prepared according to the manufacturer's instructions, with a concentration of 41.5g/L for the Slanetz–Bartley agar and 26.5 g/L for the Chromocult Coliform agar medium, sterilized in a water bath, allowed to reach a temperature of about 47–50 °C, and then poured into Petri dishes. A quantity of 2 mg of each NS oxide was weighed and placed in a test tube containing 9 mL of sterile distilled water and 1 mL of bacterial suspension.

The positive control is represented by the sample with 9 mL of sterile distilled water and 1 mL of bacterial suspension. The number of microorganisms estimated to grow on the positive control medium was approximately 300 *Escherichia coli* colonies/1mL sample and 50 enterococcal colonies/1 mL filtered sample.

Before being immersed in the test tubes with 10 mL of artificial sample, the NS oxides were sterilized under the UV lamp in the microbiological niche for 15 min.

The test tubes in which the NS oxides were introduced were incubated in the thermostat at a temperature of 25 °C, for about 30 min, to observe their bactericidal and bacteriostatic action on the microorganisms. After this time, from each test tube, 1mL of sample was filtered through the filter membranes (with a pore size of 0.45 μm) for the determination of *E. coli* and *E. faecalis*, and the rest of the samples with microorganisms and oxides of Zn and Mg were maintained for up to 5 h under the same environmental conditions (25 °C, in the dark). The membranes were placed in Petri dishes on specific culture media for the development of typical colonies of *Escherichia coli* and *Enterococcus faecalis*. Petri dishes were incubated in thermostats at 37 °C for 24 h for Coliform bacteria (*E. coli*) and 48 h for *Enterococcus faecalis*.

4. Conclusions

The biogenic synthesis approach offers several advantages over traditional chemical methods, including eco-friendliness, biocompatibility, and control over NS size and shape.

The synthesis of ZnO and MgO NSs using ovalbumin allows to produce materials with varied morphologies, which can be controlled by modifying the concentration of metal ions. The specific mechanism can be influenced by factors such as metal ion concentration and pH.

Characterization techniques like ATR-FTIR, XRD, SEM, and UV-VIS are used to analyze the surface chemistry, size, crystallinity, and shape of the synthesized ZnO and MgO NSs. The study demonstrates the ability to control particle size and morphology through variations in metal ion concentration, enabling tailored properties for specific applications. The SEM analysis revealed the tendency of ZnO to form elongated structures and of MgO to form semi-spherical shapes, influenced by ovalbumin.

The study highlights the versatility of ovalbumin as a biogenic agent, leveraging its functional groups for efficient metal ion chelation and stabilization during nanoparticle synthesis. By understanding and optimizing the synthesis process, researchers can tailor nanomaterial properties for diverse applications, including antibacterial treatments, photocatalysis, and environmental purification. Furthermore, the use of acetate precursors instead of traditional nitrates offers an eco-friendlier alternative, reducing harmful byproducts and improving overall sustainability.

ZnO_1M NSs biogenically synthesized with ovalbumin are more suitable for applications requiring higher photocatalytic activity in the UV range, or where surface sensitivity is crucial (sensors or antibacterial applications), while the ZnO_2M NSs are more suitable for advanced optoelectronic applications, durable devices, and UV protection, due to their higher Eg values and better crystalline quality.

MgO_1M NSs biogenically synthesized with ovalbumin are suitable for industrial applications where stability is a priority, such as refractory materials, gas adsorption, and optical layers. MgO_2M NSs are ideal for applications requiring intense surface interactions, such as catalysis, water treatment, and antibacterial applications.

In conclusion, the findings of this study pave the way for the broader adoption of biogenic methods in nanotechnology. Ovalbumin-mediated synthesis presents a scalable and sustainable solution for producing high-quality ZnO and MgO nanoparticles and addressing global challenges in the environmental and biomedical fields. This work contributes to the development of greener synthesis pathways, promoting innovation in the creation of nanostructured materials for a sustainable future.

Author Contributions: Conceptualization, A.-G.S. and M.O.; methodology, A.-G.S.; software, D.A.N.; validation, A.-G.S.; formal analysis, S.G.M. and M.O.; investigation, D.A.N., S.G.M., E.M.M., E.A.V., D.I. and G.C.; resources, A.-G.S. and M.O.; data curation, E.A.V. and E.M.M.; writing—original draft preparation, A.-G.S.; writing—review and editing, A.-G.S. and M.O.; visualization, M.O. and Ș.H.A.; supervision, A.-G.S. and Ș.H.A. All authors have read and agreed to the published version of the manuscript.

Funding: This research received no external funding.

Institutional Review Board Statement: Not applicable.

Informed Consent Statement: Not applicable.

Data Availability Statement: Data are contained within the article.

Conflicts of Interest: The authors declare no conflicts of interest.

References

1. Mudalige, T.; Qu, H.; Van Haute, D.; Ansar, S.M.; Paredes, A.; Ingle, T. Characterization of Nanomaterials: Tools and Challenges. In *Nanomaterials for Food Applications*; Elsevier: Amsterdam, The Netherlands, 2018; pp. 313–353. [CrossRef]
2. Kaliva, M.; Vamvakaki, M. Nanomaterials Characterization. In *Polymer Science and Nanotechnology: Fundamentals and Applications*; Elsevier: Amsterdam, The Netherlands, 2020; pp. 401–433. [CrossRef]
3. Shaji, A.; Zachariah, A.K. Surface Area Analysis of Nanomaterials. In *Thermal and Rheological Measurement Techniques for Nanomaterials Characterization*; Elsevier: Amsterdam, The Netherlands, 2017; Volume 3, pp. 197–231. [CrossRef]
4. Plaiasu, A.G.; Ducu, M.C.T.L.; Moga, S.G.; Negrea, A.D.; Modan, E.M. Nanostructured Transition Metal Oxides Obtained by SPVD. *Manuf. Rev.* **2020**, *7*, 12. [CrossRef]

5. Stepan, T.; Tété, L.; Laundry-Mottiar, L.; Romanovskaia, E.; Hedberg, Y.S.; Danninger, H.; Auinger, M. Effect of Nanoparticle Size on the Near-Surface PH-Distribution in Aqueous and Carbonate Buffered Solutions. *Electrochim. Acta* **2022**, *409*, 139923. [CrossRef]
6. Pachiyappan, J.; Gnanasundaram, N.; Rao, G.L. Preparation and Characterization of ZnO, MgO and ZnO–MgO Hybrid Nanomaterials Using Green Chemistry Approach. *Results Mater.* **2020**, *7*, 100104. [CrossRef]
7. Zhao, J.; Mu, F.; Qin, L.; Jia, X.; Yang, C. Synthesis and Characterization of MgO/ZnO Composite Nanosheets for Biosensor. *Mater. Chem. Phys.* **2015**, *166*, 176–181. [CrossRef]
8. Hafef, O.; Othman, Z.J.; Megdich, M.; Matoussi, A. Conduction Mechanism and Dielectric Properties of ZnO/MgO Solid Composites. *Appl. Phys. A Mater. Sci. Process* **2017**, *123*, 95. [CrossRef]
9. Theerthagiri, J.; Salla, S.; Senthil, R.A.; Nithyadharseni, P.; Madankumar, A.; Arunachalam, P.; Maiyalagan, T.; Kim, H.S. A Review on ZnO Nanostructured Materials: Energy, Environmental and Biological Applications. *Nanotechnology* **2019**, *30*, 392001. [CrossRef]
10. Rode, C.; Zieger, M.; Wyrwa, R.; Thein, S.; Wiegand, C.; Weiser, M.; Ludwig, A.; Wehner, D.; Hipler, U.-C. Antibacterial Zinc Oxide Nanoparticle Coating of Polyester Fabrics. *J. Text. Sci. Technol.* **2015**, *1*, 65–74. [CrossRef]
11. Chen, F.; Yan, T.H.; Bashir, S.; Liu, J.L. Synthesis of Nanomaterials Using Top-down Methods. In *Advanced Nanomaterials and Their Applications in Renewable Energy*, 2nd ed.; Elsevier: Amsterdam, The Netherlands, 2022; pp. 37–60. [CrossRef]
12. Carneiro, S.V.; Oliveira, J.J.P.; Rodrigues, V.S.F.; Lima, J.P.O.; do Nascimento, J.H.O.; Santos-Oliveira, R.; Fechine, L.M.U.D.; Freire, R.M.; Fechine, P.B.A. Recent Advances in Nanostructured Materials: A Look at the Applications in Optical Chemical Sensing. *Mater. Today Nano* **2023**, *22*, 100345. [CrossRef]
13. Negrescu, A.M.; Killian, M.S.; Raghu, S.N.V.; Schmuki, P.; Mazare, A.; Cimpean, A. Metal Oxide Nanoparticles: Review of Synthesis, Characterization and Biological Effects. *J. Funct. Biomater.* **2022**, *13*, 274. [CrossRef]
14. Calinescu, V.M.; Oproescu, M.; Iana, V.G.; Ducu, C.M.; Schiopu, A.G. Morphological Changes of Metal Oxides Through the Solar Physical Vapor Deposition Processs. *Arch. Metall. Mater.* **2024**, *69*, 535–540. [CrossRef]
15. Maruthai, J.; Muthukumarasamy, A.; Baskaran, B. Optical, Biological and Catalytic Properties of ZnO/MgO Nanocomposites Derived via Musa Paradisiaca Bract Extract. *Ceram. Int.* **2018**, *44*, 13152–13160. [CrossRef]
16. Selvi, K.T.; Mangai, K.A.; Priya, M.; Sagadevan, S. Investigation of the Dielectric and Impedance Properties of ZnO/MgO Nanocomposite. *Phys. B Condens. Matter* **2020**, *594*, 412355. [CrossRef]
17. Vargas, M.A.; Rivera-Muñoz, E.M.; Diosa, J.E.; Mosquera, E.E.; Rodríguez-Páez, J.E. Nanoparticles of ZnO and Mg-Doped ZnO: Synthesis, Characterization and Efficient Removal of Methyl Orange (MO) from Aqueous Solution. *Ceram. Int.* **2021**, *47*, 15668–15681. [CrossRef]
18. Plaiaşu, A.-G.; Iordache, D.M. Morphological Characterization of Oxide Nanopowders. 2017. Available online: https://revroum.lew.ro/wp-content/uploads/2017/10/Art%2004.pdf (accessed on 10 November 2024).
19. Bachhav, K.; Garde, A.S. Versatile Synthesis of Zinc Oxide Nanoparticles via Chemical Route: A Review. *Mater. Today Proc.* **2023**, *103*, 228–236. [CrossRef]
20. Plăiaşu, A.-G.; Abrudeanu, M.; Dicu, M.M.; Monty, C. Elaboration and Nanostructural Study of Pure and Al Doped ZnO Nanopowders. *J. Optoelectron. Adv. Mater.* **2014**, *16*, 1116–1120.
21. Aslinjensipriya, A.; Narmadha, S.; Deepapriya, S.; John, D.R.; Grace, I.S.; Reena, R.S.; Chamundeeswari, A.; Jose, M.; Jerome, D.S. Synthesis and Characterization of ZnO Nanoparticles by Novel Sol Gel Technique. In *AIP Conference Proceedings*; American Institute of Physics Inc.: College Park, MD, USA, 2020; Volume 2244. [CrossRef]
22. Modan, E.M.; Ducu, C.M.; Moga, S.G.; Negrea, D.A.; Șchiopu, A.-G.; Ahmed, O. Ultrasound and microwave assisted hydrolysis of nanostructured magnesium oxide for impregnation of polyester fibre filters. *Bull. Ser. B* **2024**, *86*, 109–118.
23. Elena Stoica, A.; Cătălina Bîrcă, A.; Loredana Pițigoi, M.; Mihai Grumezescu, A.; Ștefan Vasile, B.; Iordache, F.; Ficai, A. Nanostructured zinc oxide for wound dressings. *Bull. Ser. B* **2024**, *86*, 161–174.
24. Valtsifer, V.A.; Sivtseva, A.V.; Kondrashova, N.B.; Shamsutdinov, A.S.; Averkina, A.S.; Valtsifer, I.V.; Feklistova, I.N.; Strelnikov, V.N. Influence of Synthesis Conditions on the Properties of Zinc Oxide Obtained in the Presence of Nonionic Structure-Forming Compounds. *Nanomaterials* **2023**, *13*, 2537. [CrossRef]
25. Preda, M.D.; Popa, M.L.; Neacșu, I.A.; Grumezescu, A.M.; Ginghină, O. Antimicrobial Clothing Based on Electrospun Fibers with ZnO Nanoparticles. *Int. J. Mol. Sci.* **2023**, *24*, 1629. [CrossRef]
26. Kakhramanov, N.T.; Azizov, A.G.; Osipchik, V.S.; Mamedli, U.M.; Arzumanova, N.B. Nanostructured Composites and Polymer Materials Science. *Int. Polym. Sci. Technol.* **2017**, *44*, 37–48. [CrossRef]
27. Ogunyemi, S.O.; Zhang, M.; Abdallah, Y.; Ahmed, T.; Qiu, W.; Ali, M.A.; Yan, C.; Yang, Y.; Chen, J.; Li, B. The Bio-Synthesis of Three Metal Oxide Nanoparticles (ZnO, MnO_2, and MgO) and Their Antibacterial Activity Against the Bacterial Leaf Blight Pathogen. *Front. Microbiol.* **2020**, *11*, 588326. [CrossRef] [PubMed]
28. Eissa, D.; Hegab, R.H.; Abou-Shady, A.; Kotp, Y.H. Green Synthesis of ZnO, MgO and SiO_2 Nanoparticles and Its Effect on Irrigation Water, Soil Properties, and Origanum Majorana Productivity. *Sci. Rep.* **2022**, *12*, 5780. [CrossRef] [PubMed]

29. Seghir, B.B.; Hima, M.; Moulatti, F.; Sahraoui, I.; Ben Amor, I.; Zeghoud, S.; Hemmami, H.; Kouadri, I.; Ben Amor, A.; Messaoudi, M.; et al. Exploring the Antibacterial Potential of Green-Synthesized MgO and ZnO Nanoparticles from Two Plant Root Extracts. *Nanomaterials* **2023**, *13*, 2425. [CrossRef] [PubMed]
30. Aalami, Z.; Hoseinzadeh, M.; Hosseini Manesh, P.; Aalami, A.H.; Es'haghi, Z.; Darroudi, M.; Sahebkar, A.; Hosseini, H.A. Synthesis, Characterization, and Photocatalytic Activities of Green Sol-Gel ZnO Nanoparticles Using Abelmoschus Esculentus and Salvia Officinalis: A Comparative Study versus Co-Precipitation-Synthesized Nanoparticles. *Heliyon* **2024**, *10*, e24212. [CrossRef]
31. Hussain, I.; Singh, N.B.; Singh, A.; Singh, H.; Singh, S.C. Green Synthesis of Nanoparticles and Its Potential Application. *Biotechnol. Lett.* **2016**, *38*, 38–545. [CrossRef]
32. Vijan, E.A.; Modan, E.M.; Moga, S.G.; Negrea, D.A.; Schiopu, A.-G.; Oproescu, M.; Istrate, D. Assisted Egg White Biogenic Synthesis for Elaboration of ZnO Nanoparticles. *Crystals* **2025**, *15*, 71. [CrossRef]
33. Gherbi, B.; Laouini, S.E.; Meneceur, S.; Bouafia, A.; Hemmami, H.; Tedjani, M.L.; Thiripuranathar, G.; Barhoum, A.; Menaa, F. Effect of PH Value on the Bandgap Energy and Particles Size for Biosynthesis of ZnO Nanoparticles: Efficiency for Photocatalytic Adsorption of Methyl Orange. *Sustainability* **2022**, *14*, 11300. [CrossRef]
34. Kulkarni, D.; Sherkar, R.; Shirsathe, C.; Sonwane, R.; Varpe, N.; Shelke, S.; More, M.P.; Pardeshi, S.R.; Dhaneshwar, G.; Junnuthula, V.; et al. Biofabrication of Nanoparticles: Sources, Synthesis, and Biomedical Applications. *Front. Bioeng. Biotechnol.* **2023**, *11*, 1159193. [CrossRef]
35. Harish, V.; Ansari, M.M.; Tewari, D.; Gaur, M.; Yadav, A.B.; García-Betancourt, M.L.; Abdel-Haleem, F.M.; Bechelany, M.; Barhoum, A. Nanoparticle and Nanostructure Synthesis and Controlled Growth Methods. *Nanomaterials* **2022**, *12*, 3226. [CrossRef]
36. Lu, R.; Yang, D.; Cui, D.; Wang, Z.; Guo, L. Egg White-Mediated Green Synthesis of Silver Nanoparticles with Excellent Biocompatibility and Enhanced Radiation Effects on Cancer Cells. *Int. J. Nanomed.* **2012**, *7*, 2101–2107. [CrossRef]
37. Al-Senani, G.M.; Al-Fawzan, F.F.; Alshabanat, M.; Abd-Elkader, O.H.; Nasrallah, M.; Nasrallah, M. Biosynthesis Effect of Egg White on Formation and Characteristics of NiO/$NiCo_2O_4$ Nanocomposites. *Crystals* **2023**, *13*, 1579. [CrossRef]
38. Schiopu, A.-G.; Oproescu, M.; Iana, V.G.; Ducu, C.M.; Moga, S.G.; Vîlcoci, D.S.; Cîrstea, G.; Calinescu, V.M.; Ahmed, O. Synthesis and Characterization of ZnO-Nanostructured Particles Produced by Solar Ablation. *Materials* **2023**, *16*, 6417. [CrossRef]
39. Haque, M.J.; Bellah, M.M.; Hassan, M.R.; Rahman, S. Synthesis of ZnO Nanoparticles by Two Different Methods & Comparison of Their Structural, Antibacterial, Photocatalytic and Optical Properties. *Nano Express* **2020**, *1*, 010007. [CrossRef]
40. Ahmed, F.; Arshi, N.; Jeong, Y.S.; Anwar, M.S.; Dwivedi, S.; Alsharaeh, E.; Koo, B.H. Novel Biomimatic Synthesis of ZnO Nanorods Using Egg White (Albumen) and Their Antibacterial Studies. *J. Nanosci. Nanotechnol.* **2016**, *16*, 5959–5965. [CrossRef] [PubMed]
41. Weijers, M.; Barneveld, P.A.; Cohen Stuart, M.A.; Visschers, R.W. Heat-induced Denaturation and Aggregation of Ovalbumin at Neutral PH Described by Irreversible First-order Kinetics. *Protein Sci.* **2003**, *12*, 2693–2703. [CrossRef]

Disclaimer/Publisher's Note: The statements, opinions and data contained in all publications are solely those of the individual author(s) and contributor(s) and not of MDPI and/or the editor(s). MDPI and/or the editor(s) disclaim responsibility for any injury to people or property resulting from any ideas, methods, instructions or products referred to in the content.

molecules

MDPI

Article

Bimodal Poly(lactic-co-glycolic acid) Nanocarrier with Zinc Oxide and Iron Oxide for Fluorescence and Magnetic Resonance Imaging

Thúlio Wliandon Lemos Barbosa [1,2,*], Laurent Lemaire [2,3], Isabelle Verdu [2], Larissa Santos [1], Natália Galvão de Freitas [1], Mariana Picchi Salto [1] and Leila Aparecida Chiavacci [1,*]

[1] School of Pharmaceutical Sciences, São Paulo State University (UNESP), Araraquara 14800-903, SP, Brazil; l.santos@unesp.br (L.S.); n.freitas@unesp.br (N.G.d.F.); mariana.psalto@gmail.com (M.P.S.)
[2] National Institute of Health and Medical Research (INSERM), National Centre for Scientific Research (CNRS), Materials, Engineering, Nanosciences, and Technologies (MINT), Research and Training System-Interactions, Catalysis, Applications, and Technologies (SFR ICAT), University of Angers, F49000 Angers, France; laurent.lemaire@univ-angers.fr (L.L.); isabelle.verdu@univ-angers.fr (I.V.)
[3] Platform for Research in Imaging and Multimodal Spectroscopy (PRISM), SFR ICAT, University of Angers, F49000 Angers, France
* Correspondence: thulio.lemos@unesp.br (T.W.L.B.); leila.chiavacci@unesp.br (L.A.C.)

Abstract: Zinc oxide (ZnO) and iron oxide (IO) nanoparticles have been identified as promising candidates for biomedical applications, based on their unique physicochemical properties. The association of these nanoparticles in a single system creates a bimodal entity, allowing the excellent luminescent properties of ZnO quantum dots to be combined with the contrast agent of IO for magnetic resonance imaging (MRI). The present study focuses on the luminescent and MRI properties of a new poly(lactic-co-glycolic acid) (PLGA) nanocarrier system formulation containing ZnO NPs and IO NPs in different nominal ratios. Microscopic analysis (TEM and SEM) reveals a circular morphology with IO and ZnO NPs. The average diameter of the particles was determined to be 220 nm, as measured by DLS. The luminescence results indicate that the PLGA system shows strong emission in the visible range, and the MRI analysis shows a high *r2* relaxivity of 171 mM^{-1} s^{-1} at 7T. The optimized formulation, exhibiting a molar ratio of Fe:Zn ranging from 1:10 to 1:13 (mol:mol), demonstrates superior fluorescence and MRI performance, underscoring the significance of nanoparticle composition in bimodal imaging applications. The systems evaluated demonstrate no toxicity in the THP-1 cells for doses of up to 128 µg mL^{-1}, with efficient labeling after 4 h of incubation, yielding images of strong luminescence and T2 contrast. The PLGA:ZnO:IO system demonstrates considerable potential as a bimodal platform for diagnostic imaging.

Keywords: contrast agents; zinc oxide; iron oxide; poly(lactic-co-glycolic acid); fluorescence imaging; magnetic resonance imaging

1. Introduction

Quantum dots (QDs) or semiconductor materials stand out for their ability to produce high-resolution images due to their unique luminescent and electrical properties resulting from quantum confinement. QDs are particularly useful in diagnostic imaging, due to their ability to enhance image contrast through fluorescence, in combination with dedicated contrast agents for magnetic resonance imaging (MRI) [1–5]. They have also been used in photodynamic therapy [6–8], controlled drug delivery [9–11], and cell markers [12,13].

The toxicity of QDs is dependent on their physicochemical properties and environmental conditions, such as charge, size, concentration, and surface coating [14]. If the QDs' core is based on metals such as cadmium and selenium, which have high quantum yields, their use is limited as they are toxic (e.g., CdTe QDs and CdSe/ZnS QDs) [14–16]; this does not seem to be the case for zinc-based QDs.

Zinc oxide is a semiconductor employed frequently due to its biocompatibility, chemical stability, biodegradability, biosafety, and excellent optical and electrical properties. Its versatility enables applications in chemical detection, biosensors, photocatalysts, and other biomedical uses [17]. Its characteristics include a wide band gap of 3.37 eV and a significant exciton binding energy of 60 meV at room temperature (RT), which contribute to its efficient light absorption and emission properties [18,19]. Furthermore, research has been conducted on its application in the domain of fluorescence imaging for the detection of tumor cells, resulting in a high fluorescence yield [17,20,21].

MRI techniques can also employ nanoparticle-based contrast agents, such as superparamagnetic iron oxide nanoparticles (SPIONs). SPIONs, in their magnetite form, exhibit superparamagnetic properties that make them responsive to the external magnetic fields used in MRI [22]. This enables a strong interaction with the magnetic fields of the MRI equipment, resulting in a high-contrast image signal. In addition to its magnetic properties, iron oxide finds application in cancer treatment through magnetic hyperthermia, nanocatalysis, and the generation of reactive oxygen species to induce cancer cell apoptosis [23].

These two compounds, iron oxide nanoparticles (IO NPs) and zinc oxide nanoparticles (ZnO NPs), are interesting due to their unique physicochemical properties, low cost, and the non-toxicity of the zinc and iron elements [24]. IO stands out for its magnetic properties [25–28], and the ZnO NP is known for its luminescent properties [29–32]. However, studies investigating the concomitant use of ZnO and IO as bimodal imaging agents are limited [33,34]. In Gupta et al. [33], a core (IO) shell (ZnO) structure is reported, along with its biocompatibility and capacity to label cells. In Lai et al. [34], research was carried out on the in vivo biosynthesis of ZnO and IO nanoclusters in Alzheimer models. Indeed, after the administration of iron(II) chloride and zinc gluconate, the formation and accumulation of metallic nanoclusters in the brains of mice were detected using fluorescence and magnetic resonance imaging.

To the best of our knowledge, no studies have proposed a bimodal imaging system based on ZnO and IO within a polymeric system, such as poly(Lactic-co-Glycolic Acid) (PLGA), which promotes stability and biocompatibility, while maintaining reduced toxicity of inorganic compounds and promoting vectorization for specific targeting, with potential application as a theranostic drug [35]. However, there are reports on ZnO-encapsulated PLGA, especially for antimicrobial activity [36–40], and IO-encapsulated PLGA for photodynamic therapy and drug delivery for diseases such as cancer [41–46]. The objective was to develop a biocompatible and stable PLGA system that contains both nanoparticles, maintaining their fluorescence and magnetic properties to provide a bimodal contrast agent (Figure 1). A simple emulsion and solvent evaporation method was developed, and an extensive study was conducted to optimize the system. The interaction between the two nanoparticles, based on their magnetic and luminescent properties, was investigated. Finally, a study assessed the cellular labeling and potential toxicity. This study utilized high-quality images via fluorescence and MRI to provide comprehensive insights into the system's performance.

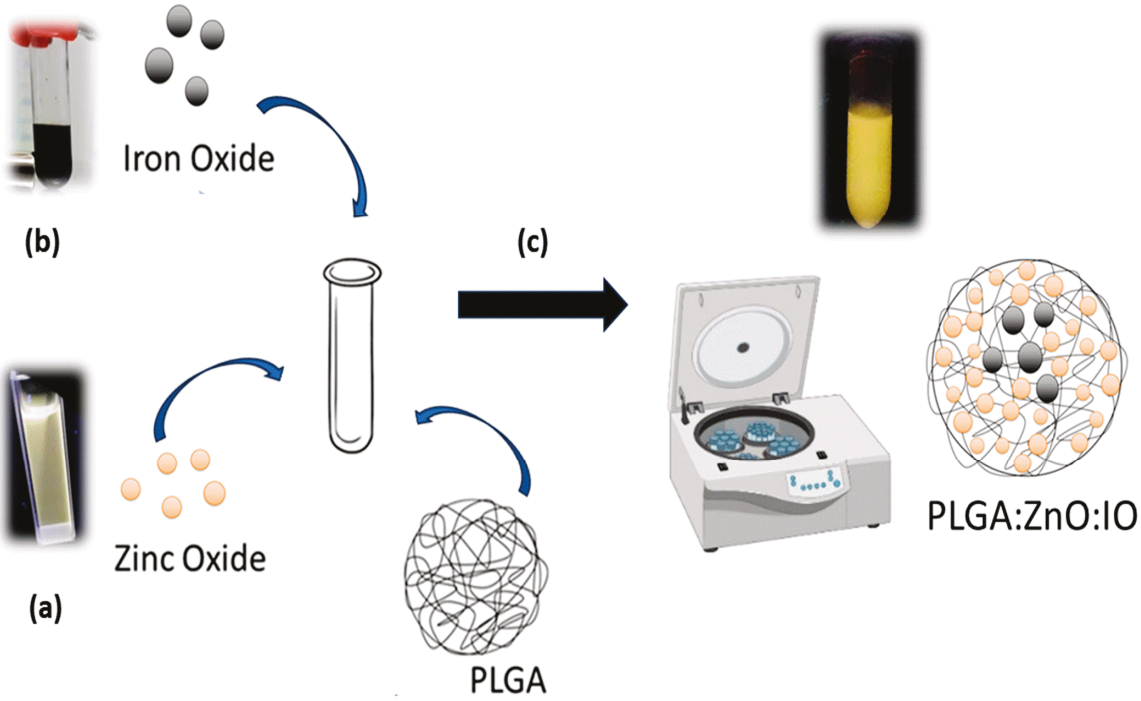

Figure 1. Synthesis scheme of PLGA particles containing ZnO NPs and SPIONs. (**a**) sol-gel method for ZnO NPs, adapted from Spanhel and Anderson [47]; (**b**) co-precipitation method for IO NPs, adapted from Babes et al. (1999) [48]; and (**c**) PLGA particles produced by a simple solvent evaporation emulsion reaction, adapted from Luque-Michel et al. (2021) [45].

2. Results and Discussion

The nominal ratio between PLGA, ZnO, and IO was assessed to ensure that the resulting product exhibits favorable luminescent and magnetic characteristics. For instance, a sample with a nominal PLGA:ZnO:IO ratio of 10:1:1 (*w*:*w*:*w*, mg) indicates the intended use of 10 mg PLGA, 1 mg ZnO, and 1 mg IO.

During the experiments, interactions between ZnO, iron oxide, and PLGA influenced the luminescence and magnetic intensity of the materials. These interactions were analyzed, providing insights into the system's stability.

2.1. Stability Assessment of the PLGA System: Hydrodynamic Diameter Distribution Analysis

The particle size distribution of the PLGA systems was determined using the intensity-weighted mean hydrodynamic diameter (d.nm) (Table 1). The stability in the PVA and T80 surfactant systems, at concentrations of 0.4% and 0.3%, respectively, was evaluated on the day of synthesis and 15 days post-synthesis.

The diameter of PLGA-IO NPs with varying IO ratios exhibited no significant changes following a 15-day storage, as indicated in Table 1. Additionally, the hydrodynamic diameter of the PLGA:IO particles exhibited uniformity across varying IO ratios, with an average measurement of 150 nm. Particle uniformity was corroborated by the polydispersity index (PDI) values. Even after a 15-day storage period at 4 °C, the particles exhibited stability in suspension. The observed diameter of PLGA particles falls within the optimal range of 100 to 300 nm for effective cell incorporation [49].

The average diameter of PLGA:ZnO particles is approximately 220 nm. This diameter is greater than that of PLGA:IO particles (~150 nm), with a statistically significant difference ($p < 0.05$). This observation indicates that there are distinct interaction behaviors associated with the loading of ZnO NPs into PLGA. The diameter remained consistent after 15 days of storage at 4° C, indicating robust stability under these conditions.

Table 1. Stability study of PLGA suspensions after particle synthesis and following a 15-day storage period in suspension. DLS analysis.

PLGA:IO (*w*:*w*, mg)	Synthesis		15 Days	
	Z-Average (d.nm)	PDI	Z-Average (d.nm)	PDI
10:1	152.1 ± 0.907	0.099 ± 0.026	149.5 ± 0.411	0.120 ± 0.015
10:2	146.8 ± 0.800	0.128 ± 0.013	144.9 ± 3.107	0.174 ± 0.024
10:3	148.7 ± 1.457	0.106 ± 0.007	148.1 ± 0.818	0.136 ± 0.014
10:4	147.8 ± 0.568	0.184 ± 0.017	145.4 ± 2.931	0.164 ± 0.010
PLGA:ZnO (*w*:*w*, mg)	**Synthesis**		**15 days**	
	Z-average (d.nm)	**PDI**	**Z-average (d.nm)**	**PDI**
10:2	251.5 ± 1.473	0.118 ± 0.016	243.0 ± 1.082	0.096 ± 0.022
10:4	211.4 ± 10.95	0.205 ± 0.014	254.2 ± 1.950	0.189 ± 0.023
10:6	224.6 ± 2.948	0.078 ± 0.040	226.3 ± 1.952	0.069 ± 0.025
10:8	219.4 ± 1.266	0.093 ± 0.016	214.8 ± 1.450	0.095 ± 0.002
PLGA:ZnO:IO (*w*:*w*:*w*, mg)	**Synthesis**		**15 days**	
	Z-average (d.nm)	**PDI**	**Z-average (d.nm)**	**PDI**
10:8:1	247.0 ± 2.254	0.157 ± 0.020	236.0 ± 2.227	0.144 ± 0.019
10:8:2	280.3 ± 2.887	0.204 ± 0.042	270.1 ± 5.508	0.191 ± 0.022
10:8:3	236.1 ± 1.589	0.233 ± 0.006	277.1 ± 9.296	0.289 ± 0.109
10:8:4	264.6 ± 7.534	0.288 ± 0.034	318.6 ± 69.12	0.409 ± 0.113
PLGA:ZnO:IO (*w*:*w*:*w*, mg)	**Synthesis**		**15 days**	
	Z-average (d.nm)	**PDI**	**Z-average (d.nm)**	**PDI**
10:4:1	193.8 ± 0.265	0.061 ± 0.012	200.1 ± 0.448	0.091 ± 0.017
10:6:1	235.0 ± 0.758	0.066 ± 0.021	222.0 ± 1.778	0.096 ± 0.030
10:8:1	247.0 ± 2.254	0.157 ± 0.020	236.0 ± 2.227	0.144 ± 0.019

For PLGA:ZnO:IO, the diameter of the particles ranged from 190 to 250 nm; this is a range similar to that of PLGA:ZnO synthesized without IO (211 to 250 nm). Over a 15-day storage period at 4 °C, formulations with higher IO content in PLGA:ZnO:IO exhibited particle growth, possibly due to interparticle interactions leading to aggregation. The increase in IO NPs may promote aggregation, likely due to a decrease in surface charge between IO particles at neutral pH during the PLGA formulation process [50]. Consequently, it is essential to determine the appropriate IO NP concentration to prevent excessive aggregation.

On the other hand, when the amount of IO was kept constant and the amount of ZnO was increased, no significant increase in the diameter of the PLGA particles was observed. Unlike IO NPs, ZnO NPs remain stable when the suspension pH is in the range of 7–8 [51]. Furthermore, although an increase in NP concentration can influence the particle aggregation, the amount of ZnO used in the formulations was not sufficient to induce an increase in PLGA particle diameter.

2.2. Characterization of the PLGA System: Transmission Electron Microscopy (TEM) and Scanning Electron Microscopy (SEM) Analysis

The morphology of the NPs was analyzed by TEM, and the elemental analysis of iron and zinc elements in the PLGA systems was conducted by a combination of SEM and EDS analysis (Figure 2).

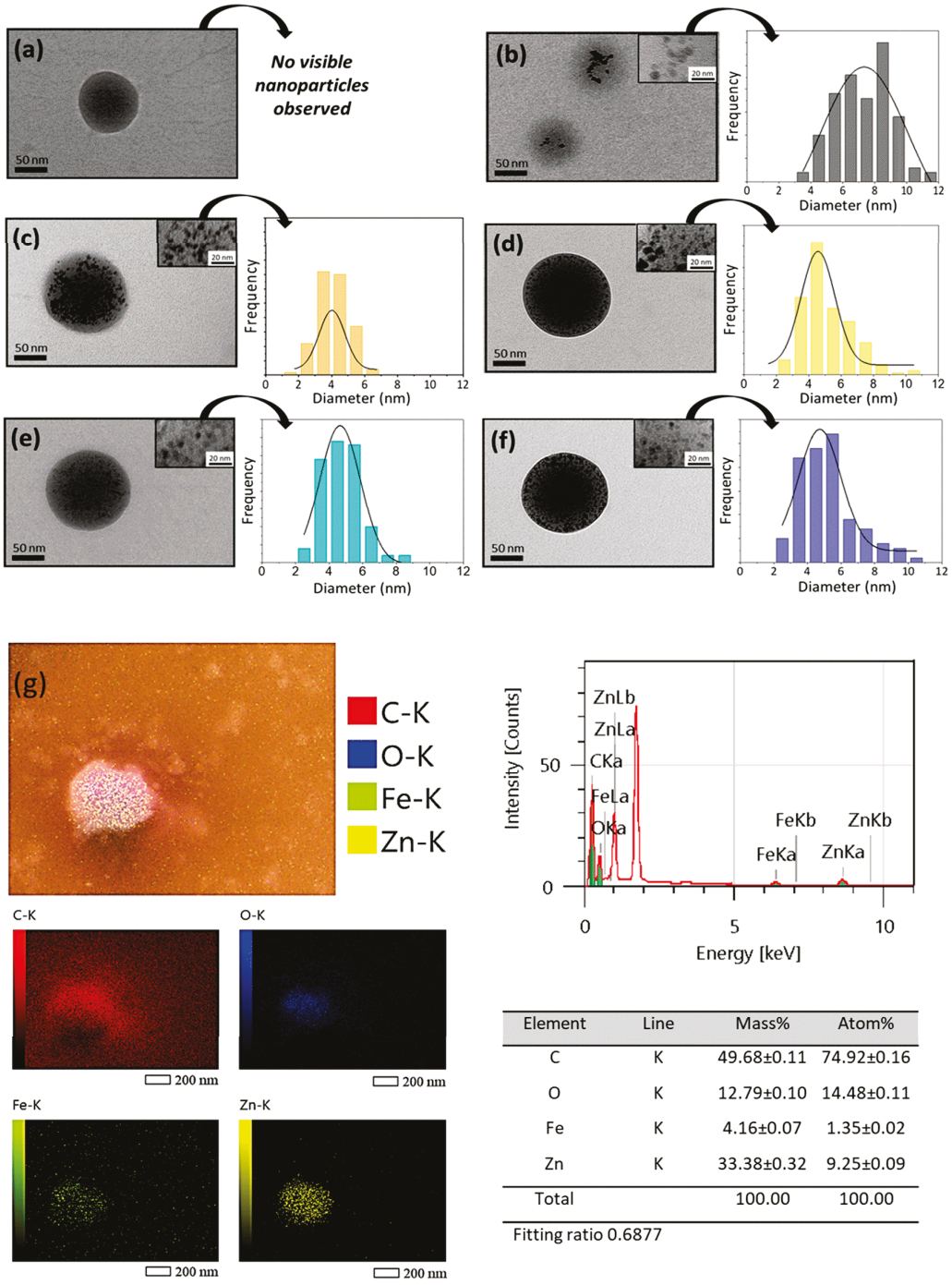

Element	Line	Mass%	Atom%
C	K	49.68±0.11	74.92±0.16
O	K	12.79±0.10	14.48±0.11
Fe	K	4.16±0.07	1.35±0.02
Zn	K	33.38±0.32	9.25±0.09
Total		100.00	100.00

Fitting ratio 0.6877

Figure 2. TEM images of PLGA particles (**a**–**f**). (**a**) PLGA unloaded; (**b**) PLGA:IO 10:1; (**c**) PLGA:ZnO 10:6; (**d**) PLGA:ZnO:IO 10:6:1; (**e**) PLGA:ZnO 10:8; and (**f**) PLGA:ZnO:IO 10:8:1. Gaussian distribution curve representing the NP diameter calculation based on the presence of ZnO and IO NPs as determined by TEM analysis; (**g**) SEM image of the PLGA:ZnO:IO 10:6:1 sample. Energy-dispersive X-ray spectroscopy (EDS) analysis is presented, showing the detection of the elements O-K, C-K, Zn-K, and Fe-K. The corresponding EDS spectrum and elemental mapping are displayed, confirming the distribution and composition of these elements within the sample.

Additionally, PLGA particles containing only ZnO or IO NPs manifested as black dots, a phenomenon not observed in the image of unloaded PLGA. The diameter of the ZnO and IO NP was calculated by utilizing the Gaussian curve (Figure 2), and the resulting data are presented in Table 2.

Table 2. The average diameter of ZnO and IO was analyzed by TEM and calculated using a Gaussian curve, while the zeta potential of the PLGA systems in water was measured before the lyophilization process.

PLGA:ZnO:IO	Average Diameter NPs (nm)	Zeta Potential
10:0:0	-	-21.3 ± 1.0
10:6:0 (ZnO)	4.73 ± 0.16	-12.2 ± 1.6
10:8:0 (ZnO)	4.56 ± 0.16	-17.5 ± 0.8
10:0:1 (IO)	7.33 ± 0.28	-25.4 ± 0.2
10:6:1 (ZnO + IO)	4.03 ± 0.10	-33.2 ± 1.4
10:8:1 (ZnO + IO)	4.64 ± 0.14	-31.9 ± 1.0

The ZnO NPs present in the PLGA:ZnO 10:6 and 10:8 formulations have an average diameter of 4.73 nm and 4.56 nm, respectively. These results are consistent with those previously reported for ZnO NPs [52]. In the PLGA:IO 10:1 formulation, the IO NPs exhibited an average diameter of 7.33 nm, with the TEM analysis of isolated IO NPs revealing a comparable diameter of 8.07 nm (Figure S1).

Although there is no significant difference in the average diameters of the NPs observed in PLGA 10:8:1 or 10:6:1 (4.64 ± 0.14 nm and 4.03 ± 0.10 nm, respectively) compared to PLGA:ZnO 10:8 or 10:6 (4.73 ± 0.16 nm and 4.56 ± 0.16 nm, respectively), it can be noted that the formulations with IO (PLGA:ZnO:IO 10:8:1 and 10:6:1) exhibit a broader distribution, with NPs larger than 6 nm, which is consistent with the PLGA:IO 10:1 sample, while the formulations without IO (PLGA:ZnO 10:8 and 10:6) show a narrower distribution.

These results suggest that the NPs were successfully incorporated into the PLGA system. Elemental analysis through SEM images followed by EDS was performed to confirm the incorporation of ZnO and IO NPs. Furthermore, the integrated SEM and EDS analysis (Figure 2g) revealed that zinc and iron elements were predominantly situated within the PLGA:ZnO:IO particles, indicating their efficient incorporation into the polymeric matrix. These findings complement and reinforce the TEM results.

The surface charge was also studied using zeta potential (ZP) before the lyophilization (Table 2). The results indicate that the IO NP, in the presence of the ZnO NP, caused an increase in the zeta potential value of the PLGA particles. This increase in zeta potential may contribute to enhanced colloidal stability within the system, which can be attributed to the inhibition of particle aggregation.

2.3. PLGA Particles Incorporating Zinc Oxide and Iron Oxide Nanoparticles: Analysis of Luminescent Properties

The spectra demonstrating luminescence (emission and absorption) are presented in Figure 3. The luminescent properties of the PLGA system were adjusted based on the excitation (absorption) and emission spectra of pristine ZnO synthesized in previous work by our team [53]. The synthesized ZnO NP, with a diameter ranging from 3 to 4 nm, exhibits a peak emission at ~540 nm when excited at 343 nm. The excitation wavelength of ZnO typically varies around 350 nm, with a decrease in emission capability at longer wavelengths, generally starting from ~365 nm. This variation in the emission spectrum is attributed to the diameter of the produced ZnO NPs [54].

The behavior of the emission spectra varies with the concentration of ZnO in the PLGA polymer system. Therefore, 343 nm is a suitable excitation wavelength for evaluating ZnO luminescence, as it avoids excitation loss regardless of NP diameter or concentration. Notably, the luminescence intensity increases with increasing ZnO concentration in the polymer system (Figure 3b). The PLGA:ZnO 10:8 sample exhibits the highest luminescence intensity, although it is similar to PLGA:ZnO 10:6, suggesting a possible plateau in luminescence intensity. No luminescence was observed in the PLGA:ZnO 10:2 sample, and a

low luminescence intensity of the PLGA:ZnO 10:4 sample was observed, despite several attempts, suggesting that there is a minimum concentration of ZnO required for the luminescent properties to manifest. Based on these observations, the minimum and maximum concentrations of ZnO and IO in the PLGA preparation were evaluated (Figure 3c–f).

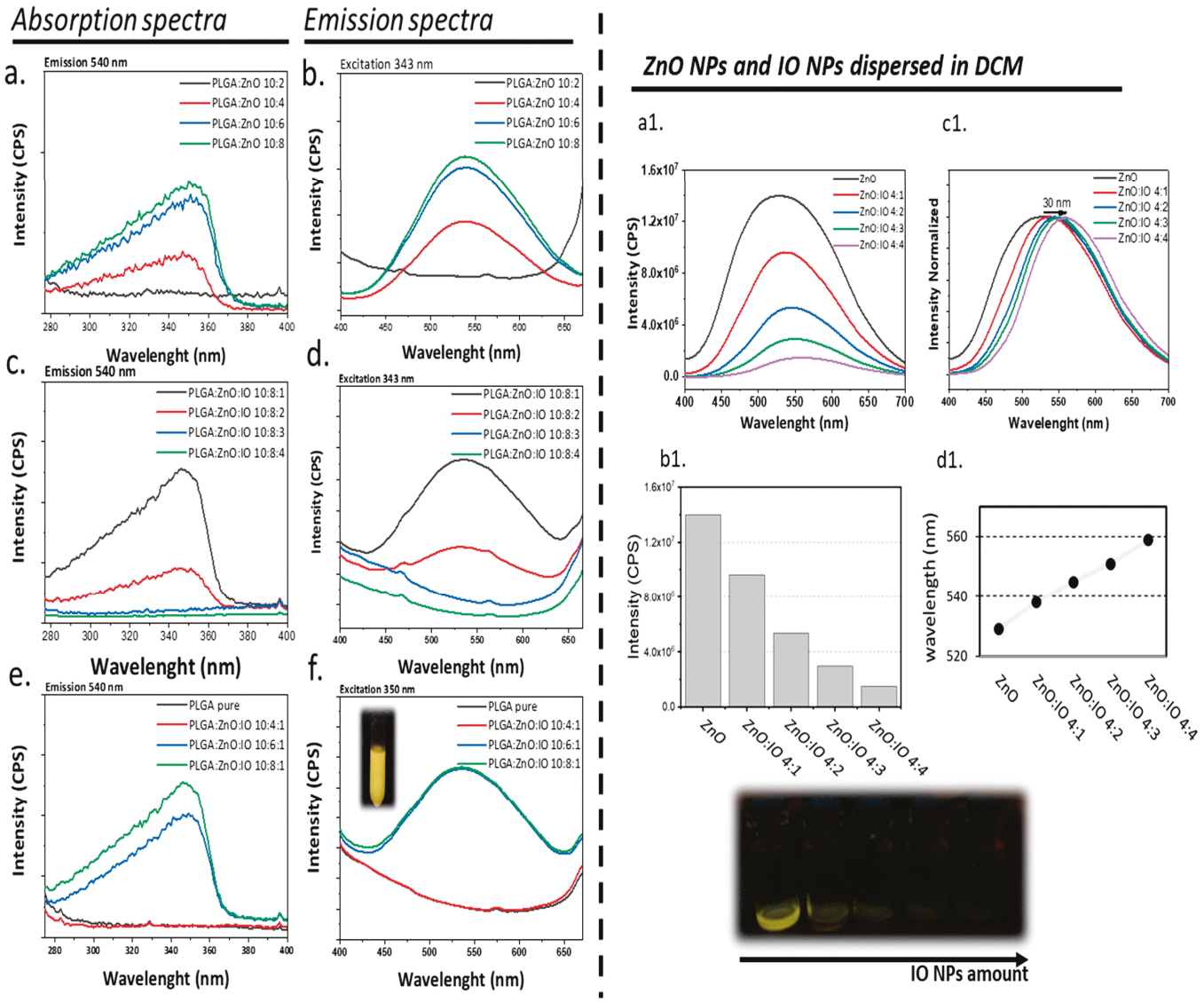

Figure 3. Fluorescence spectra of PLGA samples: absorption spectra and emission spectra for PLGA:ZnO samples (**a**,**b**), PLGA:ZnO:IO samples with the same quantity of ZnO and varying amounts of IO (**c**,**d**), and PLGA:ZnO:IO samples with the same quantity of IO and varying amounts of ZnO (**e**,**f**). The insets (**a1**–**d1**) highlight the fluorescence assay of ZnO NPs and IO NPs dispersed in dichloromethane (DCM), with a constant quantity of ZnO and varying amounts of IO: (**a1**) emission spectra upon excitation at 343 nm, (**b1**) maximum emission intensity as a function of IO concentration, (**c1**) normalized emission spectra, and (**d1**) maximum emission wavelength as a function of IO concentration.

If the amount of ZnO affects the luminescence intensity of PLGA systems, the presence and amount of IO also impact the luminescence, as shown in Figure 3c,d. PLGA:ZnO:IO 10:8:1 shows robust luminescence intensity. However, doubling the amount of IO in the formulation process to produce the PLGA:ZnO:IO 10:8:2 sample reduced the luminescence intensity. At higher IO amounts, luminescence becomes negligible. Consequently, the optimal IO nominal concentration for assessing luminescence in the current PLGA:ZnO:IO samples is determined by a quantity of 1 mg.

In the analysis of Figure 3e,f, where the ZnO concentration is varied while the IO concentration is kept constant, the emission remains constant for the PLGA:ZnO:IO 10:6:1 and 10:8:1 samples, but not for the PLGA:ZnO:IO 10:4:1 sample. This latter formulation was synthesized several times, consistently yielding the same result. The last one was synthesized multiple times, consistently producing the same result. Therefore, a minimum of 6 mg of ZnO is necessary to impart luminescent properties to this material when a nominal amount of 1 mg of IO is present in the PLGA particle preparation. An initial amount of ZnO NPs between 6 and 8 mg can ensure a luminescence plateau in samples containing 1 mg of IO.

Regarding the luminescent properties and ICP results of different Zn and Fe concentrations (Table 3), the quantified ZnO content for PLGA:ZnO:IO at 10:6:1 and 10:8:1 was 50.01 ± 0.34 mM and 45.57 ± 0.42 mM, respectively. These values indicate a saturation point for ZnO incorporation in the PLGA matrix, which is consistent with the observed luminescence intensity plateau. In formulations containing only ZnO, the luminescence intensity increased with the nominal ZnO concentration, as expected. However, in systems co-loaded with ZnO and IO, the presence of IO NPs interfered with the luminescent response. According to the ICP data, the IO:ZnO ratio shifted from 1:10 to 1:13 as the formulation changed from PLGA:ZnO:IO 10:6:1 to 10:8:1. While absorption intensity (Figure 3e) increased with higher ZnO content relative to IO, this variation had no significant effect on emission intensity at the excitation wavelength of 343 nm.

Table 3. Relaxivity (*r2*) of PLGA:ZnO:IO samples, followed by ICP results of Zn and Fe elements and their ratio.

Samples	Fe (μM)	Zn (μM)	Fe:Zn (mol:mol)	*r2* (mM^{-1} s^{-1})
PLGA:IO 10:1	4.15 ± 0.33	-	-	356.38
PLGA:ZnO:IO 10:6:1	4.98 ± 0.26	50.01 ± 0.34	1:10	171.50
PLGA:ZnO:IO 10:8:1	3.44 ± 0.20	45.57 ± 0.42	1:13	90.62

The results show that increasing the nominal concentration of IO significantly affects the material's luminescent properties. To investigate the interaction between IO and ZnO NPs under controlled conditions, we conducted a study using different nominal concentrations of IO while keeping the nominal concentration of ZnO dispersed in DCM (Figure 3a1–d1). These results allow us to draw two important conclusions. First, an increase in IO concentration can reduce the luminescence intensity of the dispersion. Second, as the IO concentration increases, there is a 30 nm "red shift" in the maximum emission wavelength. Consequently, the luminescence properties of the ZnO NP can be influenced not only by its concentration in the PLGA particles, but also by the presence of the IO NP.

This phenomenon is attributed to a specific property of iron in fluorescent compounds known as the quenching effect, where the reduction in luminescence intensity occurs due to several factors. In the case of iron oxide and zinc oxide, this is facilitated by the energy transfer process [55]. The fluorescence of the molecule is quenched due to an energy transfer from the lowest excited singlet state to another electronic state of the metal, resulting in a loss of fluorescence [56].

2.4. PLGA Particles Incorporating Zinc Oxide and Iron Oxide: Analysis of Magnetic Resonance Imaging Properties

Magnetic resonance imaging (MRI) was used to evaluate the magnetic properties of PLGA particles containing ZnO and IO. Samples of PLGA:ZnO:IO 10:6:1 and 10:8:1 were

analyzed as they exhibited the highest luminescence properties. The MRI images are shown in Figure 4.

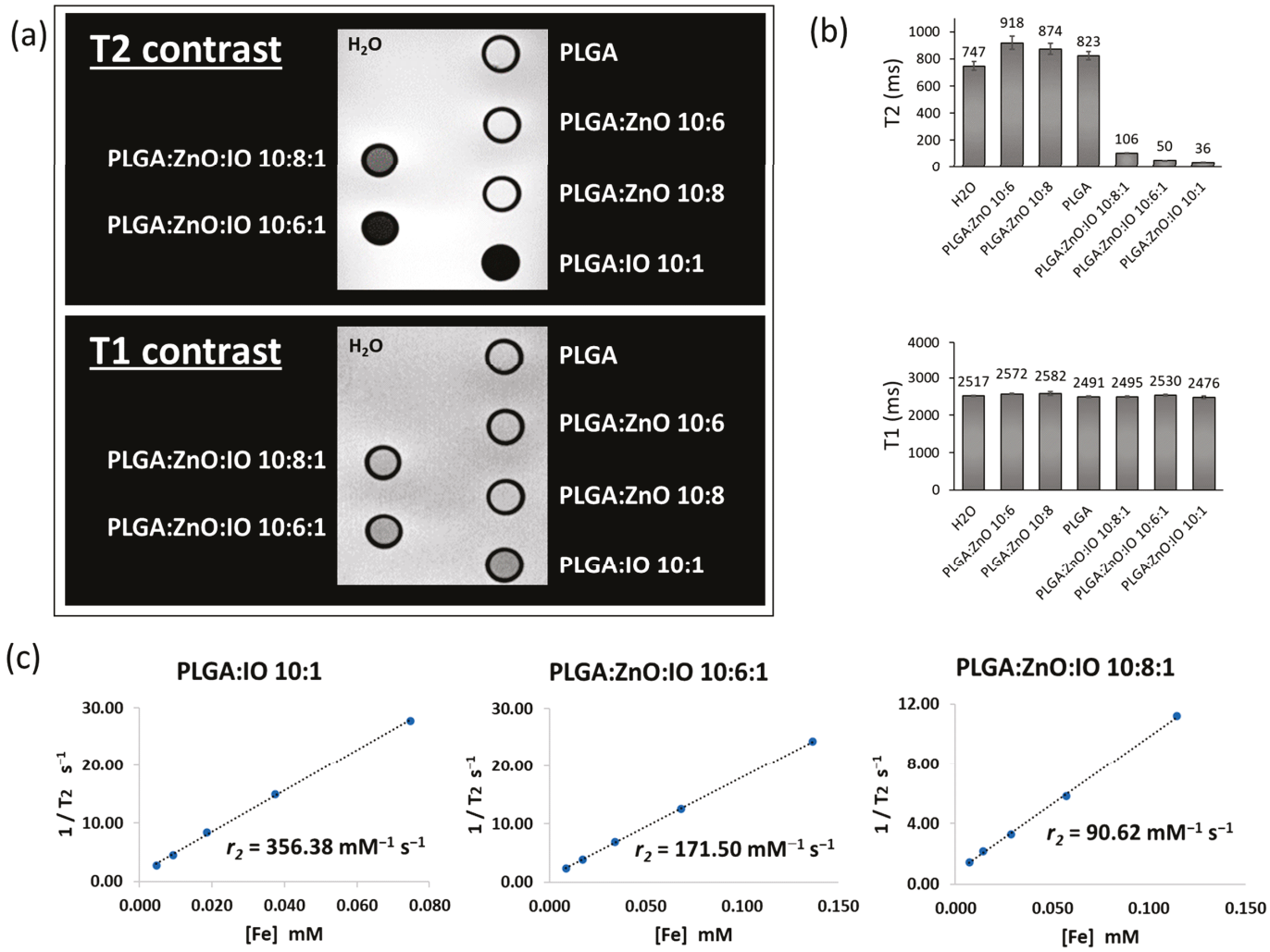

Figure 4. MRI characterization of PLGA samples: (**a**) *T*2-weighted (TE = 64 ms and TR = 2000 ms) and *T*1-weighting images (TE = 8 ms and TR = 400 ms) of PLGA samples acquired at 7T. The concentration of the samples is fixed at 2.5 mg mL^{-1}; (**b**) *T*2 and *T*1 values of the PLGA samples (n = 3, mean ± SD); (**c**) relaxivity calculation for PLGA samples containing IO and ZnO:IO. The calculation was made based on the concentration of iron in each sample based on ICP results.

To calculate the relaxivity for each sample, the concentration of Fe was measured by ICP (Table 3). The relaxivity value (r) was determined using the relaxivity linearity plot (Figure 4c), according to Equation (1):

$$\frac{1}{T} = r[Fe] + \frac{1}{T_0} \quad (1)$$

where $1/T$ is the relaxation rate (inverse of the relaxation time T) in s^{-1}, r is the relaxivity, $[Fe]$ is the iron concentration in mM, and $1/T_0$ is the intercept, representing the relaxation in the absence of iron. The relaxivity values are summarized in Table 3.

As shown in Figure 4a,b, an effect on the *T*2-weighted image is observed when IO is present (samples of PLGA:IO 10:1, PLGA:ZnO:IO 10:6:1, and PLGA:ZnO:IO 10:8:1), with the most significant effect observed for the PLGA containing only IO. Quantitative analysis of these images confirms a reduction in *T*2 values for PLGA:IO 10:1 (36 ± 1 ms) and PLGA:ZnO:IO 10:6:1 and 10:8:1 (50 ± 1 ms and 106 ± 1 ms, respectively) compared

to unloaded PLGA (823 ± 25 ms). On the *T*1-weighted images, a very limited effect was observed, as is commonly seen with NPs [57,58]. The *T*2 and *T*1 results related to different concentrations of iron are shown in Table S1 and Figure S2.

The *r2* results (Figure 4c) demonstrate high relaxivity, which is probably associated with aggregation of IO NPs [57]. Interestingly, the presence of ZnO NPs negatively impacts the PLGA system's relaxivity. This may be related to the organization of IO NPs within the PLGA particle, where the ZnO NP seems to limit the aggregation of IO, as observed in the TEM and SEM images presented in Figure 2 (Section 2.2). The addition of ZnO NPs can act as a spacer, reducing the dipolar interactions between the magnetic moments of IO NPs [59].

According to the ICP results shown in Table 3, it can be observed that the amount of zinc is approximately ten times higher than that of iron in moles. Additionally, this ratio increases with the nominal concentration of ZnO in the formulation (Fe:Zn, 1:10 to 1:13). Since the ratios can affect the aggregation state of the iron oxide NPs, this may explain why the *r2* value of the PLGA:ZnO:IO 10:8:1 formulation is lower than that of the PLGA:ZnO:IO 10:6:1 formulation.

2.5. PLGA Particles Incorporating Zinc Oxide and Iron Oxide: Analysis of Cytotoxicity and Cellular Labelling

THP-1 cells, a human monocytic cell line capable of differentiating into highly phagocytic macrophages, were used in this study. The cytotoxicity assay was performed with unloaded PLGA particles, as well as those loaded with IO, ZnO, or both, evaluating their effects as a function of particle concentration and incubation time (Figure 5). None of the tested systems induced a statistically significant reduction in cell viability, regardless of the dose or incubation period.

A cellular labelling assay was conducted to evaluate the ability of PLGA samples to mark THP-1 cells (Figure 5e–h). The labelling efficiency was evaluated after 4 h (Figure 5e) and 24 h (Figure 5f) of incubation, using luminescence testing based on the properties of ZnO.

After the 4 h incubation period, only the cells incubated with ZnO NP-containing PLGA were detectable using luminescence (Figure 5g), in a concentration-dependent manner (Figure 5e). The PLGA and PLGA-IO samples were used as controls to demonstrate the absence of fluorescence in cells without ZnO.

On the other hand, increasing the incubation time up to 24 h led to a reduction in luminescence (Figure 5e–g). One hypothesis to explain this observation is that, over time, the particles undergo cellular metabolism, where the acidic pH dissolves the luminescent ZnO, thus accounting for the loss of luminescence [60]. A study conducted by Lallo et al. (2022) revealed that ZnO behaves differently in more acidic pH environments, leading to its dissolution [53]. Another study by Cai et al. (2017) revealed that the endocytosis of tumor cells can dissolve ZnO when in contact with the lower pH of the cellular metabolism [61].

The cellular uptake assessed using MRI after 4h incubation (Figure 5h) showed that PLGA particles containing IO, such as PLGA:IO and PLGA:ZnO:IO, provided a strong *T*2 contrast, showing that the double-labelled PLGA particles were also detectable using MRI. These results indicate that this approach could be promising for biomedical imaging applications.

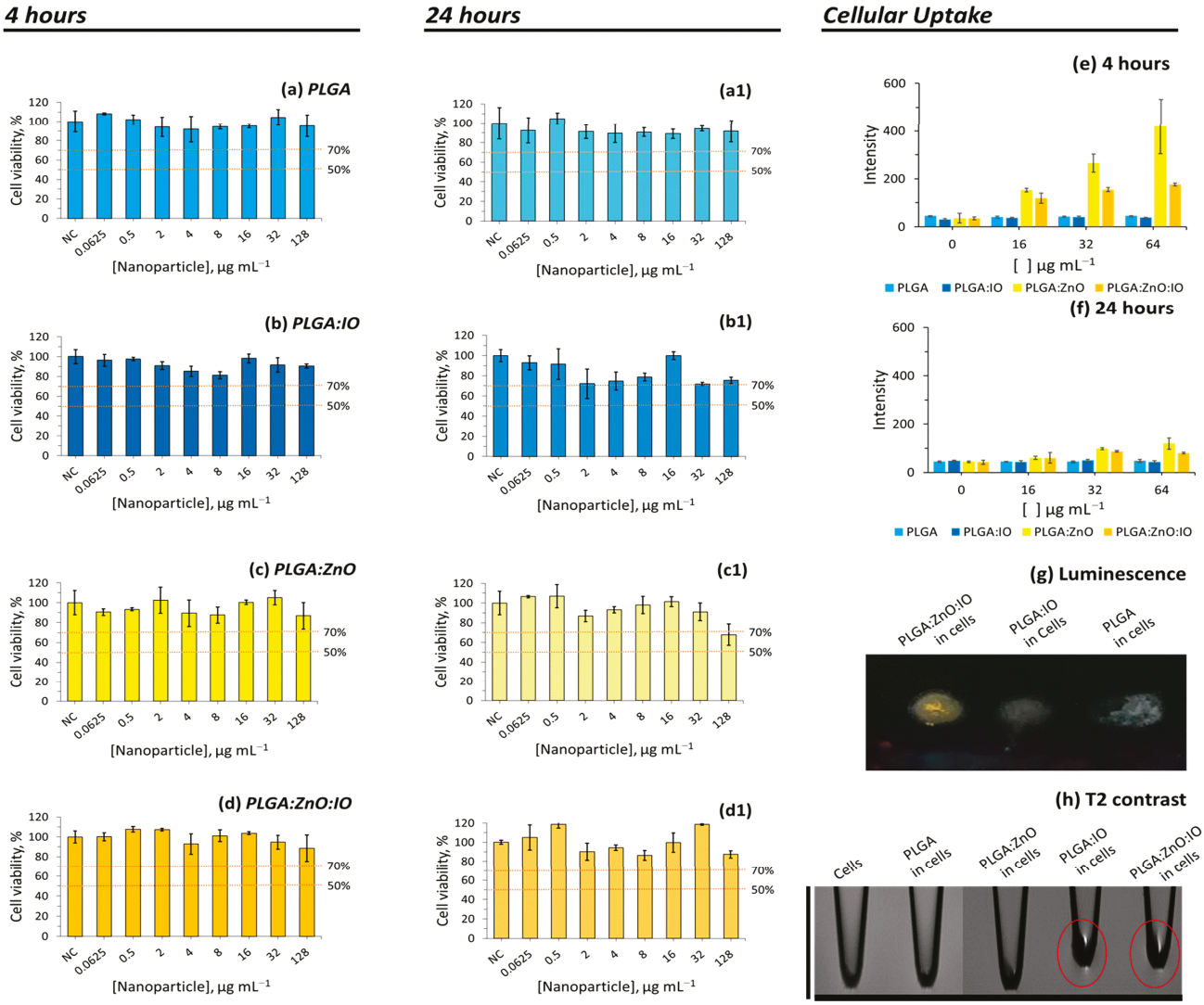

Figure 5. Resazurin cytotoxicity assay of PLGA particles: cell viability versus concentration of PLGA samples after incubating for 4 h (**a**–**d**) and 24 h (**a1**–**d1**) (n = 3, mean ± SD) (NC = negative control). Kruskal–Wallis followed by Dunn's test compared with NC ($p > 0.05$); uptake of PLGA particles containing ZnO and IO NPs by cells assessed through luminescence assay at incubation times of 4 h (**e**) and 24 h (**f**), with an excitation wavelength of 343 nm and an emission wavelength of 540 nm (n = 3, mean ± SD). UV chamber luminescence (λ_{ex} = 245 nm) of uptake cells is shown in (**g**), and uptake of cells assessed by MRI test using $T2$ contrast (TR = 3000 ms and TE = 7.5 ms) is shown in (**h**).

3. Materials and Methods

3.1. Materials

Zinc acetate dihydrate $C_4H_6O_4Zn.2H_2O$, iron (II) chloride hexahydrate 98%, iron (III) chloride hexahydrate 97%, tetramethylammonium hydroxide pentahydrate 97% (TMAOH), oleic acid 90%, perchloric acid, poly(lactic-co-glycolic acid) polymer (Resomer RG 503H, PLGA 50:50), Tween 80 (Polysorbate 80) (T80), triethylamine, dichloromethane (DCM), and polyvinylalkohol 20–98 (PVA) were purchased from Sigma-Aldrick® (Saint Louis, MO, USA); lithium hydroxide monohydrate $LiOH.H_2O$ Chemicals™ (Ribeirão Preto, Brazil); ethanol 99.5%(Qhemis, São Paulo, Brazil); ethyl acetate 99.8% Fisher Chemical™ (Loughborough, UK). The water Milli-Q was obtained by an ultrapurification process in Merck™ Millipore (Trosly-Breuil, France).

3.2. Synthesis

3.2.1. Zinc Oxide NPs

ZnO NPs were obtained by a sol-gel method according to Spanhel and Anderson (1991) [47], with some modifications. It consists of 2 main stages: (1) Formation of acetyl zinc acetate precursor: Zinc acetate hexahydrate and 50 mL of ethyl alcohol were added in a refluxing system at 98 °C for 2 h, obtaining a solution of 0.1 M. After this step, the solution was cooled at RT and diluted to a final concentration of 0.05 M. (2) Formation of the ZnO colloidal suspension: the colloidal suspension of ZnO was carried out by a hydrolysis and condensation reaction, in high power ultrasound (frequency 37, power 70%), at 60 °C, for 60 min, using lithium hydroxide (LiOH) as a hydrolysis agent. The 1:1 molar ratio of Zn:OH was used.

The coating method with oleic acid was performed following the procedure described by Manaia et al. (2015) [62], with some modifications. For that, 75 µL of oleic acid was added to 10 mL of the pre-prepared QD ethanolic suspension. The final concentration of oleic acid was 18.57 mM. The reaction was made at 30 min, up to 60 °C with stirring at 400 rpm. The suspension was stored overnight at RT (25 °C). The final suspension was washed 3 times with 10 mL of ethanol and centrifuged at 2000 rpm at RT. The centrifuged sample was diluted in DCM to a final concentration of 40 mg mL^{-1}. The ZnO NPs were characterized by X-ray diffraction (XRD) and absorbance measurements, with detailed results presented in Figure S3.

3.2.2. Superparamagnetic Iron Oxide NPs (SPIONs)

The synthesis of IO NPs was made according to Babes et al. (1999) [48], with some modifications. Solutions of 0.2 mL of $FeCl_2.4H_2O$ 0.314 M and $FeCl_3.6H_2O$ 0.666 M were added dropwise in 2 mL of 1 M TMAOH solution, magnetically stirred at RT for 5 min. Then, the solution was transferred to a 75 °C water bath, and 75 µL of oleic acid was added, stirred for 15 min, and stirred for 15 min at RT. The final solution was neutralized using 2 mL of $HCLO_4$ 1 M, then washed 10 times with pure water and 3 times with ethanol PA. The final product was dried and dispersed in DCM in a concentration of 40 mg mL^{-1}.

3.2.3. PLGA Particles

The synthesis of the PLGA system dispersed in water was conducted following the procedure of a simple solvent evaporation emulsion reaction made by Luque-Michel et al. (2021) [45], with some modifications. Initially, 10 mg of PLGA (Resomer RG 503H) was dissolved in 0.8 mL of a mixture of triethylamine and acetyl acetate solution (1:1000). Subsequently, 0.2 mL of the contrast agent in DCM was added at the appropriate concentration. This solution was added dropwise into 2 mL of T80 1% under continuous agitation at RT. The mixture was sonicated using an ultrasonic probe system at 20 W for 20 s. The resulting emulsion was added dropwise to a solution of T80 0.3% and PVA 0.4%, and the mixture was kept under constant agitation for 1.5 h with the flask uncapped. The dispersion was then centrifuged and washed three times with pure water. The final product was dispersed in water containing trehalose 37% (a nominal amount based on trehalose:PLGA, *w*:*w*).

3.3. Characterization

3.3.1. Evaluation of Luminescent Properties

The photoluminescence properties were evaluated by measuring the spectra of emission by photoluminescence (PL) and the excitation spectra by photoluminescence excitation (PLE). The spectra were recorded in the UV–visible range on a spectrophotometer Fluorolog™ 3 at RT, equipped with a double excitation monochromator, and a Hamamatsu™

R928 photomultiplier with a Xe lamp (450 W). The wavelength of emission and excitation was based on the previous wavelength test.

3.3.2. Transmission Electron Microscopy

TEM images were obtained with a JEOL Electron Microscope (model JEM-1400; SUPER TWIN) (JOEL Ltd., Tokyo, Japan) operated at 600 kV of 60 magnitude. The samples dispersed in water were deposited on carbon grids. Image analysis was performed by ImageJ software (version 1.53t, National Institute of Health, Bethesda, MD, USA) with 20 and 50 nm scale bars.

3.3.3. Scanning Electron Microscopy and Energy-Dispersive X-Ray Spectroscopy (EDS)

SEM was carried out to evaluate the visual aspects of the nanocrystals. The samples were carbon-coated to about 15 nm thickness using a Sample Sputter Coater SCD 050™ (Bal-Tec, Wallruf, Germany) for 70 s. After that, SEM pictures were taken using a scanning electron microscope SM300™ (TOPCON, Singapore) instrument.

Additionally, the elemental composition was determined using energy-dispersive X-ray spectroscopy (EDS) attached to the SEM. EDS spectra were obtained from selected areas of the samples, enabling qualitative and semi-quantitative identification of the elements present in the NP. The data were analyzed using JSM-IT500HR (JEOL ltd., Tokyo, Japan), providing information on the elemental distribution across the particle.

3.3.4. Inductively Coupled Plasma Mass Spectrometry (ICP-MS)

Iron and zinc concentrations were measured using inductively coupled plasma mass spectrometry (ICP-MS), following the protocol established in collaboration with the Institute of Chemical Sciences of the University of Rennes (ISCR).

3.3.5. Evaluation of Particle Diameter Distribution and Zeta Potential

Particle diameter distribution and zeta potential measurements were performed using a Malvern Dynamic Light Scattering (DLS) system (Malvern™, Malvern, UK). The samples were diluted in distilled water to achieve an optimal count rate (>300 kcps) and attenuation level (attn) between 6 and 9, following the equipment's operational parameters. The dilution factor was adjusted empirically to ensure reliable measurements. All measurements were conducted at 25 °C, and the results were collected in triplicate.

3.3.6. Magnetic Resonance Imaging

The magnetic resonance imaging (MRI) was carried out using a 7T scanner (Biospec 70/20 Avance III, Bruker™, Wissembourg, France) equipped with a BGA12S gradient system (675 mT/m) applying a magnetic field of 7 Tesla at room temperature. Emission and reception were ensured by a 72 mm diameter resonator. Sets of spin echo sequences weighted in $T1$ or $T2$ were acquired using variable repetition times (from 200 to 10,000 ms), with a fixed echo time of 8 ms and a fixed repetition time of 2000 ms for variable echo times (ranging from 8 to 200 ms). In both cases, images were acquired with a field of view = 6 cm × 4 cm, a matrix = 256 × 192, and a slice thickness of 2 mm.

3.4. Biological Analysis

3.4.1. Cytotoxicity Assay Using Resazurin Test

The cell uptake assay was made using the THP-1 human monocytic cell line, which was obtained from ATCC, catalog number TIB-202. The differentiation of THP-1 cells into macrophage-like cells was induced by adding phorbol 12-myristate-13-acetate (PMA, Sigma-Aldrich™, Burlington, MA, USA) at a concentration of 100 nM at the time of seeding (time 0). The cells were incubated with PMA for 48 h before further experiments.

The cells were plated in a 96-well plate with a seeding density of 8.5×10^3 cells per well. After 24 h, PLGA NPs were introduced at concentrations ranging from 0.078 to 128 μg mL^{-1}, followed by a 4 h and 24 h incubation period. Subsequently, the cells were washed and allowed to grow for an additional 24 h before the addition of 20 μL of a 25 μg mL^{-1} resazurin solution in phosphate-buffered saline (PBS). After 4 h, the wells were analyzed using the EnSpire™ microplate reader (PerkinElmer, Waltham, MA, USA) at 570 nm wavelength excitation, and the baseline emission was corrected at 590 nm. The percentage of viable cells was calculated using Equation (2):

$$Viable\ cells\ (\%) = \frac{(O.D.\ sample - O.D.\ media)}{(O.D.\ cells - O.D.\ media)} \times 100 \quad (2)$$

where viable cells (%) represent the percentage of living cells in the sample, *O.D. sample* is the optical density of the sample with cells, O.D. media is the optical density of the cell-free medium, and O.D. cells is the optical density of a sample with a known number of viable cells. The analyses were conducted in triplicate. A statistical analysis was carried out using the Kruskal–Wallis test followed by Dunn's test, to compare the viability between the concentrations of PLGA samples and the control, as well as between different incubation times. A significance level of 0.05 was considered for all analyses. Data processing and statistical tests were conducted using GraphPad Prism 9.

3.4.2. Cellular Uptake

The cellular uptake assay was performed using the TPH-1 cell line. The cells were seeded onto a 24-well plate with a seeding density of 8.5×10^3 cells per well. The concentration between 16 and 64 μg mL^{-1} was tested according to the cytotoxicity assay for the different samples. Incubation times were fixed at 4 and 24 h. After the incubation, the cells were washed to remove the NPs not captured by the cells. Fluorescence analyses were carried out using EnSpire™ microplate reader (PerkinElmer, Waltham, MA, USA), with excitation at 343 nm and emission at 540 nm. MRI analyses of the cells were performed according to the procedures outlined in Section 3.3.6, following a 4 h incubation period.

4. Conclusions

In this study, we present a nanoscale bimodal contrast agent for fluorescence and magnetic resonance imaging, formulated using poly(lactic-co-glycolic acid) (PLGA) encapsulating zinc oxide (ZnO) and iron oxide (IO) nanoparticles. Before the biological assessment on THP-1 cells, an extensive investigation into the interaction of these oxides and their impact on imaging properties was conducted. Our findings demonstrate the potential of PLGA:ZnO:IO particles for biomedical applications; this is attributed to their combined luminescent and magnetic properties. This bifunctional nanosystem holds promise for advanced imaging modalities in biomedical research and clinical diagnostics.

Supplementary Materials: The following supporting information can be downloaded at: https://www.mdpi.com/article/10.3390/molecules30081818/s1, Figure S1. TEM analyses of IO NPs; Table S1. Results of *T*2 and *T*1 in different concentrations of PLGA systems; Figure S2. Relaxivity values (r1 and r2); Figure S3. Characterization of ZnO NP [63–65].

Author Contributions: Conceptualization, T.W.L.B., L.L. and L.A.C.; methodology, T.W.L.B., L.L., I.V. and L.A.C.; software, T.W.L.B. and L.L.; validation, T.W.L.B. and L.L.; formal analysis, T.W.L.B., L.L., I.V., L.S. and N.G.d.F.; investigation, T.W.L.B., L.L. and L.A.C.; resources, L.L. and L.A.C.; data curation, T.W.L.B., L.L. and I.V.; writing—original draft preparation, T.W.L.B., L.S. and N.G.d.F.; writing—review and editing, T.W.L.B., L.L., M.P.S. and L.A.C.; visualization, T.W.L.B., L.L. and L.A.C.;

supervision, L.L. and L.A.C.; project administration, L.L. and L.A.C.; funding acquisition, L.L. and L.A.C. All authors have read and agreed to the published version of the manuscript.

Funding: The authors acknowledge the financial support of CAPES-finance code 001 (Grant number: 88887.529995/2020-00), CAPES-Print code 41/2017 (Grant number: 88887.696991/2022-00), CNPQ (Grant number: 301994/2022-6).

Institutional Review Board Statement: Not applicable.

Informed Consent Statement: Not applicable.

Data Availability Statement: Data will be made available on request.

Acknowledgments: The authors would like to express their gratitude to CAPES, CAPES Print, and CNPQ for funding the project, as well as to the *MINT laboratories* and the University of Angers for their support and col-laboration. We would like to also thank Prism platform for providing access to the *MRI facility*, *SCIAM facility* and especially Romain Mallet for the TEM images acquisition, Bertrand Lefeuvre for the ICP analysis at *Institut des Sciences Chimiques* of Rennes (Fr), and Marina Paiva Abuçafy for the SEM images acquisition at Chemical Institute of *Unesp—Araraquara*.

Conflicts of Interest: The authors declare no conflicts of interest.

Abbreviations

The following abbreviations are used in this manuscript:

DCM	Dichloromethane
EDS	Energy-Dispersive Spectroscopy
IO	Iron Oxide
MRI	Magnetic Resonance Imaging
NC	Negative Control
NP	Nanoparticle
PDI	Polydispersity Index
PLGA	Poly(lactic-co-glycolic acid)
PVA	Polyvinyl Alcohol
RT	Room Temperature
SEM	Scanning Electronic Microscopy
SPION	Superparamagnetic Iron Oxide Nanoparticles
T80	Tween 80
TEM	Transmission Electronic Microscopy
TE	Echo Time
THP-1	(Human monocytic cell line)
TR	Repetition Time
ZnO	Zinc Oxide

References

1. Yang, D.; Wei, X.; Piao, Z.; Cui, Z.; He, H.; Wen, Z.; Zhang, W.; Wang, L.; Mei, S.; Guo, R. Constructing Bimodal Nanoprobe Based on Gd:AgInS2/ZnS Quantum Dots for Fluorometric/Magnetic Resonance Imaging in Mesenchymal Stem Cells. *J. Mater. Sci. Technol.* **2023**, *148*, 116–122. [CrossRef]
2. Molaei, M.J. Turmeric-Derived Gadolinium-Doped Carbon Quantum Dots for Multifunctional Fluorescence Imaging and MRI Contrast Agent. *J. Lumin.* **2023**, *257*, 119692. [CrossRef]
3. Huang, X.; Wang, Z.; Li, S.; Lin, S.; Zhang, L.; Meng, Z.; Zhang, X.; Sun, S.K. Non-Invasive Diagnosis of Acute Kidney Injury Using Mn-Doped Carbon Dots-Based Magnetic Resonance Imaging. *Biomater. Sci.* **2023**, *11*, 4289–4297. [CrossRef]
4. Jin, L.; Bai, W.; Yu, S.; Zhang, J. One-Pot Preparation of Mn_3O_4/GSH/CdTe Quantum Dots Complex for T1-Weighted MRI/Fluorescence Detection of H_3PO_4. *Talanta* **2023**, *263*, 124713. [CrossRef]
5. Xu, Y.Q.; Zang, L.Y.; Gao, H.Y.; Peng, J.; Zheng, D.Y.; Liu, C.; Liu, X.J.; Cheng, D.B.; Zhu, C.N. Cu-In-S/ZnS:Gd^{3+} Quantum Dots with Isolated Fluorescent and Paramagnetic Modules for Dual-Modality Imaging in Vivo. *Colloids Surf. B Biointerfaces* **2023**, *223*, 113158. [CrossRef]

6. Ren, C.; Hu, D.; Cui, Y.; Chen, P.; Xu, X.; Cheng, J.; He, T. Ag-Doped InP/ZnS Quantum Dots for Type-I Photosensitizers. *Chem. Commun.* **2023**, *59*, 2311–2314. [CrossRef]
7. Liu, F.; Lin, J.; Luo, Y.; Xie, D.; Bian, J.; Liu, X.; Yue, J. Sialic Acid-Targeting Multi-Functionalized Silicon Quantum Dots for Synergistic Photodynamic and Photothermal Cancer Therapy. *Biomater. Sci.* **2023**, *11*, 4009–4021. [CrossRef] [PubMed]
8. Bao, Y.; Wu, X.; Bo, B.; Qin, J.; Zhang, Y.; Wu, X.; Li, X.; Wang, Y.; Peng, H. Synthesis of NIR-II Fluorescent Hybrid Ag_2S/ZnPc Nanoparticles for in Vitro Photodynamic Therapy. *ChemNanoMat* **2023**, *9*, e202200570. [CrossRef]
9. Singh, B.; Singh, S.; Gautam, A.; Sutherland, A.; Pal, K. Preparation and Characterization of PLA Microspheres as Drug Delivery System for Controlled Release of Cetirizine with Carbon Dots as Drug Carrier. *Polym. Bull.* **2023**, *80*, 5741–5757. [CrossRef]
10. Kurniawan, D.; Mathew, J.; Rahardja, M.R.; Pham, H.P.; Wong, P.C.; Rao, N.V.; Ostrikov, K.; Chiang, W.H. Plasma-Enabled Graphene Quantum Dot Hydrogels as Smart Anticancer Drug Nanocarriers. *Small* **2023**, *19*, 2206813. [CrossRef]
11. Mohammed-Ahmed, H.K.; Nakipoglu, M.; Tezcaner, A.; Keskin, D.; Evis, Z. Functionalization of Graphene Oxide Quantum Dots for Anticancer Drug Delivery. *J. Drug Deliv. Sci. Technol.* **2023**, *80*, 104199. [CrossRef]
12. Lv, Y.; Wang, P.; Li, J.; Li, N.; Xu, D.; Wu, R.; Shen, H.; Li, L.S. Establishment of a Ca(II) Ion-Quantum Dots Fluorescence Signal Amplification Sensor for High-Sensitivity Biomarker Detection. *Anal. Chim. Acta* **2023**, *1237*, 340534. [CrossRef] [PubMed]
13. Magdy, G.; Elmansi, H.; Belal, F.; El-Deen, A.K. Doped Carbon Dots as Promising Fluorescent Nanosensors: Synthesis, Characterization, and Recent Applications. *Curr. Pharm. Des.* **2022**, *29*, 415–444. [CrossRef] [PubMed]
14. Hardman, R. A Toxicologic Review of Quantum Dots: Toxicity Depends on Physicochemical and Environmental Factors. *Environ. Health Perspect.* **2006**, *114*, 165–172. [CrossRef]
15. Winnik, F.M.; Maysinger, D. Quantum Dot Cytotoxicity and Ways to Reduce It. *Acc. Chem. Res.* **2013**, *46*, 672–680. [CrossRef]
16. Hoshino, A.; Hanada, S.; Yamamoto, K. Toxicity of Nanocrystal Quantum Dots: The Relevance of Surface Modifications. *Arch. Toxicol.* **2011**, *85*, 707–720. [CrossRef]
17. Ortiz-Casas, B.; Galdámez-Martínez, A.; Gutiérrez-Flores, J.; Baca Ibañez, A.; Kumar Panda, P.; Santana, G.; de la Vega, H.A.; Suar, M.; Gutiérrez Rodelo, C.; Kaushik, A.; et al. Bio-Acceptable 0D and 1D ZnO Nanostructures for Cancer Diagnostics and Treatment. *Mater. Today* **2021**, *50*, 533–569. [CrossRef]
18. Norek, M. Approaches to Enhance UV Light Emission in ZnO Nanomaterials. *Curr. Appl. Phys.* **2019**, *19*, 867–883. [CrossRef]
19. Xu, X.; Chen, Y.; Zhang, G.; Bian, H.; Zhao, M.; Ma, S. Optical Properties and the Band-Gap Variation in Diverse Zn1-XSnxO Nanostructures. *Superlattices Microstruct.* **2018**, *123*, 349–357. [CrossRef]
20. Ibraheem, S.; Kadhim, A.A.; Kadhim, K.A.; Kadhim, I.A.; Jabir, M. Zinc Oxide Nanoparticles as Diagnostic Tool for Cancer Cells. *Int. J. Biomater.* **2022**, *2022*, 2807644. [CrossRef]
21. Wanas, W.; Abd El-Karaem, S.A.; Ebrahim, S.; Soliman, M.; Karim, M. Cancer Bioimaging Using Dual Mode Luminescence of Graphene/FA-ZnO Nanocomposite Based on Novel Green Technique. *Sci. Rep.* **2023**, *13*, 27. [CrossRef] [PubMed]
22. Rahman, M. Magnetic Resonance Imaging and Iron-Oxide Nanoparticles in the Era of Personalized Medicine. *Nanotheranostics* **2023**, *7*, 424–449. [CrossRef]
23. Liu, M.; Ye, Y.; Ye, J.; Gao, T.; Wang, D.; Chen, G.; Song, Z. Recent Advances of Magnetite (Fe_3O_4)-Based Magnetic Materials in Catalytic Applications. *Magnetochemistry* **2023**, *9*, 110. [CrossRef]
24. Egorova, K.S.; Ananikov, V.P. Toxicity of Metal Compounds: Knowledge and Myths. *Organometallics* **2017**, *36*, 4071–4090. [CrossRef]
25. Edis, Z.; Wang, J.; Waqas, M.K.; Ijaz, M.; Ijaz, M. Nanocarriers-Mediated Drug Delivery Systems for Anticancer Agents: An Overview and Perspectives. *Int. J. Nanomed.* **2021**, *16*, 1313–1330. [CrossRef] [PubMed]
26. Fernández-Barahona, I.; Muñoz-Hernando, M.; Ruiz-Cabello, J.; Herranz, F.; Pellico, J. Iron Oxide Nanoparticles: An Alternative for Positive Contrast in Magnetic Resonance Imaging. *Inorganics* **2020**, *8*, 28. [CrossRef]
27. Calsolaro, F.; Garello, F.; Cavallari, E.; Magnacca, G.; Trukhan, M.V.; Valsania, M.C.; Cravotto, G.; Terreno, E.; Martina, K. Amphoteric β-Cyclodextrin Coated Iron Oxide Magnetic Nanoparticles: New Insights into Synthesis and Application in MRI. *Nanoscale Adv.* **2025**, *7*, 155–168. [CrossRef]
28. Lu, K.; Zhang, R.; Wang, H.; Li, C.; Yang, Z.; Xu, K.; Cao, X.; Wang, N.; Cai, W.; Zeng, J.; et al. PEGylated Ultrasmall Iron Oxide Nanoparticles as MRI Contrast Agents for Vascular Imaging and Real-Time Monitoring. *ACS Nano* **2025**, *19*, 3519–3530. [CrossRef]
29. Sreenan, B.; Kafil, V.; Hunt, T.; Shin, S.H.R.; Brennan, A.A.; Thallapally, P.K.; Tal-Gan, Y.; Zhu, X. Luminescent ZnO-Carbon Hybrid Nanomaterials: Synthesis, Characterization, Emission Mechanism, and Applications. *ACS Appl. Opt. Mater.* **2025**, *3*, 698–711. [CrossRef]
30. Babayevska, N.; Kustrzyńska, K.; Przysiecka, Ł.; Jarek, M.; Jancelewicz, M.; Iatsunskyi, I.; Dydak, K.; Skupin-Mrugalska, P.; Janiszewska, E. Doxorubicin and ZnO-Loaded Gadolinium Oxide Hollow Spheres for Targeted Cancer Therapy and Bioimaging. *Spectrochim. Acta Part A Mol. Biomol. Spectrosc.* **2025**, *333*, 125903. [CrossRef]
31. Mehto, A.; Shukla, P. Bioimaging Potential: Comparative Study of ZnO Nanoparticles Synthesized via Green and Chemical Routes. *Next Nanotechnol.* **2025**, *7*, 100118. [CrossRef]

32. Verma, A.K.; Lakshmi, G.B.V.S.; Dhiman, T.K.; Hashmi, S.Z.H.; Kumar, A.; Solanki, P.R. Optical Tuning of Polymer Functionalized Zinc Oxide Quantum Dots as a Selective Probe for the Detection of Antibiotics. *Sci. Rep.* **2025**, *15*, 1648. [CrossRef]
33. Gupta, J.; Hassan, P.A.; Barick, K.C. Core-Shell Fe_3O_4@ZnO Nanoparticles for Magnetic Hyperthermia and Bio-Imaging Applications. *AIP Adv.* **2021**, *11*, 25207. [CrossRef]
34. Lai, L.; Jiang, X.; Han, S.; Zhao, C.; Du, T.; Rehman, F.U.; Zheng, Y.; Li, X.; Liu, X.; Jiang, H.; et al. In Vivo Biosynthesized Zinc and Iron Oxide Nanoclusters for High Spatiotemporal Dual-Modality Bioimaging of Alzheimer's Disease. *Langmuir* **2017**, *33*, 9018–9024. [CrossRef]
35. Rocha, C.V.; Gonçalves, V.; da Silva, M.C.; Bañobre-López, M.; Gallo, J. PLGA-Based Composites for Various Biomedical Applications. *Int. J. Mol. Sci.* **2022**, *23*, 2034. [CrossRef]
36. Burmistrov, D.; Serov, D.; Grigorieva, D.; Simakin, A. Physicochemical, Antibacterial, and Cytotoxic Properties of Composite Materials Based on Biodegradable Poly (Lactic-Co-Glycolic Acid) Functionalized with ZnO Nanoparticles. *BIO Web Conf.* **2023**, *57*, 02005. [CrossRef]
37. Ostovar, S.; Pourmadadi, M.; Zaker, M.A. Co-Biopolymer of Chitosan/Carboxymethyl Cellulose Hydrogel Improved by Zinc Oxide and Graphene Quantum Dots Nanoparticles as PH-Sensitive Nanocomposite for Quercetin Delivery to Brain Cancer Treatment. *Int. J. Biol. Macromol.* **2023**, *253*, 127091. [CrossRef]
38. Li, S.; Yin, J.; Xu, L. Batch Fabrication and Characterization of ZnO/PLGA/PCL Nanofiber Membranes for Antibacterial Materials. *Fibers Polym.* **2022**, *23*, 1225–1234. [CrossRef]
39. Stanković, A.; Sezen, M.; Milenković, M.; Kaišarević, S.; Andrić, N.; Stevanović, M. PLGA/Nano-ZnO Composite Particles for Use in Biomedical Applications: Preparation, Characterization, and Antimicrobial Activity. *J. Nanomater.* **2016**, *2016*, 9425289. [CrossRef]
40. Mozaffari, A.; Mirzapour, S.M.; Rad, M.S.; Ranjbaran, M. Cytotoxicity of PLGA-Zinc Oxide Nanocomposite on Human Gingival Fibroblasts. *J. Adv. Periodontol. Implant. Dent.* **2023**, *15*, 27–33. [CrossRef]
41. Ayyanaar, S.; Kesavan, M.P. Magnetic Iron Oxide Nanoparticles@lecithin/Poly (l-Lactic Acid) Microspheres for Targeted Drug Release in Cancer Therapy. *Int. J. Biol. Macromol.* **2023**, *253*, 127480. [CrossRef] [PubMed]
42. Senturk, F.; Cakmak, S. Fabrication of Curcumin-Loaded Magnetic PEGylated-PLGA Nanocarriers Tagged with GRGDS Peptide for Improving Anticancer Activity. *MethodsX* **2023**, *10*, 102229. [CrossRef] [PubMed]
43. Pereira, E.D.; de Souza Junior, F.G.; Pinto, J.C.; Filho, S.T.; Pal, K.; dos Santos Pyrrho, A.; da Costa, R.C.; da Cunha, B.P.; da Silveira Maranhão, F.; de Almeida, T.M. Evaluation of Hyperthermic Potential and Acute Toxicity of PLGA-PEG/Magnetite Microspheres Loaded with Oxaliplatin Using Mice as a Test System. *Macromol. React. Eng.* **2023**, *17*, 2300005. [CrossRef]
44. Gupta, A.; Niveria, K.; Chandpa, H.H.; Singh, M.; Kumar, V.; Meena, J. Stimuli Responsive Magnetic-Silica-Poly Lactic-Co-Glycolic Acid Hybrid Nanoparticles for Targeted Cancer Chemo-Immunotherapy. *Drug Deliv. Transl. Res.* **2024**, *14*, 2712–2726. [CrossRef]
45. Luque-Michel, E.; Lemaire, L.; Blanco-Prieto, M.J. SPION and Doxorubicin-Loaded Polymeric Nanocarriers for Glioblastoma Theranostics. *Drug Deliv. Transl. Res.* **2021**, *11*, 515–523. [CrossRef]
46. Luque-Michel, E.; Sebastian, V.; Larrea, A.; Marquina, C.; Blanco-Prieto, M.J. Co-Encapsulation of Superparamagnetic Nanoparticles and Doxorubicin in PLGA Nanocarriers: Development, Characterization and in Vitro Antitumor Efficacy in Glioma Cells. *Eur. J. Pharm. Biopharm.* **2019**, *145*, 65–75. [CrossRef]
47. Spanhel, L.; Anderson, M.A. Semiconductor Clusters in the Sol-Gel Process: Quantized Aggregation, Gelation, and Crystal Growth in Concentrated ZnO Colloids. *J. Am. Chem. Soc.* **1991**, *113*, 2826–2833. [CrossRef]
48. Babes, L.; Denizot, B.; Tanguy, G.; Le Jeune, J.J.; Jallet, P. Synthesis of Iron Oxide Nanoparticles Used as MRI Contrast Agents: A Parametric Study. *J. Colloid. Interface Sci.* **1999**, *212*, 474–482. [CrossRef]
49. Chiu, H.I.; Samad, N.A.; Fang, L.; Lim, V. Cytotoxicity of Targeted PLGA Nanoparticles: A Systematic Review. *RSC Adv.* **2021**, *11*, 9433–9449. [CrossRef]
50. Baalousha, M. Aggregation and Disaggregation of Iron Oxide Nanoparticles: Influence of Particle Concentration, PH and Natural Organic Matter. *Sci. Total Environ.* **2009**, *407*, 2093–2101. [CrossRef]
51. Mohd Omar, F.; Abdul Aziz, H.; Stoll, S. Aggregation and Disaggregation of ZnO Nanoparticles: Influence of PH and Adsorption of Suwannee River Humic Acid. *Sci. Total Environ.* **2014**, *468–469*, 195–201. [CrossRef]
52. Lallo da Silva, B.; Caetano, B.L.; Chiari-Andréo, B.G.; Pietro, R.C.L.R.; Chiavacci, L.A. Increased Antibacterial Activity of ZnO Nanoparticles: Influence of Size and Surface Modification. *Colloids Surf. B Biointerfaces* **2019**, *177*, 440–447. [CrossRef] [PubMed]
53. Lallo da Silva, B.; Garcia, M.M.; Oshiro-Junior, J.A.; Sato, M.R.; Caetano, B.L.; Chiavacci, L.A. Modified Zinc Oxide Nanoparticles against Multiresistant Enterobacteriaceae: Stability, Growth Studies, and Antibacterial Activity. *J. Sol-Gel Sci. Technol.* **2022**, *101*, 244–255. [CrossRef]
54. Caetano, B.L.; Silva, M.N.; Santilli, C.V.; Briois, V.; Pulcinelli, S.H. Unified ZnO Q-Dot Growth Mechanism from Simultaneous UV–Vis and EXAFS Monitoring of Sol-Gel Reactions Induced by Different Alkali Base. *Opt. Mater.* **2016**, *61*, 92–97. [CrossRef]

55. Ashley, J.; Manikova, P. Fluorescent Sensors. In *Fundamentals of Sensor Technology: Principles and Novel Designs*; Woodhead Publishing: Cambridge, UK, 2023; pp. 147–161. [CrossRef]
56. Liang, L.; Chen, J.; Liu, X. Lanthanide-Doped Upconversion Nanomaterials. In *Comprehensive Inorganic Chemistry III*, 3rd ed.; Elsevier: Amsterdam, The Netherlands, 2023; Volume 1–10, pp. 439–485. [CrossRef]
57. Ragheb, R.R.T.; Kim, D.; Bandyopadhyay, A.; Chahboune, H.; Bulutoglu, B.; Ezaldein, H.; Criscione, J.M.; Fahmy, T.M. Induced Clustered Nanoconfinement of Superparamagnetic Iron Oxide in Biodegradable Nanoparticles Enhances Transverse Relaxivity for Targeted Theranostics. *Magn. Reson. Med.* **2013**, *70*, 1748–1760. [CrossRef]
58. Geraldes, C.F.G.C. Rational Design of Magnetic Nanoparticles as T1–T2 Dual-Mode MRI Contrast Agents. *Molecules* **2024**, *29*, 1352. [CrossRef]
59. Fleutot, S.; Nealon, G.L.; Pauly, M.; Pichon, B.P.; Leuvrey, C.; Drillon, M.; Gallani, J.-L.; Guillon, D.; Donnio, B.; Begin-Colin, S. Spacing-Dependent Dipolar Interactions in Dendronized Magnetic Iron Oxide Nanoparticle 2D Arrays and Powders. *Nanoscale* **2013**, *5*, 1507. [CrossRef]
60. Mudunkotuwa, I.A.; Rupasinghe, T.; Wu, C.M.; Grassian, V.H. Dissolution of ZnO Nanoparticles at Circumneutral PH: A Study of Size Effects in the Presence and Absence of Citric Acid. *Langmuir* **2012**, *28*, 396–403. [CrossRef]
61. Cai, X.; Luo, Y.; Yan, H.; Du, D.; Lin, Y. PH-Responsive ZnO Nanocluster for Lung Cancer Chemotherapy. *ACS Appl. Mater. Interfaces* **2017**, *9*, 5739–5747. [CrossRef]
62. Manaia, E.B.; Kaminski, R.C.K.; Caetano, B.L.; Briois, V.; Chiavacci, L.A.; Bourgaux, C. Surface Modified Mg-Doped ZnO QDs for Biological Imaging. *Eur. J. Nanomed.* **2015**, *7*, 109–120. [CrossRef]
63. Ba-Abbad, M.M.; Kadhum, A.A.H.; Mohamad, A.B.; Takriff, M.S.; Sopian, K. Visible Light Photocatalytic Activity of Fe^{3+}-Doped ZnO Nanoparticle Prepared via Sol-Gel Technique. *Chemosphere* **2013**, *91*, 1604–1611. [CrossRef] [PubMed]
64. Sekar, A.D.; Muthukumar, H.; Chandrasekaran, N.I.; Matheswaran, M. Photocatalytic Degradation of Naphthalene Using Calcined Fe–ZnO/ PVA Nanofibers. *Chemosphere* **2018**, *205*, 610–617. [CrossRef] [PubMed]
65. Krobthong, S.; Wongrerkdee, S.; Pimpang, P.; Moungsrijun, S.; Sujinnapram, S.; Nilphai, S.; Rungsawang, T.; Wongrerkdee, S. ZnO Nanoparticles Coprecipitation with Aluminum and Copper Ions for Efficient Photocatalytic Degradation of Commercial Glyphosate. *Integr. Ferroelectr.* **2022**, *222*, 69–83. [CrossRef]

Disclaimer/Publisher's Note: The statements, opinions and data contained in all publications are solely those of the individual author(s) and contributor(s) and not of MDPI and/or the editor(s). MDPI and/or the editor(s) disclaim responsibility for any injury to people or property resulting from any ideas, methods, instructions or products referred to in the content.

molecules

MDPI

Article

Construction and Anti-Cancer Activity of a Self-Assembly Composite Nano-Delivery System Loaded with Curcumin

Liang Chen [1], Qiao Wu [2], Chen Yang [1], Xiulan Xin [1], Zhaochu Xu [1], Shuai Luo [1] and Hao Liang [2,*]

[1] School of Bioengineering, Beijing Polytechnic University, Beijing 100176, China; chenliang@bpi.edu.cn (L.C.); yangchen2000521@126.com (C.Y.); xinxiulan@bpi.edu.cn (X.X.); xuzhaochu@bpi.edu.cn (Z.X.); luoshuai@bpi.edu.cn (S.L.)
[2] State Key Laboratory of Chemical Resource Engineering, Beijing University of Chemical Technology, Beijing 100029, China; wuqiao@mail.buct.edu.cn
* Correspondence: lianghao@mail.buct.edu.cn

Abstract: Natural products possess potent pharmacological activities and health benefits. However, drawbacks such as water insolubility, poor stability, and low bioavailability limit their practical applications. This research is dedicated to the development of suitable natural self-assembled nano-delivery systems to encapsulate natural molecule drugs, improving their dispersion and stability in aqueous solution. As a model drug, curcumin (Cur) was encapsulated in zinc–adenine nanoparticles (Zn–Adenine), based on the self-assembly of a coordination matrix material. Hyaluronic acid (HA) was further functionalized on the surface of Cur@(Zn–Adenine) to realize a tumor-targeted delivery system. The morphology was characterized through TEM and zeta potential analyses, while the encapsulation mechanism of the nanoparticles was researched via XRD and FTIR. The formed Cur@(Zn–Adenine)@HA nanoparticles exhibited good drug loading efficiency and drug loading rate. Moreover, compared to free Cur, Cur-loaded (Zn–Adenine)@HA showed enhanced pH stability and thermal stability. In particular, Cur@(Zn–Adenine)@HA demonstrated excellent biocompatibility and strong specificity for targeting CD44 protein on cancer cells. The above results indicate that (Zn–Adenine)@HA NPs can serve as an effective nano-delivery system for hydrophobic substances.

Keywords: natural self-assembled nano-delivery system; curcumin; hyaluronic acid; adenine; anti-cancer

1. Introduction

Curcumin (Cur), a type of polyphenol, is extracted from the rootstalk of Zingiberaceae plants. Its chemical structure is shown in Figure 1. Its molecular formula is $C_{21}H_{20}O_6$, and its molecular weight is 368.39 g/mol. Cur forms orange–yellow water insoluble crystals, but is soluble in glacial acetic acid, ethanol, methanol, acetone, and other organic reagents. It has strong coloring properties and is sensitive to light, heat, and other environmental factors [1,2].

Cur is a globally recognized natural pigment. It is generally applied in the food industry and has also been used as a natural treatment for cancer, inflammation, viral infections, and other diseases. Cur has low toxicity to normal cells but can induce the death of a variety of animal and human tumor cell lines, including lung, gastric, breast, colon, and prostatic cancers, and malignant melanoma [3,4]. Cur impedes the proliferation of tumor cells by suppressing multiple signal transduction pathways, disrupting cell cycles, and inducing apoptosis. Its molecular targets include NF-κB and AP-1 (activator protein 1), STAT3 (signal transducer and activator of transcription 3), and other carcinogenesis-related signaling

proteins involved in the occurrence and development of cancer [5,6]. In a small-cell lung cancer model, Yang et al. found that Cur effectively reduced STAT3 phosphorylation, affecting cell proliferation, migration, invasion, apoptosis, and other behaviors, as well as altering the expression of proliferative proteins and prohibitin, thereby inhibiting tumor growth and angiogenesis [7]. However, its peculiarities, such as poor water insolubility, low stability, limited bioavailability, etc., have become major obstacles to its application in the medical field [8]. The advent of nanotechnology has helped to overcome these limitations.

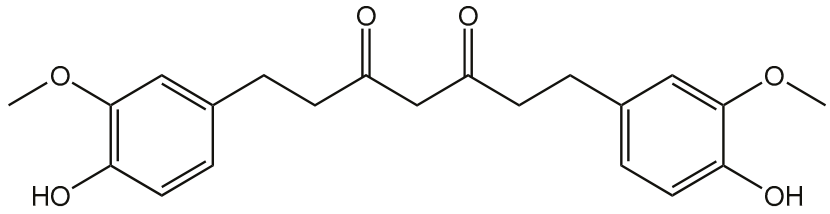

Figure 1. Structure of Cur.

Multifunctional drug delivery systems, enlightened by nanotechnology and high polymer chemistry—including lipid-based carriers (liposomes and lipid granules), polymer-based carriers (polymer nanospheres, micelle, and gelatum), and inorganic nanoparticles (gold and magnetic silicon dioxide)—are widely used in clinical medicine. These systems enhance drug absorption and distribution, improving therapeutic efficacy and drug safety [9]. Natural self-assembled drug delivery systems (NSADDS) are nano-carriers formed from natural biomaterials that spontaneously form into nanoscale structures such as inerratic spherical shapes, circular cylinders, or thin slices. These carriers exhibit enhanced penetration and retention and can be used to protect and transport active functional substances [10–12]. Compared with traditional embedding techniques, NSADDS offer size-dependent behaviors and specific biodistribution properties that benefit the targeted delivery of drugs and nutritious compounds [13,14]. Furthermore, biodegradable NSADDS increase the bioavailability of active molecules, enable the controlled and sustained release of guest molecules, and promote the targeted delivery of active molecules [15].

Metal biomolecule frameworks (MBioFs), built from biological components as single structural units and varying in modality and properties, have potential applications in separation and catalysis fields due to their high specific recognition and structural diversity [16]. Most importantly, based on their biological characteristics and biocompatibility, MBioFs are more suitable for drug dispensing and other medical applications. Along with developments in material science and pharmacology, the use of MBioFs composed of metal ions and nucleic acid components has become an important strategy for clinical cancer treatment and drug management due to their accessibility, biocompatibility, low cost, nanoscale size, high drug-loading efficiency, and self-assembly characteristics [17–20]. Adenine, a nucleic alkaline base that can be readily obtained from biomass, coordinates with multiple metal ions via its heterocycle and imidazole nitrogen atoms to form MBioFs, promoting its biological application potential [21–24]. Previous research has proven that zinc and adenine can self-assemble into porous materials suitable for drug storage and release, making zinc–adenine a preferred material for multifunctional drug delivery platforms [25]. Hyaluronic acid (HA), a major constituent of the human extracellular matrix, specifically binds the transmembrane receptor CD44 protein receptor, which is overexpressed on the surface of cancer cells. This property can be used for targeted tumor drug delivery [26–28]. Due to its biocompatibility, non-toxicity, and degradability in vivo, HA is also used as a controlled-release carrier for drugs [29–31].

In this study, we encapsulated Cur in zinc–adenine nanoparticles (Cur@(Zn–Adenine)NPs) and further functionalized (Cur@(Zn–Adenine)@HA NPs) the surface of Cur@Zn–Adenine with

HA via electrostatic adsorption. Our aim was to build a tumor-targeted drug delivery system, providing an experimental and theoretical basis for targeted cancer therapy.

2. Results and Discussion

2.1. Preparation of Cur@(Zn-Adenine)@HA

Cur@(Zn–Adenine)@HA NPs were prepared using a one-pot process. In HEPES buffer solution, adenine coordinated with Zn^{2+} ions through its heterocycle and imidazole nitrogen atoms. During self-assembly, Cur was encapsulated within the MOF. HA was subsequently introduced to functionalize the surface of Cur@(Zn–Adenine), promoting cell uptake.

As shown in Figure 2, the aqueous solution (a) of Cur appeared as a turbid, insoluble yellow liquid. Cur@(Zn–Adenine) (b) formed an aggregated orange precipitate. After HA modification, Cur@(Zn–Adenine)@HA (c) became a dispersed suspension with a slight color change.

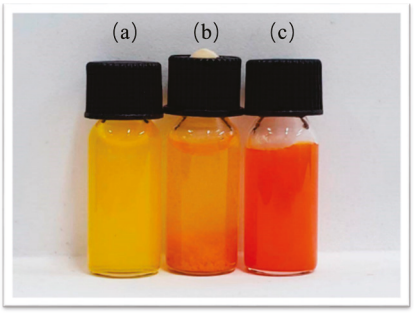

Figure 2. Photo of free Cur in water (**a**), Cur@(Zn-Adenine) (**b**), Cur@(Zn-Adenine)@HA (**c**).

2.2. DLE and DLC of Cur@(Zn-Adenine)@HA

The absorbance of Cur standard solutions was measured using UV–Vis spectroscopy. As shown in Figure 3, a standard curve was established with the following linear regression equation: $y = 0.1568x + 0.0296$ ($R^2 = 0.9993$), where y represents absorbance and x denotes Cur concentration (μg/mL). The encapsulation efficiency of Cur@(Zn–Adenine) was 98.9 ± 1.24%. After HA modification, the drug loading capacity (DLC) of Cur@(Zn–Adenine)@HA reached 18.6 ± 0.65%. The results show that (Zn–Adenine)@HA is a highly suitable nanoplatform for delivering hydrophobic compounds.

2.3. Characterization of Cur@(Zn-Adenine)@HA

Cur@(Zn–Adenine), Cur@(Zn–Adenine)@HA, and (Zn–Adenine)@HA were characterized using TEM, grain diameter and electric potential, XRD, and FTIR. UV was also used to scan the full wavelength range of 200 nm–700 nm for the above sample.

Through TEM, we observed the nanostructure of Zn–Adenine, Cur@(Zn–Adenine), and Cur@(Zn–Adenine)@HA. As shown in Figure 4, Zn–Adenine exhibits an amorphous extended network structure that was easy to reunite. After Cur loading, the network structure expanded—consistent with its subsidence behavior in water. Compared with Cur@(Zn–Adenine), Cur@(Zn–Adenine)@HA presented a well-defined spherical structure with better dispersibility, which is beneficial for intravenous injection and to achieve the EPR effect [32].

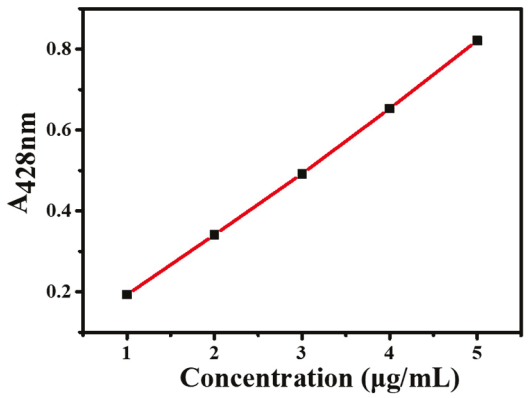

Figure 3. Standard curve of Cur.

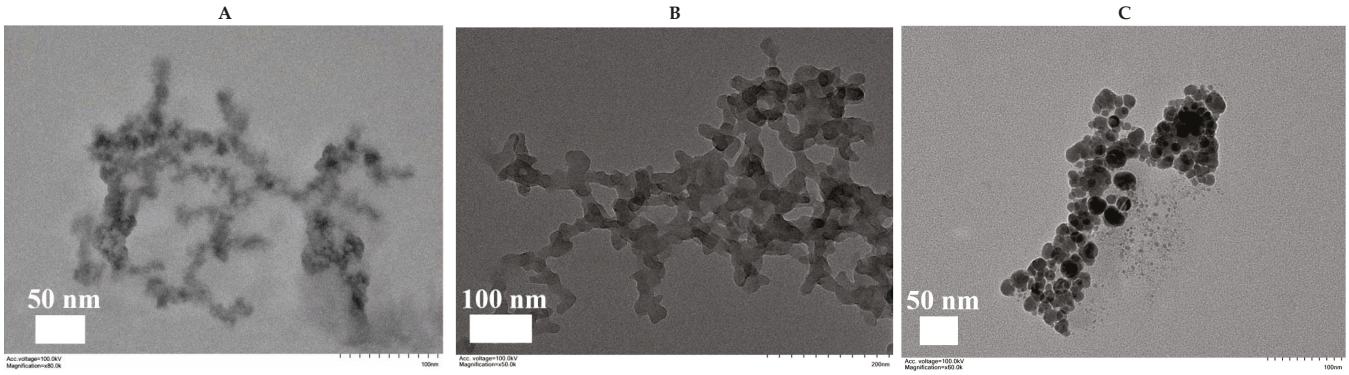

Figure 4. (**A**) TEM images of Zn-Adenine. (**B**) TEM images of Cur@(Zn-Adenine). (**C**) TEM images of Cur@(Zn-Ade nine)@HA.

The optical properties of NPs were recorded using UV spectra. As shown in Figure 5, Cur@(Zn–Adenine) displays a UV–visible absorption pattern combining Cur and Zn–Adenine. Cur@(Zn–Adenine)@HA showed a similar ultraviolet absorption trend to Cur@(Zn–Adenine). The UV absorption peak of free Cur at 427 mm red-shifted to 520 nm and 510 nm in the absorption spectrum of Cur@(Zn–Adenine) and Cur@(Zn–Adenine)@HA, respectively. These results indicate that Cur was successfully enveloped in the Zn–Adenine and (Zn–Adenine)@HA NPs, and that this envelopment partially altered the UV absorption of Cur [33].

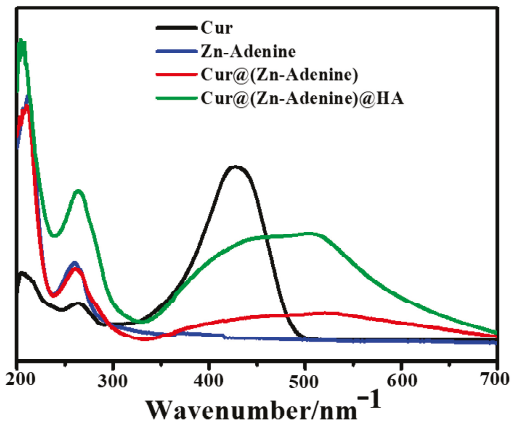

Figure 5. The UV spectra of Cur, Zn-Adenine, Cur@(Zn-Adenine), and Cur@(Zn-Adenine)@HA.

In addition, the surface potential of nanoparticles was measured. As shown in Figure 6, the HA surface was negatively charged (−16.97 mV), and the zeta electric potential of Cur@(Zn–Adenine) (9.20 mV) was almost the same as that of Zn–Adenine (9.27 mV). The

zeta electric potential of Cur@(Zn–Adenine)@HA and (Zn–Adenine)@HA was significantly reduced to −29.8 mV and −27.7 mV, respectively. Zeta potential was employed to assess the colloidal stability of the nanoparticles. The study revealed a significant increase in the magnitude of zeta potential following HA modification, indicating enhanced nanoparticle stability and improved resistance to sedimentation in solution.

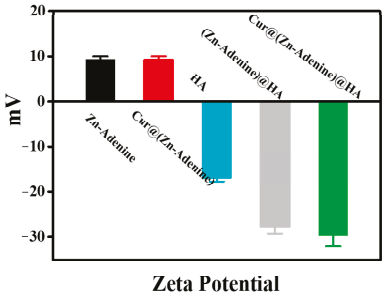

Figure 6. The zeta potentials of Zn-Adenine, Cur@(Zn-Adenine), HA, (Zn-Adenine)@HA, and Cur@(Zn-Adenine)@HA.

XRD was used to verify the successful structuring of the nanoplatform. As shown in Figure 7, Cur@(Zn–Adenine) closely matched the amorphous state of Zn–Adenine, and the crystalline peak of Cur was completely covered. This indicated that Cur was enveloped in Zn–Adenine, and that drug loading did not destroy the structural integrity of the nanoparticles. (Zn–Adenine)@HA and Cur@(Zn–Adenine)@HA showed different XRD patterns compared to Zn–Adenine, Cur@(Zn–Adenine), and HA, due to their good dispersibility [34]. On the other hand, TEM detected that after HA modification, the appearance of Cur@(Zn–Adenine) changed to a nearly spherical shape, which also contributed to the changes observed in XRD [35].

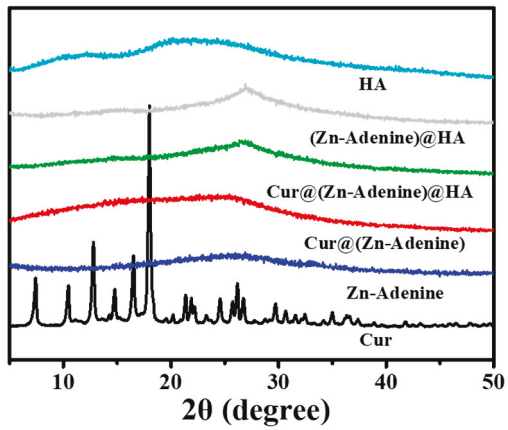

Figure 7. The XRD patterns of Cur, Zn-Adenine, Cur@(Zn-Adenine), Cur@(Zn-Adenine)@HA, (Zn-Adenine)@HA, and HA.

Figure 8A presents the FTIR spectrum of Cur and NPs between 4000 and 400 cm^{-1}, and Figure 8B shows an enlarged view of 1800–550 cm^{-1}. In Cur@(Zn–Adenine)@HA, the characteristic peaks of Cur at 1628 (C=O stretching) and 1602 cm^{-1} (aromatic series C=C stretching) disappear. The peaks of Cur located at 1510 (C=O stretching), 1427 (olefin bending vibration bonded by C-H and benzene ring), and at 1028 and 960 cm^{-1} (C=O stretching) shift separately to 1511, 1409, 1030, and 966 cm^{-1} in the Cur@(Zn–Adenine)@HA optical spectrum. It is speculated that the benzene ring structure in Cur undergoes π-π stacking with the aromatic ring structure in Adenine, slightly altering the vibration peak displacement on the benzene ring of Cur [36,37]. Moreover, the peak located at 1623 cm^{-1} in the amide I band of HA corresponds to the peak located at 1604 cm^{-1} in the Cur@(Zn–Adenine)@HA spectrum, which corresponds to changes caused by asymmetric tensile

vibration of the -COO anion [38]. These results further confirmed that Cur was loaded into Zn–Adenine and that HA was successfully modified onto the surface of Cur@(Zn–Adenine).

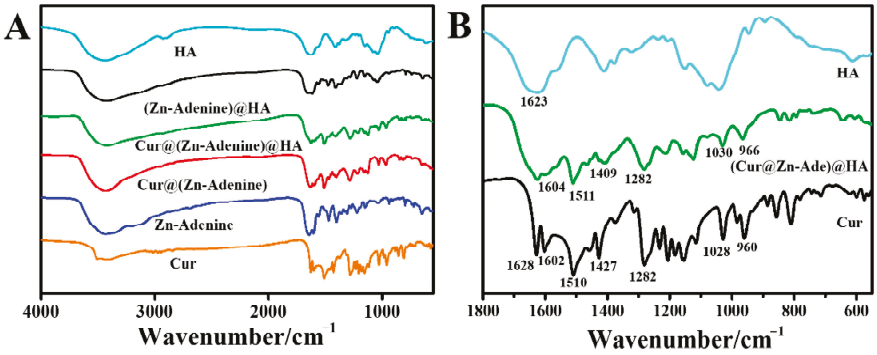

Figure 8. (**A**) FT-IR spectra of Cur, Zn-Adenine, Cur@(Zn-Adenine), Cur@(Zn-Adenine)@HA, (Zn-Adenine)@HA, and HA. (**B**) the enlarged FT-IR spectra of Cur, Cur@(Zn-Adenine)@HA and HA in the range 1800–550 cm^{-1}.

2.4. Stability of Cur@(Zn-Adenine)@HA

At different pH values, and with all other test and commissioning conditions kept the same, the photophobic reaction was carried out for 120 min. The relative intensity of free Cur, Cur@(Zn–Adenine), and Cur@(Zn–Adenine)@HA in PBS solution (10 mM, 25 °C) is shown in Figure 9. After reacting for 120 min in the solution at pH 5.5 and 7.4, the Cur content dropped to below 40%. By contrast, Cur@(Zn–Adenine) showed a loss of less than 10% in both solutions, while Cur@(Zn–Adenine)@HA experienced a content loss of approximately 25.3% in the pH = 5.5 solution.

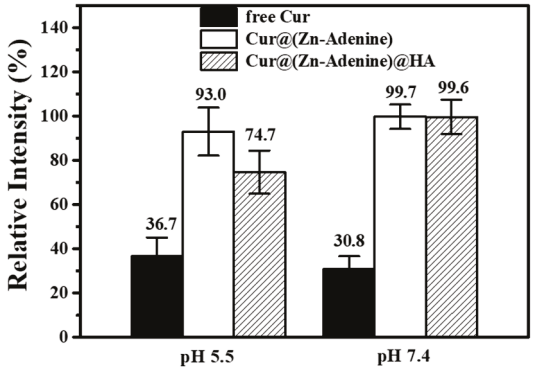

Figure 9. Stability of free and NPs loaded Cur in PBS solution (pH 5.5 or 7.4) after 120 min.

Subsequently, we studied the degradation kinetics of free and enveloped Cur in aqueous solution. As shown in Figure 10A, in PBS solution at pH = 5.5, the relative intensity of free Cur and Cur-loaded NPs gradually decreased over time. Only 49.19% of free Cur remained after 60 min, then gradually degraded, with relative intensity dropping to 36.69% after 120 min. Cur in Cur@(Zn–Adenine) still retained above 90% after 120 min, while Cur in Cur@(Zn–Adenine)@HA degraded 23.64% after 60 min and then remained stable. As shown in Figure 10B, in PBS solution with pH = 7.4, the relative intensity of free Cur rapidly decreased to 41.63% within 15 min. By contrast, Cur in Cur@(Zn–Adenine) and Cur@(Zn–Adenine)@HA showed almost no degradation within 120 min. The results showed that the envelopment of Zn–Adenine and (Zn–Adenine)@HA could both significantly enhance the pH stability of Cur, but the effect of (Zn–Adenine)@HA was slightly weaker, possibly because the modification of HA made the NPs more dispersed in aqueous solution, increasing their contact with the external environment and, hence, weakening stability.

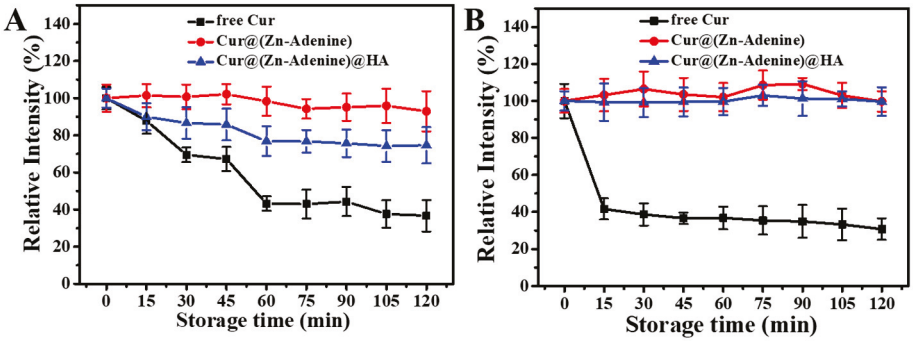

Figure 10. (**A**) Degradation kinetics of free and NPs loaded Cur in PBS solution (pH 5.5) for 120 min. (**B**) Degradation kinetics of free and NPs loaded Cur in PBS solution (pH 7.4) for 120 min.

During heat treatment at 80 °C, degradation kinetics curves of free Cur and NP-loaded Cur are shown in Figure 11. Free Cur showed rapid degradation within 45 min, rapidly reducing to 23.34%, and then degraded slowly, with the final relative intensity reduced to 9.12% after 120 min. Cur loaded by Zn–Adenine and (Zn–Adenine)@HA showed a rapid degradation process within 15 min, then degraded more slowly. After heat treatment for 120 min, the stability of Cur was increased more than four times. This showed that the envelopment of Zn–Adenine and (Zn–Adenine)@HA could improve the heat stability of Cur.

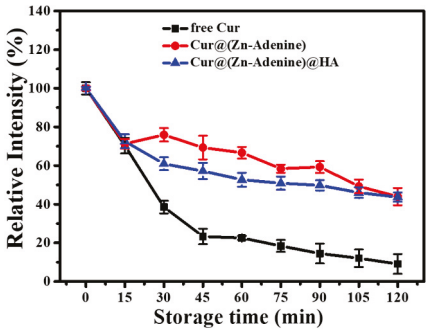

Figure 11. Degradation kinetics of free and NPs loaded Cur in PBS solution (pH 7.4) at 80 °C for 120 min.

2.5. Cellular Uptake of Cur@(Zn-Adenine)@HA

Due to its specific recognition with the CD44 receptor on the tumor cell surface, HA has been widely researched and applied to the field of targeted antitumor drugs. The uptake of free Cur and Cur-loaded NPs by A549 cells was explored through CLSM. Commercial fluorescent dye PI (red) was used to characterize cell morphology, and the green fluorescence of Cur indicated cellular uptake of the NPs. A Cur concentration of 5 μg/mL was selected as the final equivalent administration concentration. DMSO-treated cells were used as the control, and Cur, Cur@(Zn–Adenine), and Cur@(Zn–Adenine)@HA were used separately to treat monolayer cells for 4 h. In order to verify the HA targeting mechanism, competitive treatment with excess HA was performed—that is, free HA was used to preprocess cells and then had uptake of Cur@(Zn–Adenine)@HA. As shown in Figure 12, cells treated with free Cur showed weak green fluorescence, indicating a low uptake of Cur. Cells treated with Cur@(Zn–Adenine) and Cur@(Zn–Adenine)@HA showed stronger Cur fluorescence, and HA-modified NPs showed brighter fluorescence and wider distribution. This showed that the modification with Zn–Adenine and HA could promote the absorption of NPs by cells and that HA's targeting of cancer cells could promote drug endocytosis. After A549 cells were pretreated with HA, the fluorescence signal of Cur@(Zn–Adenine)@HA in the cells was significantly reduced, indicating a specific

competitive relationship between Cur@(Zn–Adenine)@HA and HA for the CD44 receptor overexpressed on the cell surface.

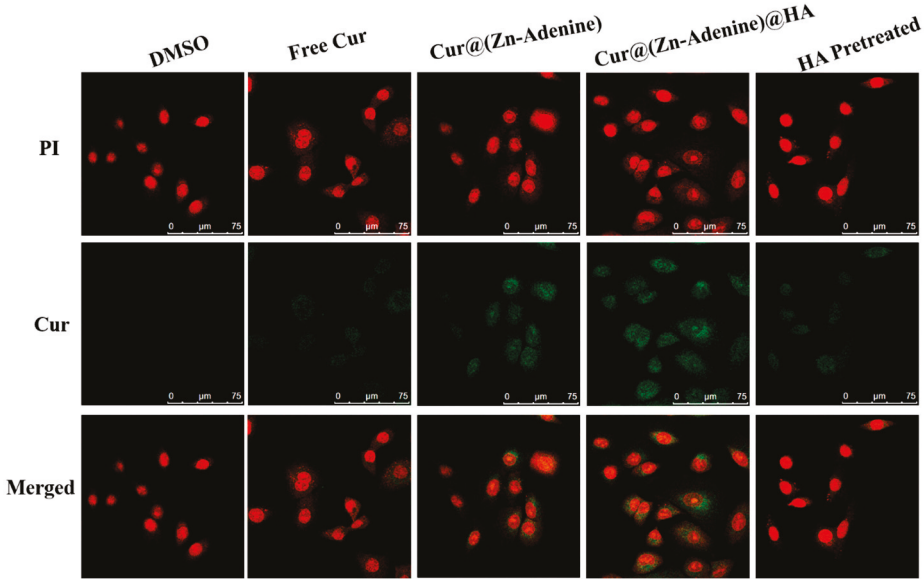

Figure 12. CLSM images on A549 cells incubated with DMSO, free Cur, Cur@(Zn-Adenine), Cur@(Zn-Adenine)@HA, and Cur@(Zn-Adenine)@HA after HA pretreated.

Figure 14 shows a CLSM diagram of cells treated with Cur@(Zn–Adenine)@HA for 0.5 h, 2 h, and 4 h, and as time went on, the green fluorescence intensity in the cells gradually increased, indicating that the release behavior of Cur in A549 cells was time-dependent. This durative release is the basis for prolonged drug therapy. In short, the results showed that Cur@(Zn–Adenine)@HA could effectively increase the accumulation of Cur in cells and enhance the therapeutic effect through tumor cell-targeted drug endocytosis between HA and the CD44 receptor.

2.6. Cytotoxicity of Cur@(Zn-Adenine)@HA

Through a quantitative cytotoxicity method, the inhibitory effects of free Cur, Cur@(Zn–Adenine), and Cur@(Zn–Adenine)@HA on A549 cells were studied under the same effective Cur concentration. As shown in Figure 13, with increasing Cur concentration, the cell survival rates of free Cur, Cur@(Zn–Adenine), and Cur@(Zn–Adenine)@HA gradually declined, indicating that both free Cur and Cur-loaded NPs had an inhibitory effect on tumor cells. When the Cur concentration was 1 μg/mL, the cell survival rate of free Cur was 97.32%, that of Cur@(Zn–Adenine) was 83.18%, and that of Cur@(Zn–Adenine)@HA was 76.92%. At a Cur concentration of 7 μg/mL, free Cur induced only 30.83% cell death, Cur@(Zn–Adenine) induced 44.94% cell death, and Cur@(Zn–Adenine)@HA induced 79.69% cell death, with its cancer cell suppression effect increasing about 2.58 times compared to free Cur. When the concentration reached 10 μg/mL, free Cur caused a 61.21% cell death rate, Cur@(Zn–Adenine) 80.65%, and Cur@(Zn–Adenine)@HA as high as 84.5%. The results showed that Cur@(Zn–Adenine) could increase the bioavailability of Cur, and after HA modification, its anticancer effect was significantly increased, which could be attributed to improved stability. Cur showed massive degradation in the weakly acidic tumor environment, while the enveloping carrier enabled effective and continuous release. On the other hand, the targeting effect of HA on cancer cells promoted drug endocytosis of drugs and enabled cumulative drug release in the cells.

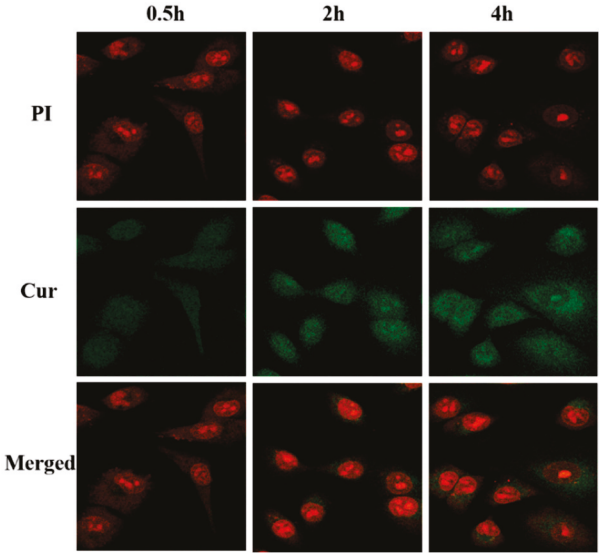

Figure 13. CLSM images on A549 cells incubated with Cur@(Zn-Adenine)@HA for 0.5 h, 2 h, and 4 h.

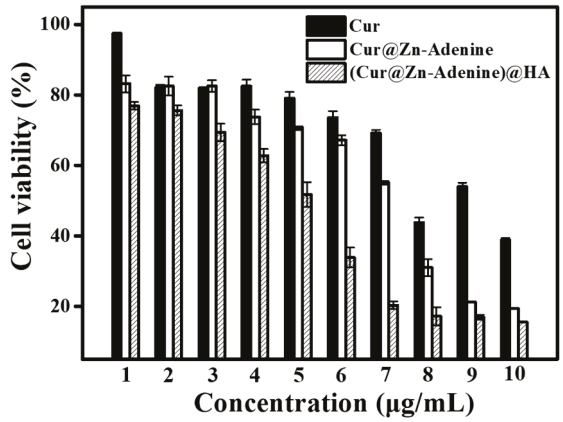

Figure 14. Anti-proliferation activity free Cur, Cur@(Zn-Adenine) and Cur@(Zn-Adenine)@HA against A549 cells.

2.7. Live/Dead Cell Staining Assay

The CLSM observation of NPs' inhibitory effect on cancer cells was assisted by a cell death and survival experiment. In this experiment, Calcein-AM marked live cells with green fluorescence, while PI stained dead cells with red. As shown in Figure 15, DMSO and free Cur showed almost no toxicity to A549 cells, and all the cells were in good condition. Cell death was observed in cells treated with both Cur@(Zn–Adenine) and Cur@(Zn–Adenine)@HA. However, the limited cytotoxic effect was likely due to the abbreviated 5-hour treatment duration, during which the cumulative release of encapsulated Cur in Zn–Adenine and (Zn–Adenine)@HA carriers remained insufficient to achieve complete tumor cell eradication.

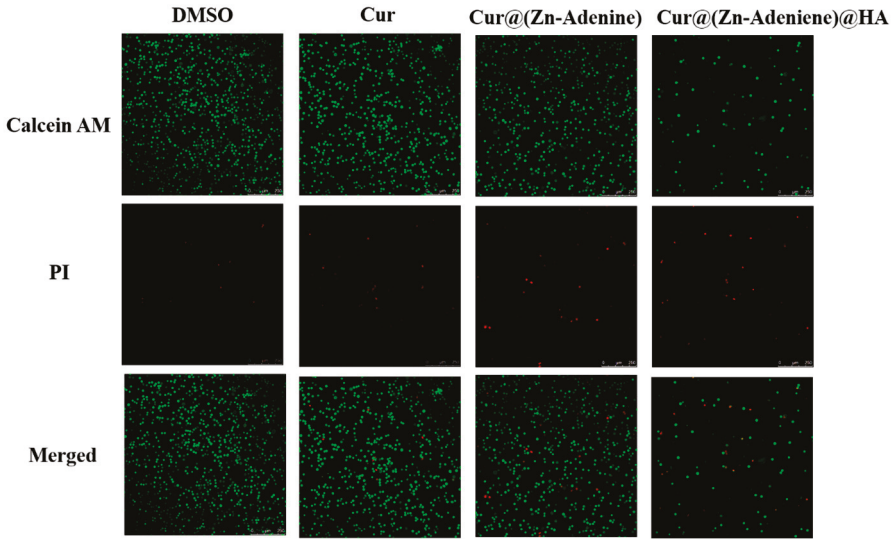

Figure 15. CLSM images of Calcein AM and PI stained A549 cells treated with DMSO, Cur, Cur@(Zn-Adenine), and Cur@(Zn-Adenine)@HA. Scale bar = 250 μm.

2.8. Cancer Cell Targeting of Cur@(Zn-Adenine)@HA

The cancer cell targeting of HA was based on the specific recognition between HA and the CD44 protein receptor overexpressed on the surface of cancer cells. The interaction between HA and the CD44 receptor on the surface of A549 cells was verified through experiments. After incubating A549 cells with HA solution for 12 h, cells were treated at Cur@(Zn–Adenine)@HA concentrations of 1–10 μg/mL. As shown in Figure 16, when the Cur concentration was 1–7 μg/mL, the inhibition rate of Cur@(Zn–Adenine)@HA on A549 cells was almost negligible. When the Cur concentration rose from 8 to 10 μg/mL, the cell survival rate was still above 70%. This finding showed that after competitive inhibition of HA, the targeting specificity of Cur@(Zn–Adenine)@HA, mediated by HA, weakened. As a result, its recognition of tumor cells was reduced, and the endocytosis of the drug by cells was affected. The above results demonstrated that the surface modification role of HA remarkably improved the cellular uptake and anticancer effect of NPs.

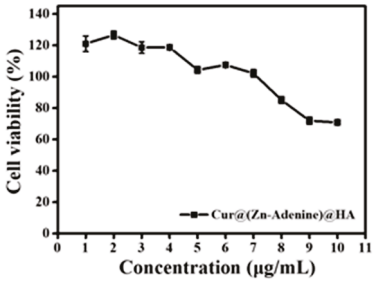

Figure 16. Anti-proliferation activity of Cur@(Zn-Adenine)@HA after HA pre-incubated with A549 cells.

3. Materials and Methods

3.1. Materials

Cur and HA were purchased from Meilunbio (Dalian, China). Adenine, $Zn(NO_3)_2 \cdot 6H_2O$, and HEPES buffer solution were obtained from Aladdin (Shanghai, China). Ethanol and acetonitrile were purchased from Mcklin (Shanghai, China).

PBS (pH = 5.5, 7.4), DMEM, DMSO, and FBS were obtained from Servicebio (Wuhan, China). A549 cells (glandular cancer human alveolus base epithelial cells) were obtained from the Cell Resource Center of Peking Union Medical College.

3.2. Preparation of Cur@(Zn-Adenine)@HA

Cur@(Zn–Adenine)@HA NPs were prepared using a one-pot process. Cur ethanol solution (2 mg/mL Cur), HEPES buffer solution (50 mM, pH = 7.4), $Zn(NO_3)_2 \cdot 6H_2O$ water solution (50 mM), adenine water solution (10 mM), and HA water solution (1 mg/mL) were prepared separately. Then, 4 mL of adenine water solution, 4 mL of Cur ethanol solution, and 4 mL of $Zn(NO_3)_2 \cdot 6H_2O$ water solution were added sequentially into 20 mL of HEPES buffer solution, followed by intense agitation (800 rpm/min) of the mixture in the dark for 2 h. The suspension was centrifuged, and the precipitate at the bottom was washed with deionized water three times to obtain Cur@(Zn–Adenine) NPs, which were used either in the next reaction or freeze-dried for backup. Zn–Adenine NPs were prepared using the same method. The collected Cur@(Zn–Adenine) NPs were dispersed in 5 mL of deionized water, then poured into a small beaker filled with 20 mL of HA solution. The mixture was stirred vigorously for 4 h. After centrifugation for 30 min to remove unlinked HA, the precipitate at the bottom was washed with deionized water three times to obtain Cur@(Zn–Adenine)@HA NPs.

3.3. DLE and DLC of Cur@(Zn-Adenine)@HA

A 1 mg/mL Cur solution in ethanol was stepwise diluted to concentrations of 1, 2, 3, 4, and 5 μg/mL. The Cur standard solutions were then analyzed by UV–Vis spectroscopy at a detection wavelength of 428 nm to establish a standard curve.

A weighed amount of Cur-loaded NPs powder was dissolved in ethanol solution, sonicated in a water bath for 30 min, then further diluted to a suitable concentration with ethanol solution, and tested for Cur content through UV. The Cur content at the initial time was set to 100%. The embedding rate and drug loading rate were calculated according to the Cur standard curve and Equations (1) and (2).

$$\text{Embedding rate (\%)} = \text{Content of Cur in Cur@(Zn-Adenine)/ total amount of Cur added} \times 100\% \quad (1)$$

$$\text{Drug loading rate (\%)} = \text{Content of Cur in Cur@(Zn-Adenine)@HA/total amount of nano particles added} \times 100\% \quad (2)$$

3.4. Characterization of Cur@(Zn-Adenine)@HA

Solutions of Zn–Adenine, Cur@(Zn–Adenine), and Cur@(Zn–Adenine)@HA were diluted to appropriate concentrations, minimally spotted onto ultrathin silicon wafers/400-mesh copper grids, and air-dried at room temperature. Morphological characterization was performed using transmission electron microscopy (TEM).

HA, Zn–Adenine, Cur@(Zn–Adenine), Cur@(Zn–Adenine)@HA, and (Zn–Adenine)@HA solutions were equally diluted under identical conditions. Surface zeta potential was determined using a dynamic light scattering instrument equipped with zeta potential measurement capability.

Appropriate amounts of dried powders of HA, Zn–Adenine, Cur@(Zn–Adenine), Cur@(Zn–Adenine)@HA, and (Zn–Adenine)@HA were evenly spread on clean sample holders. Structural analysis was conducted via X-ray diffraction (XRD) with a scan rate of 10°/min over a 2θ range of 5°–40° and a step size of 0.02°.

3.5. Stability of Cur@(Zn-Adenine)@HA

The influence of temperature (80 °C) and pH (7.4, 5.5) on NPs stability was examined. For temperature stability, Cur@(Zn–Adenine) and Cur@(Zn–Adenine)@HA of equal Cur concentration were dispersed in PBS buffer solution (pH = 7.4, 10 mM), and a Cur solution of the same concentration (PBS, pH = 7.4, 10 mM) served as the control. For the stability of

NPs in a pH = 5.5 solution, the buffer solution of 10 mM, pH = 7.4 was replaced with a PBS of 10 mM, pH = 5.5. The test duration was 2 h.

3.6. Cell Lines and Cell Culture

A549 cells (glandular cancer human alveolus base epithelial cells) were cultured in DMEM containing 10% fetal calf serum (FBS) and 1% double-resistance (100 U/mL streptomycin and 100 U/mL penicillin). Incubator conditions: 37 °C, 5% CO_2.

3.7. Cellular Uptake of Cur@(Zn-Adenine)@HA

A549 cells were seeded in glass-bottom confocal dishes at a density of 40,000 cells per mL (200 μL per dish) and incubated for 12 h. Solutions of Cur, Cur@(Zn–Adenine), and Cur@(Zn–Adenine)@HA were diluted with culture medium to achieve a final Cur concentration of 5 μg/mL. Cells were then treated with these solutions and co-incubated for 4 h. CLSM images of A549 were acquired to observe cellular uptake of Cur, Cur@(Zn–Adenine), and Cur@(Zn-Adenine)@HA. The selected Cur final concentration was 5 μg/mL; cells were incubated for 4 h, and captured laser confocal microscope (CLSM) images of A549 cells for Cur, Cur@(Zn–Adenine), and Cur@(Zn–Adenine)@HA were captured. Particularly, CLSM images of cells and Cur@(Zn–Adenine)@HA were also captured after 0.5 h, 2 h, and 4 h to assess changes in cell uptake over time. For inhibition studies, A549 cells were pretreated with 2 mg/mL free HA for 4 h, then Cur@(Zn–Adenine)@HA was incubated with the cells for 4 h. CLSM images were taken to observe the influence of HA inhibition on the cellular uptake of Cur@(Zn–Adenine)@HA.

3.8. Cytotoxicity of Cur@(Zn-Adenine)@HA

The cytotoxicity of Cur@(Zn–Adenine)@HA against A549 cells was evaluated using a CCK-8 kit and compared with free Cur and Cur@(Zn–Adenine). A549 cells in the logarithmic growth phase were trypsinized, centrifuged, and adjusted to a density of 4000 cells/mL. Cells were seeded into 96-well plates and incubated for 12 h to allow attachment. Subsequently, cells were treated with Zn-Adenine or (Zn–Adenine)@HA across a concentration range of 0–100 μg/mL. After treatment, CCK-8 reagent diluted in culture medium (10 μL per well) was added to each well, followed by incubation in the dark for 1 h. Absorbance was measured at 450 nm using a microplate reader to determine cell viability.

3.9. Live/Dead Cell Staining Assay

A549 cells were inoculated into laser confocal wells at 5×10^5 cells/well and incubated for 24 h. After removing the medium, each well received 100 μL of solution (Cur concentration: 5 μg/mL), pre-dissolved in DMSO and diluted with DMEM, was added to each well for Cur, Cur@(Zn–Adenine), and Cur@(Zn–Adenine)@HA and cultured for 5 h. The control group included cells only treated with DMSO. All the experimental groups and control groups were washed once with PBS, followed by the addition of Calcein-AM/PI in PBS solution. Samples were incubated at 37 °C for 15 min. Each hole was fully washed 3 times with PBS and kept away from light before CLSM observation.

3.10. Cancer Cell Targeting of Cur@(Zn-Adenine)@HA

After preprocessing A549 cells with HA (2 mg/mL) for 12 h, Cur@(Zn–Adenine)@HA with a concentration range of 1–10 μg/mL was added to incubate for 72 h. The CCK-8 test kit was used to test cell survival rate and evaluate cell viability.

3.11. Statistical Analysis

All experiments were performed in triplicate. Data are expressed as X ± SD, and variance analysis was performed using Origin 9.

4. Conclusions

In this study, a Bio-MOF nano drug-loading system based on Zn–Adenine was successfully prepared, and Cur loading was carried out. In addition, HA with specific recognition characteristics for cancer cells was modified on its surface, forming a targeted delivery system, Cur@(Zn–Adenine)@HA NPs. Cur@(Zn–Adenine)@HA NPs showed a high embedding rate (98.9 ± 1.24%) and high drug loading rate (18.6 ± 0.65%) and were well-dispersed in aqueous solution, thus improving the subsidence behavior of the original MOF material. Their structure and formation mechanism were explored through various means of characterization. Cur@(Zn–Adenine)@HA NPs significantly improved the heat stability of the embedded drug Cur and increased its stability in weakly acidic tumor environments (pH = 5.5) by more than two times. Its stability in physiological pH increased by about 3.2 times, helping to protect the loss of encapsulated drug due to degradation during transportation before reaching tumor cells. Compared with the equivalent dose of free Cur or Cur@(Zn–Adenine), Cur@(Zn-Adenine)@HA NPs more effectively reduced the survival rate of A549 cells. When Cur concentration was 7 μg/mL, its cancer cell suppression effect increased about 2.58 times compared with free Cur. Furthermore, the research results showed that Cur@(Zn–Adenine)@HA NPs achieved targeted delivery and controlled release of Cur through the specific binding of HA to the highly expressed receptor CD44 on the surface of cancer cells. This promoted drug endocytosis and accumulation in the cells while reducing harm to normal cells. In summary, the (Zn-Adenine)@HA NPs constructed in this study facilitate the endocytosis of A549 cells through CD44 receptor-specific interactions, enabling targeted delivery and controlled release of hydrophobic sensitive drugs while enhancing their stability under physiological conditions, demonstrating great potential as a versatile drug delivery platform. However, in order to apply them and explore their impact on human health, follow-up studies on (Zn–Adenine)@HA NPs are still required. These include investigating the bioactivity of the nanoplatform's encapsulated molecules after body fluid circulation, their release mechanism in the human body, and their transmission behavior and absorption mechanism in animal systems, with the expectation of promoting their future application in the medical field.

Author Contributions: L.C. and Q.W. conducted the research; C.Y. and X.X. analyzed the data; Z.X. and S.L. wrote the paper; L.C. and H.L. provisioned study materials, instrumentation, and computing resources. All authors have read and agreed to the published version of the manuscript.

Funding: This study was supported by The Project of Beijing Educational Science Planning (grant No. CDDB22223). Funder: L.C.

Institutional Review Board Statement: Not applicable.

Informed Consent Statement: Not applicable.

Data Availability Statement: The data presented in this study are available on request from the corresponding author.

Conflicts of Interest: The authors declare no conflicts of interest.

References

1. Perrone, D.; Ardito, F.; Giannatempo, G.; Dioguardi, M.; Troiano, G.; Lo, R.L.; DE Lillo, A.; Laino, L.; Lo, M.L. Biological and therapeutic activities, and anticancer properties of curcumin. *Exp. Ther. Med.* **2015**, *10*, 1615–1623. [CrossRef] [PubMed]
2. Li, S.; Fang, C.; Zhang, J.; Liu, B.; Wei, Z.; Fan, X.; Sui, Z.; Tan, Q. Catanionic lipid nanosystems improve pharmacokinetics and anti-lung cancer activity of curcumin. *Nanomedicine* **2016**, *12*, 1567–1579. [CrossRef] [PubMed]
3. Elmegeed, G.A.; Yahya, S.M.; Abd-Elhalim, M.M.; Mohamed, M.S.; Mohareb, R.M.; Elsayed, G.H. Evaluation of heterocyclic steroids and curcumin derivatives as anti-breast cancer agents: Studying the effect on apoptosis in MCF-7 breast cancer cells. *Steroids* **2016**, *115*, 80–89. [CrossRef]
4. Yallapu, M.M.; Khan, S.; Maher, D.M.; Ebeling, M.C.; Sundram, V.; Chauhan, N.; Ganju, A.; Balakrishna, S.; Gupta, B.K.; Zafar, N.; et al. Anti-cancer activity of curcumin loaded nanoparticles in prostate cancer. *Biomaterials* **2014**, *35*, 8635–8648. [CrossRef]
5. Lopez-Lazaro, M. Anticancer and carcinogenic properties of curcumin: Considerations for its clinical development as a cancer chemopreventive and chemotherapeutic agent. *Mol. Nutr. Food Res.* **2008**, *52* (Suppl. 1), S103–S127. [CrossRef]
6. Shehzad, A.; Wahid, F.; Lee, Y.S. Curcumin in cancer chemoprevention: Molecular targets, pharmacokinetics, bioavailability, and clinical trials. *Arch. Pharm.* **2010**, *343*, 489–499. [CrossRef]
7. Yang, C.L.; Liu, Y.Y.; Ma, Y.G.; Xue, Y.X.; Liu, D.G.; Ren, Y.; Liu, X.B.; Li, Y.; Li, Z. Curcumin blocks small cell lung cancer cells migration, invasion, angiogenesis, cell cycle and neoplasia through Janus kinase-STAT3 signalling pathway. *PLoS ONE* **2012**, *7*, e37960. [CrossRef] [PubMed]
8. Subramanian, A.P.; Jaganathan, S.K.; Manikandan, A.; Pandiaraj, K.N.; Gomathi, N.; Supriyanto, E. Recent trends in nano-based drug delivery systems for efficient delivery of phytochemicals in chemotherapy. *RSC Adv.* **2016**, *6*, 48294–48314. [CrossRef]
9. Cui, W.; Li, J.; Decher, G. Self-Assembled smart nanocarriers for targeted drug delivery. *Adv. Mater.* **2016**, *28*, 1302–1311. [CrossRef]
10. Duan, X.; Chen, H.; Fan, L.; Kong, J. Drug Self-Assembled delivery system with dual responsiveness for cancer chemotherapy. *ACS Biomater. Sci. Eng.* **2016**, *2*, 2347–2354. [CrossRef]
11. Li, Y.; Wang, Y.; Huang, G.; Gao, J. Cooperativity principles in Self-Assembled nanomedicine. *Chem. Rev.* **2018**, *118*, 5359–5391. [CrossRef]
12. Jin, Y.; Xin, R.; Ai, P.; Chen, D. Self-assembled drug delivery systems 2. Cholesteryl derivatives of antiviral nucleoside analogues: Synthesis, properties and the vesicle formation. *Int. J. Pharm.* **2008**, *350*, 330–337. [CrossRef]
13. Qin, S.Y.; Zhang, A.Q.; Cheng, S.X.; Rong, L.; Zhang, X.Z. Drug self-delivery systems for cancer therapy. *Biomaterials* **2017**, *112*, 234–247. [CrossRef] [PubMed]
14. Jaiswal, S.; Mishra, P. Co-delivery of curcumin and serratiopeptidase in HeLa and MCF-7 cells through nanoparticles show improved anti-cancer activity. *Mater. Sci. Eng. C Mater. Biol. Appl.* **2018**, *92*, 673–684. [CrossRef]
15. Lu, H.; Wang, Q.; Li, G.; Qiu, Y.; Wei, Q. Electrospun water-stable zein/ethyl cellulose composite nanofiber and its drug release properties. *Mater. Sci. Eng. C Mater. Biol. Appl.* **2017**, *74*, 86–93. [CrossRef] [PubMed]
16. Wu, H.; Tian, C.; Zhang, Y.; Yang, C.; Zhang, S.; Jiang, Z. Stereoselective assembly of amino acid-based metal-biomolecule nanofibers. *Chem. Commun.* **2015**, *51*, 6329–6332. [CrossRef] [PubMed]
17. Pu, F.; Ren, J.; Qu, X. Nucleobases, nucleosides, and nucleotides: Versatile biomolecules for generating functional nanomaterials. *Chem. Soc. Rev.* **2018**, *47*, 1285–1306. [CrossRef]
18. Joarder, B.; Chaudhari, A.K.; Nagarkar, S.S.; Manna, B.; Ghosh, S.K. Amino acid based dynamic metal-biomolecule frameworks. *Chemistry* **2013**, *19*, 11178–11183. [CrossRef]
19. Liang, H.; Lin, F.; Zhang, Z.; Liu, B.; Jiang, S.; Yuan, Q.; Liu, J. Multicopper laccase mimicking nanozymes with nucleotides as ligands. *ACS Appl. Mater. Interfaces* **2017**, *9*, 1352–1360. [CrossRef]
20. Lippert, B.; Sanz, M.P. The renaissance of Metal-Pyrimidine nucleobase coordination chemistry. *Acc. Chem. Res.* **2016**, *49*, 1537–1545. [CrossRef]
21. Mohapatra, B.; Pratibha; Verma, S. Directed adenine functionalization for creating complex architectures for material and biological applications. *Chem. Commun.* **2017**, *53*, 4748–4758. [CrossRef] [PubMed]
22. An, J.; Geib, S.J.; Rosi, N.L. Cation-triggered drug release from a porous zinc-adeninate metal-organic framework. *J. Am. Chem. Soc.* **2009**, *131*, 8376–8377. [CrossRef] [PubMed]
23. Sushrutha, S.R.; Hota, R.; Natarajan, S. Adenine-Based coordination polymers: Synthesis, structure, and properties. *Eur. J. Inorg. Chem.* **2016**, *2016*, 2962–2974. [CrossRef]
24. Purohit, C.S.; Verma, S. A luminescent silver-adenine metallamacrocyclic quartet. *J. Am. Chem. Soc.* **2006**, *128*, 400–401. [CrossRef]
25. An, J.; Farha, O.K.; Hupp, J.T.; Pohl, E.; Yeh, J.I.; Rosi, N.L. Metal-adeninate vertices for the construction of an exceptionally porous metal-organic framework. *Nat. Commun.* **2012**, *3*, 604. [CrossRef]
26. Luan, S.; Zhu, Y.; Wu, X.; Wang, Y.; Liang, F.; Song, S. Hyaluronic-Acid-Based pH-Sensitive nanogels for Tumor-Targeted drug delivery. *ACS Biomater. Sci. Eng.* **2017**, *3*, 2410–2419. [CrossRef]

27. Huang, G.; Huang, H. Hyaluronic acid-based biopharmaceutical delivery and tumor-targeted drug delivery system. *J. Control. Release* **2018**, *278*, 122–126. [CrossRef]
28. Wolf, K.J.; Kumar, S. Hyaluronic Acid: Incorporating the Bio into the Material. *ACS Biomater. Sci. Eng.* **2019**, *5*, 3753–3765. [CrossRef] [PubMed]
29. Xu, W.; Qian, J.; Hou, G.; Wang, Y.; Wang, J.; Sun, T.; Ji, L.; Suo, A.; Yao, Y. A dual-targeted hyaluronic acid-gold nanorod platform with triple-stimuli responsiveness for photodynamic/photothermal therapy of breast cancer. *Acta Biomater.* **2019**, *83*, 400–413. [CrossRef]
30. Spadea, A.; Rios, D.L.R.J.; Tirella, A.; Ashford, M.B.; Williams, K.J.; Stratford, I.J.; Tirelli, N.; Mehibel, M. Evaluating the efficiency of hyaluronic acid for tumor targeting via CD44. *Mol. Pharm.* **2019**, *16*, 2481–2493. [CrossRef]
31. Ossipov, D.A. Nanostructured hyaluronic acid-based materials for active delivery to cancer. *Expert Opin. Drug Deliv.* **2010**, *7*, 681–703. [CrossRef] [PubMed]
32. Zhang, H.; Li, Q.; Liu, R.; Zhang, X.; Li, Z.; Luan, Y. A versatile prodrug strategy to in situ encapsulate drugs in MOF nanocarriers: A case of Cytarabine-IR820 prodrug encapsulated ZIF-8 toward Chemo-Photothermal therapy. *Adv. Funct. Mater.* **2018**, *28*, 1802830. [CrossRef]
33. Song, L.; Pan, Z.; Zhang, H.; Li, Y.; Zhang, Y.; Lin, J.; Su, G.; Ye, S.; Xie, L.; Li, Y.; et al. Dually folate/CD44 receptor-targeted self-assembled hyaluronic acid nanoparticles for dual-drug delivery and combination cancer therapy. *J. Mater. Chem. B* **2017**, *5*, 6835–6846. [CrossRef] [PubMed]
34. Shi, Z.; Chen, X.; Zhang, L.; Ding, S.; Wang, X.; Lei, Q.; Fang, W. FA-PEG decorated MOF nanoparticles as a targeted drug delivery system for controlled release of an autophagy inhibitor. *Biomater. Sci.* **2018**, *6*, 2582–2590. [CrossRef]
35. Jing, Y.; Wang, J.; Yu, B.; Lun, J.; Cheng, Y.; Xiong, B.; Lei, Q.; Yang, Y.; Chen, L.; Zhao, M. A MOF-derived ZIF-8@Zn1-xNixO photocatalyst with enhanced photocatalytic activity. *RSC Adv.* **2017**, *7*, 42030–42035. [CrossRef]
36. Zhang, X.; Liu, L.; Huang, L.; Zhang, W.; Wang, R.; Yue, T.; Sun, J.; Li, G.; Wang, J. The highly efficient elimination of intracellular bacteria via a metal organic framework (MOF)-based three-in-one delivery system. *Nanoscale* **2019**, *11*, 9468–9477. [CrossRef]
37. Govindaraj, P.; Kandasubramanian, B.; Kodam, K.M. Molecular interactions and antimicrobial activity of curcumin (Curcuma longa) loaded polyacrylonitrile films. *Mater. Chem. Phys.* **2014**, *147*, 934–941. [CrossRef]
38. Cai, W.; Gao, H.; Chu, C.; Wang, X.; Wang, J.; Zhang, P.; Lin, G.; Li, W.; Liu, G.; Chen, X. Engineering phototheranostic nanoscale Metal-Organic frameworks for multimodal Imaging-Guided cancer therapy. *ACS Appl. Mater. Interfaces* **2017**, *9*, 2040–2051. [CrossRef]

Disclaimer/Publisher's Note: The statements, opinions and data contained in all publications are solely those of the individual author(s) and contributor(s) and not of MDPI and/or the editor(s). MDPI and/or the editor(s) disclaim responsibility for any injury to people or property resulting from any ideas, methods, instructions or products referred to in the content.

molecules

MDPI

Article

Physicochemical and Multimodal Imaging Properties of Core–Shell Ln_2O_3@Carbon Nanoparticles (Ln = Tb and Ho)

Huan Yue [1,†], Tirusew Tegafaw [1], Shuwen Liu [1], Ying Liu [1], Dejun Zhao [1], Endale Mulugeta [1], Xiaoran Chen [1], Ahrum Baek [2], Kwon Seok Chae [3], Jihyun Kim [4], Yongmin Chang [5,*] and Gang Ho Lee [1,*]

[1] Department of Chemistry, College of Natural Sciences, Kyungpook National University, Taegu 41566, Republic of Korea; tirukorea@gmail.com (T.T.); djzhao.chem@gmail.com (D.Z.)
[2] Institute of Biomedical Engineering Research, School of Medicine, Kyungpook National University, Taegu 41944, Republic of Korea
[3] Department of Biology Education, Teachers' College, Kyungpook National University, Taegu 41566, Republic of Korea
[4] Department of Chemistry Education, Teachers' College, Kyungpook National University, Taegu 41566, Republic of Korea; jkim23@knu.ac.kr
[5] Department of Molecular Medicine, School of Medicine, Kyungpook National University, Taegu 41944, Republic of Korea
* Correspondence: ychang@knu.ac.kr (Y.C.); ghlee@mail.knu.ac.kr (G.H.L.)
† Current address: College of Chemistry and Environmental Engineering, Pingdingshan University, Pingdingshan 467000, China.

Abstract: In this study, core–shell Ln_2O_3@carbon nanoparticles (core = Ln_2O_3 and shell = carbon; Ln = Tb and Ho) were synthesized for the first time by preparing Ln_2O_3 nanoparticles through a polyol method, followed by carbon coating using D-glucose as a carbon precursor in aqueous media. The synthesized Ln_2O_3@carbon nanoparticles exhibited good colloidal stability in solution and very low toxicity in in vitro cellular cytotoxicity tests. They exhibited paramagnetic magnetization values that increased with increasing applied field strength, resulting from spin–orbit magnetic moments of 4f-electrons; hence, they yielded negligible r_1 (<0.1 $s^{-1}mM^{-1}$) and appreciable r_2 values (3.446 and 3.677 $s^{-1}mM^{-1}$ for Ln = Tb and Ho, respectively) at 3 T, highlighting their potential as T_2 MRI contrast agents, particularly at high MR fields. In addition, the carbon coating shell exhibited photoluminescence at 460 nm, suitable for applications in fluorescence imaging probes.

Keywords: core-shell nanoparticle; Ln_2O_3@carbon (Ln = Tb and Ho); cellular toxicity; relaxivity; T_2 MRI contrast agent; photoluminescence

1. Introduction

Nanomedicine, i.e., nanotechnology-based medicine, has attracted great attention owing to its strong potential to overcome the limitations of conventional medicine, thus representing a breakthrough in disease treatments [1–3]. Among various examples, nanoparticle-based contrast agents for magnetic resonance imaging (MRI) are emerging as potential alternatives to the conventional molecular imaging contrast agents employed in MRI, such as Gd(III)-chelates [4–6], because they can provide enhanced imaging performances, reduced dosages, longer blood circulation times, and targeted theranosis [7–9].

The MRI contrast agents function by enhancing the proton spin relaxation rates at their accumulation region, leading to contrast enhancement [4–6,10]. Various types of nanoparticle-based negative (T_2) MRI contrasts have been introduced to date [11–19]; however, large nanoparticles [diameter (d) > 5 nm], such as superparamagnetic iron oxide nanoparticles (SPIONs), tend to exhibit long-term accumulation in the body, thus

potentially causing biotoxic effects such as back pain [20–22]. Another system suitable for use as T_2 MRI contrast agents is lanthanide (Ln)-based nanoparticles [12]. However, ultrasmall nanoparticles (d < 3 nm) are extremely useful as T_2 MRI contrast agents owing to their renal excretion ability [23–25]. Lanthanide (Ln)-based nanoparticles are ideal systems for this purpose, because their magnetic properties are nearly independent of the size and the surface-coating ligand [26,27], enabling their fabrication in ultrasmall sizes and their surface to be coated with any kind of ligand. The most effective T_2 relaxation results from electron spin–orbit magnetic moments of fast moving 4f electrons, because they can exclusively induce T_2 relaxation along with minimal T_1 relaxation [28,29], in contrast to pure electron spin magnetic moments of slow moving 3d or 4f electrons, which induce strong T_1 relaxations [28,30–32]. Therefore, ultrasmall Ln_2O_3 nanoparticles (Ln = Tb and Ho) are ideal systems to serve as highly effective T_2 MRI contrast agents, owing to the high paramagnetic electron spin–orbit moments of Tb and Ho, resulting from their 4f electrons [12,29,33] and renal excretion ability [23–25].

In this study, carbon-coated ultrasmall Ln_2O_3 nanoparticles (i.e., core–shell Ln_2O_3 @carbon; Ln = Tb and Ho) were synthesized for the first time to demonstrate their potential as T_2 MRI contrast agents. Ultrasmall Ln_2O_3 nanoparticles were synthesized via a polyol method and then coated with carbon by reducing D-glucose with NaOH in the presence of the nanoparticles in aqueous media. Carbon, as a key element in living organisms, is nontoxic and thus suitable for use as a surface-coating material for biomedical applications [34–37]. In addition, as confirmed in this study, carbon nanomaterials emit photons in the visible region [38–40], which makes them useful as fluorescent imaging probes. To investigate their potential as T_2 MRI contrast agents, we assessed various physicochemical properties, including in vitro cellular toxicities and water proton spin relaxivities.

2. Results

2.1. Physicochemical Properties

2.1.1. Particle Size

To confirm the successful synthesis of ultrasmall core–shell Ln_2O_3@carbon nanoparticles (Ln = Tb and Ho), the synthesized materials were characterized using various techniques. As shown by high-resolution transmission electron microscopy (HRTEM) images (Figure 1a), the Ln_2O_3@carbon nanoparticles had particle diameters ranging from 2 to 4 nm, with average values (d_{avg}) of 3.0 and 2.9 nm for Ln = Tb and Ho, respectively (Table 1), as estimated using log-normal function fits to the observed particle diameter distributions (Figure 1b). Clear lattice fringes were observed, confirming the successful synthesis of the Ln_2O_3 nanoparticles. In addition, energy dispersive X-ray spectroscopy (EDS) exhibited the presence of Tb and Ho in the nanoparticles (Figure 1c).

Table 1. Summarized physicochemical properties of core–shell Ln_2O_3@carbon nanoparticles (Ln = Tb and Ho).

Core Nanoparticle	d_{avg} (nm)	a_{avg} (nm)	ζ (mV)	Carbon Coating Amount (wt.%)		Net M at 2 T (emu/g)	r_1 ($s^{-1}mM^{-1}$)	r_2 ($s^{-1}mM^{-1}$)
				TGA	EA			
Tb_2O_3	3.0	19.5	−48.2	57.7	59.5	3.37	0.086	3.446
Ho_2O_3	2.9	21.5	−40.2	58.5	61.8	3.82	0.093	3.677

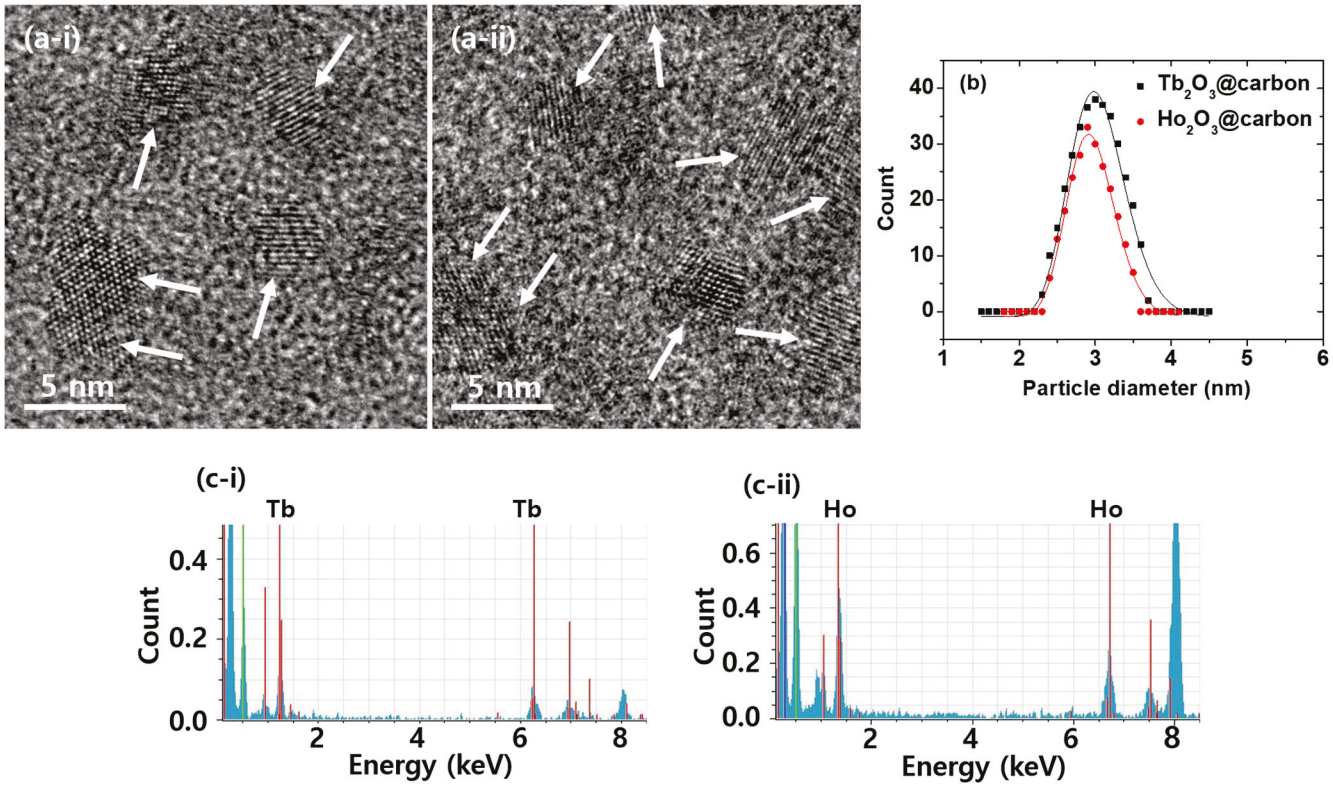

Figure 1. (**a**) HRTEM images of core–shell Ln_2O_3@carbon nanoparticles. Arrows indicate nanoparticles. (**b**) Log-normal function fits to observed particle diameter distributions. (**c**) EDS spectra. Ln = (**i**) Tb and (**ii**) Ho in (**a**,**c**).

2.1.2. Hydrodynamic Diameter

The average hydrodynamic diameter (a_{avg}) of the Ln_2O_3@carbon nanoparticles was estimated to be 19.5 and 21.5 nm for Ln = Tb and Ho, respectively, from log-normal function fits to the observed dynamic light scattering (DLS) patterns (Figure 2a; Table 1). The larger a_{avg} than d_{avg} values are due to the carbon coating and water hydration layer around the nanoparticles, because the surface functional groups of the carbon shells are -OH groups originating from D-glucose, used as a carbon precursor. This was supported by the highly negative zeta potentials (ζ) of the core–shell nanoparticles, i.e., −48.2 and −40.2 mV for Ln = Tb and Ho, respectively (Figure 2b; Table 1).

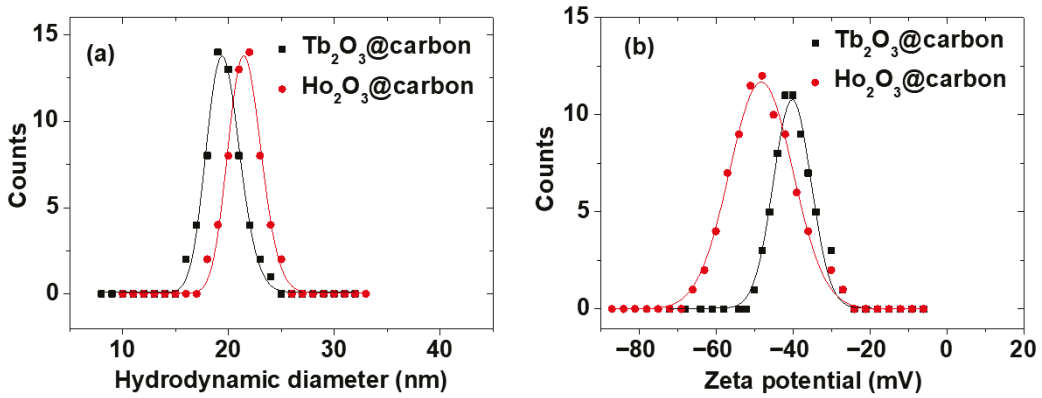

Figure 2. (**a**) DLS patterns and log-normal function fits to estimate a_{avg} values and (**b**) zeta potential curves of core–shell Ln_2O_3@carbon nanoparticles (Ln = Tb and Ho) dispersed in triple-distilled water.

2.1.3. Colloidal Stability

The physicochemical properties and performance of nanoparticles may be affected by colloidal stability, and thus good colloidal stability is crucial for biomedical applications [41]. The colloidal stability of the ultrasmall core–shell Ln_2O_3@carbon nanoparticles (Ln = Tb and Ho) was investigated in triple-distilled water, sodium acetate buffer (pH = 7), and 10% fetal bovine serum (FBS) solutions at 1, 3, and 7 days (Figure 3a). As shown in Figure 3a, all solution samples were transparent, with no nanoparticle precipitation for up to 7 days, demonstrating their good colloidal stability. Moreover, Figure 3b shows that all nanoparticle solution samples except triple-distilled water exhibited laser scattering (i.e., Tyndall effect), confirming the good colloidal dispersion of the carbon-coated nanoparticles in triple-distilled water.

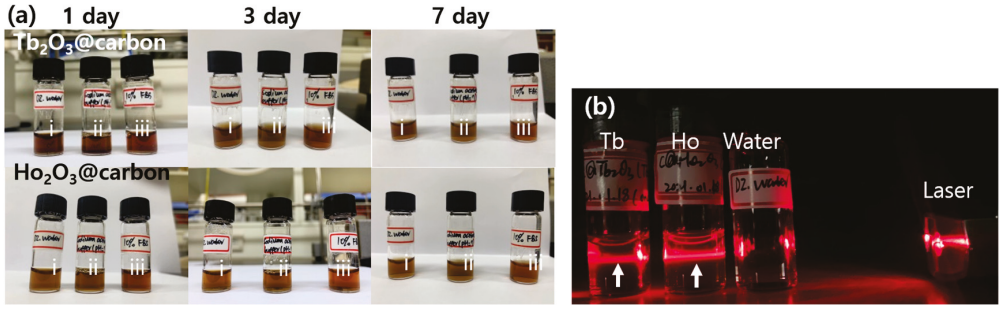

Figure 3. (**a**) Photographs of solutions containing core–shell Ln_2O_3@carbon nanoparticles (Ln = Tb and Ho) in (i) triple-distilled water, (ii) sodium acetate buffer (pH = 7), and (iii) 10% FBS solutions at 1, 3, and 7 days. (**b**) Laser scattering (or Tyndall effect, indicated with vertical arrows, measured using a commercial laser pointer with 650 nm wavelength) of triple-distilled water (used as reference) and core–shell Ln_2O_3@carbon nanoparticles (Ln = Tb and Ho) dispersed in triple-distilled water.

2.1.4. Crystallinity

As shown by the X-ray diffraction (XRD) patterns in Figure 4a,b, the ultrasmall core–shell Ln_2O_3@carbon nanoparticles (Ln = Tb and Ho) exhibited very broad peaks (bottom patterns), indicating an amorphous structure due to their ultrasmall particle sizes; on the other hand, a cubic phase (top patterns) was observed after thermalgravimetric analysis (TGA), with lattice constants (a) of 10.57 and 10.61 Å for Ln = Tb and Ho, respectively, using Bragg's equation, consistent with the literature values (10.72 and 10.6186 Å for Ln = Tb and Ho, respectively) [42,43].

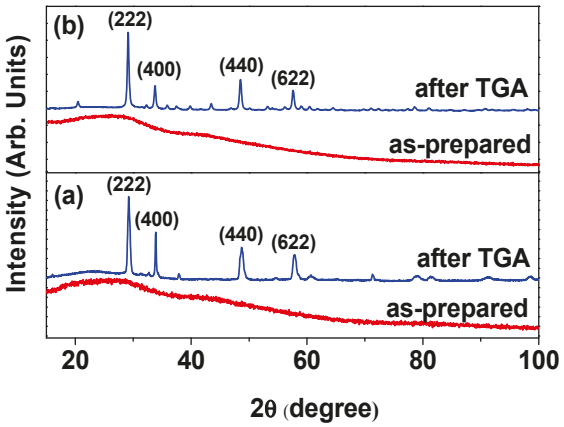

Figure 4. XRD patterns of core–shell Ln_2O_3@carbon nanoparticles before (**bottom**) and after (**top**) TGA: Ln = (**a**) Tb and (**b**) Ho. All peaks after TGA could be assigned with (hkl) Miller indices of cubic structure (card no. 00-021-1208 and 01-083-0923 for Tb and Ho, respectively), but only four strong peaks were assigned.

2.1.5. Carbon Coating Results

The carbon coating of the core–shell Ln_2O_3@carbon nanoparticles was analyzed through Fourier transform-infrared (FT-IR) absorption spectroscopy, Raman spectroscopy, elemental analysis (EA), and TGA. The FT-IR absorption spectra of nanoparticle samples and reference materials (i.e., D-glucose, carbon nanoparticles made from D-glucose, bare Ln_2O_3 nanoparticles after TGA) are displayed in Figure 5a,b for Ln = Tb and Ho, respectively. The C=C stretching-related G and D bands at 1577 and 1383 cm^{-1} [44,45], respectively, which also appeared in the FT-IR spectrum of the carbon nanoparticles, confirmed the presence of the carbon coating shell on the Ln_2O_3 nanoparticle surface. The strong O–H and C–O stretching peaks at 3252 and 1053 cm^{-1}, respectively, indicated the presence of a large amount of −OH groups on the carbon coating shell, because D-glucose was used as the carbon source. The C–H stretching peak at 2943 cm^{-1} also confirmed the presence of the carbon coating on the nanoparticle surface. The G and D bands also appeared at 1569 and 1412 cm^{-1}, respectively, in the Raman spectra (λ_{ex} = 532 nm) shown in Figure 6a (Ln = Tb) and Figure 6b (Ln = Ho), further confirming the presence of the carbon coating on the nanoparticle surface [45,46].

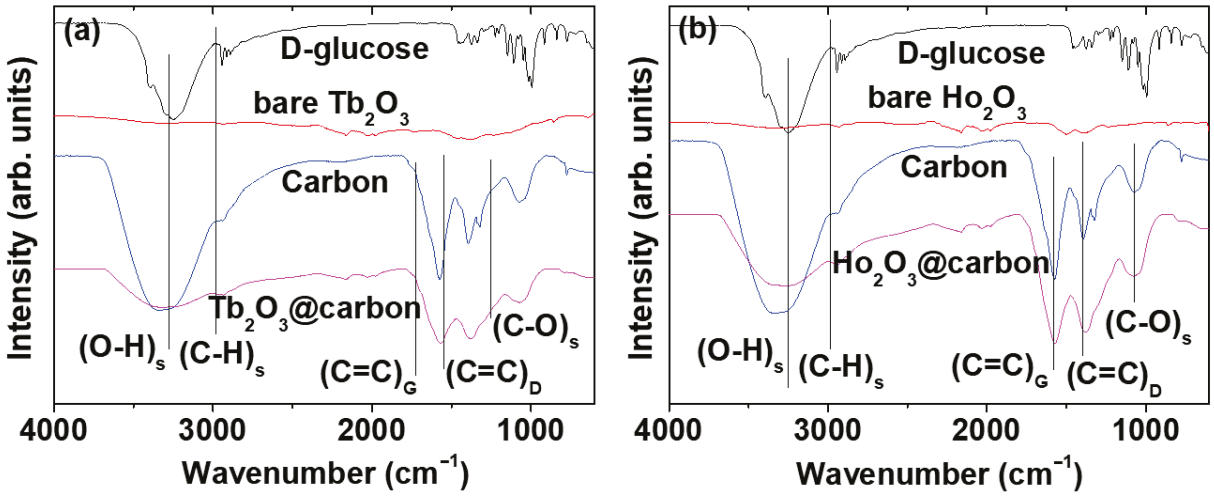

Figure 5. FT-IR absorption spectra of core–shell Ln_2O_3@carbon nanoparticles, D-glucose, bare Ln_2O_3 nanoparticles, and carbon nanoparticles (used as references): Ln = (**a**) Tb and (**b**) Ho. Subscripts s, G, D indicate "stretch", "G-band", and "D-band", respectively.

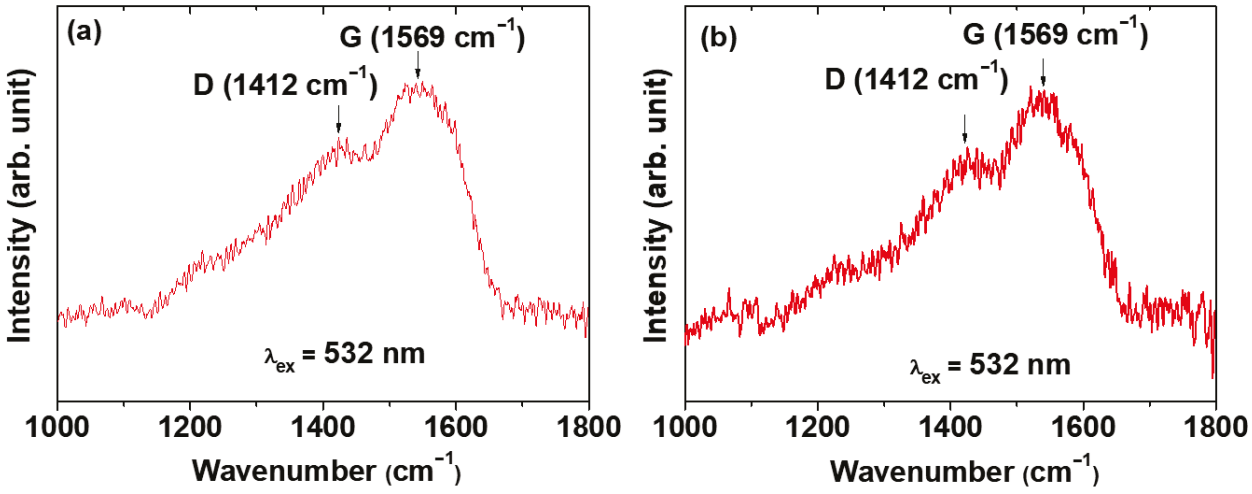

Figure 6. Raman spectra (λ_{ex} = 532 nm) of core–shell Ln_2O_3@carbon nanoparticles: Ln = (**a**) Tb and (**b**) Ho.

The carbon coating amount on the nanoparticle surface was estimated from the TGA curves (Figure 7). The initial mass losses of 9.0 and 7.2 wt.% were due to water and air desorption from the powder samples of the core–shell Ln_2O_3@carbon nanoparticles (Ln = Tb and Ho). The subsequent mass losses, estimated as 57.7 and 58.5 wt.% for Ln = Tb and Ho, respectively, were due to the removal of carbon coating from the nanoparticle surface through an oxidation reaction with flowing hot air (Table 1). The remaining masses of 33.3 and 34.3 wt.% after TGA were due to the Ln_2O_3 nanoparticles (Ln = Tb and Ho, respectively), as identified from their XRD patterns (top patterns in Figure 4a,b).

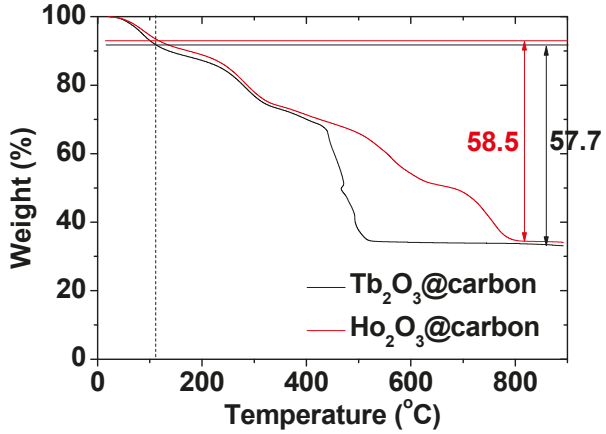

Figure 7. TGA curves of core–shell Ln_2O_3@carbon nanoparticles (Ln = Tb and Ho). Air and water desorption occurred before the vertical dotted line at ~110 °C and after it, the removal of carbon coating from the nanoparticle surface occurred.

The EA data provided in Table 1 show carbon coating amounts of 59.5 and 61.8 wt.% for core–shell Ln_2O_3@carbon nanoparticles (Ln = Tb and Ho, respectively), consistent with the TGA data. In addition, compared to the D-glucose ($C_6H_{12}O_6$, C:H:O = 1:2:1), the estimated C:H:O ratios were 1:1.3:0.6 for Ln = both Tb and Ho; this indicated the presence of a large amount of H and O in carbon coating shells, consistent with the observation of C–H and O–H stretching peaks in the FT-IR absorption spectra.

2.2. Magnetic Properties

The magnetic properties of powder samples of the core–shell Ln_2O_3@carbon nanoparticles (Ln = Tb and Ho) were characterized by measuring their magnetization versus applied magnetic field (M–H) curves at T = 300 K. The measured M values were corrected using the net masses of the Ln_2O_3 nanoparticles only (without carbon coating), which were estimated from the TGA curves. The mass-corrected net M values were used in the plots shown in Figure 8. The net M values were appreciable at room temperature and increased linearly with increasing H, reaching values of 3.37 and 3.82 emu/g at room temperature and H = 2 T (Table 1). These magnetization values are approximately ten times higher than 0.37 emu/g of carbon nanoparticles [47]. Therefore, the contribution of surface-coating carbon shells to magnetic moments of the nanoparticles is negligible. The magnetic moment of Ho_2O_3@carbon nanoparticles was slightly higher than that of Tb_2O_3@carbon nanoparticles because of a slightly higher magnetic moment of Ho^{3+} ($^5I_8$) compared to Tb^{3+} ($^7F_6$) [48]. This behavior confirms the paramagnetic nature of the Ln_2O_3@carbon nanoparticles, similar to the bulk [49–52], suggesting that they will induce stronger transverse (T_2) water proton spin relaxations with increasing H.

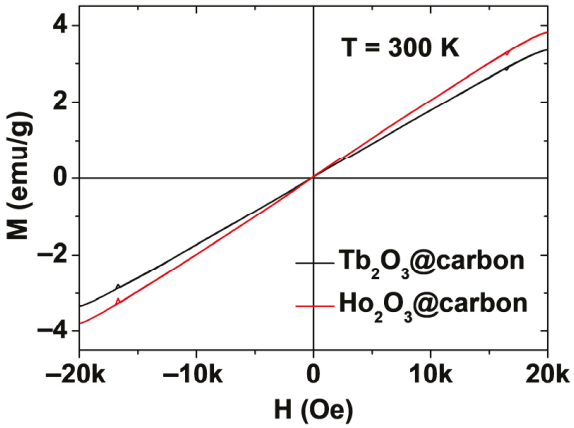

Figure 8. M–H curves of core–shell Ln_2O_3@carbon nanoparticles (Ln = Tb and Ho) at T = 300 K. The plots show the net M values of the core nanoparticles only.

2.3. In Vitro Cellular Cytotoxicity

The in vitro cell viability of the core–shell Ln_2O_3@carbon nanoparticles (Ln = Tb and Ho) was assessed using NCTC1469 and DU145 cell lines, and the results were compared to those obtained for the bare Ln_2O_3 nanoparticles. As shown in Figure 9a,b for Ln = Tb and Ho, respectively, the nanoparticles exhibited low cellular toxicity up to a measured Ln concentration of 500 μM after 48 h incubation, whereas the bare nanoparticles showed high toxicity, demonstrating the importance of the carbon coating in order to ensure a low toxicity of the nanoparticles. As shown in Figure 9c, the optical microscope images of the cells treated with 500 μM Ln (Ln = Tb and Ho) nanoparticle solutions after 48 h of incubation were similar to those of control cells (i.e., labeled as 0, untreated cells with nanoparticle solutions), confirming the low toxicity of the carbon-coated nanoparticles.

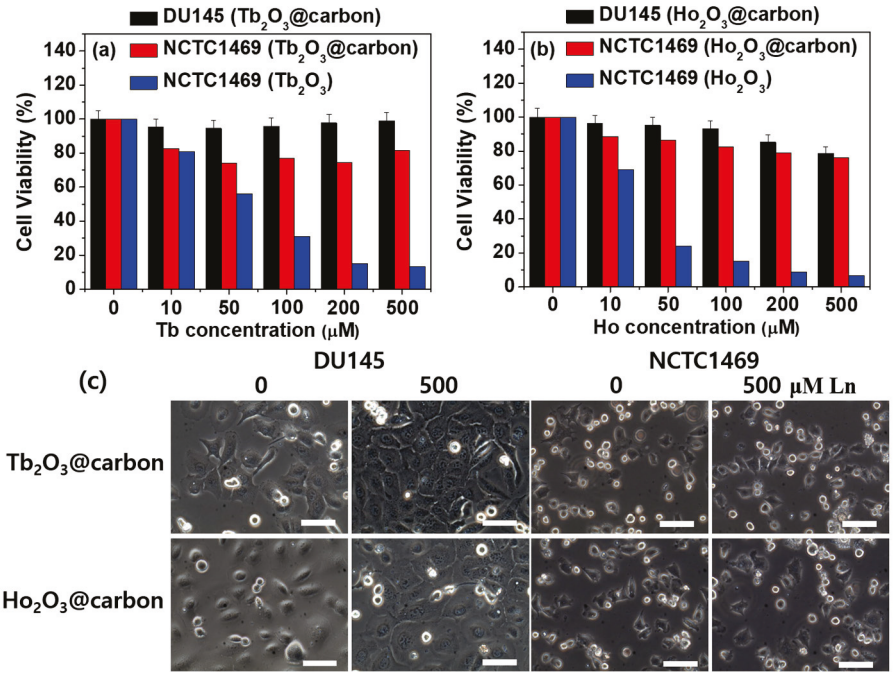

Figure 9. In vitro cell viabilities of core–shell Ln_2O_3@carbon nanoparticles in NCTC1469 and DU145 cells: Ln = (**a**) Tb and (**b**) Ho. (**c**) Optical microscope images of NCTC1469 and DU145 cells after treatment with 0 (control) and 500 μM Ln nanoparticle solutions (Ln = Tb and Ho) after 48 h. Scale bars indicate 70 μm.

2.4. Water Proton Spin Relaxivities

As shown in Figure 10a,b, the inverse $1/T_1$ and $1/T_2$ water proton spin relaxation times of the core–shell Ln_2O_3@carbon nanoparticles (Ln = Tb and Ho) dispersed in triple-distilled water were plotted as a function of the Ln concentration, and the corresponding longitudinal (r_1) and transverse (r_2) relaxivity values were estimated from the corresponding slopes, respectively. The r_1 values were negligible, i.e., 0.086 and 0.093 $s^{-1}mM^{-1}$ for Ln = Tb and Ho, respectively, whereas the r_2 values were appreciable, i.e., 3.446 and 3.677 $s^{-1}mM^{-1}$ for Ln = Tb and Ho, respectively (Table 1). The negligible r_1 values are attributed to the spin–orbit magnetic moments of fast moving 4f-electrons of Tb and Ho [28,48], while the appreciable r_2 values are due to the appreciable magnetic moments of the nanoparticles [53,54], as observed in the M–H curves in Figure 8. However, the r_2 values will increase with increasing H, because the paramagnetic M values of the nanoparticles increase with H, as shown in Figure 8.

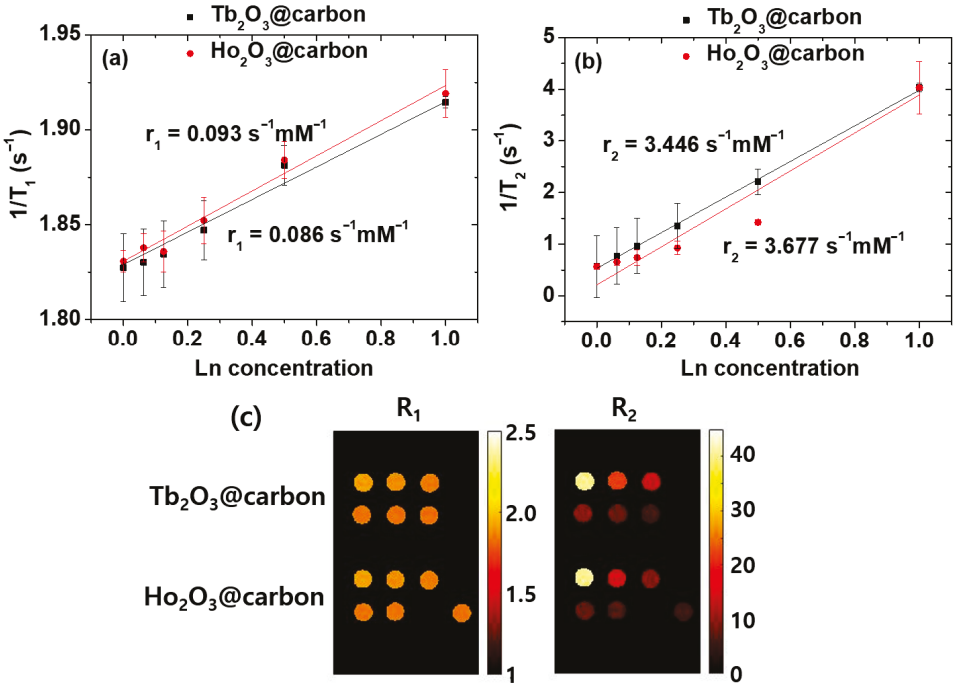

Figure 10. Plots of inverse (**a**) $1/T_1$ and (**b**) $1/T_2$ water proton spin relaxation times, along with (**c**) R_1 and R_2 map images of core–shell Ln_2O_3@carbon nanoparticles (Ln = Tb and Ho) dispersed in triple-distilled water as a function of Ln concentration.

As shown in Figure 10c, the R_1 maps of the nanoparticles exhibited negligible dose-dependent contrast changes, whereas appreciable changes were observed in the R_2 map images, demonstrating the ability of the nanoparticles to induce negative contrasts in vitro and thus their potential to serve as T_2 MRI contrast agents.

2.5. Fluorescent Properties

The carbon nanomaterials have unique photofluorescence properties in the visible region, making them suitable as fluorescent imaging probes [55–57]. The core–shell Ln_2O_3@carbon nanoparticles (Ln = Tb and Ho) dispersed in triple-distilled water exhibited photoluminescence (PL) under 365 nm UV irradiation, which is close to the excitation wavelength of the surface-coating carbon shells (available from a commercial UV lamp, VL-6.LC, Vilber Lourmat, Collégien, France), displaying a sky-blue emission color originating from the surface-coating carbon shells [47] (Figure 11a). As shown in Figure 11b, the nanoparticles exhibited PL spectra between 410 and 560 nm, originating from the surface-coating

carbon shells [47], with emission maxima (λ_{em}) at 460 nm at an excitation wavelength (λ_{ex}) of 370 nm, demonstrating their potential as fluorescent imaging probes. This visible emission is suitable for in vivo skin and in vitro cellular imaging owing to its limited penetration depth. In addition, we observed emission peaks from the core Tb_2O_3 nanoparticles at λ_{ex} of 260 nm (Figure 11c), indicating that both the core and the carbon-coating shell in core–shell Tb_2O_3@carbon nanoparticles will be useful for fluorescent imaging.

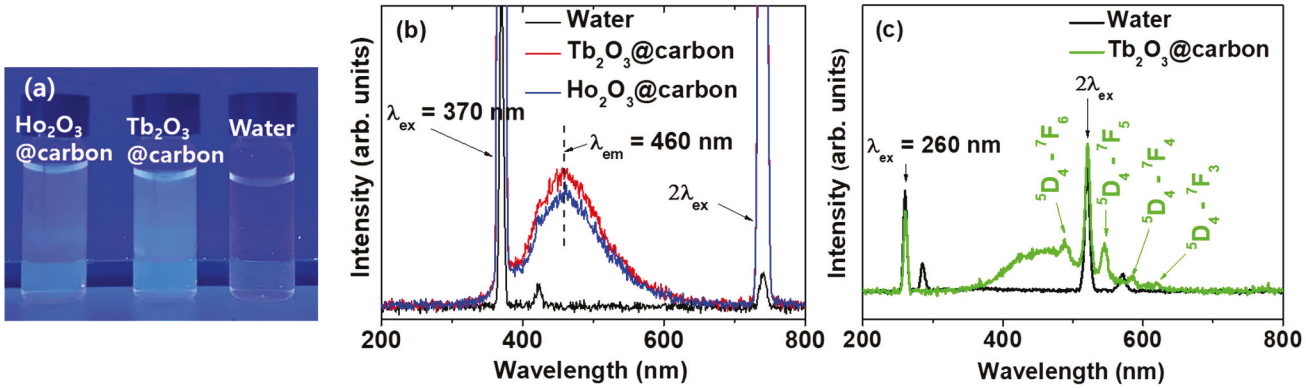

Figure 11. (**a**) Photographs under 365 nm UV irradiation and (**b**) PL spectra of core–shell Ln_2O_3@carbon nanoparticles (Ln = Tb and Ho) (λ_{ex} = 370 nm) and (**c**) core–shell Tb_2O_3@carbon nanoparticles (λ_{ex} = 260 nm) dispersed in triple-distilled water. Water was used as reference.

3. Discussion

In this study, ultrasmall core–shell Ln_2O_3@carbon nanoparticles (Ln = Tb and Ho) were successfully synthesized, as confirmed via various analytical techniques. The carbon coating shell endowed the nanoparticles with multifunctional properties, i.e., good colloidal stability, reduced toxicity, and photoluminescence in the visible region centered at 460 nm. Because the carbon coating shell was synthesized using D-glucose as a carbon source, it contained numerous hydrophilic −OH groups, as confirmed by FT-IR absorption spectroscopy (Figure 5a,b) and EA (discussed at the last paragraph in Section 2.1.5), thus yielding highly negative zeta potentials (Figure 2b) and good colloidal stability in solution (Figure 3a). Moreover, the core–shell Ln_2O_3@carbon nanoparticles exhibited almost complete nontoxicity in in vitro cellular toxicity tests using NCTC1469 and DU145 cells, whereas the bare Ln_2O_3 nanoparticles were toxic (Figure 9a,b). This is because carbon, as one of the most common elements in living organisms, is nontoxic [34–37] and can thus be used as nanoparticle coating materials.

The paramagnetic moments of the core–shell Ln_2O_3@carbon nanoparticles (Ln = Tb and Ho) exhibited a linear increase with increasing H, with appreciable net magnetic moments of 3.37 and 3.82 emu/g at room temperature and H = 2 T (Figure 8). These appreciable paramagnetic moments at clinical fields originate from the high spin–orbit magnetic moments of the fast-moving 4f-electrons of Tb^{3+} ($^7F_6$) and Ho^{3+} ($^5I_8$) [48]. Therefore, the nanoparticles can induce strong T_2 water proton spin relaxations with negligible induction of T_1 relaxations [53,54], in contrast to Gd^{3+} (s = 7/2), Fe^{3+} (s = 5/2), and Mn^{2+} (s = 5/2) (particularly Gd^{3+}), which can induce strong T_1 and T_2 water proton spin relaxations owing to their pure electron spin magnetic moments originating from slow moving 4f- or 3d-electrons [28,30–32]. Therefore, the magnetic moments of the nanoparticles resulted in negligible r_1 (i.e., 0.086 and 0.093 $s^{-1}mM^{-1}$ for Ln = Tb and Ho, respectively) and appreciable r_2 (i.e., 3.446 and 3.677 $s^{-1}mM^{-1}$ for Ln = Tb and Ho, respectively) values (Figure 10a,b). Under these r_1 and r_2 values, the core–shell Ln_2O_3@carbon nanoparticles can serve as T_2 MRI contrast agents because they can exclusively induce T_2 relaxations while

causing minimal T_1 relaxations, as demonstrated in vitro by negligible and appreciable dose-dependent contrast changes observed in the R_1 and R_2 map images, respectively.

As provided in Table 2, the r_1 and r_2 values of our nanoparticles are similar to those of carbon-coated Dy_2O_3 nanoparticles [12] because of similar spin–orbit electronic magnetic moments of Tb^{3+}, Dy^{3+}, and Ho^{3+}, but are considerably smaller than those of carbon-coated Gd_2O_3 nanoparticles [40] because of different (i.e., pure spin) electronic magnetic moments of Gd^{3+} as mentioned above. Compared to free lanthanide metal ions [58] (Table 2), the r_1 values of our carbon-coated nanoparticles are slightly smaller owing to fewer water coordination numbers in nanoparticles than in free lanthanide metal ions, but our r_2 values are higher owing to the high density of lanthanide metal ions in the nanoparticles.

Table 2. Comparison of r_1 and r_2 values for core–shell Ln_2O_3@carbon nanoparticles (Ln = Gd, Tb, Dy, and Ho).

Core Nanoparticle or Free Ion	d_{avg} (nm)	r_1 ($s^{-1}mM^{-1}$)	r_2 ($s^{-1}mM^{-1}$)	Applied Field (T)	Ref
Tb_2O_3	3.0	0.086	3.446	3	This study
Ho_2O_3	2.9	0.093	3.677	3	This study
Dy_2O_3	3.0	0.1	5.7	3	[12]
Gd_2O_3	3.1	16.26	24.12	3	[40]
Gd^{3+}	-	15.1	17.9	4.7	[58]
Dy^{3+}	-	0.652	0.688	4.7	[58]
Ho^{3+}	-	0.494	0.530	4.7	[58]

4. Materials and Methods

4.1. Materials

$LnCl_3 \cdot 6H_2O$ (99.9%; Ln = Tb and Ho), D-glucose (>99.5%), NaOH (>99.9%), and triethylene glycol (TEG) (99%) were purchased from Sigma-Aldrich, St. Louis, MO, USA, and used as received. Ethanol (99%) was purchased from Duksan, Ansan, Republic of Korea, and used as received. Triple-distilled water was obtained using a Pure Power I+ system (Human Co., Ltd., Seoul, Republic of Korea). The human prostate carcinoma cell line DU145 and mouse liver normal hepatocyte cell line NCTC 1469, used in this study, were obtained from the American Type Culture Collection (Rockville, MD, USA) and the Korean Cell Line Bank (Seoul, Republic of Korea), respectively.

4.2. Synthesis of Ultrasmall Core–Shell Ln_2O_3@Carbon Nanoparticles (Ln = Tb and Ho)

Ultrasmall core–shell Ln_2O_3@carbon nanoparticles (Ln = Tb and Ho) were synthesized in two steps (Figure 12a,b): (i) synthesis of ultrasmall Ln_2O_3 nanoparticles in TEG and (ii) carbon coating of the above nanoparticles using D-glucose as a carbon source in an aqueous solution. In the first step, we prepared a precursor solution [made by dissolving 1.0 mmol of $LnCl_3 \cdot 6H_2O$ (Ln = Tb or Ho) in 20 mL of TEG within a 100 mL three-necked round bottom flask] and a solution of 4 mmol of NaOH in 10 mL of TEG contained in a 50 mL beaker. The temperature was controlled by suspending the reaction flask in a silicone oil bath placed on a hot plate. After dissolution of $LnCl_3 \cdot 6H_2O$ in TEG via magnetic stirring at 60 °C under atmospheric conditions, followed by the addition of the NaOH solution until the solution pH reached 9 to 10, the temperature of the mixed solution was slowly raised to 110 °C and maintained for 6 h. After being cooled to room temperature, the solution was diluted with 500 mL of ethanol in a beaker, then magnetically stirred for ~5 min, and kept in a refrigerator (at ~4 °C) until the nanoparticles settled to the beaker bottom.

After decanting the top transparent liquid, the remaining Ln_2O_3 nanoparticle solution was diluted with ethanol again: this washing process was repeated three times to remove unreacted precursors, NaOH, and TEG. Ethanol was removed from the product solution by diluting it with 100 mL of triple-distilled water and then concentrating it to ~10 mL using a rotary evaporator. In the second step, the above concentrated Ln_2O_3 nanoparticle solution was added to a mixture consisting of 1.0 mmol of D-glucose dissolved in 10 mL of triple-distilled water within a 100 mL three-necked round bottom flask; the mixed solution was magnetically stirred for 30 min, followed by the addition of NaOH solution (4 mmol of NaOH in 5 mL of triple-distilled water) until the solution pH reached 9–10. The mixed solution was magnetically stirred at ~95 °C for 2 h to make the solution color black. After being cooled to room temperature, the solution was transferred to a dialysis bag (MWCO ~2000 amu) and dialyzed against triple-distilled water for 3 days with magnetic stirring; outside water was replaced with fresh water three times. Then, half of the solution volume was concentrated to a powder by freeze-drying it in vacuum prior to characterization.

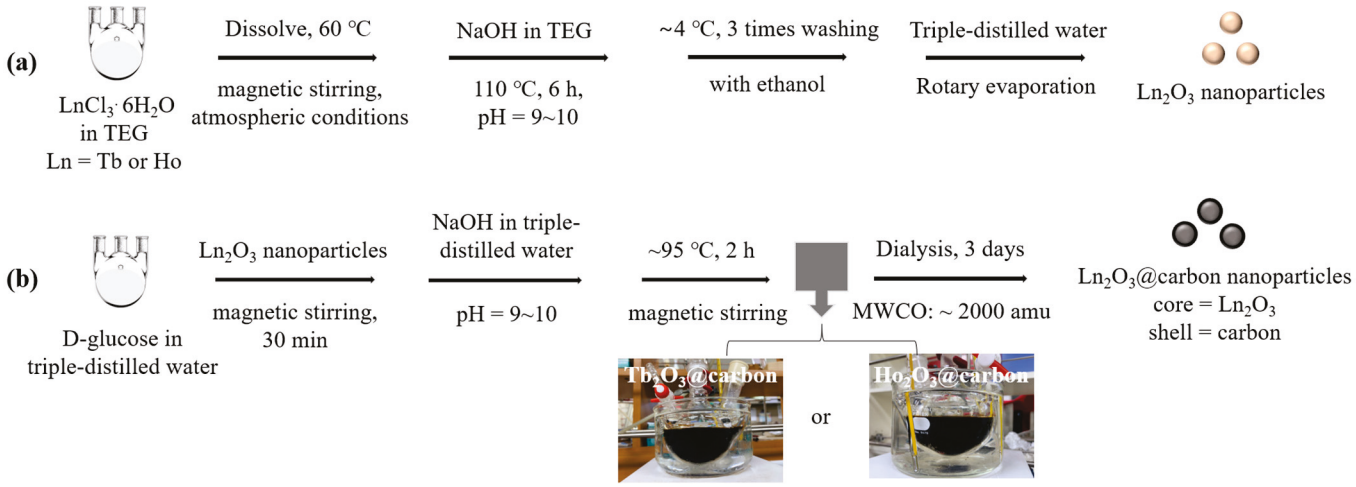

Figure 12. Synthesis of ultrasmall core–shell Ln_2O_3@carbon nanoparticles (Ln = Tb and Ho) in two steps: (**a**) synthesis of ultrasmall Ln_2O_3 nanoparticles in TEG and (**b**) carbon coating of these nanoparticles using D-glucose as carbon source in aqueous solution.

4.3. Characterization Experiments

HRTEM (Titan G2 ChemiSTEM CS Probe, FEI, Hillsboro, OR, USA) was used to measure the d values of the ultrasmall core–shell Ln_2O_3@carbon nanoparticles (Ln = Tb and Ho) at a 200kV acceleration voltage. The Ln concentration in an aqueous nanoparticle suspension sample was measured using inductively coupled plasma-atomic emission spectrometry (ICP-AES, Optima 7300DV& Avio500, Perkin Elmer, Waltham, MA, USA). A multi-purpose XRD spectrometer (X'PERT PRO MRD, Philips, The Netherlands) with unfiltered CuKα radiation (λ = 0.154184 Å) was used to determine the crystal structure of the power samples before and after TGA. A DLS particle size analyzer (Zetasizer Nano ZS, Malvern, UK) was used to measure the hydrodynamic diameter (a) and zeta potential values of the ultrasmall core–shell Ln_2O_3@carbon nanoparticles dispersed in an aqueous solution. An FT-IR absorption spectrometer (Galaxy 7020A, Mattson Instruments, Inc., Madison, WI, USA) was used to analyze the carbon coating on the nanoparticle surfaces by recording the corresponding spectra using KBr pellets of powder samples. To estimate the carbon coating amount on the nanoparticle surface, an SDT-Q600 analyzer (TA Instruments, New Castle, DE, USA) was used to record the TGA curves of powder samples between room temperature and 900 °C under air flow. EA (Flash 2000, ThermoFisher, Waltham, MA, USA) was used to analyze the surface composition (C/H/O) and coating amount

using powder samples. A Raman spectrometer (InVia Reflex, Renishaw, West Dundee, IL, USA) was used to record Raman spectra of the carbon coatings using power samples. Finally, vibrating sample magnetometry (VSM, 7407-S, LakeShore, Westerville, OH, USA) was used to measure the magnetic properties of the nanoparticles using powder samples at room temperature.

4.4. In Vitro Cellular Cytotoxicity Assay

The in vitro cellular cytotoxicity of the aqueous nanoparticle suspension samples was assessed using a Luminescent Cell Viability Assay (CellTiter-Glo, Promega, Madison, WI, USA) and a luminometer (Victor 3, Perkin Elmer, Waltham, MA, USA) to quantify the adenosine triphosphate (ATP) levels in live cells. DU145 and NCTC1469 cells were seeded onto a 24-well cell culture plate, followed by incubation for 24 h (5×10^4 cell density, 500 μL cells per well, 5% CO_2, and 37 °C). Each nanoparticle suspension sample (2 μL), prepared at various concentrations (10, 50, 100, 200, and 500 μM Tb or Ho) by dilution of the original concentrated suspension with a sterile phosphate-buffered saline (PBS) solution, was dropped onto the cells, followed by incubation for 48 h. After three cell viability tests, the obtained values were normalized to those of the control (i.e., untreated) cells.

4.5. Measurements of Relaxometric Properties

The T_1 and T_2 water proton spin relaxation times, along with R_1 and R_2 map images, were measured with a 3 T MRI scanner (Signa Advantage 3 T, GE Medical System, Chicago, IL, USA) equipped with a knee coil at 22 °C, using a series of nanoparticle suspension samples (1.0, 0.5, 0.25, 0.125, 0.0625, and 0.0 mM Tb or Ho) prepared by dilution of the original concentrated samples with triple-distilled water. The r_1 and r_2 values were estimated from the slopes of $1/T_1$ and $1/T_2$ plots, respectively, versus the Tb or Ho concentration. The T_1 relaxation times were determined using an inversion recovery method. The Carr–Purcell–Meiboom–Gill pulse sequence for multiple spin-echo measurements was used to obtain the T_2 relaxation times. Typical imaging parameters for T_1 (T_2) relaxation time measurements were as follows: slice thickness = 5 (5) mm, repetition time = 2000 (2000) ms, echo time = 18 (15, 50, 45, . . ., 480) ms, number of averaging = 1 (1), echo train length = 17 (1), flip angle = 120 (180) degree, matrix size = 320 × 192 (320 × 192), and field of view = 180 × 108 (180 × 108).

5. Conclusions

In this study, ultrasmall core–shell Ln_2O_3@carbon nanoparticles (Ln = Tb and Ho) were synthesized for the first time and their physicochemical properties, including in vitro cellular cytotoxicities and water proton spin relaxivities, were characterized as follows.

(1) The ultrasmall core–shell Ln_2O_3@carbon nanoparticles (Ln = Tb and Ho) showed nearly monodisperse size distributions (d_{avg} = ~3 nm), along with good colloidal stability and low cellular cytotoxicity.
(2) The ultrasmall core–shell Ln_2O_3@carbon nanoparticles (Ln = Tb and Ho) also exhibited negligible r_1 (i.e., 0.086 and 0.093 $s^{-1}mM^{-1}$) and appreciable r_2 (i.e., 3.446 and 3.677 $s^{-1}mM^{-1}$) values for Ln = Tb and Ho, respectively, demonstrating their potential to serve as T_2 MRI contrast agents, particularly at high applied fields.
(3) The carbon-coating shell exhibited photoluminescence at 460 nm, suitable for application in fluorescent imaging probes. Therefore, the present nanoparticles have dual imaging properties, making them suitable for T_2 MRI and fluorescent imaging applications, highlighting their novelty.

Author Contributions: Conceptualization, H.Y., T.T. and S.L.; methodology, H.Y., T.T. and S.L.; formal analysis, H.Y., S.L., T.T., Y.L., D.Z., E.M. and X.C.; investigation, H.Y., A.B., K.S.C. and J.K.; writing—original draft preparation, H.Y.; writing—review and editing, Y.C. and G.H.L.; funding acquisition, J.K., Y.C. and G.H.L. All authors have read and agreed to the published version of the manuscript.

Funding: This research was funded by the Basic Science Research Program of the National Research Foundation (NRF) funded by the Korea government (Ministry of Science, and Information and Communications Technology: MSIT) (Basic Research Laboratory, No. RS-2024-00406209) and NRF funded by the Ministry of Education (Post-Doc. Growth Type Cooperational Research, No. RS-2024-00459895).

Institutional Review Board Statement: Not applicable.

Informed Consent Statement: Not applicable.

Data Availability Statement: The original contributions presented in this study are included in the article. Further inquiries can be directed to the corresponding authors.

Conflicts of Interest: The authors declare no conflicts of interest.

References

1. Kazi, R.N.A.; Hasani, I.W.; Khafaga, D.S.; Kobba, S.; Farhan, M.; Aatif, M.; Muteeb, G.; Fahim, Y.A. Nanomedicine: The Effective Role of Nanomaterials in Healthcare from Diagnosis to Therapy. *Pharmaceutics* **2025**, *17*, 987. [CrossRef] [PubMed]
2. Chohan, D.P.; Dey, B.; Tarkunde, A.; Vyas, V.; Sarkar, S.D.; Sundara, B.K. Advancing Autonomous Nanomedicine: Bridging the Gap from Concept to Potential Clinical Studies. *J. Cluster Sci.* **2024**, *35*, 2607–2635. [CrossRef]
3. Liu, Q.; Zou, J.; Chen, Z.; He, W.; Wu, W. Current research trends of nanomedicines. *Acta Pharm. Sin. B* **2023**, *13*, 4391–4416. [CrossRef]
4. Caravan, P.; Ellison, J.J.; McMurry, T.J.; Lauffer, R.B. Gadolinium(III) Chelates as MRI Contrast Agents: Structure, Dynamics, and Applications. *Chem. Rev.* **1999**, *99*, 2293–2352. [CrossRef]
5. Blomqvist, L.; Nordberg, G.F.; Nurchi, V.M.; Aaseth, J.O. Gadolinium in Medical Imaging—Usefulness, Toxic Reactions and Possible Countermeasures—A Review. *Biomolecules* **2022**, *12*, 742. [CrossRef]
6. Costelloe, C.M.; Amini, B.; Madewell, J.E. Risks and Benefits of Gadolinium-Based Contrast-Enhanced MRI. *Semin Ultrasound CT MR* **2020**, *41*, 170–182. [CrossRef]
7. Yu, X.; Zhang, Q.; Wang, L.; Zhang, Y.; Zhu, L. Engineered nanoparticles for imaging and targeted drug delivery in hepatocellular carcinoma. *Exp. Hematol. Oncol.* **2025**, *14*, 62. [CrossRef]
8. Tegafaw, T.; Liu, S.; Ahmad, M.Y.; Saidi, A.K.A.A.; Zhao, D.; Liu, Y.; Nam, S.-W.; Chang, Y.; Lee, G.H. Magnetic Nanoparticle-Based High-Performance Positive and Negative Magnetic Resonance Imaging Contrast Agents. *Pharmaceutics* **2023**, *15*, 1745. [CrossRef]
9. MacDonald, D.; van Veggel, F.C.J.M.; Tomanek, B.; Blasiak, B. Contrast Enhancement in MRI Using Combined Double Action Contrast Agents and Image Post-Processing in the Breast Cancer Model. *Materials* **2023**, *16*, 3096. [CrossRef]
10. Wahsner, J.; Gale, E.M.; Rodríguez-Rodríguez, A.; Caravan, P. Chemistry of MRI Contrast Agents: Current Challenges and New Frontiers. *Chem. Rev.* **2019**, *119*, 957–1057. [CrossRef] [PubMed]
11. Brune, N.; Mues, B.; Buhl, E.M.; Hintzen, K.-W.; Jockenhoevel, S.; Cornelissen, C.G.; Slabu, I.; Thiebes, A.L. Dual Labeling of Primary Cells with Fluorescent Gadolinium Oxide Nanoparticles. *Nanomaterials* **2023**, *13*, 1869. [CrossRef]
12. Yue, H.; Park, J.A.; Ho, S.L.; Ahmad, M.Y.; Cha, H.; Liu, S.; Tegafaw, T.; Marasini, S.; Ghazanfari, A.; Kim, S.; et al. Class of Efficient T_2 Magnetic Resonance Imaging Contrast Agent: Carbon-Coated Paramagnetic Dysprosium Oxide Nanoparticles. *Pharmaceuticals* **2020**, *13*, 312. [CrossRef] [PubMed]
13. Cabrera-García, A.; Vidal-Moya, A.; Bernabeu, A.; Pacheco-Torres, J.; Checa-Chavarria, E.; Fernández, E.; Botella, P. Gd-Si Oxide Nanoparticles as Contrast Agents in Magnetic Resonance Imaging. *Nanomaterials* **2016**, *6*, 109. [CrossRef] [PubMed]
14. Ortega-Berlanga, B.; Betancourt-Mendiola, L.; del Angel-Olarte, C.; Hernández-Adame, L.; Rosales-Mendoza, S.; Palestino, G. An Overview of Gadolinium-Based Oxide and Oxysulfide Particles: Synthesis, Properties, and Biomedical Applications. *Crystals* **2021**, *11*, 1094. [CrossRef]
15. Atabaev, T.S.; Shin, Y.C.; Song, S.-J.; Han, D.-W.; Hong, N.H. Toxicity and T_2-Weighted Magnetic Resonance Imaging Potentials of Holmium Oxide Nanoparticles. *Nanomaterials* **2017**, *7*, 216. [CrossRef]
16. Garifo, S.; Vangijzegem, T.; Stanicki, D.; Laurent, S. A Review on the Design of Carbon-Based Nanomaterials as MRI Contrast Agents. *Molecules* **2024**, *29*, 1639. [CrossRef]

17. Geraldes, C.F.G.C. Rational Design of Magnetic Nanoparticles as T_1–T_2 Dual-Mode MRI Contrast Agents. *Molecules* **2024**, *29*, 1352. [CrossRef] [PubMed]
18. Fernández-Barahona, I.; Muñoz-Hernando, M.; Ruiz-Cabello, J.; Herranz, F.; Pellico, J. Iron Oxide Nanoparticles: An Alternative for Positive Contrast in Magnetic Resonance Imaging. *Inorganics* **2020**, *8*, 28. [CrossRef]
19. Aboushoushah, S.F.O. Iron oxide nanoparticles enhancing magnetic resonance imaging: A review of the latest advancements. *J. Sci. Adv. Mater. Devices* **2025**, *10*, 100875. [CrossRef]
20. Vakili-Ghartavol, R.; Momtazi-Borojeni, A.A.; VakiliGhartavol, Z.; VakiliGhartavol, H.T.; Jaafari, M.R.; Jaafari, S.; Bidgoli, S.A. Toxicity assessment of superparamagnetic iron oxide nanoparticles in different tissues. *Artif. Cells Nanomed. Biotechnol.* **2020**, *48*, 443–451. [CrossRef]
21. Wei, H.; Hu, Y.; Wang, J.; Gao, X.; Qian, X.; Tang, M. Superparamagnetic Iron Oxide Nanoparticles: Cytotoxicity, Metabolism, and Cellular Behavior in Biomedicine Applications. *Int. J. Nanomed.* **2021**, *16*, 6097–6113. [CrossRef]
22. Jarockyte, G.; Daugelaite, E.; Stasys, M.; Statkute, U.; Poderys, V.; Tseng, T.-C.; Hsu, S.-H.; Karabanovas, V.; Rotomskis, R. Accumulation and Toxicity of Superparamagnetic Iron Oxide Nanoparticles in Cells and Experimental Animals. *Int. J. Mol. Sci.* **2016**, *17*, 1193. [CrossRef] [PubMed]
23. Li, X.; Sun, Y.; Ma, L.; Liu, G.; Wang, Z. The Renal Clearable Magnetic Resonance Imaging Contrast Agents: State of the Art and Recent Advances. *Molecules* **2020**, *25*, 5072. [CrossRef]
24. Yin, R.; Zhang, X.; Ge, J.; Wen, L.; Chen, L.; Zeng, J.; Li, Z.; Gao, M. Recent Advances in Renal Clearable Inorganic Nanoparticles for Cancer Diagnosis. *Part. Part. Syst. Charact.* **2021**, *38*, 2000270. [CrossRef]
25. Longmire, M.; Choyke, P.L.; Kobayashi, H. Clearance Properties of Nano-sized Particles and Molecules as Imaging Agents: Considerations and Caveats. *Nanomedicine* **2008**, *3*, 703–717. [CrossRef]
26. Cotton, F.A.; Wilkinson, G. *Advanced Inorganic Chemistry*, 4th ed.; A Wiley-Interscience Publication: New York, NY, USA, 1980; p. 984.
27. Liu, S.; Yue, H.; Ho, S.L.; Kim, S.; Park, J.A.; Tegafaw, T.; Ahmad, M.Y.; Kim, S.; Saidi, A.K.A.A.; Zhao, D.; et al. Polyethylenimine-Coated Ultrasmall Holmium Oxide Nanoparticles: Synthesis, Characterization, Cytotoxicities, and Water Proton Spin Relaxivities. *Nanomaterials* **2022**, *12*, 1588. [CrossRef] [PubMed]
28. Lauffer, R.B. Paramagnetic Metal Complexes as Water Proton Relaxation Agents for NMR Imaging: Theory and Design. *Chem. Rev.* **1907**, *87*, 901–927. [CrossRef]
29. Marasini, S.; Yue, H.; Ho, S.L.; Park, J.A.; Kim, S.; Jung, K.-H.; Cha, H.; Liu, S.; Tegafaw, T.; Ahmad, M.Y.; et al. Synthesis, Characterizations, and 9.4 Tesla T_2 MR Images of Polyacrylic Acid-Coated Terbium(III) and Holmium(III) Oxide Nanoparticles. *Nanomaterials* **2021**, *11*, 1355. [CrossRef]
30. Miao, X.; Ho, S.L.; Tegafaw, T.; Cha, H.; Chang, Y.; Oh, I.T.; Yaseen, A.M.; Marasini, S.; Ghazanfari, A.; Yue, H.; et al. Stable and Non-Toxic Ultrasmall Gadolinium Oxide Nanoparticle Colloids (Coating Material = Polyacrylic Acid) as High-Performance T_1 Magnetic Resonance Imaging Contrast Agents. *RSC Adv.* **2018**, *8*, 3189–3197. [CrossRef]
31. Fang, J.; Chandrasekharan, P.; Liu, X.-L.; Yang, Y.; Lv, Y.-B.; Yang, C.-T.; Ding, J. Manipulating the surface coating of ultra-small Gd_2O_3 nanoparticles for improved T_1-weighted MR imaging. *Biomaterials* **2014**, *35*, 1636–1642. [CrossRef]
32. Zhang, D.; Zhang, J.; Bian, X.; Zhang, P.; Wu, W.; Zuo, X. Iron Oxide Nanoparticle-Based T_1 Contrast Agents for Magnetic Resonance Imaging: A Review. *Nanomaterials* **2025**, *15*, 33. [CrossRef] [PubMed]
33. Marasini, S.; Yue, H.; Ho, S.L.; Jung, K.-H.; Park, J.A.; Cha, H.; Ghazanfari, A.; Ahmad, M.Y.; Liu, S.; Jang, Y.J.; et al. D-Glucuronic Acid-Coated Ultrasmall Paramagnetic Ln_2O_3 (Ln = Tb, Dy, and Ho) Nanoparticles: Magnetic Properties, Water Proton Relaxivities, and Fluorescence Properties. *Eur. J. Inorg. Chem.* **2019**, *34*, 3832–3839. [CrossRef]
34. Holmannova, D.; Borsky, P.; Svadlakova, T.; Borska, L.; Fiala, Z. Carbon Nanoparticles and Their Biomedical Applications. *Appl. Sci.* **2022**, *12*, 7865. [CrossRef]
35. Rajakumar, G.; Zhang, X.-H.; Gomathi, T.; Wang, S.-F.; Ansari, M.A.; Mydhili, G.; Nirmala, G.; Alzohairy, M.A.; Chung, I.-M. Current Use of Carbon-Based Materials for Biomedical Applications—A Prospective and Review. *Processes* **2020**, *8*, 355. [CrossRef]
36. Simon, J.; Flahaut, E.; Golzio, M. Overview of Carbon Nanotubes for Biomedical Applications. *Materials* **2019**, *12*, 624. [CrossRef]
37. Malode, S.J.; Pandiaraj, S.; Alodhayb, A.; Shetti, N.P. Carbon Nanomaterials for Biomedical Applications: Progress and Outlook. *ACS Appl. Bio Mater.* **2024**, *7*, 752–777. [CrossRef]
38. Zhang, Y.; Xiao, J.; Zhuo, P.; Yin, H.; Fan, Y.; Liu, X.; Chen, Z. Carbon Dots Exhibiting Concentration-Dependent Full-Visible Spectrum Emission for Light-Emitting Diode Applications. *ACS Appl. Mater. Interfaces* **2019**, *11*, 46054–46061. [CrossRef]
39. Mandal, T.; Mishra, S.R.; Singh, V. Comprehensive advances in the synthesis, fluorescence mechanism and multifunctional applications of red-emitting carbon nanomaterials. *Nanoscale Adv.* **2023**, *5*, 5717–5765. [CrossRef] [PubMed]
40. Yue, H.; Marasini, S.; Ahmad, M.Y.; Ho, S.L.; Cha, H.; Liu, S.; Jang, Y.J.; Tegafaw, T.; Ghazanfari, A.; Miao, X.; et al. Carbon-coated ultrasmall gadolinium oxide (Gd_2O_3@C) nanoparticles: Application to magnetic resonance imaging and fluorescence properties. *Coll. Surf. A* **2020**, *586*, 124261. [CrossRef]

41. Schubert, J.; Chanana, M. Coating Matters: Review on Colloidal Stability of Nanoparticles with Biocompatible Coatings in Biological Media, Living Cells and Organisms. *Curr. Med. Chem.* **2018**, *25*, 4553–4586. [CrossRef]
42. Tang, Q.; Shen, J.; Zhou, W.; Zhang, W.; Yu, W.; Qian, Y. Preparation, characterization and optical properties of terbium oxide nanotubes. *J. Mater. Chem.* **2003**, *13*, 3103–3106. [CrossRef]
43. Boutahar, A.; Moubah, R.; Hlil, E.K.; Lassri, H.; Lorenzo, E. Large reversible magnetocaloric effect in antiferromagnetic Ho_2O_3 powders. *Sci. Rep.* **2017**, *7*, 13904. [CrossRef]
44. Kaufman, J.H.; Metin, S.; Sapersrein, D.D. Symmetry breaking in nitrogen-doped amorphous carbon: Infrared observation of the Raman-active 6 and D bands. *Phys. Rev. B* **1989**, *39*, 13053–13060. [CrossRef] [PubMed]
45. Malard, L.M.; Pimenta, M.A.; Dresselhaus, G.; Dresselhaus, M.S. Raman spectroscopy in graphene. *Phys. Rep.* **2009**, *473*, 51–87. [CrossRef]
46. Bokobza, L.; Bruneel, J.-L.; Couzi, M. Raman Spectra of Carbon-Based Materials (from Graphite to Carbon Black) and of Some Silicone Composites. *C J. Carbon Res.* **2015**, *1*, 77–94. [CrossRef]
47. Tegafaw, T.; Oh, I.T.; Cha, H.; Yue, H.; Miao, X.; Ho, S.L.; Ahmad, M.Y.; Marasini, S.; Ghazanfari, A.; Kim, H.-K.; et al. Facile synthesis of stable colloidal suspension of amorphous carbon nanoparticles in aqueous medium and their characterization. *J. Phys. Chem. Solids* **2018**, *120*, 96–103. [CrossRef]
48. Greenwood, N.N.; Earnshaw, A. *Chemistry of the Elements*; Butterworth-Heinemann: New York, NY, USA, 1997; p. 1243.
49. MacChesney, J.B.; Williams, H.J.; Sherwood, R.C.; Potter, J.F. Magnetic Properties of the Terbium Oxides at Temperatures between 1.4° and 300° K. *J. Appl. Phys.* **1966**, *37*, 1435. [CrossRef]
50. Shinde, K.P.; Nan, W.Z.; Tien, M.V.; Lin, H.; Park, H.-R.; Yu, S.-C.; Chung, K.C. Magnetocaloric effect in rare earth Ho_2O_3 nanoparticles at cryogenic temperature. *J. Magn. Magn. Mater.* **2020**, *500*, 166391. [CrossRef]
51. Lal, H.B.; Pratap, V.; Kumar, A. Magnetic susceptibility of heavy rare-earth sesquioxides. *Pramana* **1978**, *10*, 409–412. [CrossRef]
52. Xu, W.; Kattel, K.; Park, J.Y.; Chang, Y.; Kim, T.J.; Lee, G.H. Paramagnetic nanoparticle T_1 and T_2 MRI contrast agents. *Phys. Chem. Chem. Phys.* **2012**, *14*, 12687–12700. [CrossRef]
53. Roch, A.; Gossuin, Y.; Muller, R.N.; Gillis, P. Superparamagnetic colloid suspensions: Water magnetic relaxation and clustering. *J. Magn. Magn. Mater.* **2005**, *293*, 532–539. [CrossRef]
54. Roch, A.; Muller, R.N.; Gillis, P. Theory of proton relaxation induced by superparamagnetic particles. *J. Chem. Phys.* **1999**, *110*, 5403–5411. [CrossRef]
55. Yang, S.-T.; Wang, X.; Wang, H.; Lu, F.; Luo, P.G.; Cao, L.; Meziani, M.J.; Liu, J.-H.; Liu, Y.; Chen, M.; et al. Carbon Dots as Nontoxic and High-Performance Fluorescence Imaging Agents. *J. Phys. Chem. C* **2009**, *113*, 18110–18114. [CrossRef] [PubMed]
56. Zhang, Y.-Y.; Wu, M.; Wang, Y.-Q.; He, X.-W.; Li, W.-Y.; Feng, X.-Z. A new hydrothermal refluxing route to strong fluorescent carbon dots and its application as fluorescent imaging agent. *Talanta* **2013**, *117*, 196–202. [CrossRef] [PubMed]
57. Ou, S.-F.; Zheng, Y.-Y.; Lee, S.-J.; Chen, S.-T.; Wu, C.-H.; Hsieh, C.-T.; Juang, R.-S.; Peng, P.-Z.; Hsueh, Y.-H. N-Doped Carbon Quantum Dots as Fluorescent Bioimaging Agents. *Crystals* **2021**, *11*, 789. [CrossRef]
58. Din, R.N.; Venu, A.C.; Rudszuck, T.; Vallet, A.; Favier, A.; Powell, A.K.; Guthausen, G.; Ibrahim, M.; Kramer, S. Longitudinal and Transverse 1H Nuclear Magnetic Resonance Relaxivities of Lanthanide Ions in Aqueous Solution up to 1.4 GHz/33 T. *Molecules* **2024**, *29*, 4956. [CrossRef]

Disclaimer/Publisher's Note: The statements, opinions and data contained in all publications are solely those of the individual author(s) and contributor(s) and not of MDPI and/or the editor(s). MDPI and/or the editor(s) disclaim responsibility for any injury to people or property resulting from any ideas, methods, instructions or products referred to in the content.

molecules

MDPI

Article

Antimicrobial Functionalized Mesoporous Silica FDU-12 Loaded with Bacitracin

Dan Adrian Vasile [1,2,3], Ludmila Motelica [2,3,4], Luiza-Andreea Mîr [1,2,3,5], Gabriel Vasilievici [5], Oana-Maria Memecică [6], Ovidiu Cristian Oprea [2,3,7,8], Adrian-Vasile Surdu [1,2,3,9], Roxana Doina Trucă [2,3], Cristina Chircov [1,2,3], Bogdan tefan Vasile [2,3,4], Zeno Dorian Ghizdavet [1,2,3], Denisa Ficai [1,2,3,7,8], Ana-Maria Albu [6], Radu Pericleanu [10], Andreea tefania Dumbravă [10], Mara-Mădălina Mihai [11,12], Irina Gheorghe-Barbu [10,12] and Anton Ficai [1,2,3,8,*]

1 Department of Science and Engineering of Oxide Materials and Nanomaterials, Faculty of Chemical Engineering and Biotechnologies, National University of Science and Technology POLITEHNICA Bucharest, Gh. Polizu 1-7, 011061 Bucharest, Romania; vasile.surdu@unitbv.ro (A.-V.S.); cristina.chircov@upb.ro (C.C.)
2 National Research Center for Food Safety, National University of Science and Technology POLITEHNICA Bucharest, Splaiul Independentei 313, 060042 Bucharest, Romania; ludmila.motelica@upb.ro (L.M.); ovidiu73@yahoo.com (O.C.O.)
3 National Center for Micro and Nanomaterials, National University of Science and Technology POLITEHNICA Bucharest, Splaiul Independentei 313, 060042 Bucharest, Romania
4 Advanced Research Center for Innovative Materials, Products and Processes, National University of Science and Technology POLITEHNICA Bucharest, 313 Splaiul Independentei, 060042 Bucharest, Romania
5 National Institute for Research & Development in Chemistry and Petrochemistry–ICECHIM, Spl. Independentei 202, 060021 Bucharest, Romania; gvasilievici@icechim.ro
6 Department of Bioresources and Polymer Sciences, Faculty of Chemical Engineering and Biotechnologies, National University of Science and Technology POLITEHNICA Bucharest, Gh. Polizu 1-7, 011061 Bucharest, Romania
7 Department of Inorganic Chemistry, Physical Chemistry and Electrochemistry, Faculty of Chemical Engineering and Biotechnologies, National University of Science and Technology POLITEHNICA Bucharest, Gh. Polizu 1-7, 011061 Bucharest, Romania
8 Academy of Romanian Scientists, Ilfov Street 3, 050044 Bucharest, Romania
9 Department of Materials Science, Faculty of Materials Science and Engineering, Transilvania University of Brasov, 29 Eroilor Blvd., 500036 Brasov, Romania
10 Department of Botany and Microbiology, Faculty of Biology, University of Bucharest, Intr. Portocalelor No. 1–3, 060101 Bucharest, Romania
11 Department of Oncologic Dermatology, Elias Emergency University Hospital, Carol Davila University of Medicine and Pharmacy, 020021 Bucharest, Romania
12 The Research Institute of the University of Bucharest (ICUB), B.P Hasdeu No. 7, 050095 Bucharest, Romania
* Correspondence: anton.ficai@upb.ro

Abstract

The threats leading to the extinction of humanity accelerate the evolution and development of materials that are capable of providing conditions for preserving health and, implicitly, life. In our work, we developed drug delivery systems based on mesoporous silica which can deliver an antibiotic, bacitracin, in a more controlled manner. The synthesis of the FDU-12 was performed through a sol–gel method and alternatively functionalized with -NH_2 groups or with poly(N-acryloylmorpholine) chains. The loading of bacitracin was performed using the vacuum-assisted method we successfully used to load these mesoporous materials preferentially within the pores as proved by the TGA-DSC results. The release was performed in two types of simulated body fluid (SBF) and this process was evaluated with chromatographic method using UV detection. The obtained data were fitted in three mathematical models of kinetic drug release (Weibull model, Korsmeyer–Peppas model, and nonlinear regression). The antimicrobial evaluation demonstrated that bacitracin-loaded FDU-12 formulations exhibited strong activity

against both reference and clinical *Staphylococcus* strains. At sub-inhibitory concentrations, all formulations significantly reduced microbial adherence and biofilm formation, although certain strain-dependent stimulatory effects were observed. Furthermore, exposure to sub-MIC levels modulated the production of soluble virulence factors (hemolysins, lipase, and amylase), in a formulation- and strain-dependent manner, underscoring the ability of surface-functionalized FDU-12 carriers to influence bacterial pathogenicity while enhancing antimicrobial efficacy.

Keywords: mesoporous silica; poly(N-acryloylmorpholine); bacitracin; drug delivery; vacuum-assisted loading; surface functionalization; skin infection; kinetic model; antimicrobial; anti-biofilm virulence factors modulation; *Staphylococcus* spp.

1. Introduction

Antimicrobial resistance (AMR) is a global challenge that threatens public health and food security, while also being a cause of the slowed progress towards the United Nations proposed sustainable development goals. Various factors, such as improper use of antimicrobial drugs or inadequate sanitation, can help increase the number of cases of AMR and spread this phenomenon [1]. In todays world, the number of deaths linked to antimicrobial resistance diseases is estimated at 700,000 per year, revealing a potential increase to 10 million in 2050 [2]. The sixth-highest cause for AMR-attributable deaths is represented by bacterial infections of the skin and of subcutaneous tissues [3].

The development and use of nanomaterial-based drug delivery systems can be a key advantage in this fight against microbes. This type of system allows, in addition to the targeted dosing of the drug, the long-term maintenance of an optimal therapeutic concentration in the area of the body affected by disease [4]. Since their discovery [5,6] and their first use as a drug delivery system [7], mesoporous silica micro/nanoparticles are not yet part of many drug formulations approved by authorities, despite their numerous characteristics such as biocompatibility, versatility for functionalization, or high drug-loading capacity [8,9]. There are many examples of mesoporous silica particles loaded with different antibiotics: vancomycin [10], tetracycline [11], cefepime [12], ampicillin [13], amoxicillin [14], aminoglycosides [15], and rifampicin [16].

Due to the presence of silanol groups on the surface, these materials can be functionalized, and this process can improve their properties or provide them with new ones, depending on the applications for which they are intended to be used. The surface of these materials can be functionalized with inorganic particles [17,18], different organic functional groups [19,20], or polymers [21,22], especially to help increase the loading capacity and to improve control of the release process, or they can be functionalized with DNA [23,24], polysaccharides [25], lipids [26–28], proteins [29,30], or antibodies [31,32], especially to increase their biocompatibility or to facilitate targeted drug delivery [33].

Among the many functionalization agents that can be used to modify the surface, N-acryloyl-morpholine (NAM) is a disubstituted acrylamide derivative, with an inherently hydrophilic nature and solubility in a wide variety of solvents, from aqueous to organic ones (e.g., chloroform, tetrahydrofuran, 1, 4-dioxane) [34], inducing some specific functionality.

The choice of NAM as a monomer for the modification of silica substrate by graft polymerization is justified, first in terms of its good biocompatibility and secondly by the antigenic effect of its polymers. The presence of pNAM grafts is expected to support and enhance both the biocompatibility and release of the drug loaded on this substrate [35].

https://doi.org/10.3390/molecules31020340

Since the pNAM sequence is generated directly on the silica support, on which free radical initiation centers were previously generated, the approached process is of type graft on the surface.

For generating graft initiation centers, a radical redox initiation using cerium sulfate (CS) was preferred, to the detriment of initiating the process with high energy or microwave radiation. This choice is justified by the limitations aimed at degrading the substrate, namely the energy cost. In addition, redox initiation, assuming ambient working temperatures, promotes the growth of polymers on the modified substrate, to the detriment of the development of independent polymerization in the reaction medium [36–40].

The mechanism by which Ce^{4+} ions generate free radicals (initiation centers) on various substrates that possess functional reactive groups (OH; NH_2) is not generalized. An accepted theory for OH group substrates is the formation of an initiator complex involving OH groups and the Ce^{4+} ion, following the transfer of complex electrons dissociating with the release of Ce^{3+} and the formation of a radical center at the atom adjacent to the OH group [41].

In this paper, we developed three systems based on a type of mesoporous silica with cage structure FDU-12 which were kept unfunctionalized or functionalized with aminopropyl groups or pNAM and loaded with bacitracin. The mesoporous materials with 3D-pore systems are better in terms of facilitating mass diffusion and transportation compared with materials with 1D channels [42], while the choice of FDU-12 was performed based on the larger and more tunable pore diameter, making it implicitly more suitable for loading high molecular compounds such as peptides and small proteins [43], and also considering the intention to develop tunable DDS with shutter-like behavior. Bacitracin is a polypeptidic antibiotic, and was discovered in 1945 during the treatment of a knee injury and isolated from *Bacillus licheniformis* [44]. The mechanism of action is through inhibition of the linear peptidoglycan chains, which are one of the main components of bacterial cell membranes [45]. Due to its nephrotoxicity [46], bacitracin is used often through topical administration, especially against Gram-positive bacteria such as *Staphylococcus aureus*, *Staphylococcus epidermidis*, and *Streptococcus pyogenes* [47–50]. The interactions between bacitracin and the substrate is particularly influenced due to the surface chemistry of the material as follows: the amino groups modify the surface charge, being positive at physiological pH values, and increase the hydrophilic character due to formation of hydrogen bonds [51,52], while the pNAM is known to increase colloidal stability and to reduce protein adhesion to the surface of the material, since it is highly biocompatible [53].

The study also aimed to evaluate the antimicrobial efficiency, anti-adherence activity, and effects on virulence factor expression of bacitracin and bacitracin-loaded mesoporous silica FDU-12 formulations (FDU-12, FDU-12–NH_2, and FDU-12pNAM) against both reference and clinical *Staphylococcus* strains. The objective was to elucidate how surface functionalization of the FDU-12 carrier and different bacitracin concentrations influence bacterial growth inhibition, biofilm formation, and the production of soluble virulence factors, thereby assessing the potential of these systems as advanced antimicrobial delivery systems. To ensure a comprehensive assessment of the antimicrobial performance of the bacitracin-loaded FDU-12 systems, both reference and clinical *Staphylococcus* strains were included. Reference strains of *S. aureus* and *S. epidermidis* serve as genetically stable, well-characterized models that allow reproducible measurement of baseline antimicrobial activity and facilitate comparison with previously published data. In contrast, clinical isolates typically exhibit substantially greater phenotypic and genotypic heterogeneity, including altered susceptibility patterns, heightened biofilm-forming ability, and adaptive regulatory shifts shaped by host-associated selective pressures and prior antibiotic exposure. Incorporating clinical *S. aureus* isolates therefore provides a more realistic and clini-

https://doi.org/10.3390/molecules31020340

cally relevant representation of the challenges posed by contemporary infections, particularly those involving persistent or device-associated biofilms. By evaluating antimicrobial activity across both reference strains and clinically adapted pathogens, the study strengthens the translational relevance of its findings. This integrated approach ensures that the antimicrobial potential of the FDU-12–based delivery systems is characterized under conditions that more accurately reflect real-world clinical scenarios.

2. Results and Discussion

2.1. The Determination of Grafting Degree

After performing the calculations, results were obtained as follows: the grafting degree was 32%, the global grafting yield was 7.8%, and the conversion to grafted polymer was 20%. Since the role of polymer grafts is exclusively to protect the antibiotic loaded on silica, the obtained values are satisfactory. The conversion of monomer to graft can also be interpreted as molarities, so one can estimate that the size of the grafts is about 2000 Da, corresponding to a GPn of about 14 NAM.

2.2. Zeta Potential Analysis

The zeta potential values of the discharged samples were as follows: for FDU-12, a value of—26.85 mV; for FDU-12-NH_2, a value of—2.73 mV; and for FDU-12-pNAM, a value of—16.53 mV. The change in potential value demonstrates a compositional change in surface area of FDU-12. There is a drastic reduction in the potential for FDU-12-NH_2 (24.12 mV) compared to the modified pNAM (10.32 mV) sample. These values are, on the one hand, the consequence of the chemical nature of the graft, but on the other hand, they also represent the degree of grafting, graft–graft interactions, and graft–substrate interactions, respectively. APTES compatibility with the silica substrate favors a higher load with aminopropyl sequences, which reduces the surface potential due to the cationic character of the propyl sequence. Thus, the material assembly will function as a proton absorber but, on the other hand, it will favor aggregation with blood sequences and activate the immune system [54–56].

A decrease of only 10 mV in potential at pNAM grafting demonstrates a mean grafting density (32%) with oligomeric sequences that do not interact with the substrate due to steric hindrance. Thus it can be said that these grafts function as sequestrants which control the respective absorption and desorption processes of the active substance. On the other hand, it shows good colloidal stability [57].

2.3. SEM Analysis

The morphology of FDU-12-pNAM is shown in the SEM images (Figure 1). The samples have particles between 1.8 μm and 4.2 μm with a mean diameter of 2.5 μm. After functionalization, the particle size is not modified considerably, and when compared with the pristine FDU-12, the sizes expressed in the literature are quite similar [58]. Instead, the shape of the particles became more irregular and more dispersed, probably due to electrostatic repulsion and steric effects [59,60]. The loading process does not increase significantly the particle size, confirming the fact that the majority of bacitracin is present in the mesopores framework and not on the surface of the support material.

2.4. TEM Analysis

Figure 2 highlights the TEM images of the FDU-12 sample. They reveal the highly porous particles with well-ordered and uniform pores. This type shows a structure with the highest packing density of perfect spheres. Also the formation of stacking faults can be observed in the mesopore framework [61].

https://doi.org/10.3390/molecules31020340

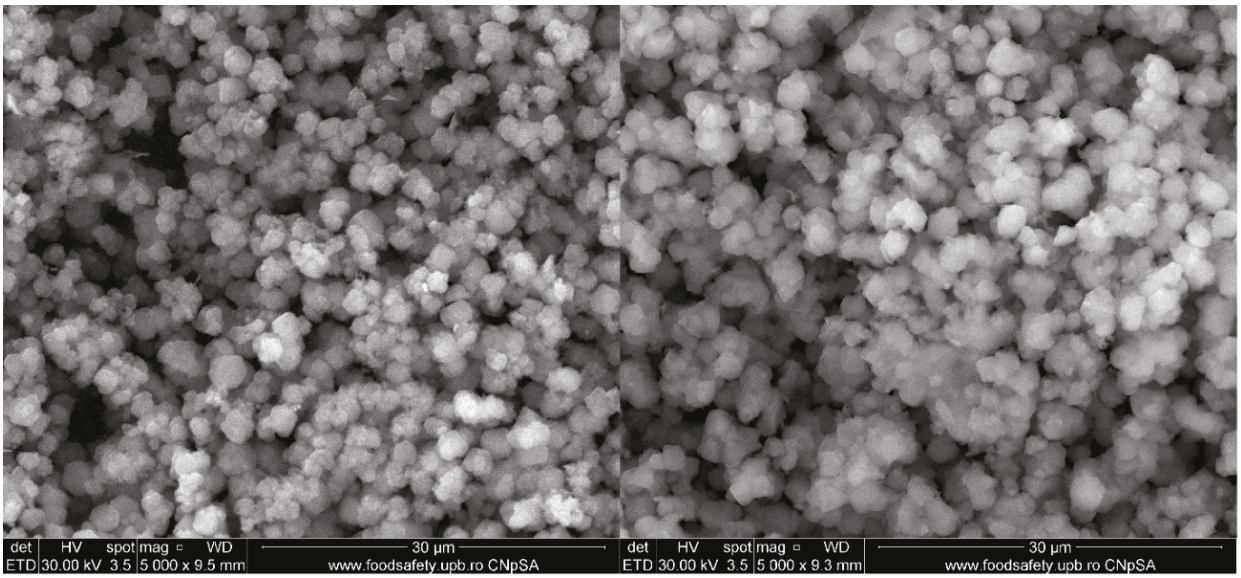

Figure 1. SEM images of FDU-12-pNAM (**left,** unloaded sample; **right,** the loaded one).

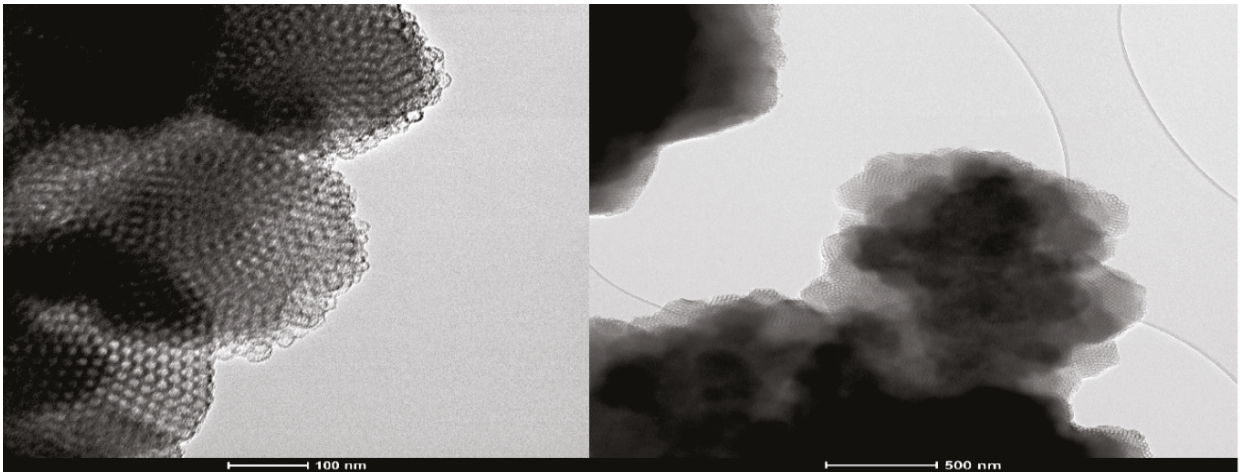

Figure 2. TEM images of FDU-12 sample.

2.5. N_2 Absorption/Desorption Analysis

The values of parameters such as surface area or pore volume have a major influence in the efficiency of a drug delivery system. A higher surface area is associated often with a higher loading drug capacity and a slower release, while a large pore size can lead to a faster release rate of the drug [62]. According to Figure 3a, all the samples present a type IV hysteresis loop that is specific for mesoporous materials [63]. Certainly, the loading of the mesoporous structures with bacitracin lead to a major modification of the absorption–desorption isotherms with N_2 and these hysteresis loops are not so visible because of the partial loading of the pores with bacitracin.

https://doi.org/10.3390/molecules31020340

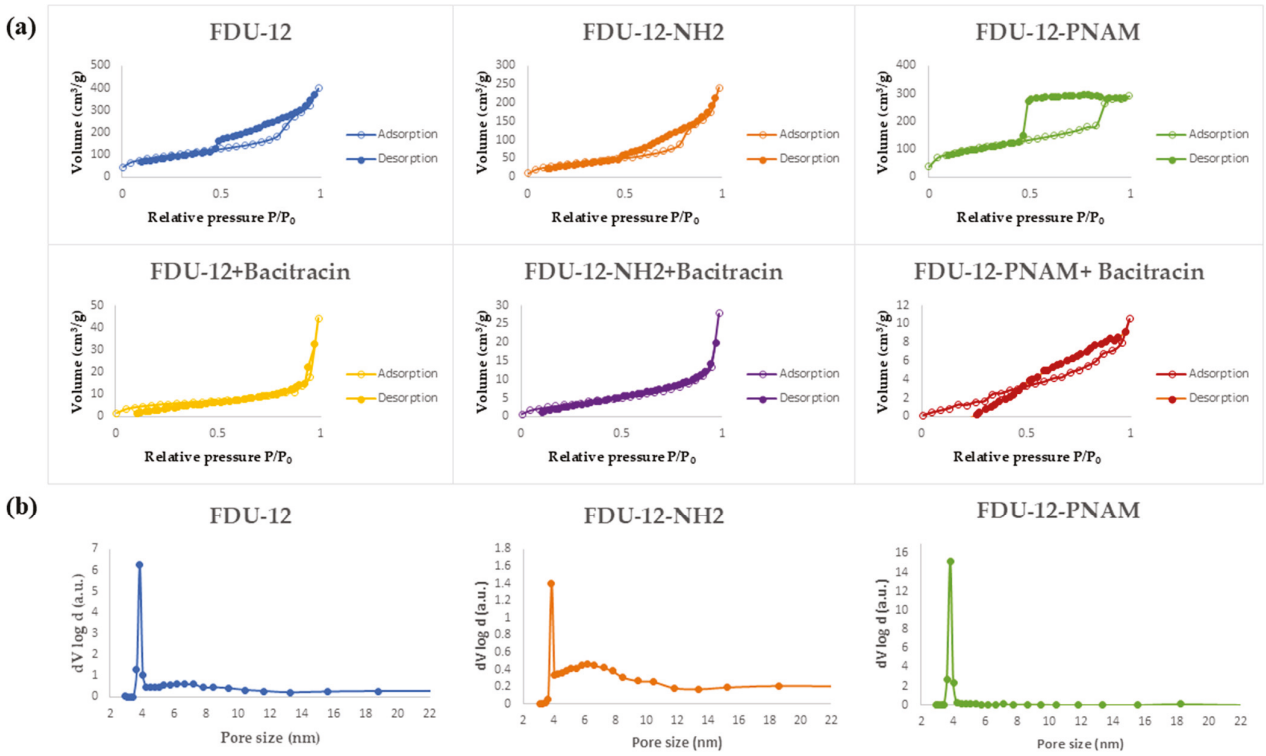

Figure 3. (**a**) N_2 adsorption/desorption isotherms of the loaded and unloaded samples and (**b**) the pore-size distributions based on BJH method.

The pore-size distributions obtained through the BJH method applied to the adsorption branch of the isotherms (Figure 3b) reveal, for all samples, a high peak at a value of ~4 nm, meaning that this pore size is representative of all three supports, which means that the modification is mainly occurring on the surface of the particles and not inside the pores.

Table 1 summarizes the surface area and pore volume determined from BET analysis. It can be seen that the aminopropyl-functionalization process with APTES led to a considerable decrease in the specific surface area, with the explanation being that the aminopropyl groups are not only attached on the surface of the material but also inside the pores, which is comparable with the process of functionalization with the pNAM chains, which are mainly on the surface of the material. For the loaded samples, these parameters have much lower values, highlighting the presence of bacitracin inside the pores.

Table 1. Textural characteristics of unloaded and loaded samples according to physisorption curves.

Sample	BET Surface Area (m^2/g)	Total Pore Volume (cm^3/g)
FDU-12	470.8	0.435
FDU-12 + Bacitracin	18.92	0.06829
FDU-12-NH_2	129.3	0.3725
FDU-12-NH_2 + Bacitracin	12.12	0.04312
FDU-12-pNAM	347.5	0.4499
FDU-12-pNAM + Bacitracin	7.13	0.01631

2.6. XRD Analysis

Figure 4 shows the SAXS pattern of the calcined sample FDU-12. The diffractogram reveals peaks assigned to (110) and (311) Miller indices. These peaks are correlated with the diffraction pattern of a face-centered cubic (fcc) structure, with a space group of Fm-3m. The broadening of peaks can be due to polydispersity, disorder, or crystal defects, which can also contribute to this phenomenon [64–66].

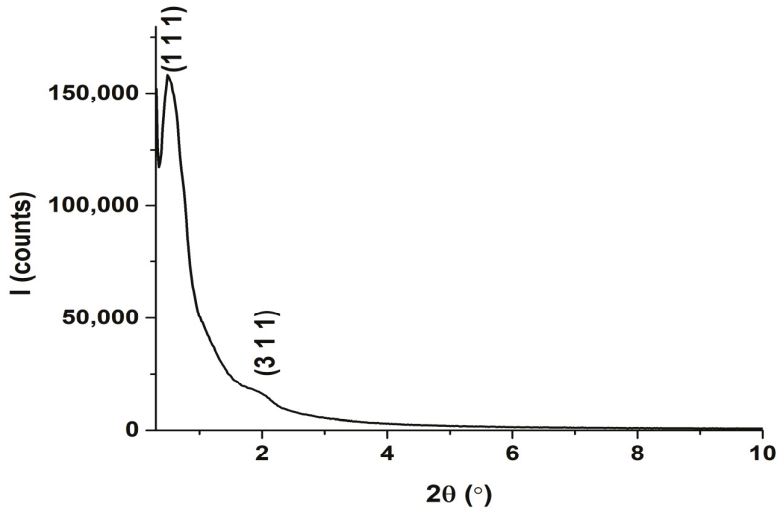

Figure 4. Small-angle diffractogram for FDU-12.

2.7. FT-IR Analysis

The FT-IR data (Figure 5) show specific mesoporous silica peaks for unloaded samples: the asymmetric stretching vibration of Si-O-Si are approximatively at 1060 cm^{-1} and from the same group the symmetric stretching vibrations are at 800 cm^{-1}. At 440 $cm^{-1,}$ the peak associated with the stretching vibration of the Si-O bond can be seen [67]. The functionalized unloaded samples present specific functional group peaks: for the aminopropyl-functionalized sample, the peak occurs around 3200 cm^{-1}, and the peak corresponding to $–NH_2$ stretching is present with low intensity due to the low degree of functionalization, while the polymer-functionalized sample at 1629 cm^{-1} represents the peak of the C=O stretching vibration of amide group. For the loaded samples the specific peaks belonging to bacitracin can be identified, if we overlap the spectra of pure bacitracin and the spectra of the loaded samples. Can be observed similar peaks confirming the presence of bacitracin, especially in the region 1380 cm^{-1}–1800 cm^{-1} (marked in the Figure 5 with a black circle). Also, outside this region, there is a peak at the 3300 cm^{-1} band resulting from the -NH/-OH stretching vibrations [68]. The specific peaks (Table 2) of the bacitracin are slightly shifted, proving that there are interactions developing between the support and the antibiotic.

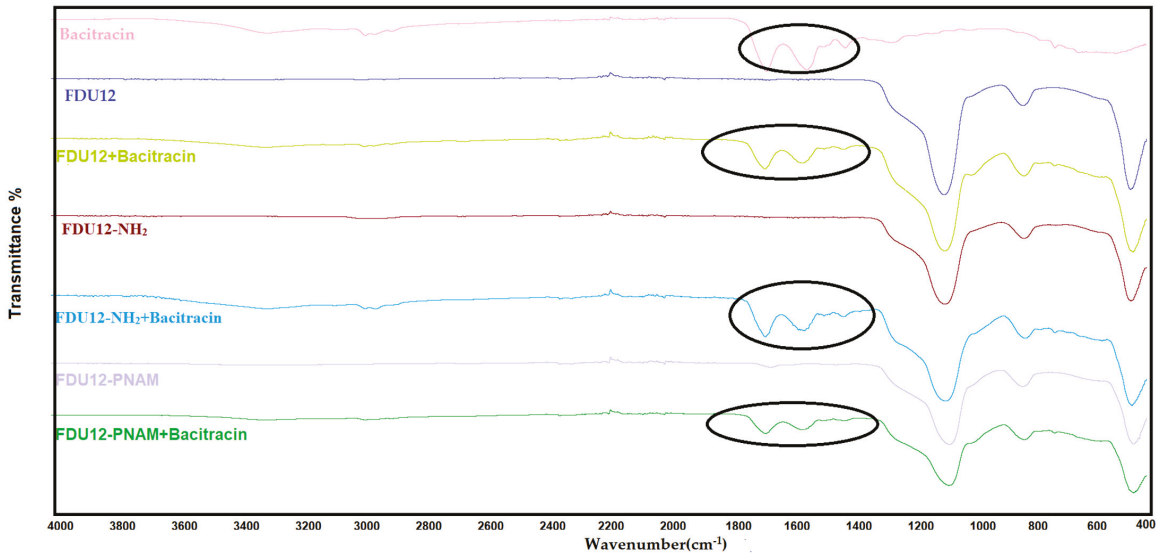

Figure 5. Infrared spectra of samples before and after loading of bacitracin (oval areas indicate the spectral regions that prove the presence of the bacitracin loaded into the mesoporous silica).

Table 2. Principal peaks of bacitracin.

Group	Bacitracin	FDU-12 + Bacitracin	FDU-12-NH_2 + Bacitracin	FDU-12-pNAM + Bacitracin
N–H stretching (amide A, peptide NH)	3279	3285	3276	3285
Aliphatic, aromatic -CH stretching	2960	2963	2961	2963
Amide I band (C=O stretching of peptide bond)	1644	1652	1647	1647
Amide II band (N–H bending + C–N stretching)	1512	1526	1522	1526
Symmetric COO^- stretching	1386	1394	1394	1388
C-S stretching	699	700	698	699

2.8. TG-DSC Analysis

The efficiency of functionalization processes and the efficiency of loading with bacitracin in materials can both be evaluated with the thermal analysis TGA-DSC. In the first case the blank is the unfunctionalized sample and in the second one it is the unloaded sample. As can be seen in Figure 6a, after the aminopropyl-functionalization process the mass loss of sample achieves an addition of 6.95% and after the grafting of polymer the mass loss is increased by 8.8%.

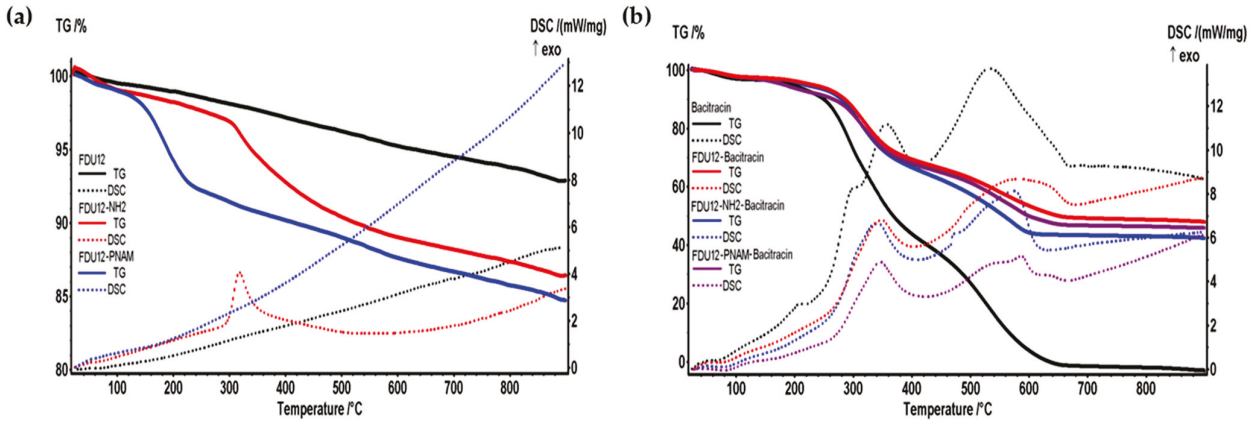

Figure 6. (**a**) TGA-DSC curves of unloaded samples (unfunctionalized FDU-12, the aminopropyl-functionalized one and the sample with the pNAM grafted). (**b**) The thermal analysis for the bacitracin and bacitracin-loaded samples.

For FDU-12 and FDU-12-NH_2 the mass loss recorded in the range RT-120 °C was low because it represents the amount of weakly bounded water, as well as physically adsorbed molecules from the surface and inside the pores [69]. After 120 °C the water bounded into the pores of silica is lost, together with condensation of -OH moieties and the process of densification of silica takes place. The pNAM organic part is degraded mostly at the temperature interval 120–250 °C, when a mass loss of 6.52% is recorded. The lack of a clear thermal effect indicates that the process is a mix of decomposition, fragmentation, and oxidation of the smaller molecules. In the interval 250–440 °C, the organic part that is introduced in the FDU-12–NH_2 functionalization process is oxidized, and the process is accompanied by an exothermic effect with maximum value at 318.1 °C (Figure 6a). The table below (Table 3) presents the principal data from the thermal analysis for unfunctionalized and functionalized FDU-12 samples.

https://doi.org/10.3390/molecules31020340

Table 3. Thermal behavior of simple and functionalized FDU-12.

Sample	Mass Loss (%)				Residual Mass (%@900 °C)	Estimated Load (%)
	RT-120 °C	120–250 °C	250–440 °C	440–900 °C		
FDU-12	0.63	0.87	1.76	3.90	92.89	-
FDU-12-NH_2	1.15	1.26	5.99	5.23	86.43	6.95
FDU-12-pNAM	1.26	6.52	2.48	5.00	84.72	8.80
FDU-12-Bacitracin	2.55	3.58	27.04	18.92	47.90	48.43
FDU-12-NH_2-Bacitracin	2.66	3.94	30.11	20.88	42.36	50.99
FDU-12-pNAM-Bacitracin	2.94	5.99	25.65	19.63	45.81	45.93
Bacitracin	3.33	6.74	51.87	41.19	0	-

Thermal analyses for the loaded samples are similar due to the dominance of the degradation pathway of bacitracin that represents about half of the samples mass (Figure 6b). Up to 120 °C, the mass loss is ~3%, representing elimination of the residual solvent molecules. The degradation of the organics starts after 250 °C, in a series of degradative–oxidative processes, as indicated by the multiple exothermic peaks from 337 to 349 °C and 574–587 °C (for the loaded samples). These exothermic effects appear shifted when compared with the thermal analysis of the bacitracin; additionally, the effects from 209 and 299 °C are missing in the loaded samples. This confirms the successful loading process and indicates possible bonds between bacitracin and the FDU support.

After 440 °C, the residual carbonaceous mass is burned away when a second high mass loss is recorded (Table 3).

The incorporation of bacitracin through the vacuum-assisted method in all samples was very efficient. The aminopropyl-functionalized sample has a higher loading content, perhaps due to the formation of a higher number of hydrogen bonds between bacitracin and the support.

2.9. HPLC-DAD Release Evaluation

The release profile of bacitracin in SBF is presented in Figure 7a. It can be observed that the drug delivery systems induce an extended release of bacitracin over time. The maximum recovery regarding the bulk sample (95.32%) occurred in the first 75 min, and for FDU-12-NH_2, the maximum (59.66%) is reached at 5 h, while for pristine FDU-12 (65.49%) and for the one with pNAM grafting, the maximum of 64.52% is reached over 24 h.

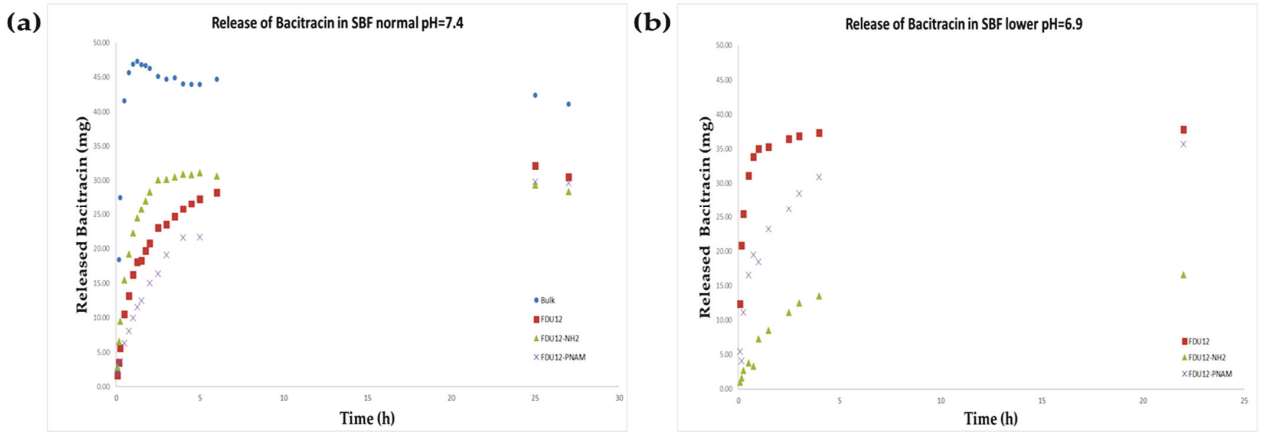

Figure 7. Release of bacitracin in SBF medium at (**a**) normal pH (7.4) and (**b**) lower pH (6.9).

Regarding the release behavior in the SBF with lower pH (pH = 6.9, Figure 7b), the release profile is different. All samples reach the maximum of released bacitracin at approximately the same timepoint, over 22 h. The aminopropyl-functionalized sample has the lowest release content of 32.94%, the unfunctionalized sample has a maximum of 75.75%, and the pNAM-grafted sample has a maximum release of 75.11%. Bacitracin being an amphiphilic peptide when is in a medium with a lower pH, it has more protonated groups. Regarding the contribution of the support, J.M. Rosenholm et al. demonstrate the fact that on the surface, they consist of approximatively 20% silanol groups with a $pK_a < 2$ (isolated silanol groups), while the remaining 80% have a $pK_a>8$ (geminal and vicinal silanol groups) [70]. So, in the case of the unfunctionalized FDU-12, there are more negative charges on the surface at a higher pH, and implicitly more electrostatic interactions with bacitracin. For FDU-12-NH_2, the release is delayed in the medium with the lower pH because the amino groups of the support are more polarized and act as a gate based on electrostatic repulsion, which keeps the bacitracin inside the pores and thus slows down the release process. It is known that the tertiary amino groups from poly(N-acryloylmorpholine) free molecule in aqueous solution have a pK_a of around 8.3 [71], so it is expected to be protonated and, like in the case of FDU-12-NH_2, to have a role in delaying bacitracin release. But for the pNAM chains being grafted, these values of pK_a can be influenced by electrostatic interactions with the surface or by ionic strength and composition of SBF medium. In comparison with the release in SBF at normal physiological pH (7.4), the samples FDU-12 and FDU-12-pNAM have an enhanced release process in the medium with lower pH. Also, based on our measurements, even after 74 h, the concentration of released bacitracin continues to be high (70.28% for FDU-12 and 70.54% for FDU-12-pNAM).

2.10. Kinetic Models

Data fitting for W and K-P models led to the values of (a, b) and (k, n) given in Table 4. In the same Table, R^2 values prove that both models performed well ($R^2 \geq 0.94$), noticing that W model covers 100% of the original datasets rather than only 60%, as in the case of the K-P model. When tested for all datasets, the K-P model recorded a decrease in efficiency ($0.66 \leq R^2 \leq 0.94$).

Table 4. Parameters and R^2 values of the three models used. Weibull model used 100% of the datasets, Korsmeyer–Peppas model used 60%, while Logarithmic regression used both.

pH	Sample	W 100%			K-P 60%			LnR	
		a	b	R^2	K	n	R^2	R^2 100%	R^2 60%
7.4	FDU-12	30.440	0.719	0.98	0.080	0.500	0.98	0.85	0.85
	FDU-12-NH_2	35.733	0.930	0.98	0.120	0.420	0.97	0.56	0.99
	FDU-12-pNAM	58.718	0.770	0.99	0.050	0.640	0.99	0.96	0.94
6.9	FDU-12	7.792	0.792	0.99	0.290	0.280	0.94	0.58	0.95
	FDU-12-NH_2	86.920	0.903	0.99	0.033	0.688	0.97	0.91	0.85
	FDU-12-pNAM	17.244	0.643	0.99	0.100	0.500	0.95	0.89	0.94

Logarithmic regression (LnR) generally performed better in the case of 60% data fitting ($0.85 \leq R^2 \leq 0.99$), as in the case of 100% ($0.56 \leq R^2 \leq 0.96$).

Models parameters and R^2 values of the three models used are shown in Table 4, describing two cases: (i) pH = 7.4 and (ii) pH = 6.9. From the analysis of R^2 values, it could be found that W model is the best one, even though it was fitted with the entire database.

When the three models were fitted for 100% of the datasets, the W model was the closest one to the experimental curve, as shown in Figure 8a. Also, LnR and K-P tend to provide closer results.

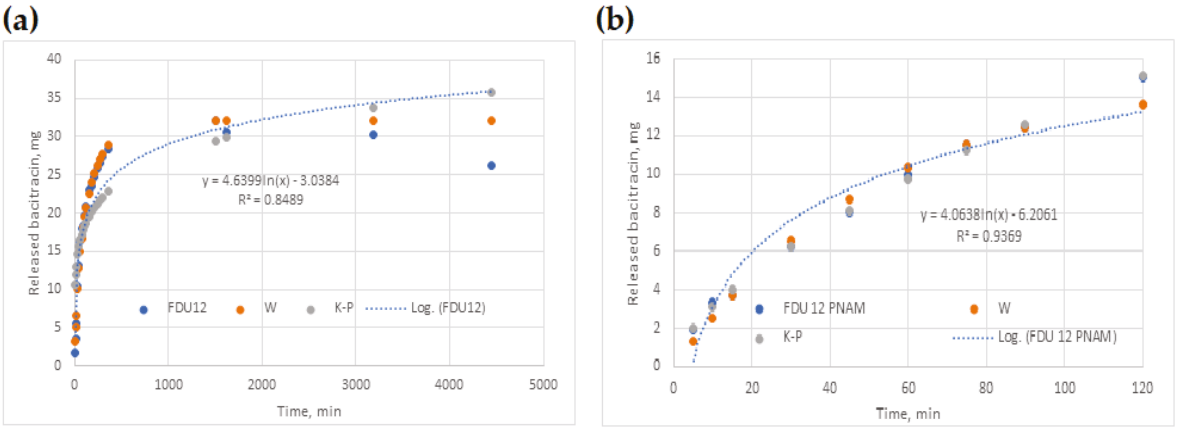

Figure 8. Release curve fitted by the three models in the case of (**a**) FDU-12, for 100% datasets used and pH 7.4; (**b**) FDU-12-pNAM, for 60% datasets used and pH 7.4.

Figure 8b shows the case when all three models were fitted for 60% of the datasets, with W and K-P being both close to the experimental points.

2.11. Antimicrobial Activity of Bacitracin and FDU-12/FDU-12-NH_2/FDU-12-pNAM Loaded with Bacitracin Against Reference and Clinical Gram-Positive Strains

2.11.1. Qualitative Screening of the Antimicrobial Activity of FDU-12/FDU-12-NH_2/FDU-12-pNAM Loaded with Bacitracin Against Reference and Clinical Gram-Positive Strains

The qualitative evaluation of the antimicrobial activity of bacitracin and FDU-12/FDU-12-NH_2/FDU-12-pNAM loaded with bacitracin (B0 = bacitracin; B1 = FDU-12 + Bacitracin; B4 = FDU-12-NH_2 + Bacitracin; BP = FDU-12-pNAM + Bacitracin) against reference and clinical Gram-positive strains belonging to *S. aureus*, demonstrated the efficiency in the following decreasing order, revealed by the inhibition zone diameters: B0 [*S. epidermidis* ATCC 12228 = *S. aureus*$_{30}$ = *S. aureus*$_{32}$ = *S. aureus*$_{39}$ă= *S. aureus*$_{44}$ă= *S. aureus*$_{59}$ă= *S. aureus*$_{68}$ă= *S. aureus*$_{100}$ (AU = 3) > *S. aureus* ATCC 25923 = *S. aureus*$_{60}$ (AU = 2)]; B1 [*S. epidermidis* ATCC 12228 (AU = 3) > *S. aureus* ATCC 25923 = *S. aureus*$_{30}$ = *S. aureus*$_{32}$ = *S. aureus*$_{39}$ă= *S. aureus*$_{44}$ă= *S. aureus*$_{59}$ă= *S. aureus*$_{60}$ = *S. aureus*$_{68}$ă= *S. aureus*$_{100}$ (AU = 2)]; BP [*S. epidermidis* ATCC 12228 = *S. aureus* ATCC 25923 = *S. aureus*$_{30}$ = *S. aureus*$_{32}$ = *S. aureus*$_{39}$ă= *S. aureus*$_{44}$ă= *S. aureus*$_{59}$ă= *S. aureus*$_{60}$ = *S. aureus*$_{68}$ă= *S. aureus*$_{100}$ (AU = 2)] and B4 (*S. epidermidis* ATCC 12228 = *S. aureus* ATCC 25923 = *S. aureus*$_{30}$ = *S. aureus*$_{32}$ = *S. aureus*$_{39}$ă= *S. aureus*$_{44}$ă= *S. aureus*$_{59}$ă= *S. aureus*$_{68}$ă= *S. aureus*$_{100}$ (AU = 2) > *S. aureus*$_{60}$ (AU = 1)] (Table 5, Figure 9).

https://doi.org/10.3390/molecules31020340

Table 5. The inhibition zones diameters (mm) and the corresponding AU of the tested formulations against *S. aureus* ATCC 25923, *S. epidermidis* ATCC 12228, and clinical *S. aureus* isolates (AU—arbitrary units; ZD = inhibition zone diameter).

	Bacterial Strains																			
	***S. aureus* ATCC 25923**		***S. epidermidis* ATCC 12228**		***S. aureus* 30**		***S. aureus* 32**		***S. aureus* 39**		***S. aureus* 44**		***S. aureus* 59**		***S. aureus* 60**		***S. aureus* 68**		***S. aureus* 100**	
Tested Formulation	**ZD**	**AU**	**ZD**	**AU**	**ZD**	**AU**	**ZD**	**AU**	**ZD**	**AU**	**ZD**	**AU**	**ZD**	**AU**	**ZD**	**AU**	**ZD**	**AU**	**ZD**	**AU**
B0	19	2	25	3	21	3	21	3	22	3	22	3	23	3	20	2	21	3	21	3
B1	16	2	21	3	18	2	19	2	17	2	19	2	20	2	15	2	18	2	17	2
B4	11	2	17	2	13	2	14	2	15	2	14	2	13	2	10	1	14	2	14	2
BP	14	2	19	2	15	2	15	2	16	2	17	2	17	2	14	2	17	2	16	2

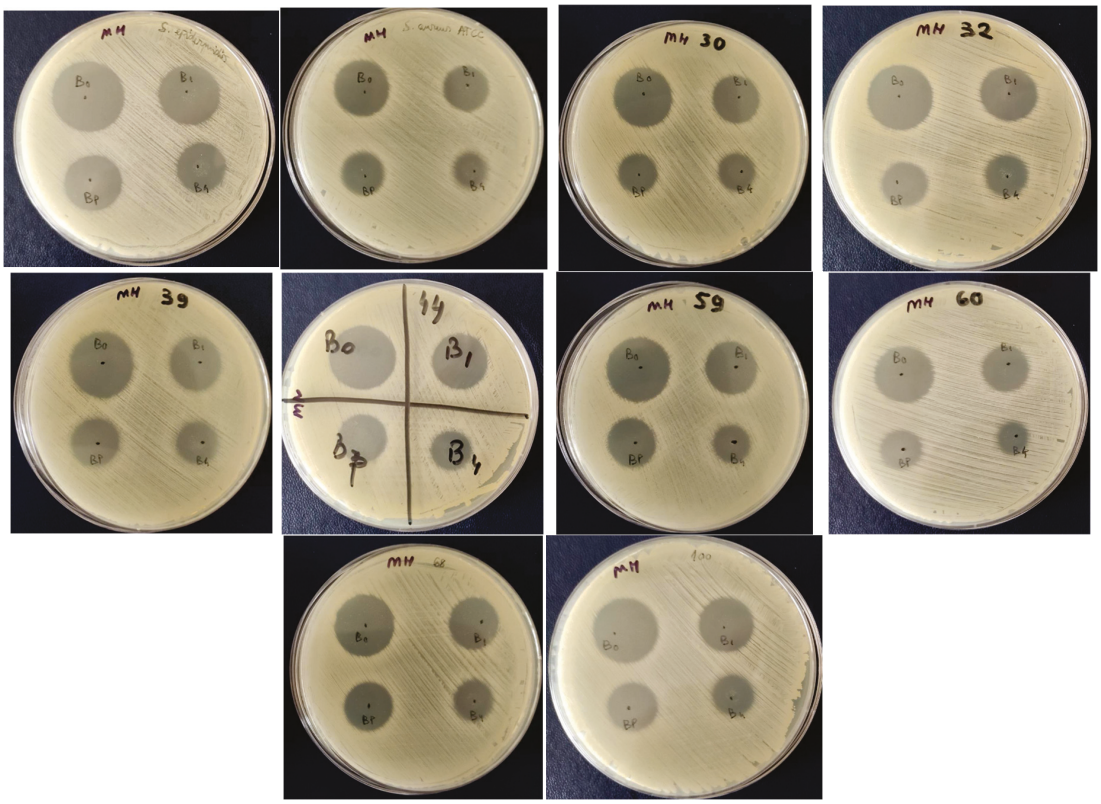

Figure 9. Qualitative screening of the antimicrobial activity Bacitracin and Bacitracin–FDU-12 derivatives against reference and clinical *S. aureus* strains.

2.11.2. Quantitative Evaluation of the Antimicrobial Activity of Bacitracin and Bacitracin–FDU-12 Derivatives

Following the quantitative evaluation of the antimicrobial activity of Bacitracin and Bacitracin–FDU-12 derivatives against both reference and clinical *S. aureus* strains, the highest efficiency was observed for the reference strain *S. epidermidis* ATCC 12228, with the MIC values ranked as follows: B0 (0.09 mg/mL) > B1 (0.19 mg/mL) > BP (0.29 mg/mL) > B4 (0.78 mg/mL). This was followed by *S. aureus* ATCC 25923, showing a similar trend: B0 (0.14 mg/mL) > BP (0.39 mg/mL) > B1 (0.78 mg/mL) > B4 (2.34 mg/mL) (Table 6, Figure 10).

https://doi.org/10.3390/molecules31020340

Table 6. Mean MIC values obtained from the quantitative evaluation of the antimicrobial activity of Bacitracin and Bacitracin–FDU-12 derivatives against reference strains and clinical isolates of *S. aureus*.

	B0		B1		BP		B4	
	MIC Mean (mg/mL)	St. Dev.	MIC Mean (mg/mL)	St. Dev.	MIC Mean (mg/mL)	St. Dev.	MIC Mean (mg/mL)	St. Dev.
S. aureus ATCC 25923	0.14	0.07	0.78	0	0.39	0	2.34	1.11
S. epidermidis ATCC 12228	0.09	0	0.19	0	0.29	0.14	0.78	0
60	0.39	0	2.34	1.11	1.56	0	1.17	0.55
59	0.39	0	1.56	0	1.56	0	3.13	0
44	0.39	0	0.59	0.28	1.56	0	4.69	2.21
100	0.39	0	0.78	0	1.56	0	7.81	6.63
32	0.39	0	1.17	0.55	1.56	0	7.81	6.63
39	0.19	0	0.59	0.28	0.78	0	3.13	0
30	0.39	0	1.56	0	1.56	0	3.13	0
68	1.56	0	6.25	0	3.125	0	9.38	4.42

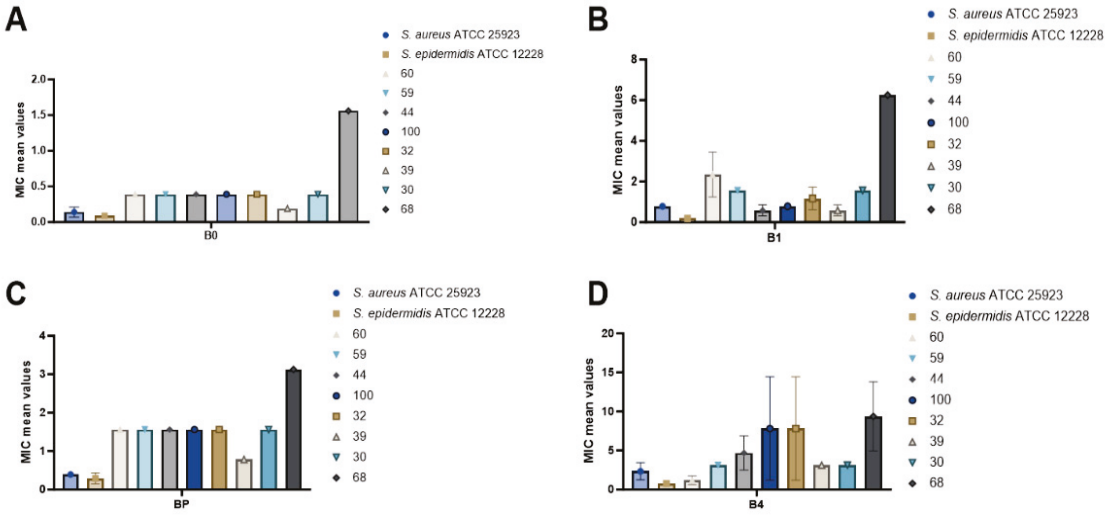

Figure 10. Average MIC values for the tested solutions ((**A**)—B0; (**B**)—B1; (**C**)—BP and (**D**)—B4) against *S. aureus* ATCC 25923, *S. epidermidis* ATCC 12228, and clinical *S. aureus* isolates.

For clinical *S. aureus* isolates, the antimicrobial efficiency decreased in the following order: B0 > B1 > BP > B4 (Table 6, Figure 10). When comparing the activity of each formulation across the tested strains, patterns were observed as follows:

- B0: *S. epidermidis* ATCC 12228 (0.09 mg/mL) > *S. aureus* ATCC 25923 (0.14 mg/mL) > clinical *S. aureus* strain 39 (0.19 mg/mL).
- B1: *S. epidermidis* ATCC 12228 (0.19 mg/mL) > *S. aureus* strain 39 = strain 44 (0.58 mg/mL).
- BP: *S. epidermidis* ATCC 12228 (0.29 mg/mL) > *S. aureus* ATCC 25923 (0.39 mg/mL) > *S. aureus* strain 39 (0.78 mg/mL).
- B4: *S. epidermidis* ATCC 12228 (0.78 mg/mL) > *S. aureus* strain 60 (1.17 mg/mL) (Table 6, Figure 11).
- Notably, three of the tested formulations, B0 (pure Bacitracin), B1 (FDU-12 + Bacitracin), and BP (FDU-12-pNAM + Bacitracin), exhibited significant antimicrobial activity against the clinical *S. aureus* strain 39 (Table 6, Figure 10).

The reduced susceptibility of clinical *S. aureus* isolates to bacitracin and its derivatives is likely attributable to a combination of genetic, physiological, and ecological adaptations that arise during infection and clinical antibiotic exposure. Unlike reference strains, clinical isolates typically display substantial genomic heterogeneity, including point mutations,

gene amplifications, and acquisition of mobile genetic elements (e.g., plasmids, transposons, SCCmec elements) that encode resistance determinants and stress–response functions [72,73]. These features emerge under sustained selective pressures in vivo, where bacterial populations must withstand host immune defenses, nutrient limitation, oxidative stress, and repeated or sub-optimal antibiotic treatments [74]. Furthermore, clinical isolates frequently exhibit an enhanced capacity for biofilm formation on host tissues or indwelling medical devices. The resultant extracellular polymeric matrix impedes antimicrobial diffusion, alters local microenvironmental conditions (e.g., pH, oxygen tension), and supports the formation of metabolically inactive persister cells, collectively reducing the efficacy of bacitracin-based formulations and contributing to persistent infection phenotypes [73,75]. In addition, strain-specific variation in the activity of global regulatory systems such as *agr*, *sarA*, and *sigB* modulates the expression of virulence determinants, cell-envelope modifying enzymes, and stress–response pathways, thereby influencing both antimicrobial susceptibility and adaptive survival strategies relative to reference strains [76,77].

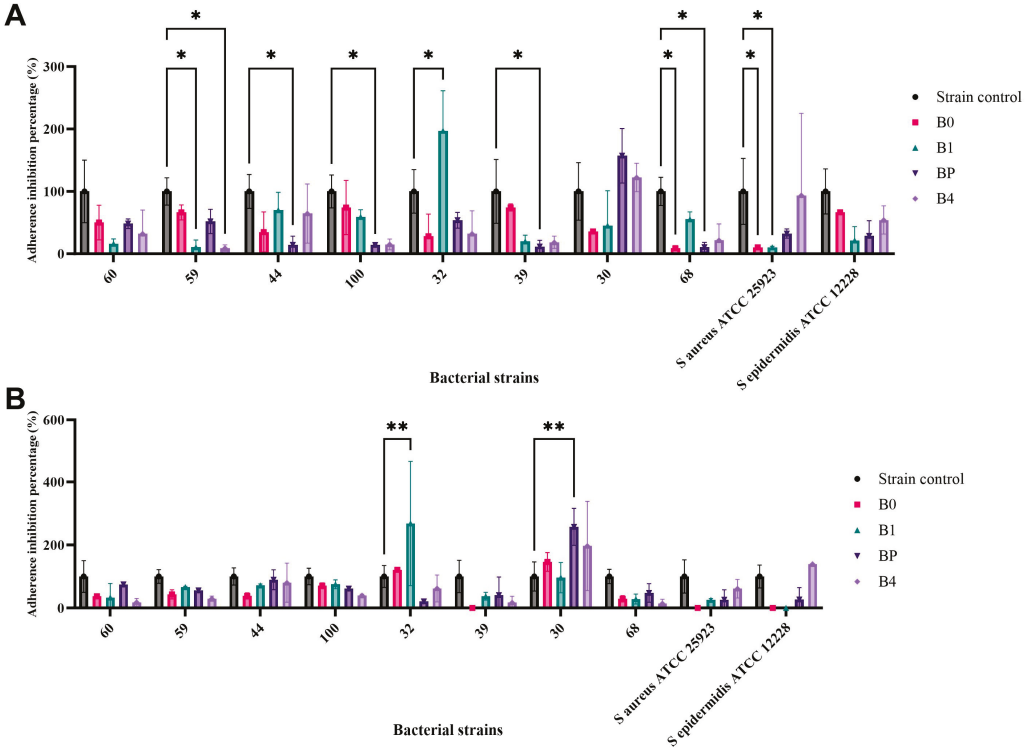

Figure 11. Percentage of adherence inhibition (%MAI) for the tested Bacitracin and Bacitracin–FDU-12 formulations at sub-inhibitory concentration ((**A**) MIC/2 and (**B**) MIC/4) against *S. aureus* ATCC 25923, *S. epidermidis* ATCC 12228, and clinical *S. aureus* isolates. Statistical significance was determined using Dunnetts multiple comparisons test (* $p < 0.05$, ** $p < 0.01$).

Several studies have reported variable susceptibility of *S. aureus* to bacitracin, with MIC values ranging from 16 to 64 µg/mL for susceptible isolates and higher for clinical or multidrug-resistant strains [78]. This pattern is consistent with the higher MIC values observed in the present study, suggesting decreased susceptibility among clinical isolates. The higher numerical MICs can be attributed to the fact that values were expressed per total formulation mass (mg/mL) rather than per active bacitracin content, reflecting the well-known mass-of-carrier effect in mesoporous silica nanoparticle-based antibiotic systems. As highlighted in previous studies, functionalized mesoporous silica nanoparticle

maintain or only slightly modify the intrinsic antimicrobial activity of the incorporated drug unless specifically designed for controlled release or synergistic delivery [79].

2.11.3. The Impact of Bacitracin and Bacitracin–FDU-12 Derivatives on Biofilm Formation by *S. aureus* ATCC 25923, *S. epidermidis* ATCC 12228, and Clinical *S. aureus* Isolates

At sub-inhibitory concentrations corresponding to MIC/2, all four tested formulations exhibited a reduction in biofilm formation relative to the untreated control (100%). Specifically, significant decreases in biofilm formation ability were observed as follows. B0: *S. aureus* strain 68 (91%, $p = 0.032$) and *S. aureus* ATCC 25923 (89.7%, $p = 0.036$); B1: *S. aureus* ATCC 25923 (89.8%, $p = 0.036$) and *S. aureus* strain 59 (89.4%, $p = 0.037$); BP: *S. aureus* strain 68 (89.5%, $p = 0.036$), strain 39 (88.3%, $p = 0.040$), and strain 100 (85.9%, $p = 0.047$); B4: *S. aureus* strain 59 (90.9%, $p = 0.033$). These findings indicate a marked inhibitory effect on biofilm formation at relatively low (sub-MIC) concentrations, suggesting potent anti-biofilm activity of the tested compounds. In contrast, B1 treatment resulted in a statistically significant increase in biofilm formation for *S. aureus* strain 32, with an MAI value of 97.19% ($p = 0.020$) compared to the untreated control, indicating a strain-dependent response (Table 7, Figure 11A).

Table 7. Percentage of microbial adherence inhibition (%MAI) of *S. aureus* ATCC 25923, *S. epidermidis* ATCC 12228, and clinical *S. aureus* isolates in the presence of Bacitracin and Bacitracin–FDU-12 derivatives at sub-inhibitory concentration (MIC/2).

	Strain Control		**B0**			**B1**			**BP**			**B4**		
	M	**SD**	**M**	**SD**	***p***	**M**	**SD**	***p***	**M**	**SD**	***p***	**M**	**SD**	***p***
60	100	50.04	50.13	27.70	0.392	16.21	7.75	0.055	48.27	7.58	0.360	32.18	37.92	0.1538
59	100	21.88	66.29	12.00	0.714	10.61	11.50	0.04	51.97	19.50	0.425	9.10	5.37	0.0332
44	100	27.06	34.98	32.10	0.181	69.75	28.93	0.782	14.31	14.11	0.048	64.55	47.3.8	0.6781
100	100	26.38	74.22	43.37	0.860	59.04	11.61	0.56	14.03	0.15	0.047	15.02	8.60	0.0507
32	100	34.95	28.05	35.47	0.120	197.19	64.17	0.021	53.79	12.60	0.459	32.01	36.87	0.1523
39	100	51.24	74.36	5.80	0.86	19.76	10.14	0.070	11.71	9.94	0.040	18.44	9.94	0.0643
30	100	46.22	35.96	1.140	0.191	45.20	55.97	0.311	157.11	43.75	0.277	122.35	22.73	0.9092
68	100	22.69	8.96	4.16	0.033	55.50	11.54	0.492	10.56	7.75	0.037	21.66	26.10	0.0798
SA	100	52.77	10.26	1.951	0.036	10.26	1.99	0.036	32.47	7.363	0.1565	93.72	131.46	0.9991
SE	100	36.08	66.67	1.79	0.721	21.31	22.38	0.078	28.69	24.465	0.1248	54.22	22.67	0.4676

M—mean value; SD—Standard Deviation; *p*—*p* value; SA—*S. aureus* ATCC 25923; SE—*S. epidermidis* ATCC 12228.

At sub-inhibitory concentrations corresponding to MIC/4, the impact of B1 (FDU-12 + Bacitracin), and BP (FDU-12-pNAM + Bacitracin) on biofilm formation by *S. aureus* strain 32 and *S. aureus* strain 30, respectively, showed a statistically significant increase in bacterial adherence to the inert substratum, with an MAI% of 268.15% ($p = 0.0016$) and 257.35 ($p = 0.0032$) relative to the strain control (Table 8, Figure 11B).

Table 8. Percentage of microbial adherence inhibition (%MAI) of *S. aureus* ATCC 25923, *S. epidermidis* ATCC 12228, and clinical *S. aureus* isolates in the presence of Bacitracin and Bacitracin–FDU-12 derivatives at sub-inhibitory concentration (MIC/4).

	Strain control		**B0**			**B1**			**BP**			**B4**		
	M	**SD**	**M**	**SD**	***p***	**M**	**SD**	***p***	**M**	**SD**	***p***	**M**	**SD**	***p***
60	100	50.04	37.07	0.33	0.429	33.23	44.35	0.376	74.85	5.61	0.945	18.07	12.37	0.211
59	100	21.88	43.48	14.50	0.52	66.11	2.75	0.860	55.50	3.00	0.711	29.61	8.12	0.331
44	100	27.06	38.45	9.81	0.448	71.70	4.50	0.919	89.77	31.28	0.99	80.38	61.94	0.977
100	100	26.38	70.58	8.97	0.909	75.26	13.82	0.948	61.43	6.32	0.799	39.66	3.90	0.466
32	100	34.95	121.45	4.67	0.968	268.15	197.20	0.002	20.79	5.13	0.236	62.05	42.94	0.808
39	100	51.24	0	0	0.093	37.47	12.42	0.434	40.98	57.13	0.485	17.27	19.87	0.204
30	100	46.22	146.06	29.83	0.687	96.03	48.02	>0.999	257.36	58.81	0.003	196.68	141.49	0.109
68	100	22.69	29.15	10.02	0.325	28.48	15.89	0.318	47.74	29.69	0.589	14.38	13.14	0.180
SA	100	52.77	0	0	0.093	25.57	4.55	0.285	26.49	31.40	0.295	61.41	29.45	0.799
SE	100	36.08	0	0	0.093	0	0	0.093	26.79	37.89	0.298	139.03	1.49	0.792

M—mean value; SD—Standard Deviation; *p*—*p* value; SA—*S. aureus* ATCC 25923; SE—*S. epidermidis* ATCC 12228.

The obtained results showed that at MIC/2, all formulations reduced microbial adherence and biofilm formation in several *S. aureus* strains (approximately 86–91% inhibition). However, at MIC/4, a strain-dependent increase in biofilm formation was observed (B1 in *S. aureus* strain 32 and BP in *S. aureus* strain 30), indicating that lower sub-inhibitory concentrations may stimulate biofilm development. This outcome is consistent with other studies reporting that sub-inhibitory levels of different antibiotics can either suppress or induce biofilm formation in *S. aureus*, depending on the antibiotic type, concentration, and genetic background of the strain. Such findings underscore the dual nature of sub-inhibitory antibiotic exposure and reinforce the importance of avoiding under-dosing, particularly when using carrier-based formulations [80]. Therefore, anti-biofilm efficiency should be validated across a range of sub-MICs to accurately assess formulation performance and minimize the risk of biofilm stimulation.

Evaluation of Bacitracin and Bacitracin–FDU-12 derivatives at sub-inhibitory concentrations (MIC/2 and MIC/4) revealed pronounced differences in biofilm-associated responses between reference and clinical *S. aureus* isolates. While all formulations produced consistent biofilm inhibition at MIC/2, several clinical isolates displayed concentration-dependent and strain-specific increases in adherence at MIC/4. This paradoxical enhancement of biofilm formation at lower antimicrobial exposure levels is characteristic of clinical isolates with highly plastic or deregulated biofilm regulatory systems. Sub-inhibitory antimicrobial concentrations can act as environmental cues that activate stress–responsive pathways, downregulate quorum-sensing systems (particularly *agr*), or upregulate adhesion encoding genes and polysaccharide intercellular adhesin synthesis, thereby promoting compensatory biofilm production. These divergent behaviors highlight fundamental differences in regulatory circuit dynamics between reference strains and clinical isolates, underscoring the complexity of bacterial adaptation under sub-inhibitory antibiotic stress.

2.11.4. The Influence of Bacitracin and Bacitracin–FDU-12 Formulations at Sub-Inhibitory Concentration (MIC/2 and MIC/4) on the Ability of Bacterial Strains to Secrete Soluble Virulence Factors

Lecithinase Production

The effect of Bacitracin and Bacitracin–FDU-12 formulations on lecithinase activity was assessed across six bacterial strains.

For *S. aureus* ATCC 25923, lecithinase production remained largely unchanged following treatment, with no statistically significant differences compared to the untreated control. Nonetheless, a moderate inhibitory effect was detected in the presence of Bacitracin (B0) at sub-inhibitory concentrations (MIC/2 and MIC/4), resulting in 25% and 12.5% reduction in enzyme activity, respectively, suggesting a strain-dependent response (Supplementary Table S2, Table 9). In contrast, exposure to the composite formulations B1 and BP led to a stimulatory effect on lecithinase production, with the most pronounced increase (37.5%) observed at the MIC/2 concentration.

Table 9. A summary table of the qualitative effects of Bacitracin and Bacitracin-FDU-12 formulations at sub-inhibitory concentration (MIC/2 and MIC/4) on *S. aureus* lecithinase activity.

Lecithinase		B0			B1			BP			B4		
Tested Strains	Subinhibitory Concentration	Positive Effect	Negative Effect	No Significant Effect	Positive Effect	Negative Effect	No Significant Effect	Positive Effect	Negative Effect	No Significant Effect	Positive Effect	Negative Effect	No Significant Effect
S. aureus ATCC 25923	MIC/2												
	MIC/4												
68	MIC/2												
	MIC/4												
32	MIC/2												
	MIC/4												
59	MIC/2												
	MIC/4												
60	MIC/2												
	MIC/4												
100	MIC/2												
	MIC/4												

Legend: gray—no statistically significant differences.

For the *S. aureus* clinical isolates, no statistically significant differences in lecithinase production were observed compared to the untreated control. In *S. aureus* strain 68, inhibitory effects were detected in the presence of B0 at MIC/4 (25%), B4 at MIC/2 (50%), and BP at MIC/2 (25%) (Supplementary Table S3, Table 9). In *S. aureus* strain 32, a moderate inhibition was observed with BP at MIC/2 and MIC/4 (12.5% and 25%, respectively) (Supplementary Table S4, Table 9). The remaining *S. aureus* clinical strains exhibited a dose-dependent response. For instance, in *S. aureus* strain 100, modest inhibition was recorded with B0 (MIC/4), B1 (MIC/2), and BP (MIC/2) treatments (22.3%). Conversely, in *S. aureus* strains 59 and 60, lecithinase secretion was stimulated in the presence of B1 at MIC/2 and B4 at MIC/4, showing up to 28.5% enhancement compared to the control (Supplementary Table S5, Table 9).

Caseinase Production

The effect of Bacitracin and Bacitracin–FDU-12 formulations at sub-inhibitory concentrations on caseinase activity was evaluated in ten bacterial strains. In *S. aureus* ATCC 25923, caseinase production remained largely unaffected by treatment, with no statistically significant differences relative to the untreated control (Supplementary Table S6, Table 10). Among the clinical isolates, the response varied depending on the formulation and concentration applied. For instance, stimulation of caseinase secretion was observed in *S. aureus* strain 39 following exposure to B0 at MIC/2 and BP at MIC/4 (57.15%, $p = 0.0036$), as well as in *S. aureus* strain 59 with B1 at MIC/2 and BP at both sub-inhibitory concentrations (50%, $p = 0.0144$) and in *S. aureus* strain 100 with B1 at MIC/4 (50%, $p = 0.0144$). Conversely, inhibition of caseinase activity was detected under treatment with B1 at MIC/4, BP at MIC/4, and B4 at MIC/2, resulting in 35.8%, 42.9%, and 42.9% reduction, respectively ($p = 0.0489$) (Supplementary Table S6, Table 10), in the case of *S. aureus* strain 44. For the remaining strains, no statistically significant differences in enzyme production were noted compared to the control (Supplementary Tables S7 and S8, Table 10).

https://doi.org/10.3390/molecules31020340

Table 10. A summary table of the qualitative effects of Bacitracin and Bacitracin-FDU-12 formulations at sub-inhibitory concentration (MIC/2 and MIC/4) on *S. aureus* caseinase activity.

Caseinase		B0			B1			BP			B4		
	Subinhibitory Concentration	Positive Effect	Negative Effect	No Significant Effect	Positive Effect	Negative Effect	No Significant Effect	Positive Effect	Negative Effect	No Significant Effect	Positive Effect	Negative Effect	No Significant Effect
SA	MIC/2 MIC/4												
30	MIC/2 MIC/4												
32	MIC/2 MIC/4												
39	MIC/2 MIC/4												
44	MIC/2 MIC/4												
59	MIC/2 MIC/4												
60	MIC/2 MIC/4												
100	MIC/2 MIC/4												
68	MIC/2 MIC/4												
SE	MIC/2 MIC/4												

SA—*S. aureus* ATCC 25923; SE—*S. epidermidis* ATCC 12228. Legend: gray—no statistically significant differences; green—stimulation; red—inhibition.

Amylase Secretion

The impact of Bacitracin and Bacitracin–FDU-12 formulations at sub-inhibitory concentrations on amylase activity was assessed in ten bacterial strains. In the reference strains, amylase secretion remained largely unaffected by treatment, with no statistically significant differences compared to the untreated control (Supplementary Table S10, Table 11). The highest inhibition of enzyme production was observed in two clinical isolates, *S. aureus* 68 and *S. aureus* 100, following exposure to B1 at MIC/2, and to BP and B4 at both sub-inhibitory concentrations, resulting in a 50% reduction in activity ($p \leq 0.0001$) (Supplementary Table S9, Table 11). Similarly, *S. aureus* 59 exhibited marked inhibition of amylase secretion when treated with B0, B1, and BP at MIC/2 and MIC/4 (50%, $p = 0.0024$). In contrast, *S. aureus* strain 39 demonstrated enhanced amylase production in the presence of B1 at MIC/4, with a 66.7% increase relative to the control ($p = <0.0001$) (Supplementary Table S10, Table 11).

Table 11. A summary table of the qualitative effects of Bacitracin and Bacitracin-FDU-12 formulations at sub-inhibitory concentration (MIC/2 and MIC/4) on *S. aureus* amylase activity.

Amylase		B0			B1			BP			B4		
	Subinhibitory Concentration	Positive Effect	Negative Effect	No Significant Effect	Positive Effect	Negative Effect	No Significant Effect	Positive Effect	Negative Effect	No Significant Effect	Positive Effect	Negative Effect	No Significant Effect
SA	MIC/2 MIC/4												
30	MIC/2 MIC/4												
32	MIC/2 MIC/4												
39	MIC/2 MIC/4												
44	MIC/2 MIC/4												
59	MIC/2 MIC/4												
60	MIC/2 MIC/4												
100	MIC/2 MIC/4												
68	MIC/2 MIC/4												
SE	MIC/2 MIC/4												

SA—*S. aureus* ATCC 25923; SE—*S. epidermidis* ATCC 12228. Legend: gray—no statistically significant differences; green—stimulation; red—inhibition.

Lipase Secretion

The effect of Bacitracin and Bacitracin–FDU-12 formulations at sub-inhibitory concentrations on lipase activity was evaluated in nine bacterial strains. The strongest inhibitory response was recorded for *S. epidermidis* ATCC 12228, showing a 77% reduction in lipase production after treatment with B4 at MIC/2 ($p = < 0.0001$), followed by B0 at MIC/4

(62%, $p = 0.0018$), B0 at MIC/2 (54%, $p = 0.0082$), and B4 at MIC/4 (54%, $p = 0.0082$) (Supplementary Table S11, Table 12). In contrast, several *S. aureus* clinical isolates exhibited stimulation of lipase secretion under specific treatment conditions; for instance, exposure to B0 at MIC/2 and BP at MIC/4 in *S. aureus* strain 39 (57%, $p = 0.0044$); B1 at MIC/2 and BP at both sub-inhibitory concentrations in *S. aureus* strain 59 (50%, $p = 0.0165$); and B1 at MIC/4 in *S. aureus* strain 100 (50%, $p = 0.0165$) (Supplementary Table S11, Table 12). For *S. aureus* strain 68, lipase activity remained comparable to that of the untreated control, with no statistically significant differences detected (Supplementary Table S12, Table 12).

Table 12. A summary table of the qualitative effects of Bacitracin and Bacitracin-FDU-12 formulations at sub-inhibitory concentration (MIC/2 and MIC/4) on *S. aureus* lipase activity.

Lipase		B0			B1			BP			B4		
	Subinhibitory Concentration	Positive Effect	Negative Effect	No Significant Effect	Positive Effect	Negative Effect	No Significant Effect	Positive Effect	Negative Effect	No Significant Effect	Positive Effect	Negative Effect	No Significant Effect
SA	MIC/2 MIC/4												
32	MIC/2 MIC/4												
39	MIC/2 MIC/4												
44	MIC/2 MIC/4												
59	MIC/2 MIC/4												
60	MIC/2 MIC/4												
100	MIC/2 MIC/4												
68	MIC/2 MIC/4												
SE	MIC/2 MIC/4												

SA—*S. aureus* ATCC 25923; SE—*S. epidermidis* ATCC 12228. Legend: gray—no statistically significant differences; green—stimulation; red—inhibition.

Hemolysin Production

The effect of Bacitracin and Bacitracin–FDU-12 formulations at sub-inhibitory concentrations on hemolysin production was evaluated in nine *S. aureus* strains. A significant reduction in hemolysin synthesis was observed in several strains, indicating inhibition of virulence factor expression. The strongest inhibitory response was recorded for *S. aureus* strain 100 treated with Bacitracin (B0) at MIC/2 and MIC/4, showing a 79% decrease compared to the untreated control ($p < 0.0001$). This was followed by *S. aureus* strain 30 (B1, MIC/2 and MIC/4; 77% inhibition, $p < 0.0001$), *S. aureus* strain 32 (B1, MIC/2 and MIC/4; 75% inhibition, $p < 0.0001$), and *S. aureus* strain 59 (B4, MIC/4; 50% inhibition, $p < 0.0001$) (Supplementary Table S13, Table 13).

Table 13. A summary table of the qualitative effects of Bacitracin and Bacitracin-FDU-12 formulations at sub-inhibitory concentration (MIC/2 and MIC/4) on *S. aureus* hemolysin activity.

Hemolysin		B0			B1			BP			B4		
	Subinhibitory Concentration	Positive Effect	Negative Effect	No Significant Effect	Positive Effect	Negative Effect	No Significant Effect	Positive Effect	Negative Effect	No Significant Effect	Positive Effect	Negative Effect	No Significant Effect
SA	MIC/2 MIC/4												
30	MIC/2 MIC/4												
32	MIC/2 MIC/4												
39	MIC/2 MIC/4												
44	MIC/2 MIC/4												
59	MIC/2 MIC/4												
60	MIC/2 MIC/4												
100	MIC/2 MIC/4												
68	MIC/2 MIC/4												

SA—*S. aureus* ATCC 25923. Legend: gray—no statistically significant differences; green—stimulation; red—inhibition.

Conversely, a statistically significant increase in hemolysin production was detected in two clinical isolates: *S. aureus* strain 60 exposed to B0 at MIC/2 (157% of control, $p < 0.0001$) and *S. aureus* strain 39 exposed to B1 at MIC/4 (150% of control, $p < 0.0001$) (Supplementary Table S13, Table 13).

In the present study, sub-inhibitory exposure to the tested formulations produced strain-specific alterations in the expression of soluble virulence factors, including hemolysins, lipase, amylase, caseinase, and lecithinase, ranging from pronounced inhibition to measurable stimulation. Such variability likely reflects differential engagement of stress–response systems and transcriptional regulators that coordinate virulence expression in *S. aureus*. Overall, these findings illustrate that the antibacterial formulations interact with clinical isolates in multifaceted ways that extend beyond growth inhibition, affecting biofilm development, virulence regulation, and adaptive physiological states.

These findings are consistent with previous data demonstrating that antibiotics at sub-inhibitory concentrations can modulate *S. aureus* virulence through global regulatory systems such as *agr* and *sarA*, as well as through stress–response pathways. Notably, cell wall active agents often enhance the production of different exotoxins, whereas ribosome-targeting antibiotics tend to suppress them [81]. Our results extend this paradigm by showing that carrier functionalization specifically, -NH_2, pNAM, or unmodified FDU-12 surfaces can further influence both the direction and magnitude of virulence modulation, likely due to differences in local drug release kinetics and surface cell interactions. This observation highlights an underexplored aspect of mesoporous silica nanoparticle systems. Recent studies have emphasized that rational surface engineering of mesoporous silica nanoparticles can be strategically employed to modulate bacterial adherence, biofilm formation, and the modulation of virulence-associated phenotypes, thereby supporting the rationale for the functionalization strategies implemented in this study [82].

3. Materials and Methods

3.1. Materials

All reagents in this study were used without further purification. Triblock co-polymer Pluronic F127, trimethylbenzene (TMB), tetraethylortosilicate (TEOS), aminopropyl- triethoxysilane (APTES), KCl, NaCl, $MgCl_2 \cdot 6H_2O$, $CaCl_2$, trishidroxiethylaminomethan, toluene, bacitracin, HCl, H_2SO_4, $NaHCO_3$, N-acryloylmorpholine, $CeSO_4$ were obtained from Sigma-Aldrich Merck (Dartmand, Germany).

3.2. Methods

3.2.1. Mesoporous Silica Nanoparticles FDU-12 Synthesis

The synthesis of the FDU-12 mesoporous silica nanoparticles was performed according to the method developed by Yu et al. [83] and based on a sol–gel method using Pluronic F127 as soft template and TMB as a swelling agent dissolved with KCl in a solution of HCl 2 M. After 24 h of stirring the silica source, TEOS is added and is left to mix for another 24 h. The next step is to put the sample at thermal treatment for 3 days at 100 °C, then it is filtered and left to dry at ambient temperature. To remove the organic template, the material is calcinated for 6 h at 550 °C. The schematic preparation procedure is presented in Figure 12.

https://doi.org/10.3390/molecules31020340

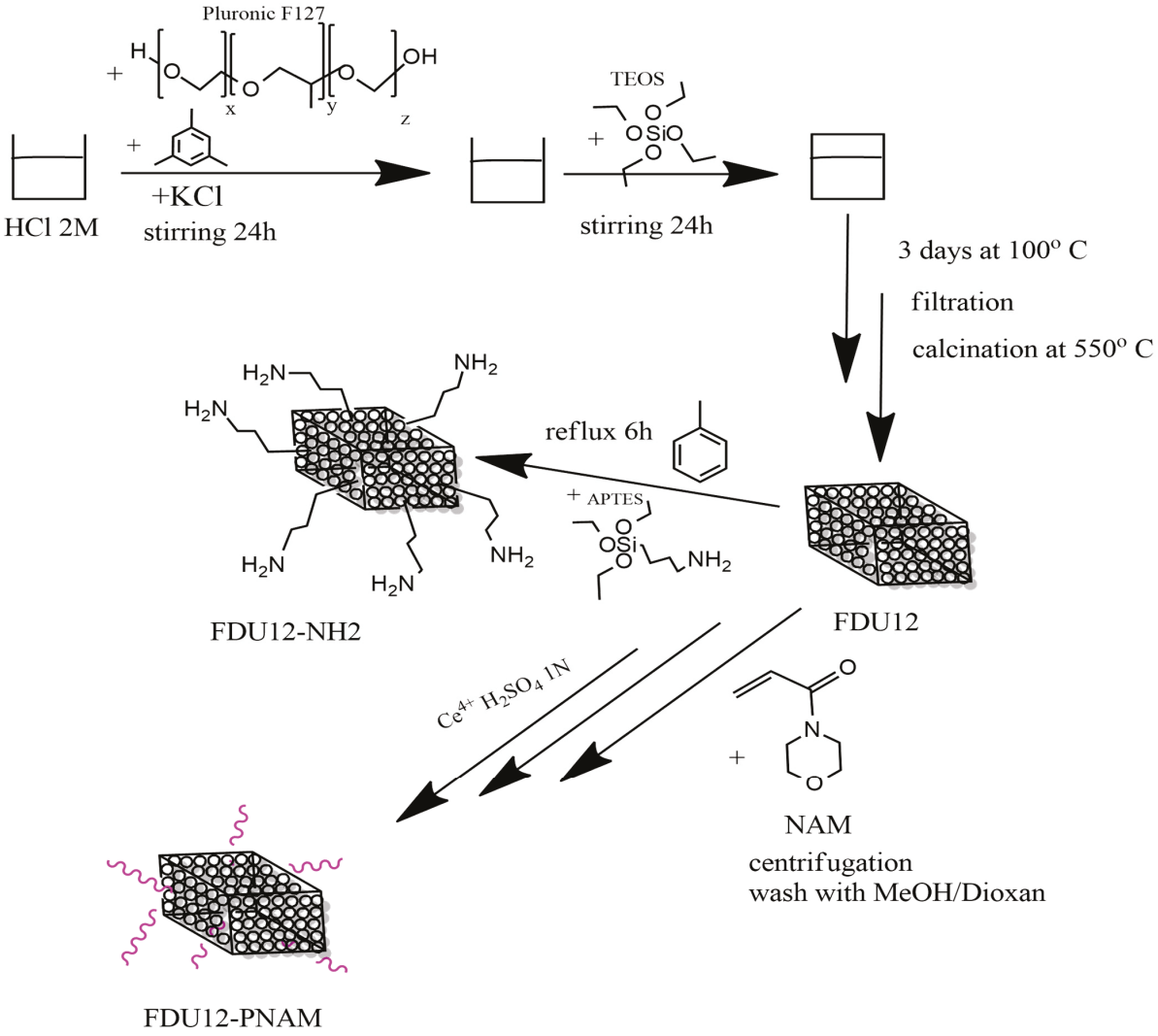

Figure 12. Schematic synthesis of samples.

3.2.2. Functionalization of FDU-12 with Aminopropyl Groups

For aminopropyl-functionalization, the FDU-12 sample is first dried in a vacuum oven for 1 h at 40 °C. After that, the sample is immersed in toluene where APTES is added and it is maintained for a minimum of 6 h at reflux [84]. For better efficiency of the functionalization process, the quantity of APTES is optimized based on the estimation of the number of hydroxyl groups from the surface of FDU-12 [85].

3.2.3. Functionalization of FDU-12 with pNAM

The modification of the FDU-12 substrate with NAM started from a substrate composition that was calculated based on the predetermined structural-dimensional characteristics of silica: average content of OH groups of 3.02×10^{-3} mmol OH/g. So, n_{Ce4+}/mol OH = 10^{-3}; $n_{NAM} = n_{OH}$; $[M]_0 = 3$ mol/L. As a source of Ce^{4+}, a solution of $Ce(SO_4)_2$ in H_2SO_4 1N (3×10^{-4} mol/L) was used as solvent dioxane.

The synthesis procedure is as follows: dispersion of mesoporous silica FDU-12 in the solvent at room temperature (about 15 min at 700 rot/min); addition of the initiator solution, keeping the same conditions for about 15 min; addition of monomer, conditioning by nitrogen purging; stabilization of temperatures at 35 °C with the same stirring regime; and maintenance of the reaction mass under these conditions for 6 h. When stopping the process, the cooled reaction mass is centrifuged (30,000 rot/min), separated, and washed with CH_3OH/Dioxan mixture (1:9 vol) until colorless and dried at 40 °C for 24 h.

https://doi.org/10.3390/molecules31020340

3.2.4. The Determination of Grafting Degree

The grafting degree, obtained after grafting, is calculated using relation Equation (1):

$$\%\ \text{grafting} = \frac{m_{\text{modified silica}} - m_{\text{silica}}}{m_{\text{silica}}} \times 100 \quad (1)$$

where m_{silica} is the initial mass of silica used in reaction (g); $m_{\text{modified silica}}$ is the mass of grafted silica after washing and drying (g).

The global grafting yield was calculated using relation Equation (2):

$$\text{global yield} = \frac{m_{\text{modified silica}}}{m_{\text{modified silica}} + m_{\text{monomer}}} \times 100 \quad (2)$$

where m_{monomers} is the initial mass of monomer(s) introduced in the grafting reaction (g).

The conversion of the monomer to grafted polymer was calculated using Equation (3):

$$\text{conversion to grafted polymer} = \frac{m_{\text{modified silica}-m_{\text{silica}}}}{m_{\text{monomer}}} \times 100 \quad (3)$$

3.2.5. Loading of Bacitracin in the Pores of the Samples

Due to its high solubility in water, the loading of the bacitracin was performed using the vacuum-assisted method developed by our group, from aqueous solution [10,69,85]. The first step is devoted to the removal of water and air from pores of the FDU-12 mesoporous material (1 g) and was achieved by vacuum drying at room temperature with a vacuum rate of about 0.1 bars. After the drying step, 1 g of bacitracin dissolved in 3 mL water was injected over the FDU-12 powder and allowed to be absorbed into the pores, at 1 bar. After this step, drying was achieved by applying a vacuum rate of 0.1 bar for about 30–60 min.

3.2.6. Release of Bacitracin in Simulated Body Fluid (SBF)

The evaluation of the delivery of bacitracin was performed by placing ~100 mg of sample in 200 mL of simulated body fluid (SBF), keeping it at 37 °C, with stirring at 300 rpm. At each timepoint, 1 mL of liquid is collected and 1 mL of SBF is added back to compensate for the removed solution. The release process was performed in two types of SBF medium, with both having compositions similar to that of blood, and the first medium had a pH value of 7.4 [86] and the second one had a lower pH, at a value of 6.9, which mimics a blood infection [87]. When monitoring the bacitracin level, a high-pressure liquid chromatography separation method coupled with UV detection using a Diode Array Detector (HPLC-DAD) was used according to British Pharmacopeia [88]. The chromatographic conditions are summarized in Supplementary Table S1.

From a stock solution of bacitracin, 6 standardized solutions were obtained (in the same solvent as the release medium), corresponding to 1, 5, 25, 50, 100, 500 ppm. The standards are injected and the correlation between concentration and absorbance was determined based on linear equation of the curve from the graph: f(Area) = Concentration. The relative released bacitracin content is expressed as a percentage reported to the total content of bacitracin from the samples.

3.2.7. Kinetic Models

Various kinetic models are available to address the issue of drug release modeling, with targeted applications for specific materials and shapes [89]. Among these models, three kinetic models were tested to fit the released bacitracin curve, i.e., Weibull model (denoted herein as W), Korsmeyer–Peppas model (denoted as K-P), and nonlinear regres-

https://doi.org/10.3390/molecules31020340

sion (natural logarithm regression, denoted as LnR). Weibull model is defined according to Equation (4) [90]:

$$M = M_{\infty}\left(1 - e^{-\frac{t^b}{a}}\right) \quad (4)$$

where a—scale factor; b—shape factor; t—time; and M_{∞} is the maximum value of the released bacitracin mass, M, in mg. Parameters a and b are to be calculated during the fitting process. Other versions of the exponent were tested with poor results.

The Korsmeyer–Peppas model, given in Equation (5), has other two parameters that need to be obtained, i.e., k and n.

$$M = M_{\infty} \cdot k \cdot t^n \quad (5)$$

As a peculiar feature, the K-P model could use only 60% of datasets in order to be effective [89] as compared to the W model. The effectiveness of using 60% of datasets as compared to 100% for the K-P model was also assessed.

Pairs of parameters (a, b) and (k, n), for the two models (W and K-P) were obtained by using the Generalized Reduced Gradient method; determination coefficients R^2 between fitted and experimental results were also calculated and used to compare effectiveness. Natural logarithmic regression (LnR) was also used to evaluate whether a simpler, yet more effective equation could be identified.

3.2.8. Characterization of Samples

Transmission Electron Microscopy (TEM) was used to provide information about the particle size and morphology of the material. The instrument used was a High-Resolution 80-200 TITAN THEMIS transmission microscope equipped with an Image Corrector 4 EDXS detectors in the column, manufactured by FEI (Hillsboro, OR, USA).

Scanning Electron Microscopy (SEM) was performed with a Inspect F50 microscope (FEI Company, Eindhoven, The Netherlands), and was equipped with a Schottky Field Emission source and a system capable of providing a vacuum in the sample chamber of 6×10^{-4} Pa. The acceleration voltage is controlled and varies from 200 V to 30 kV and the sample current is 200 nA. For analysis the samples were coated with a silver layer. For measurements the images were processed with ImageJ software, version 1.54g.

For confirmation of the specific cage structure of FDU-12, the X-ray diffraction (XRD) technique was used. The analysis was performed using CuKα PAN Analytical Empyrean powder diffractometer (PANalytical, Almelo, The Netherlands) in the Bragg–Brentano configuration. The measurement parameters included a 2θ angle range of 0.5–10, with a step size of 0.0256° and a time per step of one second.

The functional groups of samples were investigated with Fourier Transform-Infrared Spectroscopy (FT-IR) which was performed using a Nicolet iS50 FTIR with DTGS ATR detector (Thermo Fisher Scientific, Madison, WI, USA) by co-addition of 64 scans in the 4000–400 cm^{-1} interval, at a resolution of 8 cm^{-1}. The validation of the presence of bacitracin in samples can be obtained through this type of analysis.

For determination of zeta potential, the analyses were performed in triplicate. First, the samples were dispersed in pure water using an ultrasonic bath, then they were placed inside the measurement cell of DelsaMax Pro equipment (Backman Coulter, Brea, CA, USA).

The efficiency of the functionalization process and of the loading process can be estimated according to data obtained from thermogravimetric analysis combined with differential scanning calorimetry (TGA-DSC). The instrument used was a Netzsch 449C STA Jupiter (Netzsch-Gerätebau GmbH, Selb, Germany) that worked from room temperature up to 900 °C with a heating rate of 10 °C/min in dry air (10 mL/min).

https://doi.org/10.3390/molecules31020340

The textural properties were determined by N_2 physisorption measurements at 77 K using a NOVA 2200e-Quantachrome Analyzer porosimeter (Anton Paar, Graz, Austria). Pore volume was estimated from the quantity of absorbed N_2 at a relative pressure P/P_0 = 0.9. Pore-size distribution was obtained from the isotherm desorption by applying the Barett–Joyner–Halenda (BJH) method. The specific surface area was determined using the Brunauer–Emmett–Teller (BET) equation.

3.2.9. Evaluation of Antimicrobial Activity of Mesoporous Silica FDU-12 Loaded with Bacitracin Against *Staphylococcus* spp. Strains

The antimicrobial activity of mesoporous silica FDU-12 formulations loaded with bacitracin at different concentrations designated as B_0 (bacitracin only), B_1 (FDU-12 + bacitracin), B_4 (FDU-12–NH_2 + bacitracin), and BP (FDU-12–pNAM + bacitracin) was evaluated using both qualitative and quantitative antimicrobial assays.

Qualitative Screening of Mesoporous Silica FDU-12 Formulations Loaded with Bacitracin

The qualitative antimicrobial activity of mesoporous silica FDU-12 formulations loaded with bacitracin at different concentrations was evaluated. Antimicrobial screening was carried out against the reference strains *Staphylococcus aureus* ATCC 25923 and *Staphylococcus epidermidis* ATCC 12228, which were purchased from the American Type Culture Collection, (ATCC, Manassas, VA, USA), as well as eight clinical *S. aureus* isolates previously obtained and characterized from patients with hidradenitis suppurativa [91]. The evaluation was conducted using a modified disk diffusion method as previously described [92,93]. Standardized bacterial suspensions adjusted to a 0.5 McFarland standard (approximately 1.5×10^8 CFU/mL) were uniformly inoculated onto the surfaces of Mueller Hinton (MH) agar plates. Subsequently, 10 µL aliquots of each bacitracin-loaded FDU-12 formulation (100 mg/mL) were spotted onto the inoculated plates. Following incubation at 37 °C for 24 h under aerobic conditions, antimicrobial efficiency was evaluated by measuring the diameters of the resulting inhibition zones. The inhibition was expressed in arbitrary activity units (AU) and defined as follows: AU 0 = no inhibition (0 mm); AU 1 = weak inhibition (<10 mm); AU 2 = moderate inhibition (10–20 mm); and AU 3 = strong inhibition (21–30 mm).

Quantitative Evaluation of Antimicrobial Activity of Mesoporous Silica FDU-12 Formulations Loaded with Bacitracin

The quantitative assessment of the antimicrobial activity of tested formulations (B_0; B_1; B_4; and BP) was performed using the broth microdilution method in sterile 96-well microtiter plates. Serial twofold dilutions of each tested solution were prepared in Mueller–Hinton (MH) broth to yield final concentrations ranging from 50 to 0.09 mg/mL. A standardized bacterial suspension adjusted to 0.5 McFarland standard (1.5×10^8 CFU/mL) was inoculated into each well to obtain a final inoculum representing 10% of the total well volume (100 µL). Plates were incubated at 37 °C for 24 h under aerobic conditions, and bacterial growth was measured spectrophotometrically at 620 nm (Thermo Scientific™ Multiskan™ GO). The minimum inhibitory concentration (MIC) was defined as the lowest concentration, showing complete growth inhibition. MIC values were obtained from triplicate assays, corrected for blanks, and expressed as mean ± standard deviation.

Evaluation of the Effect of Mesoporous Silica FDU-12 Formulations Loaded with Bacitracin on Microbial Adherence to an Inert Substratum

The effect of bacitracin-loaded FDU-12, FDU-12–NH_2, and FDU-12–pNAM formulations on the adherence capacity of microbial strains to an inert substratum was evaluated

https://doi.org/10.3390/molecules31020340

using the crystal violet microtiter plate assay. The percentage of microbial adherence inhibition (%MAI) was calculated according to the following formula, Equation (6):

$$\%\text{MAI} = \frac{(As - Ablank)}{(Ac - Ablank)} \times 100 \quad (6)$$

where As is the absorbance at 490 nm of treated samples, and Ac is the absorbance at 490 nm of the control [94].

Evaluation of the Influence of Bacitracin and Bacitracin–FDU-12 Derivatives on the Modulation of Soluble Virulence Factors

The effect of bacitracin and FDU-12, FDU-12–NH_2, and FDU-12–pNAM loaded with bacitracin at different concentrations on the production of soluble virulence factors was investigated as previously described [95,96]. Microbial strains were cultivated in the presence of sub-inhibitory concentrations (MIC/2 and MIC/4) of each formulation on differential solid media supplemented with 5% sheep blood, 2.5% egg yolk, 1% starch, 1% Tween 80, and 15% soluble casein, to evaluate the modulation of virulence factor production, including hemolysins, lecithinase, amylase, lipase, and caseinase. The influence on virulence factor secretion was quantified according to the following relationship expressed by Equation (7):

$$\text{Inhibition } \% = \frac{(D2 - C2)}{(D1 - C1)} \times 100 \quad (7)$$

where C1—diameter of culture spot untreated with B and FDU-12/FDU-12-NH_2/FDU-12-pNAM loaded with B—control; D1—the diameter of the clear/precipitated zone around the culture spot untreated with B and FDU-12/FDU-12-NH_2/FDU-12-pNAM loaded with B-control; C2—diameter of culture spot treated with B and FDU-12/FDU-12-NH_2/FDU-12-pNAM loaded with B—sample; and D2—the diameter of the clear/precipitated zone around the culture spot treated with MIC/2 of B and FDU-12/FDU-12-NH_2/FDU-12-pNAM loaded with B—sample.

Statistical Analysis

The results obtained from antimicrobial activity, anti-adherence, and virulence modulation assays were analyzed using GraphPad Prism version 10.0.0 for Windows (GraphPad Software, Boston, MA, USA, www.graphpad.com). Data are presented as mean ± standard deviation (SD). Statistical significance was assessed using two-way ANOVA followed by Dunnetts multiple comparison test, with $p < 0.05$ considered statistically significant.

4. Conclusions

FDU-12 was prepared and modified with two functionalization agents, aminopropyltriethoxysilane and poly(N-acryloyl-morpholine). Starting from these three supports, the loading of the bacitracin was performed and the release was evaluated considering two different simulated body fluids with same components but slightly different pH (pH = 7.4—standard and pH = 6.9—slightly acidic, conditions which can simulate infections) and found out that the surface modification can affect the release behavior, these systems being pH-sensitive.

Bacitracin exhibited strong antimicrobial activity against both reference and clinical *Staphylococcus* strains, while its incorporation into mesoporous silica FDU-12 derivatives maintained or slightly modulated this effect depending on the functionalization. The bacitracin-loaded FDU-12 formulations, particularly FDU-12–pNAM and FDU-12–NH_2, demonstrated notable anti-adherence and biofilm inhibitory properties, though their effi-

https://doi.org/10.3390/molecules31020340

cacy was strain and concentration-dependent. Exposure to sub-inhibitory concentrations revealed variable modulation of soluble virulence factors, with some formulations reducing hemolysin, lipase, and amylase production, while others induced mild stimulatory effects in certain isolates. Overall, mesoporous silica carriers preserved bacitracins antimicrobial potency and enhanced its anti-biofilm potential, but sub-inhibitory exposure may differentially influence bacterial virulence expression, underscoring the importance of formulation selection and dosage optimization in therapeutic applications.

Supplementary Materials: The following supporting information can be downloaded at: https://www.mdpi.com/article/10.3390/molecules31020340/s1, Table S1: Chromatographic conditions of HPLC-DAD method.; Table S2: The influence of Bacitracin and Bacitracin–FDU-12 formulations at the corre-sponding subinhibitory MIC/2 and MIC/4 concentrations on lecithinase production in the selected *S. aureus* ATCC 25923 strain; Table S3: The influence of Bacitracin and Bacitracin–FDU-12 formula-tions at the corresponding subinhibitory MIC/2 and MIC/4 concentrations on lecithinase produc-tion in the selected clinical *S. aureus* 68 strain; Table S4: The influence of Bacitracin and Bacitracin–FDU-12 formulations at the corresponding subinhibitory MIC/2 and MIC/4 concentrations on le-cithinase production in the selected clinical *S. aureus* 32 strain; Table S5: The influence of Bacitracin and Bacitracin–FDU-12 formulations at the corresponding subinhibitory MIC/2 and MIC/4 con-centrations on lecithinase production in the selected clinical *S. aureus* 59, *S. aureus* 60, *S. aureus* 100 strain; Table S6: The influence of Bacitracin and Bacitracin–FDU-12 formulations at the corresponding subinhibitory MIC/2 and MIC/4 concentrations on caseinase production in the selected *S. aureus* strains; Table S7: The influence of Bacitracin and Bacitracin–FDU-12 formulations at the corresponding subinhibitory MIC/2 and MIC/4 concentrations on caseinase production in the selected *S. aureus* 68 strain; Table S8: The in-fluence of Bacitracin and Bacitracin–FDU-12 formulations at the corresponding subinhibitory MIC/2 and MIC/4 concentrations on caseinase production in the selected *S. epidermidis* ATCC 12228 strain; Table S9: The influence of Bacitracin and Bacitracin–FDU-12 formulations at the corresponding subinhibitory MIC/2 and MIC/4 concentrations on amylase production in the selected *S. aureus* 60, *S. aureus* 100 strain; Table S10: The influence of Bacitracin and Bacitracin–FDU-12 formulations at the corresponding subinhibitory MIC/2 and MIC/4 concentrations on amylase production in the selected *S. aureus* ATCC 25923, *S. epidermidis* ATCC 12228, *S. aureus* 30, *S. aureus* 32, *S. aureus* 39, *S. aureus* 44, *S. aureus* 59, *S. aureus* 60 strains; Table S11: The influence of Bacitracin and Bacitracin–FDU-12 formulations at the corresponding subinhibitory MIC/2 and MIC/4 concentrations on lipase production in the selected *S. aureus* ATCC 25923, *S. epidermidis* ATCC 12228, *S. aureus* 32, *S. aureus* 39, *S. aureus* 44, *S. aureus* 59, *S. aureus* 60, *S. aureus* 100 strains; Table S12: The influence of Bacitracin and Bacitracin–FDU-12 formulations at the corresponding subinhibitory MIC/2 and MIC/4 concentrations on lipase production in the selected *S. aureus* 68 strain; Table S13: The influence of Bacitracin and Bacitracin–FDU-12 formulations at the corresponding subinhibitory MIC/2 and MIC/4 concentrations on hemolysin production in the selected *S. aureus* ATCC 25923, *S. aureus* 30, *S. aureus* 32, *S. aureus* 39, *S. aureus* 44, *S. aureus* 59, *S. aureus* 60, *S. aureus* 68, *S. aureus* 100 strains.

Author Contributions: Conceptualization, D.A.V. and A.F.; methodology, A.F. and D.F.; validation, D.A.V., D.F. and A.F.; formal analysis, D.A.V., O.C.O., B..V., L.M., L.-A.M., C.C., O.-M.M., A.-V.S., G.V., R.D.T., A.-M.A., R.P., A..D., M.-M.M., Z.D.G. and I.G.-B.; investigation, D.A.V., O.C.O., B..V., L.M., L.-A.M., C.C., O.-M.M., A.-V.S., G.V., R.D.T., A.-M.A., R.P., A..D., M.-M.M., Z.D.G. and I.G.-B.; resources, A.F. and D.F.; data curation, D.A.V., O.C.O., B..V., L.M., L.-A.M., C.C., O.-M.M., A.-V.S., G.V., R.D.T., A.-M.A., R.P., A..D., M.-M.M. and I.G.-B.; writing—original draft preparation, D.A.V.; writing—review and editing, A.F., A.-M.A., I.G.-B. and D.F.; visualization, D.A.V. and A.F.; supervision A.F. and D.F. All authors have read and agreed to the published version of the manuscript.

Funding: The APC was funded by the National University of Science and Technology POLITEHNICA Bucharest and the University of Bucharest.

Institutional Review Board Statement: This study was conducted in accordance with the Declaration of Helsinki and approved by the Ethics Commission of the Elias University Emergency Hospital, Bucharest (no.6081/2025-10-24).

Informed Consent Statement: Informed consent was obtained from all subjects involved in the study.

Data Availability Statement: The research date will be available upon request.

Acknowledgments: This research was supported by UEFISCDI through the projects Nanostructured Bone Grafts with Predetermined Properties CollNanoBone project number 29ROMD/20.05.2024 and by the project PN-IV-P7-7.1-PED-2024-2249 (9PED/2025). Most of the analyses were realized within the CNMN IOSIN infrastructure funded by the Romanian Government via the Ministry of Research and Education.

Conflicts of Interest: The authors declare no conflicts of interest.

References

1. FAO; WHO; UNEP. *Antimicrobial Resistance and the United Nations Sustainable Development Cooperation Framework: Guidance for United Nations Country Teams*; FAO: Rome, Italy, 2021; p. 24.
2. Adebisi, Y.A.; Ogunkola, I.O. The global antimicrobial resistance response effort must not exclude marginalised populations. *Trop. Med. Health* **2023**, *51*, 33. [CrossRef] [PubMed]
3. Monk, E.J.M.; Jones, T.P.W.; Bongomin, F.; Kibone, W.; Nsubuga, Y.; Ssewante, N.; Muleya, I.; Nsenga, L.; Rao, V.B.; van Zandvoort, K. Antimicrobial resistance in bacterial wound, skin, soft tissue and surgical site infections in Central, Eastern, Southern and Western Africa: A systematic review and meta-analysis. *PLoS Glob. Public Health* **2024**, *4*, e0003077. [CrossRef] [PubMed]
4. Moritz, M.; Geszke-Moritz, M. Mesoporous Materials as Elements of Modern Drug Delivery Systems for Anti-Inflammatory Agents: A Review of Recent Achievements. *Pharmaceutics* **2022**, *14*, 1542. [CrossRef]
5. Beck, J.S.; Vartuli, J.C.; Roth, W.J.; Leonowicz, M.E.; Kresge, C.T.; Schmitt, K.D.; Chu, C.T.W.; Olson, D.H.; Sheppard, E.W.; McCullen, S.B.; et al. A New Family of Mesoporous Molecular-Sieves Prepared with Liquid-Crystal Templates. *J. Am. Chem. Soc.* **1992**, *114*, 10834–10843. [CrossRef]
6. Inagaki, S.; Fukushima, Y.; Kuroda, K. Synthesis of Highly Ordered Mesoporous Materials from a Layered Polysilicate. *J. Chem. Soc. Chem. Comm.* **1993**, 680–682. [CrossRef]
7. Vallet-Regi, M.; Rámila, A.; del Real, R.P.; Pérez-Pariente, J. A new property of MCM-41: Drug delivery system. *Chem. Mater.* **2001**, *13*, 308–311. [CrossRef]
8. Brezoiu, A.M.; Prundeanu, M.; Berger, D.; Deaconu, M.; Matei, C.; Oprea, O.; Vasile, E.; Negreanu-Pîrjol, T.; Muntean, D.; Danciu, C. Properties of *Salvia officinalis* L. and *Thymus serpyllum* L. Extracts Free and Embedded into Mesopores of Silica and Titania Nanomaterials. *Nanomaterials* **2020**, *10*, 820. [CrossRef]
9. Petrisor, G.; Motelica, L.; Ficai, D.; Trusca, R.D.; Surdu, V.A.; Voicu, G.; Oprea, O.C.; Ficai, A.; Andronescu, E. New Mesoporous Silica Materials Loaded with Polyphenols: Caffeic Acid, Ferulic Acid and p-Coumaric Acid as Dietary Supplements for Oral Administration. *Materials* **2022**, *15*, 7982. [CrossRef]
10. Dolete, G.; Purcareanu, B.; Mihaiescu, D.E.; Ficai, D.; Oprea, O.C.; Bîrca, A.C.; Chircov, C.; Vasile, B.S.; Vasilievici, G.; Ficai, A.; et al. A Comparative Loading and Release Study of Vancomycin from a Green Mesoporous Silica. *Molecules* **2022**, *27*, 5589. [CrossRef]
11. Koneru, B.; Shi, Y.; Wang, Y.C.; Chavala, S.H.; Miller, M.L.; Holbert, B.; Conson, M.; Ni, A.; Di Pasqua, A.J. Tetracycline-Containing MCM-41 Mesoporous Silica Nanoparticles for the Treatment of *Escherichia coli*. *Molecules* **2015**, *20*, 19690–19698. [CrossRef]
12. Najafi, A.; Khosravian, P.; Validi, M.; Daryasari, M.P.; Drees, F.; Gholipour, A. Antimicrobial action of mesoporous silica nanoparticles loaded with cefepime and meropenem separately against multidrug-resistant (MDR). *J. Drug Deliv. Sci. Tec.* **2021**, *65*, 102757. [CrossRef]
13. Nairi, V.; Medda, L.; Monduzzi, M.; Salis, A. Adsorption and release of ampicillin antibiotic from ordered mesoporous silica. *J. Colloid Interf. Sci.* **2017**, *497*, 217–225. [CrossRef] [PubMed]
14. Marcelo, G.A.; Duarte, M.P.; Oliveira, E. Gold@mesoporous silica nanocarriers for the effective delivery of antibiotics and bypassing of β-lactam resistance. *SN Appl. Sci.* **2020**, *2*, 1354. [CrossRef]

15. Berger, D.; Bajenaru, L.; Nastase, S.; Mitran, R.A.; Munteanu, C.; Matei, C. Influence of structural, textural and surface properties of mesostructured silica and aluminosilicate carriers on aminoglycoside uptake and in vitro delivery. *Microporous Mesoporous Mater.* **2015**, *206*, 150–160. [CrossRef]
16. Subramaniam, S.; Thomas, N.; Gustafsson, H.; Jambhrunkar, M.; Kidd, S.P.; Prestidge, C.A. Rifampicin-Loaded Mesoporous Silica Nanoparticles for the Treatment of Intracellular Infections. *Antibiotics* **2019**, *8*, 39. [CrossRef]
17. Volcanes Moreno, V.; Yohai, L.; Procaccini, R.; Pellice, S. Silver-functionalized mesoporous silica nanoparticle coatings: Optimal thermal stability and ionic activity for antimicrobial applications. *Colloids Surf. A Physicochem. Eng. Asp.* **2025**, *711*, 136387. [CrossRef]
18. Ghobadi, M.; Salehi, S.; Ardestani, M.T.S.; Mousavi-Khattat, M.; Shakeran, Z.; Khosravi, A.; Cordani, M.; Zarrabi, A. Amine-functionalized mesoporous silica nanoparticles decorated by silver nanoparticles for delivery of doxorubicin in breast and cervical cancer cells. *Eur. J. Pharm. Biopharm.* **2024**, *201*, 114349. [CrossRef]
19. Falahati, M.; Saboury, A.A.; Mamani, L.; Shafiee, A.; Rafieepour, H.A. The effect of functionalization of mesoporous silica nanoparticles on the interaction and stability of confined enzyme. *Int. J. Biol. Macromol.* **2012**, *50*, 1048–1054. [CrossRef]
20. Sevimli, F.; Ylmaz, A. Surface functionalization of SBA-15 particles for amoxicillin delivery. *Microporous Mesoporous Mater.* **2012**, *158*, 281–291. [CrossRef]
21. Lawal, U.; Kumar, N.; Samyuktha, R.; Gopi, A.; Robert, V.; Pugazhenthi, G.; Loganathan, S.; Valapa, R.B. Poly (lactic acid)/amine grafted mesoporous silica-based composite for food packaging application. *Int. J. Biol. Macromol.* **2024**, *277*, 134567. [CrossRef]
22. Gan, Q.; Zhu, J.; Yuan, Y.; Liu, H.; Qian, J.; Li, Y.; Liu, C. A dual-delivery system of pH-responsive chitosan-functionalized mesoporous silica nanoparticles bearing BMP-2 and dexamethasone for enhanced bone regeneration. *J. Mater. Chem. B* **2015**, *3*, 2056–2066. [CrossRef] [PubMed]
23. Hai, L.; Jia, X.; He, D.; Zhang, A.; Wang, T.; Cheng, H.; He, X.; Wang, K. DNA-Functionalized Hollow Mesoporous Silica Nanoparticles with Dual Cargo Loading for Near-Infrared-Responsive Synergistic Chemo-Photothermal Treatment of Cancer Cells. *ACS Appl. Nano Mater.* **2018**, *1*, 3486–3497. [CrossRef]
24. He, D.; He, X.; Wang, K.; Chen, M.; Cao, J.; Zhao, Y. Reversible stimuli-responsive controlled release using mesoporous silica nanoparticles functionalized with a smart DNA molecule-gated switch. *J. Mater. Chem.* **2012**, *22*, 14715–14721. [CrossRef]
25. Pandele, A.M.; Andronescu, C.; Ghebaur, A.; Garea, S.A.; Iovu, H. New Biocompatible Mesoporous Silica/Polysaccharide Hybrid Materials as Possible Drug Delivery Systems. *Materials* **2019**, *12*, 15. [CrossRef]
26. LaBauve, A.E.; Saada, E.A.; Jones, I.K.A.; Mosesso, R.; Noureddine, A.; Techel, J.; Gomez, A.; Collette, N.; Sherman, M.B.; Serda, R.E.; et al. Lipid-coated mesoporous silica nanoparticles for anti-viral applications via delivery of CRISPR-Cas9 ribonucleoproteins. *Sci. Rep.* **2023**, *13*, 6873. [CrossRef]
27. Costa-e-Sá, F.; Comís-Tuche, M.; Spuch, C.; Castanheira, E.M.S.; Veloso, S.R.S. Sequential release of drugs from dual-delivery plasmonic nanogels containing lipid-gated mesoporous silica-coated gold nanorods. *J. Drug Deliv. Sci. Tec.* **2024**, *96*, 105723. [CrossRef]
28. El-Feky, A.S.; Noor, N.A.; Mohammed, F.F.; Fahmy, H.M. Biodistribution and toxicity assessment of gallic acid (GA)-loaded mesoporous silica nanoparticles coated with lipid in male wistar rats: A comprehensive investigation. *J. Drug Deliv. Sci. Tec.* **2024**, *99*, 105970. [CrossRef]
29. Pandita, D.; Munjal, A.; Poonia, N.; Awasthi, R.; Kalonia, H.; Lather, V. Albumin-Coated Mesoporous Silica Nanoparticles of Docetaxel: Preparation, Characterization, and Pharmacokinetic Evaluation. *Assay Drug Dev. Technol.* **2021**, *19*, 226–236. [CrossRef]
30. Nguyen, C.T.; Webb, R.I.; Lambert, L.K.; Strounina, E.; Lee, E.C.; Parat, M.O.; McGuckin, M.A.; Popat, A.; Cabot, P.J.; Ross, B.P. Bifunctional Succinylated ε-Polylysine-Coated Mesoporous Silica Nanoparticles for pH-Responsive and Intracellular Drug Delivery Targeting the Colon. *ACS Appl. Mater. Interfaces* **2017**, *9*, 9470–9483. [CrossRef]
31. Mandal, T.; Beck, M.; Kirsten, N.; Lindén, M.; Buske, C. Targeting murine leukemic stem cells by antibody functionalized mesoporous silica nanoparticles. *Sci. Rep.* **2018**, *8*, 989. [CrossRef]
32. Tsai, C.-P.; Chen, C.-Y.; Hung, Y.; Chang, F.-H.; Mou, C.-Y. Monoclonal antibody-functionalized mesoporous silica nanoparticles (MSN) for selective targeting breast cancer cells. *J. Mater. Chem.* **2009**, *19*, 5737–5743. [CrossRef]
33. Bharti, C.; Nagaich, U.; Pal, A.K.; Gulati, N. Mesoporous silica nanoparticles in target drug delivery system: A review. *Int. J. Pharm. Investig.* **2015**, *5*, 124–133. [CrossRef] [PubMed]
34. Agosto, F.; Charreyre, M.-T.; Veron, L.; Llauro, M.-F.; Pichot, C. Kinetic Study of Free-Radical Solution Copoly- merization of N-Acryloylmorpholine with an Activated Ester-Type Monomer, N-Acryloxysuccinimide. *Macromol. Chem. Phys.* **2001**, *202*, 1689–1699. [CrossRef]
35. DAgosto, F.; Charreyre, M.-T.; Pichot, C. Side-Product of N-Acryloyloxysuccinimide Synthesis or Useful New Bifunctional Monomer? *Macromol. Biosci.* **2001**, *1*, 322–328.
36. Bruce, C. Surface Modification of Cellulose by Covalent Grafting and Physical Adsorption for Biocomposite Applications. Ph.D. Thesis, KTH Royal Institute of Technology, Stockholm, Sweeden, 2014.

37. Rani, G.U.; Mishra, S.; Sen, G.; Jha, U. Polyacrylamide grafted Agar: Synthesis and applications of conventional and microwave assisted technique. *Carbohydr. Polym.* **2012**, *90*, 784–791. [CrossRef]
38. Güven, O. Ionizing radiation: A versatile tool for nanostructuring of polymers. *Pure Appl. Chem.* **2016**, *88*, 1049–1061. [CrossRef]
39. Galos, J. Microwave processing of carbon fibre polymer composites: A review. *Polym. Polym. Compos.* **2021**, *29*, 151–162. [CrossRef]
40. Wang, Y.; Di, Y.; Shaobo, D.; He, Z.; Zhang, X.; Shi, J.; Lan, T. Study on initiating approach of (3-(tert-butylperoxy)propyl) trimethoxysilane on the polymerization of acrylonitrile as an initiator. *Des. Monomers Polym.* **2017**, *20*, 468–475. [CrossRef]
41. Metzler, M.; Chyliska, M.; Kaczmarek, H. Preparation and characteristics of nanosilver composite based on chitosan-graft-acrylic acid copolymer. *J. Polym. Res.* **2015**, *22*, 146. [CrossRef]
42. Fan, J.; Yu, C.; Gao, F.; Lei, J.; Tian, B.; Wang, L.; Luo, Q.; Tu, B.; Zhou, W.; Zhao, D. Cubic mesoporous silica with large controllable entrance sizes and advanced adsorption properties. *Angew. Chem.* **2003**, *42*, 3146–3150. [CrossRef]
43. Xu, B.; Li, S.; Shi, R.; Liu, H. Multifunctional mesoporous silica nanoparticles for biomedical applications. *Signal Transduct. Target. Ther.* **2023**, *8*, 435. [CrossRef]
44. Johnson, B.A.; Anker, H.; Meleney, F.L. Bacitracin: A New Antibiotic Produced by a Member of the B. Subtilis Group. *Science* **1945**, *102*, 376–377. [CrossRef] [PubMed]
45. Vardanyan, R.S.; Hruby, V.J. 32—Antibiotics. In *Synthesis of Essential Drugs*; Vardanyan, R.S., Hruby, V.J., Eds.; Elsevier: Amsterdam, The Netherlands, 2006; pp. 425–498.
46. Injectable bacitracin linked with nephrotoxicity and hypersensitivity. *React. Wkly.* **2021**, *1837*, 5. [CrossRef]
47. Grumezescu, A.M.; Ghitulica, C.D.; Voicu, G.; Huang, K.S.; Yang, C.H.; Ficai, A.; Vasile, B.S.; Grumezescu, V.; Bleotu, C.; Chifiriuc, M.C. New silica nanostructure for the improved delivery of topical antibiotics used in the treatment of staphylococcal cutaneous infections. *Int. J. Pharm.* **2014**, *463*, 170–176. [CrossRef] [PubMed]
48. Drapeau, G.; Petitclerc, E.; Toulouse, A.; Marceau, F. Dissociation of the antimicrobial activity of bacitracin USP from its reno-vascular effects. *Antimicrob. Agents Chemother.* **1992**, *36*, 955–961. [CrossRef]
49. Ao, H.; Duan, K.; Zhang, D.; Xun, X.; Feng, F.; Liu, H.; Li, J.; Li, Y.; Wan, Y. Biofunctionalized bacterial cellulose grafted with bacitracin for wound healing. *J. Mater. Sci.* **2024**, *59*, 10987–10997. [CrossRef]
50. Zhang, Z.; Guo, J.; He, Y.; Han, J.; Chen, M.; Zheng, Y.; Zhang, S.; Guo, S.; Shi, X.; Yang, J. An injectable double network hydrogel with hemostasis and antibacterial activity for promoting multidrug-resistant bacteria infected wound healing. *Biomater. Sci.* **2022**, *10*, 3268–3281. [CrossRef]
51. Martínez Carmona, M.; Ho, Q.; Morand, J.; Garcia, A.; Ortega-Forte, E.; Erthal, L.; Ruiz-Hernandez, E.; Santana, M.; Ruiz, J.; Vallet-Regí, M.; et al. Amino-Functionalized Mesoporous Silica Nanoparticle-Encapsulated Octahedral Organoruthenium Complex as an Efficient Platform for Combatting Cancer. *Inorg. Chem.* **2020**, *59*, 10275–10284. [CrossRef]
52. Musso, G.; Bottinelli, E.; Celi, L.; Magnacca, G.; Berlier, G. Influence of surface functionalization on the hydrophilic character of mesoporous silica nanoparticles. *Phys. Chem. Chem. Phys.* **2015**, *17*, 13882–13894. [CrossRef]
53. Neumann-Tran, T.; López-Iglesias, C.; Navarro, L.; Quaas, E.; Achazi, K.; Biglione, C.; Klinger, D. Poly(N-acryloylmorpholine) Nanogels as Promising Materials for Biomedical Applications: Low Protein Adhesion and High Colloidal Stability. *ACS Appl. Polym. Mater.* **2023**, *5*, 7718–7732. [CrossRef]
54. Boussif, O.; Lezoualch, F.; Zanta, M.A.; Mergny, M.D.; Scherman, D.; Demeneix, B.; Behr, J.P. A versatile vector for gene and oligonucleotide transfer into cells in culture and in vivo: Polyethylenimine. *Proc. Natl. Acad. Sci. USA* **1995**, *92*, 7297–7301. [CrossRef]
55. Yezhelyev, M.V.; Qi, L.; ORegan, R.M.; Nie, S.; Gao, X. Proton-sponge coated quantum dots for siRNA delivery and intracellular imaging. *J. Am. Chem. Soc.* **2008**, *130*, 9006–9012. [CrossRef] [PubMed]
56. Lee, Y.; Miyata, K.; Oba, M.; Ishii, T.; Fukushima, S.; Han, M.; Koyama, H.; Nishiyama, N.; Kataoka, K. Charge-conversion ternary polyplex with endosome disruption moiety: A technique for efficient and safe gene delivery. *Angew. Chem. Int. Ed.* **2008**, *47*, 5163–5166. [CrossRef] [PubMed]
57. Pochapski, D.J.; Carvalho dos Santos, C.; Leite, G.W.; Pulcinelli, S.H.; Santilli, C.V. Zeta Potential and Colloidal Stability Predictions for Inorganic Nanoparticle Dispersions: Effects of Experimental Conditions and Electrokinetic Models on the Interpretation of Results. *Langmuir ACS J. Surf. Colloids* **2021**, *37*, 13379–13389. [CrossRef] [PubMed]
58. Cao, Z.; Duan, A.; Zhao, Z.; Li, J.; Wei, Y.; Jiang, G.; Liu, J. A simple two-step method to synthesize the well-ordered mesoporous composite Ti-FDU-12 and its application in the hydrodesulfurization of DBT and 4,6-DMDBT. *J. Mater. Chem. A* **2014**, *2*, 19738–19749. [CrossRef]
59. Dong, H.; Yang, H.; Du, Q.; Zhang, T.; Liu, Q. Ultrasonication-assisted Synthesis of α, β-Unsaturated Compounds Catalyzed by Amino-functionalized FDU-12 Catalyst. *ChemistrySelect* **2019**, *4*, 1463–1469. [CrossRef]
60. Ghaforinejad, H.; Mazaheri, H.; Hassani Joshaghani, A.; Marjani, A. Study on novel modified large mesoporous silica FDU-12/polymer matrix nanocomposites for adsorption of Pb(II). *PLoS ONE* **2021**, *16*, e0245583. [CrossRef]

61. Sakamoto, Y.; Han, L.; Che, S.; Terasaki, O. Structural Analyses of Intergrowth and Stacking Fault in Cage-Type Mesoporous Crystals. *Chem. Mater.* **2009**, *21*, 223–229. [CrossRef]
62. Bavnhøj, C.G.; Knopp, M.M.; Madsen, C.M.; Löbmann, K. The role interplay between mesoporous silica pore volume and surface area and their effect on drug loading capacity. *Int. J. Pharm. X* **2019**, *1*, 100008. [CrossRef]
63. Sing, K. Reporting Physisorption Data for Gas/Solid Systems with Special Reference to the Determination of Surface Area and Porosity. *Pure Appl. Chem.* **1982**, *54*, 2201–2218. [CrossRef]
64. Carmona, D.; Balas, F.; Santamaria, J. Pore ordering and surface properties of FDU-12 and SBA-15 mesoporous materials and their relation to drug loading and release in aqueous environments. *Mater. Res. Bull.* **2014**, *59*, 311–322. [CrossRef]
65. Meoto, S.; Kent, N.; Nigra, M.M.; Coppens, M.-O. Effect of stirring rate on the morphology of FDU-12 mesoporous silica particles. *Microporous Mesoporous Mater.* **2017**, *249*, 61–66. [CrossRef]
66. Mitran, R.-A.; Lincu, D.; Berger, D.; Matei, C. FDU-12 cubic mesoporous silica as matrix for phase change materials using bismuth or stearic acid. *J. Therm. Anal. Calorim.* **2022**, *147*, 14097–14106. [CrossRef]
67. Alahmadi, S.M.; Mohamad, S.; Maah, M.J. Synthesis and characterization of mesoporous silica functionalized with calix[4]arene derivatives. *Int. J. Mol. Sci.* **2012**, *13*, 13726–13736. [CrossRef] [PubMed]
68. Al-Thubiani, A.S.A.; Maher, Y.A.; Fathi, A.; Abourehab, M.A.S.; Alarjah, M.; Khan, M.S.A.; Al-Ghamdi, S.B. Identification and characterization of a novel antimicrobial peptide compound produced by Bacillus megaterium strain isolated from oral microflora. *Saudi Pharm. J.* **2018**, *26*, 1089–1097. [CrossRef]
69. Petrior, G.; Motelica, L.; Ficai, D.; Ilie, C.-I.; Truc, R.D.; Surdu, V.-A.; Oprea, O.-C.; Mr, A.-L.; Vasilievici, G.; Semenescu, A.; et al. Increasing Bioavailability of Trans-Ferulic Acid by Encapsulation in Functionalized Mesoporous Silica. *Pharmaceutics* **2023**, *15*, 660. [CrossRef]
70. Rosenholm, J.M.; Czuryszkiewicz, T.; Kleitz, F.; Rosenholm, J.B.; Lindén, M. On the nature of the Brønsted acidic groups on native and functionalized mesoporous siliceous SBA-15 as studied by benzylamine adsorption from solution. *Langmuir ACS J. Surf. Colloids* **2007**, *23*, 4315–4323. [CrossRef]
71. Arsenie, L.V.; Hausig, F.; Kellner, C.; Brendel, J.C.; Lacroix-Desmazes, P.; Ladmiral, V.; Catrouillet, S. Stimuli-Responsive Thiomorpholine Oxide-Derived Polymers with Tailored Hydrophilicity and Hemocompatible Properties. *Molecules* **2022**, *27*, 4233. [CrossRef]
72. Lindsay, J.A. Staphylococcus aureus genomics and the impact of horizontal gene transfer. *Int. J. Med. Microbiol.* **2014**, *304*, 103–109. [CrossRef]
73. Touaitia, R.; Mairi, A.; Ibrahim, N.A.; Basher, N.S.; Idres, T.; Touati, A. Staphylococcus aureus: A Review of the Pathogenesis and Virulence Mechanisms. *Antibiotics* **2025**, *14*, 470. [CrossRef]
74. de Jong, N.W.M.; van Kessel, K.P.M.; van Strijp, J.A.G. Immune Evasion by *Staphylococcus aureus*. *Microbiol. Spectr.* **2019**, *7*. [CrossRef]
75. Moormeier, D.E.; Bayles, K.W. Staphylococcus aureus biofilm: A complex developmental organism. *Mol. Microbiol.* **2017**, *104*, 365–376. [CrossRef] [PubMed]
76. Jenul, C.; Horswill, A.R. Regulation of *Staphylococcus aureus* Virulence. *Microbiol. Spectr.* **2019**, *7*. [CrossRef] [PubMed]
77. Cheung, A.L.; Zhang, G. Global regulation of virulence determinants in Staphylococcus aureus by the SarA protein family. *Front. Biosci. A J. Virtual Libr.* **2002**, *7*, d1825–d1842. [CrossRef]
78. Suzuki, M.; Yamada, K.; Nagao, M.; Aoki, E.; Matsumoto, M.; Hirayama, T.; Yamamoto, H.; Hiramatsu, R.; Ichiyama, S.; Iinuma, Y. Antimicrobial ointments and methicillin-resistant *Staphylococcus aureus* USA300. *Emerg. Infect. Dis.* **2011**, *17*, 1917–1920. [CrossRef]
79. Castillo, R.R.; Vallet-Regi, M. Recent Advances Toward the Use of Mesoporous Silica Nanoparticles for the Treatment of Bacterial Infections. *Int. J. Nanomed.* **2021**, *16*, 4409–4430. [CrossRef]
80. Elawady, R.; Aboulela, A.G.; Gaballah, A.; Ghazal, A.A.; Amer, A.N. Antimicrobial Sub-MIC induces Staphylococcus aureus biofilm formation without affecting the bacterial count. *BMC Infect. Dis.* **2024**, *24*, 1065. [CrossRef]
81. Hodille, E.; Rose, W.; Diep, B.A.; Goutelle, S.; Lina, G.; Dumitrescu, O. The Role of Antibiotics in Modulating Virulence in Staphylococcus aureus. *Clin. Microbiol. Rev.* **2017**, *30*, 887–917. [CrossRef]
82. Colilla, M.; Vallet-Regí, M. Targeted Stimuli-Responsive Mesoporous Silica Nanoparticles for Bacterial Infection Treatment. *Int. J. Mol. Sci.* **2020**, *21*, 8605. [CrossRef]
83. Yu, T.; Zhang, H.; Yan, X.; Chen, Z.; Zou, X.; Oleynikov, P.; Zhao, D. Pore structures of ordered large cage-type mesoporous silica FDU-12s. *J. Phys. Chem. B* **2006**, *110*, 21467–21472. [CrossRef]
84. Alazzawi, H.F.; Salih, I.K.; Albayati, T.M. Drug delivery of amoxicillin molecule as a suggested treatment for COVID-19 implementing functionalized mesoporous SBA-15 with aminopropyl groups. *Drug Deliv.* **2021**, *28*, 856–864. [CrossRef] [PubMed]
85. Petrisor, G.; Ficai, D.; Motelica, L.; Trusca, R.; Alexandra Catalina, B.; Vasile, B.; Voicu, G.; Oprea, O.; Semenescu, A.; Ficai, A.; et al. Mesoporous Silica Materials Loaded with Gallic Acid with Antimicrobial Potential. *Nanomaterials* **2022**, *12*, 1648. [CrossRef]

86. Yilmaz, B.; Pazarceviren, A.E.; Tezcaner, A.; Evis, Z. Historical development of simulated body fluids used in biomedical applications: A review. *Microchem. J.* **2020**, *155*, 104713. [CrossRef]
87. Chrusch, C.; Bautista, E.; Jacobs, H.K.; Light, R.B.; Bose, D.; Duke, K.; Mink, S.N. Blood pH level modulates organ metabolism of lactate in septic shock in dogs. *J. Crit. Care* **2002**, *17*, 188–202. [CrossRef] [PubMed]
88. European Directorate for the Quality of Medicines. Monographs A-K, Bacitracin. In *European Pharmacopeia 10.0*; Council of Europe: Strasbourg, France, 2020; Volume 2, pp. 1913–1917.
89. Dash, S.; Murthy, P.N.; Nath, L.; Chowdhury, P. Kinetic modeling on drug release from controlled drug delivery systems. *Acta Pol. Pharm.* **2010**, *67*, 217–223.
90. Corsaro, C.; Neri, G.; Mezzasalma, A.M.; Fazio, E. Weibull Modeling of Controlled Drug Release from Ag-PMA Nanosystems. *Polymers* **2021**, *13*, 2897. [CrossRef]
91. Cucu, C.I.; Giurcăneanu, C.; Poenaru, E.; Popa, L.G.; Popa, M.I.; Chifiriuc, M.C.; Lazăr, V.; Holban, A.M.; Gheorghe-Barbu, I.; Muntean, A.A.; et al. Phenotypic and Genotypic Bacterial Virulence and Resistance Profiles in Hidradenitis Suppurativa. *Int. J. Mol. Sci.* **2025**, *26*, 3502. [CrossRef]
92. Corbu, V.M.; Georgescu, A.M.; Marinas, I.C.; Pericleanu, R.; Mogos, D.V.; Dumbrava, A.S.; Marinescu, L.; Pecete, I.; Vassu-Dimov, T.; Czobor Barbu, I.; et al. Phenotypic and Genotypic Characterization of Resistance and Virulence Markers in Candida spp. Isolated from Community-Acquired Infections in Bucharest, and the Impact of AgNPs on the Highly Resistant Isolates. *J. Fungi* **2024**, *10*, 563. [CrossRef]
93. Maximov, M.V.; Maximov, O.C.; Motelica, L.; Ficai, D.; Oprea, O.C.; Trusca, R.D.; Balahura, L.R.; Pericleanu, R.; Dumbrava, A.S.; Corbu, V.M.; et al. Comprehensive Evaluation of 45S5 Bioactive Glass Doped with Samarium: From Synthesis and Physical Properties to Biocompatibility and Antimicrobial Activity. *Coatings* **2025**, *15*, 404. [CrossRef]
94. Corbu, V.M.; Gheorghe, I.; Marinas, I.C.; Geana, E.I.; Moza, M.I.; Csutak, O.; Chifiriuc, M.C. Demonstration of Allium sativum Extract Inhibitory Effect on Biodeteriogenic Microbial Strain Growth, Biofilm Development, and Enzymatic and Organic Acid Production. *Molecules* **2021**, *26*, 7195. [CrossRef]
95. Gheorghe-Barbu, I.; Corbu, V.M.; Vrancianu, C.O.; Marinas, I.C.; Popa, M.; Dumbrava, A.S.; Nita-Lazar, M.; Pecete, I.; Muntean, A.A.; Popa, M.I.; et al. Phenotypic and Genotypic Characterization of Recently Isolated Multidrug-Resistant Clinical and Aquatic Strains and Demonstration of Silver Nanoparticle Potency. *Microorganisms* **2023**, *11*, 2439. [CrossRef]
96. Trusca, B.S.; Gheorghe-Barbu, I.; Manea, M.; Ianculescu, E.; Barbu, I.C.; Marutescu, L.G.; Ditu, L.M.; Chifiriuc, M.C.; Lazar, V. Snapshot of Phenotypic and Molecular Virulence and Resistance Profiles in Multidrug-Resistant Strains Isolated in a Tertiary Hospital in Romania. *Pathogens* **2023**, *12*, 609. [CrossRef]

Disclaimer/Publisher's Note: The statements, opinions and data contained in all publications are solely those of the individual author(s) and contributor(s) and not of MDPI and/or the editor(s). MDPI and/or the editor(s) disclaim responsibility for any injury to people or property resulting from any ideas, methods, instructions or products referred to in the content.

molecules

MDPI

Article

Biodistribution of Tc-99m-Labeled Solid Lipid Nanoparticles and Evaluation of Their Possibility as a Radiopharmaceutical

Hayrettin Eroglu [1,*], Arif Kürsad Ayan [2] and Ayse Yenilmez [3]

[1] Department of Chemical Engineering, Faculty of Engineering and Architecture, Erzurum Technical University, 25110 Erzurum, Türkiye
[2] Department of Nuclear Medicine, Samsun Medicana Hospital, 55100 Samsun, Türkiye; ayankursad@gmail.com
[3] Department of Mathematics and Science Education, Faculty of Education, Van Yüzüncü Yıl University, 65080 Van, Türkiye; ayseyenilmez@yyu.edu.tr
* Correspondence: hayrettin.eroglu@erzurum.edu.tr; Tel.: +90-0442-4445388-2696

Abstract

Solid lipid nanoparticles (SLNs) are submicron colloidal systems widely investigated as drug carriers; however, their intrinsic biodistribution properties are also critical when SLNs are considered for diagnostic imaging. In the present proof-of-concept study, drug-free SLNs were evaluated exclusively as a radiolabeled imaging agent rather than as a drug delivery system. SLNs were radiolabeled with Technetium-99m (^{99m}Tc), and their in vivo biodistribution was investigated using gamma camera imaging, ex vivo organ counting, and confocal microscopy. SLNs were prepared by a microemulsion–low-temperature solidification method and characterized by dynamic light scattering (DLS), scanning electron microscopy (SEM), and differential scanning calorimetry (DSC). Radiolabeling efficiency was determined by instant thin-layer chromatography (ITLC) and exceeded 95%. Following intravenous administration in a rabbit model, dynamic scintigraphic imaging demonstrated predominant uptake in the liver and spleen. These findings were quantitatively confirmed by ex vivo biodistribution analysis at 4 h post-injection and qualitatively supported by confocal microscopy of liver and spleen tissues. The results indicate that ^{99m}Tc-labeled SLNs behave as RES-targeting radiocolloids and may serve as potential agents for liver–spleen scintigraphy.

Keywords: solid lipid nanoparticle; Tc-99m; scintigraphy; drug delivery; biodistribution

1. Introduction

Molecular imaging is pivotal in contemporary nuclear medicine, facilitating noninvasive viewing of physiological and functional processes in vivo. Scintigraphic techniques depend on the preferential accumulation of radiopharmaceuticals in specific organs, with imaging quality influenced by the target-to-background activity ratio. Conventional radiocolloids utilized for liver–spleen scintigraphy, despite their extensive clinical application, exhibit various drawbacks, such as diverse particle properties, inadequate control over biodistribution, and constrained possibilities for systematic physicochemical modification. As a result, there is persistent interest in creating alternative nanoscale imaging agents that integrate reliable in vivo behavior with advantageous safety and imaging characteristics [1–5].

Recently, nanoparticle-based systems have arisen as interesting platforms for bioimaging owing to their adjustable size, surface properties, and interactions with biological

systems. SLNs consist of physiological lipids and are distinguished by their great biocompatibility, low toxicity, and colloidal stability. Although SLNs have been thoroughly examined as drug delivery vehicles, their inherent biodistribution characteristics—regardless of any encapsulated drug—have garnered very little focus, especially concerning diagnostic nuclear imaging. The colloidal characteristics of SLNs and their tendency for absorption by the reticuloendothelial system (RES) indicate their potential suitability for applications necessitating targeted localization in the liver and spleen [6–10].

Technetium-99m (^{99m}Tc) is the predominant radionuclide utilized in nuclear medicine due to its advantageous physical characteristics, which encompass a 6 h half-life, ideal gamma emission energy (140 keV), extensive availability, and economic viability. Since technetium has chemically different oxidation states, it can be used in the design of various radiopharmaceuticals for its selective uptake in different organs of the body. The integration of gamma camera imaging with ^{99m}Tc-labeled nanoparticles facilitates real-time, non-invasive evaluation of biodistribution and organ uptake, rendering them exceptionally appealing for the assessment of innovative radiopharmaceutical platforms.

Liver–spleen scintigraphy is a recognized nuclear medicine procedure utilized for assessing hepatic and splenic disorders, relying on the localization of intravenously administered radiopharmaceuticals within the blood pool or reticuloendothelial system (RES) cells of the liver and spleen, subsequently detected by gamma cameras that capture emitted gamma radiation. In this context, SLNs have garnered heightened interest as radiolabeled nanoplatforms owing to their lipid-based composition, colloidal stability, and advantageous nano-bio interaction characteristics. Numerous studies have examined the biodistribution of radiolabeled SLNs employing various radionuclides, labeling methodologies, and administration routes. Inhaled ^{99m}Tc-HMPAO-labeled SLNs preferentially accumulated in lymph nodes, indicating their potential for lymphatic targeting, whereas drug-loaded SLNs radiolabeled with ^{99m}Tc or ^{64}Cu exhibited organ-specific uptake patterns, including accumulation in the brain and RES, thereby affirming their viability for diagnostic imaging [11–14]. Nonetheless, most of this research predominantly concentrated on SLNs as drug delivery vehicles, highlighting the biodistribution of the encapsulated drug rather than the in vivo dynamics of the carrier system itself. Comprehending the inherent biodistribution of SLNs is essential for both the precise interpretation of imaging outcomes and the logical design of nanoparticle-based systems for biomedical applications. Due to their low toxicity, advantageous surface characteristics, and colloidal structure, SLNs are especially appropriate for radiolabeling and reticuloendothelial system (RES)-based imaging. Their physicochemical properties indicate possible application as radiocolloidal agents for liver–spleen scintigraphy, commonly employed to assess organ morphology, localized lesions, metastatic involvement, residual splenic tissue, and congenital defects [15–23].

The aim of the present study is to assess SLNs as a radiopharmaceutical platform, independent of drug delivery factors. SLNs were radiolabeled with ^{99m}Tc, and their in vivo biodistribution was examined using gamma camera imaging, ex vivo organ biodistribution analysis, and confocal microscopy after intravenous delivery in a rabbit model. This study thoroughly evaluates the uptake of RES and imaging features of ^{99m}Tc-labeled SLNs, investigating their viability as radiocolloids for liver–spleen scintigraphy and establishing a basis for further optimization and translational assessment. In our prior research, curcumin- and silymarin-loaded SLNs radiolabeled with ^{99m}Tc were assessed as a drug delivery method; however, the current study diverges by concentrating on the biodistribution and imaging capabilities of the SLN carrier itself, independent of any therapeutic cargo.

https://doi.org/10.3390/molecules31040654

2. Results and Discussion

2.1. Characterization of the SLNs

Among the most important data used to determine the physicochemical properties of colloidal carrier systems are particle size and size distribution. Especially in carrier systems such as suspension and emulsion, the particle size of the product is a key determinant for developing a successful formulation in terms of physical–chemical stability and efficacy [24].

Since the size and surface charge of nanoparticles determine the path they take in the biological environment, it is crucial to study the characterization of these structures in detail. As shown in Figure 1, the SLNs exhibited an average particle size of 146.8 $\pm$ 6.2 nm. The polydispersity index is 0.554 $\pm$ 0.03, and the zeta potential is -16.4 ± 2.5 mV, indicating that the suspension consists of negatively charged (anionic) particles. Zeta potential is also an important parameter that affects the probability of recognition of particles by the RES (reticuloendothelial system) and the stability of the formulation [25–29]. Particle size, size distribution, and surface properties are acknowledged as the primary factors influencing the in vivo behavior of lipid-based nanocarriers after intravenous delivery. In this work, SLNs demonstrated a mean hydrodynamic diameter of 146.8 $\pm$ 6.2 nm, positioning them within the size range associated with expedited identification and sequestration by the reticuloendothelial system (RES). This observation aligns closely with classical SLN studies conducted by Mehnert and Mäder, as well as recent analyses compiled by Hallan et al. [30], which highlighted that lipid nanoparticles within the 100–200 nm range are effectively opsonized and eliminated by hepatic and splenic macrophages, rather than persisting in systemic circulation for extended periods. The elevated polydispersity index (PDI = 0.554 $\pm$ 0.03) indicates a heterogeneous particle population, typical of solid lipid nanoparticles (SLNs) produced using microemulsion-based, low-energy solidification methods. Britto et al. [31] established that low-energy approaches inherently provide wider size distributions than high-pressure homogenization while maintaining good reproducibility and biological relevance, especially for applications that do not necessitate prolonged circulation periods. Significantly, Danaei et al. [27] and later researchers have demonstrated that wider size distributions can improve phagocytic uptake by offering subpopulations of particles that are ideally sized for macrophage internalization. In this scenario, the observed PDI is not a constraint but rather a contributing factor to the robust RES targeting noted in vivo. Zeta potential examinations indicated a moderately negative surface charge of -16.4 ± 2.5 mV. According to the comprehensive analysis by Hallan et al., weakly negative lipid nanoparticles demonstrate increased serum protein adsorption, facilitating opsonization and subsequent macrophage-mediated elimination. Arroyo-Nogales et al. [32] also emphasized that nanoparticles devoid of steric shielding (e.g., PEGylation) are preferentially recognized by immune cells, especially macrophages, due to unobstructed surface–protein interactions. Consequently, the surface charge properties of the current SLNs elucidate their swift accumulation in the liver and spleen, distinctly distinguishing them from long-circulating stealth nanocarriers.

Scanning electron microscopy (SEM) was employed to qualitatively examine the surface morphology of the lyophilized SLN formulation. The SEM images (Figure 2) show particulate structures with relatively smooth surfaces, which are suggestive of a predominantly spherical morphology. SEM analysis verified the creation of distinct, mostly spherical nanoparticles with smooth surfaces, demonstrating effective lipid solidification and structural integrity post-lyophilization. This shape aligns with SLNs generated using microemulsion–solidification methods, as documented in formulation-centric research and current reviews of lipid nanocarrier structures.

https://doi.org/10.3390/molecules31040654

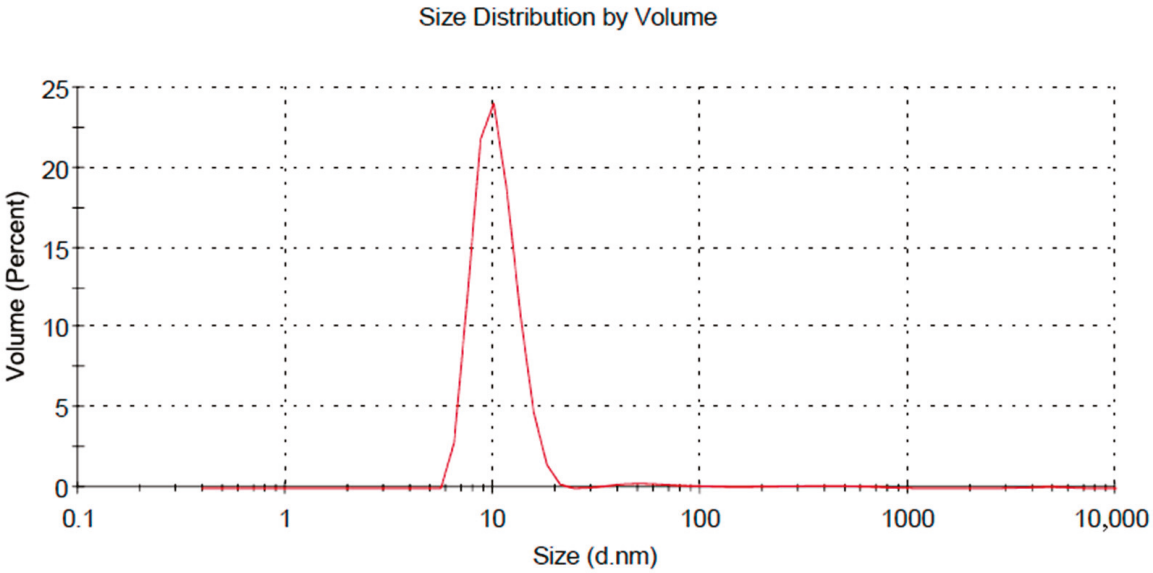

Figure 1. Particle size characterization of SLNs.

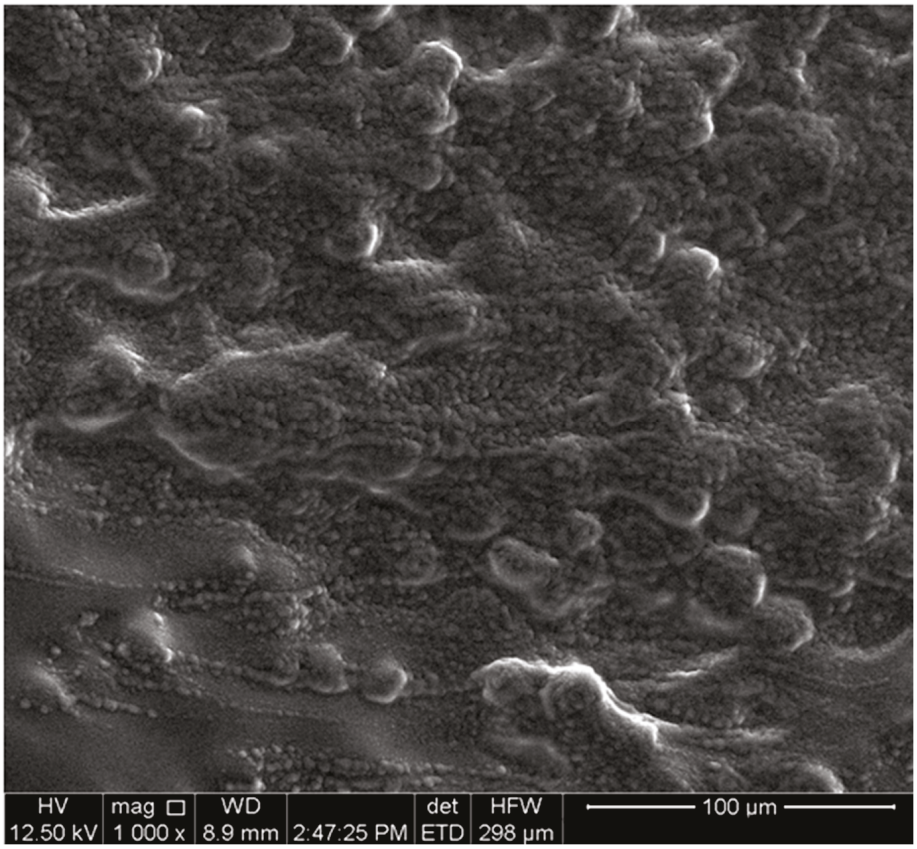

Figure 2. Scanning Electron Microscopy image (SEM) of the SLNs.

Polymorphism is defined as the formation of multiple crystal forms as a result of the same molecules being organized in different crystal arrangements. Although polymorphic structures are the same in terms of chemical composition, they can exhibit distinct differences in properties such as solubility, stability, and melting point. It is possible to find various polymorphic forms, such as α, β^{-}, and β, in SLNs prepared with low-melting lipids. Among these forms, the α structure tends to change first to the β^{-} form and then to the β form, which is more stable. The β polymorph is considered the most stable structure, while the β^{-} form is a metastable intermediate stage. The polymorphism observed in lipids,

https://doi.org/10.3390/molecules31040654

on the other hand, is mostly due to differences in the partial arrangement of hydrocarbon chains and different arrangements of fatty acid chains. The DSC method allows us to study the differences in the physical properties of lipids and polymorphic transformations by measuring the energy and temperature changes that occur during the phase changes of a substance. In the literature, it has been shown in many studies that the physical state and lipid structure of the drug encapsulated in nanoparticles have important effects on the release profile of the drug.

In this study, DSC analyses were performed for both prepared SLNs and pure Compritol®. Upon examination of Figure 3, a distinct endothermic peak was observed for Compritol® at approximately 79 °C. In contrast, colloidal SLNs have a lower melting temperature, and the endothermic peak occurs at 67 °C. This temperature drop suggests that the lipid matrix transitions to a more disordered, i.e., amorphous, structure when it transforms into a nanoparticle structure. Within the scope of radiolabeling studies, the efficiency of marking SLNs with ^{99m}Tc was determined as 95% ± 4 (n = 3) at room temperature using the ITLC method. This high marking efficiency reveals that SLNs can connect strongly and effectively with ^{99m}Tc. DSC research indicated a significant decrease in the melting temperature of Compritol® during nanoparticle production, signifying a partial loss of crystallinity and heightened structural disorder within the lipid matrix. Hallan et al. [30] highlighted that defective or partially amorphous lipid configurations are characteristic of SLNs and significantly influence molecular mobility, surface accessibility, and interactions with external agents. In radiopharmaceutical development, diminished crystallinity is beneficial since it enhances the binding of technetium complexes to the lipid matrix and minimizes the risk of radionuclide release during circulation.

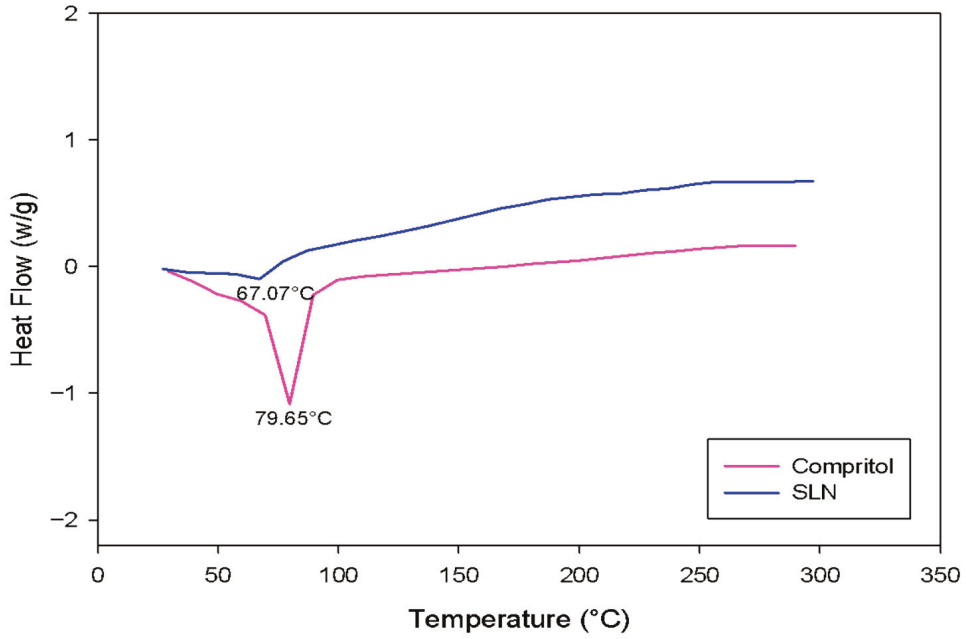

Figure 3. Differential calorimeter (DSC) thermogram curves of Compritol® and SLNs.

2.2. Radiolabeling

The radiolabeling efficiency surpassed 95%, validating the effective link between ^{99m}Tc and the SLN system. No substantial thyroid or stomach absorption was detected in vivo, signifying little dissociation of free pertechnetate. This observation aligns with prior publications on lipid-based nanoparticles, wherein stable radiolabeling was attained through optimum reduction conditions and suitable lipid habitats [31]. From a comprehensive nanomedicine viewpoint, Arroyo-Nogales et al. [32] underscored that the durability of nanoparticles in vivo should be assessed not only in relation to chemical integrity but also

https://doi.org/10.3390/molecules31040654

to their biological destiny. The observed biodistribution indicates a stable nanoparticle–radionuclide complex that maintains its structural integrity sufficiently to arrive at and be processed by RES organs.

2.3. Gamma Scintigraphy and Biodistribution Study

Measurement, characterization, and imaging of biological processes at the molecular and cellular level in living organisms constitute the field of molecular imaging. MRI (magnetic resonance imaging), X-ray-CT (X-ray computed tomography), SPECT (single-photon-emitting computed tomography), and PET (positron-emitting computed tomography) are some of the molecular imaging approaches. Since molecular imaging is considered noninvasive, it provides more reliable and accurate results than in vitro/ex vivo studies. Non-invasive imaging can be used for early diagnosis of diseases (in particular cancer) and to determine the stage of the disease. Frequent and multiple imaging processes open the door to customized medicine by providing a wide framework for evaluating the efficiency of treatment regimes for diseases. SPECT and PET are radionuclide-based molecular imaging techniques. The greatest advantages of radionuclide-based molecular imaging techniques over other imaging approaches are that they are very sensitive (at the picomolar level), they are quantitative, and they do not have a barrier for tissue penetration. For this purpose, the biodistribution of ^{99m}Tc-SLN in rabbits was evaluated noninvasively using SPECT. Images were taken using a gamma camera after the IV administration of ^{99m}Tc-SLN. Dynamic images were evaluated, and the regions showing radioactivity uptake were determined. These dynamic images are given in Figure 4.

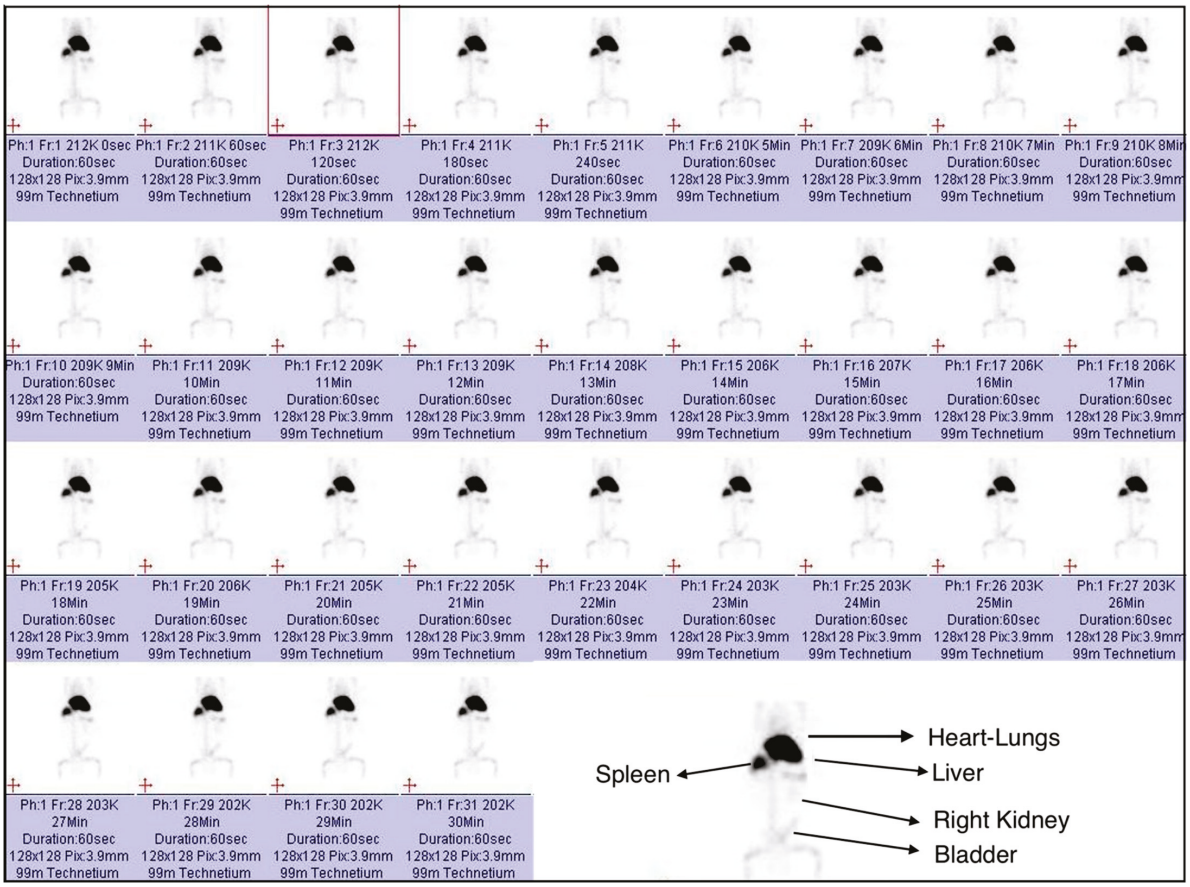

Figure 4. Scintigraphy images of a Rabbit after intravenous injection of ^{99m}Tc-SLN.

When Figure 4 is analyzed, uptake can be seen in the heart, the lungs, the liver, the spleen, the kidneys, and the bladder.

https://doi.org/10.3390/molecules31040654

Organ distribution of ^{99m}Tc-SLN in the rabbit that was sacrificed four hours after the IV injection is presented in Table 1. The presence of activity per gram in the liver (0.73%) and the spleen (0.59%) tissue of the rabbit supports the uptake of a significant amount of colloidal particles. It could be suggested that the radioactivity recorded in these organs is due to the uptake in RES cells.

Table 1. Biodistribution (%ID/g) with gamma counting of ^{99m}Tc-SLN in a rabbit following intravenous injection at 4 h, values represent mean ± SD (n = 3).

Organ	%ID/Organ	%ID/g
Spleen	1.24 ± 0.11	0.59 ± 0.03
Liver	51.62 ± 0.16	0.73 ± 0.01
Right Kidney	1.04 ± 0.13	0.09 ± 0.04
Left Kidney	1.09 ± 0.07	0.09 ± 0.03
Stomach	1.65 ± 0.58	0.23 ± 0.03
Bone	0.35 ± 0.09	0.02 ± 0.00
Intestine	2.08 ± 0.17	0.19 ± 0.08
Lungs	13.55 ± 0.29	0.35 ± 0.11
Heart	10.71 ± 0.06	0.21 ± 0.07

When the ex vivo biodistribution in the rabbit is analyzed, it is observed that the main uptake is in the liver and the spleen. The uptake in the kidneys and the bladder is interpreted as physiological uptake due to excretion of ^{99m}Tc-SLNs through the kidneys and the bladder. In other words, it could be suggested that the clearance route of ^{99m}Tc-SLNs is through the kidneys and the hepatobiliary system. The fact that no significant ^{99m}Tc-SLN activity was observed in the thyroid or the stomach during the ex vivo biodistribution study indicates that the stability of ^{99m}Tc-SLN was good when the radiolabeling procedure summarized in this study was used. Moreover, the activity (0.02%) in the bones shows the uptake of a small part of these particles in the bone marrow. The uptake observed in the lungs may be attributed to the size of the SLNs, as pulmonary capillaries can partially restrict the passage of larger particles; however, the absence of any clinical complications in the experimental animal indicates that this transient retention did not result in embolism. In conclusion, the results in the ex vivo biodistribution study are in line with the scintigraphic images.

Dynamic scintigraphic imaging demonstrated predominant uptake in the liver and spleen, with secondary activity observed in the lungs, kidneys, and bladder. Ex vivo biodistribution quantitatively validated these results. This organ distribution pattern is typical of non-stealth lipid nanoparticles and closely resembles the RES-mediated biodistribution documented for SLNs and other lipid-based nanocarriers in the recent literature.

Arroyo-Nogales et al. [32] examined techniques, including PEGylation and hybrid lipid-inorganic structures, to circumvent immune clearance for oncological purposes, while also emphasizing that immune recognition is not intrinsically negative but rather contingent on the application. In this study, quick RES absorption is not a limitation but the desired functional result, establishing ^{99m}Tc-SLNs as radio colloidal imaging agents rather than prolonged circulation delivery vehicles.

The observed moderate pulmonary absorption can be ascribed to transitory capillary filtration of bigger particle fractions, a phenomenon well documented for nanoparticles above approximately 100 nm. Britto et al. [31] observed that particle size heterogeneity affects early biodistribution patterns, without necessarily causing pathological retention when formulations are maintained within submicron dimensions.

Renal and bladder function suggest partial elimination through the urinary tract, possibly associated with smaller particles or breakdown products, whereas hepatobiliary activity indicates macrophage processing and biliary excretion. The observed combined

clearance routes align with classical radiocolloids and further reinforce the functional parallel between sentinel lymph nodes and clinically utilized liver–spleen imaging agents.

2.4. Confocal Microscopy Study

Considering the increased uptake of ^{99m}Tc-SLN in the liver and the spleen together with the results of the histopathological analysis of liver and spleen tissues of the sacrificed rabbit using the confocal microscopy, it was concluded that the SLNs passed to the liver and the spleen effectively without impairment following the intravenous administration. The passage of ^{99m}Tc radiolabeled SLN to the rabbit's spleen and liver is shown in Figures 5 and 6, respectively. These images are in line with the scintigraphic findings.

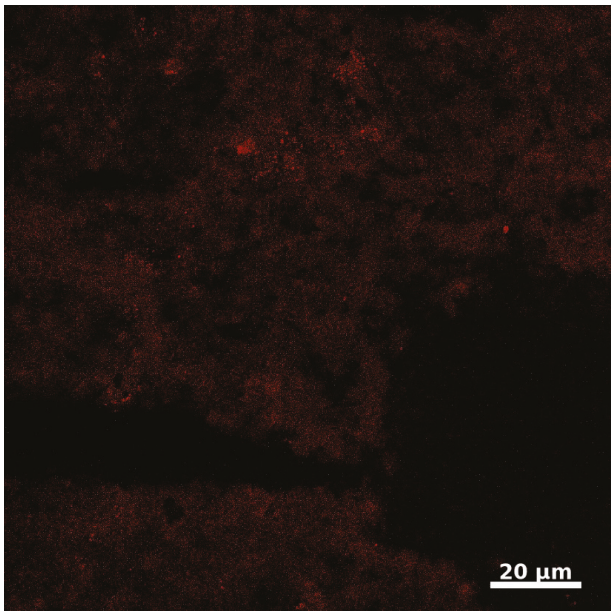

Figure 5. Confocal microscopy image of cryosections of rabbit spleen 4 h after intravenous injection of ^{99m}Tc-SLN (×400).

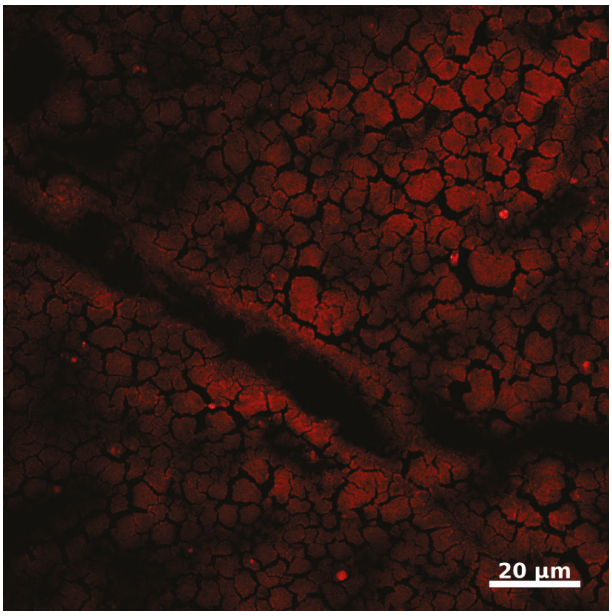

Figure 6. Confocal microscopy image of cryosections of rabbit liver 4 h after intravenous injection of ^{99m}Tc-SLN (×400).

https://doi.org/10.3390/molecules31040654

Confocal microscopy of cryosections from the liver and spleen offered direct visual validation of SLN localization within reticuloendothelial system tissues. These results enhance scintigraphic and quantitative biodistribution data and correspond with the macrophage-centric processing routes identified for lipid nanoparticles in various biological situations.

The current findings indicate that the physicochemical characteristics of SLNs—particle size, size distribution, surface charge, and lipid matrix organization—collectively determine their in vivo activity. The robust alignment between experimental findings and the current literature validates that the biodistribution profile of ^{99m}Tc-SLNs is foreseeable, mechanistically based, and appropriate for their intended use as RES-targeting radiopharmaceuticals. Moreover, it shows that the SLNs have the potential to be a selective drug carrier to the liver and the spleen.

3. Summary and Conclusions

SLNs are colloidal carriers in submicron sizes that are developed as an alternative to traditional carrier systems (emulsions, liposomes, polymeric nanoparticles, etc.). In order to use SLNs radiolabeled with ^{99m}Tc as the radiocolloid agent in colloid scintigraphy, this study focused on analyzing the feasibility of using SLNs for diagnosis purposes in nuclear medicine, in particular, in RES scintigraphy. For this reason, SLNs are successfully prepared and radiolabeled with ^{99m}Tc. The experimental studies conducted showed that the SLNs were localized effectively in the RES organs, and therefore, there is great potential for using them to target the RES organs, in particular, the liver and spleen. Radiolabeling, on the other hand, helped us observe these particles in the living organism noninvasively. Using this method, the performance of other nano-sized drug carrier systems used in the diagnosis and treatment of diseases can be evaluated without sacrificing many animals. Moreover, this nanosystem might be a promising strategy for the delivery of drugs used in the treatment of liver and spleen diseases.

4. Materials and Methods

4.1. Materials

Compritol® 888 ATO (glyceryl behenate) was purchased from Gattefossé (Lyon, France). Tween 80, soy lecithin, and stannous chloride dihydrate were purchased from Merck (Merck KGaA, Darmstadt, Germany). Xylazine was obtained from Bioveta (Bioveta, a.s., Ivanovice na Hané, Czech Republic). Ketamine was obtained from Pfizer (Pfizer Inc., New York, NY, USA). ^{99}Mo/^{99m}Tc kits were obtained from ELUMATIC-III® CIS bio international, RADMED (İstanbul, Turkey). ^{99m}Tc extraction was performed in Ataturk University Faculty of Nuclear Medicine, Erzurum, Turkey. All other solvents and reagents were of analytical grade.

4.2. Preparation of SLNs

This study utilized Compritol® 888 ATO (glyceryl behenate) as a solid lipid, soy lecithin as a lipophilic surfactant, and Tween 80® as a hydrophilic surfactant. SLNs were synthesized using microemulsion and sonication techniques at reduced temperatures. A distinct microemulsion is created when the matrix lipid content is around 5% (w/v), the surfactant content is about 15% (w/v), and the co-surfactant concentration is roughly 12% (w/v). Briefly, Compritol® 888 ATO was heated slightly above its melting point of 80 °C. The aqueous surfactant mixture was dropped with a magnetic stirrer into the lipid, which melted at 80 °C. It was then homogenized at 10,000 rpm for 5 min to produce a pre-emulsion. An ultrasonic probe was inserted into the pre-emulsion using a VCX750 ultrasonic processor (Sonics & Materials, Inc., Newtown, CT, USA). Power output with an amplitude of 70% was delivered for 20 min, resulting in droplet fragmentation through sonic cavita-

https://doi.org/10.3390/molecules31040654

tion and the subsequent generation of nanoparticles. Then, the *o*/*w* nanoemulsion was transferred to glass vials and promptly cooled to room temperature to produce SLNs.

In addition, the prepared SLNs were kept in the freezer for 24 h at −86 °C and then placed in the lyophilizer. The lyophilized powder obtained at the end of the lyophilization process, which was carried out in 24 h at 0.011 mbar and −60 °C, was stored at +4 °C.

4.3. Studies to Determine the Characterization of the SLNs

Dynamic light scattering (DLS) measurements were conducted on freshly generated aqueous solid lipid nanoparticle (SLN) dispersions before lyophilization. Prior to measurement, the dispersions were suitably diluted with distilled water to get optimal scattering intensity and to reduce multiple scattering effects. Measurements of particle size and size distribution were conducted using Malvern Mastersizer 2000 equipment (Malvern Instruments Ltd., Worcestershire, UK), which operates on the concept of dynamic light scattering, with triplicate measurements taken at 25 °C.

Scanning electron microscopy (SEM) (FEI Inspect S50, FEI Company, Hillsboro, OR, USA) was used to study the morphology of SLN. For SEM investigation of the freeze-dried nanoparticles, a random sample was positioned on a copper stub and sputter-coated with a gold–palladium alloy to reduce surface charging before acquiring SEM pictures.

The thermal stability of SLNs was determined using the Netzsch STA 409 PC Luxx Thermal analyzer (NETZSCH-Gerätebau GmbH, Selb, Germany). Analysis of SLNs pulverized by lyophilization was performed in an alumina crucible against a blank reference in a nitrogen atmosphere fed at a heating rate of 10 °C/min, a temperature range of 25 °C to 300 °C, and a flow rate of 30 mL/min.

4.4. Radiolabeling

Radiolabeling of SLNs with 99mTc was done in the radiopharmacy laboratory of the Nuclear Medicine Department in Ataturk University.

Similar to the methods indicated in previous studies, SLNs were radiolabeled with Tc-99m using Tin Chloride Dihydrate ($SnCl_2.2H_2O$) as the reducing agent. Briefly, 20 μg of Tin Chloride Dihydrate ($SnCl_2.2H_2O$) was added to 2 mCi pertechnetate (TcO_4^-), and the pH of the solution was adjusted to 6.5 using sodium bicarbonate. Then, 1 mL SLN was added to this solution and incubated at room temperature for 10 min. Quality control studies were performed in line with the previously mentioned methods. The radiolabeling technique was evaluated with the preparative thin-layer chromatography induced by silica gel-loaded fiber strips (2 × 8 cm). Radiolabeled complex (3 μL) was dropped 1 cm above the lower part of the ITLC-SG strip using an insulin syringe and moved up to a height of approximately 7 cm using 100% acetone as the mobile phase. The ITLC-SG strip was cut into two equal halves, and the radioactivity in each half was counted using a well-type gamma counter. (Biodex, Atomlab 200 model dose calibrator, Erzurum, Turkey) Free TcO_4^- was separated from the labeled complex at the bottom part of the strip and migrated towards the front part. The radiolabeled complex remained at the point of application. The excess of tin chloride used to reduce the pertechnetate resulted in the formation of unwanted radiocolloids. Therefore, the percentage of radiocolloid was determined using pyridine:acetic acid:water (3:5:1.5). Whilst the colloids remained at the bottom part of the strip, free pertechnetate and radiolabeled complex moved towards the front part of the strip. The net amount of 99mTc-SLNs was calculated by subtracting the activity migrating in the acetone from the pyridine:acetic acid:water mixture. All measurements were performed in triplicate, and results were expressed as mean ± standard deviation.

https://doi.org/10.3390/molecules31040654

4.5. Gamma Scintigraphy Studies

In the studies, a white New Zealand male rabbit weighing 3.5–4 kg was kept under controlled laboratory conditions, with a 12 h light and a 12 h dark cycle, a temperature of 22 ± 2 °C, and a relative humidity of 45–50%. The rabbit, which was fed with standard feed pellets and tap water before the experiment, was not given a special diet regimen before the experiment and was starved during the experiment. Animal studies were carried out with the permission of the ethics committee numbered 2015-83443830/891 from the Atatürk University Animal Experiments Local Ethics Committee.

The activity of the ^{99m}Tc-labeled SLNs to be administered to the rabbit was adjusted to be approximately 2 mCi per 1.2 mL. The rabbit, which was anesthetized with intramuscular injection of 1 mL of ketamine and 1 mL of xylazine, was placed in a supine position on the appropriate-sized plate. The prepared radioactive solution was administered i.v through the dorsal ear vein and planar imaging was performed with a Gamma camera at certain time intervals. Necessary precautions were taken to prevent urine contamination. Dynamic images were recorded in 128 × 128 matrices with a low-energy general-purpose collimator-compatible gamma camera (Siemens Medical Systems, Inc., Hoffman Estates, IL 60195, USA).

4.6. Ex Vivo Biodistribution Study

In vivo biodistribution of SLNs after the IV injection was evaluated using a gamma camera (SPECT). These values were compared with ex vivo biodistribution in the organs obtained with the gamma counter. An ex vivo biodistribution study was conducted approximately four hours after the IV administration of the ^{99m}Tc radiolabeled SLNs. The rabbit was sacrificed using a high dose of anesthetic (100 mg/kg) sodium thiopental. Then, the relevant organs of the rabbit were removed. Tissue samples were washed with saline and weighed. Radioactivity was measured with a well-type gamma counter calibrated for ^{99m}Tc energy. The results were expressed for each organ as a percentage of the injected dose per gram and organ (%ID/g and %ID/organ) of the tissue, taking into account the decay correction following the IV administration.

$$\%ID/g \text{ of the tissue} = [(\text{count in the sample})/(\text{sample weight} \times \text{total counts injected after decay correction})] \times 100$$

4.7. Histopathological Analysis of the Presence of SLNs in the Liver and the Spleen

After the images of the rabbit and radioactive measurements in the organs, it was determined that the liver and spleen had the highest attachment capacity. Therefore, after tissue samples were taken from the liver and spleen and frozen, frozen cryosections of the samples were analyzed under a confocal microscope (Zeiss LSM 710, New York, NY, USA) at 400× magnification.

Author Contributions: Conceptualization, H.E., A.Y., and A.K.A.; methodology, A.Y.; validation, H.E., A.Y., and A.K.A.; formal analysis, H.E., A.Y.; investigation, A.Y.; resources, H.E., A.Y., and A.K.A.; data curation, A.Y.; writing—original draft preparation, A.Y.; writing—review and editing, A.Y.; visualization, A.Y.; supervision, H.E., A.Y. All authors have read and agreed to the published version of the manuscript.

Funding: This research received no external funding.

Institutional Review Board Statement: The animal study was conducted in accordance with the relevant institutional guidelines and ethical standards, and the protocol was approved by the Atatürk University Animal Experiments Local Ethics Committee (Approval No. 83443830/891) on 27 February 2015.

Data Availability Statement: The data presented in this study are available upon request from the authors.

Conflicts of Interest: The authors declare no conflict of interest.

Abbreviations

Tc-99m	Technetium-99 Metastable
SLNs	Solid Lipid Nanoparticles
RES	Reticuloendothelial System
DLS	Dynamic Light Scattering
SEM	Scanning Electron Microscopy
DSC	Differential Scanning Calorimetry
IV	Intravenously
SPECT	Single-Photon-Emitting Computed Tomography
keV	Kiloelectron Volt
HMPAO	Hexamethylpropylene Amine Oxime
Na	Sodium
Cu	B
Mo	Molybdenum
μ	Micro
mCi	Millicruie

References

1. Eroglu, H.; Yenilmez, A. An Investigation of the Usability of Solid Lipid Nanoparticles Radiolabelled with Tc-99m as Imaging Agents in Liver-Spleen Scintigraphy. *J. Biomed. Nanotechnol.* **2016**, *12*, 1501–1509. [CrossRef] [PubMed]
2. Farokhzad, O.C.; Langer, R. Nanomedicine: Developing Smarter Therapeutic and Diagnostic Modalities. *Adv. Drug Deliv. Rev.* **2006**, *58*, 1456–1459. [CrossRef] [PubMed]
3. Youan, B.B.C. Impact of Nanoscience and Nanotechnology on Controlled Drug Delivery. *Nanomedicine* **2008**, *3*, 401–406. [CrossRef] [PubMed]
4. Ayan, A.K.; Yenilmez, A.; Eroglu, H. Evaluation of radiolabeled curcumin-loaded solid lipid nanoparticles usage as an imaging agent in liver-spleen scintigraphy. *Mater. Sci. Eng. C Mater. Biol. Appl.* **2017**, *75*, 663–670. [CrossRef]
5. Eroglu, H.; Ayan, A.K.; Yenilmez, A. Research for a new imaging agent: In vivo examination of silymarin loaded solid lipid nanoparticles radiolabeled with ^{99m}Tc in rabbits. *Inorg. Chem. Commun.* **2024**, *163*, 112328. [CrossRef]
6. Gindy, M.E.; Prud'homme, R.K. Multifunctional Nanoparticles for Imaging, Delivery and Targeting in Cancer Therapy. *Expert Opin. Drug Deliv.* **2009**, *6*, 865–878. [CrossRef]
7. Kim, K.; Kim, J.H.; Park, H.; Kim, Y.S.; Park, K.; Nam, H.; Lee, S.; Park, J.H.; Park, R.W.; Kim, I.S.; et al. Tumor-Homing Multifunctional Nanoparticles for Cancer Theragnosis: Simultaneous Diagnosis, Drug Delivery, and Therapeutic Monitoring. *J. Control. Release* **2010**, *146*, 219–227. [CrossRef]
8. Hong, H.; Zhang, Y.; Sun, J.; Cai, W. Molecular Imaging and Therapy of Cancer with Radiolabeled Nanoparticles. *Nano Today* **2009**, *4*, 399–413. [CrossRef]
9. Yeong, C.H.; Cheng, M.H.; Ng, K.H. Therapeutic Radionuclides in Nuclear Medicine: Current and Future Prospects. *J. Zhejiang Univ. Sci. B* **2014**, *15*, 845–863. [CrossRef]
10. Tyagi, N.; Arora, S.; Deshmukh, S.K.; Singh, S.; Marimuthu, S.; Singh, A.P. Exploiting Nanotechnology for the Development of MicroRNA-Based Cancer Therapeutics. *J. Biomed. Nanotechnol.* **2016**, *12*, 28–42. [CrossRef]
11. Andreozzi, E.; Seo, J.W.; Ferrara, K.; Louie, A. Novel Method to Label Solid Lipid Nanoparticles with 64Cu for Positron Emission Tomography Imaging. *Bioconjug. Chem.* **2011**, *22*, 808–818. [CrossRef] [PubMed]
12. Videira, M.A.; Botelho, M.F.; Santos, A.C.; Gouveia, L.F.; de Lima, J.J.; Almeida, A.J. Lymphatic Uptake of Pulmonary Delivered Radiolabelled Solid Lipid Nanoparticles. *J. Drug Target.* **2002**, *10*, 607–613. [CrossRef] [PubMed]
13. Banerjee, I.; De, K.; Chattopadhyay, S.; Bandyopadhyay, A.K.; Misra, M. An Easy and Effective Method for Radiolabelling of Solid Lipid Nanoparticles. *J. Radioanal. Nucl. Chem.* **2014**, *302*, 837–843. [CrossRef]
14. Kakkar, V.; Mishra, A.K.; Chuttani, K.; Kaur, I.P. Proof of Concept Studies to Confirm the Delivery of Curcumin Loaded Solid Lipid Nanoparticles (C-SLNs) to Brain. *Int. J. Pharm.* **2013**, *448*, 354–359. [CrossRef]
15. Rai, S.; Paliwal, R.; Gupta, P.N.; Khatri, K.; Goyal, A.K.; Vaidya, B.; Vyas, S.P. Solid Lipid Nanoparticles (SLNs) as a Rising Tool in Drug Delivery Science: One Step up in Nanotechnology. *Curr. Nanosci.* **2008**, *4*, 30–44. [CrossRef]

16. Kathe, N.; Henriksen, B.; Chauhan, H. Physicochemical Characterization Techniques for Solid Lipid Nanoparticles: Principles and Limitations. *Drug Dev. Ind. Pharm.* **2014**, *40*, 1565–1575. [CrossRef]
17. de Mendoza, A.E.H.; Campanero, M.A.; Mollinedo, F.; Blanco-Prieto, M.J. Lipid Nanomedicines for Anticancer Drug Therapy. *J. Biomed. Nanotechnol.* **2009**, *5*, 323–343. [CrossRef]
18. Shivananjegowda, M.G.; Hani, U.; Osmani, R.A.M.; Alamri, A.H.; Ghazwani, M.; Alhamhoom, Y.; Rahamathulla, M.; Paranthaman, S.; Gowda, D.V.; Siddiqua, A. Development and Evaluation of Solid Lipid Nanoparticles for the Clearance of Aβ in Alzheimer's Disease. *Pharmaceutics* **2023**, *15*, 221. [CrossRef]
19. Renukuntla, J.; Peterson-Sockwell, S.; Clark, B.A.; Godage, N.H.; Gionfriddo, E.; Bolla, P.K.; Boddu, S.H.S. Design and Preclinical Evaluation of Nicotine–Stearic Acid Conjugate-Loaded Solid Lipid Nanoparticles for Transdermal Delivery: A Technical Note. *Pharmaceutics* **2023**, *15*, 1043. [CrossRef]
20. Creteanu, A.; Lisa, G.; Vasile, C.; Popescu, M.-C.; Spac, A.F.; Tantaru, G. Development of Solid Lipid Nanoparticles for Controlled Amiodarone Delivery. *Methods Protoc.* **2023**, *6*, 97. [CrossRef]
21. Santonocito, D.; Sarpietro, M.G.; Castelli, F.; Lauro, M.R.; Torrisi, C.; Russo, S.; Puglia, C. Development of Solid Lipid Nanoparticles as Dry Powder: Characterization and Formulation Considerations. *Molecules* **2023**, *28*, 1545. [CrossRef] [PubMed]
22. Aldayel, T.S.; Badran, M.M.; Alomrani, H.A.; AlFaris, N.A.; Altamimi, Z.J.; Alqahtani, S.A.; Nasr, A.F.; Ghaffar, S.; Orfali, R. Chitosan-Coated Solid Lipid Nanoparticles as an Efficient Avenue for Boosted Biological Activities of *Aloe perryi*: Antioxidant, Antibacterial, and Anticancer Potential. *Molecules* **2023**, *28*, 3569. [CrossRef] [PubMed]
23. Stendahl, J.C.; Sinusas, A.J. Nanoparticles for Cardiovascular Imaging and Therapeutic Delivery, Part 1: Compositions and Features. *J. Nucl. Med.* **2015**, *56*, 1469–1475. [CrossRef] [PubMed]
24. Demirel, M.; Yazan, Y. Katı Lipit Nanopartiküller (SLN). *FABAD J. Pharm. Sci.* **2000**, *25*, 167–179.
25. Aburahma, M.H.; Badr-Eldin, S.M. Compritol 888 ATO: A Multifunctional Lipid Excipient in Drug Delivery Systems and Nanopharmaceuticals. *Expert Opin. Drug Deliv.* **2014**, *11*, 1865–1883. [CrossRef]
26. Mehnert, W.; Mäder, K. Solid lipid nanoparticles: Production, characterization and applications. *Adv. Drug Deliv. Rev.* **2012**, *64*, 83–101. [CrossRef]
27. Danaei, M.; Dehghankhold, M.; Ataei, S.; Hasanzadeh Davarani, F.; Javanmard, R.; Dokhani, A.; Khorasani, S.; Mozafari, M.R. Impact of Particle Size and Polydispersity Index on the Clinical Applications of Lipidic Nanocarrier Systems. *Pharmaceutics* **2018**, *10*, 57. [CrossRef]
28. Sayed, S.; Elsharkawy, F.M.; Amin, M.M.; Shamsel-Din, H.A.; Ibrahim, A.B. Brain targeting efficiency of intranasal clozapine-loaded mixed micelles following radiolabeling with Technetium-99m. *Drug Deliv.* **2021**, *28*, 1524–1538. [CrossRef]
29. Liu, J.; Liu, Z.; Pang, Y.; Zhou, H. The interaction between nanoparticles and immune system: Application in the treatment of inflammatory diseases. *J. Nanobiotechnol.* **2022**, *20*, 127. [CrossRef]
30. Hallan, S.S.; Ferrara, F.; Cortesi, R.; Sguizzato, M. Potential of the nano-encapsulation of antioxidant molecules in wound healing applications: An innovative strategy to enhance the bio-profile. *Molecules* **2025**, *30*, 641. [CrossRef]
31. Britto, N.T.; Montanheri, L.R.; Pelin, J.N.; Siqueira, R.A.; Alves, M.D.S.; Martins, T.S.; Hamley, I.W.; Lopes, P.S.; Leite-Silva, V.R.; Andreo-Filho, N. Development and Optimization of Resveratrol-Loaded NLCs via Low-Energy Methods: A Promising Alternative to Conventional High-Energy or Solvent-Based Techniques. *Processes* **2026**, *14*, 393. [CrossRef]
32. Arroyo-Nogales, A.; Plaza-Palomo, G.; González-Larre, J.; Jiménez-Falcao, S.; Baeza, A. Silicasomes in Oncology: From Conventional Chemotherapy to Combined Immunotherapy. *Molecules* **2025**, *30*, 1257. [CrossRef]

Disclaimer/Publisher's Note: The statements, opinions and data contained in all publications are solely those of the individual author(s) and contributor(s) and not of MDPI and/or the editor(s). MDPI and/or the editor(s) disclaim responsibility for any injury to people or property resulting from any ideas, methods, instructions or products referred to in the content.

molecules

MDPI

Article

Nanostructured Lipid Carriers as Physicochemical Modulators of Complex Natural Extracts: Release Behavior and Bile-Induced Remodeling in Biorelevant Media

Javiera Carrasco-Rojas [1], Javiera Solas-Soto [2], Rubén Veas-Albornoz [2], Carlos F. Lagos [2,3], Mario J. Simirgiotis [4], Francisco Arriagada [1] and Andrea C. Ortiz [2,*]

[1] Departamento de Ciencias y Tecnología Farmacéutica, Facultad de Ciencias Químicas y Farmacéuticas, Universidad de Chile, Santiago 8380494, Chile; javiera.carrasco@uchile.cl (J.C.-R.); francisco.arriagada@ciq.uchile.cl (F.A.)
[2] Escuela de Química y Farmacia, Facultad de Ciencias, Universidad San Sebastián, Lota 2465, Santiago 7510157, Chile; jsolass@correo.uss.cl (J.S.-S.); ruben.veas@uss.cl (R.V.-A.); carlos.lagos@uss.cl (C.F.L.)
[3] Centro Basal Ciencia & Vida, Fundación Ciencia & Vida, Av. del Valle Norte 725, Santiago 8580702, Chile
[4] Instituto de Farmacia, Facultad de Ciencias, Universidad Austral de Chile, Campus Isla Teja, Valdivia 5090000, Chile; mario.simirgiotis@uach.cl
* Correspondence: andrea.ortizo@uss.cl

Abstract

Propolis is a chemically complex natural product with recognized antioxidant potential, but its compositional heterogeneity and poor aqueous solubility complicate formulation and interpretation of in vitro release behavior. In this study, a nanostructured lipid carrier (NLC) based on Gelucire® 44/14 was developed as a physicochemical platform to modulate the accessibility of a selected Chilean ethanolic propolis extract. Propolis extracts from different origins were first screened using complementary antioxidant assays (DPPH, ABTS, ORAC, FRAP), leading to the selection of the Peñaflor extract, which exhibited the highest phenolic content (~41 mg GAE/g) and antioxidant capacity. The selected extract was incorporated into NLCs with encapsulation efficiencies above 90%, a narrow size distribution (~200 nm), and high stability over 90 days. Under simple aqueous conditions, propolis release remained limited (<15% over 6 h), consistent with diffusion- and partition-controlled transport. In simulated gastrointestinal media containing bile components, pronounced pH- and composition-dependent effects were observed. While fed-state intestinal conditions induced extensive morphological remodeling without increasing the analytically accessible fraction (<3% at 4 h), fasted-state intestinal media promoted a higher accessible fraction (~14% within 1 h) without complete carrier disruption, as confirmed by transmission electron microscopy. Preliminary cytocompatibility studies in HepG2 cells showed acceptable viability at 10–40 μg/mL and concentration-dependent effects at higher doses. Overall, this work demonstrates that bile components modulate propolis accessibility through dynamic partitioning and colloidal reorganization rather than simple carrier breakdown, providing a physicochemical framework for future digestion and absorption studies.

Keywords: nanostructured lipid carriers; propolis; biorelevant gastrointestinal media; HepG2

1. Introduction

Propolis is a chemically complex resinous material produced by bees through the transformation of plant-derived exudates, and it is widely recognized for its rich content of

polyphenols, flavonoids, and other redox-active constituents [1]. Owing to this composition, propolis has been associated with antioxidant, antimicrobial, and anti-inflammatory properties, motivating sustained interest in pharmaceutical and nutraceutical research [2,3]. However, propolis does not represent a single, well-defined chemical entity; its composition is highly heterogeneous and strongly dependent on botanical source, geographic origin, and local environmental conditions, leading to pronounced variability even among samples collected within geographically close regions [4,5]. This intrinsic heterogeneity poses challenges for formulation development and complicates the interpretation of in vitro performance data.

From a physicochemical standpoint, additional limitations arise from the poor aqueous solubility and marked lipophilicity of many propolis constituents [6]. Under gastrointestinal conditions, these properties may restrict the fraction of compounds that become analytically accessible, resulting in low apparent release or activity values that reflect formulation-dependent partitioning phenomena rather than insufficient intrinsic chemical potential [7,8]. Consequently, conventional in vitro assays may underestimate or misrepresent the functional behavior of propolis if the formulation context, phase behavior, and analytical readouts are not carefully considered.

Several delivery systems have been explored to improve the stability and bioavailability of propolis and other polyphenol-rich natural extracts, including liposomes, polymeric particles, and solid lipid nanoparticles (SLNs) [9]. Liposomal systems are attractive due to their biocompatibility and ability to encapsulate both hydrophilic and lipophilic compounds [6]; however, their phospholipid bilayers may be destabilized under gastrointestinal conditions, particularly in the presence of bile salts and digestive surfactants, leading to membrane disruption and premature compound leakage [10]. Polymeric carriers such as PLGA-based microspheres can provide controlled release and protection against degradation, but their preparation typically involves multistep processes and organic solvents, which may complicate large-scale production and limit encapsulation efficiency for chemically heterogeneous extracts. In addition, their degradation behavior and release kinetics in the digestive environment may be difficult to predict [11,12]. Conventional SLNs have also been investigated for natural product delivery; however, their highly ordered lipid matrices often restrict drug accommodation and may promote compound expulsion during lipid crystallization, particularly when accommodating complex lipophilic mixtures [13].

In this context, nanostructured lipid carriers (NLCs) have emerged as versatile colloidal systems for the incorporation of poorly water-soluble compounds and complex natural extracts [14]. By combining solid and liquid lipid components, NLCs form partially disordered matrices capable of accommodating high payloads while maintaining colloidal stability [15]. For chemically heterogeneous natural extracts such as propolis, where multiple constituents with different polarity and partitioning behavior coexist, this structural characteristic is particularly advantageous because it enables the incorporation of diverse lipophilic constituents while minimizing crystallization-induced expulsion phenomena [16]. Importantly, NLCs should not be regarded solely as passive encapsulation vehicles. Their internal organization, interfacial properties, and interactions with surrounding media govern not only loading efficiency and physical stability but also the fraction of encapsulated compounds that become accessible under specific physicochemical environments [17]. In this sense, lipid-based nanocarriers can actively modulate compound partitioning, apparent release, and analytical accessibility, particularly in complex biorelevant media.

For chemically heterogeneous systems such as propolis, rational extract selection represents a critical initial step. Antioxidant profiling, when interpreted as a physicochemical descriptor rather than a direct predictor of biological efficacy, provides a comparative chemical framework to guide this selection. The use of complementary antioxidant assays

https://doi.org/10.3390/molecules31061028

offers an integrated view of redox-related properties and reduces the risk of advancing extracts whose apparent activity is dominated by assay-specific effects or narrow subsets of reactive constituents [18]. This strategy is especially relevant when the objective is to investigate how a lipid-based nanosystem modulates accessibility and release behavior, rather than to rank extracts solely on the basis of bioactivity claims.

In parallel, the gastrointestinal environment introduces additional complexity for lipid-based nanocarriers. Bile salts and phospholipids are surface-active amphiphiles capable of inducing interfacial remodeling, mixed colloid formation, and redistribution of lipophilic compounds [19]. Importantly, structural alteration of lipid carriers in bile-containing media does not necessarily translate into proportional increases in analytically measured release, as morphological changes and assay-accessible fractions represent distinct physicochemical readouts. Understanding this distinction is essential for the rational interpretation of release data obtained in biorelevant media.

Unlike most previous studies on propolis delivery systems, which primarily focus on improving encapsulation efficiency or biological activity, the present work investigates how a lipid nanosystem modulates the physicochemical accessibility and apparent release of a chemically complex extract under biorelevant gastrointestinal conditions. Specifically, this study aimed to develop and characterize a Gelucire®-based nanostructured lipid carrier loaded with a selected Chilean propolis extract from the Metropolitan Region and to investigate how simulated gastrointestinal environments containing bile components influence carrier structure and apparent propolis release. We hypothesized that the nanostructured lipid carrier would behave as a retentive lipid matrix under simple aqueous buffer conditions, while bile salts and phospholipids present in biorelevant media would induce composition- and pH-dependent interfacial remodeling and redistribution of propolis into mixed colloidal assemblies. Such processes were expected to alter the assay-accessible fraction without necessarily implying complete carrier disintegration. To address these questions, propolis extracts from different local origins were first screened using complementary antioxidant assays to support rational extract selection. The selected extract was subsequently incorporated into NLCs, followed by systematic evaluation of loading efficiency, colloidal properties, and physical stability. Release behavior was assessed in aqueous buffers and bile-component-containing simulated gastrointestinal media, alongside morphological analysis by transmission electron microscopy. Finally, a preliminary cytocompatibility assessment in HepG2 cells was conducted to support the potential relevance of the developed nanosystem for future biomedical applications.

2. Results and Discussion

2.1. Antioxidant Profile of Propolis Extracts as a Physicochemical Criterion for Nanosystem Design

The antioxidant characterization of the ethanolic propolis extracts (EPE) was conducted as an initial physicochemical screening step to support the rational selection of the extract to be incorporated into the NLC. Given the well-known compositional heterogeneity of propolis, the use of complementary antioxidant assays provides an integrated chemical description of its redox-related properties, rather than a direct prediction of biological efficacy [20]. In this context, antioxidant profiling was intentionally employed as a comparative physicochemical descriptor to guide formulation decisions while minimizing assay-specific bias. The results obtained for total phenolic content (TPC) and antioxidant assays are summarized in Table 1. TPC analysis revealed marked quantitative differences among the extracts, with the Peñaflor sample exhibiting the highest phenolic content (~41 mg GAE/g extract), followed by Pirque (~37 mg GAE/g extract) and Pudahuel (~35 mg GAE/g extract). These differences are consistent with the strong influence of botanical origin and local vegetation on the chemical fingerprint of Chilean propolis, even

https://doi.org/10.3390/molecules31061028

within geographically close areas of the Metropolitan Region [21]. From a physicochemical perspective, higher TPC values indicate a greater density of redox-active moieties capable of participating in electron transfer and hydrogen atom donation processes [22]. However, it should be emphasized that TPC alone does not establish a linear or universal relationship with antioxidant performance, reinforcing the need for complementary functional assays.

Table 1. Antioxidant profile and total phenolic content of free propolis extracts from Peñaflor, Pirque, and Pudahuel, evaluated by DPPH•, ABTS•$^+$, ORAC, FRAP, and total phenolic content (TPC) assays.

Sample	DPPH• [a]	ABTS•$^+$ [a]	ORAC [b]	FRAP [b]	TPC [c]
Peñaflor	53.4 ± 0.02	2.6 ± 0.08	867.2 ± 4.02	222.9 ± 0.06	40.7 ± 0.02
Pirque	65.4 ± 0.02	14.2 ± 0.04	472.3 ± 1.17	215.9 ± 0.02	36.6 ± 0.02
Pudahuel	68.3 ± 0.02	17.9 ± 0.01	321.6 ± 2.95	204.4 ± 0.02	35.4 ± 0.03

[a] Antiradical DPPH and ABTS activities are expressed as μg/mL; [b] Expressed as μmol Trolox/g Extract; [c] Total phenolic content (TPC) expressed as mg gallic acid equivalent GAE/g extract.

Radical scavenging assays further supported this comparative trend. In both DPPH• and ABTS•$^+$ assays, the Peñaflor propolis extract displayed the lowest SC50 values (53.4 μg/mL and 2.6 μg/mL, respectively), indicating higher apparent scavenging efficiency than the Pirque and Pudahuel extracts (Table 1). Although DPPH• and ABTS•$^+$ are often grouped as conceptually similar assays, their distinct radical species, solvent environments, and reaction mechanisms provide complementary information [23]. The consistent ranking observed across both assays suggests that the superior performance of the Peñaflor extract is not an assay-dependent artifact but rather reflects a broader compositional advantage within the limits of chemical redox-based measurements.

Additional insight was provided by the ORAC and FRAP assays, which probe different antioxidant mechanisms. ORAC values, reflecting the ability to scavenge peroxyl radicals under kinetic conditions, were markedly higher for the Peñaflor extract (~867 μmol Trolox/g) than for Pirque (~472 μmol Trolox/g) and Pudahuel (~322 μmol Trolox/g), indicating a pronounced difference in the capacity to delay oxidative chain reactions over time. In contrast, FRAP values followed the same general ranking but exhibited a narrower quantitative separation among extracts (Table 1). Although these differences are modest, their consistency with the trends observed in TPC, DPPH•, ABTS•$^+$, and ORAC supports their interpretation as part of a coherent multidimensional physicochemical profile rather than as isolated numerical descriptors. Such partial divergence among assays is expected for complex natural matrices and underscores the importance of interpreting antioxidant data collectively rather than relying on a single metric [24]. Importantly, the convergence of all applied assays toward the same extract as the most redox-active supports the robustness of the selection strategy. This robustness should be understood strictly within the framework of in vitro chemical characterization and does not imply predictive value for in vivo antioxidant efficacy. Rather than advancing an extract based on a single antioxidant endpoint, the combined evaluation of TPC, radical scavenging capacity and reducing power enables identification of the extract with the most balanced and consistent redox-related properties. From a formulation standpoint, this approach minimizes the risk of advancing an extract whose apparent antioxidant performance is driven by assay-specific effects or by a limited subset of reactive constituents [25]. Based on this integrated antioxidant profiling, the Peñaflor ethanolic propolis extract was selected as the most suitable candidate for incorporation into NLC system. This selection does not imply superior biological activity per se but instead identifies an extract with higher chemical reducing capacity and radical reactivity, properties that are particularly relevant when evaluating how a lipid-based nanosystem modulates payload accessibility, release behavior and apparent antioxidant response.

https://doi.org/10.3390/molecules31061028

It is worth emphasizing that antioxidant assays performed directly on propolis-loaded NLC formulations do not provide a direct measure of the intrinsic antioxidant capacity of the encapsulated extract. In such dispersions, the observed response is governed by the fraction of phenolic compounds that are accessible to the reaction medium during the assay time scale, which may include surface-associated molecules or compounds released from the carrier [13]. Consequently, antioxidant measurements on NLC formulations were not used as selection criteria and are reported only as Supplementary Information (Table S1), as they primarily reflect the fraction of antioxidants accessible during the assay rather than the total antioxidant content of the encapsulated system. This approach avoids overinterpretation of formulation-dependent assay effects and ensures that both extract selection and nanosystem design remain grounded in sound physicochemical reasoning while explicitly acknowledging the methodological limitations of antioxidant screening assays.

2.2. Rational Selection of Propolis Loading

Several propolis-to-lipid ratios (expressed as g propolis extract equivalents per g Gelucire® 44/14 (main lipid material)) were systematically evaluated to identify a formulation window that maximized effective encapsulation rather than nominal loading (Figure 1). Increasing the propolis content beyond this window led to a pronounced reduction in encapsulation efficiency, with high nominal loadings (e.g., 0.6 g propolis extract equivalents/g lipid material) resulting in efficiencies of only ~20–25%. In contrast, a propolis loading of 0.15 g propolis extract equivalents/g lipid material consistently preserved encapsulation efficiencies above 90%. Increasing the concentration to 0.6 g ethanolic propolis extract per 1 g of lipid resulted in a sharp decline in propolis encapsulation efficiency. This behavior reflects the finite solubilization and accommodation capacity of the lipid matrix for chemically heterogeneous natural extracts and highlights the importance of distinguishing between nominal loading and physically retained payload.

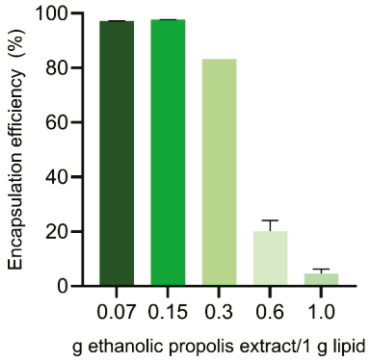

Figure 1. Encapsulation efficiency of ethanolic propolis extract from Peñaflor in the NLC. $n = 3$.

Such behavior is consistent with the literature on NLC systems loaded with complex natural extracts, which typically report encapsulation efficiencies ranging from 60% to 80% as a practical compromise between loading and stability [26]. The comparatively high encapsulation efficiency achieved here can be rationalized by the physicochemical characteristics of Gelucire® 44/14, which, despite being classified as a lipid, exhibits self-emulsifying behavior due to its amphiphilic composition. This property facilitates the incorporation of compounds spanning a broad lipophilicity range, including moderately polar polyphenolic constituents. In addition, the intrinsic structural disorder of NLCs, arising from the combination of solid and liquid lipid phases, generates multiple molecular imperfections and free volume within the lipid matrix. These structural features are known to favor the accommodation and retention of bioactive compounds relative to fully crys-

talline lipid systems. For propolis in particular, the predominance of lipophilic flavonoids and related phenolic compounds further promotes favorable partitioning into the lipid domains, enhancing entrapment and reducing expulsion during nanosystem formation and storage [27]. On this basis, a propolis loading of 0.15 g propolis extract equivalents/g lipid material was selected as a rational formulation entry point for subsequent physicochemical, release, and biorelevant media studies.

2.3. Characterization of NLC and NLC-Pe

The physicochemical properties of the unloaded NLC and propolis-loaded formulation (NLC–Pe) are summarized in Table 2. The unloaded NLC exhibited a hydrodynamic diameter of 150 ± 3 nm, which increased to 207 ± 2 nm upon incorporation of the ethanolic propolis extract. This size increase is consistent with successful incorporation of extract constituents within the lipid matrix and has been widely reported for NLC systems loaded with natural products [28,29].

Table 2. Physicochemical characterization of NLC and NLC-Pe, showing hydrodynamic diameter (nm ± SD), polydispersity index (± SD) and zeta potential (mV ± SD) (n = 3).

Nanosystem	Hydrodynamic Diameter (nm ± SD)	Polydispersity Index (±SD)	Zeta Potential (mV ± SD)
NLC	150.4 ± 3.2	0.11 ± 0.01	−10.3 ± 0.5
NLC-Pe	206.5 ± 1.9	0.12 ± 0.01	−8.0 ± 0.4

In both formulations, the PdI remained below 0.15, indicating narrow size distributions and good colloidal homogeneity. Zeta potential values were moderately negative (−10.3 mV and −8.0 mV for the NLC and NLC-Pe, respectively). Although, the zeta potential varied after the incorporation of EPE, the magnitude of this change is not expected to compromise colloidal stability. Instead, colloidal stability in this system is primarily governed by steric stabilization provided by the poly (ethylene glycol) chains present in Gelucire®, which form a hydrated interfacial layer that limits particle-particle interactions even at relatively low electrostatic potentials.

Long-term colloidal stability studies further supported the robustness of the formulation. Over a storage period of 90 days at both 4 °C and 25 °C, no meaningful changes in hydrodynamic diameter, PdI, or zeta potential were observed (Figure 2). Importantly, encapsulation efficiency remained consistently above 96% at 30, 60, and 90 days, indicating minimal payload expulsion over time. Together, these results demonstrate that the selected propolis loading yields an NLC system with high physicochemical stability and retention capacity, suitable for subsequent evaluation under biorelevant release conditions.

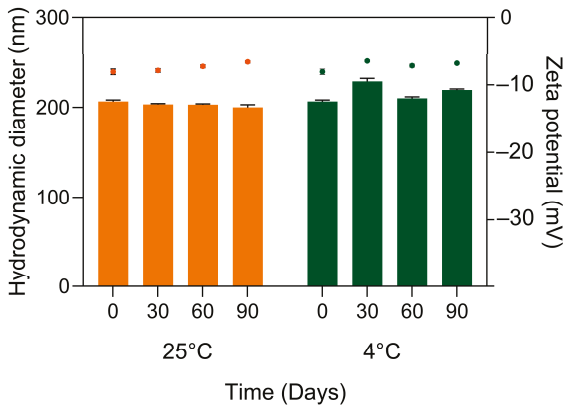

Figure 2. Colloidal stability of NLC and NLC-Pe over 0, 30, 60, and 90 days of storage at 25 °C and 4 °C (n = 3). Bar represents hydrodynamic diameter, while dots represent zeta potential.

2.4. Release Behavior in Aqueous Buffers

Because propolis is a chemically complex natural extract composed of numerous phenolic constituents rather than a single defined compound, release profiles were expressed as the cumulative mass of propolis extract equivalents (μg) detected in the external medium. This representation provides a direct estimate of the amount of extract that becomes analytically accessible under the tested conditions. Consequently, the reported values reflect the fraction of propolis that partitions into or becomes solubilized within the surrounding medium, rather than complete depletion of the extract from the lipid carrier.

In acidic buffer (pH 2.0), NLC–Pe exhibited minimal release, reaching approximately 967 μg after 4 h, indicating strong payload retention under gastric-like aqueous conditions (Figure 3a). At pH 6.8, release followed a biphasic profile, with an initial increase to ~1100 μg within the first hour, followed by a slower phase reaching ~1900 μg after 6 h (Figure 3b). This change in slope is consistent with an initial readily accessible fraction (surface-associated or near-surface domains) followed by a slower transport process from deeper regions of the lipid matrix. Such behavior indicates that release under these simple aqueous conditions is governed primarily by diffusion and matrix-partitioning processes within the lipid carrier, rather than by aqueous pH alone. Importantly, the moderate difference observed between the two buffers is consistent with a retentive lipid matrix in which internal diffusion and lipid-extract interactions limit the direct influence of bulk pH on the analytically accessible fraction of propolis. These observations indicate that, under simple aqueous conditions, the nanosystem provides a suitable platform to examine how bile components modulate payload accessibility in more complex biorelevant media.

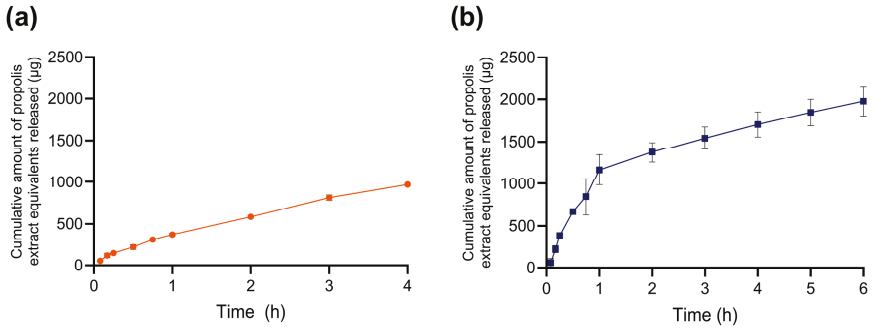

Figure 3. Apparent cumulative release profile of ethanolic propolis extract from NLC-Pe in aqueous buffers at (**a**) pH 2.0 and (**b**) pH 6.8. data are shown as mean ± SD (n = 3).

2.5. Effect of Bile-Component-Containing Media on Apparent Release and Morphology

Bile salts are not passive solubilizers; they are highly surface-active amphiphiles capable of displacing interfacial layers, forming mixed micelles with phospholipids, and promoting lipid reorganization and solubilization processes [30]. Accordingly, the presence of bile salts and phospholipids markedly altered both the apparent release behavior and morphology of NLC-Pe in a pH- and composition-dependent manner. In the FaSSGF, which contains lecithin together with a low concentration of sodium taurocholate, apparent release remained low, reaching only ~550 μg after 2 h (Figure 4a), in line with limited propolis accessibility under strongly acidic conditions. Nevertheless, TEM images revealed increased morphological heterogeneity compared to freshly prepared NLC-Pe, including irregular and globular features (Figure 5b). These observations suggest bile-component-induced interfacial perturbation without extensive depletion of the propolis payload. Such behavior is consistent with previous reports showing that bile salts can induce permeability defects or partial structural rearrangements at sub-solubilizing conditions, producing visible morphological changes that do not necessarily translate into large increases in soluble payload during short time windows [31,32]. Therefore, under our conditions, this

low micromolar taurocholate concentration is sufficient to perturb interfacial organization but remains far below levels typically associated with extensive lipid solubilization.

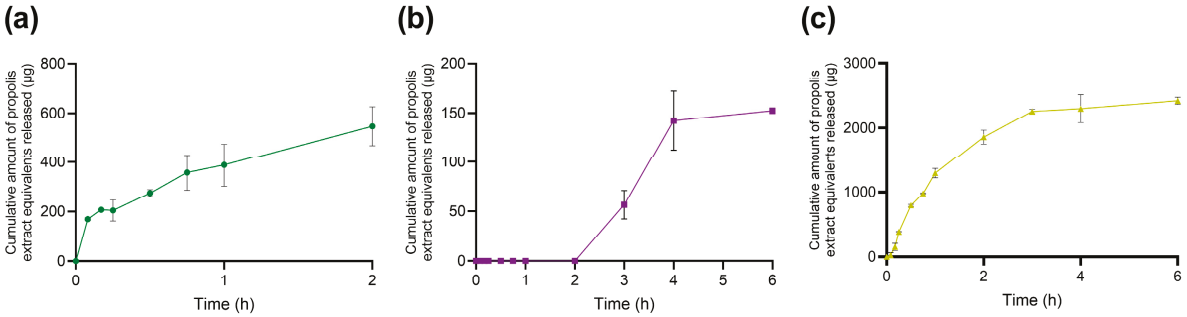

Figure 4. Apparent release profile of the ethanolic propolis extract from NLC-Pe in simulated gastrointestinal media containing bile components: (**a**) FaSSGF, (**b**) FeSSIF, and (**c**) FaSSIF. Data are shown as mean ± SD (n = 3).

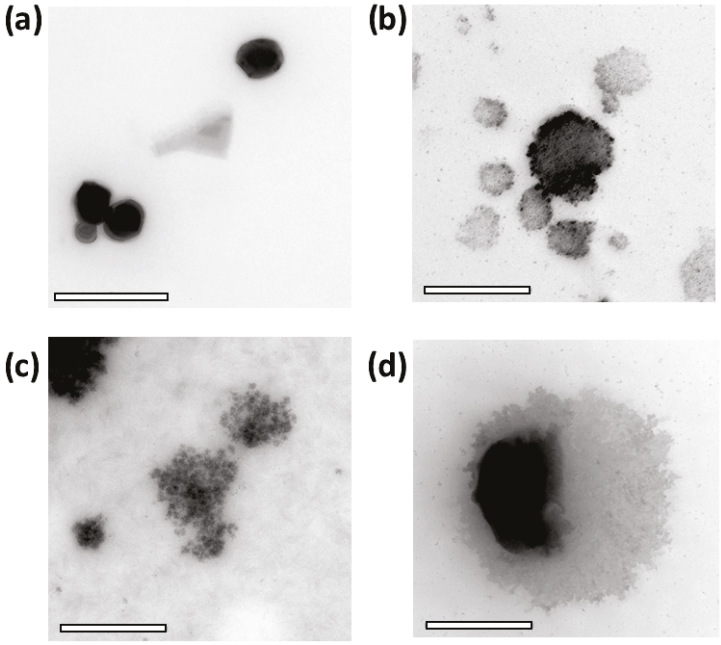

Figure 5. Transmission electron microscopy (TEM) images of (**a**) freshly prepared NLC-Pe (control), (**b**) NLC-Pe after incubation in FaSSGF, (**c**) NLC-Pe after incubation in FeSSIF, and (**d**) NLC-Pe after incubation in FaSSIF. All micrographs were acquired under identical imaging conditions at 20,000× magnification. Scale bar: 500 nm.

In FeSSIF, pronounced morphological remodeling was evident by TEM, including fragmentation and aggregation into smaller lipid domains (Figure 5d). Despite this extensive structural alteration, apparent propolis release remained very low, with little to no release detected initially and only ~150 µg after 6 h (Figure 4b). This apparent divergence between morphology and release is not unexpected in complex biorelevant media and can be rationalized by several non-mutually exclusive physicochemical factors. First, colloidal sequestration and phase partitioning are favored under FeSSIF conditions. Many phenolic constituents of propolis exhibit pH-dependent ionization behavior, and at mildly acidic pH they may remain less ionized and preferentially associated with hydrophobic or colloidal domains rather than partitioning into the assay-accessible aqueous phase. In this context, the high bile salt and phospholipid content of FeSSIF strongly promotes the formation of mixed lipid–bile assemblies that redistribute propolis within colloidal structures without necessarily increasing the analytically measurable fraction, as widely discussed

for FaSSIF/FeSSIF media [33]. Second, the relatively high ionic strength characteristic of FeSSIF may contribute to aggregation-driven masking of release by compressing the electrical double layer and enhancing interparticle attraction, in line with classical DLVO considerations [34]. Such aggregation or bridging of remodeled lipid fragments can reduce the effective interfacial area available for net desorption of propolis markers into the sampled phase, while still yielding "damaged" or heterogeneous morphologies by TEM. Finally, it is important to emphasize that structural disruption and analytical accessibility represent fundamentally different readouts: TEM provides information on morphological states (e.g., fragments, aggregates, globules), whereas the release assay quantifies only the fraction that becomes accessible under the specific sampling and separation conditions employed. In bile-rich media, a substantial fraction of propolis may remain associated with lipid fragments or mixed colloids that are not fully represented in the quantified fraction, resulting in low apparent release despite pronounced morphological changes [31]. While these mechanisms cannot be directly disentangled within the scope of the present experiments, the combined release and TEM data support a coherent physicochemical framework for interpreting the observed behavior. Taken together, FeSSIF at pH 5.0 can be viewed as a condition that strongly remodels the carrier while simultaneously retaining or re-sequestering propolis within bile–phospholipid–lipid colloids.

In contrast, FaSSIF promoted a rapid increase in apparent release, reaching ~14% within the first hour, followed by a plateau at ~2400 μg up to 6 h (Figure 4c). This behavior is consistent with the rapid establishment of a partition equilibrium between the lipid matrix and bile component mixed colloids, yielding a larger assay-accessible fraction under fasted-state intestinal conditions. TEM images revealed altered particles surrounded by halo-like and globular features, indicative of lipid redistribution and secondary colloidal structures rather than complete carrier disintegration (Figure 5d). Notably, these results highlight that morphological alteration and apparent release are not linearly correlated in bile-component-containing media. In particular, FeSSIF induces extensive structural remodeling while retaining propolis within mixed colloidal assemblies, whereas FaSSIF favors higher analytical accessibility despite lower bile salt concentrations.

Although the simulated intestinal media used here did not include lipolytic enzymes, the observed remodeling is mechanistically relevant. Bile salts are known to condition lipid interfaces and facilitate subsequent lipase/colipase action by displacing interfacial material and organizing mixed assemblies [35,36]. Accordingly, the present results isolate the physicochemical contribution of bile components to carrier remodeling and payload accessibility. Fully dynamic digestion studies incorporating enzymatic lipolysis are expected to further modulate these processes and warrant dedicated investigation beyond the scope of the present work [35,37].

This overall interpretation is also consistent with prior studies demonstrating that bile salts can remodel lipid-based carriers without a one-to-one correspondence between structural alteration and the analytically recovered released fraction. In multiple lipid systems, taurocholate or cholate has been shown to trigger interfacial destabilization, vesicle–micelle transitions, or fragmentation under certain compositions and concentration windows, while substantial payload remains associated with mixed colloids or lipid remnants depending on pH and medium composition [31,36,38,39]. Collectively, these studies also emphasize that bile salts do not universally "destroy" lipid carriers in a single step; rather, they promote dynamic reorganization and partitioning processes whose analytical manifestation depends strongly on medium composition and the definition of the measured phase [40,41].

2.6. Assessment of Release Under Near-Physiological pH (pH 7.4)

To further explore release behavior once bile-driven perturbation is no longer dominant, NLC-Pe was evaluated in buffer at near-physiological pH (7.4). Under these conditions, release increased gradually from ~20% at 12 h to ~30% at 24 h, approaching ~40% after 72 h (Figure 6). This sustained release profile is consistent with diffusion- and partition-controlled transport from internal lipid domains over extended times scales. While this experiment does not model absorption or cellular uptake, it supports the premise that a substantial fraction of propolis remains kinetically retained within the lipid matrix and can be released under less aggressive aqueous conditions.

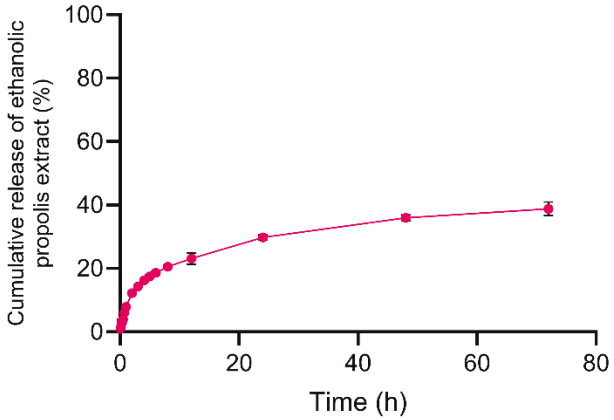

Figure 6. Apparent release profile of ethanolic propolis extract from NLC-Pe in buffer at pH 7.4. data are shown as mean ± SD (n = 3). Percentage release was calculated relative to the initial amount of propolis encapsulated in the NLC formulation.

Comparable trends have been reported for other lipid-based nanosystems. Bidabad et al., observed approximately 20% release of propolis from liposomes after 48 h at pH 7.4 [42], whereas Aytekin et al. reported release values ranging from 40 to 80%, depending on propolis loading and formulation composition [43]. In hybrid systems, Bose et al., showed that increasing the amount and complexity of lipid layers around PLGA nanoparticles significantly delayed payload release compared to polymeric controls [44]. Taken together, these findings support the notion that lipid components can effectively slow the release of propolis constituents, likely reflecting their preferential partitioning into hydrophobic domains within the carrier matrix.

2.7. Cell Viability Assessment

Cell viability was evaluated as a preliminary cytocompatibility screening rather than a comprehensive toxicological assessment. The selection of the HepG2 cell line was based on its extensive use as an in vitro human hepatic model for nanocarrier cytocompatibility and toxicity screening, as well as its relevance for evaluating potential systemic toxicity of drug delivery systems. The liver represents the primary organ involved in xenobiotic metabolism and nanoparticle clearance, making hepatocyte-derived models particularly relevant for preliminary safety assessment of nanomaterials [45,46]. The tested concentration range was selected to enable comparison with previously reported propolis-based and lipid-based nanosystems evaluated under similar in vitro conditions. Accordingly, the results should be interpreted in the context of relative cytocompatibility and concentration—dependent trends rather than absolute toxicity thresholds [47,48].

Free ethanolic propolis extract from Peñaflor did not reduce HepG2 viability within the 10–40 µg/mL range, with cell viability remaining at or above 100% after both 24 and 48 h of exposure (Figure 7). This response is consistent with the antioxidant-rich composi-

tion of the extract and suggests the absence of acute cytotoxic effects at low to moderate concentrations under the tested conditions [48]. When the lipid carrier was evaluated independently (blank NLC), a moderate reduction in cell viability was observed at increasing concentrations, with values decreasing below ~80% from 40 μg/mL onward, suggesting that the lipid nanocarrier itself may contribute partially to the observed cytotoxicity at higher doses, likely through enhanced cellular interactions or membrane perturbation. In contrast, NLC-Pe formulations exhibited a clear concentration-dependent effect. High cell viability was maintained at 10 and 20 μg/mL, whereas progressive reduction was observed at higher concentrations. At 80 μg/mL, cell viability dropped to approximately 20–30%, and at 100 μg/mL a near-complete loss of viability was detected at both 24 and 48 h. The stronger reduction observed for NLC-Pe compared with blank NLC suggests that the incorporation of propolis into the lipid nanocarrier increases the effective intracellular exposure to bioactive propolis constituents, thereby amplifying their biological activity. This behavior likely reflects a combination of factors, including increased intracellular exposure to propolis constituents and the presence of lipid components that may enhance cellular uptake or membrane interactions at higher concentrations [49]. Comparable trends have been reported for other propolis-loaded nanosystems, although absolute viability thresholds vary widely across studies. Syaifie et al., reported lower HepG2 viability for a chitosan-based nanosystem loaded with Indonesian propolis at similar concentrations, highlighting the influence of extract composition and carrier chemistry on cellular response [50]. On the other hand, Amin et al., showed that a nanoemulsion loaded with Egyptian propolis requires approximately 90.8 μg/mL to halve the viability of HepG2 [51]. In contrast, Tzankova et al. reported acceptable cell viability for both free propolis and propolis incorporated into a micellar system at concentrations exceeding 50 μg/mL in the same cell line [52]. Taken together, these observations underscore that the cytocompatibility of propolis-loaded nanosystems does not follow a universal trend but is strongly dependent on the chemical composition of the extract, the nature of the carrier, and the resulting interactions with cells. In this context, the present results indicate that NLC–Pe exhibits acceptable cytocompatibility at concentrations relevant for in vitro evaluation, while higher concentrations induce a predictable, dose-dependent reduction in viability. These findings support the suitability of the selected formulation for further mechanistic and biopharmaceutical investigations, while also highlighting the need for careful dose selection in future biological studies.

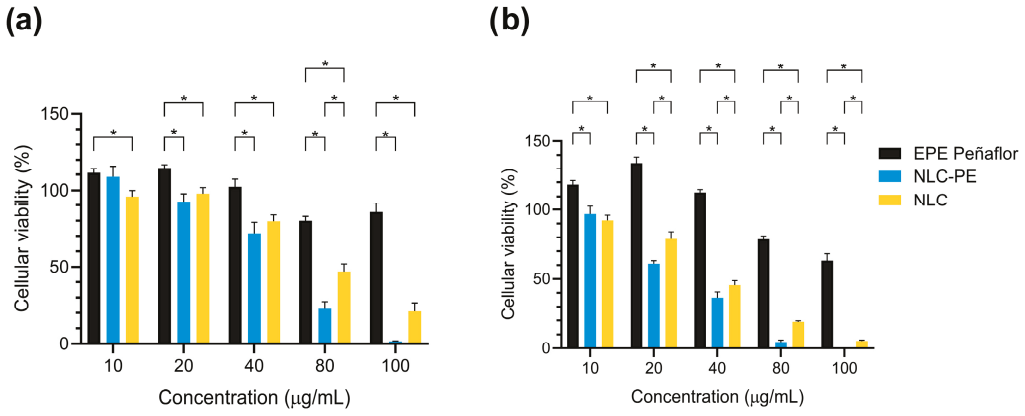

Figure 7. MTT-based cell viability of free ethanolic propolis extract, NLC, and NLC-Pe after (**a**) 24 h and (**b**) 48 h of exposure. * Indicates statistically significant differences. Data are shown as mean ± SD (n = 3).

3. Materials and Methods

3.1. Materials

Gelucire® 44/14 was donated by Gattefossé (Saint-Priest, France). Miglyol® 812, Tween® 80, dimethyl sulfoxide (DMSO, Molecular Biology grade), Folin–Ciocalteu reagent, sodium carbonate (Na_2CO_3), gallic acid, 2,2-diphenyl-1-picrylhydrazyl (DPPH•, ≥90%), ABTS Single Reagent, fluorescein, 2,2′-Azobis(2-amidinopropane) dihydrochloride (AAPH, 97%), sodium chloride (NaCl), L-α-lecithin (lecithin), pepsin, hydrochloric acid (HCl), sodium taurocholate, sodium hydroxide, acetic acid, sodium phosphate dibasic (Na_2HPO_4), 3-(4,5-dimethylthiazol-2-yl)-2,5-diphenyltetrazolium (MTT, ≥97.5%), and Amicon® Ultra 10 kDa were purchased from Merck (Merck KGaA, Darmstadt, Germany). SnakeSkin™ dialysis tubing (cellulose membrane, 10 kDa MWCO) was purchased from Thermo Fisher Scientific (Carlsbad, CA, USA). Chilean crude propolis samples were obtained from three locations in the Metropolitan Region of Chile: Peñaflor (33°37′00″ S, 70°55′00″ W), Pudahuel (33°26′42″33 S, 70°44′28″7 W), and Pirque (33°37′48″ S, 70°34′12″ W). Dulbecco's Modified Eagle Medium (DMEM high-glucose; Cat# SH30243.02), phosphate-buffered saline (PBS, without calcium and magnesium; Cat# SH302560.1), fetal bovine serum (FBS; Cat# SV30160.03), and penicillin/streptomycin (Cat# SH40003.01) solution were obtained from Cytiva (Marlborough, MA, USA). Trypsin-EDTA solution (0.25%; Cat# 25200-072) was purchased from Thermo Fischer Scientific (Gibco, Waltham, MA, USA). Ultra-pure water (18.2 MΩ·cm) was produced using a Simplicity System from Millipore (Merck KGaA, Darmstadt, Germany). All materials were used as received without any further purification.

3.2. Methods

3.2.1. Extraction and Dewaxing of Raw Propolis

Ethanolic propolis extracts (EPEs) were prepared according to the methodology described by Valenzuela-Barra et al., with minor modifications [53]. Briefly, raw propolis samples, previously cleaned to remove hive residues, foreign materials, and insects, were macerated in technical-grade ethanol (95%) at a 1:5 (*w*/*v*) ratio and maintained at 4–8 °C for approximately 24 h. Subsequently, the mixtures were heated in a thermostatically controlled water bath at 70 °C for 30 min and then returned to 4–8 °C for an additional 24 h. The resulting suspensions were then cold-filtered under reduced pressure to remove waxes. To enhance extraction efficiency, the temperature cycle and subsequent filtration step were repeated once. Combined filtrates were concentrated under reduced pressure using a rotary evaporator at 50 °C. The concentrated EPEs were dried in a vacuum oven at 45–50 °C for 72 h until constant weight was achieved. Finally, the dried extracts were stored protected from light until further use. Extraction yield was calculated based on the recovery of dry mass.

3.2.2. Antioxidant Profile and Total Phenolic Content

The antioxidant profile of free propolis extracts and propolis-loaded NLC was evaluated using complementary spectrophotometric and fluorimetric assays in order to assess both reducing capacity and radical scavenging capacity. All determinations were performed using a microplate reader (BioTek Instruments, Inc., Winooski, VT, USA). Each analysis was conducted at least in triplicate.

Total phenolic content (TPC) was determined using a modified Folin–Ciocalteu colorimetric method [22]. Free propolis extracts were dissolved in ethanol, while propolis-loaded NLC were dispersed under mild agitation to obtain homogeneous suspensions. Aliquots of each sample were mixed with 10% Folin–Ciocalteu reagent and allowed to react for a short pre-incubation period (2 min at 40 °C). Subsequently, 5% Na_2CO_3 solution was added, and the reaction mixtures were incubated for 20 min at 40 °C, and absorbance was

https://doi.org/10.3390/molecules31061028

measured at 765 nm. Gallic acid was used as reference standard, and results were expressed as milligrams of gallic acid equivalents per gram of dry sample (mg GAE/g).

The free radical scavenging capacity against DPPH• was evaluated by determining the concentration required to inhibit 50% of the radical signal (SC_{50}) [54]. Sample solutions or dispersions (50 μL) were mixed with 150 μL of ethanolic DPPH• solution (156 μM) and incubated in the dark at room temperature to allow reaction completion (30 min). Absorbance was recorded at 517 nm, and SC_{50} values were expressed as μg/mL.

The ABTS$\bullet^+$ scavenging capacity was assessed by determining the SC_{50} value following incubation of the samples with a pre-formed ABTS radical cation solution [55]. Sample aliquots (50 μL) were mixed with 150 μL of ABTS radical solution (169 μM) during a fixed incubation period (30 min) in the absence of light; then, absorbance was measured at 732 nm. The antioxidant capacity (SC_{50}) was expressed as μg/mL.

The Ferric-Reducing Antioxidant Power (FRAP) assay was used to assess the reducing capacity of the samples based on the reduction of the Fe^{3+}–TPTZ complex to its ferrous form [56]. Briefly, 10 μL of sample aliquots were mixed with freshly prepared FRAP reagent (290 μL) and incubated in the dark for 60 min. Absorbance was measured at 593 nm, and results were expressed as μmol Trolox equivalents per gram of sample (μmol Trolox/g).

The Oxygen Radical Absorbance (ORAC) assay was performed to evaluate peroxyl radical scavenging activity using fluorescein as a fluorescent probe [57]. To this, 45 μL of samples were pre-incubated with 175 μL of fluorescein solution (108 nM) at 37 °C for 30 min, followed by the addition of AAPH (18 mM) as a peroxyl radical generator. Fluorescence decay was monitored every 2 min during 2 h at excitation and emission wavelengths of 480 and 520 nm, respectively. Antioxidant capacity was quantified by calculating the area under the fluorescence decay curve and expressed as micromoles of Trolox equivalents per gram of sample (μmol Trolox/g).

3.2.3. Fabrication of Nanostructured Lipid Carrier and Propolis Incorporation

Nanostructured lipid carriers (NLCs) were prepared using a slow-drip hot emulsification method, as previously described by our group, with minor adaptations [58]. The lipid phase consisted of Gelucire® 44/14, Miglyol® 812, and Tween® 80, while ultrapure water (Milli Q®) was used as the aqueous phase. Briefly, Gelucire® 44/14, Miglyol® 812 and Tween® 80 were combined and heated to 85 °C in a round-bottom flask under gentle stirring to obtain a homogeneous molten lipid phase. In parallel, the aqueous phase was heated to the same temperature. When both phases reached the temperature, the aqueous phase was slowly dripped onto the lipid phase under constant stirring (400 rpm). The mixture was cooled at 4 °C for at least 30 min without stirring to promote lipid solidification and nanoparticle formation.

For propolis incorporation, the ethanolic propolis extract (EPE) was added directly to the lipid phase prior to emulsification. The fabrication process was otherwise identical to that described above. The amount of propolis incorporated was selected according to the highest percentage of incorporation, and the resulting formulation was denominated NLC-P.

3.2.4. Colloidal Characterization of NLC and NLC-P

The hydrodynamic diameter and polydispersity index (PdI) of NLC and NLC-P were evaluated by dynamic light scattering (DLS), while zeta potential was determined by laser Doppler electrophoresis using a Zetasizer Nano ZS90 (Malver Instruments, Malver, UK). Samples were diluted 1:10 in deionized water and analyzed at a wavelength of 633 nm with a detection angle of 173° and equilibration time of 120 s. Each reported value corresponds to the average of three independent measurements, each consisting of eleven

https://doi.org/10.3390/molecules31061028

determinations. The pH of the dispersion medium (deionized water) was not adjusted and was approximately 6.5 under the experimental conditions.

In addition, colloidal stability in the time was measured by three months at 4 °C and 25 °C. Hydrodynamic diameter, PdI and zeta potential were monitored at predefined time points and compared with freshly prepared formulations.

3.2.5. Evaluation of Propolis Loading Capacity

The maximum loading capacity of the selected propolis in the NLC system was systematically evaluated by varying the propolis-to-lipid ratio. Propolis concentrations of 1.0, 0.6, 0.3, 0.15, and 0.07 g of propolis per 1 g of Gelucire® 44/14 were investigated. To quantify the propolis incorporation, NLC-Pe formulations were subjected to ultrafiltration in 10,000 Da MWCO Amicon® Ultra at 6900× *g* for 10 min. The ultrafiltrate containing the non-encapsulated fraction was collected and analyzed spectrophotometrically.

Propolis concentrations were determined by UV–Vis spectroscopy at 283 nm using a Genesys 180 UV–Vis spectrophotometer (Thermo Scientific, Waltham, MA, USA). Quantification was performed using a calibration curve constructed from serial dilutions of the same ethanolic propolis extract used for nanoparticle preparation [26]. Because propolis is a chemically complex natural extract composed of multiple phenolic and flavonoid constituents rather than a single defined compound, the analytical objective of this method was to estimate the total amount of extract present in the sample rather than quantify individual molecular species [59,60]. Accordingly, measured concentrations were expressed as propolis extract equivalents, determined by interpolation from the calibration curve.

The drug loading and incorporation efficiency percentages were determined according to the following Equation (1):

$$\%\ \text{Encapsulation efficiency}\ (\%EE) = \frac{\text{Propolis}_{\text{total}} - \text{Propolis}_{\text{free}}}{\text{Propolis}_{\text{total}}} * 100 \quad (1)$$

where $\text{Propolis}_{\text{total}}$ corresponds to the initial amount of propolis added during formulation and $\text{Propolis}_{\text{free}}$ corresponds to the amount detected in the ultrafiltrate.

3.2.6. In Vitro Release Study

Release studies were performed under gastrointestinally relevant residence times using both standard aqueous buffers and the bile-component-containing simulated media. Propolis release from the NLC formulation was determined using the dialysis bag method designed to monitor the fraction of propolis that becomes accessible to the surrounding medium. Briefly, SnakeSkin™ dialysis tubing (10 kDa MWCO) was preconditioned according to the manufacturer's instructions and filled with a defined volume of NLC-Pe dispersion. The dialysis bags (3 mL) were immersed in 30 mL of release medium maintained at 37 ± 0.5 °C under continuous agitation (100 rpm) using an orbital incubator shaker (LabTech, LSI-3016R, Bucheon, Korea). At predetermined time points, aliquots (1.5 mL) were withdrawn from the external medium and immediately replaced with an equal volume of fresh medium to maintain sink conditions. Release experiments in standard aqueous buffers were performed at pH 1.2 and pH 6.8 for 2 h and 6 h, respectively, in accordance with gastrointestinally relevant residence times.

Propolis concentration in the collected samples was quantified by spectrophotometry at 283 nm as described above. Based on the measured concentration and the sampling volume, the cumulative amount of propolis extract equivalents released into the medium was calculated and expressed as μg of propolis extract equivalents. Results are therefore reported as cumulative apparent release over time. Because bile-component-containing media generate mixed colloidal structures capable of solubilizing lipophilic compounds,

the measured values represent the analytically accessible fraction of propolis in the external medium, rather than complete depletion of propolis from the carrier or total nanoparticle disintegration. This distinction is well established for FaSSIF- and FeSSIF-type media, where solubilization and partitioning phenomena strongly depend on the colloidal phase behavior and analytical separation conditions [33].

3.2.7. In Vitro Release Study in Simulated Gastrointestinal Media Containing Bile Components

To investigate the physicochemical response of propolis-loaded NLC under biorelevant conditions, release studies were conducted in simulated gastrointestinal media containing bile components at different pH values. A fasted-state simulated gastric fluid (FaSSGF, pH 1.6) was prepared using NaCl and lecithin (20 μM), supplemented with pepsin (0.1 g), and adjusted pH with HCl. Sodium taurocholate was included at a sub-millimolar concentration (80 μM) [61]. A fed-state simulated intestinal fluid (FeSSIF, pH 5.0) was prepared using sodium taurocholate (15 mM) and lecithin (3.75 mM), together with NaCl (11.87 g), NaOH (4.04 g), and acetic acid (8.65 g) to reach the target composition and pH. A fasted-state simulated intestinal fluid (FaSSIF, pH 6.5) was prepared using sodium taurocholate (3 mM) and lecithin (0.75 mM), with Na_2HPO_4 (3.438 g) and NaCl (6.18 g), adjusting pH with NaOH as required [62].

These media were selected because bile salts and phospholipids are known to form mixed colloidal assemblies that strongly modulate lipid solubilization, interfacial organization, and the apparent release behavior of lipid-based delivery systems [30].

It should be noted that no lipolytic enzymes were included in the simulated intestinal media. This deliberate choice was made to isolate the physicochemical contribution of bile components (bile salts and phospholipids) to carrier remodeling and payload accessibility. Enzyme-mediated lipolysis and fully dynamic digestion processes, which are known to further influence lipid-based systems, were therefore intentionally excluded and are considered beyond the scope of the present study.

3.2.8. Morphologic Analysis Before and After Exposure to the Simulated Gastrointestinal Media

Transmission electron microscopy (TEM) was employed to qualitatively assess morphological changes in NLC–Pe before and after exposure to the simulated gastrointestinal media. TEM images were acquired using a LIBRA 120 transmission electron microscope (Zeiss, Jena, Germany), and all micrographs presented were obtained under identical imaging conditions. Freshly prepared NLC-Pe were used as controls, while treated samples were recovered after incubation under the corresponding conditions (FaSSGF pH 1.6, 2 h; FeSSIF pH 5.0, 6 h; FaSSIF pH 6.5, 6 h). TEM micrographs were analyzed qualitatively to evaluate particle integrity, size heterogeneity, aggregation behavior, and the formation of secondary lipid or mixed colloidal structures. TEM analysis was intended to provide structural insight into bile-component-induced remodeling rather than quantitative size determination.

3.2.9. Cellular Viability

Cell viability of the developed formulations, free ethanolic propolis extract (EPE), unloaded NLC, and NLC-Pe, were evaluated in vitro using the colorimetric MTT assay. The human hepatocellular carcinoma cell line HepG2 (ATCC® HB-806, Manassas, VA, USA), widely used as a model for hepatotoxicity and hepatic metabolism, was employed for this purpose [26]. HepG2 cells were cultured in DMEM with high glucose content, supplemented with 10% FBS and penicillin (100 μg/mL)–streptomycin (100 μg/mL). Cultures were maintained at 37 °C in a humidified atmosphere containing 5% CO_2. Upon reaching approximately 90% confluence, cells were washed twice with 1× PBS and detached using

https://doi.org/10.3390/molecules31061028

0.25% trypsin–EDTA. Cells were then seeded into 96-well plates at a density of 1×10^4 cells per well in a final volume of 100 µL and incubated for 24 h to allow cell attachment. After the adhesion period, the culture medium was removed, and cells were treated with the different formulations diluted in supplemented culture medium. Final concentrations of 10, 20, 40, 80, and 100 µg/mL were evaluated at exposure times of 24 h and 48 h. At each time point, MTT solution was added to each well to achieve a final concentration of 0.5 mg/mL, and plates were incubated for 1.5 h at 37 °C. Absorbance was measured at 570 nm using a microplate reader (Synergy H1, BioTek, Winooski, VT, USA) with Gen5 software (v3.16) [63]. Cell viability was calculated as the percentage of absorbance relative to the negative control, according to the following equation:

$$\text{Cellular viability } (\%) = \frac{(\text{sample absorbance} - \text{blank}(\text{medium} + \text{EPE, NLC or NLC-Pe})}{\text{Mean } (\text{control absorbance} - (\text{blanck medium}))} * 100 \quad (2)$$

3.2.10. Statistical Analysis

Statistical significance was determined at $p < 0.05$ using one-way or two-way ANOVA, as appropriate, followed by Tukey's post hoc test, performed with GraphPad Prism version 8.0.1 (San Diego, CA, USA). Results are expressed as mean ± standard deviation (SD) from three independent experiments performed in triplicate.

4. Conclusions

In this study, an NLC based on Gelucire® 44/14 was successfully developed as a delivery platform for a selected Chilean ethanolic propolis extract. The resulting nanosystem exhibited high encapsulation efficiency, narrow size distribution, and sustained physicochemical stability over time, supporting its suitability for the incorporation of chemically complex natural extracts.

Release experiments in simple aqueous buffers demonstrated strong retention of propolis within the lipid matrix, consistent with diffusion- and partition-controlled transport rather than rapid carrier disintegration. In contrast, exposure to simulated gastrointestinal media containing bile components induced pronounced pH- and composition-dependent effects. It is noteworthy that the extensive morphological remodeling observed by transmission electron microscopy did not translate into proportional increases in analytically accessible propolis, underscoring the distinction between structural alteration of the carrier and measurable release. In bile-rich media, propolis largely remained associated with mixed lipid-bile colloidal assemblies, whereas fasted-state intestinal conditions favored a higher accessible fraction without complete disruption of the nanosystem.

These findings highlight that apparent release from lipid-based nanocarriers under biorelevant conditions reflects complex partitioning, redistribution, and sequestration processes rather than a simple depletion of the payload. By deliberately excluding lipolytic enzymes, the present work isolates the physicochemical contribution of bile salts and phospholipids, providing mechanistic insights into early-stage carrier remodeling prior to enzymatic digestion. Preliminary cytocompatibility studies further indicated concentration-dependent effects that are consistent with previously reported propolis-loaded nanosystems.

Overall, this work demonstrates that nanostructured lipid carriers can effectively retain and modulate the accessibility of propolis under relevant gastrointestinal conditions, and that bile-induced structural changes do not necessarily imply increased release. The results contribute to a deeper physicochemical understanding of lipid-based delivery systems for complex natural products and establish a robust framework for future studies incorporating dynamic digestion models and absorption-related processes.

https://doi.org/10.3390/molecules31061028

Supplementary Materials: The following supporting information can be downloaded at: https://www.mdpi.com/article/10.3390/molecules31061028/s1, Table S1: Antioxidant profile and total phenolic content of NLC loaded with propolis extracts from Peñaflor, Pirque, and Pudahuel, evaluated by DPPH•, ABTS•+, ORAC, FRAP, and total phenolic content (TPC) assays.

Author Contributions: Conceptualization, F.A. and A.C.O.; methodology, J.C.-R., M.J.S., F.A. and A.C.O.; software, J.C.-R. and J.S.-S.; validation, F.A. and A.C.O.; formal analysis, J.C.-R., F.A. and A.C.O.; investigation, J.C.-R., J.S.-S. and R.V.-A.; resources, C.F.L., M.J.S. and A.C.O.; data curation, J.C.-R., F.A. and A.C.O.; writing—original draft preparation, J.C.-R., J.S.-S., F.A. and A.C.O.; writing—review and editing, R.V.-A., F.A. and A.C.O.; visualization, F.A. and A.C.O.; supervision, F.A. and A.C.O.; project administration, A.C.O.; funding acquisition, C.F.L., M.J.S. and A.C.O. All authors have read and agreed to the published version of the manuscript.

Funding: This research was funded by ANID/FONDECYT Project 11240466 (Ortiz, AC), ANID/FONDECYT Project 1220075 (Simirgiotis, M.J.), Centro Basal Ciencia & Vida, FB210008, Financiamiento Basal para Centros Científicos y Tecnológicos de Excelencia de ANID (Lagos, CF).

Institutional Review Board Statement: Not applicable.

Informed Consent Statement: Not applicable.

Data Availability Statement: The manuscript and Supplementary Materials contain the reported data. Additional relevant data can be obtained upon request from the corresponding author.

Acknowledgments: We thank the SEM and TEM technical support of the Electron Microscopy Unit, a core facility—Zeiss Reference Center of Universidad Austral de Chile.

Conflicts of Interest: The authors declare no conflicts of interest.

References

1. Sarapa, A.; Peter, A.; Buettner, A.; Loos, H.M. Organoleptic and Chemical Properties of Propolis: A Review. *Eur. Food Res. Technol.* **2025**, *251*, 1331–1352. [CrossRef]
2. Zullkiflee, N.; Taha, H.; Usman, A. Propolis: Its Role and Efficacy in Human Health and Diseases. *Molecules* **2022**, *27*, 6120. [CrossRef]
3. Wieczorek, P.P.; Hudz, N.; Yezerska, O.; Horčinová-Sedláčková, V.; Shanaida, M.; Korytniuk, O.; Jasicka-Misiak, I. Chemical Variability and Pharmacological Potential of Propolis as a Source for the Development of New Pharmaceutical Products. *Molecules* **2022**, *27*, 1600. [CrossRef]
4. Kasote, D.; Bankova, V.; Viljoen, A.M. Propolis: Chemical Diversity and Challenges in Quality Control. *Phytochem. Rev.* **2022**, *21*, 1887–1911. [CrossRef]
5. Hossain, R.; Quispe, C.; Khan, R.A.; Saikat, A.S.M.; Ray, P.; Ongalbek, D.; Yeskaliyeva, B.; Jain, D.; Smeriglio, A.; Trombetta, D.; et al. Propolis: An Update on Its Chemistry and Pharmacological Applications. *Chin. Med.* **2022**, *17*, 100. [CrossRef] [PubMed]
6. Karadag, A.; Saroglu, O. Propolis-Loaded Liposomes: Characterization and Evaluation of the in Vitro Bioaccessibility of Phenolic Compounds. *ADMET DMPK* **2024**, *12*, 209–224. [CrossRef]
7. Zhang, Y.; Wang, Y.; Lu, Y.; Quan, H.; Wang, Y.; Song, S.; Guo, H. Advanced Oral Drug Delivery Systems for Gastrointestinal Targeted Delivery: The Design Principles and Foundations. *J. Nanobiotechnol.* **2025**, *23*, 400. [CrossRef]
8. Wang, S.; Zhang, Z.; Li, D.; Li, L. Elucidating Impacts of Partitioning and Transmembrane Permeability on Absorption of Chemicals in Human Gastrointestinal Tract. *Environ. Int.* **2024**, *193*, 109108. [CrossRef] [PubMed]
9. Kustiawan, P.M.; Syaifie, P.H.; Al Khairy Siregar, K.A.; Ibadillah, D.; Mardliyati, E. New Insights of Propolis Nanoformulation and Its Therapeutic Potential in Human Diseases. *ADMET DMPK* **2024**, *12*, 1–26. [CrossRef]
10. Lee, M.-K. Liposomes for Enhanced Bioavailability of Water-Insoluble Drugs: In Vivo Evidence and Recent Approaches. *Pharmaceutics* **2020**, *12*, 264. [CrossRef]
11. Alsaab, H.O.; Alharbi, F.D.; Alhibs, A.S.; Alanazi, N.B.; Alshehri, B.Y.; Saleh, M.A.; Alshehri, F.S.; Algarni, M.A.; Almugaiteeb, T.; Uddin, M.N.; et al. PLGA-Based Nanomedicine: History of Advancement and Development in Clinical Applications of Multiple Diseases. *Pharmaceutics* **2022**, *14*, 2728. [CrossRef]
12. Iadnut, A.; Mamoon, K.; Thammasit, P.; Pawichai, S.; Tima, S.; Preechasuth, K.; Kaewkod, T.; Tragoolpua, Y.; Tragoolpua, K. In Vitro Antifungal and Antivirulence Activities of Biologically Synthesized Ethanolic Extract of Propolis-Loaded PLGA Nanoparticles against Candida Albicans. *Evid.-Based Complement. Altern. Med.* **2019**, *2019*, 3715481. [CrossRef]

13. Shahab-Navaei, F.; Asoodeh, A. Synthesis of Optimized Propolis Solid Lipid Nanoparticles with Desirable Antimicrobial, Antioxidant, and Anti-Cancer Properties. *Sci. Rep.* **2023**, *13*, 18290. [CrossRef]
14. Shamsuddin, N.A.M.; Zulfakar, M.H. Nanostructured Lipid Carriers for the Delivery of Natural Bioactive Compounds. *Curr. Drug Deliv.* **2022**, *20*, 127–143. [CrossRef]
15. Nguyen, V.H.; Thuy, V.N.; Van, T.V.; Dao, A.H.; Lee, B.-J. Nanostructured Lipid Carriers and Their Potential Applications for Versatile Drug Delivery via Oral Administration. *OpenNano* **2022**, *8*, 100064. [CrossRef]
16. Prema, R.; Prabhakaran, M.; Meenakshi, M.; Sankar, C. A Comprehensive Review on Nanostructured Lipid Carriers. *J. Drug Deliv. Ther.* **2025**, *15*, 172–186. [CrossRef]
17. Viegas, C.; Patrício, A.B.; Prata, J.M.; Nadhman, A.; Chintamaneni, P.K.; Fonte, P. Solid Lipid Nanoparticles vs. Nanostructured Lipid Carriers: A Comparative Review. *Pharmaceutics* **2023**, *15*, 1593. [CrossRef]
18. Sadeer, N.B.; Montesano, D.; Albrizio, S.; Zengin, G.; Mahomoodally, M.F. The Versatility of Antioxidant Assays in Food Science and Safety—Chemistry, Applications, Strengths, and Limitations. *Antioxidants* **2020**, *9*, 709. [CrossRef] [PubMed]
19. Christfort, J.F.; Tollemeto, M.; Li, Y.; Thamdrup, L.H.E.; van Hest, J.; Boisen, A. Colloidal Interactions in Simulated Intestinal Fluids: Implications for Oral Drug Delivery at the Nanoscale. *Small Sci.* **2025**, *5*, 2500350. [CrossRef]
20. Gulcin, İ. Antioxidants: A Comprehensive Review. *Arch. Toxicol.* **2025**, *99*, 1893–1997. [CrossRef] [PubMed]
21. Alvear, M.; Santos, E.; Cabezas, F.; Pérez-SanMartín, A.; Lespinasse, M.; Veloz, J. Geographic Area of Collection Determines the Chemical Composition and Antimicrobial Potential of Three Extracts of Chilean Propolis. *Plants* **2021**, *10*, 1543. [CrossRef]
22. Pérez, M.; Dominguez-López, I.; Lamuela-Raventós, R.M. The Chemistry Behind the Folin–Ciocalteu Method for the Estimation of (Poly)Phenol Content in Food: Total Phenolic Intake in a Mediterranean Dietary Pattern. *J. Agric. Food Chem.* **2023**, *71*, 17543–17553. [CrossRef] [PubMed]
23. Shahidi, F.; Samarasinghe, A. How to Assess Antioxidant Activity? Advances, Limitations, and Applications of in Vitro, in Vivo, and Ex Vivo Approaches. *Food Prod. Process. Nutr.* **2025**, *7*, 50. [CrossRef] [PubMed]
24. Sadowska-Bartosz, I.; Bartosz, G. Evaluation of The Antioxidant Capacity of Food Products: Methods, Applications and Limitations. *Processes* **2022**, *10*, 2031. [CrossRef]
25. Munteanu, I.G.; Apetrei, C. Analytical Methods Used in Determining Antioxidant Activity: A Review. *Int. J. Mol. Sci.* **2021**, *22*, 3380. [CrossRef]
26. Shaker, S.A.; Alshufta, S.M.; Gowayed, M.A.; El-Salamouni, N.S.; Bassam, S.M.; Megahed, M.A.; El-Tahan, R.A. Propolis-Loaded Nanostructured Lipid Carriers Halt Breast Cancer Progression through miRNA-223 Related Pathways: An In-Vitro/In-Vivo Experiment. *Sci. Rep.* **2023**, *13*, 15752. [CrossRef]
27. Suhandi, C.; Wilar, G.; Mohammed, A.F.A.; Mahmoud, S.A.; Muchtaridi, M.; Shamsuddin, S.; Safuan, S.; Lesmana, R.; Hasan, N.; Zulhendri, F.; et al. Propolis-Based Nanostructured Lipid Carrier of α-Mangostin for Promoting Diabetic Wound Healing in Alloxan-Induced Mice. *J. Inflamm. Res.* **2025**, *18*, 7443–7457. [CrossRef]
28. Pardeike, J.; Hommoss, A.; Müller, R.H. Lipid Nanoparticles (SLN, NLC) in Cosmetic and Pharmaceutical Dermal Products. *Int. J. Pharm.* **2009**, *366*, 170–184. [CrossRef]
29. Mehnert, W.; Mäder, K. Solid Lipid Nanoparticles: Production, Characterization and Applications. *Adv. Drug Deliv. Rev.* **2001**, *47*, 165–196. [CrossRef]
30. Sarkar, A.; Ye, A.; Singh, H. On the Role of Bile Salts in the Digestion of Emulsified Lipids. *Food Hydrocoll.* **2016**, *60*, 77–84. [CrossRef]
31. Fatouros, D.G.; Bergenstahl, B.; Mullertz, A. Morphological Observations on a Lipid-Based Drug Delivery System during in Vitro Digestion. *Eur. J. Pharm. Sci.* **2007**, *31*, 85–94. [CrossRef]
32. Kokkona, M.; Kallinteri, P.; Fatouros, D.; Antimisiaris, S.G. Stability of SUV Liposomes in the Presence of Cholate Salts and Pancreatic Lipases: Effect of Lipid Composition. *Eur. J. Pharm. Sci.* **2000**, *9*, 245–252. [CrossRef]
33. Frank, K.J.; Westedt, U.; Rosenblatt, K.M.; Hölig, P.; Rosenberg, J.; Mägerlein, M.; Brandl, M.; Fricker, G. Impact of FaSSIF on the Solubility and Dissolution-/Permeation Rate of a Poorly Water-Soluble Compound. *Eur. J. Pharm. Sci.* **2012**, *47*, 16–20. [CrossRef]
34. Dumont, C.; Bourgeois, S.; Fessi, H.; Dugas, P.-Y.; Jannin, V. In-Vitro Evaluation of Solid Lipid Nanoparticles: Ability to Encapsulate, Release and Ensure Effective Protection of Peptides in the Gastrointestinal Tract. *Int. J. Pharm.* **2019**, *565*, 409–418. [CrossRef] [PubMed]
35. Thomas, N.; Holm, R.; Rades, T.; Müllertz, A. Characterising Lipid Lipolysis and Its Implication in Lipid-Based Formulation Development. *AAPS J.* **2012**, *14*, 860–871. [CrossRef]
36. Jannin, V.; Blas, L.; Chevrier, S.; Miolane, C.; Demarne, F.; Spitzer, D. Evaluation of the Digestibility of Solid Lipid Nanoparticles of Glyceryl Dibehenate Produced by Two Techniques: Ultrasonication and Spray-Flash Evaporation. *Eur. J. Pharm. Sci.* **2018**, *111*, 91–95. [CrossRef]

37. Williams, H.D.; Anby, M.U.; Sassene, P.; Kleberg, K.; Bakala-N'Goma, J.-C.; Calderone, M.; Jannin, V.; Igonin, A.; Partheil, A.; Marchaud, D.; et al. Toward the Establishment of Standardized in Vitro Tests for Lipid-Based Formulations. 2. The Effect of Bile Salt Concentration and Drug Loading on the Performance of Type I, II, IIIA, IIIB, and IV Formulations during in Vitro Digestion. *Mol. Pharm.* **2012**, *9*, 3286–3300. [CrossRef]
38. Lüdtke, F.L.; Fernandes, J.-M.; Gonçalves, R.F.S.; Martins, J.T.; Berni, P.; Ribeiro, A.P.B.; Vicente, A.A.; Pinheiro, A.C. Performance of β-Carotene-Loaded Nanostructured Lipid Carriers under Dynamic in Vitro Digestion System: Influence of the Emulsifier Type. *J. Food Sci.* **2024**, *89*, 3290–3305. [CrossRef]
39. Hyun, J.E.; Yi, H.-Y.; Hong, G.-P.; Chun, J.-Y. Digestion Stability of Curcumin-Loaded Nanostructured Lipid Carrier. *LWT* **2022**, *162*, 113474. [CrossRef]
40. Sun, R.; Wei, C.; Tang, X.; Sun, Y.; Ji, J. Nanostructured Lipid Carrier-Filled Hydrogel Beads for the Delivery of Curcumin: Digestion, Intestinal Permeation, and Antioxidant Bioactivity After Gastrointestinal Digestion. *Pharmaceutics* **2025**, *17*, 541. [CrossRef] [PubMed]
41. Paternostre, M.T.; Roux, M.; Rigaud, J.L. Mechanisms of Membrane Protein Insertion into Liposomes during Reconstitution Procedures Involving the Use of Detergents. 1. Solubilization of Large Unilamellar Liposomes (Prepared by Reverse-Phase Evaporation) by Triton X-100, Octyl Glucoside, and Sodium Cholate. *Biochemistry* **1988**, *27*, 2668–2677. [CrossRef] [PubMed]
42. Bidabad, S.; Ahmadpour Yazdi, H.; Zolghadr, L.; Valivand, N.; Gheibi, N. Evaluation of Liposome Encapsulated Propolis Nanoparticles on Cell Proliferation and Apoptosis in A375 Melanoma Cancer Cell Line. *Food Sci. Nutr.* **2025**, *13*, e70303. [CrossRef] [PubMed]
43. Aytekin, A.A.; Tuncay Tanrıverdi, S.; Aydın Köse, F.; Kart, D.; Eroğlu, İ.; Özer, Ö. Propolis Loaded Liposomes: Evaluation of Antimicrobial and Antioxidant Activities. *J. Liposome Res.* **2020**, *30*, 107–116. [CrossRef]
44. Bose, R.J.; Lee, S.-H.; Park, H. Lipid Polymer Hybrid Nanospheres Encapsulating Antiproliferative Agents for Stent Applications. *J. Ind. Eng. Chem.* **2016**, *36*, 284–292. [CrossRef]
45. Godoy, P.; Hewitt, N.J.; Albrecht, U.; Andersen, M.E.; Ansari, N.; Bhattacharya, S.; Bode, J.G.; Bolleyn, J.; Borner, C.; Böttger, J.; et al. Recent Advances in 2D and 3D in Vitro Systems Using Primary Hepatocytes, Alternative Hepatocyte Sources and Non-Parenchymal Liver Cells and Their Use in Investigating Mechanisms of Hepatotoxicity, Cell Signaling and ADME. *Arch. Toxicol.* **2013**, *87*, 1315–1530. [CrossRef] [PubMed]
46. Elje, E.; Mariussen, E.; Moriones, O.H.; Bastús, N.G.; Puntes, V.; Kohl, Y.; Dusinska, M.; Rundén-Pran, E. Hepato(Geno)Toxicity Assessment of Nanoparticles in a HepG2 Liver Spheroid Model. *Nanomaterials* **2020**, *10*, 545. [CrossRef]
47. Ismail, N.M. Propolis Nanoparticles Combined with Gamma-Irradiation Enhance the Potency of Anticancer Against HepG2 Cell Lines: Invitro Investigation. *BioNanoScience* **2024**, *14*, 2457–2465. [CrossRef]
48. Umthong, S.; Phuwapraisirisan, P.; Puthong, S.; Chanchao, C. In Vitro Antiproliferative Activity of Partially Purified Trigona Laeviceps Propolis from Thailand on Human Cancer Cell Lines. *BMC Complement. Altern. Med.* **2011**, *11*, 37. [CrossRef]
49. Jeitler, R.; Glader, C.; König, G.; Kaplan, J.; Tetyczka, C.; Remmelgas, J.; Mußbacher, M.; Fröhlich, E.; Roblegg, E. On the Structure, Stability, and Cell Uptake of Nanostructured Lipid Carriers for Drug Delivery. *Mol. Pharm.* **2024**, *21*, 3674–3683. [CrossRef]
50. Syaifie, P.H.; Siregar, K.A.A.K.; Fadhilah, I.; Anggraini, A.; Jauhar, M.M.; Mardliyati, E.; Puthong, S.; Meemongkolkiat, T.; Khongkarat, P.; Chanchao, C.; et al. Nanoencapsulation of East Kalimantan Propolis with Chitosan Using Modified Ionic Gelation: Enhanced Antioxidant and Selective Anticancer Activity. *Food Bioprod. Process.* **2025**, *154*, 426–439. [CrossRef]
51. Amin, A.A.; Mahmoud, K.F.; Salama, M.F.; Longo, V.; Pozzo, L.; Seliem, E.I.; Ibrahim, M.A. Characterization and Stability Evaluation of Egyptian Propolis Extract Nano-Capsules and Their Application. *Sci. Rep.* **2023**, *13*, 16065. [CrossRef]
52. Tzankova, V.; Aluani, D.; Yordanov, Y.; Kondeva-Burdina, M.; Petrov, P.; Bankova, V.; Simeonova, R.; Vitcheva, V.; Odjakov, F.; Apostolov, A.; et al. Micellar Propolis Nanoformulation of High Antioxidant and Hepatoprotective Activity. *Rev. Bras. Farmacogn.* **2019**, *29*, 364–372. [CrossRef]
53. Valenzuela-Barra, G.; Castro, C.; Figueroa, C.; Barriga, A.; Silva, X.; de las Heras, B.; Hortelano, S.; Delporte, C. Anti-Inflammatory Activity and Phenolic Profile of Propolis from Two Locations in Región Metropolitana de Santiago, Chile. *J. Ethnopharmacol.* **2015**, *168*, 37–44. [CrossRef] [PubMed]
54. Rumpf, J.; Burger, R.; Schulze, M. Statistical Evaluation of DPPH, ABTS, FRAP, and Folin-Ciocalteu Assays to Assess the Antioxidant Capacity of Lignins. *Int. J. Biol. Macromol.* **2023**, *233*, 123470. [CrossRef]
55. Ilyasov, I.R.; Beloborodov, V.L.; Selivanova, I.A.; Terekhov, R.P. ABTS/PP Decolorization Assay of Antioxidant Capacity Reaction Pathways. *Int. J. Mol. Sci.* **2020**, *21*, 1131. [CrossRef]
56. Knez, E.; Kadac-Czapska, K.; Grembecka, M. Evaluation of Spectrophotometric Methods for Assessing Antioxidant Potential in Plant Food Samples—A Critical Approach. *Appl. Sci.* **2025**, *15*, 5925. [CrossRef]
57. Asma, U.; Bertotti, M.L.; Zamai, S.; Arnold, M.; Amorati, R.; Scampicchio, M. A Kinetic Approach to Oxygen Radical Absorbance Capacity (ORAC): Restoring Order to the Antioxidant Activity of Hydroxycinnamic Acids and Fruit Juices. *Antioxidants* **2024**, *13*, 222. [CrossRef] [PubMed]

58. Ortiz, A.C.; Yañez, O.; Salas-Huenuleo, E.; Morales, J.O. Development of a Nanostructured Lipid Carrier (NLC) by a Low-Energy Method, Comparison of Release Kinetics and Molecular Dynamics Simulation. *Pharmaceutics* **2021**, *13*, 531. [CrossRef] [PubMed]
59. Popova, M.; Bankova, V.; Butovska, D.; Petkov, V.; Nikolova-Damyanova, B.; Sabatini, A.G.; Marcazzan, G.L.; Bogdanov, S. Validated Methods for the Quantification of Biologically Active Constituents of Poplar-Type Propolis. *Phytochem. Anal.* **2004**, *15*, 235–240. [CrossRef]
60. Popova, M.; Chen, C.-N.; Chen, P.-Y.; Huang, C.-Y.; Bankova, V. A Validated Spectrophotometric Method for Quantification of Prenylated Flavanones in Pacific Propolis from Taiwan. *Phytochem. Anal.* **2010**, *21*, 186–191. [CrossRef]
61. Jantratid, E.; Janssen, N.; Reppas, C.; Dressman, J.B. Dissolution Media Simulating Conditions in the Proximal Human Gastrointestinal Tract: An Update. *Pharm. Res.* **2008**, *25*, 1663–1676. [CrossRef] [PubMed]
62. Amaral Silva, D.; Al-Gousous, J.; Davies, N.M.; Bou Chacra, N.; Webster, G.K.; Lipka, E.; Amidon, G.; Löbenberg, R. Simulated, Biorelevant, Clinically Relevant or Physiologically Relevant Dissolution Media: The Hidden Role of Bicarbonate Buffer. *Eur. J. Pharm. Biopharm.* **2019**, *142*, 8–19. [CrossRef] [PubMed]
63. Carrasco-Rojas, J.; Sandoval, F.I.; Schuh, C.M.A.P.; Lagos, C.F.; Morales, J.O.; Arriagada, F.; Ortiz, A.C. NLC-Based Rifampicin Delivery System: Development and Characterization for Improved Drug Performance Against Staphylococcus Aureus. *Pharmaceutics* **2025**, *17*, 799. [CrossRef] [PubMed]

Disclaimer/Publisher's Note: The statements, opinions and data contained in all publications are solely those of the individual author(s) and contributor(s) and not of MDPI and/or the editor(s). MDPI and/or the editor(s) disclaim responsibility for any injury to people or property resulting from any ideas, methods, instructions or products referred to in the content.

molecules

MDPI

Article

A Dual-Drug Nanocarrier Strategy for Ocular Fungal Infections: Micelles Embedded in Electrospun Nanofibers

Egemen Uzel [1], Meltem Ezgi Durgun [2], Neriman Aydilek [1], Mayram Hacıoğlu [3], Sevgi Güngör [1] and Yıldız Özsoy [1,*]

[1] Department of Pharmaceutical Technology, Faculty of Pharmacy, Istanbul University, Istanbul 34126, Türkiye; egemenuzel@gmail.com (E.U.); neriman.aydilek@ogr.iu.edu.tr (N.A.); sevgi.gungor@istanbul.edu.tr (S.G.)
[2] Department of Pharmaceutical Technology, Faculty of Pharmacy, Istanbul Health and Technology University, Istanbul 34275, Türkiye; meltem.durgun@istun.edu.tr
[3] Department of Pharmaceutical Microbiology, Faculty of Pharmacy, Istanbul University, Istanbul 34126, Türkiye; mayramtuysuz@gmail.com
* Correspondence: yozsoy@istanbul.edu.tr; Tel.: +90-212-440-0000

Abstract

Ocular fungal diseases are associated with severe infection and pain and, in advanced stages, can lead to vision loss. Current treatment options are limited to the topical application of conventional drugs, and the bioavailability of these drugs is quite limited due to ocular barriers. In this study, a dual-drug nanodelivery system was developed to improve intraocular drug delivery by combining antifungal and anti-inflammatory therapies. Posaconazole (PSC), a broad-spectrum triazole antifungal agent, and dexketoprofen trometamol (DKP), a rapidly acting nonsteroidal anti-inflammatory drug, were co-loaded onto polymeric micelles and then incorporated into electrospun poly(vinyl alcohol)/poly(vinylpyrrolidone) (PVA/PVP) nanofiber intraocular implants. DSC, XRD, FTIR, and FESEM analyses showed that both APIs were successfully converted into nanofiber form without disrupting the micelle structure. Comparative studies with DKP solution and PSC commercial oral suspension (Noxafil® 40 mg/mL) showed that the produced micelle-loaded nanofibers provided sustained release and significantly increased ex vivo ocular permeation and penetration. In vitro antifungal activity tests demonstrated efficacy against *Candida albicans*, and HET-CAM toxicity tests showed that the micelle-loaded nanofibers were non-irritating and suitable for ocular application. Overall, the micelle-loaded electrospun nanofiber ocular inserts developed in this study represent a promising platform for combined antifungal and anti-inflammatory ocular therapy.

Keywords: ocular drug delivery; electrospinning; nanofiber inserts; polymeric micelles; posaconazole; dexketoprofen trometamol

1. Introduction

Fungal ocular diseases are less common than bacterial or viral infections; however, if not diagnosed and treated promptly, they can lead to severe morbidity, including vision loss and even blindness, and are often accompanied by pain and inflammation. Their incidence is particularly high in tropical and subtropical regions. Globally, it is estimated that more than one million cases of fungal keratitis occur each year, with serious outcomes—including enucleation—reported in approximately 8–11% of cases. The burden of these infections is also increasing in temperate regions, driven by factors such as the rising use of contact lenses and a higher rate of environmentally related ocular trauma [1,2].

Topical antifungal agents are generally the first-line therapy for these conditions. In severe cases, treatment is often escalated to include systemic therapy and/or combination regimens in addition to topical administration. Systemic antifungals may be used in the management of fungal ocular diseases, and combination approaches frequently incorporate steroidal or non-steroidal anti-inflammatory drugs to alleviate inflammation and pain [3]. Nevertheless, both systemically administered and conventional topical formulations typically exhibit low ocular bioavailability due to the complex barrier properties of ocular tissues, including the tear film, cornea, conjunctiva, sclera, blood–aqueous humor barrier (iris–ciliary body), lens, and blood–retina barrier, which collectively present both lipophilic and hydrophilic obstacles to drug permeation and retention. For example, the ocular bioavailability of conventional eye drops is generally less than 5% [4,5].

To overcome these limitations, research interest in controlled-release platforms and nanocarrier-based delivery systems has increased substantially. Such approaches aim to prolong precorneal residence time, enhance tissue penetration, and improve ocular bioavailability, thereby increasing therapeutic efficacy while minimizing adverse effects [6,7]. In addition, accumulating evidence suggests that combined dosage forms can further improve therapeutic outcomes in various ocular disorders [8,9].

Micelles, one of the nanocarrier systems developed for ocular delivery, are nanoscale structures typically composed of a hydrophobic core and a hydrophilic shell formed from amphiphilic copolymers or surfactants. They are colloidal drug delivery systems that spontaneously assemble in solution when the polymer/surfactant concentration exceeds the critical micelle concentration (CMC) [10]. Amphiphilic surfactants or diblock copolymers self-associate to form micellar structures once a threshold concentration and/or temperature is reached [7]. Micelles generally range from 5 to 200 nm in size and may adopt diverse morphologies, including spherical, cylindrical, or star-like structures. A key feature distinguishing micelles from many other carrier systems is their ability to encapsulate not only lipophilic drugs but also hydrophilic compounds, which makes them well suited for combination drug therapy. Moreover, micellar systems can enhance the corneal permeability of topically administered drugs and are therefore considered promising candidates for delivering therapeutics targeting ocular tissues [11–13].

Nanofiber-based ocular inserts represent another drug delivery platform that has attracted increasing research interest for ocular applications. Nanofibers are nanoscale solid fibrous structures that can be fabricated from natural or synthetic polymers and typically exhibit diameters in the range of 1–1000 nm. Owing to this distinctive architecture, nanofibers are considered promising drug delivery systems and can be engineered to achieve different drug-release kinetics. As a delivery platform, nanofibers offer several advantages, including their suitability for the controlled release of both hydrophilic and lipophilic active substances as well as biomolecules (e.g., antibiotics and proteins) [14]. Additional benefits include a high surface area-to-volume ratio, high porosity, and a structure that can resemble the extracellular matrix of tissues. Moreover, their production methods are often simpler and less costly than those of many other nanostructured delivery systems. Among the available fabrication approaches, electrospinning is the most widely used technique for producing nanofibers [15].

Electrospinning generates ultrafine fibers by applying a high-voltage, low-current electrical potential and is a simple and robust method for producing nanofibers with diameters typically in the 10–1000 nm range [16]. One of its principal advantages is the high degree of control it provides over fiber morphology, enabling researchers to tailor nanofiber properties for specific applications such as tissue engineering, drug delivery, and filtration. In addition, electrospinning is a versatile technique compatible with a broad range of polymers, including natural polymers (e.g., hyaluronic acid, chitosan,

dextran, gelatin, and collagen), synthetic polymers (e.g., poly(lactic acid), poly(lactic-co-glycolic acid), poly(ε-caprolactone), poly(vinyl alcohol), and poly(vinylpyrrolidone), and their blends. This versatility facilitates the production of nanofibers with diverse physicochemical characteristics. In addition, its ability to be used in combination with other drug delivery systems (nanoparticles, dendrimers, micelles, etc.) provides a significant advantage [17–19].

Posaconazole (PSC) is a broad-spectrum second generation triazole antifungal that exhibits low minimum inhibitory concentration (MIC) values against a wide range of fungal strains. It exerts its antifungal activity by altering the fungal cell membrane, primarily through inhibition of ergosterol biosynthesis via interaction with lanosterol 14α-demethylase (CYP51). PSC is classified as a Biopharmaceutics Classification System (BCS) Class II compound, characterized by low aqueous solubility and high permeability. It is highly lipophilic, with a logP of 5.5 [20–22]. Currently, there is no commercially available ocular formulation of PSC. Notably, case reports have described therapeutic benefit even when PSC oral commercial suspension (Noxafil® 40 mg/mL) was diluted and administered topically to the eye in resistant, fungus-derived ocular infections unresponsive to other antifungal treatments [23,24]. Recent studies have increasingly explored the potential of posaconazole for ocular antifungal therapy. Durgun and colleagues optimized micellar formulations that enhanced the aqueous solubility of PSC and improved its permeability across ocular tissues [25]. In subsequent work, they focused on micelle-based in situ gelling systems to further increase the ocular bioavailability of PSC, reporting high antifungal activity without inducing ocular toxicity [26].

Nonsteroidal anti-inflammatory drugs (NSAIDs) are preferred in ocular inflammation to alleviate inflammation, pain, and photophobia. They play a critical supportive role in the treatment of ocular infections, particularly in ocular fungal infections, as an alternative to corticosteroids, which tend to exacerbate the infection [27]. Dexketoprofen trometamol (DKP) is the active S-(+)-enantiomer of ketoprofen. It has a high onset of analgesic effect and, due to its trometamol salt form, has very high sucrose solubility. It offers a better bioavailability profile and higher tolerability compared to ketoprofen. It acts by inhibiting both cyclooxygenase-1 (COX-1) and cyclooxygenase-2 (COX-2), thereby suppressing the synthesis of prostaglandins, which are key mediators of inflammation and pain [28]. Although studies on ocular drug delivery systems for various NSAIDs such as diclofenac, ketorolac, and nepafenac exist in the literature, DKP has not yet been investigated for ocular application [29]. Considering its high solubility (BCS Class I) and rapid anti-inflammatory activity [30,31], the aim is to alleviate inflammation-related tissue damage by adding DKP to the current formulation and to synergistically complement PSC in antifungal therapy.

In this study, we aimed to design an innovative "micellar nanofiber" system to enhance the aqueous solubility of PSC and improve the penetration of both active agents (PSC and DKP) into ocular tissues. To this end, drug-loaded micelles were first prepared and subsequently incorporated into polymeric nanofibers via electrospinning to produce solid-state ocular inserts. The developed combined nanocarrier platform was systematically evaluated in terms of physicochemical characterization, in vitro drug release, ex vivo permeation and penetration, and antifungal efficacy, with the goal of contributing to the existing literature on advanced ocular drug delivery systems.

A review of the literature reveals no studies describing the integration of a dual-drug antifungal-anti-inflammatory micellar electrospun nanofiber ocular implant. This study is the first of its kind. While polymeric micelles and electrospun nanofibers have been studied separately for intraocular drug delivery, the combination of "micellar nanofibers" for the simultaneous delivery of PSC, an antifungal agent, and DKP, a nonsteroidal anti-inflammatory drug, has not been previously reported. This combined delivery system

https://doi.org/10.3390/molecules31081235

strategy is designed to overcome the different biopharmaceutical limitations of each API by increasing the water solubility of PSC, controlling the release kinetics of both DKP and PSC, and improving ocular permeability-on-penetration, thus offering a multifunctional approach for the management of fungal eye infections accompanied by inflammation and pain.

2. Results

2.1. Preparation and Characterization of PSC/DKP-Loaded Polymeric Micelles

PSC/DKP-loaded polymeric micelles were successfully obtained with nanoscale dimensions appropriate for ocular delivery. Dynamic light scattering measurements showed a mean hydrodynamic diameter of 11.01 ± 0.06 nm with a low PDI of 0.078, indicating a narrow size distribution. The zeta potential of the optimized micellar formulation was −1.68 ± 0.23 mV. Drug incorporation into the micellar system was high for both actives. Encapsulation efficiencies were 97.55 ± 4.10% for DKP and 98.67 ± 4.71% for PSC. All results are summarized in Table 1.

Table 1. Physicochemical characteristics of the optimized PSC/DKP-loaded micellar formulation (*n* = 3).

Attribute	Value
Particle size (nm)	11.01 ± 0.06
PDI	0.078
Zeta potential (mV)	−1.68 ± 0.23
Encapsulation efficiency DKP (%)	97.55 ± 4.10
Encapsulation efficiency PSC (%)	98.67 ± 4.71

2.2. Characterization of Spinning Solutions

Spinning solution properties strongly govern jet stability and fiber morphology. Thus, electrical conductivity and rheological behavior were assessed as key predictors of electrospinnability. Rheograms of the electrospinning solutions are shown in Figure 1. Rheological data were fitted to mathematical models and compared based on correlation coefficients (r). The best agreement was obtained with the Herschel–Bulkley model for all tested solutions. Rheology and conductivity data are given in Table 2.

Table 2. Rheological data (Herschel–Bulkley) and electrical conductivity of electrospinning solutions (*n* = 3) (Mean ± SD).

Solution	τ_0	K	n	r	Conductivity (μS/cm)
A	−43.21 ± 8.76	10.96 ± 1.09	0.68 ± 0.02	0.9997	5732 ± 6.24
P	−17.67 ± 2.78	6.76 ± 0.52	0.65 ± 0.01	0.9999	7490.67 ± 22.28
AP	−123.17 ± 57.33	35.89 ± 16.15	0.57 ± 0.07	0.9995	5920.33 ± 9.29
P(−M)	−50.80 ± 28.48	10.81 ± 6.27	0.64 ± 0.08	0.9996	2139 ± 6.24

τ_0: The yield stress, K: The consistency index (Pa·s), n: The flow behavior index, r: The correlation coefficient.

2.3. Characterization of Micellar Nanofiber Inserts

2.3.1. Drug Content and Encapsulation Efficiency

The drug content in the nanofiber inserts was measured by HPLC using the sample preparation procedure described in "Section 4.2" of this article. Encapsulation efficiencies determined from samples collected at different locations of the nanofiber mats are presented in Table 3.

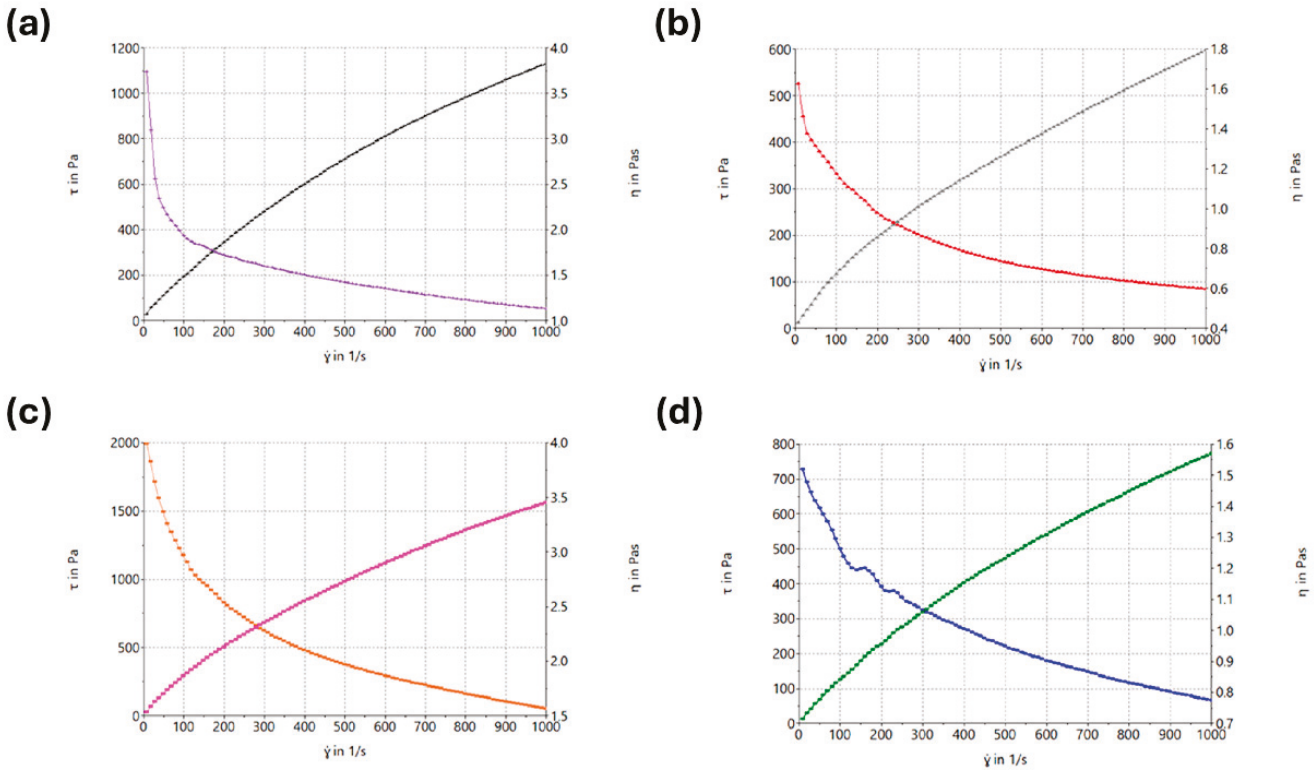

Figure 1. Rheograms of electrospinning solutions of nanofiber formulations. (**a**) Nanofiber-A electrospinning solution, (**b**) Nanofiber-P electrospinning solution, (**c**) Nanofiber-AP electrospinning solution, and (**d**) Nanofiber-P-(−M) electrospinning solution.

Table 3. Nanofiber insert properties and drug content (n = 3) (Mean ± SD).

Nanofiber	Fiber Diameter (nm)	Insert Diameter (mm)	Thickness (mm)	Weight (mg)	DKP (*EE*%)	PSC (*EE*%)
NF-A	185.4 ± 62.5	5.80 ± 0.01	0.32 ± 0.01	3.62 ± 0.08	86.65 ± 2.75	75.48 ± 5.30
NF-P	229.2 ± 87.7	5.80 ± 0.03	0.44 ± 0.03	5.42 ± 0.06	93.47 ± 1.59	90.33 ± 3.42
NF-AP	410 ± 139	5.80 ± 0.01	0.51 ± 0.03	8.32 ± 0.16	94.78 ± 1.18	91.51 ± 5.37

2.3.2. Thickness, Diameter, and Weight

Physical characterization of micelle-loaded nanofiber inserts showed in Table 3.

2.3.3. FESEM Imagining and Fiber Diameter

FESEM images and fiber diameter distribution histograms are provided in Figure 2.

2.3.4. Differential Scanning Calorimetry (DSC) Analysis

DSC thermograms showed in Figure 3.

2.3.5. X-Ray Diffraction (XRD) Mapping

XRD diffractograms presented in Figure 4.

2.3.6. Fourier-Transform Infrared Spectroscopy (FTIR, ATR-FTIR) Analysis

ATR-FTIR spectra of the pure components, physical mixtures, and produced nanofibers are presented in Figure 5.

2.4. In Vitro Drug Release

In vitro release was evaluated for the micellar formulation, a Noxafil® + DKP control solution diluted to the same DKP/PSC concentrations as the micelles, and the nanofiber

inserts Nanofiber-A, -P, -AP, -P(−M), and -AP(−M) using a 0.45 µm cellulose acetate membrane in Franz diffusion cells. Here, the suffix "(−M)" denotes nanofiber formulations prepared without micellar encapsulation (i.e., PSC and DKP were incorporated directly into the polymer solution rather than being pre-loaded into micelles). Cumulative release (µg/cm^2) was monitored over 8 h. Time-dependent drug release graphs from DKP and PSC carrier systems are given in Figures 6 and 7, respectively.

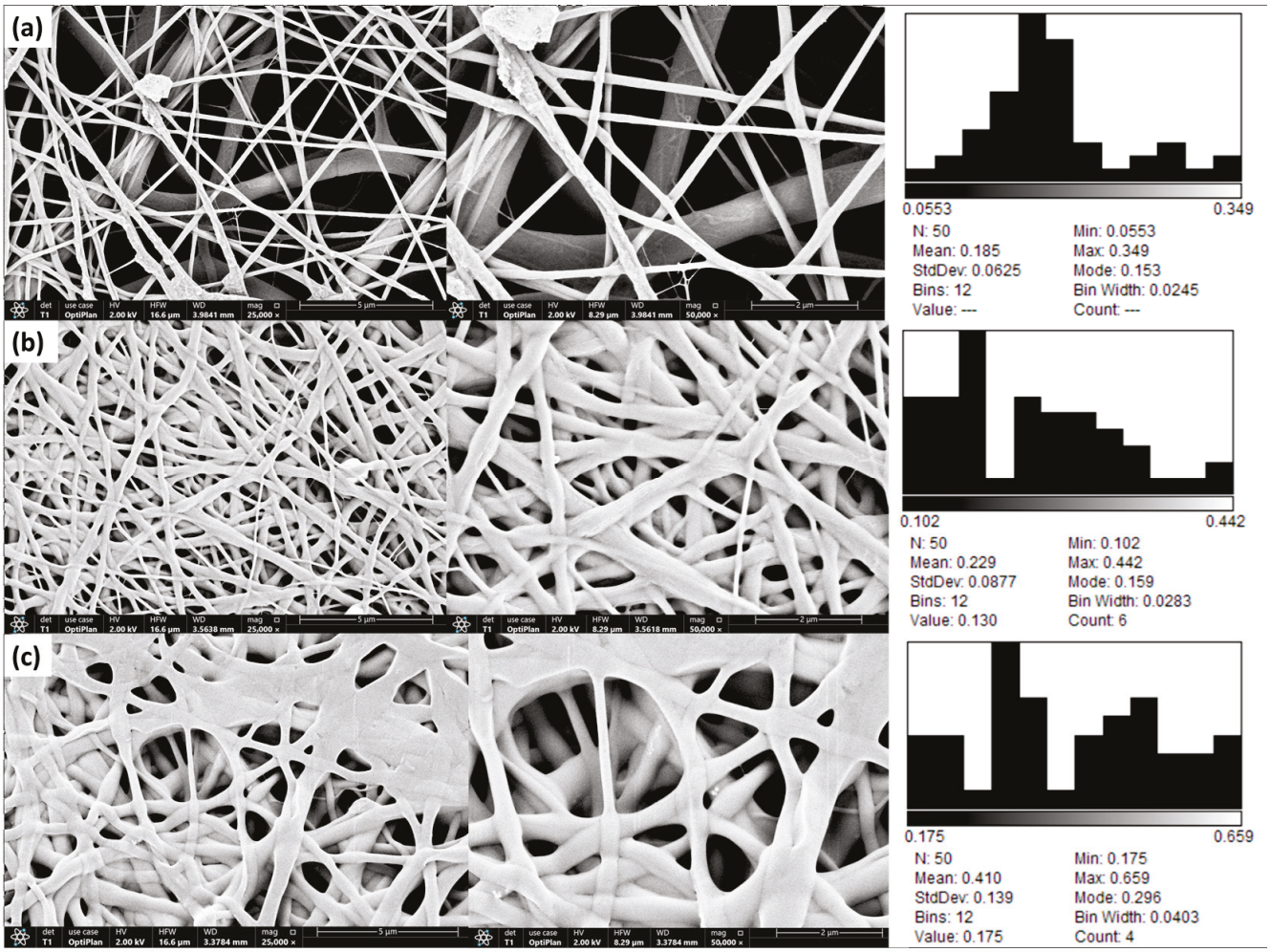

Figure 2. FESEM imaging findings at 25,000× and 50,000× magnification (n = 50): (**a**) Nanofiber-A, (**b**) Nanofiber-P, and (**c**) Nanofiber-AP.

2.5. Ex Vivo Permeation and Penetration Studies

2.5.1. Ex Vivo Permeation Studies

Ex vivo permeation experiments were conducted using bovine cornea and sclera for the micellar formulation, Nanofiber-AP, and a control solution consisting of a mixture of Noxafil® diluted to 250 µg/mL PSC and DKP solution at 10 mg/mL. The studies were performed using Valia–Chien diffusion cells as described before. The donor and receptor phase volumes were 2 mL for corneal cells and 3.4 mL for scleral cells. The diffusion area was 20.7 mm^2 for corneal cells and 7.2 mm^2 for scleral cells. Following isolation and cleaning, corneal and scleral tissues were mounted in the diffusion cells, and the receptor compartment was filled with artificial tear fluid containing 0.1% (w/v) SLS. Cumulative permeated amounts of DKP and PSC were calculated as µg/cm^2 over 8 h. Corneal and scleral permeation results for both DKP and PSC are shown in Figures 8 and 9, respectively. Following permeation testing, permeation parameters were calculated based on the ex vivo permeation data, and the calculated parameters are presented in Table 4.

https://doi.org/10.3390/molecules31081235

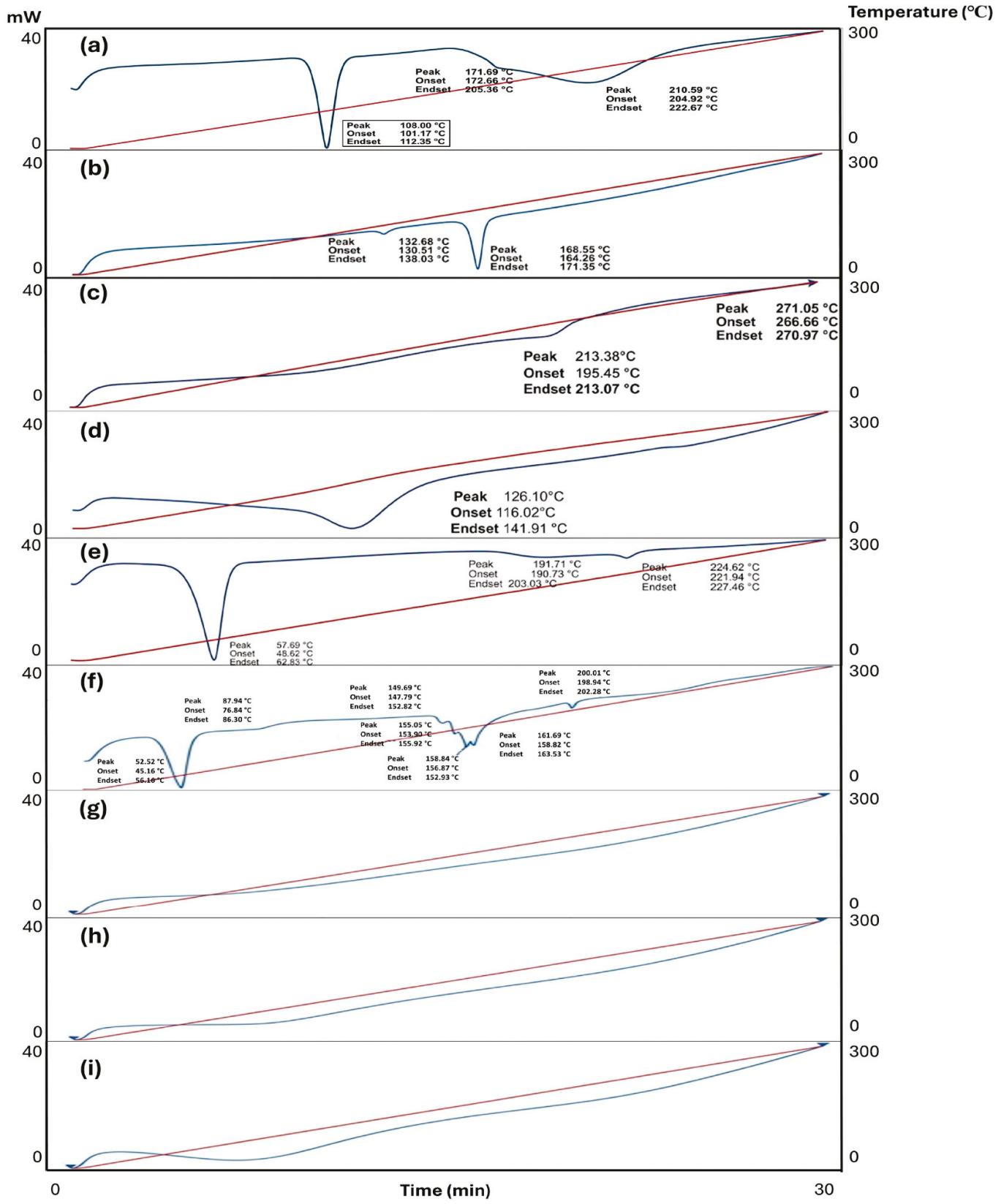

Figure 3. Thermograms of the DSC analysis. (**a**) DKP, (**b**) PSC, (**c**) PVA, (**d**) PVP, (**e**) PLU, (**f**) MIX, (**g**) NF-A, (**h**) NF-P and (**i**) NF-AP. DSC: Differential scanning calorimetry; PSC: Posaconazole; DKP: Dexketoprofen trometamol; PVA: poly(vinyl alcohol); PVP: poly(vinylpyrrolidone); PLU: Pluronic® F; NF-A: Nanofiber-A; NF-P: Nanofiber-P; NF-AP: Nanofiber-AP.

https://doi.org/10.3390/molecules31081235

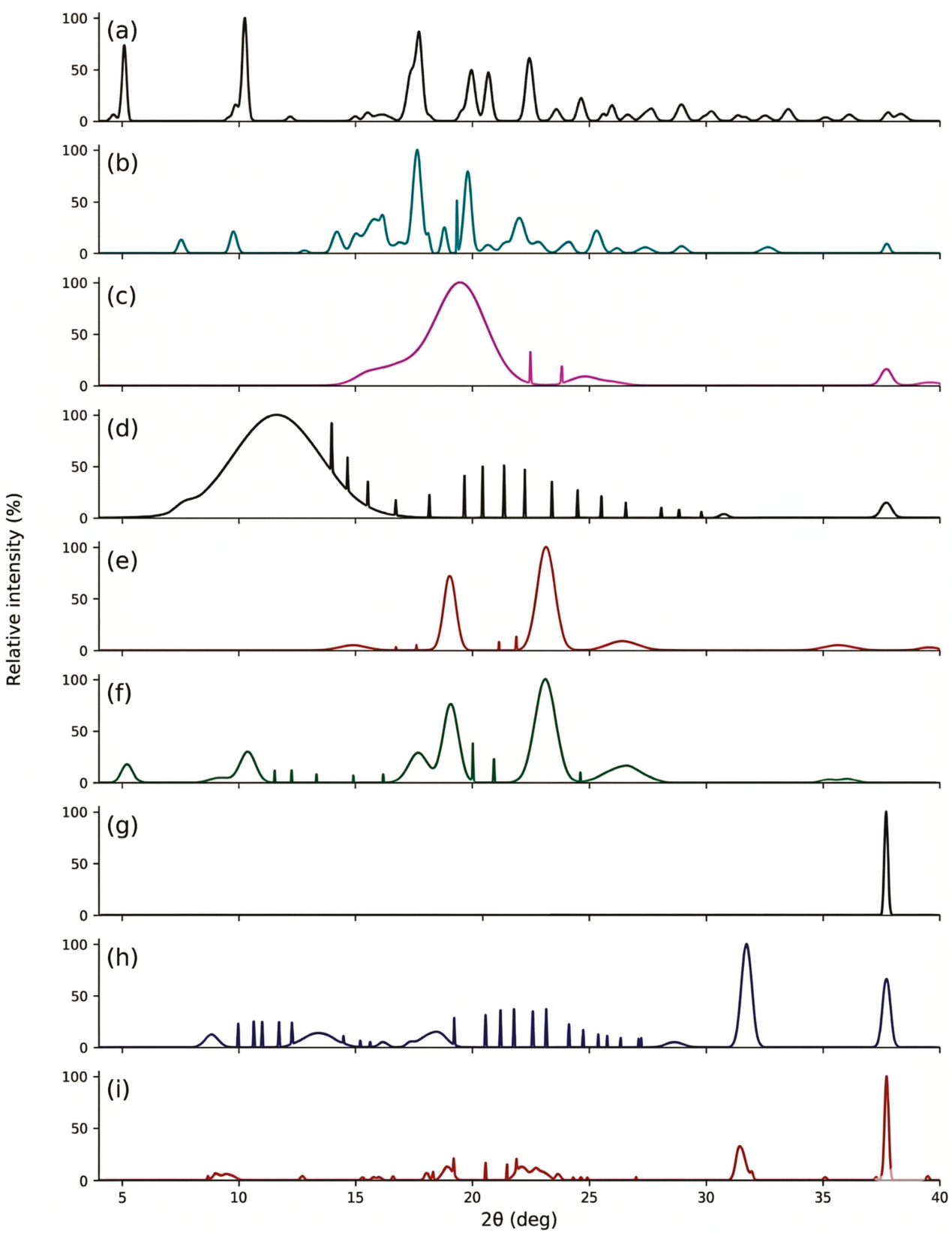

Figure 4. Results graphs of XRD analysis. (**a**) DKP, (**b**) PSC, (**c**) PVA, (**d**) PVP, (**e**) PLU, (**f**) MIX, (**g**) NF-A, (**h**) NF-P and (**i**) NF-AP. XRD: X-ray Diffraction; PSC: Posaconazole; DKP: Dexketoprofen trometamol; PVA: poly (vinyl alcohol); PVP: poly(vinylpyrrolidone); PLU: Pluronic® F; NF-A: Nanofiber-A; NF-P: Nanofiber-P; NF-AP: Nanofiber-AP.

https://doi.org/10.3390/molecules31081235

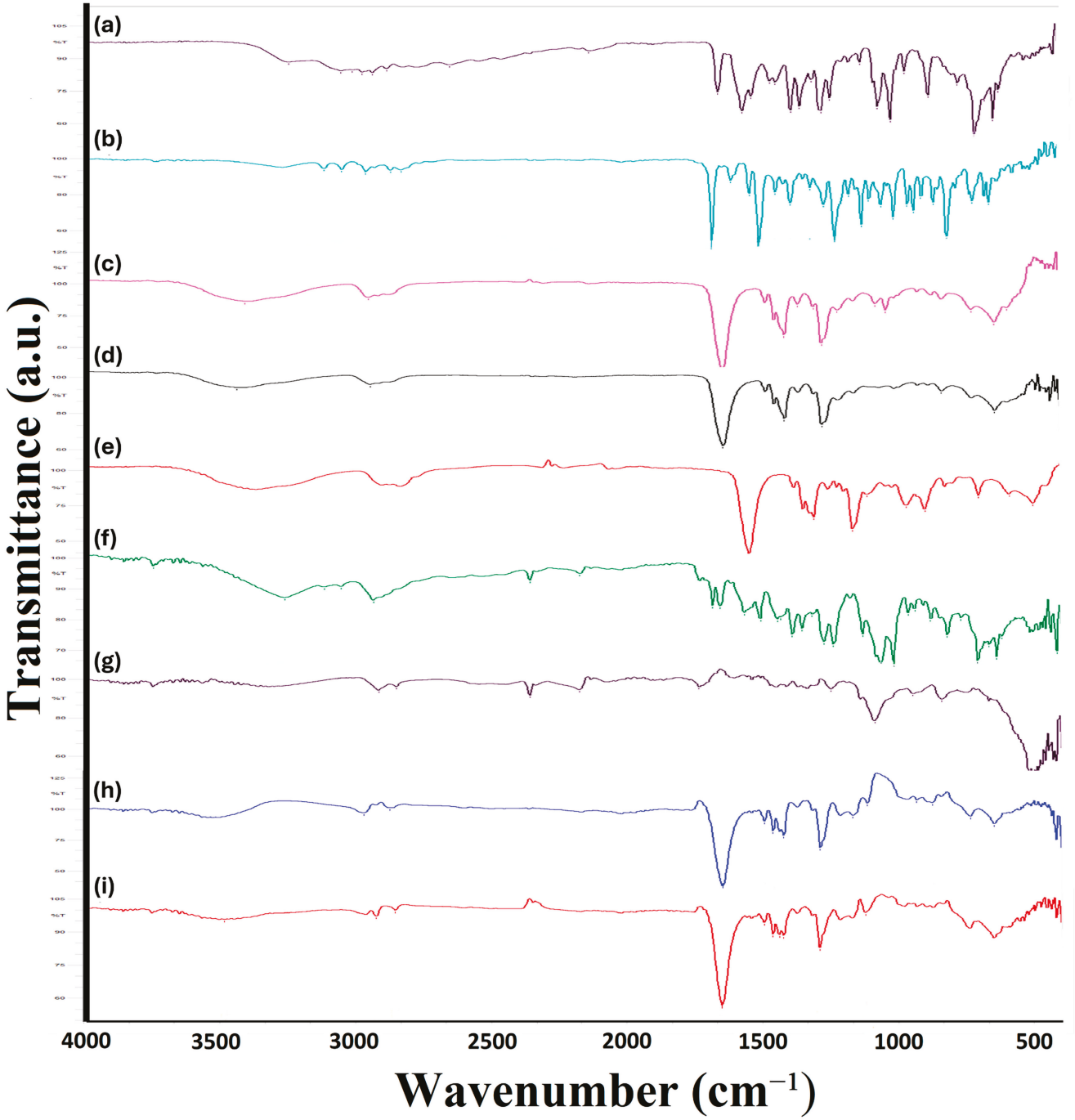

Figure 5. Results graphs of ATR-FTIR analysis (**a**) DKP, (**b**) PSC, (**c**) PVA, (**d**) PVP, (**e**) PLU, (**f**) MIX, (**g**) NF-A, (**h**) NF-P and (**i**) NF-AP. FTIR: Fourier Trans-form Infrared; PSC: Posaconazole; DKP: Dexketoprofen trometamol; PVA: poly(vinyl alcohol); PVP: poly(vinylpyrrolidone); PLU: Pluronic® F; NF-A: Nanofiber-A; NF-P: Nanofiber-P; NF-AP: Nanofiber-AP.

Table 4. Corneal and scleral permeation parameters of Micelle, Nanofiber-AP and or F68 and control (Noxafil® + DKP solution) (n = 3) (Mean ± SD).

			P_{app} (cm s^{-1})		D_{eff} (s^{-1})		J_{ss} (µg min^{-1})	
			Mean	**±SD**	**Mean**	**±SD**	**Mean**	**±SD**
Cornea	DKP	Micelle	5.69×10^{-5}	6.59×10^{-5}	2.22×10^{-5}	8.38×10^{-6}	2.31×10^{-9}	3.41×10^{-10}
		Nanofiber-AP	2.84×10^{-5}	2.99×10^{-5}	1.25×10^{-5}	6.10×10^{-6}	1.28×10^{-10}	3.30×10^{-11}
		Control	4.15×10^{-5}	5.25×10^{-5}	1.45×10^{-5}	3.96×10^{-6}	1.55×10^{-9}	1.85×10^{-10}

https://doi.org/10.3390/molecules31081235

Table 4. *Cont.*

			P_{app} (cm s^{-1})		D_{eff} (s^{-1})		J_{ss} (μg min^{-1})	
			Mean	**±SD**	**Mean**	**±SD**	**Mean**	**±SD**
Sclera	DKP	Micelle	1.37×10^{-5}	1.63×10^{-5}	4.84×10^{-6}	2.42×10^{-6}	5.56×10^{-10}	2.96×10^{-11}
		Nanofiber-AP	5.63×10^{-6}	1.79×10^{-5}	4.39×10^{-6}	2.35×10^{-6}	4.26×10^{-11}	1.58×10^{-12}
		Control	6.93×10^{-6}	2.15×10^{-5}	5.22×10^{-6}	2.74×10^{-6}	5.08×10^{-10}	2.70×10^{-11}
Cornea	PSC	Micelle	4.58×10^{-8}	6.99×10^{-8}	9.38×10^{-9}	2.88×10^{-9}	6.02×10^{-15}	7.36×10^{-16}
		Nanofiber-AP	4.28×10^{-8}	6.29×10^{-8}	1.01×10^{-8}	1.28×10^{-9}	6.60×10^{-16}	3.73×10^{-17}
		Control	1.65×10^{-9}	2.48×10^{-9}	3.60×10^{-10}	7.95×10^{-11}	2.33×10^{-16}	8.38×10^{-18}
Sclera	PSC	Micelle	1.93×10^{-8}	2.99×10^{-8}	3.17×10^{-9}	3.87×10^{-10}	2.45×10^{-15}	4.14×10^{-16}
		Nanofiber-AP	6.07×10^{-8}	8.63×10^{-8}	1.51×10^{-8}	7.77×10^{-9}	1.15×10^{-15}	5.56×10^{-16}
		Control	8.40×10^{-9}	1.20×10^{-8}	2.01×10^{-9}	8.37×10^{-10}	1.54×10^{-15}	5.88×10^{-16}

To calculate corneal D_{eff}, the thickness of bovine cornea and sclera was assumed as 0.1 cm and 0.065 cm, respectively.

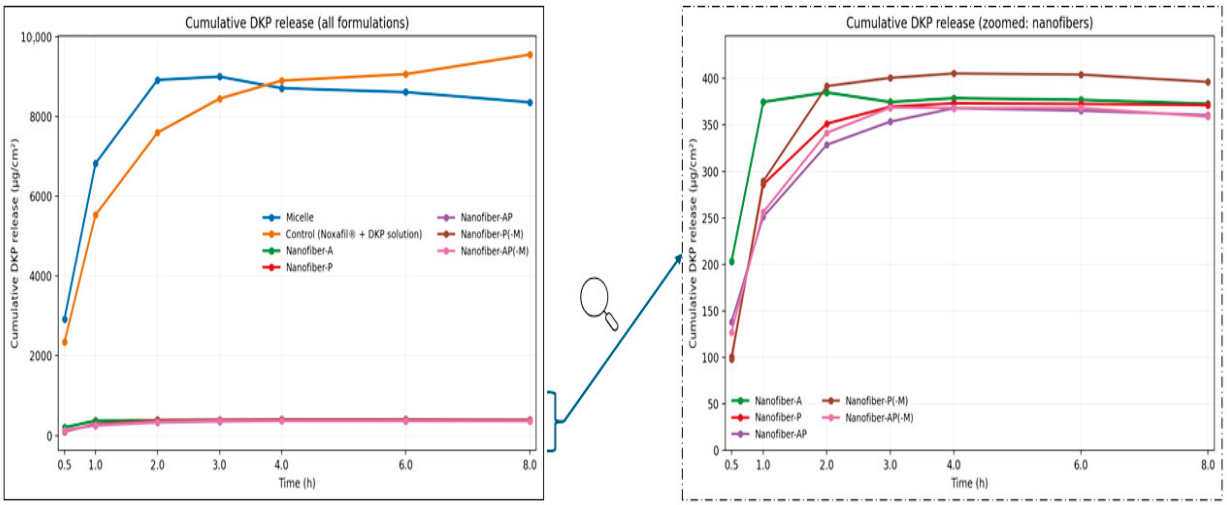

Figure 6. Cumulative DKP release profiles for micelle, nanofibers and control (n = 3). Nanofiber curves are not clearly visible due to overlapping at low concentrations; therefore, a zoomed-in plot is provided on the right, as indicated by the arrow.

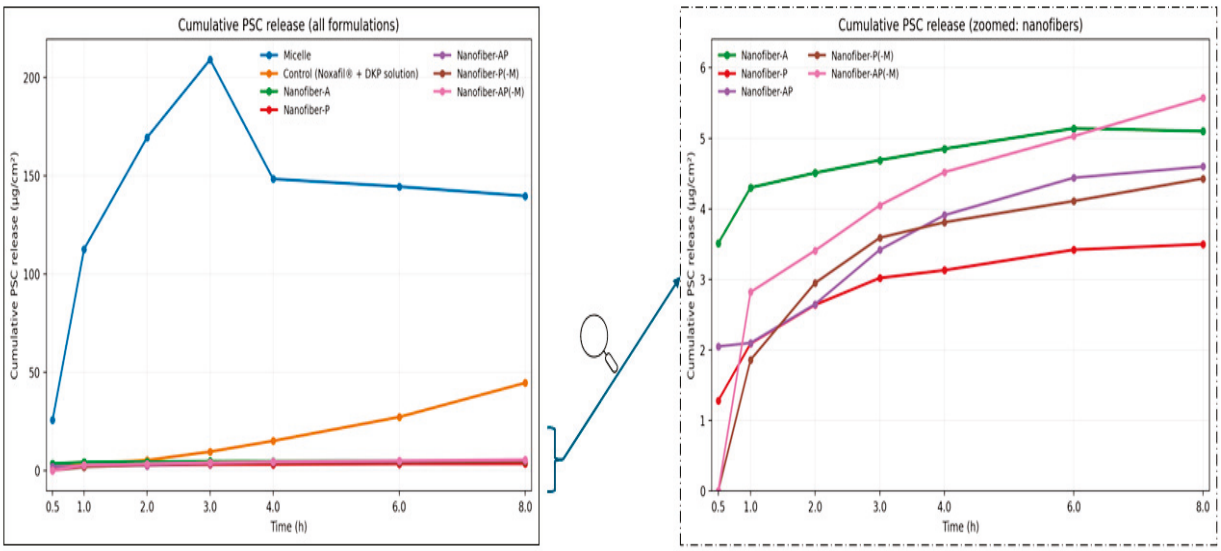

Figure 7. Cumulative PSC release profiles for micelle, nanofibers and control (n = 3). Nanofiber curves are not clearly visible due to overlapping at low concentrations; therefore, a zoomed-in plot is provided on the right, as indicated by the arrow.

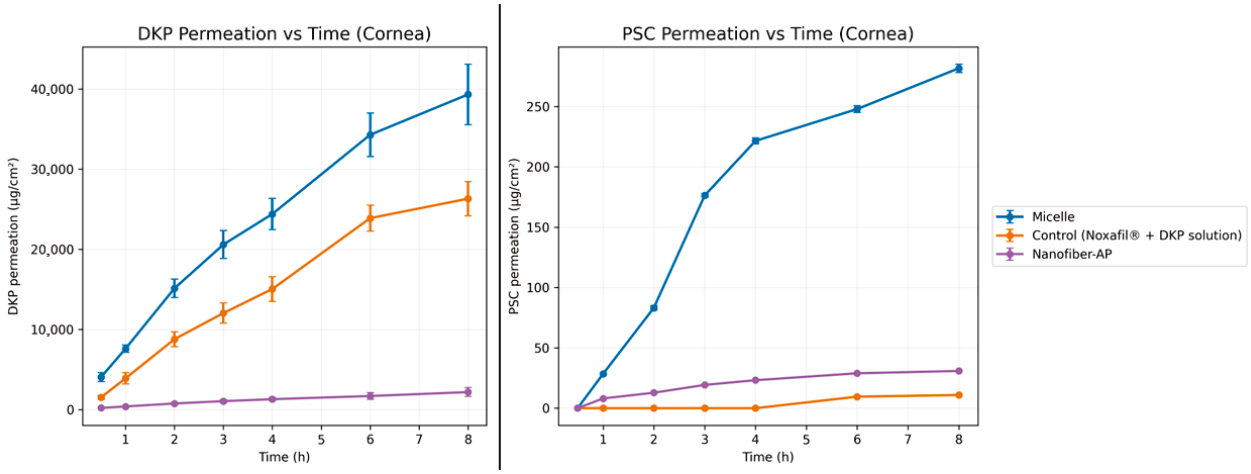

Figure 8. Ex vivo cumulative corneal DKP and PSC permeation profiles of Micelles, Nanofiber-AP and control (Noxafil® + DKP solution) (n = 3).

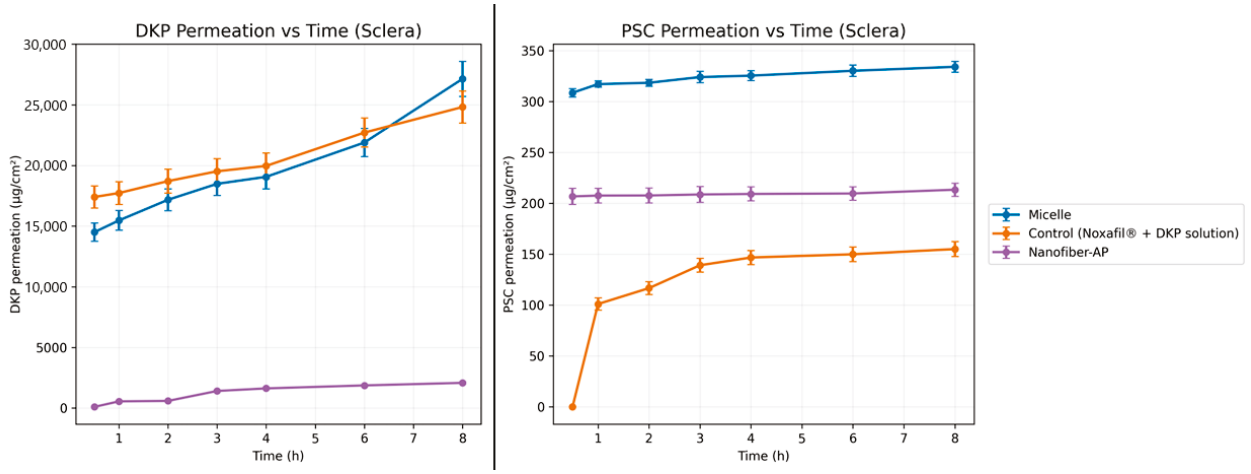

Figure 9. Ex vivo cumulative scleral DKP and PSC permeation profiles of Micelles, Nanofiber-AP and control (Noxafil® + DKP solution) (n = 3).

2.5.2. Ex Vivo Penetration Studies

Corneal and scleral penetration results for both DKP and PSC are shown in Figure 10.

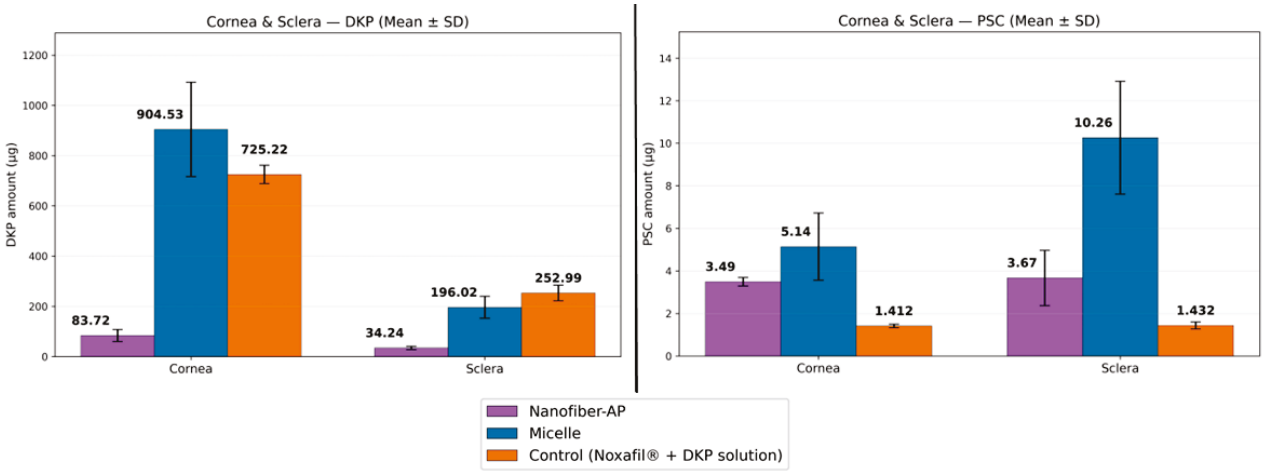

Figure 10. Ex vivo cumulative ocular DKP and PSC penetration profiles of Micelle, Nanofiber-AP and Control (Noxafil® + DKP solution) (n = 3).

https://doi.org/10.3390/molecules31081235

2.6. Antifungal Activity (Disk Diffusion)

Inhibition zone diameters (mm) obtained from the disk diffusion assay for the placebo, micellar formulation, Nanofiber-AP, the Noxafil® + DKP mixture at the same active concentrations as the micellar formulation, and the Noxafil® + DKP mixture at the same active concentrations as Nanofiber-AP are presented in Table 5.

Table 5. Zone diameters (mm) determined with the disk diffusion method of the Placebos, Micelles, Nanofiber-AP, and Controls (n = 4) (against *Candida albicans*).

Formulation	Inhibition Zone (mm) (Mean ± SD)
Placebo for micelle solution	0
Placebo for Nanofiber-AP	0
Micelles	26.25 ± 0.50
Nanofiber-AP	24.25 ± 0.50
Control mixture (same concentration as Micelle solution)	24.50 ± 0.58
Control mixture (same concentration as Nanofiber-AP)	22.00 ± 0.41

2.7. HET-CAM Irritation Test

The HET-CAM irritation assessment was performed on White Leghorn fertilized hen's eggs as described in Section 4.10. Representative images obtained from the assay are shown in Figure 11, while the irritation scores of the formulations and controls are provided in Table 6. The corresponding classification categories for HET-CAM scores are presented in Section 4.10. Each sample was applied to three different eggs (n = 3), and all CAM membranes were monitored for 300 s.

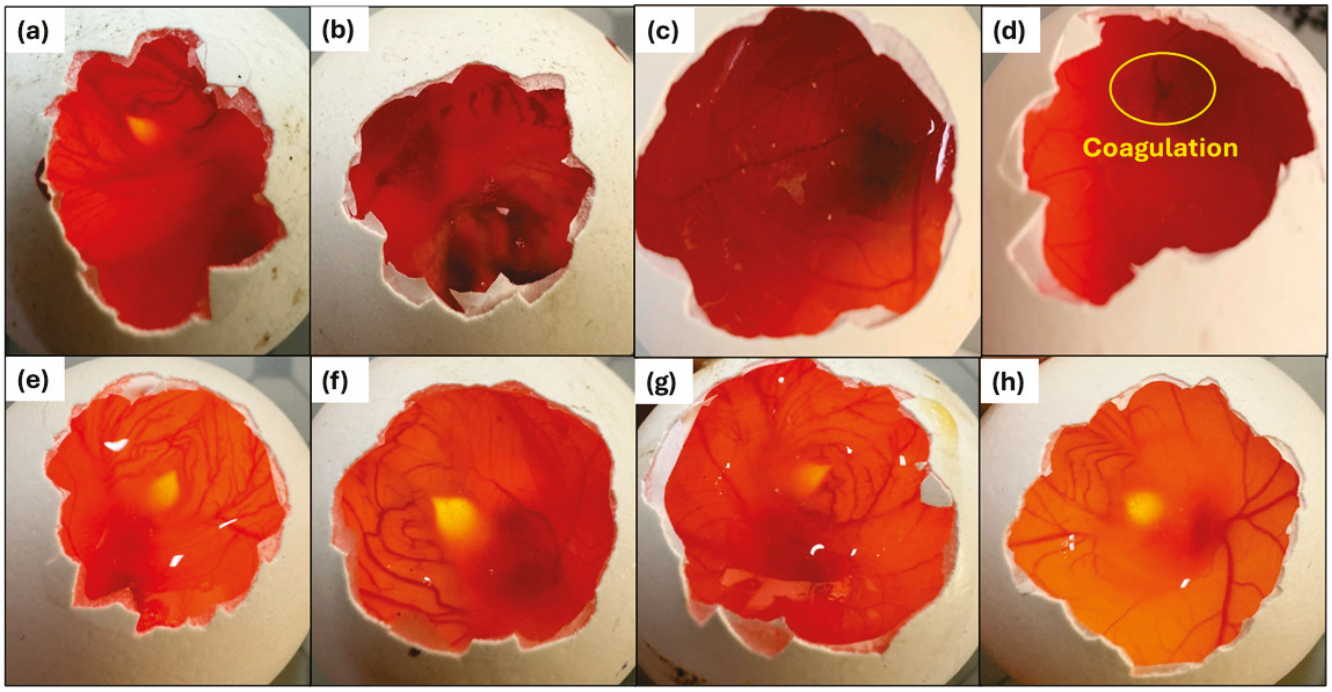

Figure 11. HET-CAM: Representative result images for prepared formulations (Nanofiber-AP, Micelle), Placebos and controls. (**a**) Negative control, (**b**) Positive control, (**c**) Placebo, (**d**) PSC solution (Noxafil), (**e**) DKP solution, (**f**) Mixture of Noxafil and DKP solution, (**g**) Micelles, (**h**) Nanofiber-AP.

During evaluation, coagulation within the first 30 s was observed in only one egg treated with the diluted Noxafil® suspension (Figure 11). According to the time-dependent HET-CAM scoring scheme, this finding corresponds to a score of 9. As the experiment

was conducted in triplicate (n = 3), this score was divided by three to obtain the mean irritation score, which was subsequently categorized as "slight" irritation based on the HET-CAM classification scheme. In contrast, no observable alterations in the vascularized chorioallantoic membrane were detected for any of the other actives or formulated systems.

Table 6. Cumulative scores and HET-CAM irritation assessment of Micelle, Nanofiber-AP, Placebos and Controls (n = 3).

Formulation	Cumulative Score	Irritation Assessment
Placebo (Micelle)	0	Practically none
Placebo (Nanofiber-AP)	0	Practically none
Micelle solution	0	Practically none
Nanofiber-AP	0	Practically none
DKP solution	0	Practically none
Diluted Noxafil®	3	Slight
Mixture of Noxafil®-DKP	0	Practically none

3. Discussion

In fungal ocular diseases, infection alone does not cause tissue damage. The process, accompanied by inflammation, progresses very painfully and the healing process is delayed [2]. The two APIs included in the formulation in this study were actually selected based on this consideration. PSC disrupts the structural integrity and fluidity of the fungal cell membrane and increases membrane permeability by inhibiting lanosterol 14α-demethylase (CYP51), a key enzyme involved in ergosterol biosynthesis. As a result, it leads to the death of the fungal cell and exhibits an anti-infective effect [22]. On the other hand, DKP, an NSAID, inhibits cyclooxygenase (COX-1 and COX-2) enzymes and provides an additional therapeutic benefit by reducing prostaglandin-mediated inflammatory responses [28]. The combined delivery of PSC and DKP in a single nanocarrier system offers a synergistic therapeutic strategy by simultaneously targeting the infectious agent and associated inflammatory processes, which can increase the overall treatment efficacy in fungal eye diseases.

3.1. Preperation and Characterization of PSC/DKP-Loaded Polymeric Micelles

The micelles produced were found to be ultra-small (11.01 $\pm$ 0.06 nm, seen in Table 1) in terms of particle size. Such ultrasmall and relatively monodisperse systems are advantageous for ocular applications, as they can spread rapidly within the tear film and may facilitate close contact with the corneal surface, potentially supporting drug transport toward anterior ocular tissues. The advantage of this ultra-small size becomes even more prominent, especially when considering the pore openings of ocular tissues. It is known that for successful corneal permeation, the particle size of nanocarriers should be smaller than 100 nm [32]. In particular, nanocarriers smaller than 20 nm can easily pass through the spaces between the collagen fibers of the corneal stroma [33].

The zeta potential of the micelles was found to be within the neutral range of mV (seen in Table 1). This near-neutral surface charge is consistent with sterically stabilized micellar systems, where colloidal stability is primarily provided by the hydrated polymeric corona rather than strong electrostatic repulsion. For nanocarriers to be more stable, the zeta potential is expected to be in the range of $\pm$30 mV [34]. However, considering that the mucin layer on the ocular surface is negatively charged, it is known that highly charged colloids, especially positively charged ones, can interact strongly with the ocular mucosa and epithelial surfaces. On the other hand, neutral systems can easily pass through mucin [35].

https://doi.org/10.3390/molecules31081235

Overall, these findings are consistent with previous reports in the literature. The micelle characteristics observed in the present study were in agreement with the results reported by Durgun et al. [25]. In addition, similar particle size and zeta potential values have been obtained in the micellar formulation study by Suksiriworapong et al., who prepared itraconazole-loaded micelles using TPGS [36], supporting the comparability of the present micellar system with previously reported TPGS-based micellar platforms.

Encapsulation activity was demonstrated, showing that both APIs could be loaded into the micelle structure with high efficiency (seen in Table 1). For PSC—an antifungal with low aqueous solubility—high loading within nanoscale micelles is particularly relevant, as it supports enhanced apparent solubility and enables delivery in an aqueous ocular-compatible form. Although DKP is intrinsically more soluble, its co-incorporation at high efficiency supports the feasibility of a combined therapy approach within a single nanocarrier system.

3.2. Characterization of Spinning Solutions

Electrospinning solutions were developed to enable the formation of continuous nanofibers and to allow incorporation of PSC and DKP either directly or via the micellar dispersion. In addition to the micelle-loaded systems, a PVP-based solution containing PSC and DKP at the same concentrations but without micellar encapsulation (i.e., the non-micellar counterpart of the Nanofiber-P system, denoted as P(−M)) was also evaluated in order to specifically assess the influence of micelles on the flow behavior and processability of the polymeric spinning solution. Conductivity values were within a range compatible with stable electrospinning.

In rheology studies, all solutions exhibited n values below 1 ($n < 1$), confirming pseudoplastic (shear-thinning) flow behavior (seen in Table 2). This rheological profile is favorable for electrospinning because it supports polymer chain entanglement and sufficient viscoelasticity at low shear while allowing smooth flow through the needle and stable jet formation under the high-shear conditions of the process. Viscosity is a critical determinant of nanofiber morphology: overly low viscosity can lead to bead formation rather than continuous fibers, whereas excessively high viscosity may cause nozzle clogging and hinder electrospinning [37].

These observations are also consistent with literature evidence. Rošic et al. reported that polymeric solutions showing shear-thinning behavior form more stable jets during electrospinning and yield more uniform fiber diameters [38]. The fact that the solutions producing the most stable jets in the present study also exhibited shear-thinning flow supports this mechanistic interpretation.

A direct comparison between solution P and P(−M) further highlights the impact of micelles on solution rheology. While both systems shared a similar polymeric base, incorporating micelles altered the flow properties: the micelle-loaded solution exhibited a higher yield stress (τ_0) but lower apparent viscosity, indicating that micelles can modify the internal microstructure of the spinning dope and thereby influence processability. This observation supports the rationale for separately examining the non-micellar counterpart when optimizing composite "micellar nanofiber" inserts.

Based on pre-optimization screening, three representative systems were selected for insert production, i.e., a PVA-dominant system (A), a PVP-dominant system (P), and a blended PVA/PVP system (AP), representing distinct polymer networks and hydration behaviors. In addition to polymer selection, PLU was incorporated in selected compositions as a processing aid to improve electrospinnability and fiber formation by modulating solution properties (e.g., surface tension and viscoelasticity), thereby enhancing jet stability and reducing the likelihood of bead formation. Under the optimized electrospinning

https://doi.org/10.3390/molecules31081235

parameters, these solutions produced reproducible nanofiber mats suitable for conversion into ocular inserts for subsequent characterization and performance testing.

3.3. Characterization of Micellar Nanofiber Inserts

3.3.1. Drug Content and Encapsulation Efficiency

Among the tested formulations, Nanofiber-AP exhibited the highest encapsulation efficiency for both active compounds, whereas the lowest values were obtained for Nanofiber-A. The relatively lower encapsulation efficiency of Nanofiber-A may be attributed to the need for a higher applied voltage during electrospinning ($\geq$25 kV) compared with the other formulations, which could potentially disrupt the micellar structure and compromise drug retention [39]. In addition, the smaller fiber diameter of Nanofiber-A and the thinner insert structure may have contributed to reduced loading; literature reports suggest a positive relationship between insert thickness and encapsulation capacity [40], and Nanofiber-A was thinner than the other formulations (seen in Table 3).

The combined use of PVA and PVP has been reported to enhance drug encapsulation in electrospun systems, likely due to interactions between hydroxyl groups of PVA and carbonyl groups of PVP, which can stabilize the fiber network and increase loading capacity [41,42]. Consistent with this rationale, the higher loading performance of the PVA/PVP blend formulation (Nanofiber-AP) in this study may be associated with improved matrix stability and drug retention. Although the encapsulation efficiencies in nanofiber formulations were generally high, the overall drug loading capacity of inserts remained lower than that of micelles (approximately ~20-fold) because electrospinning requires relatively high polymer content. Nevertheless, the inserts contained PSC at concentrations substantially above its minimum inhibitory concentration (MIC) and DKP at therapeutically relevant levels [43,44]. To confirm content uniformity across the collector-deposited mats, samples were taken from the center and peripheral regions of the nanofiber layer; the encapsulation results were consistent across locations, indicating homogeneous drug distribution.

3.3.2. Thickness, Diameter, and Weight

The maximum thickness of 0.506 $\pm$ 0.030 mm for Nanofiber-AP. These thickness values are comparable to commercially available ocular inserts, such as Ocusert® (0.3 mm) and Lacrisert® (1.27 mm), indicating that the produced inserts fall within a practical range for ocular placement. To ensure unit-size uniformity, inserts were prepared using a circular punch (diameter = 5.8 mm). In terms of dimensions, the prepared inserts were compatible with marketed products: Ocusert® is approximately 5.5 mm $\times$ 13 mm, and Lacrisert® is approximately 1.27 mm $\times$ 3.5 mm [45].

3.3.3. FESEM Imagining and Fiber Diameter

The mean fiber diameters were 185.4 $\pm$ 62.5 nm for Nanofiber-A, 229.2 $\pm$ 87.7 nm for Nanofiber-P, and 410 $\pm$ 139 nm for Nanofiber-AP. The smaller fiber diameter observed for Nanofiber-A may be explained by the higher applied voltage during electrospinning, as increased voltage has been associated with reduced fiber diameter in the literature [46]. Moreover, the relatively lower molecular weight of the PVA used in the present study may also have contributed to smaller fiber diameters [47]. In contrast, Nanofiber-AP exhibited the largest fiber diameter; this trend is consistent with the findings of Rahmani et al., who reported that fibers electrospun from PVA/PVP blends had larger diameters than fibers produced from PVA or PVP alone [48]. Multiple studies have demonstrated hydrogen bonding between the hydroxyl groups of PVA and the carbonyl groups of PVP in blended systems [49–51]. Furthermore, partial hydrogen bond formation during post-electrospinning drying has been suggested as water evaporates from the fiber network,

https://doi.org/10.3390/molecules31081235

potentially promoting fiber–fiber interactions and thickening in PVA/PVP-based mats [52]. These interactions may account for the increased diameter observed for Nanofiber-AP.

3.3.4. Differential Scanning Calorimetry (DSC) Analysis

DSC thermograms showed characteristic endothermic transitions for the pure actives at 101.17–112.35 °C for DKP and 164.26–171.35 °C for PSC, in agreement with previously reported values [53,54]. In the drug-loaded nanofiber formulations, the absence of distinct melting endotherms was interpreted as evidence of a crystalline-to-amorphous transition and/or molecular dispersion of the actives within the polymeric network. Similar loss of melting events has been reported for drug-loaded electrospun systems and has been attributed to amorphization during fiber formation [55].

3.3.5. X-Ray Diffraction (XRD) Mapping

XRD diffractograms (Figure 4) further supported these observations. The diffraction patterns of pure PSC and DKP were consistent with the literature [56,57]. In contrast, nanofiber formulations exhibited a reduction in crystalline features, as reflected by diminished sharp peaks and a more diffuse profile, indicating reduced crystallinity and supporting the formation of an amorphous dispersion in the electrospun matrices. Such peak broadening/attenuation has also been reported for PVP-based drug-loaded nanofibers and is commonly associated with amorphization and loss of long-range order [58].

3.3.6. Fourier-Transform Infrared Spectroscopy (FTIR, ATR-FTIR) Analysis

ATR-FTIR spectroscopy was used to investigate compatibility and intermolecular interactions among the actives and excipients. For DKP, characteristic absorption bands were observed in the 2900–3000 cm^{-1} region (C–H/CH_2 stretching), at 1658.78 cm^{-1} (C=O stretching), at 1570.06 cm^{-1} (N–H bending), and in the 1300–1400 cm^{-1} region (C–O stretching). For PSC, key bands appeared at 3120.82 cm^{-1} (O–H stretching), 2966.52 cm^{-1} (CH_2 stretching), 1685.79 cm^{-1} (C=O stretching), 1616.35 cm^{-1} (C=N stretching), 1508.33 cm^{-1} (aromatic skeleton vibrations), and 1450.47 cm^{-1} (C–N stretching). The excipients also showed their expected spectral features: PVA exhibited bands at 3414 cm^{-1} (O–H stretching), 2958.8 cm^{-1} (C–H stretching, CH_2), 1651.07 cm^{-1} (H–O–H bending of absorbed water), 1423.47 cm^{-1} (C–H bending), bands in the 1049–1226 cm^{-1} region (C–O stretching), and bands in the 840–920 cm^{-1} region (C–C stretching and C–OH bending). PVP showed bands at 3441.01 cm^{-1} (O–H stretching), 2951.09 cm^{-1} (C–H stretching, CH_2), 1651.07 cm^{-1} (C=O stretching), 1423.42 cm^{-1} (C–H bending), 1284.59 cm^{-1} (C–N stretching), and bands in the 1050–1100 cm^{-1} region (C–O stretching). Pluronic F127 (PLU) displayed prominent bands in the 2916–2850 cm^{-1} region (C–H stretching), in the 1450–1460 cm^{-1} region (C–H bending), at 1249.87 cm^{-1} (in-plane O–H bending), at 1087.85 cm^{-1} (C–O–C stretching of ether bonds), in the 950–960 cm^{-1} region (C–H bending related to alkyl groups), and at 840.96 cm^{-1} (out-of-plane C–H bending, CH_2). Overall, the spectra of the individual actives and excipients were consistent with literature [59–63].

Notably, while DKP- and PSC-related bands were observable in the physical mixtures, these drug-specific bands were not clearly distinguishable in the nanofiber spectra, which was interpreted as successful incorporation of the actives within the nanofiber system. Considering the dual-carrier design of this work (micelles embedded into electrospun fibers), the ATR-FTIR findings were further interpreted to support effective encapsulation of the drugs in micelles prior to electrospinning and maintenance of the overall carrier structure during fiber formation. In addition, comparison of the spectra of PVA and PVP powders with the PVA/PVP blend nanofiber (Nanofiber-AP) indicated broadening/distortion of O–H stretching bands in the 3000–3600 cm^{-1} region, which was attributed to hydrogen bonding within the blended system [64].

https://doi.org/10.3390/molecules31081235

3.4. In Vitro Drug Release

When comparing dosage forms, it should be considered that nanofiber inserts inherently contain much lower drug amounts than micellar dispersion because electrospinning requires high polymer content (approximately ~20-fold difference).

DKP exhibited a pronounced burst release across all systems, consistent with its BCS class I character and high aqueous solubility; DKP is also expected to be located mainly in the micellar shell, facilitating rapid release [65]. DKP reached maximum release by 3 h in micelles and by 4 h in most nanofiber formulations, after which a plateau was observed. Among nanofibers, the highest DKP release was obtained with Nanofiber-P(−M) (405.32 ± 10.31 μg/cm^2; 96.03 ± 2.44%), while the micellar formulation (8999.44 ± 653.51 μg/cm^2; 79.64 ± 5.78%) and control solution (9552.06 ± 176.00 μg/cm^2; 84.53 ± 1.55%) produced substantially higher DKP release due to the solution-based presentation (Figure 6).

For PSC, nanofiber formulations generally reached maximum release at 8 h, except Nanofiber-A, which peaked earlier at 6 h, likely due to its smaller fiber diameter that can accelerate release [66]. The micellar formulation reached maximum PSC release at ~3 h, whereas the control solution peaked at 8 h. Among nanofibers, Nanofiber-AP(−M) showed the highest PSC release (5.57 ± 0.39 μg/cm^2; 65.72 ± 4.68%), followed by Nanofiber-A (5.14 ± 0.21 μg/cm^2; 60.69 ± 2.54%) and Nanofiber-AP (4.60 ± 0.25 μg/cm^2; 54.30 ± 3.05%). PSC release from micelles (209.17 ± 13.05 μg/cm^2; 74.04 ± 4.62%) was markedly higher than from the control solution (44.63 ± 7.76 μg/cm^2; 15.79 ± 2.74%). A short initial lag was observed for PSC in AP(−M) and P(−M), where release began after 30 min (Figure 7).

One-way ANOVA indicated no significant differences among nanofiber formulations for DKP or PSC release ($p > 0.05$), whereas comparing all systems together (micelles, nanofibers, and control) revealed significant differences for both drugs ($p < 0.05$). Micelles and the control solution differed significantly for PSC release ($p < 0.05$) but not for DKP ($p > 0.05$), likely due to DKP's rapid release in both cases.

Finally, the PSC release profile of the micellar formulation differed from that reported for PSC-loaded micelles by Durgun et al. [25], with the present study showing a faster PSC release. A plausible explanation is the presence of DKP in the micellar shell: rapid DKP desorption could create transient voids/defects in the micellar structure and thereby facilitate PSC diffusion, accelerating release [65]. This interpretation is supported by literature on combined drug-loaded TPGS micelles; for example, Gaikwad et al. reported that micelles co-loaded with albendazole and paclitaxel exhibited a biphasic release pattern characterized by an initial burst followed by sustained release over time [67].

Release profile fitting using the Korsmeyer–Peppas model supported a predominantly non-Fickian mechanism. For all formulations, the release exponent n values were >0.89 for both DKP and PSC, indicating super case-II transport, which is commonly associated with polymer relaxation/erosion contributions in addition to diffusion.

In such systems, drug release is strongly influenced by physical changes in the polymer matrix, including swelling and erosion, which can lead to a rapid increase in the release rate. This behavior is typically observed when the drug is embedded within a highly swellable polymeric network.

In super case-II transport, drug release does not follow a linear model; instead, it commonly involves an initial burst release followed by a sustained release phase. This release pattern is particularly relevant to the formulation of controlled drug delivery systems, where achieving the desired release profile is critical for therapeutic performance [68]. Consistent with our findings, Rao et al. reported that norfloxacin-loaded ocular inserts

prepared using ethyl cellulose and PVP exhibited drug release governed by the super case-II mechanism [69].

3.5. Ex Vivo Permeation and Penetration Studies

Noxafil (40 mg/mL) and DKP solution and Nanofiber-AP were evaluated. The reason for eliminating other nanofiber formulations and conducting further studies with Nanofiber-AP is that this formulation exhibits superior overall performance for both APIs, including the highest encapsulation efficiency, clinically acceptable thickness range for ocular implants, and controlled release behavior. In addition, the combined use of PVA and PVP provided improved structural integrity and reproducibility compared to single polymer systems, making Nanofiber-AP the most representative candidate for advanced ex vivo evaluation.

3.5.1. Ex Vivo Permeation Studies

As in the in vitro release study, it should be noted that the drug amount present in the micellar dispersion and the drug amount incorporated into Nanofiber-AP produced from the micellar solution differ markedly due to the high polymer requirement of electrospinning; for the ex vivo studies, this difference was approximately ~20-fold, which should be considered during interpretation.

- Corneal Permeation

For all three systems (micelles, Nanofiber-AP, and control), the highest cumulative permeation of both drugs was observed at 8 h. At 8 h, DKP permeation through the cornea was 39,309.4 ± 3783.19 μg/cm^2 for the micellar formulation, 26,299.62 ± 2141.29 μg/cm^2 for the control solution, and 2167.24 ± 559.55 μg/cm^2 for Nanofiber-AP. At 8 h, PSC permeation through the cornea was 281.56 ± 3.44 μg/cm^2 for the micellar formulation, 10.90 ± 0.39 μg/cm^2 for the control solution, and 30.87 ± 0.17 μg/cm^2 for Nanofiber-AP. For PSC, the first detectable permeation occurred at 1 h in the micellar formulation and Nanofiber-AP, whereas no PSC permeation was detected during the first 6 h for the control solution (Figure 8). The cornea contains both lipophilic and hydrophilic barrier components; the epithelium exhibits lipophilic character, while the stroma is highly hydrophilic and constitutes a major barrier for lipophilic drugs [70,71]. In the control solution, PSC is present as free drug with very low aqueous solubility, and its particle size (1400 nm) exceeds corneal pore dimensions; therefore, only a very low permeation was detected after 6 h [72]. In corneal PSC permeation, the micellar formulation provided the highest permeation, and Nanofiber-AP showed higher permeation than the control solution despite containing approximately 10-fold lower drug concentration. The micellar formulation yielded approximately 28-fold higher PSC permeation than the control solution.

One-way ANOVA results indicated that micelles, Nanofiber-AP, and control solution differed significantly for both DKP and PSC corneal permeation ($p < 0.05$). When micelles were compared with the control solution, PSC corneal permeation differed significantly ($p < 0.05$) while DKP corneal permeation did not ($p > 0.05$). In addition, the difference between Nanofiber-AP and control solutions in corneal PSC permeation was significant ($p < 0.05$), indicating that the micelle-loaded nanofiber system increased corneal PSC permeability compared with the higher-dose control.

- Scleral Permeation

Similar to corneal experiments, the highest permeation values for both drugs were observed at 8 h. At 8 h, DKP permeation through the sclera was 27,137.62 ± 1443.32 μg/cm^2 for the micellar formulation, 24,815.53 ± 1315.85 μg/cm^2 for the control solution, and 2077.47 ± 77.03 μg/cm^2 for Nanofiber-AP. At 8 h, PSC scleral permeation was

https://doi.org/10.3390/molecules31081235

334.11 ± 5.36 μg/cm^2 for the micellar formulation, 155.06 ± 7.47 μg/cm^2 for the control solution, and 213.39 ± 6.45 μg/cm^2 for Nanofiber-AP. For the control solution, the first PSC permeation was detected at 1 h (Figure 9). The sclera has a predominantly hydrophilic character and can act as a barrier to lipophilic drugs [73]. One-way ANOVA indicated a significant difference among micelles, Nanofiber-AP, and control solution for scleral permeation ($p < 0.05$). When micelles were compared with the control solution, PSC scleral permeation differed significantly ($p < 0.05$) whereas DKP scleral permeation did not ($p > 0.05$). The difference between Nanofiber-AP and the control solution for PSC scleral permeation was also significant ($p < 0.05$), consistent with the corneal findings.

3.5.2. Ex Vivo Penetration Studies

- Corneal Penetration

For DKP, the highest corneal penetration was observed for the micellar formulation (904.531 ± 187.6 μg), followed by the control solution (725.221 ± 36.45 μg) and Nanofiber-AP (83.723 ± 24.2 μg). For corneal DKP penetration, the three groups differed significantly when evaluated collectively ($p < 0.05$), whereas the comparison between micelles and control solution did not show a significant difference ($p > 0.05$).

For PSC, the highest corneal penetration was obtained with the micellar formulation (5.144 ± 1.581 μg), followed by Nanofiber-AP (3.498 ± 0.177 μg) and the control solution (1.412 ± 0.076 μg). Corneal PSC penetration differed significantly among the three systems ($p < 0.05$). Pairwise comparisons showed significant differences between micelles vs. control solution ($p < 0.05$) and Nanofiber-AP vs. control solution ($p < 0.05$). In contrast, the difference between micelles and Nanofiber-AP for corneal PSC penetration was not significant ($p > 0.05$).

- Scleral Penetration

For DKP, the highest scleral penetration was observed in the control solution (252.999 ± 30.97 μg), followed by the micellar formulation (196.021 ± 43.64 μg) and Nanofiber-AP (34.24 ± 6.578 μg) (Figure 10). Collective analysis showed significant differences among the three groups ($p < 0.05$), while the comparison between micelles and control solution was not significant ($p > 0.05$) for DKP penetration.

For PSC, the highest scleral penetration was obtained with the micellar formulation (10.257 ± 2.654 μg), followed by Nanofiber-AP (3.666 ± 1.266 μg) and the control solution (1.432 ± 0.16 μg) (Figure 10). Scleral PSC penetration differed significantly among all groups ($p < 0.05$). Pairwise comparisons showed significant differences for micelles vs. control solution ($p < 0.05$) and Nanofiber-AP vs. control solution ($p < 0.05$). Unlike the corneal PSC penetration results, the difference between micelles and Nanofiber-AP was significant in the sclera ($p < 0.05$). Overall, PSC penetration was higher in the sclera than in the cornea, consistent with reports indicating that scleral tissue is more permissive to drug penetration compared with the cornea [74,75].

Finally, within-formulation comparisons of penetration between cornea and sclera were performed. In the micellar formulation, both DKP and PSC showed significant differences between corneal and scleral penetration ($p < 0.05$). In Nanofiber-AP, a significant difference was observed for DKP penetration ($p < 0.05$), whereas PSC penetration did not differ significantly between tissues ($p > 0.05$). A similar pattern was obtained for the control solution, with significance for DKP but not for PSC.

The ex vivo findings indicate that PSC transport across ocular tissues is strongly formulation-dependent, whereas DKP transport is comparatively less sensitive to the carrier platform. For permeation, the micellar formulation consistently enabled earlier and higher PSC passage, particularly across the cornea where the control solution showed a pronounced delay, consistent with PSC's low aqueous solubility and particulate state in the

https://doi.org/10.3390/molecules31081235

absence of a carrier. Importantly, Nanofiber-AP enhanced PSC permeation and penetration relative to the control solution despite containing ~20-fold lower drug concentration, demonstrating the functional advantage of the micelle-loaded nanofiber architecture for PSC delivery. In contrast, DKP permeation was largely governed by dose and its high intrinsic solubility/permeability (BCS Class I), which also explains why micelles and the control solution did not differ significantly for DKP in pairwise comparisons. Finally, the generally higher PSC deposition in the sclera compared with the cornea aligns with the greater permissiveness of scleral tissue to drug penetration supporting the relevance of scleral delivery routes for lipophilic compounds.

3.6. Antifungal Activity (Disk Diffusion)

The results showed that the micellar formulation produced a larger inhibition zone than its concentration-matched control solution (Noxafil® + DKP mixture). Similarly, Nanofiber-AP exhibited a higher inhibition zone diameter compared with its corresponding concentration-matched control. Notably, although Nanofiber-AP contained a lower drug dose than the micellar formulation, it generated an inhibition zone comparable to that of the micelles against *Candida albicans*. This finding was attributed to the fact that Nanofiber-AP still contained PSC at concentrations above the minimum inhibitory concentration (MIC) despite the lower dose [76].

The antifungal activity of drugs or formulations can be demonstrated using many different tests. The disk diffusion test is a standardized qualitative screening method according to CLSI M44-A2 guidelines [77] for comparatively evaluating antifungal activity between formulations containing equivalent or reduced drug concentrations. The primary goal of our study was to determine whether the production of micelles and micellar nanofibers in combination with DKP maintained or enhanced the antifungal effect of PSC. Therefore, minimum inhibitory concentration (MIC) or time-kill assay tests, which would provide a definitive pharmacodynamic result, were not preferred [78]. These studies will be conducted as part of microbiology research that will also be carried out on more advanced clinical strains.

3.7. HET-CAM Irritation Test

The observed slight irritation response associated with the diluted Noxafil® suspension may be attributed to the presence of formulation excipients and the relatively high local drug concentration upon direct CAM exposure. Importantly, the absence of coagulation, hemorrhage, or vascular lysis for all micelle-loaded nanofiber formulations indicates favorable ocular tolerability of the developed delivery systems. These findings suggest that incorporation of the active compounds into polymeric micelles and electrospun nanofibers effectively mitigates irritation potential, supporting the suitability of the formulations for ocular application. The obtained results are consistent with previously reported HET-CAM findings for similar nanocarrier-based ocular systems, including those reported by Durgun et al. [79].

4. Materials and Methods

4.1. Materials

Posaconazole (PSC) was obtained from MSN Laboratories (Hyderabad, India). Dexketoprofen trometamol (DKP) was kindly provided as a gift sample by Santa Farma (İstanbul, Türkiye). D-α-tocopheryl polyethylene glycol 1000 succinate (TPGS), poly(vinyl alcohol) (PVA; Mw: 50 kDa), poly(vinylpyrrolidone) (PVP; Mw: 1200 kDa), and Pluronic® F127 (PLU) were obtained from BASF Pharma (Ludwigshafen, Germany). Methanol (high-performance liquid chromatography (HPLC) grade), acetonitrile (HPLC grade), sodium

https://doi.org/10.3390/molecules31081235

lauryl sulfate (SLS) and sodium chloride (NaCl) were purchased from Merck (Darmstadt, Germany) and used as received. Isotonic NaCl solution (0.9% *w*/*v*) was purchased from Polifarma (Tekirdağ, Türkiye). Ultrapure water was obtained using a Milli-Q purification system (Millipore, MA, USA). All remaining reagents were of analytical grade.

Electrospinning was performed using an NE-200 electrospinning system (Inovenso, Boston, MA, USA). Dynamic light scattering (DLS) and zeta potential measurements were performed using a Zetasizer Nano ZS (Malvern Panalytical, Malvern, UK). HPLC analyses were conducted using a Shimadzu HPLC system (Shimadzu, Kyoto, Japan). ATR-FTIR spectra and DSC analyses were obtained using Shimadzu instruments (Shimadzu, Kyoto, Japan). Rheological measurements were performed using a Haake RheoStress 1 rheometer (Haake, Karlsruhe, Germany). Conductivity was measured using an Eutech Instruments PC2700 conductivity meter (Eutech Instruments, Landsmeer, The Netherlands). FESEM imaging was performed using a Thermo Scientific Apreo 2S FESEM (Thermo Fisher Scientific, Waltham, MA, USA).

4.2. Analytical Method

Quantification of PSC and DKP was carried out by HPLC using a C18 column (Inertsil ODS-3, 5 µm, 4.6 × 250 mm). The mobile phase consisted of methanol:water (80:20, *v*/*v*) adjusted to pH 3.5 with HCl. The flow rate was 0.8 mL/min, the column temperature was maintained at 35 °C, the injection volume was 20 µL, and UV detection was set at 262 nm.

Validation studies were performed in accordance with the ICH Q2(R1) guideline, assessing linearity, accuracy, precision, selectivity, and sensitivity (LOD/LOQ) [80].

4.3. Preparation and Characterization of PSC/DKP-Loaded Polymeric Micelles

4.3.1. Preparation of PSC/DKP-Loaded Polymeric Micelles

PSC/DKP-loaded polymeric micelles were prepared by a thin-film hydration method modified from the procedure reported by Durgun et al. [25]. Briefly, TPGS was dissolved in acetonitrile. PSC and DKP were dissolved separately in methanol and then added dropwise to the TPGS solution under magnetic stirring. The resulting mixture was transferred to a round-bottom flask and evaporated using a rotary evaporator (IKA®-Werke GmbH & Co. KG, Staufen, Germany) at 60 °C (120 rpm, 20 min). The pressure was then reduced to 150 mbar to remove residual solvents, forming a thin film. After an additional resting period (20 min), the film was hydrated with isotonic saline (0.9% NaCl) and mixed on the rotary evaporator at 60 °C (120 rpm) for 1 h (without changing ambient pressure). The dispersion was allowed to stand for 1 h and then filtered through a 0.45 µm PTFE membrane.

The optimized micelle formulation (M) contained PSC (250 µg/mL), DKP (10 mg/mL), and TPGS (20 mg/mL) (Table 7).

Table 7. Optimized formulation of PSC and DKP loaded micellar system.

Micelle Formulation Code	PSC Concentration	DKP Concentration	TPGS Concentration
M	250 µg/mL	10 mg/mL	20 mg/mL

4.3.2. Characterization of PSC/DKP-Loaded Polymeric Micelles

- Particle Size, Polydispersity Index (PDI), and Size Distribution

The hydrodynamic diameter and polydispersity index (PDI) of the micellar dispersions were determined by dynamic light scattering (DLS) at 25 °C using a Zetasizer Nano ZS (Malvern Panalytical, UK). Micellar dispersions were gently homogenized and transferred into disposable polystyrene cuvettes prior to measurement. Each sample was analyzed in

https://doi.org/10.3390/molecules31081235

triplicate, and each measurement consisted of 10 consecutive runs. Results were reported as mean ± standard deviation together with the intensity-based size distribution.

- Zeta Potential

Zeta potential was measured by electrophoretic light scattering using the same instrument at 25 °C. Samples were loaded into folded capillary cells according to the manufacturer's instructions, and zeta potential values were calculated using the Smoluchowski approximation [81]. Measurements were conducted in triplicate (10 runs per measurement), and results were expressed as mean ± standard deviation.

- Determination of Drug Content and Encapsulation efficiency (*EE%*)

To quantify PSC and DKP incorporated into the micellar system, micelles were disrupted with methanol to ensure complete extraction of both drugs. Briefly, 0.1 mL of micellar dispersion was diluted to 1.0 mL with methanol (1:10, *v*/*v*) and mixed thoroughly until a clear solution was obtained. The resulting solutions were analyzed by HPLC. Drug concentrations were calculated using the corresponding calibration curves.

Encapsulation efficiency (*EE%*) was calculated as the percentage of drug incorporated into the micellar formulation relative to the total amount of drug initially used in the preparation, using the following equation:

$$EE(\%) = \frac{W_{enc}}{W_{total}} \times 100 \quad (1)$$

where W_{enc} is the amount of PSC or DKP quantified after micelle disruption and W_{total} is the total amount of the respective drug (PSC or DKP) used during micelle preparation.

4.4. Optimization and Preparation of Micellar Electrospun Nanofiber Ocular Inserts

Polymeric spinning solutions were prepared using poly(vinyl alcohol) (PVA) and poly(vinylpyrrolidone) (PVP) as the main matrix-forming polymers. For blank nanofiber screening, PVA aqueous solutions were prepared in the range of 15–30% (*w*/*w*) by gradually dispersing PVA in distilled water, followed by continuous stirring at 55 °C (350 rpm, 5 h) until a clear and homogeneous solution was obtained. PVP aqueous solutions were prepared in the range of 8–25% (*w*/*w*) by dissolving PVP in distilled water under magnetic stirring at room temperature (400 rpm, 5 h) until complete dissolution. For PVA/PVP blend nanofibers, polymer blends were screened at a fixed total polymer content of 24% (*w*/*w*), while varying the PVA:PVP ratio from 20:4 to 4:20 (*w*/*w*) (i.e., 20/4, 18/6, 16/8, 12/12, 8/16, 6/18, and 4/20). Blended solutions were prepared by mixing the corresponding pre-prepared PVA and PVP solutions and further stirring at 300 rpm for 3 h to ensure uniformity.

Electrospun nanofibers were produced using an electrospinning system (Inovenso, USA). During process development, key electrospinning parameters (nozzle/needle type, applied voltage, flow rate, and tip-to-collector distance) were screened to obtain continuous, bead-free fibers and stable jet formation. Nanofibers were collected on an aluminum foil-covered collector and removed as nonwoven mats.

Following blank (drug-free) optimization, micelle-loaded nanofiber inserts were prepared by using the optimized PSC/DKP-loaded micellar dispersion as the solvent phase. In brief, the required amounts of PVA and/or PVP (and Pluronic F127, when applicable) were dissolved directly in the micellar dispersion under stirring until homogeneous spinning solutions were obtained. In micelle-based systems, preliminary trials were performed using single-polymer systems (PVA: 20–30% (*w*/*w*); PVP: 15–25% (*w*/*w*)) and PVA/PVP blends (total polymer 24% (*w*/*w*), PVA:PVP 20:4 to 4:20). In addition, Pluronic F127 (PLU) was incorporated into selected formulations as a processing aid to improve electrospinnability

https://doi.org/10.3390/molecules31081235

and fiber formation. Specifically, PLU was used to enhance jet stability and facilitate continuous, bead-free fiber production by modulating the physicochemical properties of the spinning solution (e.g., viscoelasticity and surface tension), thereby improving the overall uniformity of the electrospun mats.

Based on the preformulation/optimization outcomes, three micelle-loaded nanofiber formulations—one PVA-based, one PVP-based, and one PVA/PVP blend—were selected for further studies. The optimized compositions and electrospinning conditions are summarized in Table 8. Unless otherwise stated, electrospinning was carried out using a 0.8 mm nozzle, a flow rate of 0.3 mL/h, and a tip-to-collector distance of 18 cm, while the applied voltage was adjusted according to the formulation (Table 8). After fabrication, nanofiber mats were cut into insert units of predefined dimensions and stored in sealed packaging until characterization and performance testing. The preparation process for micelles and micelle-loaded nanofibers is schematically illustrated in Figure 12.

Table 8. Optimized micelle-loaded nanofiber formulations and electrospinning parameters (solvent phase: micellar dispersion).

Nanofiber Formulation Code	Composition (*w*/*w*, %)	Flow Rate (mL/h)	Distance (cm)	Voltage (kV)	Nozzle
Nanofiber-AP (NF-AP)	PVA (12) + PVP (12)	0.3	18	20	0.8 mm
Nanofiber-A (NF-A)	PVA (24) + PLU (1)	0.3	18	25	0.8 mm
Nanofiber-P (NF-P)	PVP (17) + PLU (1)	0.3	18	20	0.8 mm

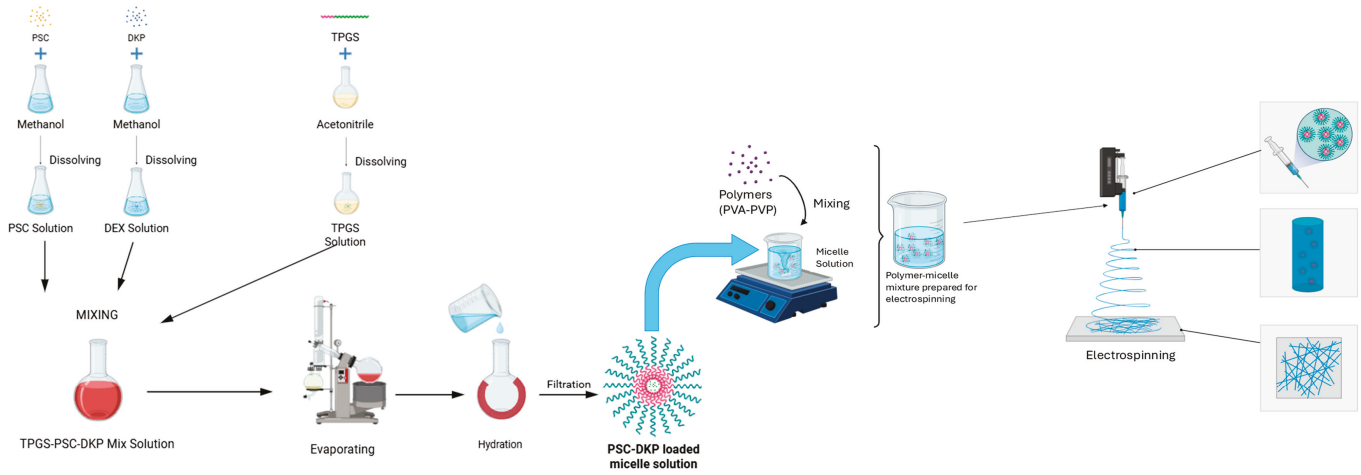

Figure 12. Schematic representation of the preparation of the micelle solution and micelle-loaded nanofibers.

For comparative assessment of the role of micellar encapsulation, control nanofibers were prepared by incorporating PSC and DKP directly into the corresponding polymer solutions (without micelles) and electrospinning under comparable conditions, as defined in the study design.

4.5. Characterization of Spinning Solutions

4.5.1. Rheology

Polymer–micelle spinning solutions were analyzed at 25 °C using a cone-plate geometry (C35 TiL; 53 µm gap; 1° cone angle). Measurements were performed over a shear rate range of 0.5–1000 s^{-1} for 60 s with 100 data points and repeated three times. Data was processed using RheoWin3 software and fitted using the power-law model.

4.5.2. Electrical Conductivity

Spinning solutions (20 g) were prepared in beakers and conductivity was measured at room temperature using a PC2700 conductivity meter.

4.6. Characterization of Nanofiber Inserts

4.6.1. Drug Content and Encapsulation Efficiency

Nanofibers (10 mg) were dissolved in 2 mL of distilled water:methanol (2:8, v/v) and shaken at 300 rpm for 24 h. Samples were centrifuged at 15,000 rpm, filtered through a 0.45 μm PTFE membrane, and analyzed by HPLC (n = 3).

4.6.2. Thickness, Diameter, and Weight

Inserts were punched into defined shapes; thickness/diameter were measured with an electronic caliper and weight with an analytical balance (n = 3).

4.6.3. FESEM Imaging and Fiber Diameter

Samples were sputter-coated with a thin gold layer prior to FESEM imaging. Fiber diameters were quantified using ImageJ software (version 1.54) from FESEM micrographs (50 measurements per formulation), and diameter histograms were plotted.

4.6.4. Differential Scanning Calorimetry (DSC)

DSC analyses were performed to determine the heat absorbed or released by micelle-loaded nanofibers during heating/cooling or isothermal conditions. Three different nanofiber formulations were evaluated. Samples were analyzed individually under a nitrogen atmosphere at a heating rate of 10 °C/min over 25–300 °C using aluminum pans. Thermograms of the nanofibers, active ingredients, and excipients were compared to assess potential incompatibilities.

4.6.5. X-Ray Diffraction (XRD)

Micelle-loaded nanofibers, active ingredients, and excipients were analyzed using a wide-angle X-ray diffractometer with a CuKα radiation source (λ = 0.154 nm) operated at 40 kV and 30 mA. Diffraction patterns were recorded over a 2θ range of 2° to 40° with a step size of 0.02°. This analysis was conducted to evaluate the crystallographic properties of the nanofiber formulations and identify differences in their solid-state characteristics.

4.6.6. Fourier-Transform Infrared Spectroscopy (FTIR, ATR-FTIR)

ATR-FTIR spectra of the active ingredients, polymers, their physical mixtures, and the produced nanofibers were collected using an ATR-FTIR instrument (Shimadzu, Kyoto, Japan). After placing the nanofibers on the ATR crystal, scans were recorded in the 4000–650 cm^{-1} range at a resolution of 4 cm^{-1}. This analysis aimed to investigate possible interactions between active compounds and excipients within the formulations.

4.7. In Vitro Release Studies

A receptor medium was selected to ensure sink conditions and reliable quantification of PSC and DKP during in vitro release testing. Based on preliminary screening, artificial tear fluid (ATF, pH 7.4) supplemented with 0.1% (w/v) sodium lauryl sulfate (SLS) was selected as the release/receptor medium, as it provided sufficient solubilization capacity for both drugs and enabled reproducible sampling throughout the experiments. ATF was prepared by dissolving NaCl (0.67 g), $NaHCO_3$ (0.20 g), $CaCl_2 \cdot 2H_2O$ (0.008 g), and KCl (0.14 g) in 100 mL ultrapure water and adjusting the pH to 7.4 with HCl.

In vitro release studies were performed using vertical Franz diffusion cells (receptor volume: 12 mL) equipped with a cellulose acetate membrane. The receptor compartment

https://doi.org/10.3390/molecules31081235

was filled with ATF containing 0.1% (*w*/*v*) SLS and equilibrated at 35.5 °C under continuous stirring to mimic the ocular surface temperature and maintain homogeneous mixing. For micelle formulations, 2 mL of PSC/DKP-loaded micellar dispersion was placed in the donor compartment. For comparator testing, diluted Noxafil® oral suspension and an aqueous DKP solution were prepared at concentrations matching those of the micellar formulation and tested under the same conditions. For nanofiber inserts, selected electrospun formulations were placed in the donor compartment; to simulate ocular hydration, 1 mL of the receptor medium was added onto the donor side to wet the insert. Control nanofibers prepared without micelles (drug directly incorporated into polymer solutions) were also evaluated in parallel.

At predetermined time points (30, 60, 120, 180, 240, 360, and 480 min), 1 mL samples were withdrawn from the receptor compartment and immediately replaced with an equal volume of fresh, pre-warmed medium to maintain constant volume and sink conditions. Samples were quantified by HPLC. Cumulative drug release was calculated and expressed as released amount per diffusion area (μg/cm^2) and/or percentage release, as appropriate (n = 3).

Release profiles of PSC and DKP from micelles and nanofibers were evaluated using KinetDS 3.0 software by fitting to appropriate kinetic models.

4.8. Ex Vivo Permeation and Penetration Studies

4.8.1. Tissue Preparation

Isolated bovine eyes were used for ex vivo studies. Until experimentation, eyes were stored at +4 °C in 0.9% isotonic NaCl solution containing penicillin G (50 U/mL) and streptomycin (50 U/mL), in accordance with the relevant guidelines. Prior to experiments, the eyes were rinsed with 0.9% isotonic NaCl to remove antibiotics and were subsequently kept for 24 h at +4 °C in the same solution. Cornea and sclera tissues were then carefully excised for ex vivo permeation experiments.

4.8.2. Permeation of PSC and DKP Through Ocular Tissues

Ex vivo permeation experiments were conducted using Valia–Chien diffusion cells. The donor and receptor chamber volumes were 2.0 mL for cornea and 3.4 mL for sclera, with diffusion areas of 20.7 mm^2 (cornea) and 7.2 mm^2 (sclera).

The receptor medium was artificial tear fluid containing 0.1% (*w*/*v*) SLS, and it was allowed to equilibrate to 35.5 °C for 30 min prior to starting the experiment. Subsequently, receptor medium and test formulations were added (2.0 mL for cornea and 3.4 mL for sclera) ensuring that no air bubbles remained; the excised tissue was positioned between donor and receptor compartments.

Permeation was evaluated comparatively for the micelle formulation, a control mixture consisting of Noxafil® diluted to 250 μg/mL PSC + DKP solution 10 mg/mL, and the selected nanofiber insert formulation (Nanofiber-AP) (n = 3). For the nanofiber condition, the insert was placed into the donor compartment and then completed with the receptor medium. Experiments were performed under stirring at 400 rpm. Samples (0.5 mL) were withdrawn from the receptor compartment at 0.5, 1, 2, 3, 4, 6, and 8 h, and the sampled volume was immediately replaced with an equal volume of fresh receptor medium. Collected samples were analyzed by HPLC after appropriate dilution. Cumulative permeated amounts over 8 h were calculated.

https://doi.org/10.3390/molecules31081235

4.8.3. Permeation Parameters and Equations

To determine permeation parameters for both PSC and DKP across cornea and sclera, the apparent permeability coefficient (P_{app}), effective diffusion coefficient (D_{eff}), and steady-state flux (J_{ss}) were calculated using the equations provided:

$$P_{app} = \frac{Q}{A \cdot C_0} \quad (2)$$

$$D_{eff} = P_{app} \cdot l \quad (3)$$

$$J_{ss} = \frac{\Delta Q}{\Delta t} \quad (4)$$

where Q is the total amount of drug permeated at time t, C_0 is the initial drug concentration in the donor phase, A is the tissue surface area, and l is the tissue thickness.

4.8.4. Penetration of PSC and DKP Across Ocular Tissues

To quantify tissue penetration, cornea and sclera were collected immediately after completion of the 8 h permeation study. Tissue integrity was confirmed by visual inspection. Each tissue sample was immersed in 4 mL methanol and extracted for 24 h on an orbital shaker. After extraction, the tissue–solvent mixture was transferred into a capped centrifuge tube and centrifuged for 10 min. The supernatant was then filtered through a 0.45 μm PTFE membrane filter, and following necessary dilutions, the amount of PSC and DKP penetrated into ocular tissues was quantified by HPLC.

4.9. Antifungal Activity (Disk Diffusion)

A disk diffusion assay was performed to evaluate the antifungal activity of the prepared formulations. *Candida albicans* (ATCC 90028) was used as the test organism. The assay was conducted according to the Clinical and Laboratory Standards Institute (CLSI) M44-A2 guideline [77]. Briefly, fungal suspensions (10^6 CFU/mL) were spread onto Mueller–Hinton agar plates (Merck, Darmstadt, Germany) (10 cm diameter) containing 25 mL medium supplemented with 2% dextrose and 0.5 mg/L methylene blue. After drying for 20 min, sterile paper disks (6 mm diameter) were placed on the agar surface. Each disk was loaded with 10 μL of the following samples: placebo, micellar formulation, the nanofiber formulation dissolved in water (Nanofiber-AP), a Noxafil®/DKP mixture containing active ingredients at concentrations matching the micellar formulation, and a Noxafil®/DKP mixture containing active ingredients at concentrations matching the nanofiber formulation. Plates were incubated at 37 ± 0.5 °C for 48 h, and inhibition zone diameters were measured in millimeters.

4.10. HET-CAM Irritation Test

The Hen's Egg Test–Chorioallantoic Membrane (HET-CAM) assay was used to assess the ocular irritation potential of the test samples as an alternative to the Draize rabbit eye test [82]. All experiments were conducted in accordance with ICCVAM recommendations [83]. Fresh, fertilized White Leghorn chicken eggs (50–60 g; not older than 7 days) were used, while excessively deformed eggs and those with cracks or thin shells were excluded. Eggs were incubated for 9 days in an automatically rotating incubator at 37.8 ± 0.3 °C and 58 ± 2% relative humidity. On day 9, eggs were candled to remove non-viable or defective specimens, and the air-cell region was marked. The marked area was opened using a rotary dental saw to access the air chamber, and the shell was carefully removed without damaging the inner membrane to expose the CAM.

Diluted Noxafil® oral suspension/DKP solution mixture, PSC-DKP loaded micelles, nanofiber (Nanofiber-AP) formulations, and their corresponding placebos were tested.

https://doi.org/10.3390/molecules31081235

A total volume of 0.3 mL of each liquid sample was applied directly onto the vascular CAM. For nanofiber formulations, the insert was placed on the CAM and then wetted with 0.3 mL isotonic water. 0.1 N NaOH and 0.9% (*w*/*v*) NaCl served as positive and negative controls, respectively. CAM responses were observed for 300 s, and the onset times of the predefined endpoints (hemorrhage, lysis, and coagulation) were recorded. Irritation scores were assigned based on the time-to-endpoint scoring scheme (Table 9). Each egg/sample was scored individually; mean scores were calculated for each test group and used to classify the irritation potential (Table 10).

Table 9. Scoring scheme for the HET-CAM test for membrane irritation.

Effect	Score at 30 s	Score at 120 s	Score at 300 s
Lysis	5	3	1
Hemorrhage	7	5	3
Coagulation	9	7	5

Table 10. Classification scheme for cumulative scores in the HET-CAM test.

Cumulative Score	Irritation Assessment
Up to 0.9	Practically none
1—4.9	Slight
5—8.9	Moderate
9 and above	Strong

4.11. Statistical Analysis

Statistical analysis was performed using GraphPad Prism 8.1.1. One-way ANOVA was applied for comparisons involving more than two groups, while Student's *t*-test was used for two-group comparisons.

5. Conclusions

In this study, innovative "micellar nanofiber" systems were developed for the treatment of ocular fungal infections by combining the broad-spectrum antifungal posaconazole (PSC) with the potent anti-inflammatory agent dexketoprofen trometamol (DKP) in both liquid (micellar) and solid (nanofiber) dosage forms. This research is distinctive in that it represents the first study to investigate ocular application of DKP and brings both agents together within a single dosage form. Within this scope, the effects of using PVA and PVP polymers, as well as their combinations, on formulation performance were also investigated. The prepared micelles exhibited an average size of 11.01 nm, while the electrospun nanofibers showed diameters within the 185–410 nm range, indicating suitable dimensions for ocular delivery. Thermal and structural analyses demonstrated that the crystalline drugs were encapsulated within the nanofiber matrix in an amorphous state, thereby significantly improving the aqueous solubility of the lipophilic PSC. According to the Korsmeyer–Peppas model, these systems provided controlled release via a super case-II transport mechanism and, in ex vivo studies, exhibited markedly higher tissue penetration and permeability in bovine cornea and sclera compared with diluted Noxafil® solution, even at lower doses for the nanofiber inserts. In addition, the developed formulations showed strong antifungal activity against *Candida albicans* and were found to be non-irritant to ocular tissues based on the HET-CAM assay. Overall, these findings indicate that the combined nanocarrier systems may offer an innovative therapeutic alternative for resistant ocular infections by simultaneously targeting infection and inflammation while improving bioavailability. In vivo studies were intentionally not included at this stage, in accordance with the 3R

principles (Replacement, Reduction, and Refinement) in animal experimentation, to avoid unnecessary animal use prior to the identification of an optimized formulation. The results obtained provide a robust foundation for future investigations.

Based on these findings, further studies may focus on optimizing the formulation using different polymers or surfactants, as well as advanced techniques such as coaxial electrospinning to enhance drug loading capacity and prolong therapeutic effects. Subsequently, in vivo studies will be conducted to evaluate the therapeutic efficacy and safety of the optimized formulations.

Author Contributions: Conceptualization, E.U., N.A., M.E.D. and M.H.; methodology, E.U. and M.E.D.; validation, E.U. and M.E.D.; formal analysis, E.U., N.A., M.E.D. and M.H.; investigation, E.U.; resources, E.U.; data curation, E.U.; writing—original draft preparation, E.U., writing—review and editing, M.E.D., S.G. and Y.Ö.; visualization, E.U.; supervision, Y.Ö.; project administration, Y.Ö.; funding acquisition, Y.Ö. All authors have read and agreed to the published version of the manuscript.

Funding: This research was funded by the Research Fund of Istanbul University (project no: 38014).

Institutional Review Board Statement: Not applicable.

Informed Consent Statement: Not applicable.

Data Availability Statement: This article is based on data obtained from Egemen Uzel's doctoral thesis. Data sharing is confidential as the study is currently undergoing a patent application process.

Acknowledgments: The authors are grateful to BASF-Turkey for their support by Kolliphor TPGS, Pluronic F127.

Conflicts of Interest: The authors declare no conflicts of interest.

Abbreviations

The following abbreviations are used in this manuscript:

CMC	Critic Micelle Concentration
COX	Cyclooxygenase
DKP	Dexketoprofen trometamol
DLS	Dynamic light scattering
DSC	Differential Scanning Calorimetry
FTIR	Fourier-Transform Infrared
HET-CAM	The Hen's Egg Test–Chorioallantoic Membrane
HPLC	High-performance liquid chromatography
NaCl	Sodium chloride
NF	Nanofiber
PDI	Polydispersity Index
PLU	Pluronic F127
PSC	Posaconazole
PVA	poly(vinyl alcohol)
PVP	poly(vinylpyrrolidone)
SLS	Sodium lauryl sulfate
TPGS	D-α-tocopheryl polyethylene glycol 1000 succinate

References

1. Walther, G.; Zimmermann, A.; Theuersbacher, J.; Kaerger, K.; von Lilienfeld-Toal, M.; Roth, M.; Kampik, D.; Geerling, G.; Kurzai, O. Eye infections caused by filamentous fungi: Spectrum and antifungal susceptibility of the prevailing agents in Germany. *J. Fungi* **2021**, *7*, 511. [CrossRef] [PubMed]
2. Clark, H.L.; Pearlman, E. Fungal Eye Infections. In *Oxford Textbook of Medical Mycology*; Oxford University Press: Oxford, UK, 2017.

3. Castano, G.; Elnahry, A.G.; Mada, P.K. Fungal keratitis. In *StatPearls [Internet]*; StatPearls Publishing: San Francisco, FL, USA, 2024.
4. Urtti, A. Challenges and obstacles of ocular pharmacokinetics and drug delivery. *Adv. Drug Deliv. Rev.* **2006**, *58*, 1131–1135. [CrossRef] [PubMed]
5. Leclercq, B.; Mejlachowicz, D.; Behar-Cohen, F. Ocular barriers and their influence on gene therapy products delivery. *Pharmaceutics* **2022**, *14*, 998. [CrossRef]
6. Subrizi, A.; Del Amo, E.M.; Korzhikov-Vlakh, V.; Tennikova, T.; Ruponen, M.; Urtti, A. Design principles of ocular drug delivery systems: Importance of drug payload, release rate, and material properties. *Drug Discov. Today* **2019**, *24*, 1446–1457. [CrossRef]
7. Cholkar, K.; Patel, S.P.; Vadlapudi, A.D.; Mitra, A.K. Novel strategies for anterior segment ocular drug delivery. *J. Ocul. Pharmacol. Ther.* **2013**, *29*, 106–123. [CrossRef]
8. Nagai, N.; Kaji, H.; Onami, H.; Ishikawa, Y.; Nishizawa, M.; Osumi, N.; Nakazawa, T.; Abe, T. A polymeric device for controlled transscleral multi-drug delivery to the posterior segment of the eye. *Acta Biomater.* **2014**, *10*, 680–687. [CrossRef]
9. Peyman, G.A.; Hosseini, K. Combination therapies in ophthalmology: Implications for intravitreal delivery. *J. Ophthalmic Vis. Res.* **2011**, *6*, 36.
10. Gote, V.; Sikder, S.; Sicotte, J.; Pal, D. Ocular drug delivery: Present innovations and future challenges. *J. Pharmacol. Exp. Ther.* **2019**, *370*, 602–624. [CrossRef]
11. Yapar, E.A.; Durgun, M.; Esentürk, I.; Güngör, S.; Özsoy, Y. Herbal bioactives for ocular drug delivery systems. In *Herbal Bioactive-Based Drug Delivery Systems*; Elsevier: Amsterdam, The Netherlands, 2022; pp. 25–61.
12. Pepić, I.; Hafner, A.; Lovrić, J.; Pirkić, B.; Filipović-Grččić, J. A nonionic surfactant/chitosan micelle system in an innovative eye drop formulation. *J. Pharm. Sci.* **2010**, *99*, 4317–4325. [CrossRef]
13. Jaiswal, M.; Kumar, M.; Pathak, K. Zero order delivery of itraconazole via polymeric micelles incorporated in situ ocular gel for the management of fungal keratitis. *Colloids Surf. B Biointerfaces* **2015**, *130*, 23–30. [CrossRef] [PubMed]
14. Uzel, E.; Durgun, M.E.; Esentürk-Güzel, İ.; Güngör, S.; Özsoy, Y. Nanofibers in ocular drug targeting and tissue engineering: Their importance, advantages, advances, and future perspectives. *Pharmaceutics* **2023**, *15*, 1062. [CrossRef]
15. Bhardwaj, N.; Kundu, S.C. Electrospinning: A fascinating fiber fabrication technique. *Biotechnol. Adv.* **2010**, *28*, 325–347. [CrossRef]
16. Megelski, S.; Stephens, J.S.; Chase, D.B.; Rabolt, J.F. Micro-and nanostructured surface morphology on electrospun polymer fibers. *Macromolecules* **2002**, *35*, 8456–8466. [CrossRef]
17. Pan, L.; Yang, J.; Xu, L. Preparation and characterization of simvastatin-loaded PCL/PEG nanofiber membranes for drug sustained release. *Molecules* **2022**, *27*, 7158. [CrossRef]
18. Deepak, A.; Goyal, A.K.; Rath, G. Nanofiber in transmucosal drug delivery. *J. Drug Deliv. Sci. Technol.* **2018**, *43*, 379–387. [CrossRef]
19. Meraz-Dávila, S.; Pérez-García, C.; Feregrino-Perez, A.A. Challenges and advantages of electrospun nanofibers in agriculture: A review. *Mater. Res. Express* **2021**, *8*, 042001. [CrossRef]
20. Long, B.; Verma, V.; Ryan, K.M.; Padrela, L. Generation and physicochemical characterization of posaconazole cocrystals using Gas Antisolvent (GAS) and Supercritical Solvent (CSS) methods. *J. Supercrit. Fluids* **2021**, *170*, 105134. [CrossRef]
21. National Center for Biotechnology Information. PubChem Compound Summary for CID 468595, Posaconazole. 22 July 2025. Available online: https://pubchem.ncbi.nlm.nih.gov/compound/Posaconazole#section=Information-Sources (accessed on 20 July 2024).
22. DrugBank. Posaconazole. 22 July 2025. Available online: https://go.drugbank.com/drugs/DB01263 (accessed on 20 July 2025).
23. Sponsel, W.; Graybill, J.; Nevarez, H.; Dang, D. Ocular and systemic posaconazole (SCH-56592) treatment of invasive Fusarium solani keratitis and endophthalmitis. *Br. J. Ophthalmol.* **2002**, *86*, 829–830. [CrossRef] [PubMed]
24. Altun, A.; Kurna, S.; Sengor, T.; Altun, G.; Olcaysu, O.; Aki, S.; Simsek, M. Effectiveness of posaconazole in recalcitrant fungal keratitis resistant to conventional antifungal drugs. *Case Rep. Ophthalmol. Med.* **2014**, *2014*, 701653. [CrossRef]
25. Durgun, M.E.; Kahraman, E.; Güngör, S.; Özsoy, Y. Optimization and characterization of aqueous micellar formulations for ocular delivery of an antifungal drug, posaconazole. *Curr. Pharm. Des.* **2020**, *26*, 1543–1555. [CrossRef]
26. Durgun, M.E.; Mesut, B.; Hacıoğlu, M.; Güngör, S.; Özsoy, Y. Optimization of the micellar-based in situ gelling systems posaconazole with quality by design (QbD) approach and characterization by in vitro studies. *Pharmaceutics* **2022**, *14*, 526. [CrossRef]
27. Knutsson, K.A.; Iovieno, A.; Matuska, S.; Fontana, L.; Rama, P. Topical corticosteroids and fungal keratitis: A review of the literature and case series. *J. Clin. Med.* **2021**, *10*, 1178. [CrossRef]
28. DrugBank. Dexketoprofen Trometamol. 25 July 2025. Available online: https://go.drugbank.com/salts/DBSALT002989 (accessed on 24 July 2025).
29. Kandarakis, S.; Petrou, P.; Papakonstantinou, E.; Spiropoulos, D.; Rapanou, A.; Georgalas, I. Ocular nonsteroidal inflammatory drugs: Where do we stand today? *Cutan. Ocul. Toxicol.* **2020**, *39*, 200–212. [CrossRef]

30. National Center for Biotechnology Information. Dexketoprofen Trometamol. 25 July 2025. Available online: https://pubchem.ncbi.nlm.nih.gov/compound/Dexketoprofen-trometamol (accessed on 24 July 2025).
31. Moore, R.A.; Barden, J. Systematic review of dexketoprofen in acute and chronic pain. *BMC Clin. Pharmacol.* **2008**, *8*, 11. [CrossRef]
32. Durgun, M.E.; Güngör, S.; Özsoy, Y. Micelles: Promising Ocular Drug Carriers for Anterior and Posterior Segment Diseases. *J. Ocul. Pharmacol. Ther.* **2020**, *36*, 323–341. [CrossRef]
33. Komai, Y.; Ushiki, T. The three-dimensional organization of collagen fibrils in the human cornea and sclera. *Investig. Ophthalmol. Vis. Sci.* **1991**, *32*, 2244–2258.
34. Bhattacharjee, S. DLS and zeta potential—What they are and what they are not? *J. Control. Release* **2016**, *235*, 337–351. [CrossRef] [PubMed]
35. Lin, S.-Y.; Wang, S.-L. Advances in simultaneous DSC–FTIR microspectroscopy for rapid solid-state chemical stability studies: Some dipeptide drugs as examples. *Adv. Drug Deliv. Rev.* **2012**, *64*, 461–478. [CrossRef]
36. Suksiriworapong, J.; Mingkwan, T.; Chantasart, D. Enhanced transmucosal delivery of itraconazole by thiolated d-α-tocopheryl poly (ethylene glycol) 1000 succinate micelles for the treatment of Candida albicans. *Eur. J. Pharm. Biopharm.* **2017**, *120*, 107–115. [CrossRef] [PubMed]
37. Liu, Z.; Ramakrishna, S.; Ahmed, I.; Rudd, C.; Liu, X. Rheological, surface tension and conductivity insights on the electrospinnability of poly (lactic-co-glycolic acid)-hyaluronic acid solutions and their correlations with the nanofiber morphological characteristics. *Polymers* **2022**, *14*, 4411. [CrossRef]
38. Rošic, R.; Pelipenko, J.; Kocbek, P.; Baumgartner, S.; Bešter-Rogač, M.; Kristl, J. The role of rheology of polymer solutions in predicting nanofiber formation by electrospinning. *Eur. Polym. J.* **2012**, *48*, 1374–1384. [CrossRef]
39. Toh, H.; Compton, R. Electrochemical detection of single micelles through 'nano-impacts'. *Chem. Sci.* **2015**, *6*, 5053–5058. [CrossRef] [PubMed]
40. Nawaz, A.; Irshad, S.; Walayat, N.; Khan, M.R.; Iqbal, M.W.; Luo, X. Fabrication and characterization of Apple-Pectin–PVA-Based nanofibers for Improved viability of Probiotics. *Foods* **2023**, *12*, 3194. [CrossRef]
41. Li, B.; Xia, X.; Chen, J.; Xia, D.; Xu, R.; Zou, X.; Wang, H.; Liang, C. Paclitaxel-loaded lignin particle encapsulated into electrospun PVA/PVP composite nanofiber for effective cervical cancer cell inhibition. *Nanotechnology* **2020**, *32*, 015101. [CrossRef]
42. Teodorescu, M.; Bercea, M.; Morariu, S. Biomaterials of PVA and PVP in medical and pharmaceutical applications: Perspectives and challenges. *Biotechnol. Adv.* **2019**, *37*, 109–131. [CrossRef]
43. Pfaller, M.; Messer, S.; Mills, K.; Bolmstrom, A.; Jones, R. Evaluation of Etest method for determining posaconazole MICs for 314 clinical isolates of Candida species. *J. Clin. Microbiol.* **2001**, *39*, 3952–3954. [CrossRef]
44. Buil, J.B.; Hagen, F.; Chowdhary, A.; Verweij, P.E.; Meis, J.F. Itraconazole, voriconazole, and posaconazole CLSI MIC distributions for wild-type and azole-resistant Aspergillus fumigatus isolates. *J. Fungi* **2018**, *4*, 103.
45. Land, D.L.; Benjamin, W.J. Sizes and shapes of conjunctival inserts. *Int. Contact Lens Clin.* **1994**, *21*, 212–217. [CrossRef]
46. Kalluri, L.; Satpathy, M.; Duan, Y. Effect of electrospinning parameters on the fiber diameter and morphology of PLGA nanofibers. *Dent. Oral Biol. Craniofacial Res.* **2021**, *4*, 10-31487. [CrossRef]
47. Ko, J.; Jun, S.; Lee, J.K.; Lee, P.C.; Jun, M.B. Effects of molecular weight and temperature on fiber diameter of poly (ε-caprolactone) melt electrospun fiber. *J. Korean Soc. Manuf. Technol. Eng.* **2015**, *24*, 160–165. [CrossRef]
48. Rahmani, F.; Ziyadi, H.; Baghali, M.; Luo, H.; Ramakrishna, S. Electrospun PVP/PVA nanofiber mat as a novel potential transdermal drug-delivery system for buprenorphine: A solution needed for pain management. *Appl. Sci.* **2021**, *11*, 2779. [CrossRef]
49. Uma Maheshwari, S.; Govindan, K.; Raja, M.; Raja, A.; Pravin, M.; Vasanth Kumar, S. Preliminary studies of PVA/PVP blends incorporated with HAp and β-TCP bone ceramic as template for hard tissue engineering. *Bio-Med. Mater. Eng.* **2017**, *28*, 401–415. [CrossRef]
50. Abou_Taleb, M. Thermal and spectroscopic studies of poly (N-vinyl pyrrolidone)/poly (vinyl alcohol) blend films. *J. Appl. Polym. Sci.* **2009**, *114*, 1202–1207. [CrossRef]
51. Uslu, İ.; Keskin, S.; Gül, A.; Karabulut, T.C.; Aksu, M.L. Preparation and properties of electrospun poly vinyl alcohol blended hybrid polymer with Aloe vera and HPMC as wound dressing. *Hacet. J. Biol. Chem.* **2010**, *38*, 19–25.
52. Wang, F.; Zhang, Z.; Yan, Y.; Shen, Z.; Wang, Q.; Gerhard, R. Surface Reconstruction on Electro-Spun PVA/PVP Nanofibers by Water Evaporation. *Nanomaterials* **2022**, *12*, 797. [CrossRef]
53. Nijhawan, M.; Godugu, M.; Saxena, T.; Farheen, T.; Dwivedi, K. Pharmaceutical co-crystals of posaconazole for improvement of physicochemical properties. *Braz. J. Pharm. Sci.* **2022**, *58*, e191024. [CrossRef]
54. Öztürk, A.A.; Akyıl, E.; Arslan, R.; Şenel, B.; Yazan, Y. Dexketoprofen trometamol loaded solid lipid nanoparticles (SLNs): Formulation, in vitro and in vivo evaluation. *J. Res. Pharm.* **2020**, *24*, 82–99. [CrossRef]
55. Reda, R.I.; Wen, M.M.; El-Kamel, A.H. Ketoprofen-loaded Eudragit electrospun nanofibers for the treatment of oral mucositis. *Int. J. Nanomed.* **2017**, *12*, 2335–2351. [CrossRef]

56. Lykouras, M.; Fertaki, S.; Orkoula, M.; Kontoyannis, C. Sample preparation of posaconazole oral suspensions for identification of the crystal form of the active pharmaceutical ingredient. *Molecules* **2020**, *25*, 6032. [CrossRef] [PubMed]
57. Rossi, P.; Paoli, P.; Chelazzi, L.; Milazzo, S.; Biagi, D.; Valleri, M.; Ienco, A.; Valtancoli, B.; Conti, L. Relationships between anhydrous and solvated species of dexketoprofen trometamol: A solid-state point of view. *Cryst. Growth Des.* **2019**, *20*, 226–236. [CrossRef]
58. Bukhary, H.; Williams, G.R.; Orlu, M. Electrospun fixed dose formulations of amlodipine besylate and valsartan. *Int. J. Pharm.* **2018**, *549*, 446–455. [CrossRef] [PubMed]
59. Ketha, N.V.D.P.; Kolli, D. Using preparative chromatography and NMR/LCMS/FT-IR, isolation, identification, and characterization of posaconazole oxidative degradation impurities. *Rasayan J. Chem.* **2022**, *15*, 619–627. [CrossRef]
60. Öztürk, A.A.; Banderas, L.M.; Otero, M.D.C.; Yenilmez, E.; Şenel, B.; Yazan, Y. Dexketoprofen trometamol-loaded poly-lactic-co-glycolic acid (PLGA) nanoparticles: Preparation, in vitro characterization and cyctotoxity. *Trop. J. Pharm. Res.* **2019**, *18*, 1–11. [CrossRef]
61. Karolewicz, B.; Górniak, A.; Owczarek, A.; Żurawska-Płaksej, E.; Piwowar, A.; Pluta, J. Thermal, spectroscopic, and dissolution studies of ketoconazole–Pluronic F127 system. *J. Therm. Anal. Calorim.* **2014**, *115*, 2487–2493. [CrossRef]
62. Baganizi, D.R.; Nyairo, E.; Duncan, S.A.; Singh, S.R.; Dennis, V.A. Interleukin-10 conjugation to carboxylated PVP-coated silver nanoparticles for improved stability and therapeutic efficacy. *Nanomaterials* **2017**, *7*, 165. [CrossRef] [PubMed]
63. Mansur, H.S.; Oréfice, R.L.; Mansur, A.A. Characterization of poly (vinyl alcohol)/poly (ethylene glycol) hydrogels and PVA-derived hybrids by small-angle X-ray scattering and FTIR spectroscopy. *Polymer* **2004**, *45*, 7193–7202. [CrossRef]
64. Mehrali, F.; Ziyadi, H.; Hekmati, M.; Faridi-Majidi, R.; Qomi, M. Kefiran/poly (vinyl alcohol)/poly (vinyl pyrrolidone) composite nanofibers: Fabrication, characterization and consideration of effective parameters in electrospinning. *SN Appl. Sci.* **2020**, *2*, 895. [CrossRef]
65. Tao, L.; Chan, J.W.; Uhrich, K.E. Drug loading and release kinetics in polymeric micelles: Comparing dynamic versus unimolecular sugar-based micelles for controlled release. *J. Bioact. Compat. Polym.* **2016**, *31*, 227–241. [CrossRef]
66. Chen, S.; Huang, X.; Cai, X.; Lu, J.; Yuan, J.; Shen, J. The influence of fiber diameter of electrospun poly (lactic acid) on drug delivery. *Fibers Polym.* **2012**, *13*, 1120–1125. [CrossRef]
67. Gaikwad, N.M.; Chaudhari, P.D.; Shaikh, K.S.; Chaudhari, S.Y.; Pathare, S.S.; Shaikh, A.A.; Aljarba, N.H.; Kumer, A.; Dhara, B. Dual drug-loaded polymeric mixed micelles for ovarian cancer: Approach to enhanced therapeutic efficacy of albendazole and paclitaxel. *J. Cell. Mol. Med.* **2024**, *28*, e18389. [CrossRef]
68. Talevi, A.; Ruiz, M.E. Korsmeyer-peppas, peppas-sahlin, and brazel-peppas: Models of drug release. In *The ADME Encyclopedia: A Comprehensive Guide on Biopharmacy and Pharmacokinetics*; Springer: Berlin/Heidelberg, Germany, 2022; pp. 613–621.
69. Rao, M.V.; Shyale, S. Preparation and evaluation of ocular inserts containing norfloxacin. *Turk. J. Med. Sci.* **2004**, *34*, 239–246.
70. Santana, C.P.; Matter, B.A.; Patil, M.A.; Silva-Cunha, A.; Kompella, U.B. Corneal permeability and uptake of twenty-five drugs: Species comparison and quantitative structure–permeability relationships. *Pharmaceutics* **2023**, *15*, 1646. [CrossRef]
71. Abdul Nasir, N.A.; Agarwal, P.; Agarwal, R.; Iezhitsa, I.; Alyautdin, R.; Nukolova, N.N.; Chekhonin, V.P.; Mohd Ismail, N. Intraocular distribution of topically applied hydrophilic and lipophilic substances in rat eyes. *Drug Deliv.* **2016**, *23*, 2765–2771. [CrossRef] [PubMed]
72. Sharpe, S.; Sequeira, J.; Harris, D.; Mahashabde, S. Antifungal Composition with Enhanced Bioavailability. U.S. Patent 20030055067A1, 20 March 2003.
73. Grytz, R.; Fazio, M.A.; Girard, M.J.; Libertiaux, V.; Bruno, L.; Gardiner, S.; Girkin, C.A.; Downs, J.C. Material properties of the posterior human sclera. *J. Mech. Behav. Biomed. Mater.* **2014**, *29*, 602–617. [CrossRef] [PubMed]
74. Gaudana, R.; Ananthula, H.K.; Parenky, A.; Mitra, A.K. Ocular drug delivery. *AAPS J.* **2010**, *12*, 348–360. [CrossRef]
75. Mofidfar, M.; Abdi, B.; Ahadian, S.; Mostafavi, E.; Desai, T.A.; Abbasi, F.; Sun, Y.; Manche, E.E.; Ta, C.N.; Flowers, C.W. Drug delivery to the anterior segment of the eye: A review of current and future treatment strategies. *Int. J. Pharm.* **2021**, *607*, 120924. [CrossRef] [PubMed]
76. Arendrup, M.; Cuenca-Estrella, M.; Donnelly, J.; Hope, W.; Lass-Flörl, C.; Rodriguez-Tudela, J.L. EUCAST technical note on posaconazole. *Clin. Microbiol. Infect.* **2011**, *17*, E16–E17. [CrossRef]
77. *CLSI M44*; Method for Antifungal Disk Diffusion Susceptibility Testing of Yeasts. Clinical and Laboratory Standards Institute: Wayne, PA, USA, 2018; p. 44.
78. Berkow, E.L.; Lockhart, S.R.; Ostrosky-Zeichner, L. Antifungal susceptibility testing: Current approaches. *Clin. Microbiol. Rev.* **2020**, *33*, e00069-19. [CrossRef]
79. Durgun, M.E.; Kahraman, E.; Hacıoğlu, M.; Güngör, S.; Özsoy, Y. Posaconazole micelles for ocular delivery: In vitro permeation, ocular irritation and antifungal activity studies. *Drug Deliv. Transl. Res.* **2022**, *12*, 662–675. [CrossRef]
80. Guideline, I.H.T. *Validation of Analytical Procedures: Text and Methodology. Q2 (R1)*; International Council for Harmonisation of Technical Requirements for Pharmaceuticals for Human Use (ICH): Geneva, Switzerland, 2005; Volume 1, p. 5.

81. Kosmulski, M.; Mączka, E. Zeta potential in dispersions of titania nanoparticles in moderately polar solvents stabilized with anionic surfactants. *J. Mol. Liq.* **2022**, *355*, 118972. [CrossRef]
82. Luepke, N.; Kemper, F. The HET-CAM test: An alternative to the Draize eye test. *Food Chem. Toxicol.* **1986**, *24*, 495–496. [CrossRef]
83. Protocol, I. *ICCVAM-Recommended Test Method Protocol: Hen's Egg Test—Chorioallantoic Membrane (HET-CAM) Test Method*; NIH Publication; NICEATM: Research Triangle Park, NC, USA, 2010; Volume, 13, pp. B30–B38.

Disclaimer/Publisher's Note: The statements, opinions and data contained in all publications are solely those of the individual author(s) and contributor(s) and not of MDPI and/or the editor(s). MDPI and/or the editor(s) disclaim responsibility for any injury to people or property resulting from any ideas, methods, instructions or products referred to in the content.

MDPI AG
Grosspeteranlage 5
4052 Basel
Switzerland
Tel.: +41 61 683 77 34

Molecules Editorial Office
E-mail: molecules@mdpi.com
www.mdpi.com/journal/molecules



Disclaimer/Publisher's Note: The title and front matter of this reprint are at the discretion of the Guest Editors. The publisher is not responsible for their content or any associated concerns. The statements, opinions and data contained in all individual articles are solely those of the individual Editors and contributors and not of MDPI. MDPI disclaims responsibility for any injury to people or property resulting from any ideas, methods, instructions or products referred to in the content.





Academic Open
Access Publishing

mdpi.com

ISBN 978-3-7258-9250-1